NASA/TM–2015-218790

Transonic Investigation of Two-Dimensional Nozzles Designed for Supersonic Cruise

Francis J. Capone and Karen A. Deere
Langley Research Center, Hampton, Virginia

August 2015

NASA STI Program . . . in Profile

Since its founding, NASA has been dedicated to the advancement of aeronautics and space science. The NASA scientific and technical information (STI) program plays a key part in helping NASA maintain this important role.

The NASA STI program operates under the auspices of the Agency Chief Information Officer. It collects, organizes, provides for archiving, and disseminates NASA's STI. The NASA STI program provides access to the NTRS Registered and its public interface, the NASA Technical Reports Server, thus providing one of the largest collections of aeronautical and space science STI in the world. Results are published in both non-NASA channels and by NASA in the NASA STI Report Series, which includes the following report types:

- TECHNICAL PUBLICATION. Reports of completed research or a major significant phase of research that present the results of NASA Programs and include extensive data or theoretical analysis. Includes compilations of significant scientific and technical data and information deemed to be of continuing reference value. NASA counter-part of peer-reviewed formal professional papers but has less stringent limitations on manuscript length and extent of graphic presentations.

- TECHNICAL MEMORANDUM. Scientific and technical findings that are preliminary or of specialized interest, e.g., quick release reports, working papers, and bibliographies that contain minimal annotation. Does not contain extensive analysis.

- CONTRACTOR REPORT. Scientific and technical findings by NASA-sponsored contractors and grantees.

- CONFERENCE PUBLICATION. Collected papers from scientific and technical conferences, symposia, seminars, or other meetings sponsored or co-sponsored by NASA.

- SPECIAL PUBLICATION. Scientific, technical, or historical information from NASA programs, projects, and missions, often concerned with subjects having substantial public interest.

- TECHNICAL TRANSLATION. English-language translations of foreign scientific and technical material pertinent to NASA's mission.

Specialized services also include organizing and publishing research results, distributing specialized research announcements and feeds, providing information desk and personal search support, and enabling data exchange services.

For more information about the NASA STI program, see the following:

- Access the NASA STI program home page at http://www.sti.nasa.gov

- E-mail your question to help@sti.nasa.gov

- Phone the NASA STI Information Desk at 757-864-9658

- Write to:
  NASA STI Information Desk
  Mail Stop 148
  NASA Langley Research Center
  Hampton, VA 23681-2199

NASA/TM–2015-218790

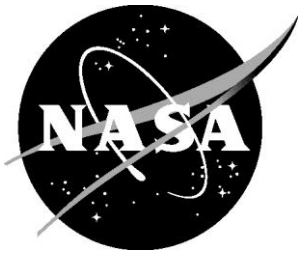

Transonic Investigation of Two-Dimensional Nozzles Designed for Supersonic Cruise

Francis J. Capone and Karen A. Deere
Langley Research Center, Hampton, Virginia

National Aeronautics and
Space Administration

Langley Research Center
Hampton, Virginia 23681-2199

August 2015

Available from:

NASA STI Program / Mail Stop 148
NASA Langley Research Center
Hampton, VA 23681-2199
Fax: 757-864-6500

Table of Contents

This page intentionally left blank.

Abstract

An experimental and computational investigation has been conducted to determine the off-design uninstalled drag characteristics of a two-dimensional convergent-divergent nozzle designed for a supersonic cruise civil transport. The overall objectives were to: (1) determine the effects of nozzle external flap curvature and sidewall boattail variations on boattail drag; (2) develop an experimental data base for 2D nozzles with long divergent flaps and small boattail angles and (3) provide data for correlating computational fluid dynamic predictions of nozzle boattail drag. The experimental investigation was conducted in the Langley 16-Foot Transonic Tunnel at Mach numbers from 0.80 to 1.20 at nozzle pressure ratios up to 9. Three-dimensional simulations of nozzle performance were obtained with the computational fluid dynamics code PAB3D using turbulence closure and nonlinear Reynolds stress modeling. The results of this investigation indicate that excellent correlation between experimental and predicted results was obtained for the nozzle with a moderate amount of boattail curvature. The nozzle with an external flap having a sharp shoulder (no curvature) had the lowest nozzle pressure drag. At a Mach number of 1.2, sidewall pressure drag doubled as sidewall boattail angle was increased from 4° to 8°. Reducing the height of the sidewall caused large decreases in both the sidewall and flap pressure drags.

Summary

An experimental and computational investigation has been conducted to determine the off-design uninstalled drag characteristics of a two-dimensional convergent-divergent nozzle designed for a supersonic cruise civil transport. The overall objectives were to: (1) determine the effects of nozzle external flap curvature and sidewall boattail variations on boattail drag; (2) develop an experimental data base for 2D nozzles with long divergent flaps and small boattail angles and (3) provide data for correlating computational fluid dynamics (CFD) predictions of nozzle boattail drag. The experimental investigation was conducted in the Langley 16-Foot Transonic Tunnel at Mach numbers from 0.80 to 1.20 at nozzle pressure ratios up to 9. Three-dimensional simulations of nozzle performance were obtained with the computational fluid dynamics code PAB3D using turbulence closure and nonlinear Reynolds stress modeling. The results of this investigation indicate that excellent correlation between experimental and predicted results was obtained for the nozzle with a moderate amount of boattail curvature. The nozzle with an external flap having a sharp shoulder (no curvature) had the lowest nozzle pressure drag. At a Mach number of 1.2, sidewall pressure drag doubled as sidewall boattail angle was increased from 4° to 8°. Reducing the height of the sidewall caused large decreases in both the sidewall and flap pressure drag forces.

Excellent correlation between experimental and CFD results were obtained for the nozzle with an external flap having a moderate amount of boattail curvature at the shoulder at all Mach numbers tested. At a Mach number of 1.20, agreement between the experimental and predicted pressures was excellent for the nozzle having a sharp corner on the external flap. The nozzle with an external flap having a sharp shoulder (no curvature) had the lowest nozzle pressure drag. Even though this nozzle had the greatest expansion of flow about the nozzle shoulder, it exhibited

more favorable pressure recovery characteristics when compared to the other three nozzles tested. At a Mach number of 1.2, sidewall pressure drag doubled as sidewall boattail angle was increased from 4° to 8°. Reducing the height of the sidewall caused large decreases in both the sidewall and flap pressure drag forces.

Introduction

The National Aeronautics and Space Administration sponsored a joint High-Speed Research Program with US airframe and propulsion companies to provide the critical high-risk technologies for a Mach 2.4, 300 passenger aircraft shown in (ref. 1). An artist concept of this aircraft is shown in figure 1(a). One task the NASA-industry team faced was what type of exhaust nozzle would be best suited for the High Speed Civil Transport (HSCT) propulsion system. The technical challenges addressed as part of the task involved developing a large nozzle with high aerodynamic efficiency, low noise, low weight and long life. Trade studies conducted during this program indicated that a very large two-dimensional convergent-divergent nozzle (2-D C-D) would be best suited to meet the very stringent noise requirements of the HSR program (fig. 1(b)). Additionally, a number of investigations conducted at both static (no external flow) and forward speeds have verified the performance characteristics of 2-D C-D nozzles (refs. 2 to 5).

The engine cycle chosen for the HSCT propulsion system was a mixed-flow turbofan. Although this cycle did have a moderate bypass ratio, a mixer-ejector type nozzle would be necessary to reduce engine noise at off-design conditions. One of the nozzle concepts considered, shown in figure 1(c), would employ a multi-lobe ejector that would entrain outside free-stream air at take-off conditions through bypass doors integrated with the nozzle. This arrangement will also help fill the nozzle at over expanded conditions. During transonic and supersonic cruise conditions, these doors would be closed since external air entrainment would not be necessary for noise abatement. Static performance of two multi-lobed mixer nozzles considered for the HSCT propulsion system is presented in reference 6.

A major problem in designing an exhaust system for a supersonic cruise vehicle is that the geometric shape must change as flight conditions vary. The nozzle exit area ratio has to be varied continuously to maintain high performance at all flight conditions from takeoff to supersonic cruise. Nozzle performance cannot be comprised at supersonic conditions since payload capacity is highly sensitive to nozzle efficiency. For example, a 1-percent decrease in nozzle performance has been estimated to be equivalent to about an 8-percent loss in payload for this class of aircraft (ref. 7).

The nozzle operates with the largest area ratio at supersonic cruise. In order to reduce flow angularity losses (flow not exiting parallel to nozzle center line), the divergent flap half-angle and thus, length, are set to provide maximum internal performance at the supersonic design point for a fully expanded area ratio. As seen in the schematic in figure 1(c), the nozzle would have very long divergent flaps and the nozzle boattail angle would essentially be at 0° at supersonic cruise conditions. At the subsonic/transonic cruise condition, the nozzle would operate at a much lower area ratio. At this condition, it is necessary to minimize nozzle boattail drag that results from not only the nozzle boattail angle but also the curvature at the start of the boattail.

The nozzle boattail drag can be a significant part of the overall drag at subsonic speeds. Several studies were also conducted that addressed installed nozzle boattail drag issues. These

studies suggested that nozzle boattail drag could be as much as 25 to 40 percent of the subsonic cruise drag (ref. 8) for the HSCT aircraft. Since limited experimental data existed for this class of nozzles, an experimental and computational program was initiated at NASA-Langley to determine the uninstalled drag characteristics of this nozzle concept. The overall objectives were to: (1) determine the effects of nozzle external flap curvature and sidewall boattail variations on boattail drag; (2) develop an experimental data base for 2D nozzles with long divergent flaps and small boattail angles and (3) provide data for correlating CFD predictions of nozzle boattail drag.

The experimental investigation was conducted in the Langley 16-Foot Transonic Tunnel at Mach numbers from 0.80 to 1.20 at nozzle pressure ratios up to 9. Three-dimensional simulations of nozzle performance were obtained with the computational fluid dynamics code PAB3D using turbulence closure and nonlinear Reynolds stress modeling.

Symbols and Abbreviations

All model forces and moments are referred to the stability axis system with the model moment reference center located at model station 35.39. A discussion of the data-reduction procedure and definitions of forces and propulsion relationships used herein are discussed in reference 9. Table 1 contains a listing of all reference dimensions.

A_e nozzle exit area, in^2

A_i internal area at metric break, in^2

A_{max} maximum model cross-sectional area, in^2

A_{ref} reference area, in^2

A_t measured nozzle throat area, in^2

A_e/A_t nozzle area ratio for ideally expanded flow

b_{ref} reference span, in.

$C_{D,f}$ nozzle skin friction drag coefficient

$C_{D,n}$ measured nozzle drag coefficient

$C_{D,p}$ integrated nozzle pressure drag coefficient, $C_{D,p,f} + C_{D,p,s}$

$C_{D,pf}$ integrated nozzle pressure drag plus estimated friction drag, $C_{D,p} + C_{D,f}$

$C_{D,p,f}$ integrated nozzle flap pressure drag coefficient (for both upper and lower flaps)

$C_{D,p,s}$ integrated nozzle sidewall pressure drag coefficient (for both sidewalls)

C_F computed thrust coefficient

$C_{F,I}$ ideal thrust coefficient

$C_{A,p,f}$ integrated nozzle flap pressure axial force coefficient (both upper and lower flaps)

$C_{A,p,s}$ integrated nozzle sidewall pressure axial force coefficient (both upper and lower flaps)

$C_{(F\text{-}Dn)}$ thrust-minus-nozzle drag force coefficient

$C_{L,p,f}$	integrated nozzle flap pressure lift coefficient (both upper and lower flaps)
$C_{L,p,s}$	integrated nozzle sidewall pressure lift coefficient (both upper and lower flaps)
$C_{N,p,f}$	integrated nozzle flap pressure normal force coefficient (both upper and lower flaps)
$C_{N,p,s}$	integrated nozzle sidewall pressure normal force coefficient (upper and lower flaps)
$C_{p,f}$	nozzle flap pressure coefficient, $(p_f - p_o)/q_o$
$C_{p,s}$	nozzle sidewall pressure coefficient, $(p_s - p_o)/q_o$
c_{ref}	reference length, in.
ΔC_D	increment in drag coefficient between measured and integrated nozzle pressure drag, $C_{D,n}$ - $C_{D,pf}$
$\Delta C_{D,p}$	jet effects parameter, $(C_{D,p})_{NPR} - (C_{D,p})_{Jet\ off}$
C-D	convergent-divergent
CFD	computational fluid dynamics
D	total center body-nozzle drag, lbf
D_f	center body friction drag, lbf
D_n	nozzle drag, lbf
EFD	experimental fluid dynamics
F	nozzle flap
F	thrust along stability axis, lbf
F_A	axial force, lbf
$(F\text{-}D_n)/F_i$	aeropropulsive parameter (thrust-minus-nozzle drag ratio)
F/F_i	static thrust ratio
F_A	axial force, lbf
$F_{A,bal}$	total axial force measured by force balance, lbf
$F_{A,mom}$	momentum tare axial force due to bellows, lbf
F_{flux}	CFD determined surface flux force, lbs
$F_{friction}$	CFD determined surface friction force, lbs
F_i	ideal isentropic gross thrust, lbf
F_j	measured thrust along the body axis, lbf
F_N	measured jet normal force, lbf

$F_{pressure}$	CFD determined surface pressure force, lbs
$F_{t,b}$	total body force vector, lbs
g	gravitational constant, 32.174 ft/sec
h_e	height of nozzle exit, in. (see fig.3)
h_m	height of nozzle, in. (see fig. 3)
h_t	height of nozzle throat, in. (see fig. 3)
HSCT	high-speed civil transport
HSR	High Speed Research program
$L_{a,f}$	circular arc portion of nozzle flap (see fig. 3), in.
$L_{a,s}$	circular arc portion of sidewall (see fig. 4), in.
L_f	length of flap (see fig.3), in.
L_n	length of nozzle (see fig.3), in.
L_s	length of sidewall flap (see fig. 4), in.
M	free-stream Mach number
MS	model station, in.
N	nozzle
N	unit normal vector
NPR	nozzle pressure ratio, $p_{t,j}/p_a$ or $p_{t,j}/p_o$
p	surface static pressure, psi
p_f	flap external static pressure, psi
p_i	average internal static pressure, psi
p_0	free-stream static pressure, psi
p_s	sidewall external static pressure, psi
$p_{t,j}$	average jet total pressure, psi
q_0	free-stream dynamic pressure, psi
R	specific gas constant, 1716 ft/sec °R
r_f	flap radius of curvature (see fig. 3), in.

$r_{f,max}$	maximum flap radius of curvature (see fig. 3), in.
r_s	sidewall radius of curvature (see fig. 4), in.
$r_{s,max}$	maximum sidewall radius of curvature (see fig. 4), in.
S	sidewall
$T_{t,j}$	average jet total temperature, °R
U	velocity vector, ft/sec
w_f	flap width, 5.492 in. (see fig. 2)
w_i	ideal weight-flow rate, lbf/sec
w_p	measured weight-flow rate, lbf/sec
w_p/w_i	discharge coefficient
x	axial distance from MS 50.90 (see fig. 3), in.
y	vertical distance (see fig. 3), in.
$y_{a,f}$	vertical distance to the terminal point of the flap circular arc (see fig. 3), in.
z	lateral distance (see fig.4), in.
$z_{a,s}$	vertical distance to the terminal point of the sidewall circular arc (see fig. 4), in.
z_e	sidewall trailing edge thickness (see fig.4), in.
2-D	two-dimensional
α	angle of attack, deg
β_f	flap boattail angle, deg
β_s	sidewall boattail angle, deg
ρ	density, slugs/ft^3

Nozzle Designs

Nozzle Sizing Criteria

For the experimental portion of this study, the 2-D C-D nozzle was sized for testing on one of the existing single-engine, propulsion simulation systems with a rectangular body at the Langley 16-Foot Transonic Tunnel (ref. 10). The system chosen has a maximum height of 6.20 inches and a maximum width of 6.80 inches that results in the nozzle having an aspect ratio of 1.10 (width to height). However, some of the full-scale nozzle concepts being considered for the HSCT vehicle, like the ones shown in figure 1, had aspect ratios of about 1.05. To account for the difference in nozzle aspect ratio, the height of the model 2-D C-D nozzle was chosen for scaling purposes, since this parameter should better represent nozzle boattail closure. This

resulted in an 8.2-percent scale model of one of the Mach 2.4 passenger aircraft being studied in the HSR program. This aircraft was about 320 ft long with a reference area of 7200 ft^2 and a reference chord of 1032.28 in. Using this model scale, an appropriate reference area was obtained to nondimensionalize nozzle drag in order to produce meaningful drag coefficients in terms of airplane drag counts (one drag count = 0.0001 in drag coefficient).

The two-dimensional convergent-divergent nozzle is a nonaxisymmetric exhaust system in which a symmetric contraction and expansion process takes place internally in the vertical plane. Basic nozzle components consist of upper and lower convergent and divergent flaps to regulate the contraction and expansion process and flat nozzle sidewalls to contain the flow laterally. The flap inner-surface (on full-scale hardware) can be varied or altered by actuators so that (1) the engine power setting (throat area) can be changed by varying the throat height and (2) the expansion surface angle (flat surface downstream of the throat) can be varied for optimum expansion of the exhaust flow. The overall nozzle geometry of the subscale 2-D C-D nozzle model is shown in figure 2 with a typical flap and sidewall setup. The overall length of the nozzle was 13.14 inches. The full-scale nozzle shown in figure 1(b) would be about 8 ft by 8 ft by 20 ft long.

All nozzles were tested with sidewalls. The height of the sidewall was fixed to a distance such that the nozzle internal flaps would not unport with the nozzle in the supersonic cruise position. In this position the boattail angle of the external flaps would be less than 4°. The sidewall cross sectional shape and maximum thickness were dictated by structural and actuation requirements for the full-scale nozzle.

External Flap and Sidewall Geometry

The geometric parameters used to define the nozzle external flap shape are shown in figure 3. The two geometric parameters varied during the test were nozzle external flap length L_f and flap radius of curvature r_f. These two parameters were nondimensionalized by the nozzle height h_m and maximum radius of curvature $r_{f,max}$. The baseline external flap had a length of 8.432 inches. A shorter flap length of 6.739 inches was also tested. Note that the overall length of the nozzle, which is representative of the full-scale nozzle, was not changed when nozzle flap length was varied. Nozzles with boattail curvature parameters $r_f/r_{f,max}$ from 0 to 1 were tested. A nozzle with no curvature would probably be the simplest to build since this flap would have a simple hinge joint. If curvature were required, some type of a sliding mechanism at the hinge joint (fig. 1) would be necessary. The term $L_{a,f}$ represents the portion of the nozzle flap that is a circular arc. Nozzle flap F1 was considered the baseline flap for this investigation since pretest predictions indicated that a nozzle with this flap external geometry would have the lowest drag. The external coordinates and location of the pressure orifices on the nozzle flaps are presented in Appendix A.

The various parameters used to define the sidewall external shape are shown in figure 4. Sidewall boattail angle β_s and radius of curvature r_s were the two geometric parameters that varied during the test. The sidewall height at the nozzle exit was 5.946 in. (see fig. 2) for sidewalls S1 to S7. An additional sidewall S8 was provided to determine the effect of sidewall height. The height of this sidewall was varied to follow the external contour of nozzle flap N1. A sketch of the nozzle flap and sidewall geometry is shown in figure 5, which also lists the summary of nozzle configurations tested. Sidewall S1 was chosen to be the baseline sidewall for this investigation. This sidewall should have the lowest drag of all the full height sidewalls tested because it had the lowest boattail angle. For a full-scale nozzle, the sidewall needs to be wide

enough to house the actuation system for the nozzle and provide structural integrity for the overall nozzle. Thus, sidewalls with larger boattail angles were provided to assess any drag penalty that might occur if such sidewalls were required for the full-scale nozzle. The external coordinates and location of the pressure orifices on the sidewalls are presented in Appendix A.

Nozzle Configurations Tested

A summary of all the nozzles tested is provided in figure 5. Nozzle configurations in which the external flap geometry was varied are presented in figure 6. The flap radius of curvature parameter was varied from 0 to 1.0 for nozzles N1, N2, N3, and N4 with the baseline flap length being held constant. The flap boattail angle β_f varied from 11.72° to 23.44° for these configurations. Flap radius of curvature $r_f/r_{f,max}$ was also varied for the nozzles with the shorter flap length as indicated by nozzles N13 and N14, all of which were tested with sidewall S1. Nozzles N11 and N12 were tested with flaps F1 and F2 with the reduced height sidewall to determine whether a drag penalty may occur for the full height sidewalls. Photographs of nozzles N1 and N11 are presented in figure 7 to show the different sidewall heights.

The nozzle configurations used to investigate sidewall boattail angle β_s and radius of curvature r_s are shown in figure 8. Sidewall boattail angle was varied from 4° to 8° for nozzles N1, N5 and N6 with $r_s/r_{s,max} = 0$. The sidewall radius of curvature parameter $r_s/r_{s,max}$ was varied from 0 to 0.4 for nozzles N5, N7, and N9 with the boattail angle at 6°, and from 0 to 1.0 for nozzles N6, N8, and N10 with the boattail angle at 8°.

All nozzles tested had the same internal geometry, because one of the objectives of this investigation was to only vary the external nozzle flap contour. Thus, any changes to external nozzle performance such as nozzle drag, should only be attributed to external flow effects over the nozzle flaps. The nozzles had a nominal throat height h_t of 2.02 inches, an exit height h_e of 2.70 inches and an area ratio A_e/A_t of 1.34 (fig. 2). The corresponding nozzle design pressure ratio was 5.0, which is where the flow in the nozzle is fully expanded and peak nozzle performance is generally expected. Static performance for each of the nozzles can be found in Appendix C. A comparison of all the nozzles static performance presented in figure 9 showed excellent agreement between all nozzles with differences of less than one-half percent in the static thrust ratio at any given pressure ratio. The maximum static pressure ratio reached was about 4.5 due to facility flow limitations.

Experimental Procedures

Wind Tunnel and Tests

The Langley 16-Foot Transonic Tunnel was a single-return atmospheric wind tunnel with a slotted octagonal test section and continuous air exchange. The wind tunnel had variable airspeeds up to a Mach number of 1.25 with test-section plenum suction used for speeds above a Mach number of 1.05. A complete description of this facility and operating characteristics can be found in reference 11.

This investigation was conducted at Mach numbers from 0.80 to 1.20. Nozzle pressure ratio was varied from jet-off up to 9, depending on Mach number. All nozzle configurations were tested at an angle of attack of 0°. Unit Reynolds number per foot varied from 3.8×10^6 to 4.2×10^6. All tests were conducted with a 0.10 in. wide boundary-layer trip consisting of a strip of No.

120 silicon carbide grit sparsely distributed in a thin film of lacquer located 1.00 in. from the tip of the forebody nose.

Air Simulation System

The nozzles were tested on an isolated, two-dimensional propulsion air-powered simulation system that was mounted in the wind tunnel by a sting/strut support system as shown in figure 10. A photograph showing this installation with nozzle N1 is presented in figure 11. The propulsion simulation system was composed of three major sections: a nose-forebody, a centerbody, and the nozzle. The nose-forebody section up to station 26.50 was nonmetric; that is, it was not attached to the strain-gage force balance. The centerbody section was made up of the low-pressure plenum, instrumentation section and transition section. The centerbody section from station 26.50 to 50.90 was rectangular in cross-section with rounded corners and had a constant width and height of 6.80 in. and 6.20 in., respectively. All sections downstream of station 26.50 were metric and mounted on the force balance. A flexible Teflon strip inserted into a circumferentially machined groove between the nose-forebody and low-pressure plenum impeded flow into or out of the internal cavity.

An external high-pressure air system provided a continuous flow of clean, dry air at a controlled temperature of about 540°R in the nozzles. This high-pressure air was brought through the support strut by six tubes that connect to a high-pressure plenum chamber. As shown in figure 10, the air was then discharged perpendicularly into the model low-pressure plenum through eight multi-holed sonic nozzles equally spaced around the high-pressure plenum. This method was designed to minimize any forces imposed by the transfer of axial momentum as the air passed from the nonmetric high-pressure plenum to the metric (mounted on the force balance) low-pressure plenum. Two-flexible metal bellows were used as seals and served to compensate for axial forces caused by pressurization.

The air was then passed from the model low-pressure plenum, through a choke plate, an instrumentation section and a transition section that provided a smooth flow path for the airflow from the round low-pressure plenum to the rectangular nozzle entrance. All nozzle configurations were attached to the transition section at model station 50.90.

Instrumentation

The Langley 1631B six-component strain-gauge balance was used to measure forces and moments on the model downstream of station 26.50. The balance limits for this balance were ±600 lbs normal force, ±800 lbs axial force and ±4,000 inch-pounds pitching moment. Flow conditions in the nozzle were determined from ten area-weighted total pressure probes and one total temperature probe located at station 45.65 in the instrumentation section, aft of the choke plate. Nozzle total pressure was determined from the average of these measurements. Weight flow of the high-pressure air supplied to the exhaust nozzle was measured by a critical flow venturi (ref. 12). Eight internal static pressures, measured at the metric break, were used to account for pressure forces at this location. All the pressures noted above were measured with individual pressure transducers.

The nozzle flaps were extensively instrumented with pressure taps because one of the primary objectives of this investigation was to provide data for correlating CFD predictions of nozzle boattail drag. The nozzle upper and lower flaps were each instrumented with two rows of pressure taps with 25 taps per row. On the upper flap, one row was located on the flap centerline

and the other was located outboard near the sidewall. On the lower flap, one row was also located on the flap centerline and the other was located midway between the flap centerline and the outer edge of the flap. For each nozzle, one sidewall was instrumented with two rows of pressure taps with 20 taps per row. These pressures were measured with electronically scanning pressure devices. The locations of each pressure tap on all flaps and sidewalls were determined from actual measurements after the pressure taps were installed and are accurate to within ±0.005 inches. These locations are presented in detail in Appendix A.

Calibration and Data Reduction Procedures

Calibration Procedure. The force balance measures the combined forces and moments due to nozzle gross thrust and the external flow field of that portion of the model aft of MS 26.5 inches. Force and moment interactions exist between the bellows-flow transfer system (fig. 10) and the force balance. Consequently, single and combined loadings of normal force, axial force and pitching moment were made with and without the jets operating with Stratford calibration nozzles (ref. 10). The calibrations performed with the jets operating give a more realistic effect of pressurizing the bellows than simply capping off the nozzles and pressurizing the flow system. Thus, in addition to the usual balance-interaction corrections applied to the force balance under combined loads, another set of corrections was applied to account for the combined loading effect of the balance with the bellows system. These calibrations were performed over a range of expected normal forces and pitching moments. The balance data were then corrected in a manner similar to that discussed in references 9 and 10.

Data Reduction. All data were recorded simultaneously on magnetic tape. Approximately 50 frames of data, taken at a rate of 10 frames per second, were taken for each data point; average values were used in data reduction computations. The average value of jet total pressure was also used in all computations. As stated in the Nozzle Design section, the nozzles were scaled to an equivalent 8.2-percent HSCT airplane so that appropriate reference dimensions could be used subsequently to non-dimensionalize drag in order to produce meaningful drag coefficients in terms of airplane drag coefficients. Thus, all aerodynamic coefficients were referenced to an equivalent reference area of 6824.4 in^2 and chord of 84.337 in.

The axial force measured by the force balance must be corrected for both a pressure-area tare force acting on the model and for momentum tare forces caused by flow in the bellows in order to achieve desired axial-force terms. The internal pressure force on the model was obtained by multiplying the difference between the average internal pressure and free-stream pressure by the affected projected area normal to the model axis. The momentum tare force was determined from calibrations using the aforementioned Stratford calibration nozzles prior to the wind tunnel investigation.

At wind-on conditions, thrust-minus nozzle drag was obtained from equation 1

$$F_A - F_j = F_{A,bal} + (p_i - p_0)A_i - F_{A,mom} + D_f \qquad (1)$$

where the first term $F_{A,bal}$ includes all pressure and viscous forces (internal and external on the afterbody and nozzle and thrust system). The second term accounts for the interior pressure forces acting at the metric break. The internal pressure at any given set of test conditions was uniform throughout the inside of the model, thus indicating no cavity flow. The tare force $F_{A,mom}$ is a momentum tare correction with the jet operating and is a function of the average bellows

internal pressure that varies with the internal chamber pressure in the supply pipe just ahead of the sonic nozzles (fig. 10). Although the bellows were designed to eliminate pressure and momentum tares, small bellows tares still exist with the jet operating. These tares result from a small pressure difference between the ends of the bellows when internal velocities are high and from small differences in the forward and aft bellows spring constants when the bellows are pressurized. The last term D_f is the friction drag of the centerbody section from stations 26.50 to 50.90.

The adjusted forces and moments measured by the force balance are transferred from the body axis of the metric portion of the model to the stability axis. The attitude of the nonmetric forebody relative to gravity was determined from a calibrated attitude indicator located in the model nose. The angle of attack, α, which is the angle between the centerbody/nozzle centerline and the relative wind, was determined by applying terms for centerbody deflection (caused when the model and balance bend under aerodynamic load) and a tunnel flow angularity term to the angle measured by the attitude indicator. The flow angularity correction was 0.1°, which is the average angle measured at the centerline of the 16-Foot Transonic Tunnel (ref. 11).

Thrust-removed (nozzle) forces and moments were obtained by subtracting the components of thrust in axial force, normal force, and pitching moment from the measured total (aerodynamic plus thrust) forces and moments. These thrust components at forward speed were determined from measured static data and were a function of free-stream and dynamic pressure. Total nozzle drag coefficient (including pressure and viscous forces) from balance measurements for only the nozzle (portion of model aft of model station 50.90) is then

$$C_{D,n} = C_{(F-D_n)} + C_F \tag{2}$$

Nozzle flap and sidewall pressure drag coefficients were determined by integration of pressures over the respective surfaces in the body axis. Integrated axial (equation 3) and normal (equation 4) pressure force coefficients for the upper and lower flap of the nozzle are simply

$$C_{A,p,f} = \sum C_{p,f,i}\left(A_{A,i}\right)/A_{ref} \tag{3}$$

$$C_{N,p,f} = \sum C_{p,f,i}\left(A_{N,i}\right)/A_{ref} \tag{4}$$

and then converted to the stability axis

$$C_{D,p,f} = C_{A,p,f}\cos a + C_{N,p,f}\sin a \tag{5}$$

Sidewall pressure drag coefficient would be obtained in a similar fashion

$$C_{D,p,s} = C_{A,p,s}\cos a + C_{N,p,s}\sin a \tag{6}$$

Nozzle discharge coefficient w_p/w_i is the ratio of measured weight flow to ideal weight flow, where ideal weight flow is based on average jet total pressure $p_{t,j}$, jet total temperature $T_{t,j}$, and the measured nozzle throat area A_t for each individual nozzle tested. Nozzle discharge coefficient is then a measure of the ability of a nozzle to pass weight flow and is reduced by any momentum and vena contracta losses (effective throat area less than measured throat area). Using the measured weight flow, ideal thrust of the nozzle can be computed from equation 7.

$$F_i = w_p \left\{ \frac{RT_{t,j}}{g^2} \left(\frac{2\gamma}{\gamma - 1} \right) \left[1 - \left(\frac{1}{\text{NPR}} \right)^{\left(\frac{\gamma - 1}{\gamma} \right)} \right] \right\}^{\left(\frac{1}{2} \right)} \qquad (7)$$

Ideal thrust is then used to compute basic propulsion performance ratios such as static thrust ratio F/F_i.

Data Repeatability. Data for this investigation was acquired within a single wind tunnel entry of the model. Short-term repeatability has been quantified in terms of a 95% confidence level for nozzle N1. Examples of short-term repeatability of integrated pressure drag values are shown in figure 12 for nozzle N1 flap and sidewall pressure drag coefficients, respectively, at a Mach number of 0.90 for seven NPR sweeps. Four of the NPR sweeps were performed at the beginning of the test and the other three were taken at the end of the test period. These figures show the residuals of the integrated pressure drag values defined as the difference in the individual measured data points from the estimated mean of the group of repeated NPR sweeps. The estimated mean was the average of the grouped data based on a piecewise, 3rd order polynomial fit of the individual NPR sweeps. Also shown with the dashed lines, are the bounds of the 95% confidence interval as a function of NPR. In general, the residuals are small over the NPR range tested. The basic data in graphical form can be found in Appendix B.

Computational Flow Solver

Governing Equations

The PAB3D computer code solves the three-dimensional, Reynolds-averaged Navier-Stokes (RANS) equations and uses one of several turbulence models for closure of the RANS equations. The governing equations are written in generalized coordinates and in conservative form. In an effort to decrease computational resources, simplified, thin-layer Navier-Stokes equations are implemented into PAB3D. This approximation neglects derivatives in the viscous terms streamwise and parallel to the surface, since they are typically negligible in comparison to the derivatives normal to the surface. Extensive details of PAB3D are found in references 13 and 14.

The flow solver was written with three numerical schemes: the flux vector scheme of van Leer (ref. 15), the flux difference-splitting scheme of Roe (ref. 16), and a modified Roe scheme used primarily for space marching solutions. These schemes implement the finite volume principle to balance the fluxes across grid cells and the upwind biased scheme of van Leer or Roe to determine fluxes at the cell interfaces. Only the inviscid terms of the flux vectors are split and upwind differenced, while the diffusion terms of the Navier-Stokes equations are centrally differenced. The details and applications of these methods are given in references 13 and 14.

For this study and other typical three-dimensional simulations, the solutions are computed with the van Leer and Roe schemes. Each iteration to a steady state in the three-dimensional computational domain includes a forward and backward relaxation sweep in the streamwise direction, while implicitly updating each cross plane.

Turbulence Modeling

Turbulence modeling is required to predict solutions for many flow fields. The PAB3D code can perform several turbulence simulations by implementing either a 1- or 2-equation turbulence model with either a linear or nonlinear Reynolds stress model. For this study, the 2-equation, viscous model was chosen because this model has proven reliable in predicting propulsive flows with mixing, separated flow regions, and jet shear layers. The nonlinear Reynolds stress model of Girimaji (ref. 17) was implemented to capture anisotropic flow features that are not resolved with the standard, linear stress-strain relationships. A modified Jones and Launder form (ref. 18) of the damping function was utilized to treat the singularity at the wall. A high Reynolds number model with no damping function was implemented in the free stream blocks.

Boundary Conditions

The PAB3D code allows for several boundary conditions at the inflow, outflow, free stream, and wall and centerline boundaries. Nozzle total temperature and total pressure with a normal fluid flow angle was used for the jet inflow boundary conditions. A jet total temperature of 528.67°R was used for all jet calculations. Riemann invariants along characteristics were used as inflow and free stream boundary conditions. A constant pressure boundary condition for subsonic outflow was used far downstream as an outflow boundary condition. A no-slip adiabatic wall boundary condition was implemented on solid surfaces to obtain viscous solutions.

Performance Calculation

The PAB3D code contains a performance module (ref. 19) that utilizes the momentum theorem applied to a user-defined control volume to calculate nozzle or aerodynamic performance. Quantities such as lift, drag, thrust, moments, heat transfer and skin friction may be computed for many complex geometric configurations and multi-stream flows. Each quantity is updated throughout the solution development to monitor convergence.

Along flow-through sections of the control volume, mass and momentum fluxes, as well as pressure forces are integrated over cell with equations 8 and 9.

$$w_p = \sum (\rho U \cdot N) \Delta A \tag{8}$$

$$F_{flux} = \sum \left[\rho U (U \cdot N) + (p - p_o) N \right] \Delta A \tag{9}$$

where D*A* is the cell face area and N is the cell face unit vector.

Along solid surfaces of the control volume, skin friction and pressure forces are calculated. Surface pressure force $F_{pressure}$ is determined by multiplying cell static pressure by cell face area using equation 10.

$$F_{pressure} = \sum \left[(p - p_o) N \right] \Delta A \tag{10}$$

The cell surface static pressure is calculated by extrapolating the cell centered static pressure to the surface where the velocity is assumed to be zero.

The skin friction force $F_{friction}$ is calculated with only the velocity gradients tangential to the surface contributing to the velocity term of the viscous stress tensor. A two point difference method was used to determine the velocity gradients; one zero-magnitude velocity vector at the surface and a second at the cell center. Sutherland's formula (ref. 20) was used to calculate the dynamic viscosity term at the surface by extrapolating the static temperature at a local cell center to the surface and using a reference viscosity and temperature condition. The total body force vector $F_{t,b}$ is defined in equation 11.

$$F_{t,b} = F_{flux} + F_{pressure} + F_{friction} \tag{11}$$

Computational Procedure

PAB3D was used to predict solutions for nozzles N1 and N3 at Mach numbers 0.90 and 1.20 with a nozzle pressure ratio of 5, which was the design pressure ratio.

The computational mesh was fully three-dimensional with 9+3 blocks defining the internal nozzle, and 9+3 blocks representing the free stream domain. The far field was located 10 body lengths upstream and downstream of the aerodynamic nose and nozzle exit, respectively. The upper and lower lateral far field boundary was located 6 body lengths above and below the aerodynamic body. The boundary layer was defined for a law-of-the-wall coordinate y+ of 0.5 on the fine mesh spacing for adequate modeling of the boundary layer flow.

The base grid is a quarter plane representation of the experimental model with 1.57 million grid points in 12 blocks. A cut 222 grid is generated by using a database reduction scheme that eliminates every other grid point in the i, j, and k directions. This cuts each grid dimension by 2, which decreases the grid count to 207,437 and substantially reduces the memory required to run the flow solver. The cut grid can also be sequenced in each direction for improved convergence rates and for grid assessment. For example, the flow solver uses alternating points in the i direction and every point in the j and k directions in a 211 sequence. Generally, a user would begin sequencing on the cut 222 grid. A pattern of 222, 221, 211, and then 111, or no sequencing might be used to assess solution behavior as more points are utilized in a particular direction. The solution is developed until convergence requirements are met at each level. Once the solution is converged on the cut 222 grid, the solution may be extrapolated to the base grid and sequencing may again be utilized.

For example, a converged solution was developed within 16.4 hours on a cut grid for nozzle N1 at M = 0.9 and NPR = 5. However, the solution was extrapolated and converged on the base level to quantify the effect of grid density. Nozzle drag coefficient decreased a mere 0.00002 in another 30 hours of computer time. Therefore, the remaining solutions were computed using sequencing only on the cut grid since the aforementioned solution was minimally dependent on doubling the grid density beyond the cut 222 level. This technique allowed for quicker solution times due to the substantially smaller memory requirement of the cut grid. Figure 13 presents typical convergence histories for Nozzle 3, and although not shown, similar results were obtained for Nozzle 1. The spikes in the residual history for Nozzle N3 at M = 0.9 and NPR = 5 exhibit locations of solution extrapolation to a finer grid level. Accordingly, small adjustments in drag coefficient, C_d, were observed at these locations, also. The solution converged at the 222 grid level after 6500 iterations, with no further change in drag coefficient as the residual continued to decrease. Drag coefficient increased a mere 1.2 percent from the 422 grid level to the 222 grid level.

Presentation of Results

Summary Data

The effect of Mach number on nozzle aeropropulsive performance parameters for nozzle N1 is presented in figure 14. Comparative and summary results from this investigation are presented graphically in figures 15 to 36. The comparisons show the correlation between the experimental and predicted results, as well as showing the effects of varying nozzle geometric parameters on the nozzle integrated pressure drags and pressure distributions at the design nozzle pressure ratio of 5.0. Although the discussion of results at this pressure ratio would generally be applicable to other pressure ratios, the relative difference between comparisons may vary.

Basic Data

All the experimental results from this investigation are presented in graphical form in Appendices D to H. Basic nozzle performance parameters for each nozzle are presented in Appendix D. Appendix E presents the effects of varying nozzle geometric parameters on the nozzle integrated pressure drag. The effects of varying nozzle geometric parameters on the nozzle integrated pressure drag values at the scheduled NPR are presented in Appendix F. Jet-effects parameter for each nozzle are presented in Appendix G. Appendix H presents the external pressure distributions for each nozzle.

An examination of the force and pressure data plots for an individual nozzle will show that at times, the force data plot may not contain as many data points as the experimental pressure data plot. During this investigation, pressure fluctuations were observed in the critical flow venturi. At times, these fluctuations would produce a sinusoidal type variation in nozzle discharge coefficient as nozzle pressure ratio was varied. Normally, there would be no variation of discharge coefficient with nozzle pressure ratio as long as the nozzle has choked flow. There are two valves in the air system for jet testing in the 16-Foot Transonic Tunnel that are used to vary mass flow and set nozzle pressure to the exhaust nozzles. One valve regulates pressure in the air line and the other is used as a throttling valve. The pressure fluctuations were caused by the pressure-regulating valve in the air system and subsequent operator problems associated with trying to set nozzle pressure ratio when these fluctuations occurred. In the past, this system has proven to be very successful in providing a very stable source of air to the exhaust nozzles. Unfortunately, repairs to the pressure-regulating valve could not be made in a timely manner and a decision was made to continue the test. After the test was completed, all discharge coefficient measurements for each of the nozzles were carefully examined. Any data point that had a value of discharge coefficient that was ± 0.015 different from the average was deleted from the data listing for the particular nozzle in question. Thus, the force data listings will not contain as many data points as the experimental pressure data listings. These pressure fluctuations should have no effect on the external pressure measurements.

Discussion of Results

Basic Nozzle Aeropropulsive Performance

Typical nozzle aeropropulsive characteristics for nozzle N1 are presented as a function of nozzle pressure ratio, NPR, for each of the Mach numbers tested in figure 14. Figure 14(a) presents the aeropropulsive parameter $(F\text{-}D_n)/F_i$ and nozzle discharge coefficient w_p/w_i. As expected because of increased drag, the aeropropulsive parameter decreases with increasing Mach number. Nozzle discharge coefficient is a measure of the ability of the nozzle to pass mass flow and is reduced from a theoretical value of 1.0 by boundary-layer thickness and non-uniform flow at the nozzle throat. Since nozzle discharge coefficient is a function only of internal nozzle geometry, it is independent of both Mach number and nozzle pressure ratio when the nozzle is choked. In addition, changes in nozzle geometry that occur downstream of the nozzle throat (supersonic exhaust) usually do not affect nozzle discharge coefficient characteristics. Thrust minus nozzle drag coefficient $C_{(F\text{-}Dn)}$ and nozzle drag coefficient $C_{D,n}$ determined from the force balance measurements are present in figure 14(b). In general, the variation of nozzle drag coefficient with nozzle pressure ratio for a particular nozzle is similar to that of axisymmetric nozzles particularly at zero degrees angle of attack. Nozzle drag decreases with initial jet operation because there is a reduction in the external flow expansion required at the nozzle exit as the exhaust flow fills the nozzle base region. This reduced expansion generally results in higher pressures on the nozzle boattail regions. Figure 14(c) presents the pressure integrated nozzle flap drag $C_{D,p,f}$, sidewall drag $C_{D,p,s}$, and total pressure drag $C_{D,p}$. Measured nozzle drag coefficient $C_{D,n}$, nozzle pressure drag plus estimated friction drag coefficient $C_{D,pf}$, and incremental drag coefficient DC_D are shown in figure 14(d). Ideally, the incremental drag coefficient should be equal to zero. However, the greatest differences seen are at jet-off conditions (NPR ~ 1.0) and result because of inaccuracies in measuring jet-off drag with the force balance. Typically, measured jet-off drag is about 2 to 3 percent of the maximum rated balance axial force where the balance has been sized to measure thrust.

Similar results for the other 13 nozzles that were tested as part of this investigation can be found in the Appendix D.

Experimental/Prediction Comparisons

Nozzle N1. A comparison between experimental and predicted pressures on flap F1 for nozzle N1 are presented in figure 15 at Mach numbers of 0.90 and 1.20 at the design nozzle pressure ratio of 5.0. At the design pressure ratio, the flow is expected to be fully expanded and peak nozzle internal performance usually occurs. The boattail radius of curvature parameter $r_f/ r_{f,max}$ was 0.40 for this flap and the sidewall was S1. Pressure distributions are compared along the flap centerline, at the flap mid station, and at the flap outboard station. At $M = 0.90$, the CFD computations tend to overpredict the expansion about the shoulder of the flap but do accurately predict the pressure recovery along the flap. Data indicates excellent agreement between predicted and experimental pressure data at $M = 1.20$ at NPR = 5. In addition, the pressure distributions across the flap are nearly identical, indicating that nearly uniform flow exists across the flap. The full height sidewalls tend to act like fences in inhibiting any communication between the sidewall and flap flows. The effects of reducing sidewall height will be discussed later in this section of the report.

The experimental and predicted nozzle pressure drag coefficients are presented in figure 16 for nozzle N1 at NPR = 5.0. Shown in this figure are the flap, sidewall, and nozzle pressure drag coefficient values where nozzle pressure drag coefficient is simply the sum of the sidewall and flap pressure drag coefficient values. As would be expected from the excellent correlation of pressures, the predicted drag coefficient values are in excellent agreement with experimental drag coefficient values at $M = 0.9$ and within 0.3 of a drag count (one drag count equals 0.0001 drag coefficient) of the experimental drag coefficient value at $M = 1.2$.

A comparison of experimental and predicted nozzle total drag coefficients is also presented in figure 16 where the nozzle total drag coefficient includes skin friction. Skin friction drag coefficient for the prediction is computed within the performance module of the PAB3D code. The skin friction drag coefficient $C_{D,f}$ is determined using the Frankl-Voishel skin friction coefficient as part of the wind tunnel standard data reduction system (ref. 9). The measured drag coefficient is obtained from the force data measurements. As was the case for the pressure drag coefficients, excellent agreement exits. The total drag coefficients agree to within one-half drag count (0.00005) at $M = 0.90$ and one drag count (0.0001) at $M = 1.20$.

Nozzle N3. Experimental and predicted pressure distribution comparisons for nozzle N3 are shown in figure 17. The boattail radius of curvature parameter was 0 for this flap, which meant it had a sharp corner at the start of the boattail. As can be seen, the agreement between the experimental and predicted pressures was not as good as was the case for nozzle N1 at $M = 0.90$. Consequently, there is a poorer correlation of flap pressure drag coefficient and nozzle total drag coefficient values (fig. 18). PAB3D predicts more flow expansion around the sharp corner than experimental data, which results in higher predicted drag. Another possible reason for this poor agreement of predicted and experimental data at $M = 0.90$ may be associated with treatment of the corner flow. Treatment of the corner flow is critical computationally at speeds less than Mach number 1. However, at $M = 1.20$, where geometrically matching the corner is not as important, agreement between the experimental and predicted pressures was similar to nozzle N1.

Effect of Nozzle Boattail Curvature

The effects of varying nozzle flap boattail radius of curvature on nozzle, flap, and sidewall pressure drag coefficient values are presented in figure 19 at the design nozzle pressure ratio of 5.0. These nozzles all had the baseline flap length $L_f/h_m = 1.4$ and were tested with sidewall S1. Although discussion of results at this pressure ratio would generally be applicable to other pressure ratios, the relative difference between comparisons may vary. Similar results at the scheduled nozzle pressure ratio can be found in Appendix F. Figure 19 also illustrates the typical breakdown of pressure drag between the nozzle flaps and the sidewalls. Generally, varying flap geometry had little or no effect on sidewall pressure drag. The breakdown of the pressure drag coefficient values is similar for the other nozzle configurations tested.

The lowest nozzle pressure drag was obtained on nozzle N3 with flap F3 that had no radius of curvature (fig. 19). This was an unexpected result because previous experience has shown that axisymmetric nozzles with a sharp shoulder generally have higher drag (ref. 8). Similar results were found for 2-D C-D nozzles in reference 22 and 23. However, these nozzles generally had shorter external flaps and because they were designed for use with subsonic cruise vehicles. In order to try to understand this result, one can examine the pressure distributions on these nozzles.

Pressure distributions along the centerline row of the top flap for nozzles N1, N2, N3, and N4 are presented at $M = 0.90$ and 1.20 at NPR = 5 in figure 20. What is shown is that even

though nozzle N3 with no curvature had the greatest expansion of flow about the nozzle shoulder, it exhibited more favorable pressure recovery characteristics when compared to the other three nozzles. Similar results were found for the pressure distributions along both the mid and outboard pressure rows (not shown).

The effects of varying nozzle flap boattail radius of curvature for nozzles with flap lengths of L_f/h_m = 1.1 are presented in figures 21 and 22. These nozzles were also tested with sidewall S1. Figure 21 shows flap pressure drag coefficient for the two nozzles tested with the smaller flap lengths. Except at M = 1.20, these two nozzles followed similar trends as the nozzles with the longer flap lengths. At M = 0.90 and 0.95, nozzle pressure drag decreased as the flap radius of curvature parameter was increased from 0.1 to 0.4.

Effect of Nozzle Flap Length

The effects of varying the nozzle flap length for flaps having a radius of curvature of 0.1 are shown in figures 23 and 24 and for those with a radius of curvature of 0.4 are illustrated in figures 25 and 26. Both nozzles (nozzles N13 and N14) with the shorter nozzle flap had higher total nozzle pressure drag at all the Mach numbers tested, except for N13 at M = 1.20. This was due primarily to these nozzles having steeper boattail angles than the nozzles with the longer flaps (nozzles N1 and N2). An examination of the pressure distributions in either figure 24 or 26 generally shows that the nozzles with the shorter flaps have poorer pressure recovery characteristics than those with the longer flaps. It is interesting to note that at M = 0.80 to 0.95, the increment in pressure drag due to the change in flap length is about the same for the nozzles having the two different radii of curvature.

Similar results at the scheduled nozzle pressure ratio can be found in Appendix F.

Effect of Sidewall Boattail Angle

The effects of varying sidewall boattail angle on nozzle, flap, and sidewall pressure drag coefficients are summarized in figure 27. There are no definite trends to changing sidewall boattail angle. For example, at M = 0.80 and 0.90, nozzle N6 with sidewall S3 having β_S = 8° had the lowest sidewall pressure drag coefficient whereas, just the opposite was true at M = 1.20. At M = 0.90 (fig. 28), it is interesting to note that although sidewall S3 exhibited greater expansion of the flow about the boattail than sidewall S1, it exhibited somewhat better recovery and lower pressure drag. Figure 28 also shows that the flow across the sidewall is somewhat non-uniform in nature since expansion outboard about the boattail is greater for all the sidewalls than at the center of the sidewall. However, flow recovers to about the same pressure coefficient levels at both locations.

At M = 1.20, sidewall pressure drag for nozzle N6 with sidewall S4 was doubled that of nozzle N1 with sidewall S1 as sidewall drag increased from .000017 to .000035 (fig. 27). Examination of the pressure distributions of figure 28 at this Mach number reveals markedly different flow characteristics across the sidewall. Along the center of the sidewall, the flow is rather benign and shows relatively little differences as β_S increased from 4° to 6°. Outboard on the sidewall, there is a rapid expansion of the flow about the shoulder for each of the boattail angles tested. The data indicates possible flow separation for the sidewalls with 6° and 8° boattail angles. Although the full-scale nozzle was designed to have a sidewall with 4° boattail angle, it became evident as the HSR program progressed that sidewalls with boattail angles

greater than 4° would probably be needed for both structural requirements and to house nozzle actuation hardware. This could pose a problem at supersonic cruise where the potential now exists for greater values of sidewall pressure drag to occur because of sidewall boattail angles would be greater than 4°.

Only at $M = 0.95$, did changing boattail angle appreciably affect flap pressure drag (fig. 27). Flap pressure drag coefficient increased 0.00011 as boattail angle increased from 4° to 6°, which was twice as large as the increase in sidewall pressure drag. This is a somewhat surprising result in that one would not expect such a strong effect of varying sidewall geometry on flap performance. This is because the full height sidewalls tend to act like fences and isolate the sidewall flow from the flow over the flap.

Similar results at the scheduled nozzle pressure ratio can be found in Appendix F.

Effect of Sidewall Boattail Curvature

Several sidewalls were tested with varying amounts of curvature with both 6° and 8° sidewall boattail angles. Some typical results for nozzles N5, N7, and N9 with $\beta_S = 6°$ are presented in figures 29 and 30 and for nozzles N6, N8, and N10 with $\beta_S = 8°$ in figures 31 and 32. Sidewall pressure drag decreased by 0.00014 as the sidewall radius of curvature $r_S / r_{S,max}$ was increased from 0 to 1.0 at $M = 1.20$. This could prove to be significant if sidewalls with boattail angles greater than 4° are needed as discussed previously. Sidewalls with full curvature would be feasible for the full-scale aircraft since the sidewalls would be fixed.

Similar results at the scheduled nozzle pressure ratio can be found in the Appendix F.

Effect of Sidewall Height

The height of the sidewall was fixed so that the nozzle internal flaps would not unport when the nozzle was in the supersonic cruise position. This type sidewall was selected to prevent impingement of any unwanted lateral nozzle exhaust on adjacent aircraft surfaces. As such, these sidewalls are very large panels that account for about 60-percent of the nozzle skin friction drag. Since these sidewalls could be also large unsupported panels, there could be an additional structural weight penalty associated with using them. To assess what drag penalties might occur with the full height sidewalls, some tests were performed with reduced height or cutback sidewalls. The height of the cutback sidewall S8 was contoured to match the external shape of flap F1. Sidewall S8 was then tested with flaps F1 and F2 to form nozzles N11 and N12 respectively (fig. 6).

Nozzle, flap and sidewall pressure drag coefficients for nozzle N1 and N11 are presented in figures 33. Significant reductions in both sidewall and flap pressure drag were obtained for the cutoff sidewall over the entire Mach number test range. For example, at $M = 0.90$, there was a 0.00012 reduction in nozzle pressure drag coefficient $C_{D,p}$ and a 0.00023 reduction in $C_{D,p}$ at $M = 1.20$. This drag reduction for the cutoff sidewall would be equivalent to at least a 0.00092 reduction in drag coefficient for the HSCT vehicle with four engines. This does not include an additional, albeit small reduction in skin-friction drag.

The flow characteristics over the nozzle flap are different for the two sidewalls as shown in figure 34. With the reduced height sidewall, the flow along the sidewall tends to accelerate around the corner onto the flap where it can become three-dimensional. The full height sidewalls

tend to act like fences that inhibit communication between the sidewall and flap flows, which results in the flow over the flap being more uniform. This is typical flow behavior for nozzles similar to nozzle N11, which has been found both experimentally (refs. 5 and 23) and computationally (ref. 24).

Similar results were also obtained for nozzle N12; however, the reduction in pressure drag was smaller than that noted for nozzle N11. (See figures 35 and 36.) Similar results at the scheduled nozzle pressure ratio can be found in Appendix F.

Conclusions

An experimental and computational investigation has been conducted to determine the off-design uninstalled drag characteristics of a two-dimensional convergent-divergent nozzle designed for a supersonic cruise civil transport. The overall objectives were to: (1) determine the effects of nozzle external flap curvature and sidewall boattail variations; (2) develop an experimental data base for 2D nozzles with long divergent flaps and small boattail angles and (3) provide data for correlating computational predictions of nozzle boattail drag. The experimental investigation was conducted in the Langley 16-Foot Transonic Tunnel at Mach numbers from 0.80 to 1.20 at nozzle pressure ratios up to 9. Three-dimensional simulations of nozzle performance were obtained with the computational fluid dynamics code PAB3D using turbulence closure and nonlinear Reynolds stress modeling. Based on the discussion of results in this paper, the following conclusions are made:

1. Excellent correlation between experimental and CFD results were obtained for the nozzle with an external flap having a moderate amount of boattail curvature at the shoulder at all Mach numbers tested. At a Mach number of 1.20, agreement between the experimental and predicted pressures was excellent for the nozzle having a sharp corner on the external flap.
2. The nozzle with an external flap having a sharp shoulder (no curvature) had the lowest nozzle pressure drag. Even though this nozzle had the greatest expansion of flow about the nozzle shoulder, it exhibited more favorable pressure recovery characteristics when compared to the other three nozzles tested.
3. At a Mach number of 1.2, sidewall pressure drag doubled as sidewall boattail angle was increased from 4° to 8°.
4. Reducing the height of the sidewall caused large decreases in both the sidewall and flap pressure drags.

NASA Langley Research Center
Hampton, VA 23681-2199
July 2015

Appendix A

Flap and Sidewall External Coordinates and Location of Pressure Orifices

This appendix presents the external coordinates of both the nozzle flaps and sidewalls. After installation, the locations of each pressure tap on all flaps and sidewalls were determined from actual measurements and are accurate to within ±0.005 inches. External coordinates for each nozzle flap and sidewall are presented in figures 37 to 50 as follows:

Appendix B

Data Repeatability

This Appendix presents the repeat data from this investigation in figures 51 to 56 as follows:

Appendix C

Static Data

This appendix presents the static data for each nozzle as a function of nozzle pressure ratio, NPR. Included in each figure are the static performance parameter F/F_i and nozzle discharge coefficient w_p/w_i. The static data are presented in figures 57 to 70 as follows:

Appendix D

Aeropropulsive Performance Data

This Appendix presents the basic nozzle performance parameters for each nozzle as a function of nozzle pressure ratio, NPR, for each of the Mach numbers tested. Included in each figure are: (a) the aeropropulsive parameter $(F\text{-}D_n)/F_i$ and nozzle discharge coefficient w_p/w_i; (b) thrust minus nozzle drag coefficient $C_{(F\text{-}Dn)}$ and measured nozzle drag coefficient $C_{D,n}$; (c) nozzle pressure drag coefficient $C_{D,p}$, flap pressure drag coefficient $C_{D,p,f}$, and sidewall pressure drag coefficient $C_{D,p,s}$; and (d) nozzle pressure drag plus nozzle friction drag coefficient $C_{D,pf}$, and incremental drag coefficient ΔC_D. The aeropropulsive performance data are presented in figures 71 to 84 as follows:

Appendix E

Integrated Pressure Drag Data

This appendix presents the effects of varying nozzle geometric parameters on the nozzle integrated pressure drags as a function of NPR. Included on each figure is: (a) integrated nozzle pressure drag coefficient, $C_{D,p}$; (b) integrated nozzle pressure drag plus estimated friction drag coefficient, $C_{D,pf}$; and (c) integrated nozzle sidewall pressure drag coefficient (for both sidewalls) $C_{D,p,s}$. The integrated pressure drag coefficient data are presented in figures 85 to 93 as follows:

Appendix F

Integrated Pressure Drag At Scheduled NPR

This appendix presents the effects of varying nozzle geometric parameters on the nozzle integrated pressure drags at the scheduled NPR. Scheduled nozzle pressure ratio is the pressure ratio that the nozzle operates at for a particular Mach number and is dependent on the engine cycle design. Included on part one of each figure are: (a) integrated nozzle pressure drag coefficient, $C_{D,p}$; (b) integrated nozzle pressure drag plus estimated friction drag coefficient, $C_{D,pf}$; and (c) integrated nozzle sidewall pressure drag coefficient (for both sidewalls) $C_{D,p,s}$. Another part of the figure presents the corresponding pressure data. The integrated pressure drag coefficient data at scheduled pressure ratio are presented in figures 94 to 111 as follows:

Appendix G

Jet Effects Drag Data

This Appendix presents the jet-effects parameter $\Delta C_{D,p}$ for each nozzle at both the design and scheduled pressure ratio NPR for each of the Mach numbers tested. The jet-effects parameter $\Delta C_{D,p}$ data are presented for each nozzle in figures 112 to 125 as follows:

Appendix H

External Pressure Distributions

This appendix presents the external pressure distributions for each nozzle. Pressure distributions measured along the top and bottom of the nozzle flaps as well as those on the nozzle sidewall are shown for each Mach number tested and are presented at four of the nozzle pressure ratios tested from jet-off (NPR = 1) to either NPR = 5 or 6.6 depending on Mach number in figures 126 to 139 as follows:

References

1. Wilhite, Allan W.; and Shaw, Robert J.: *An Overview of NASA's High Speed Research Program*. 20th ICAS Congress, Paper112, August 2000.
2. Capone, Francis J.: *Static Performance of Five Twin-Engine Nonaxisymmetric Nozzles With Vectoring and Reversing Capability*. NASA TP-1224, 1978.
3. Capone, Francis J.; and Reubush, David E.: *Effects of Varying Podded Nacelle-Nozzle Installations on Transonic Aeropropulsive Characteristics of a Supersonic Fighter Aircraft*. NASA TP-2120, 1983.
4. Leavitt, Laurence D.: *Summary of Nonaxisymmetric Nozzle Internal Performance From the NASA Langley Static Test Facility*. AIAA-85-1347, July 1985.
5. Yetter, Jeffrey A.; and Leavitt, Laurence D.: *Effects of Sidewall Geometry on the Installed Performance of Nonaxisymmetric Convergent-Divergent Nozzles*. NASA TP 1771, 1980.
6. Re, Richard J.; and Ingraldi, Anthony M.: Static Performance of Non-Axisymmetric Mixer/Ejector Nozzles With Hardwall and Acoustic Shrouds. NASA CDTM-10014, 1997.
7. Stitt, Leonard E.: *Exhaust Nozzles for Propulsion Systems with Emphasis on Supersonic Cruise Aircraft*. NASA RP-1235, May 1990.
8. Wallace, Hoyt; et al: Isolated and Installed Nozzle Boattail Drag Studies. NASA/CP-1999-209691/VOL1/PT1. December 1999.
9. Mercer, Charles E.; Berrier, Bobby L.; Capone, Francis J.; and Grayston, Alan M.: Data *Reduction Formulas for the Langley 16-Foot Transonic Tunnel: NASA Langley Research Center*. NASA TM-107646, 1992.
10. Staff of Propulsion Aerodynamics Branch: *A User's Guide To the Langley 16-Foot Transonic Tunnel Complex, Revision 1*. NASA TM-102750, rev. 1, 1990. (Supersedes NASA TM-831865, Kathryn H. Peddrew, compiler.)
11. Capone, Francis J.; Bangert, Linda S.; Asbury, Scott C.; Mills, Charles T.; and Bare, E. Ann: *The NASA Langley 16-Foot Transonic Tunnel - Historical Overview, Facility Description, Calibration, Flow Characteristics, Test Capabilities*. NASA TP-3521, 1995.
12. Berrier, Bobby L.; Leavitt, Laurence D.; and Bangert, Linda S.: *Operating Characteristics of the Multiple Critical Venturi System and Secondary Calibration Nozzles used for Weight-Flow Measurements in the Langley 16-Foot Transonic Tunnel*. NASA TM-86405, 1985.
13. Abdol-Hamid, Khaled S.: Application *of a Multiblock/Multizone Code (PAB3D) for the Three-Dimensional Navier-Stokes Equations*. AIAA-91-2155, June 1991.
14. Abdol-Hamid, Khaled S.: Implementation *of Algebraic Stress Models in a General 3-D Navier-Stokes Method (PAB3D)*. NASA CR-4702. 1995.
15. van Leer, B.: Flux-*Vector Splitting for the Euler Equations*. ICASE 1Report 82-30, 1982.
16. Roe, P. L.: *Characteristics Based Schemes for the Euler Equations*. A Numerical Review of Fluid mechanics, 1986, pp. 337-365.
17. Girimaji, S. S.: *Fully-Explicit and Self-Consistent Algebraic Reynolds Stress Model*. ICASE 95-82, December 1995.
18. Jones, W.P.; and Launder, B.E.: The *Prediction of Laminarization with a Two-Equation Model of Turbulence*. Int. J. Heat & Mass Trans., vol. 15, no. 2, Feb. 1972, pp. 301-314.

19. Carlson, John R.: A *Nozzle Internal Performance Prediction Method*. NASA TP-3221, 1992.
20. Ames Research Staff: *Equations, Table and Charts for Compressible Flow*. NACA Report 1135, 1953.
21. Pendergraft, Odis C. Jr.; Burley, James R. III.; and Bare, E. Ann: *Parametric Study of Afterbody/Nozzle Drag on Twin Two-Dimensional Convergent Divergent Nozzles at Mach Numbers From 0.60 to 1.20*. NASA TP 2640, 1986.
22. Capone, Francis J.; Mason, Mary L.; and Leavitt, Laurence, D.: *An Experimental Investigation of Thrust Vectoring Two-Dimensional Convergent-Divergent Nozzles Installed in a Twin-Engine Fighter Model at High Angles of Attack*. NASA TM-4155, 1990.
23. Compton, William B.: Comparison of Turbulence Models for Nozzle-Afterbody Flows With Propulsive Jets. NASA Technical Paper 3592, 1996.

Table 1. Reference dimensions.

Reference Area	A_{ref}	6824.407 in^2
Reference Chord	c_{ref}	84.337 in.
ReferenceSpan	b_{ref}	125.030 in.
Moment Reference Center		MS 35.39 in.
Maximum model cross-sectional area	A_{max}	40.635 in^2
Metric Break Cavity Area	A_i	40.064 in^2
Nominal nozzle exit area	A_e	14.846 in^2
Measured Throat Areas		
Configuration N-1	A_t	11.118 in^2
Configuration N-2	A_t	11.141 in^2
Configuration N-3	A_t	11.192 in^2
Configuration N-4	A_t	11.113 in^2
Configuration N-5	A_t	11.144 in^2
Configuration N-6	A_t	11.145 in^2
Configuration N-7	A_t	11.147 in^2
Configuration N-8	A_t	11.155 in^2
Configuration N-9	A_t	11.152 in^2
Configuration N-10	A_t	11.159 in^2
Configuration N-11	A_t	11.149 in^2
Configuration N-12	A_t	11.098 in^2
Configuration N-13	A_t	11.104 in^2
Configuration N-14	A_t	11.115 in^2

(a). Conceptual HSCT airplane.

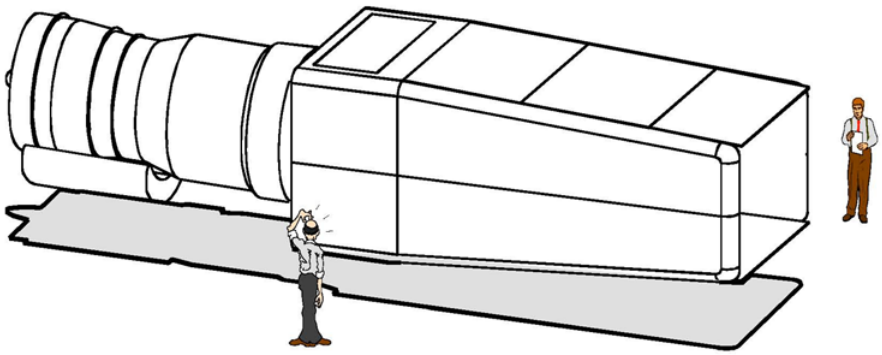

(b). Comparison of full-scale nozzle to a man.

Figure 1. Conceptual full-scale HSCT airplane exhaust nozzles.

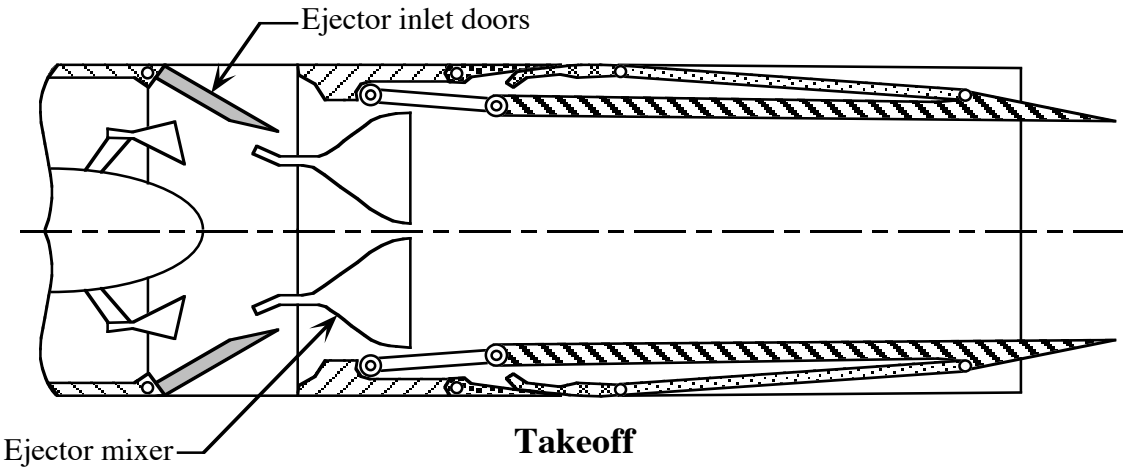

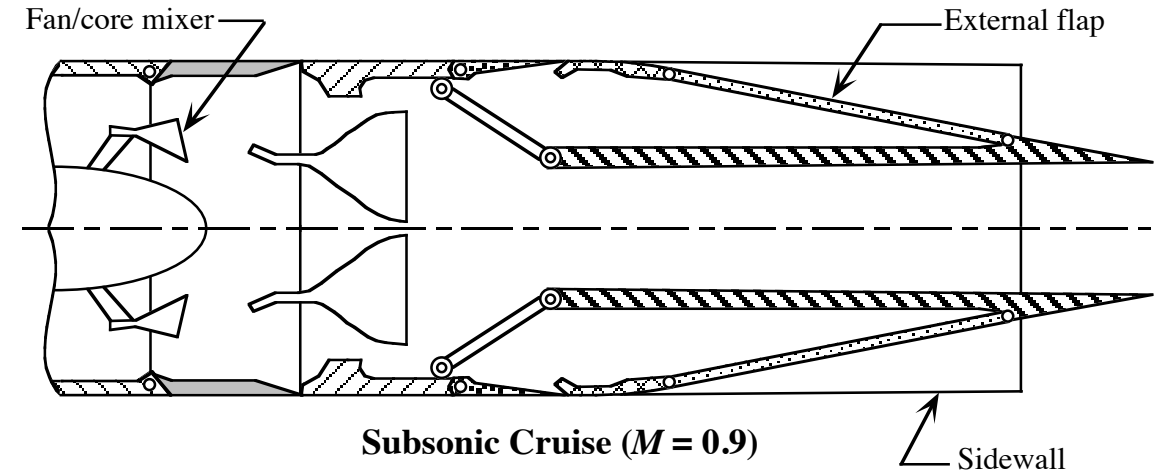

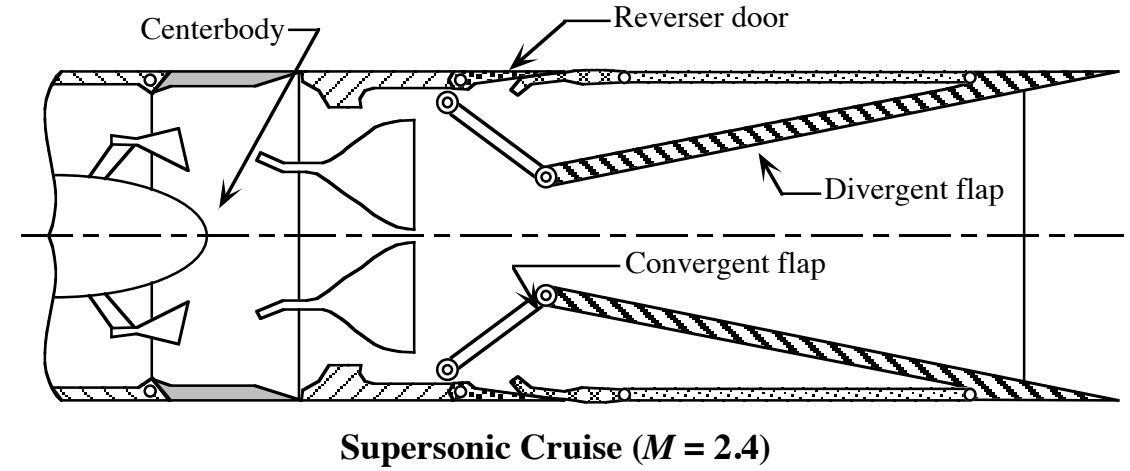

(c). Sketches of full-scale nozzle concept at three flight conditions.

Figure 1. Concluded

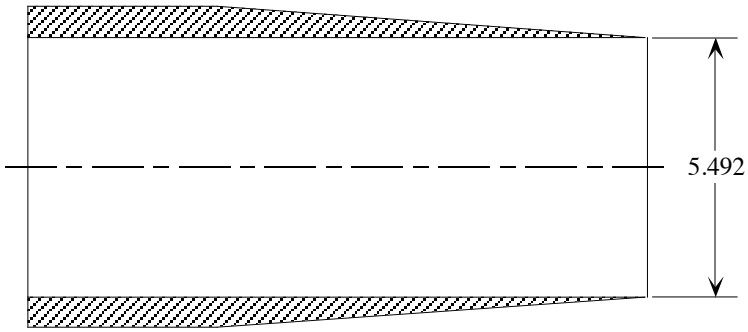

Parameter	Value
h_m, in.	6.200
h_t, in.	2.017
h_e, in	2.703
h_e / h_m	0.436
A_t, in^2	11.079
A_e, in^2	14.846
A_e / A_t	1.34
A_{max}, in^2	40.064
A_e / A_{max}	0.36

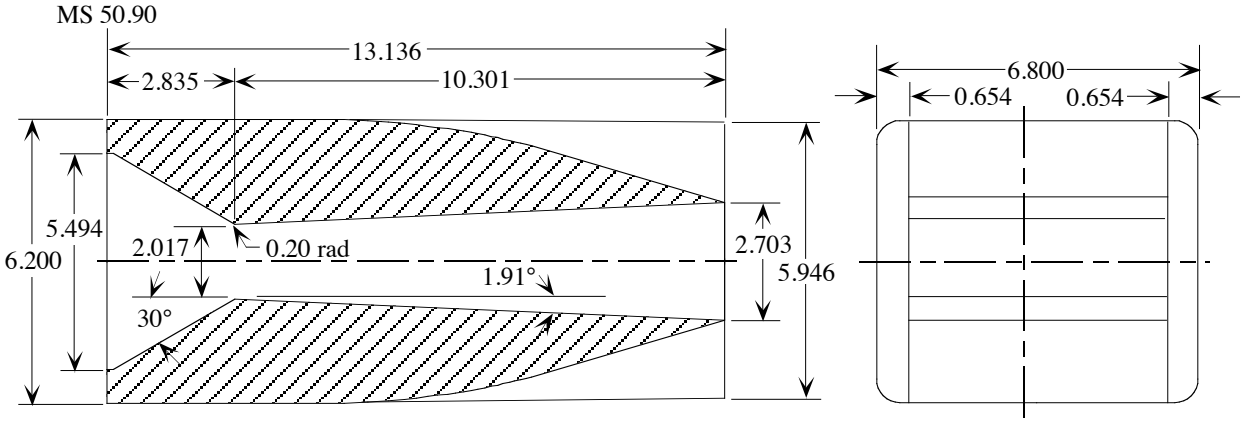

Figure 2. Overall nozzle geometry. All linear dimensions in inches.

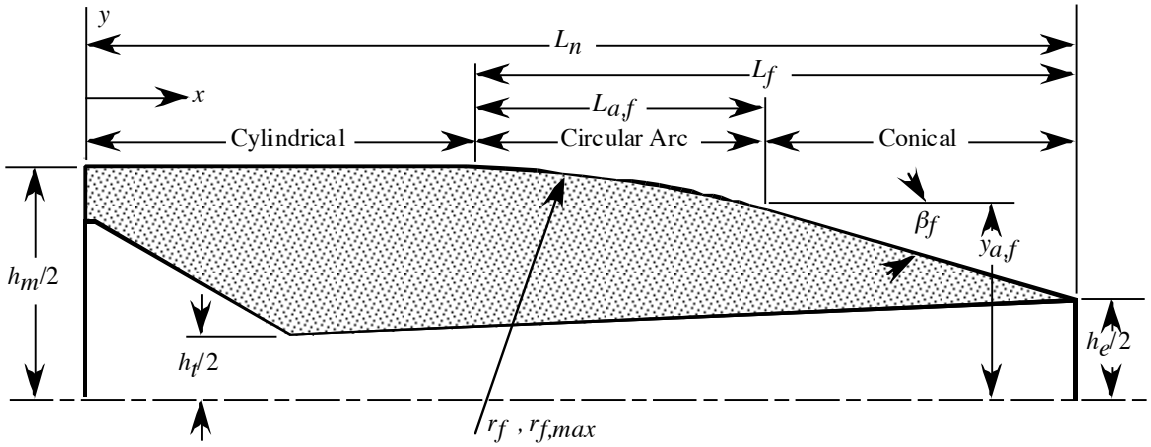

	Flap					
Parameter	F1	F2	F3	F4	F5	F6
$r_f/r_{f,max}$	0.4	0.1	0	1	0.4	0.1
β_f, *deg*	16.38	12.88	11.72	23.44	20.30	15.97
L_f/h_m	1.4	1.4	1.4	1.4	1.1	1.1
L_n, *in.*	13.136	13.136	13.136	13.136	13.136	13.136
L_f, *in.*	8.423	8.423	8.423	8.423	6.739	6.739
$L_{a,f}$, *in.*	4.856	1.548	0.0	8.423	3.904	1.245
$y_{a,f}$, *in.*	2.401	2.925	3.100	1.353	2.401	2.925
$r_{f,max}$, *in.*	43.059	69.421	83.835	21.179	28.142	45.254
r_f, *in.*	17.224	6.942	0	21.179	11.257	4.525

Figure 3. Definition of nozzle flap geometric parameters. All linear dimensions in inches.

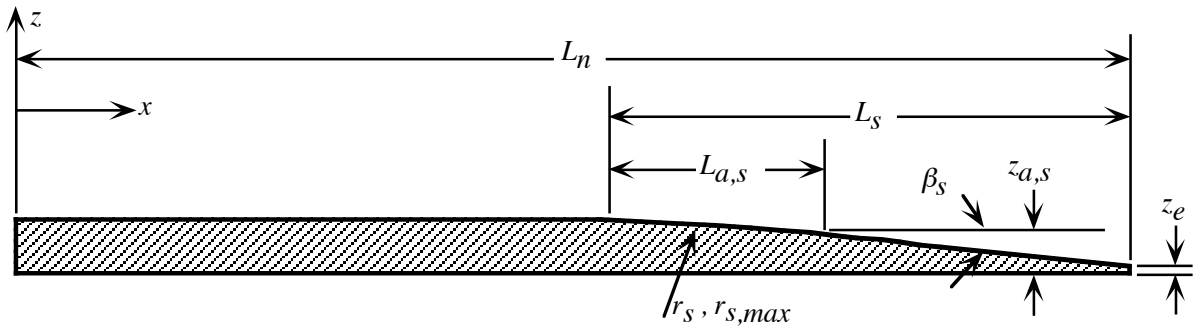

	Sidewall							
Parameter	S1	S2	S3	S4	S5	S6	S7	S8
β_s, *deg*	4.0	6.0	8.0	6.0	8.0	6.0	8.0	4.0
$r_s/r_{s,max}$	0	0	0	0.1	0.1	0.4	1.0	0
L_n, *in.*	13.136	13.136	13.136	13.136	13.136	13.136	13.136	13.136
L_s, *in.*	9.055	6.024	4.505	6.630	4.960	7.357	9.055	9.055
$L_{a,s}$, *in.*	0	0	0	1.208	0.906	4.209	9.055	0.000
$z_{a,s}$, *in.*	0.654	0.654	0.654	0.590	0.590	0.433	0.020	0.654
z_e, *in.*	0.020	0.020	0.020	0.020	0.020	0.102	0.020	0.020
$r_{s,max}$, *in.*	259.96	115.53	104.34	115.65	65.10	100.73	65.10	260.09
r_s, *in.*	0	0	0	11.565	6.510	40.292	65.102	0

Figure 4. Definition of nozzle sidewall geometric parameters. All linear dimensions in inches.

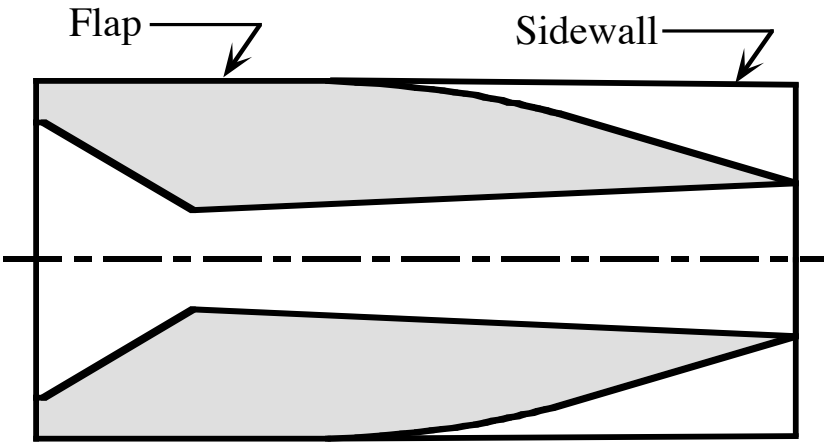

Nozzle	Nozzle Flap				Nozzle Sidewall		
	Flap	$r_f/r_{f,max}$	β_f, deg	L_f/h_m	Sidewall	β_s, deg	r_s
N3	F3	0	11.72	1.4	S1	4	0
N2	F2	0.1	12.88	1.4	S1	4	0
N1	F1	0.4	16.38	1.4	S1	4	0
N4	F4	1.0	24.44	1.4	S1	4	0
N14	F6	0.1	15.97	1.1	S1	4	0
N13	F5	0.4	20.30	1.1	S1	4	0
N5	F1	0.4	16.38	1.4	S2	6	0
N7	F1	0.4	16.38	1.4	S4	6	0.1
N9	F1	0.4	16.38	1.4	S6	6	0.4
N6	F1	0.4	16.38	1.4	S3	8	0
N8	F1	0.4	16.38	1.4	S5	8	0.1
N10	F1	0.4	16.38	1.4	S7	8	1.0
N12	F2	0.1	12.88	1.4	S8	4	0
N11	F1	0.4	16.38	1.4	S8	4	0

Figure 5. Summary of nozzle configurations tested.

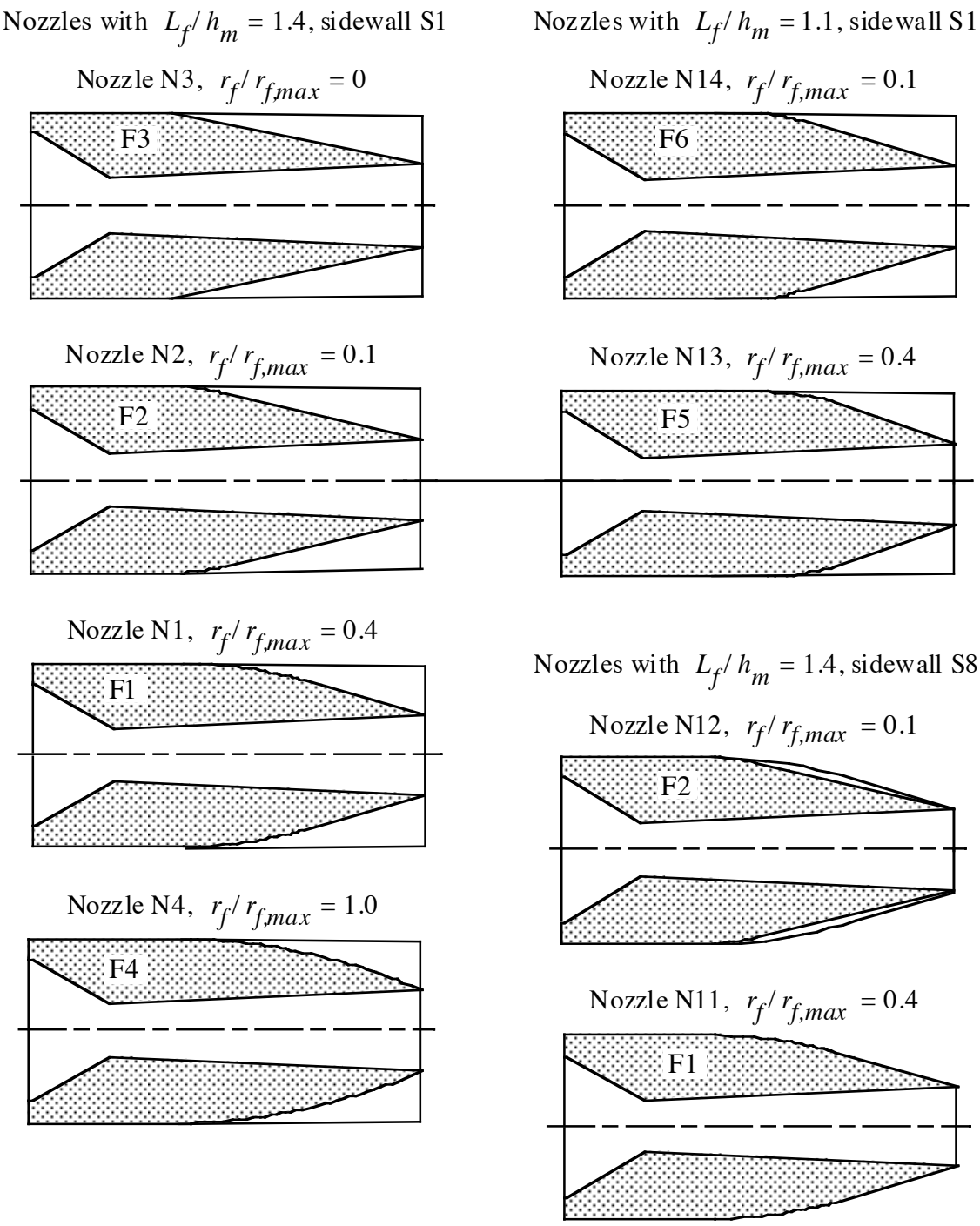

Figure 6. Sketches of nozzle configurations where the flap was varied.

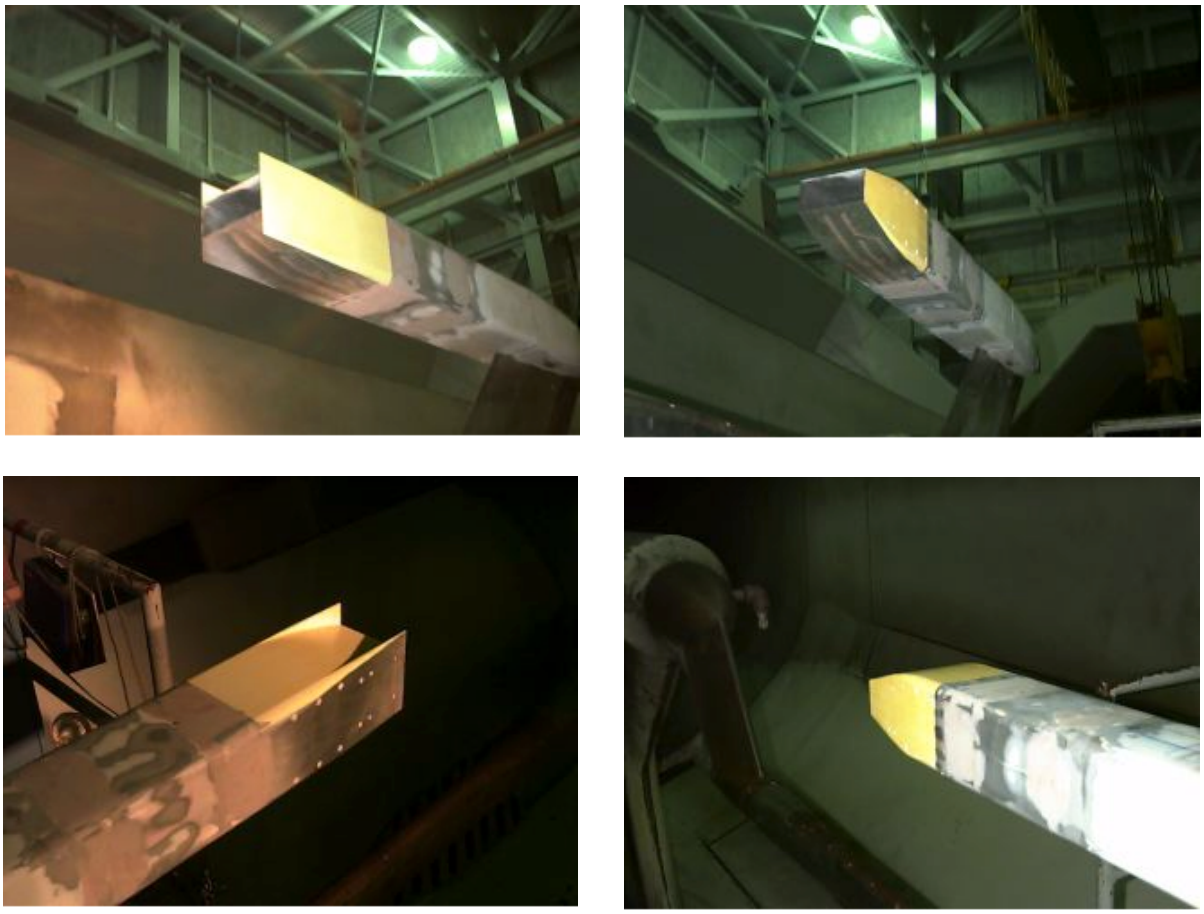

Figure 7. Photographs of nozzles N1 and N11.

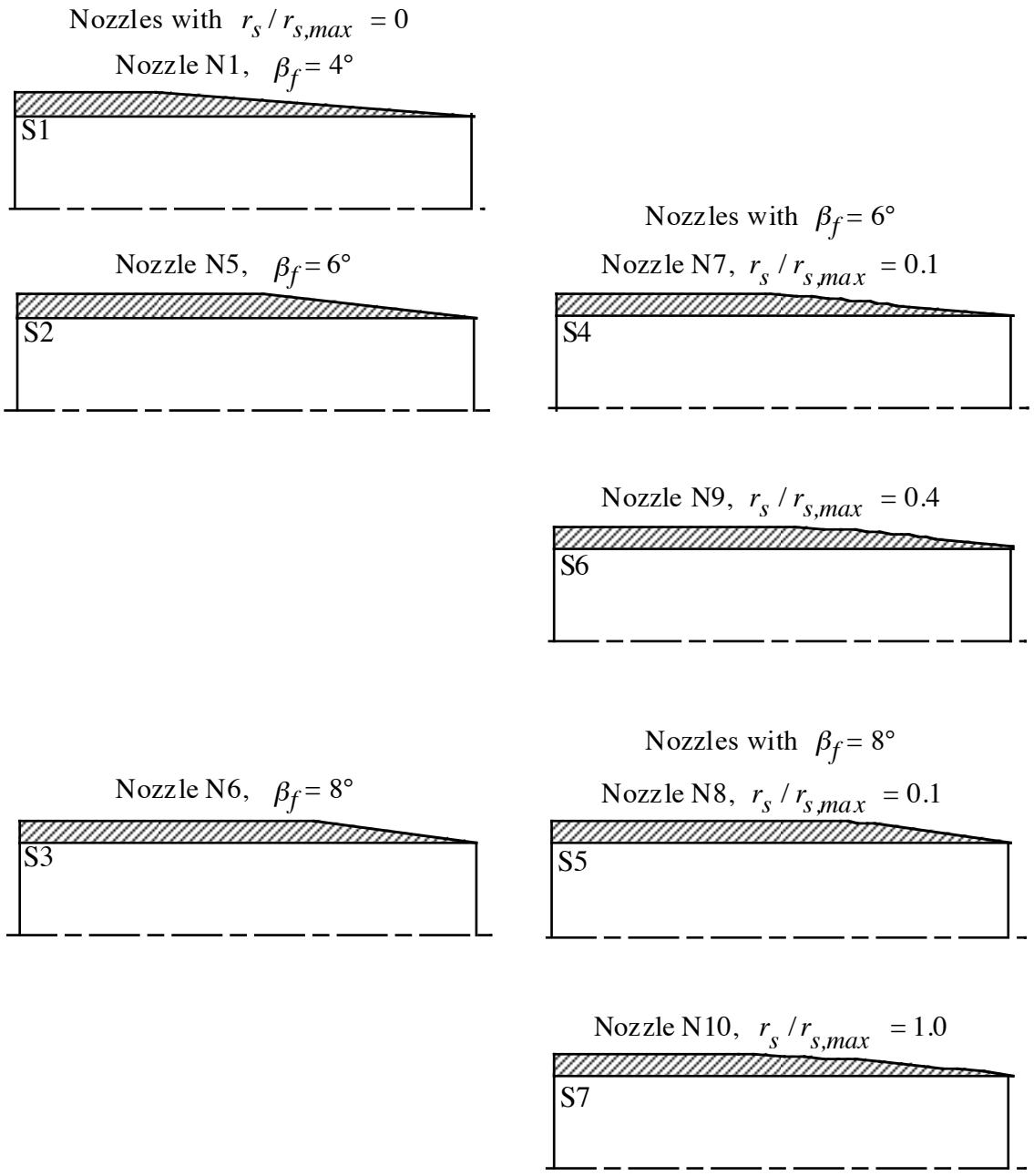

Figure 8. Sketches of nozzle configurations where sidewall was varied.

	Nozzle	Flap	L_f/h_m	$r_f/r_{f,max}$	β_f, deg	Sidewall	$r_s/r_{s,max}$	β_s, deg
○	N1	F1	1.4	0.4	16.38	S1	0	4.0
□	N2	F2	1.4	0.1	12.88	S1	0	4.0
◇	N3	F3	1.4	0	11.72	S1	0	4.0
△	N4	F4	1.4	1.0	23.48	S1	0	4.0
◺	N5	F1	1.4	0.4	16.38	S2	0	6.0
◺	N6	F1	1.4	0.4	16.38	S3	0	8.0
⏢	N7	F1	1.4	0.4	16.38	S4	0.1	6.0
◇	N8	F1	1.4	0.4	16.38	S5	0.1	8.0
◊	N9	F1	1.4	0.4	16.38	S6	0.4	6.0
⏢	N10	F1	1.4	0.4	16.38	S7	1.0	8.0
⊙	N11	F1	1.4	0.4	16.38	S8	0	4.0
⊡	N12	F2	1.4	0.4	16.38	S8	0	4.0
◈	N13	F6	1.1	0.1	15.97	S1	0	4.0
◬	N14	F5	1.1	0.4	20.30	S1	0	4.0

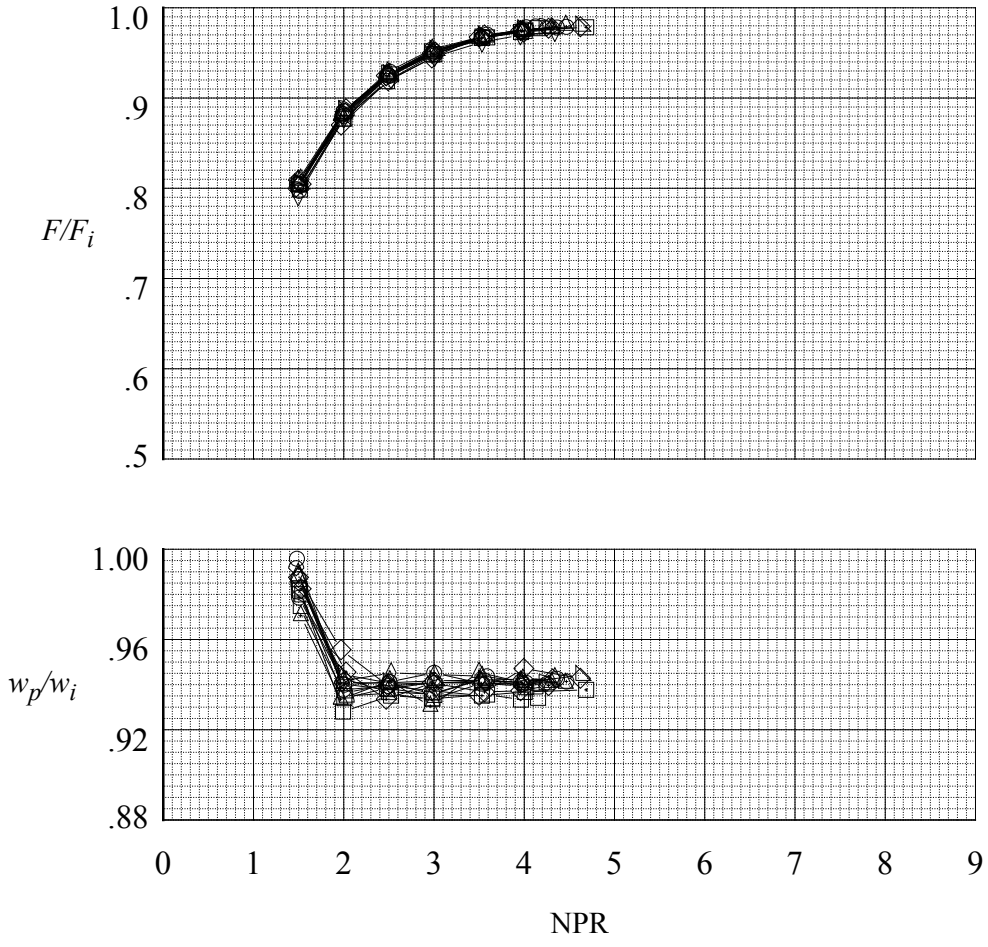

Figure 9. Static performance characteristics for all nozzles.

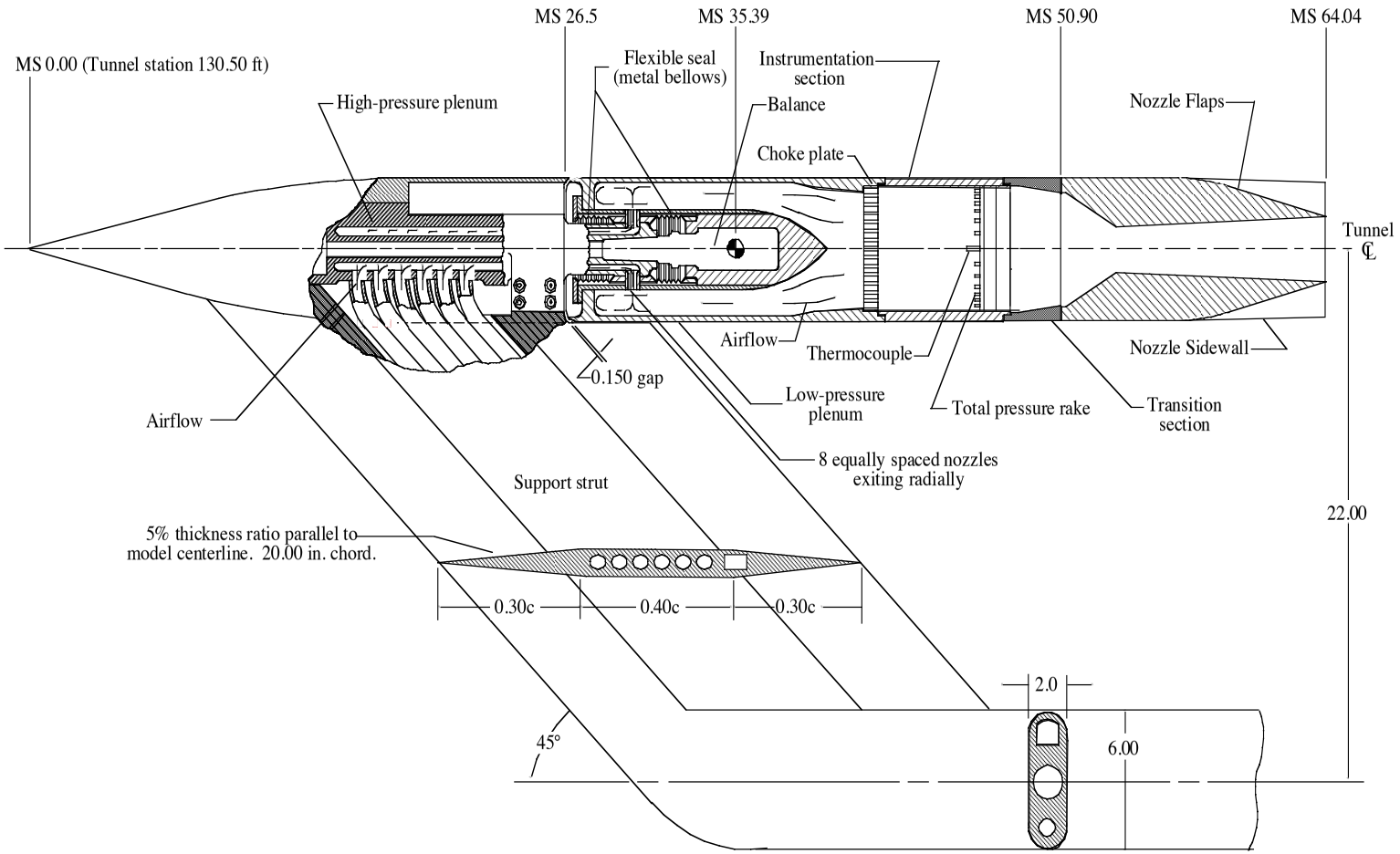

Figure10. Propulsion simulation system with typical nozzle configuration installed. All linear dimensions are given in inches.

Figure 11. Model with nozzle N1 installed in the 16-Foot Transonic Tunnel.

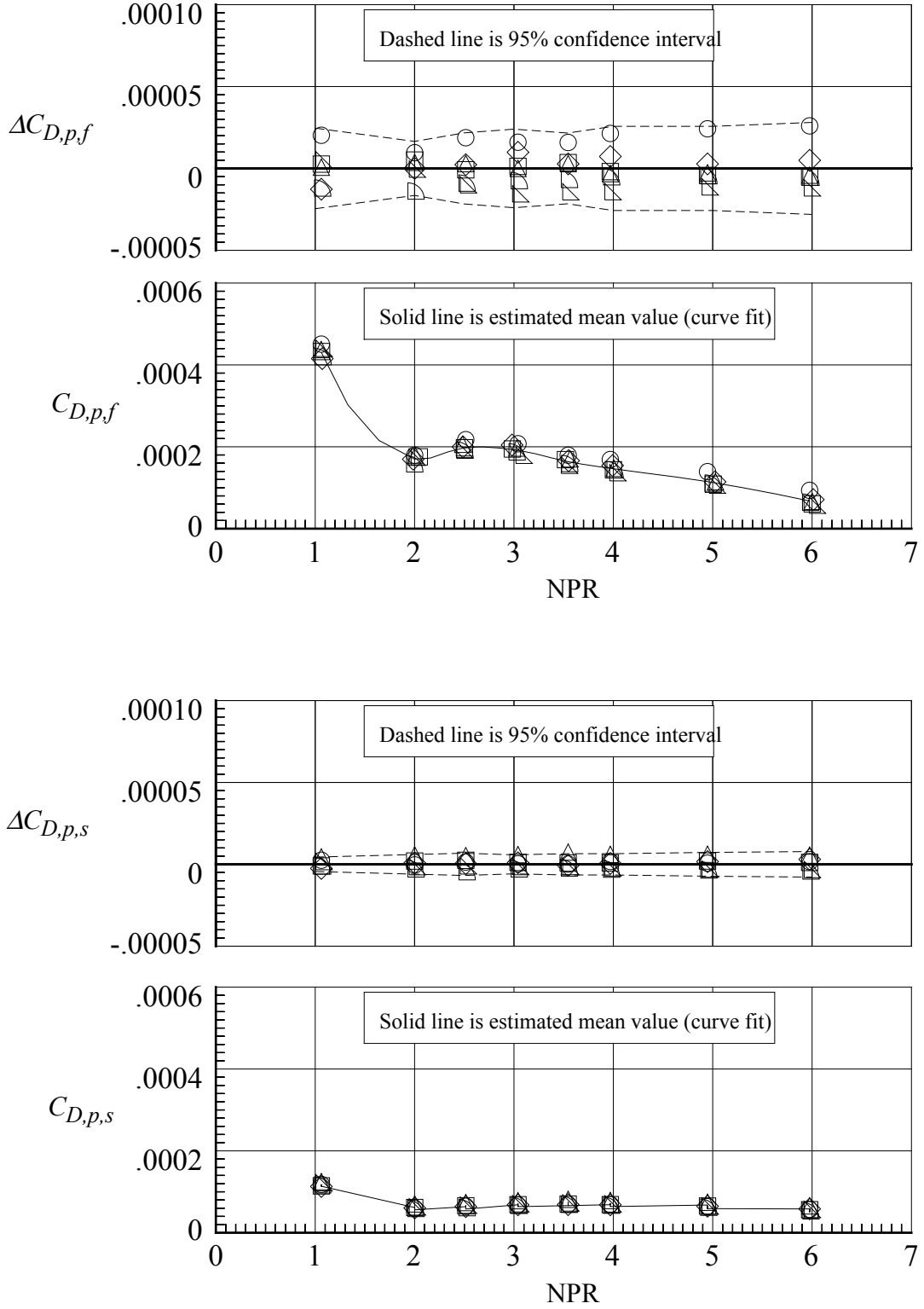

Figure 12. Short term repeatability for flap and sidewall pressure drag coefficients for nozzle N1, $M = 0.90$.

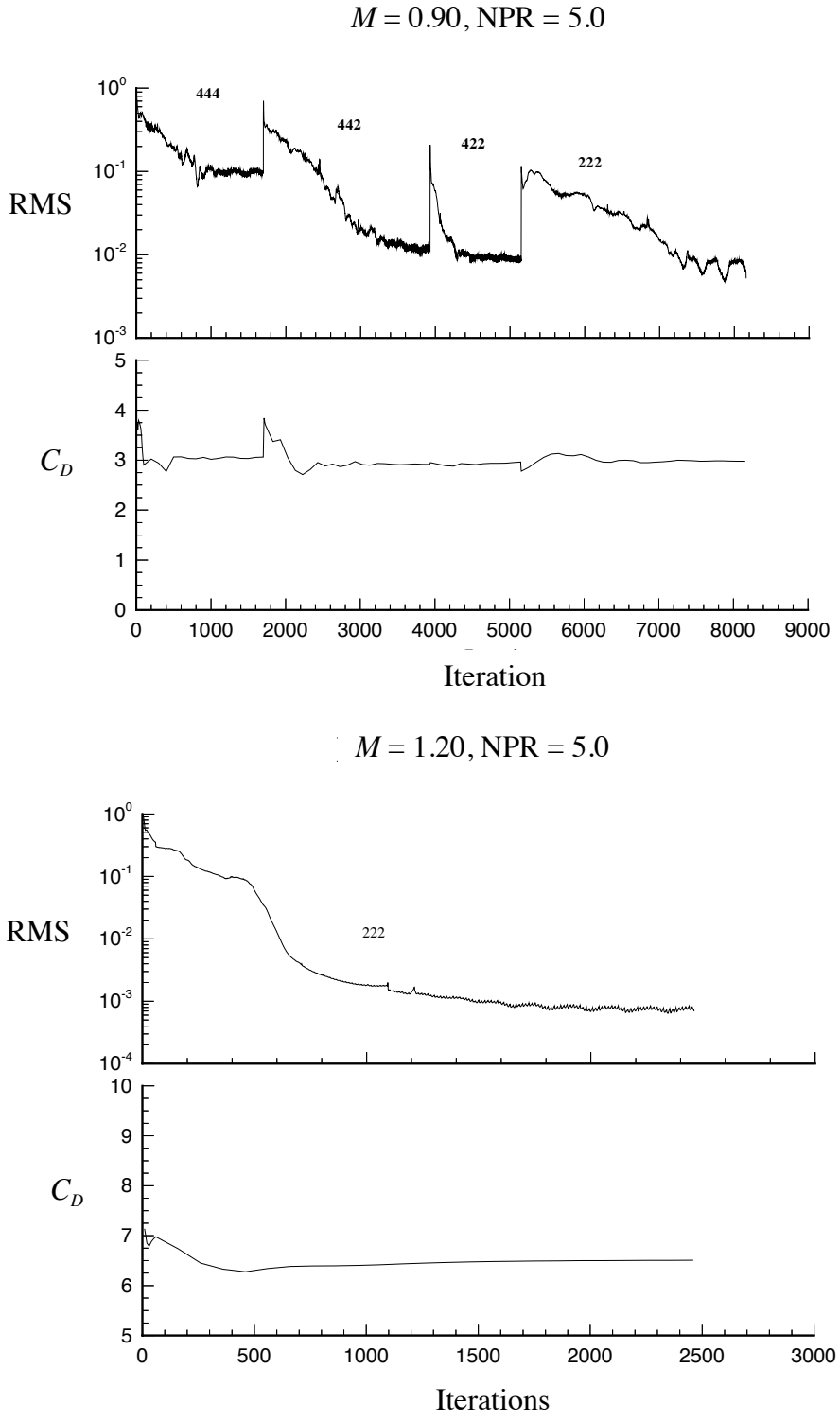

Figure 13. Residual and drag coefficient convergence history for nozzle N3.

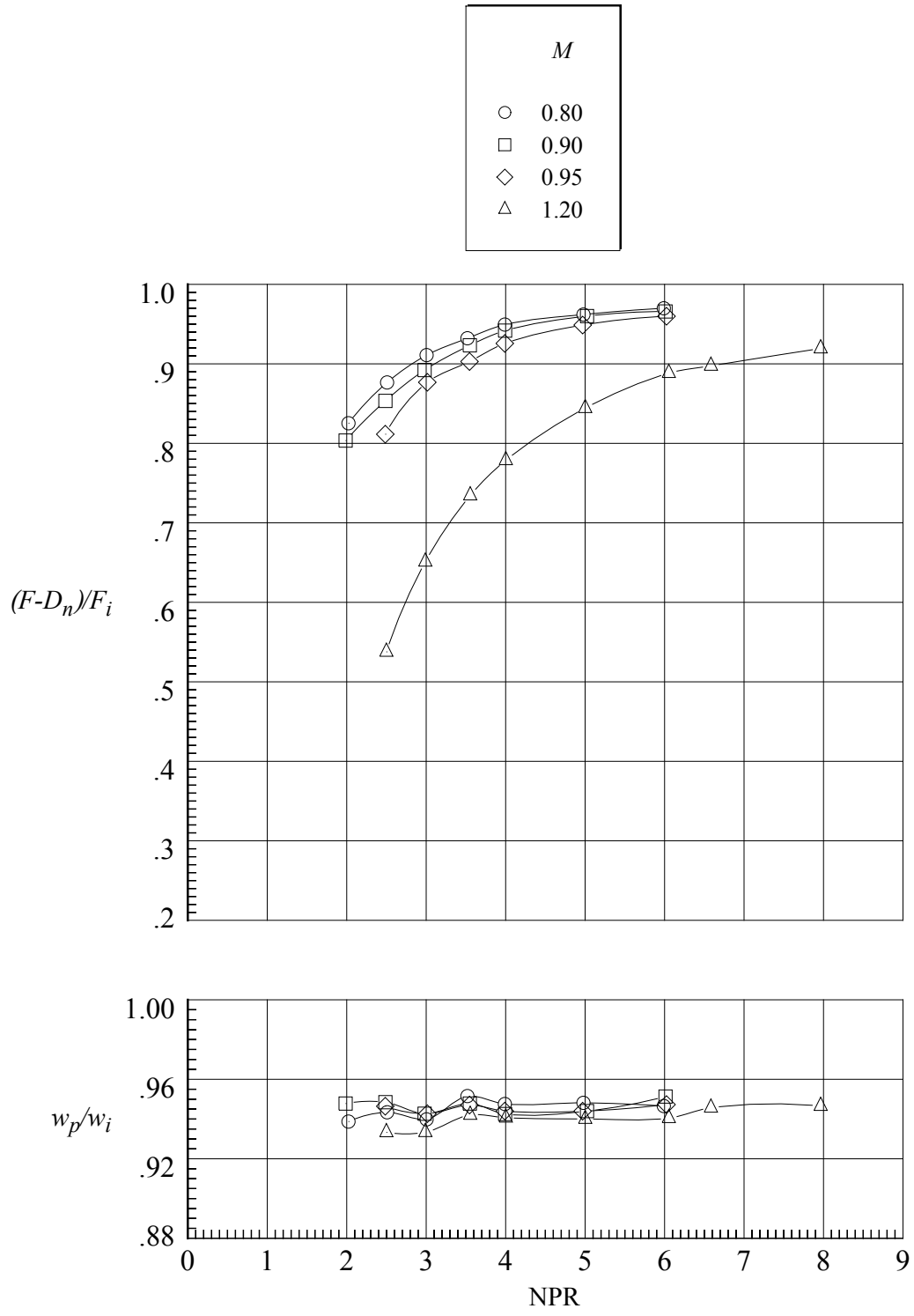

(a) Variation of $(F\text{-}D_n)/F_i$ and w_p/w_i.

Figure 14. Aeropropulsive performance for nozzle N1 with flap F1 and sidewall S1.
$r_f/r_{f,max} = 0.4$; $\beta_f = 16.38°$; $L_f/h_m = 1.4$; $\beta_s = 4.0°$; $r_s/r_{s,max} = 0$.

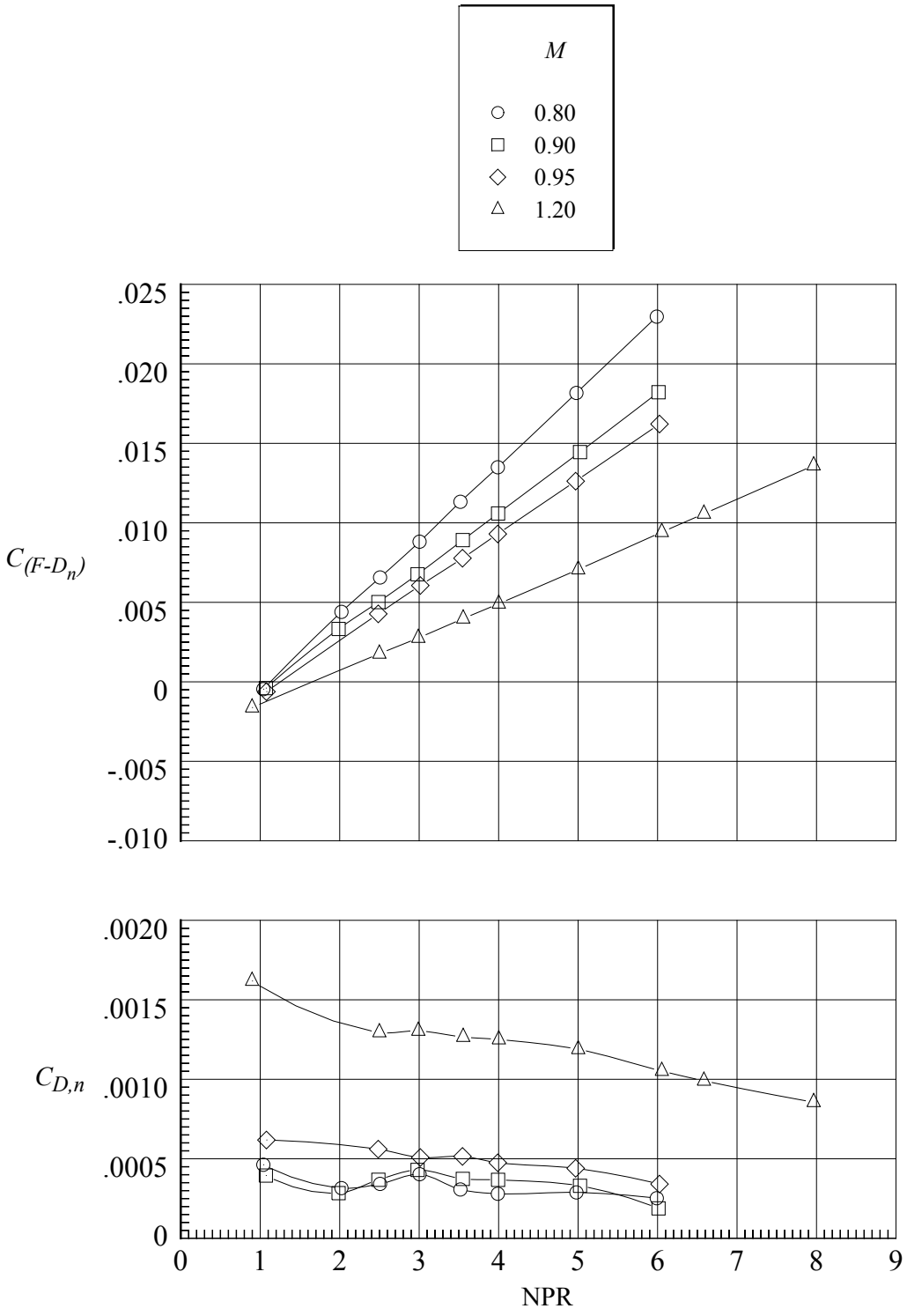

(b) Variation of $C_{(F\text{-}D_n)}$ and $C_{D,n}$.

Figure 14. Continued.

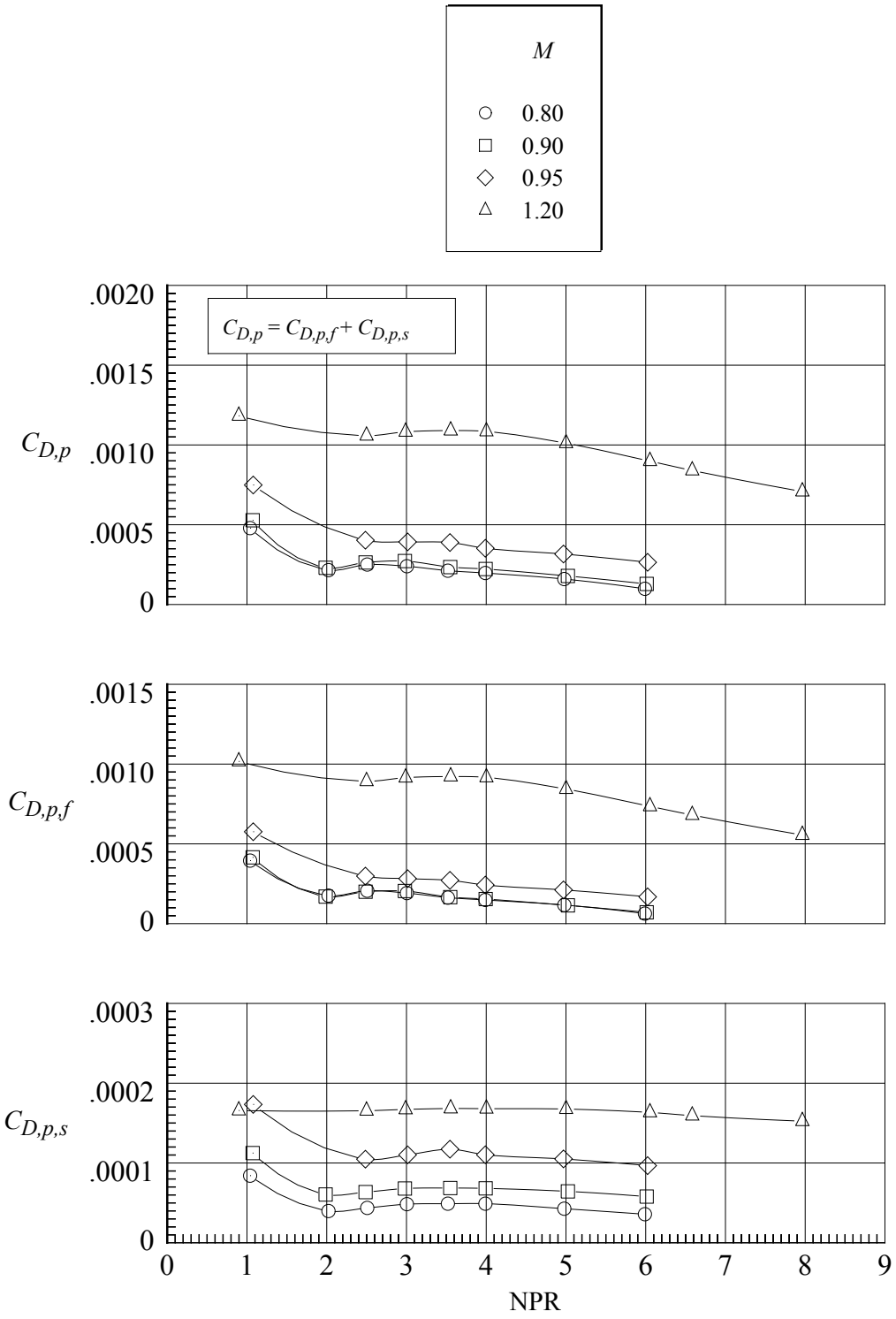

(c) Variation of $C_{D,p}$, $C_{D,p,f}$, and $C_{D,p,s}$.

Figure 14. Continued.

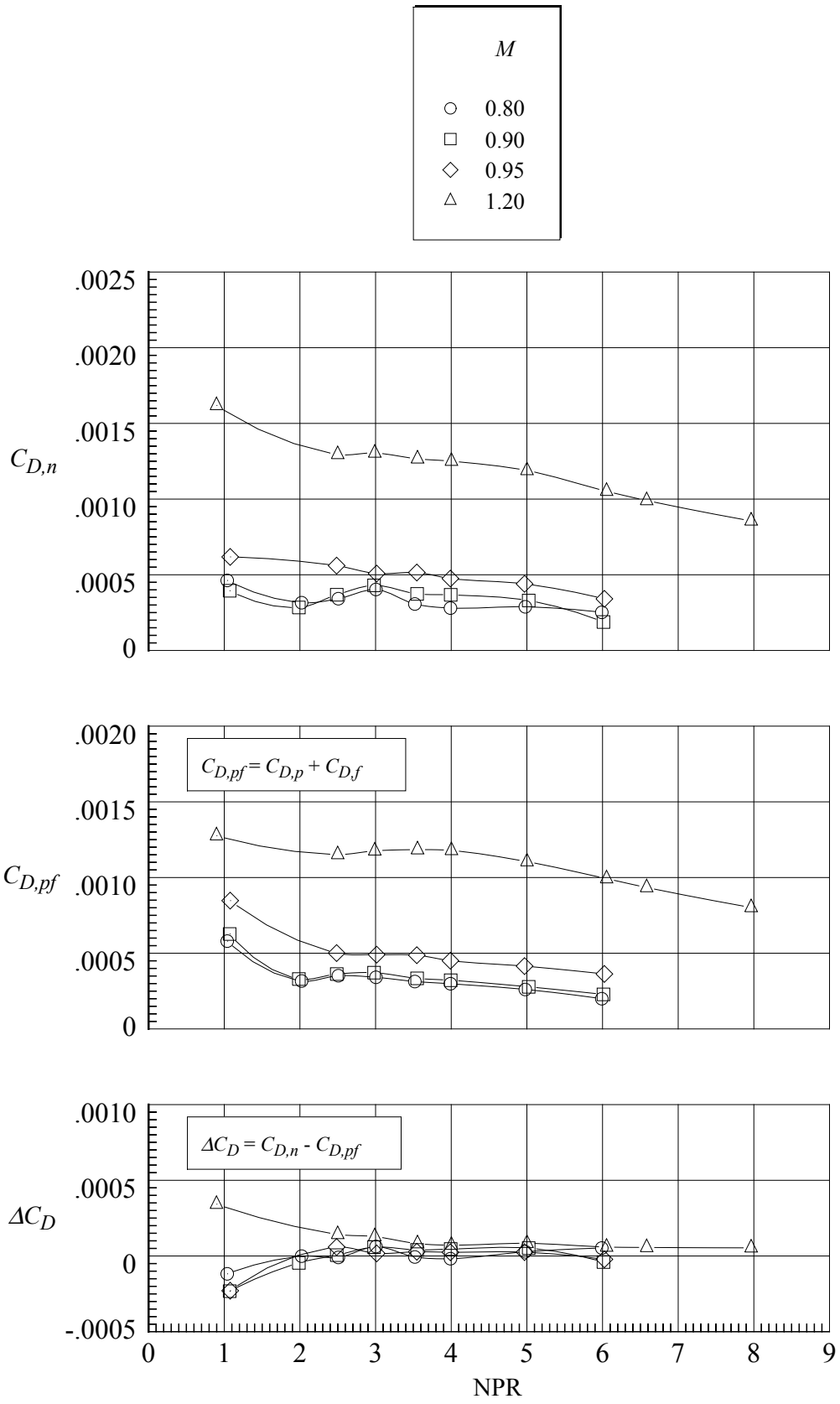

(d) Variation of $C_{D,n}$, $C_{D,pf}$, and ΔC_D.

Figure 14. Concluded.

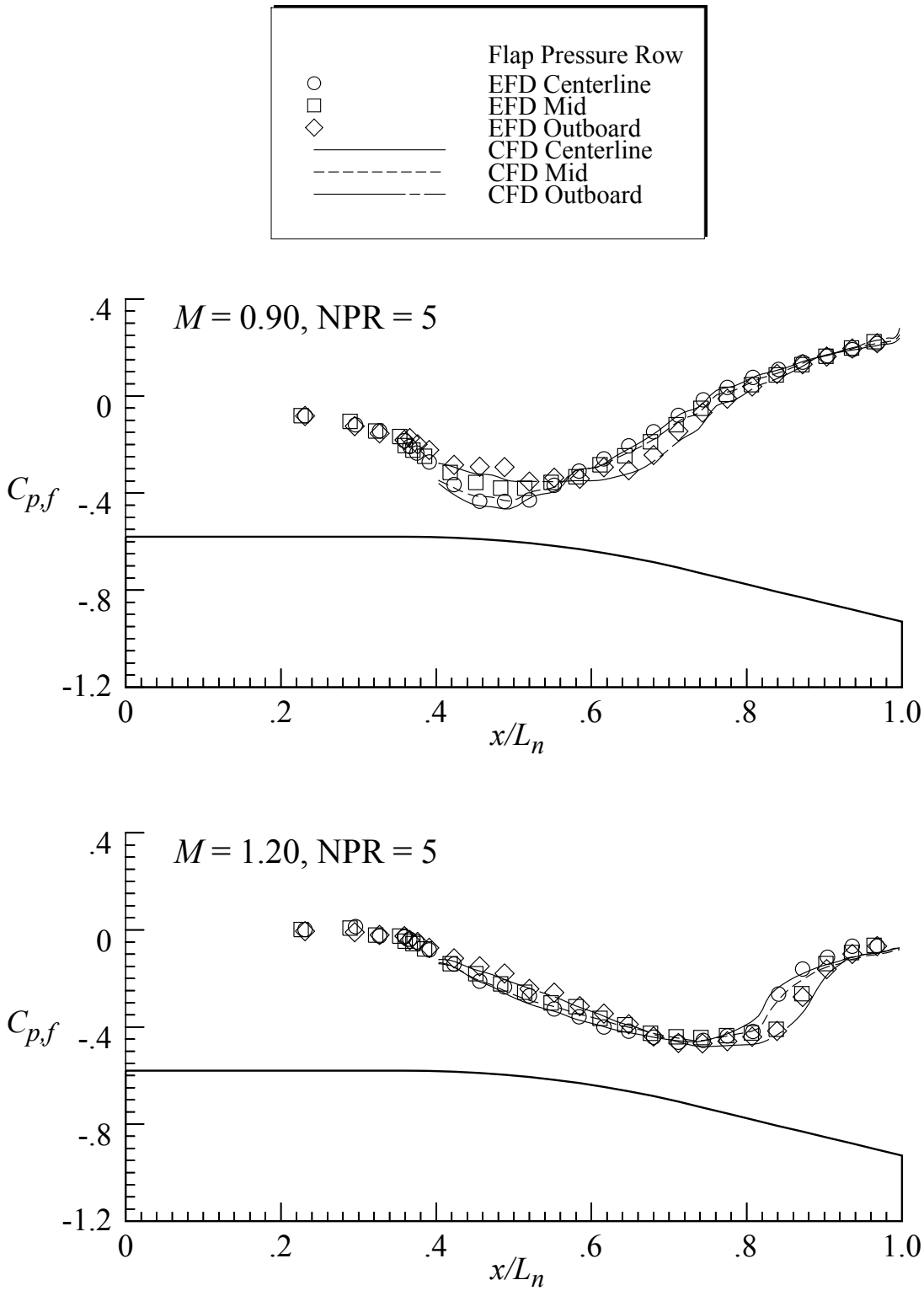

Figure 15. Comparison of experimental to predicted flap pressures for nozzle N1. $r_f/r_{f,max} = 0.4$; $\beta_f = 16.38°$; $L_f/h_m = 1.4$.

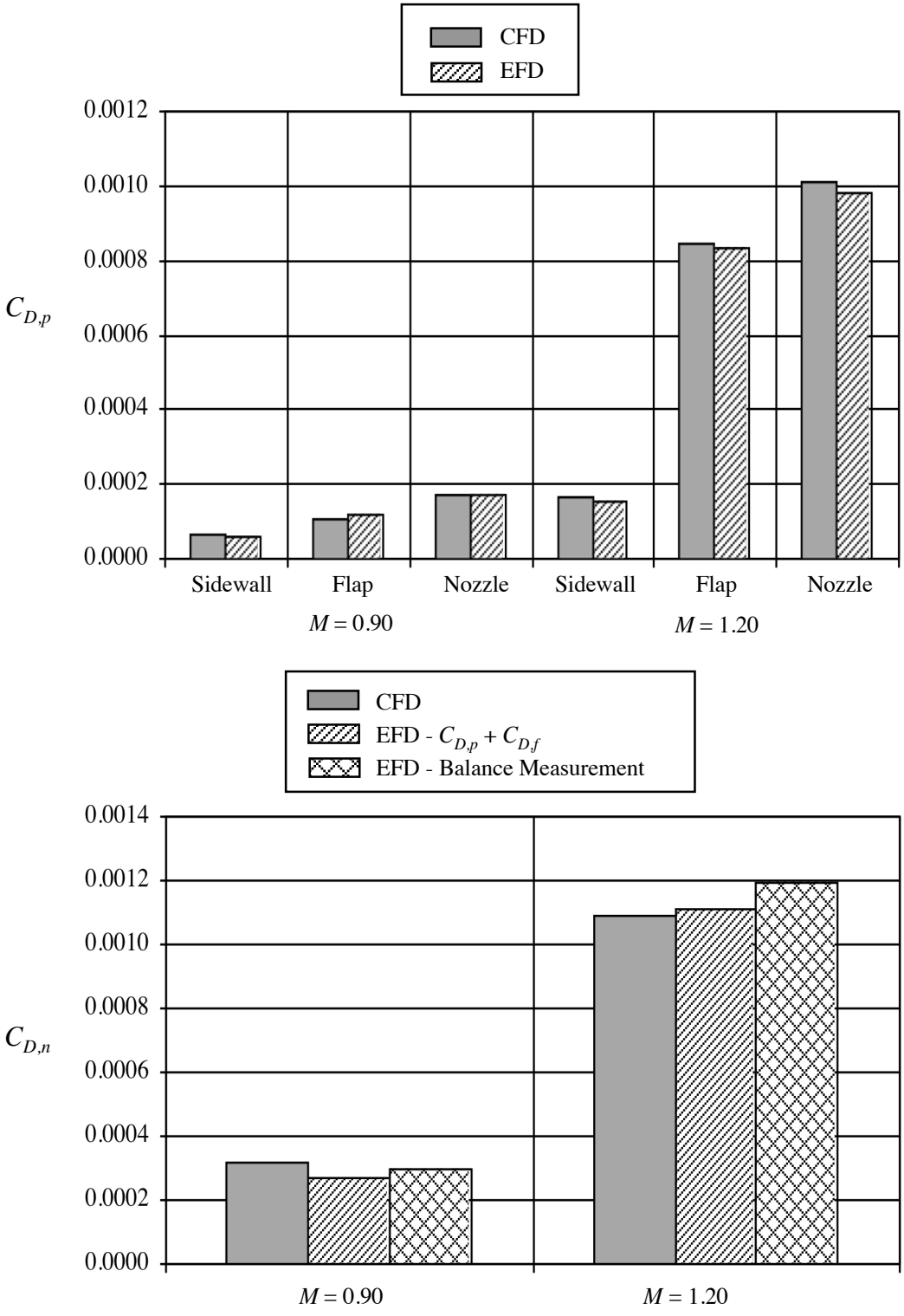

Figure 16. Comparison of experimental to predicted nozzle drag coefficients for nozzle N1. $r_f / r_{f,max} = 0.4$; $\beta_f = 16.38°$; $L_f / h_m = 1.4$; NPR = 5.0.

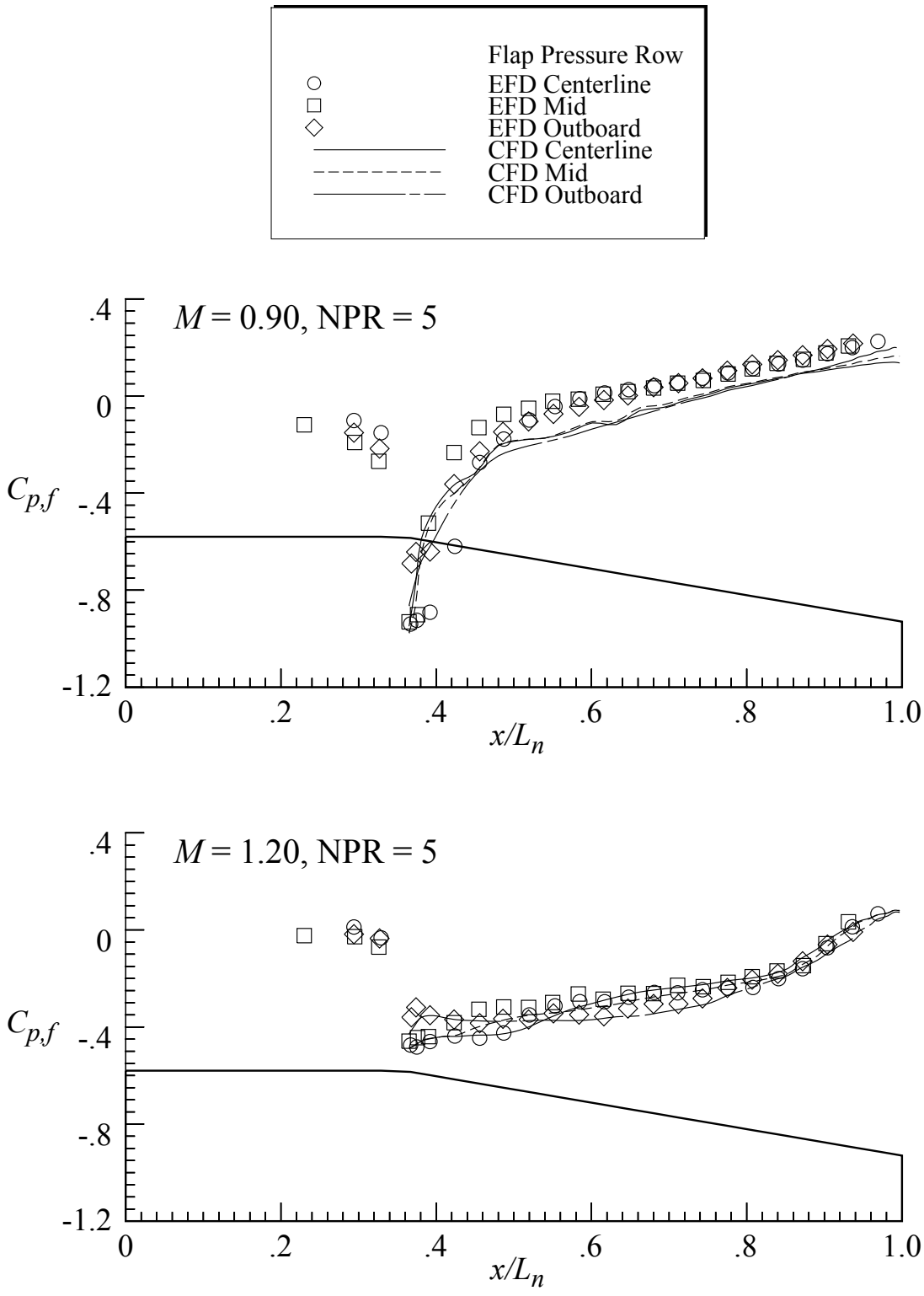

Figure 17. Comparison of experimental and predicted flap pressures for nozzle N3. $r_f/r_{f,max} = 0$; $\beta_f = 11.72°$; $L_f/h_m = 1.4$.

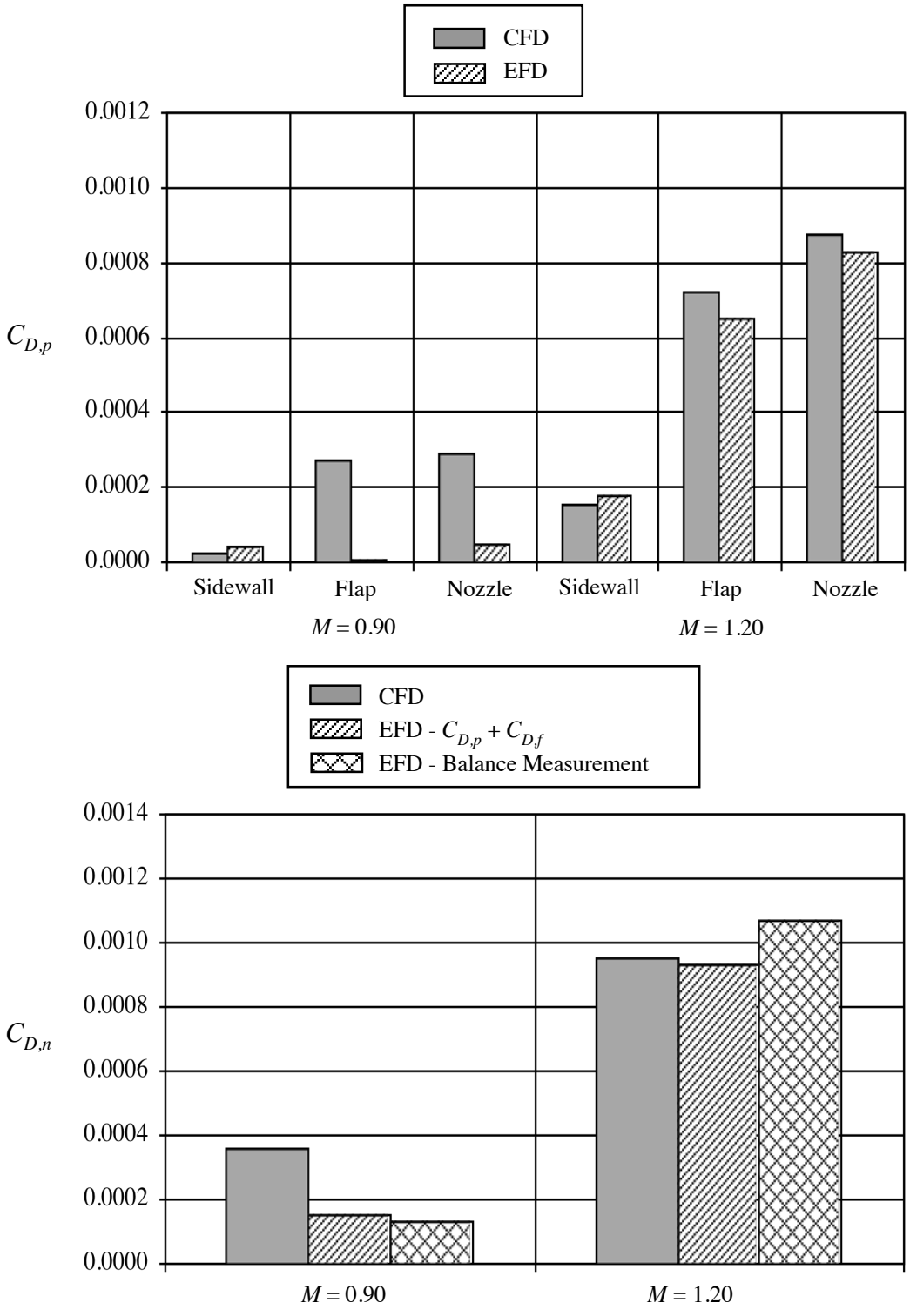

Figure 18. Comparison of experimental to predicted nozzle drag coefficients for nozzle N3. $r_f / r_{f,max} = 0$; $\beta_f = 11.72°$; $L_f / h_m = 1.4$; NPR = 5.0.

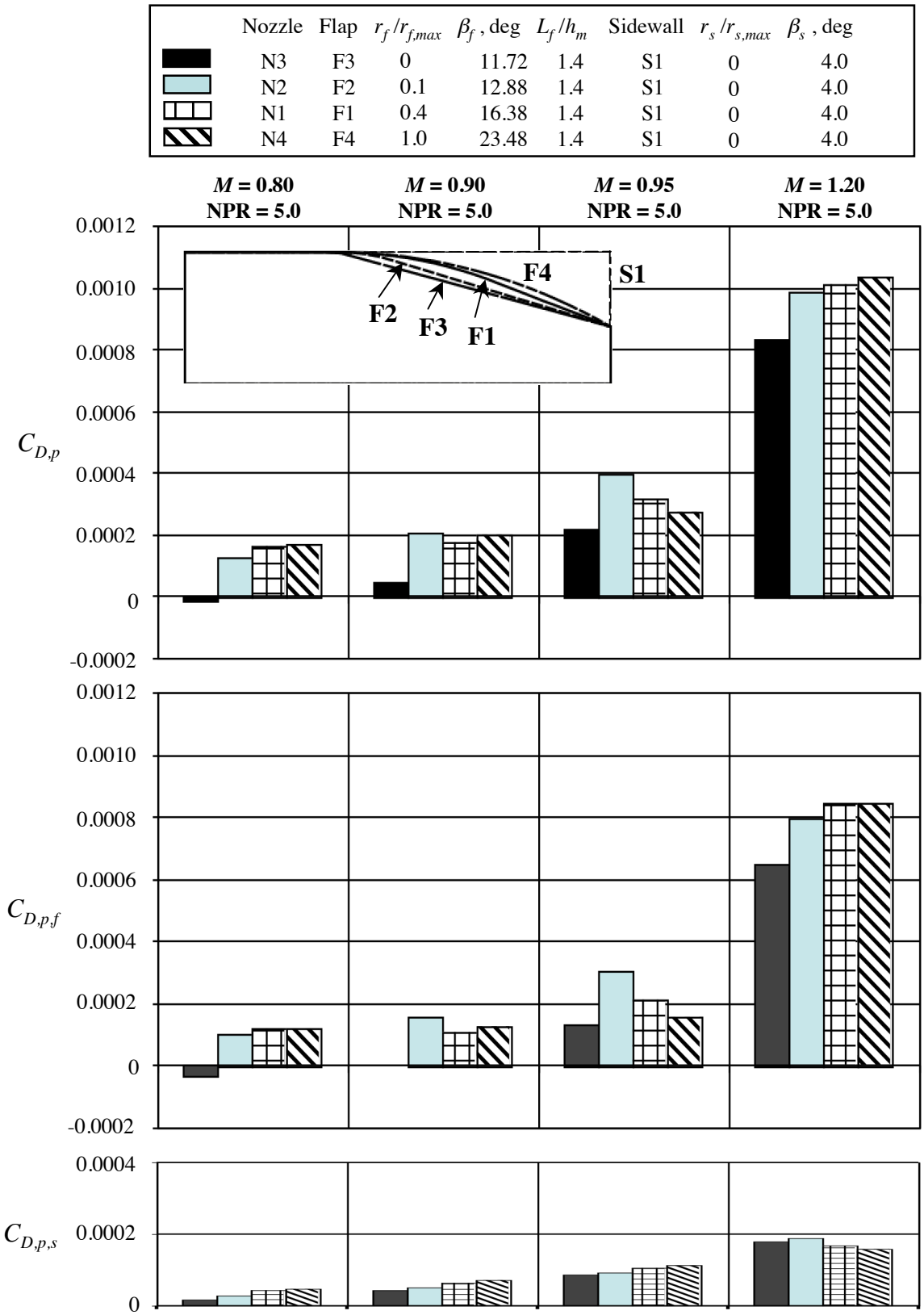

Figure 19. Effect of flap radius of curvature on pressure drag coefficients for nozzles with sidewall S1 at design NPR.

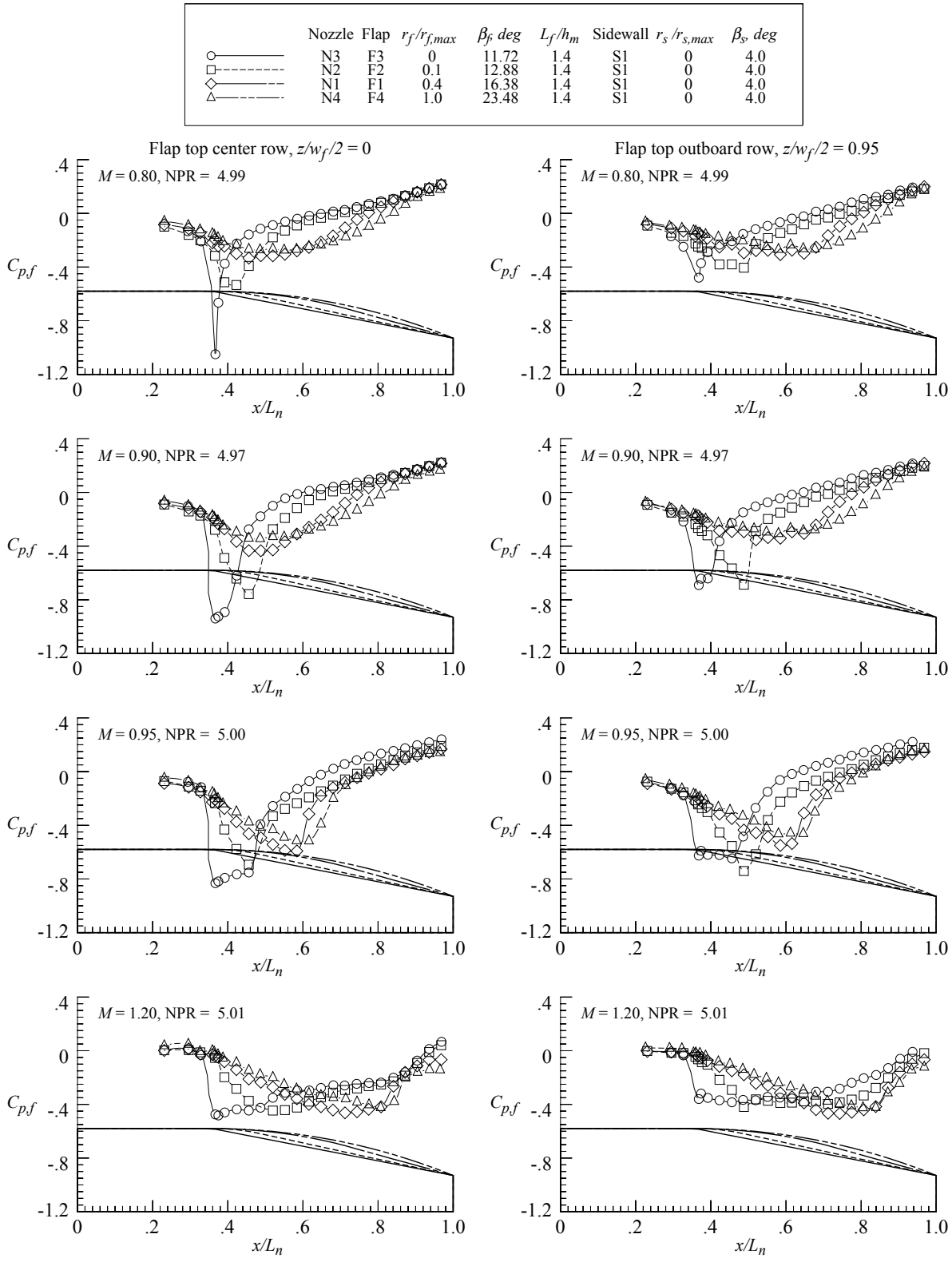

Figure 20. Effect of flap radius of curvature on upper flap pressure distributions for nozzles with sidewall S1 at design NPR.

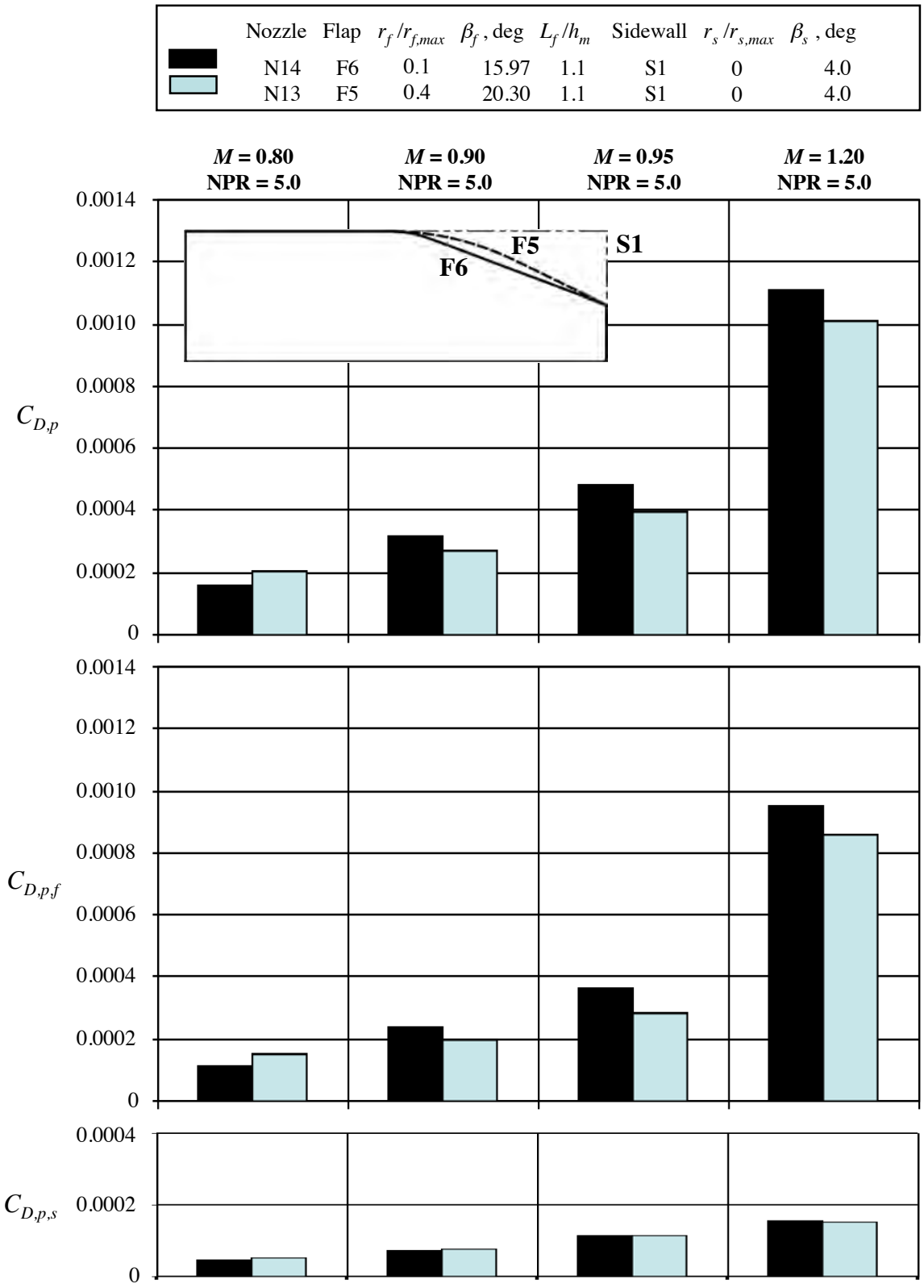

Figure 21. Effect of flap radius of curvature on pressure drag coefficients for nozzles with sidewall S1 at design NPR.

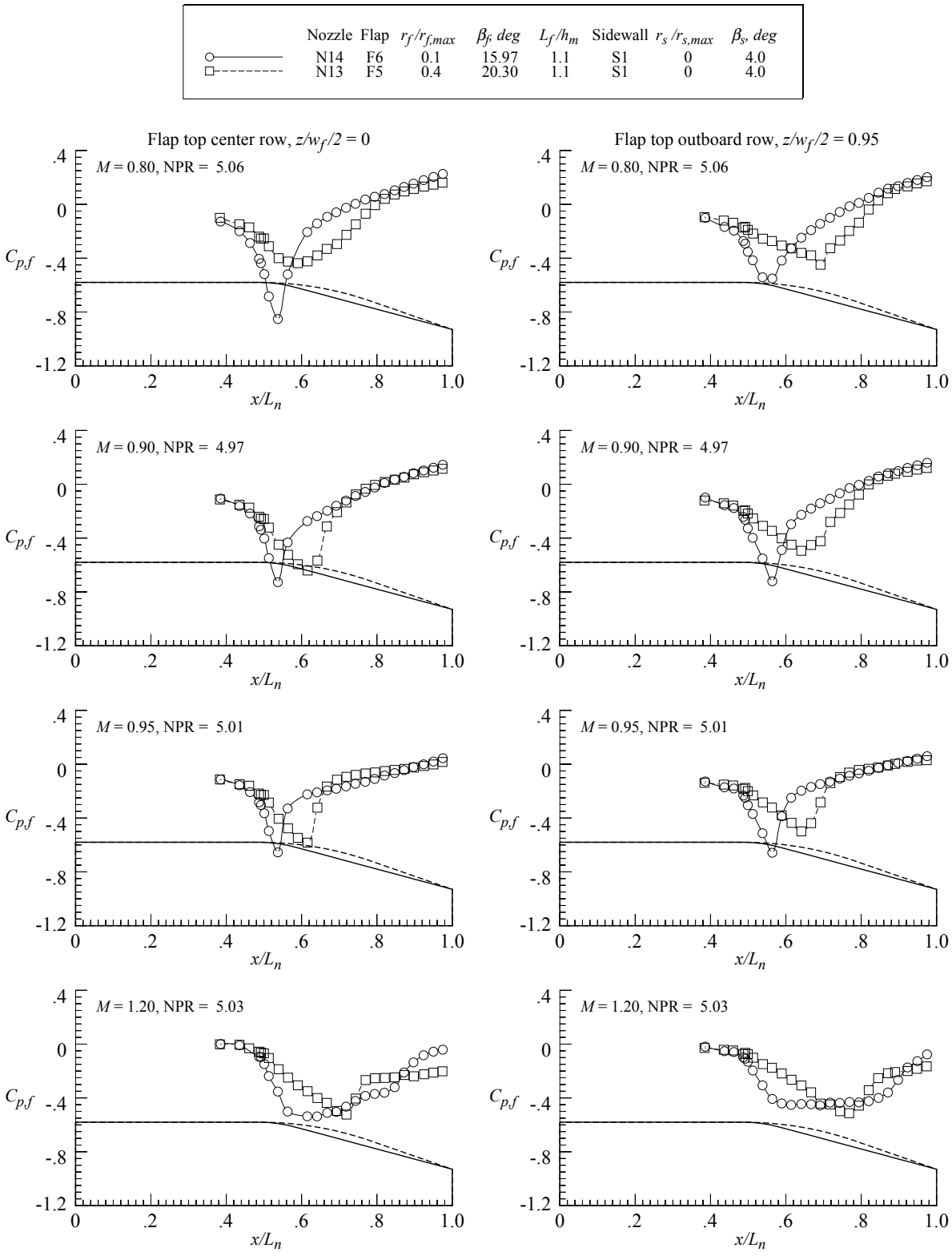

Figure 22. Effect of flap radius of curvature on upper flap pressure distributions for nozzles with sidewall S1 at design NPR.

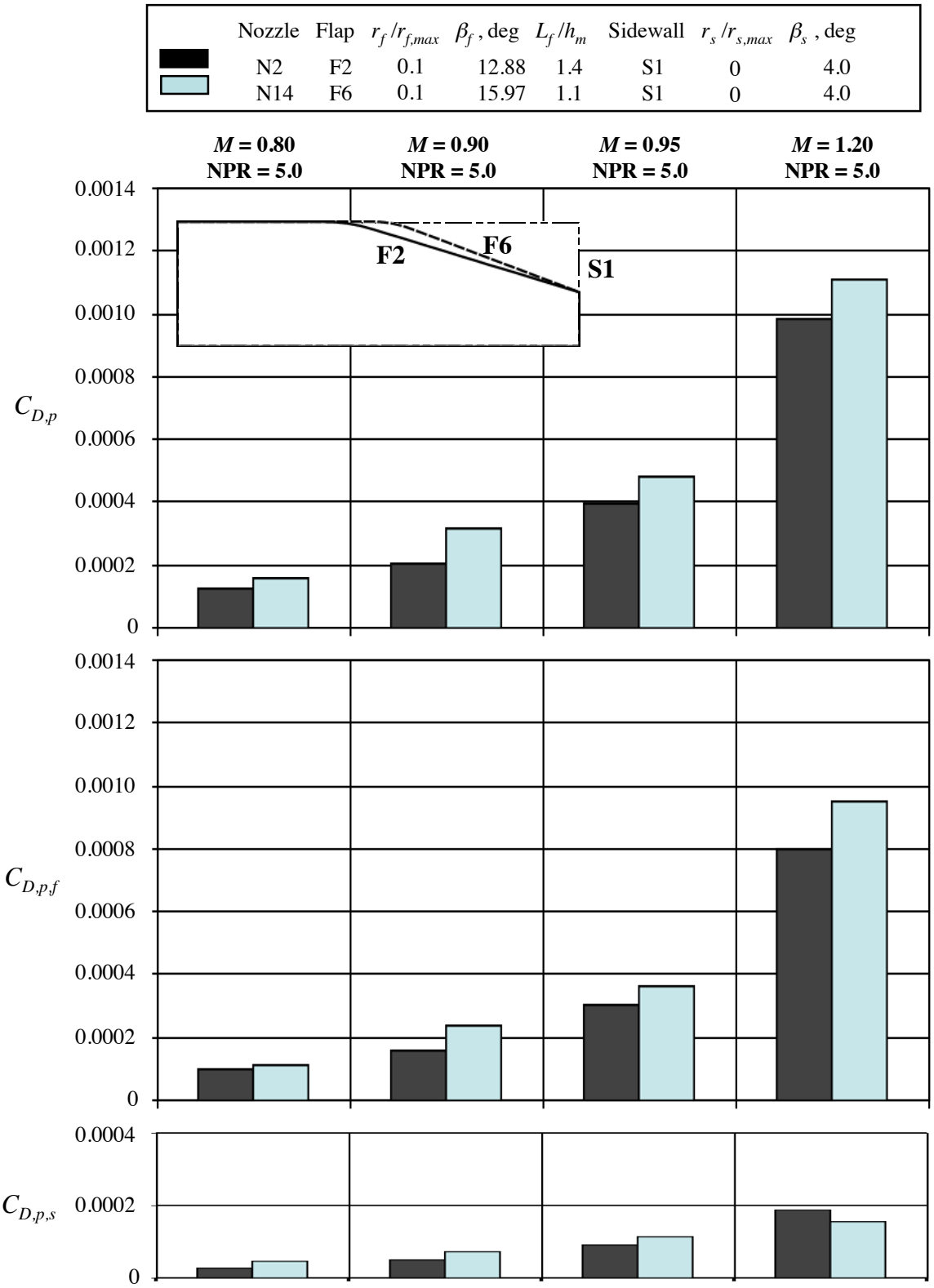

Figure 23. Effect of flap length on pressure drag coefficients for nozzles with sidewall S1 at design NPR.

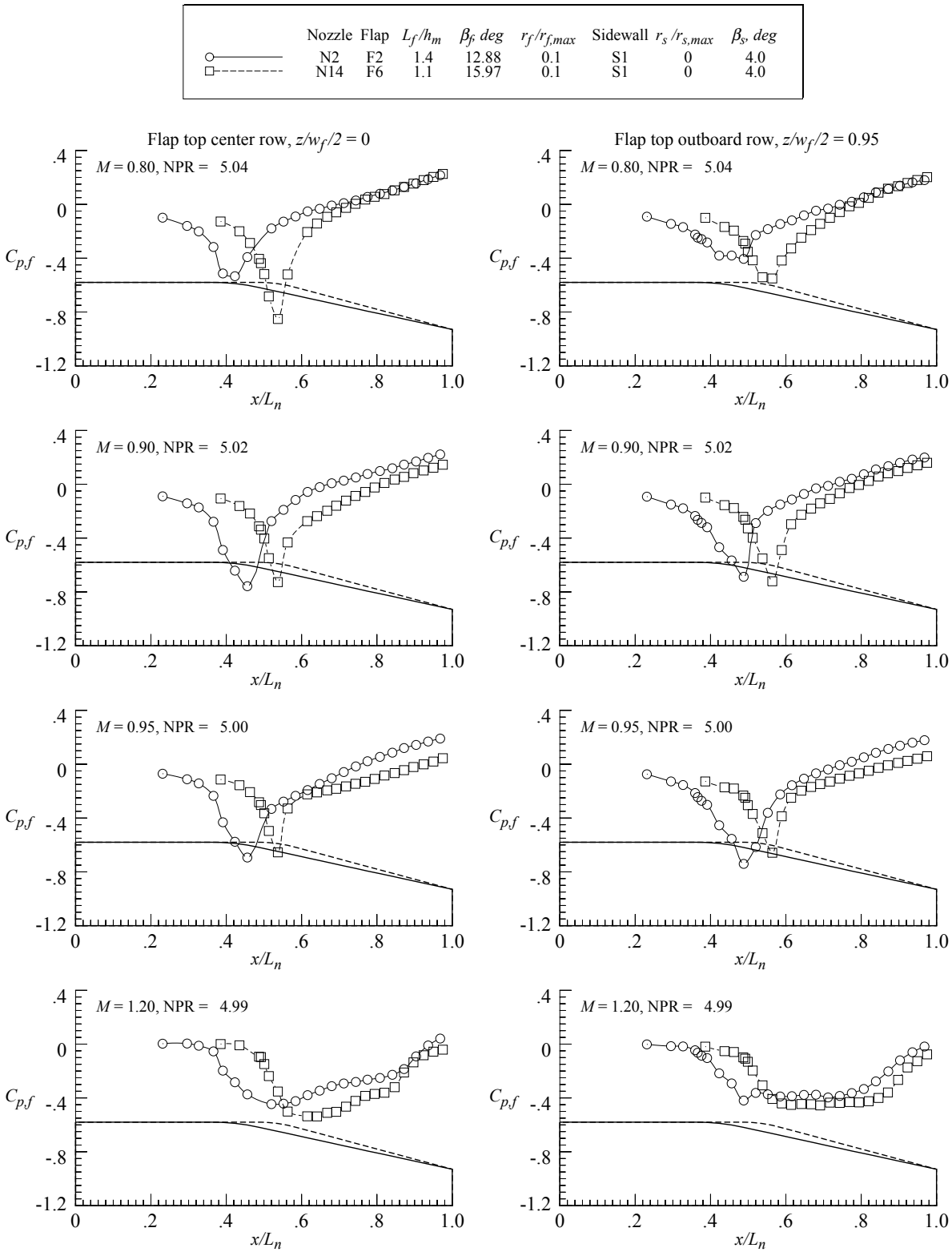

Figure 24. Effect of flap length on upper flap pressure distributions for nozzles with sidewall S1 at design NPR.

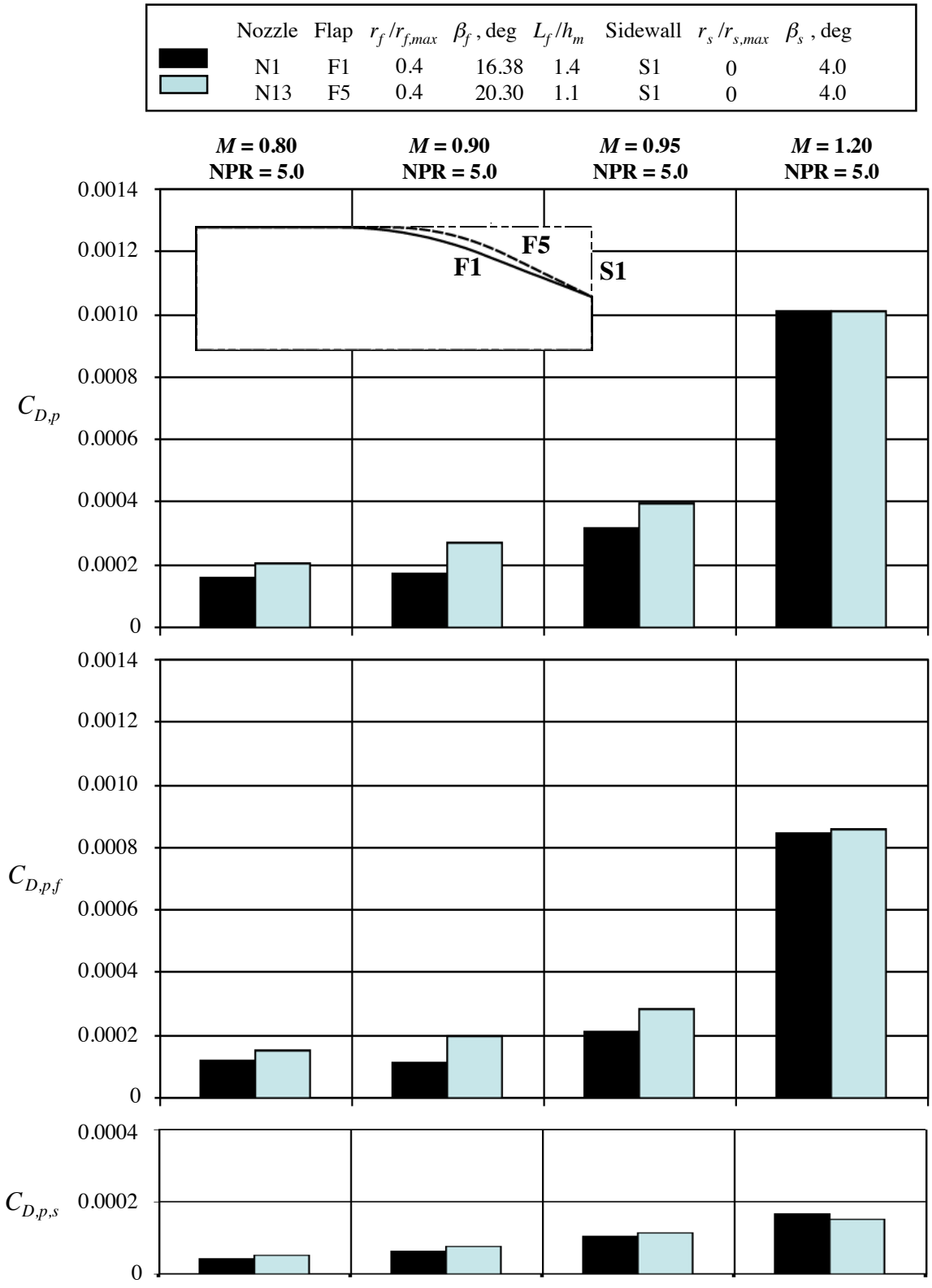

Figure 25. Effect of flap length on pressure drag coefficients for nozzles with sidewall S1 at design NPR.

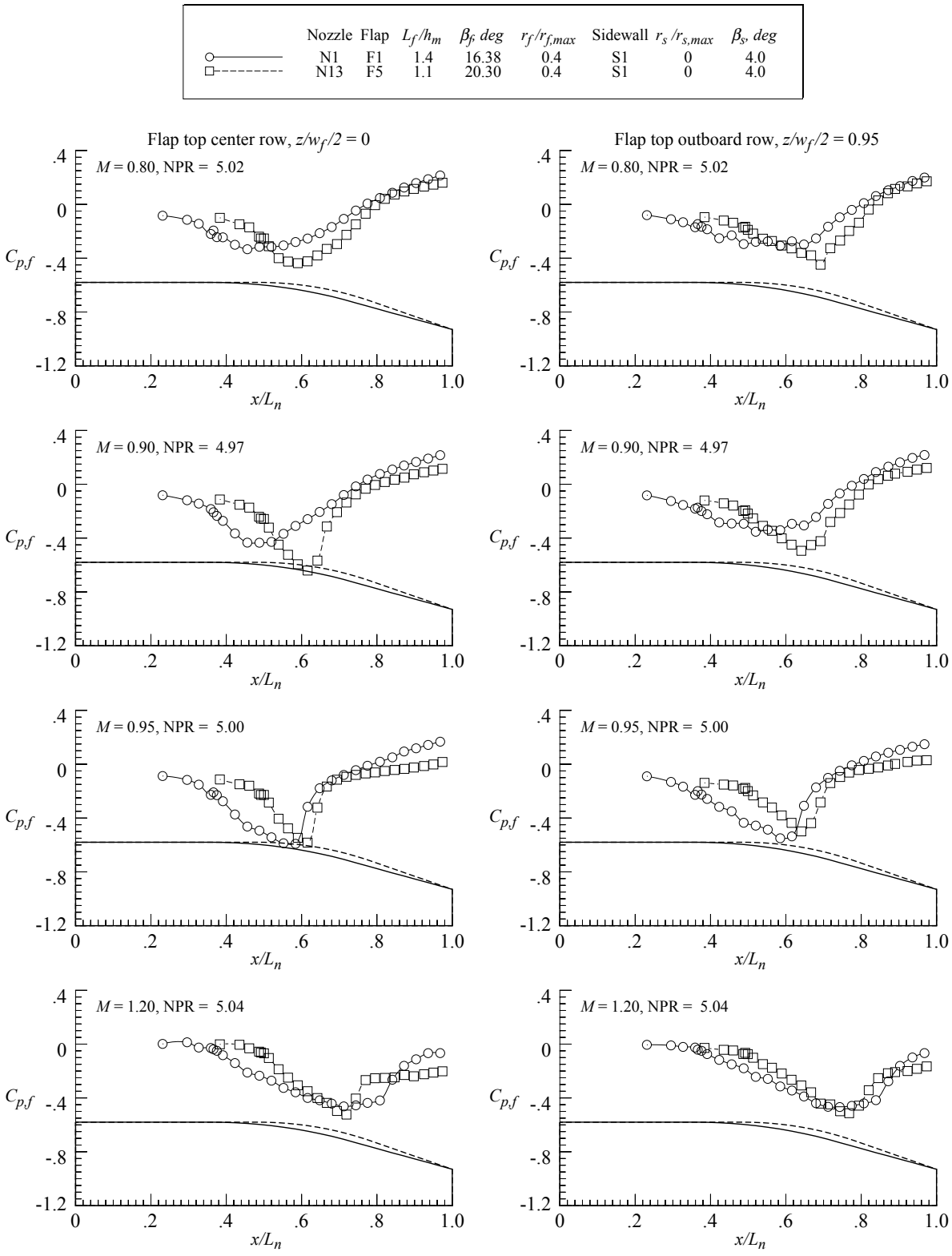

Figure 26. Effect of flap length on upper flap pressure distributions for nozzles with sidewall S1 at design NPR.

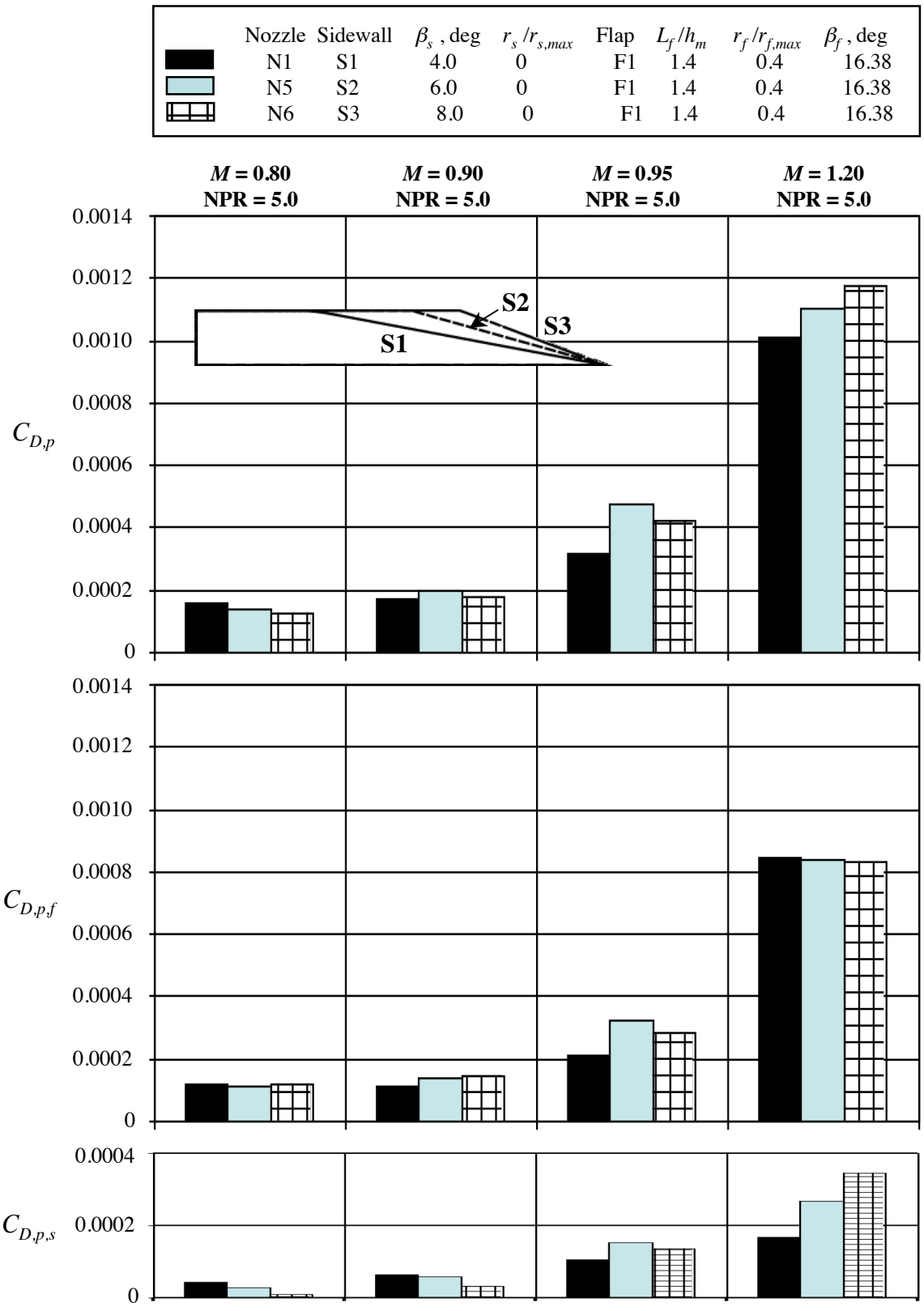

Figure 27. Effect of sidewall boattail angle on pressure drag coefficients for nozzles with flap F1 at design nozzle pressure ratio.

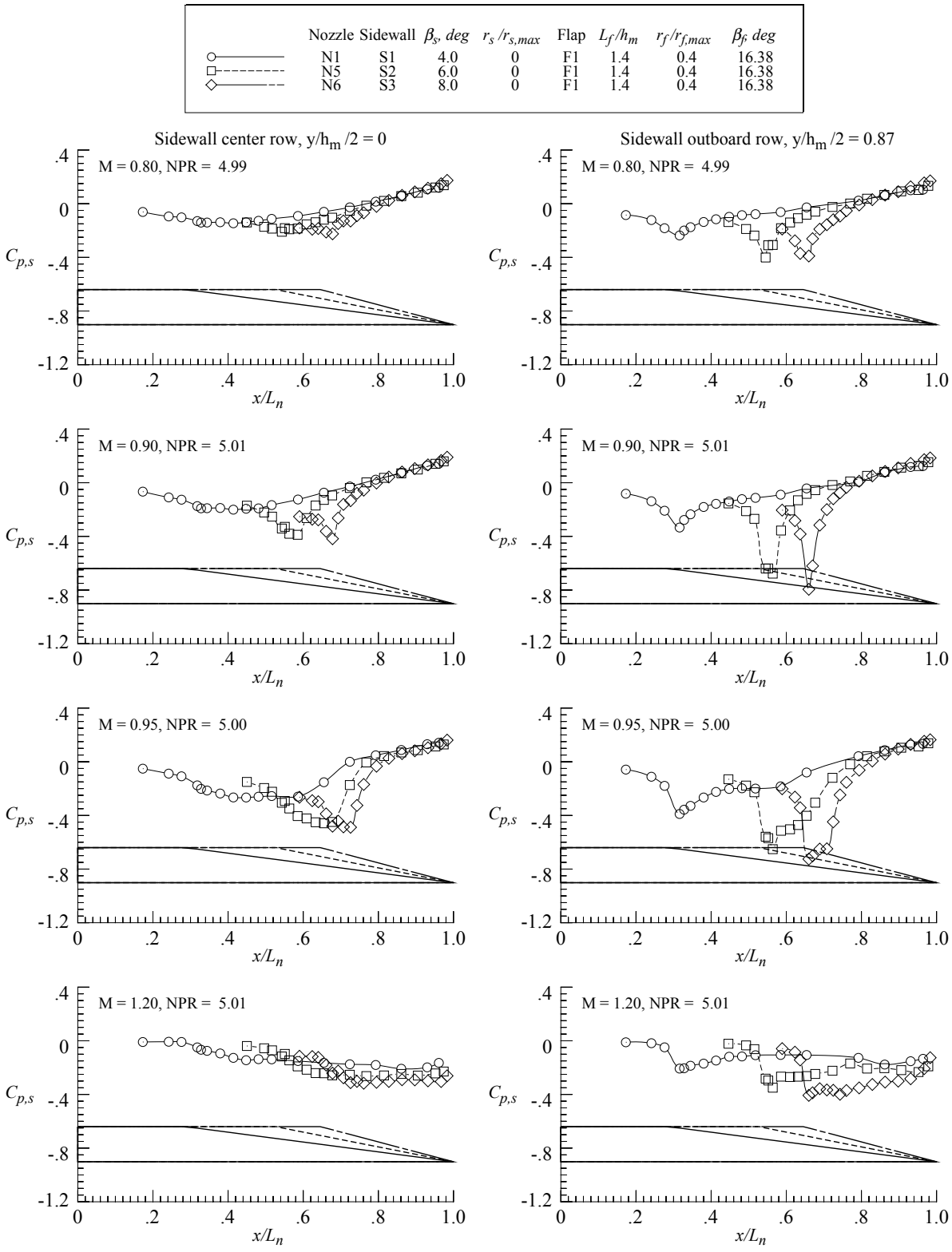

Figure 28. Effect of sidewall boattail angle on sidewall pressure distributions for nozzles with flap F1 at design NPR.

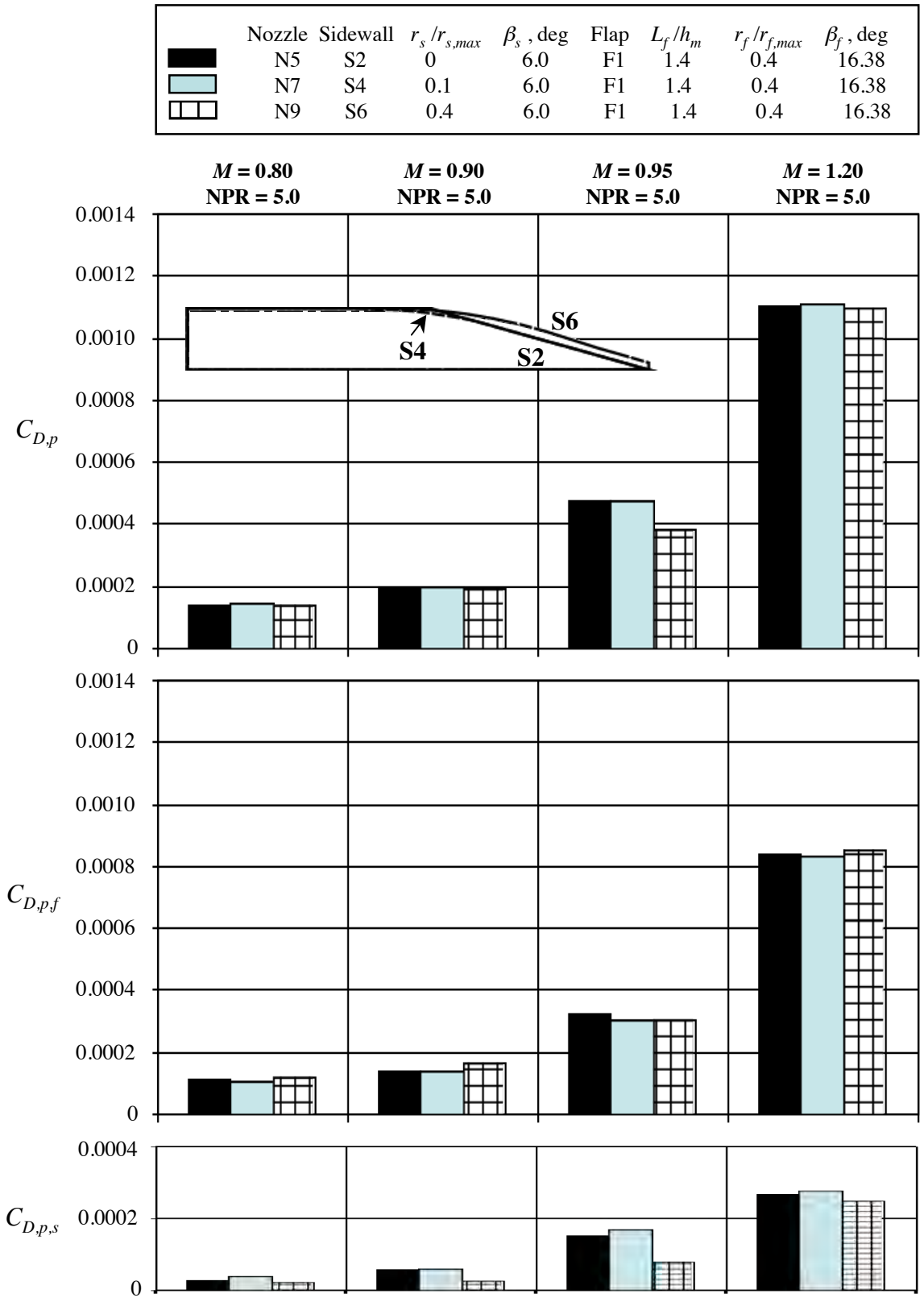

Figure 29. Effect of sidewall radius of curvature and base on pressure drag coefficients for nozzles with flap F1 at design NPR.

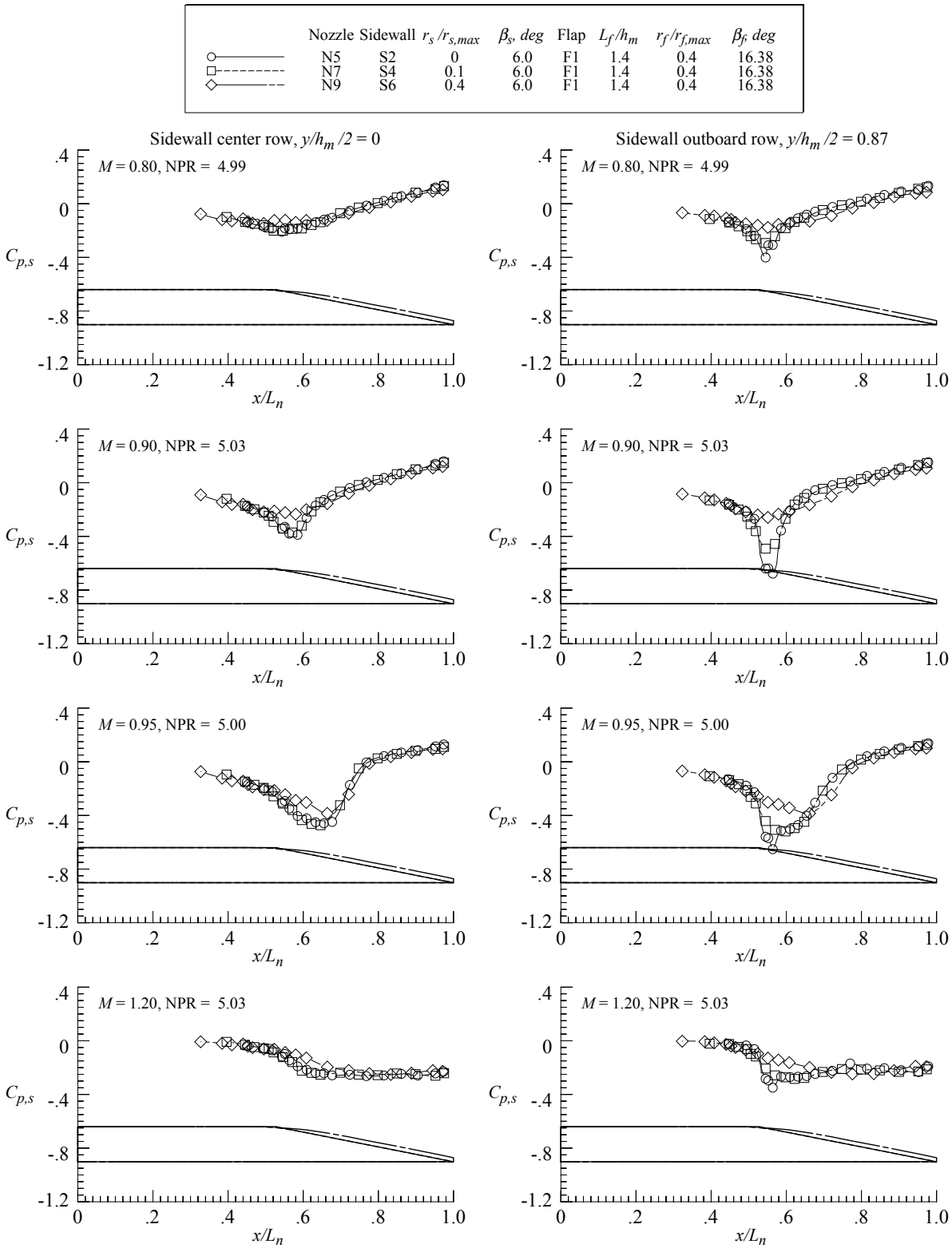

Figure 30. Effect of sidewall radius of curvature and base on sidewall pressure distributions for nozzles with flap F1 at design NPR.

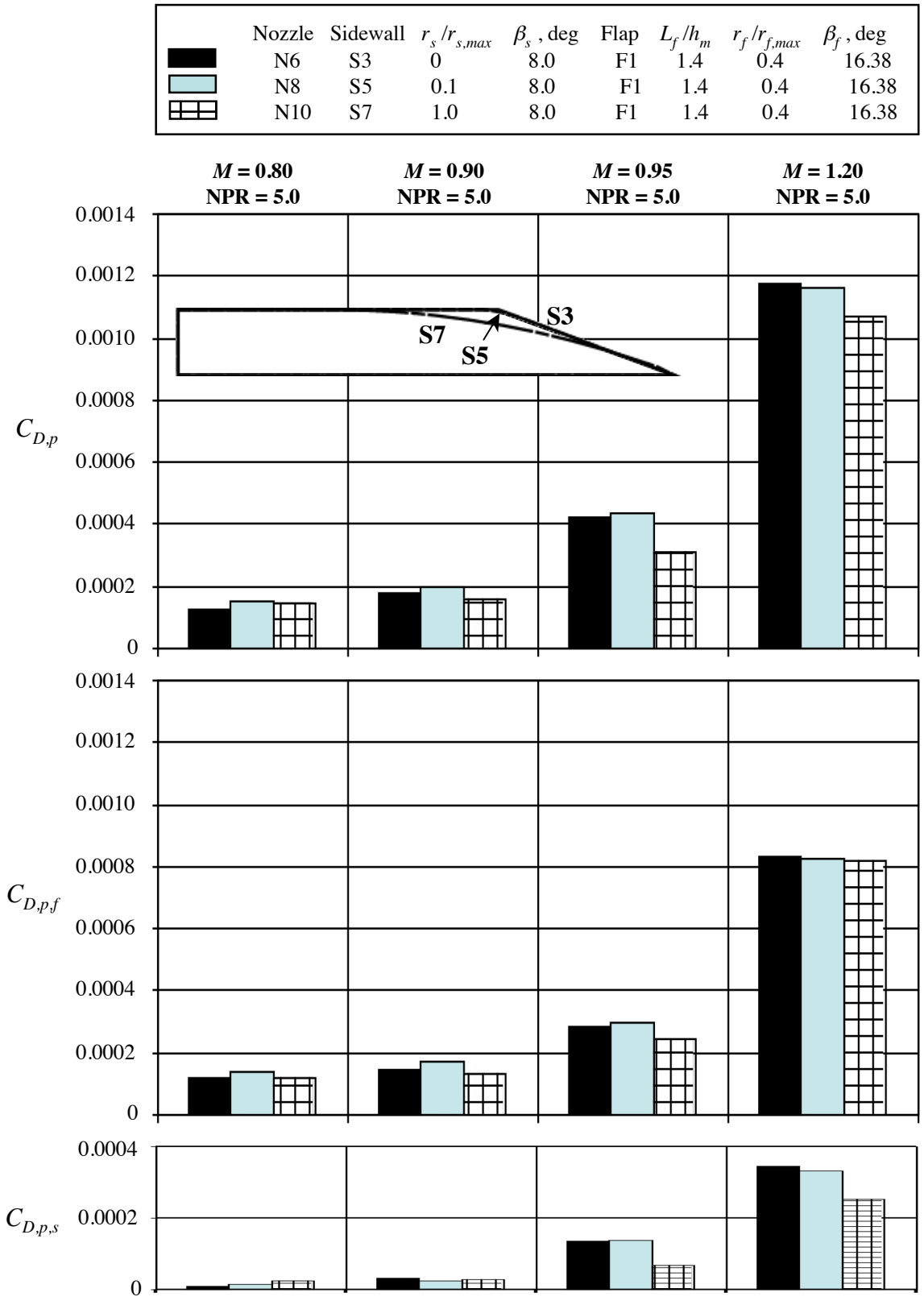

Figure 31. Effect of sidewall radius of curvature on pressure drag coefficients for nozzles with flap F1 at design NPR.

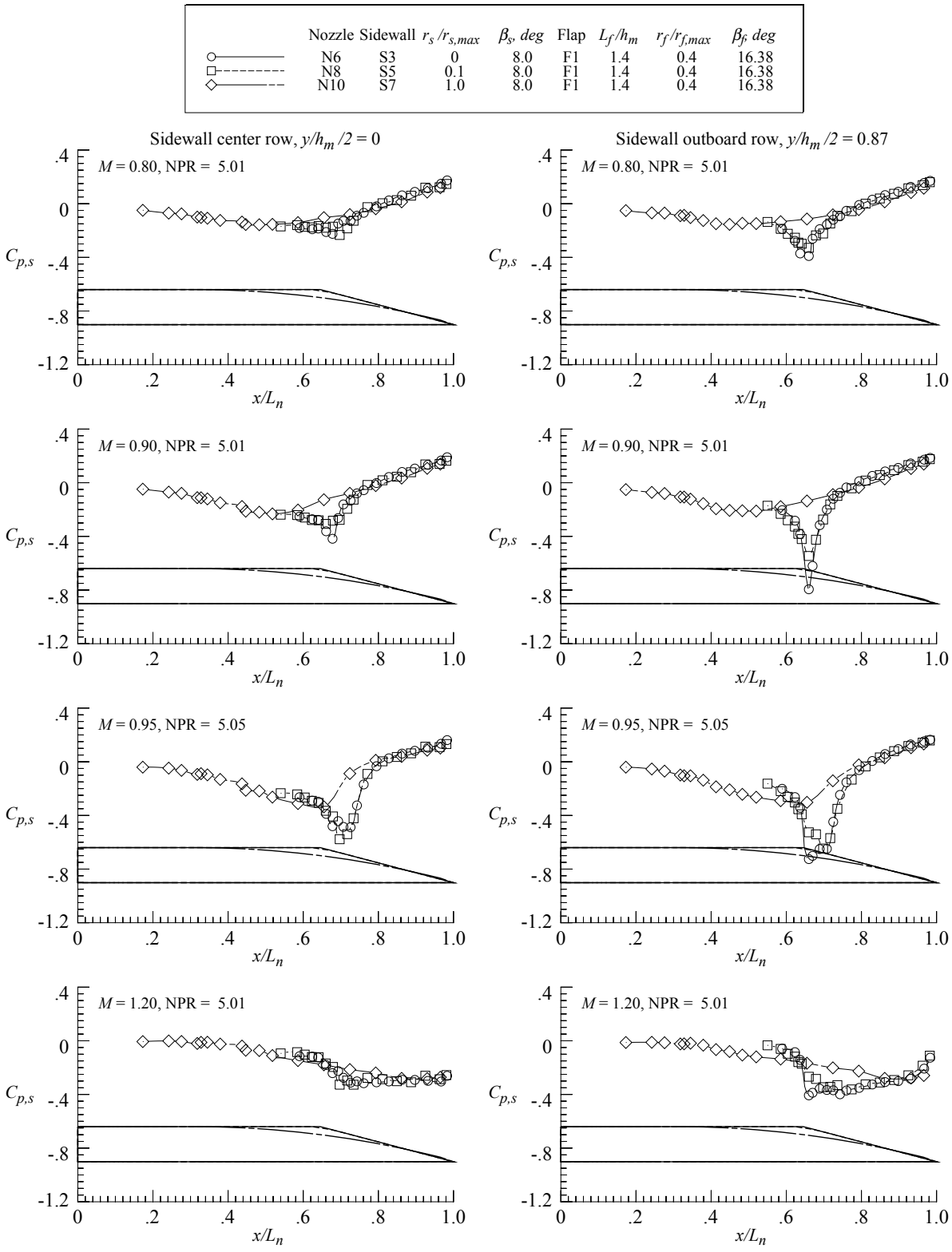

Figure 32. Effect of sidewall radius of curvature on sidewall pressure distributions for nozzles with flap F1 at design NPR.

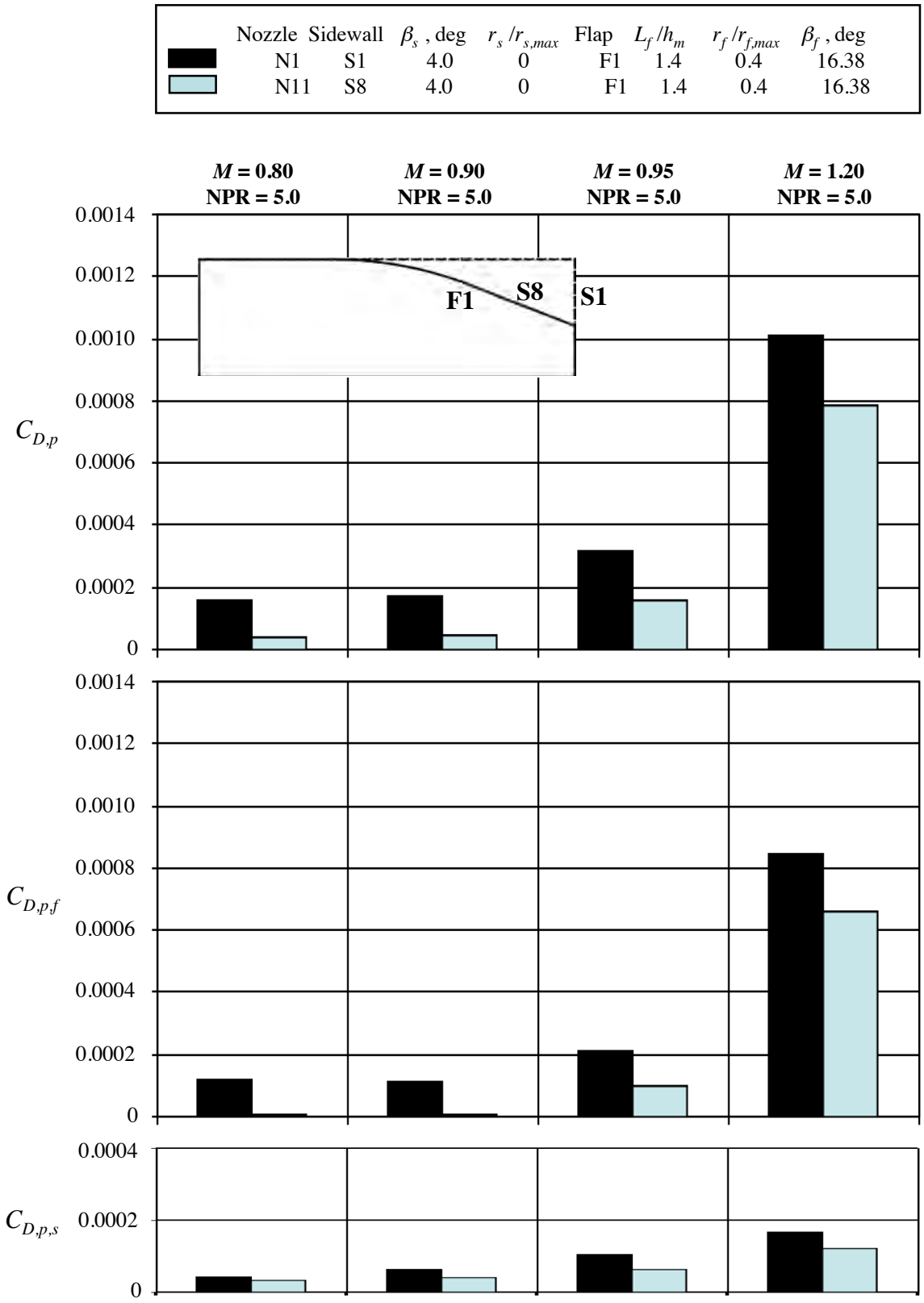

Figure 33. Effect of reduced sidewall height on pressure drag coefficients for nozzles with flap F1 at design NPR.

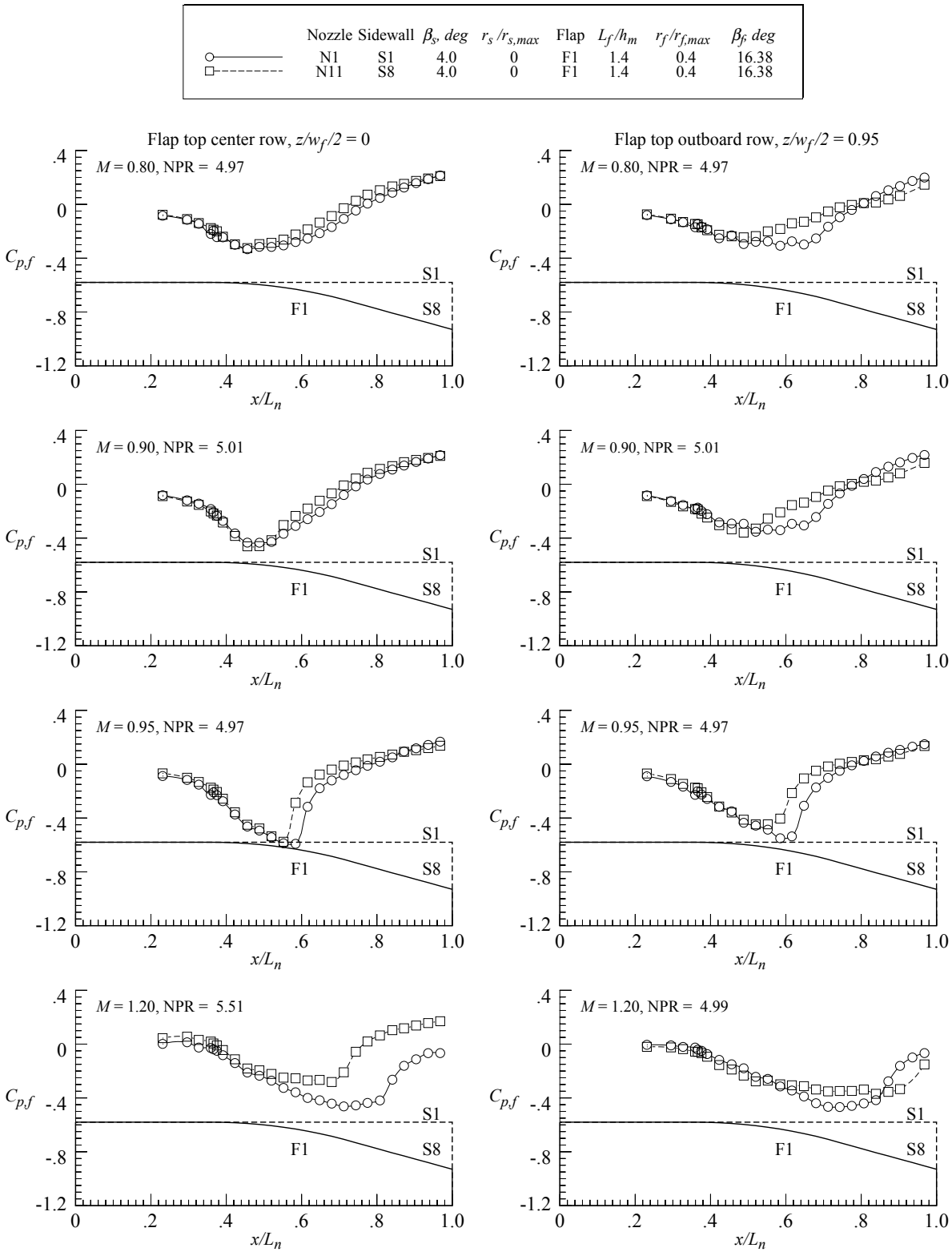

(a) Flap pressure distributions.

Figure 34. Effect of reduced sidewall height on nozzle pressure distributions for nozzles with flap F1 at design NPR.

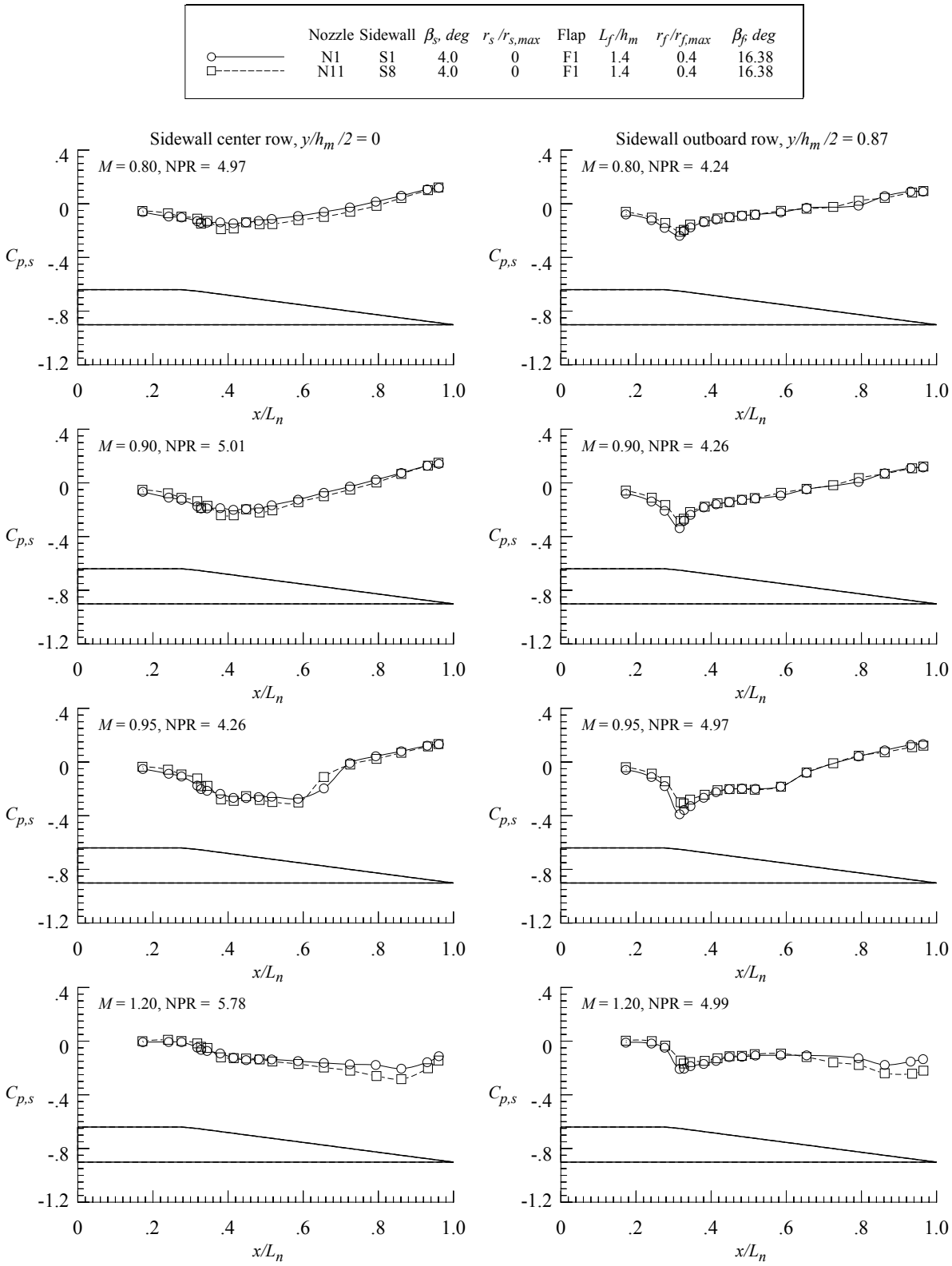

(b) Sidewall pressure distributions.

Figure 34. Concluded.

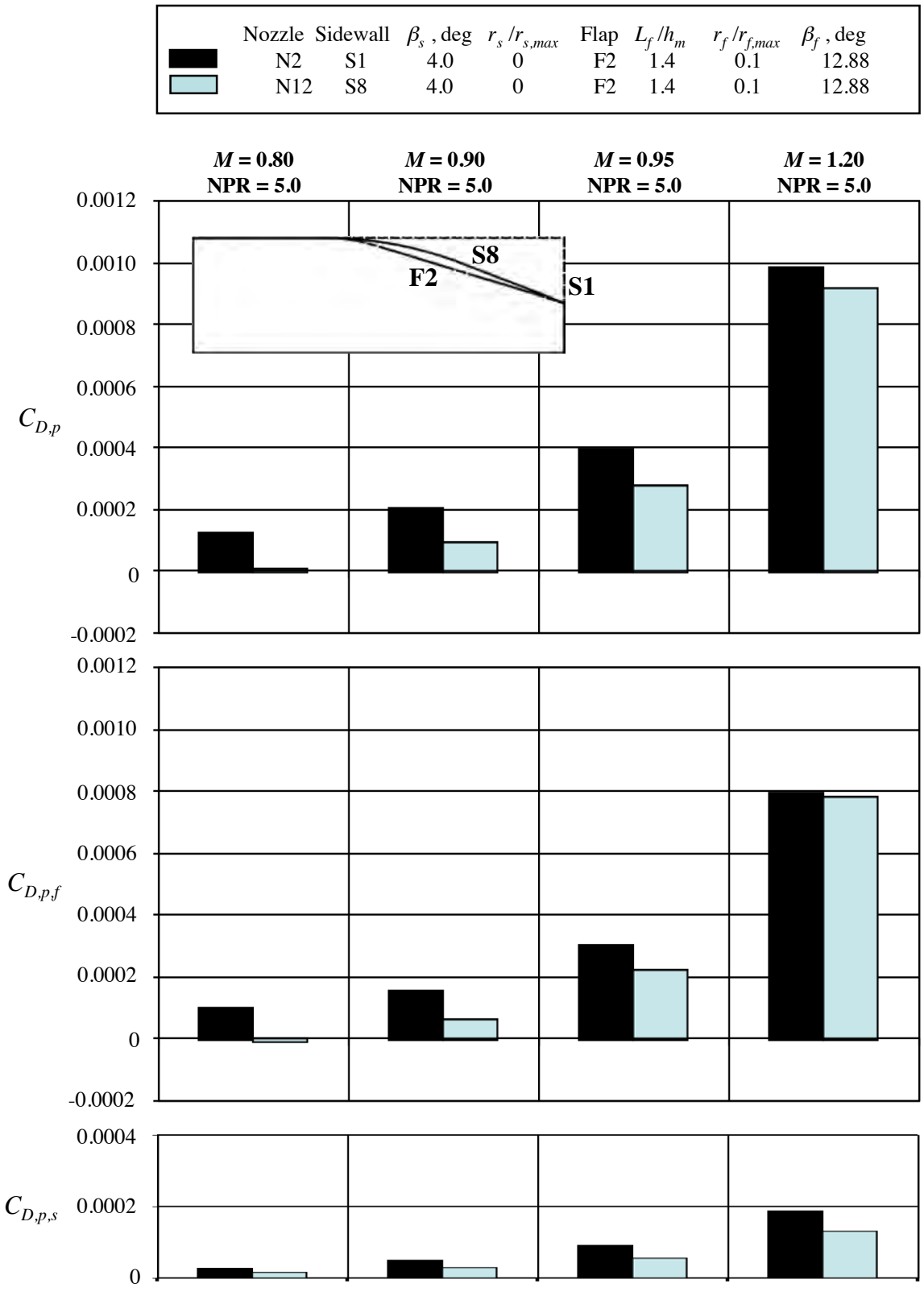

Figure 35. Effect of reduced sidewall height on pressure drag coefficients for nozzles with flap F2 at design NPR.

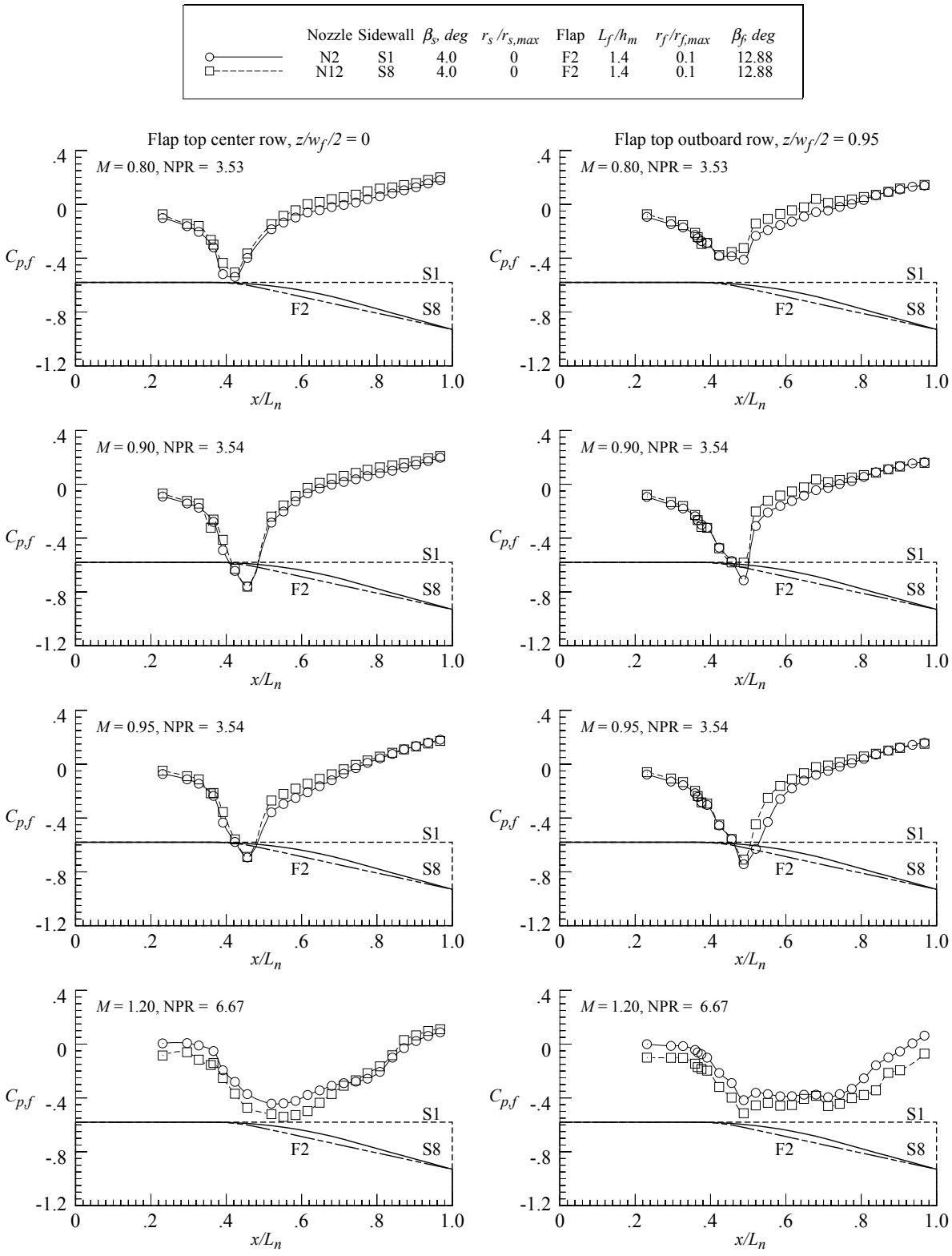

(a) Flap pressure distributions.

Figure 36. Effect of reduced sidewall height on upper flap pressure distributions for nozzles with flap F2 at design NPR.

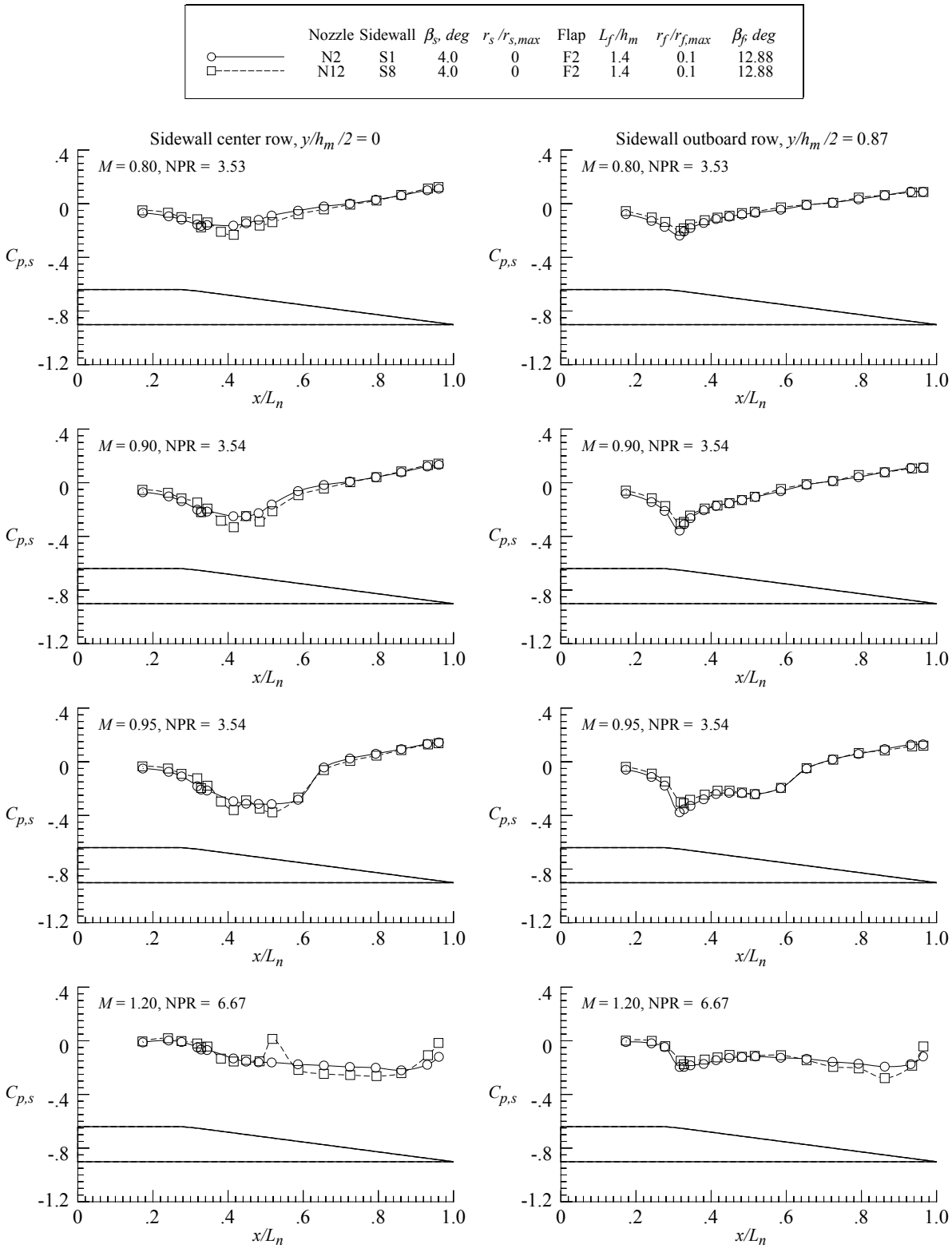

(b) Sidewall pressure distributions at design NPR.

Figure 36. Concluded.

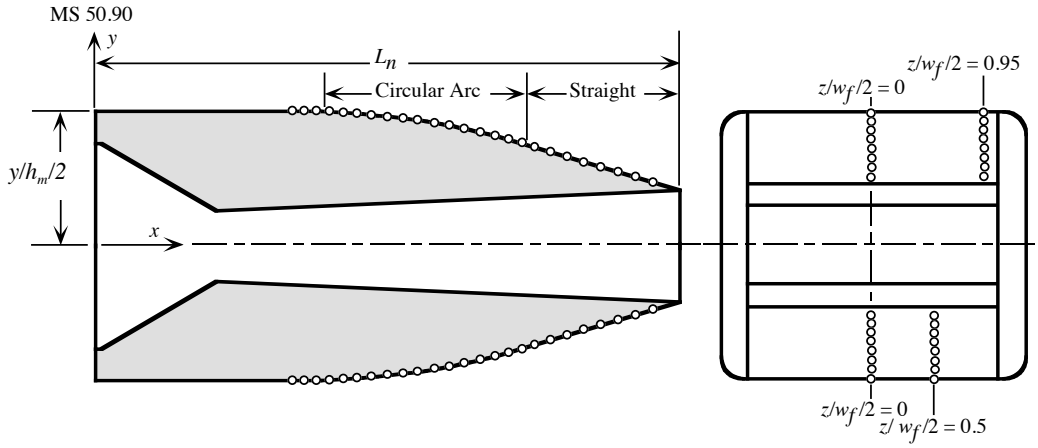

	Top centerline $z/w_f/2 = 0$		Top outboard $z/w_f/2 = 0.95$		Bottom centerline $z/w_f/2 = 0$		Bottom middle $z/w_f/2 = 0.5$	
$y/h_m/2$	x/L_n	orifice	x/L_n	orifice	x/L_n	orifice	x/L_n	orifice
1.000	0.000		0.000		0.000		0.000	
1.000	0.231	CPF26	0.231	CPF1	0.225	CPF51	0.226	CPF76
1.000	0.296	CPF27	0.295	CPF2	0.288	CPF52	0.289	CPF77
1.000	0.327	CPF28	0.327	CPF3	0.322	CPF53	0.322	CPF78
1.000	0.359	CPF29	0.359	CPF4	0.354	CPF54	0.353	CPF79
1.000	0.366	CPF30	0.366	CPF5	0.361	CPF55	0.360	CPF80
1.000	0.375	CPF31	0.376	CPF6	0.370	CPF56	0.370	CPF81
0.998	0.391	CPF32	0.391	CPF7	0.386	CPF57	0.385	CPF82
0.993	0.423	CPF33	0.423	CPF8	0.418	CPF58	0.418	CPF83
0.985	0.456	CPF34	0.456	CPF9	0.450	CPF59	0.451	CPF84
0.973	0.488	CPF35	0.488	CPF10	0.483	CPF60	0.483	CPF85
0.958	0.520	CPF36	0.520	CPF11	0.515	CPF61	0.514	CPF86
0.939	0.552	CPF37	0.552	CPF12	0.546	CPF62	0.548	CPF87
0.918	0.584	CPF38	0.585	CPF13	0.580	CPF63	0.580	CPF88
0.892	0.616	CPF39	0.616	CPF14	0.612	CPF64	0.611	CPF89
0.863	0.648	CPF40	0.648	CPF15	0.644	CPF65	0.643	CPF90
0.831	0.680	CPF41	0.680	CPF16	0.676	CPF66	0.676	CPF91
0.795	0.712	CPF42	0.712	CPF17	0.709	CPF67	0.709	CPF92
0.755	0.744	CPF43	0.743	CPF18	0.742	CPF68	0.741	CPF93
0.716	0.775	CPF44	0.775	CPF19	0.773	CPF69	0.774	CPF94
0.675	0.808	CPF45	0.807	CPF20	0.806	CPF70	0.806	CPF95
0.634	0.841	CPF46	0.839	CPF21	0.839	CPF71	0.838	CPF96
0.595	0.872	CPF47	0.872	CPF22	0.872	CPF72	0.871	CPF97
0.556	0.904	CPF48	0.903	CPF23	0.905	CPF73	0.902	CPF98
0.516	0.936	CPF49	0.936	CPF24	0.938	CPF74	0.935	CPF99
0.476	0.968	CPF50	0.968	CPF25	0.969	CPF75	0.964	CPF100
0.436	1.000		1.000		1.000		1.000	

Figure 37. Flap F1 external coordinates and location of pressure orifices.

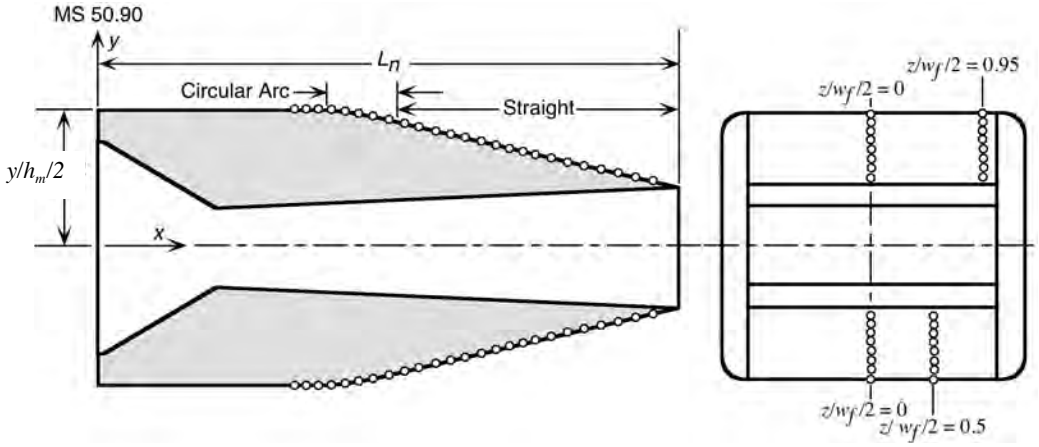

	Top centerline $z/w_f/2 = 0$		Top outboard $z/w_f/2 = 0.95$		Bottom centerline $z/w_f/2 = 0$		Bottom middle $z/w_f/2 = 0.5$	
$y/h_m/2$	x/L_n	orifice	x/L_n	orifice	x/L_n	orifice	x/L_n	orifice
1.000	0.000		0.000		0.000		0.000	
1.000	0.231	CPF26	0.231	CPF1	0.232	CPF51	0.229	CPF76
1.000	0.296	CPF27	0.295	CPF2	0.295	CPF52	0.295	CPF77
1.000	0.327	CPF28	0.327	CPF3	0.326	CPF53	0.327	CPF78
1.000	0.359	CPF29	0.359	CPF4	0.357	CPF54	0.358	CPF79
1.000	0.366	CPF30	0.366	CPF5	0.366	CPF55	0.365	CPF80
1.000	0.375	CPF31	0.376	CPF6	0.373	CPF56	0.375	CPF81
0.998	0.391	CPF32	0.391	CPF7	0.390	CPF57	0.390	CPF82
0.993	0.423	CPF33	0.423	CPF8	0.418	CPF58	0.420	CPF83
0.985	0.456	CPF34	0.456	CPF9	0.454	CPF59	0.456	CPF84
0.973	0.488	CPF35	0.488	CPF10	0.486	CPF60	0.485	CPF85
0.958	0.520	CPF36	0.520	CPF11	0.518	CPF61	0.519	CPF86
0.939	0.552	CPF37	0.552	CPF12	0.549	CPF62	0.550	CPF87
0.918	0.584	CPF38	0.585	CPF13	0.580	CPF63	0.583	CPF88
0.892	0.616	CPF39	0.616	CPF14	0.614	CPF64	0.614	CPF89
0.863	0.648	CPF40	0.648	CPF15	0.651	CPF65	0.647	CPF90
0.831	0.680	CPF41	0.680	CPF16	0.678	CPF66	0.679	CPF91
0.795	0.712	CPF42	0.712	CPF17	0.707	CPF67	0.712	CPF92
0.755	0.744	CPF43	0.743	CPF18	0.743	CPF68	0.743	CPF93
0.716	0.775	CPF44	0.775	CPF19	0.773	CPF69	0.777	CPF94
0.675	0.808	CPF45	0.807	CPF20	0.807	CPF70	0.807	CPF95
0.634	0.841	CPF46	0.839	CPF21	0.838	CPF71	0.840	CPF96
0.595	0.872	CPF47	0.872	CPF22	0.872	CPF72	0.873	CPF97
0.556	0.904	CPF48	0.903	CPF23	0.904	CPF73	0.904	CPF98
0.516	0.936	CPF49	0.936	CPF24	0.935	CPF74	0.936	CPF99
0.476	0.968	CPF50	0.968	CPF25	0.968	CPF75	0.968	CPF100
0.436	1.000		1.000		1.000		1.000	

Figure 38. Flap F2 external coordinates and location of pressure orifices.

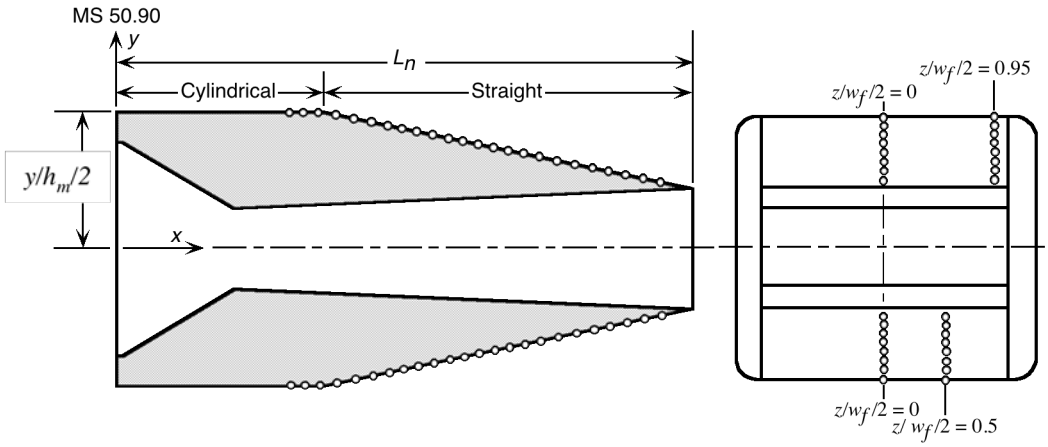

	Top centerline $z/w_f/2 = 0$		Top outboard $z/w_f/2 = 0.95$		Bottom centerline $z/w_f/2 = 0$		Bottom middle $z/w_f/2 = 0.5$	
$y/h_m/2$	x/L_n	orifice	x/L_n	orifice	x/L_n	orifice	x/L_n	orifice
1.000	0.000		0.000		0.000		0.000	
1.000	0.231	CPF26	0.231	CPF1	0.225	CPF51	0.226	CPF76
1.000	0.296	CPF27	0.295	CPF2	0.288	CPF52	0.289	CPF77
1.000	0.327	CPF28	0.327	CPF3	0.322	CPF53	0.322	CPF78
0.992	0.366	CPF30	0.366	CPF5	0.361	CPF55	0.360	CPF80
0.985	0.375	CPF31	0.376	CPF6	0.370	CPF56	0.370	CPF81
0.970	0.391	CPF32	0.391	CPF7	0.386	CPF57	0.385	CPF82
0.942	0.423	CPF33	0.423	CPF8	0.418	CPF58	0.418	CPF83
0.914	0.456	CPF34	0.456	CPF9	0.450	CPF59	0.451	CPF84
0.887	0.488	CPF35	0.488	CPF10	0.483	CPF60	0.483	CPF85
0.858	0.520	CPF36	0.520	CPF11	0.515	CPF61	0.514	CPF86
0.829	0.552	CPF37	0.552	CPF12	0.546	CPF62	0.548	CPF87
0.801	0.584	CPF38	0.585	CPF13	0.580	CPF63	0.580	CPF88
0.773	0.616	CPF39	0.616	CPF14	0.612	CPF64	0.611	CPF89
0.745	0.648	CPF40	0.648	CPF15	0.644	CPF65	0.643	CPF90
0.717	0.680	CPF41	0.680	CPF16	0.676	CPF66	0.676	CPF91
0.690	0.712	CPF42	0.712	CPF17	0.709	CPF67	0.709	CPF92
0.662	0.744	CPF43	0.743	CPF18	0.742	CPF68	0.741	CPF93
0.633	0.775	CPF44	0.775	CPF19	0.773	CPF69	0.774	CPF94
0.604	0.808	CPF45	0.807	CPF20	0.806	CPF70	0.806	CPF95
0.576	0.841	CPF46	0.839	CPF21	0.839	CPF71	0.838	CPF96
0.549	0.872	CPF47	0.872	CPF22	0.872	CPF72	0.871	CPF97
0.520	0.904	CPF48	0.903	CPF23	0.905	CPF73	0.902	CPF98
0.492	0.936	CPF49	0.936	CPF24	0.938	CPF74	0.935	CPF99
0.463	0.968	CPF50	0.968	CPF25	0.969	CPF75	0.964	CPF100
0.436	1.000		1.000		1.000		1.000	

Figure 39. Flap F3 external coordinates and location of pressure orifices.

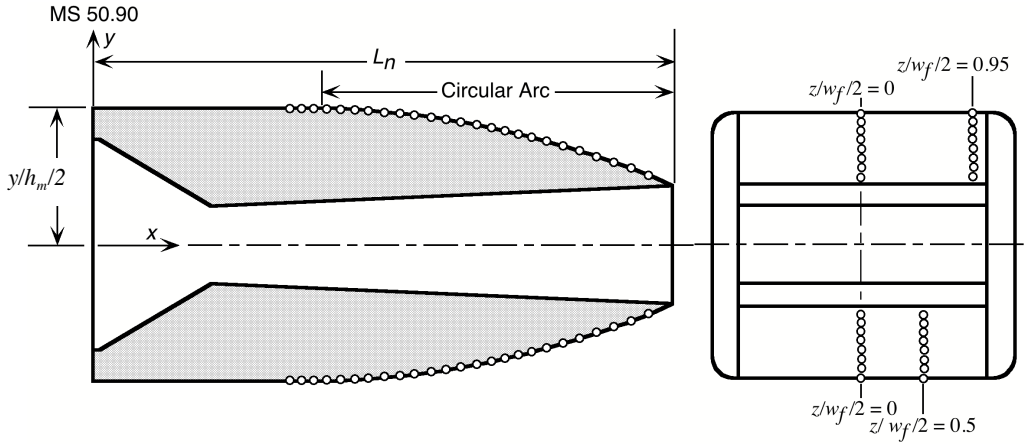

	Top centerline $z/w_f/2 = 0$		Top outboard $z/w_f/2 = 0.95$		Bottom centerline $z/w_f/2 = 0$		Bottom middle $z/w_f/2 = 0.5$	
$y/h_m/2$	x/L_n	orifice	x/L_n	orifice	x/L_n	orifice	x/L_n	orifice
1.000	0.000		0.000		0.000		0.000	
1.000	0.231	CPF26	0.226	CPF1	0.229	CPF51	0.229	CPF76
1.000	0.295	CPF27	0.290	CPF2	0.293	CPF52	0.295	CPF77
1.000	0.326	CPF28	0.323	CPF3	0.326	CPF53	0.327	CPF78
1.000	0.359	CPF29	0.354	CPF4	0.358	CPF54	0.358	CPF79
1.000	0.364	CPF30	0.360	CPF5	0.365	CPF55	0.365	CPF80
1.000	0.374	CPF31	0.371	CPF6	0.374	CPF56	0.375	CPF81
0.999	0.387	CPF32	0.386	CPF7	0.390	CPF57	0.390	CPF82
0.995	0.423	CPF33	0.420	CPF8	0.421	CPF58	0.420	CPF83
0.988	0.456	CPF34	0.451	CPF9	0.457	CPF59	0.456	CPF84
0.979	0.486	CPF35	0.485	CPF10	0.486	CPF60	0.485	CPF85
0.966	0.520	CPF36	0.515	CPF11	0.520	CPF61	0.519	CPF86
0.952	0.550	CPF37	0.548	CPF12	0.550	CPF62	0.550	CPF87
0.933	0.583	CPF38	0.580	CPF13	0.583	CPF63	0.583	CPF88
0.913	0.616	CPF39	0.612	CPF14	0.616	CPF64	0.614	CPF89
0.889	0.648	CPF40	0.646	CPF15	0.647	CPF65	0.647	CPF90
0.862	0.681	CPF41	0.677	CPF16	0.678	CPF66	0.679	CPF91
0.832	0.714	CPF42	0.710	CPF17	0.715	CPF67	0.712	CPF92
0.803	0.744	CPF43	0.742	CPF18	0.744	CPF68	0.743	CPF93
0.768	0.776	CPF44	0.774	CPF19	0.776	CPF69	0.777	CPF94
0.731	0.807	CPF45	0.805	CPF20	0.808	CPF70	0.807	CPF95
0.685	0.843	CPF46	0.839	CPF21	0.841	CPF71	0.840	CPF96
0.643	0.873	CPF47	0.871	CPF22	0.874	CPF72	0.873	CPF97
0.596	0.905	CPF48	0.902	CPF23	0.904	CPF73	0.904	CPF98
0.545	0.937	CPF49	0.934	CPF24	0.936	CPF74	0.936	CPF99
0.499	0.965	CPF50	0.968	CPF25	0.968	CPF75	0.968	CPF100
0.436	1.000		1.000		1.000		1.000	

Figure 40. Flap F4 external coordinates and location of pressure orifices.

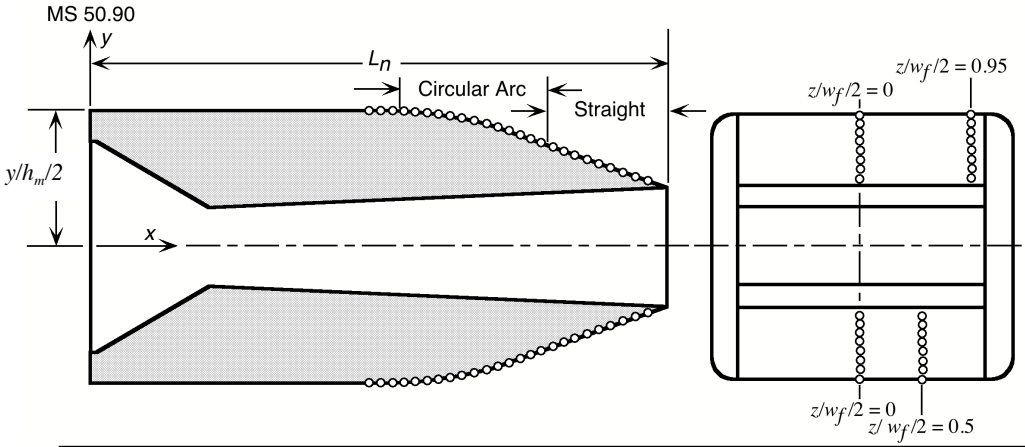

	Top centerline $z/w_f/2 = 0$		Top outboard $z/w_f/2 = 0.95$		Bottom centerline $z/w_f/2 = 0$		Bottom middle $z/w_f/2 = 0.5$	
$y/h_m/2$	x/L_n	orifice	x/L_n	orifice	x/L_n	orifice	x/L_n	orifice
1.000	0.000		0.000		0.000		0.000	
1.000	0.383	CPF26	0.384	CPF1	0.382	CPF51	0.385	CPF76
1.000	0.435	CPF27	0.435	CPF2	0.438	CPF52	0.435	CPF77
1.000	0.461	CPF28	0.460	CPF3	0.461	CPF53	0.461	CPF78
1.000	0.487	CPF29	0.487	CPF4	0.486	CPF54	0.484	CPF79
1.000	0.492	CPF30	0.492	CPF5	0.492	CPF55	0.490	CPF80
1.000	0.500	CPF31	0.499	CPF6	0.501	CPF56	0.501	CPF81
0.998	0.513	CPF32	0.513	CPF7	0.514	CPF57	0.514	CPF82
0.993	0.539	CPF33	0.539	CPF8	0.538	CPF58	0.538	CPF83
0.985	0.564	CPF34	0.563	CPF9	0.565	CPF59	0.565	CPF84
0.974	0.590	CPF35	0.589	CPF10	0.590	CPF60	0.591	CPF85
0.958	0.616	CPF36	0.615	CPF11	0.616	CPF61	0.617	CPF86
0.940	0.642	CPF37	0.641	CPF12	0.641	CPF62	0.642	CPF87
0.919	0.667	CPF38	0.667	CPF13	0.667	CPF63	0.667	CPF88
0.893	0.694	CPF39	0.692	CPF14	0.694	CPF64	0.695	CPF89
0.865	0.719	CPF40	0.718	CPF15	0.721	CPF65	0.720	CPF90
0.833	0.744	CPF41	0.744	CPF16	0.743	CPF66	0.746	CPF91
0.797	0.770	CPF42	0.768	CPF17	0.769	CPF67	0.771	CPF92
0.758	0.795	CPF43	0.794	CPF18	0.795	CPF68	0.794	CPF93
0.717	0.821	CPF44	0.820	CPF19	0.822	CPF69	0.822	CPF94
0.676	0.847	CPF45	0.845	CPF20	0.846	CPF70	0.848	CPF95
0.635	0.873	CPF46	0.871	CPF21	0.872	CPF71	0.873	CPF96
0.596	0.898	CPF47	0.897	CPF22	0.899	CPF72	0.899	CPF97
0.554	0.925	CPF48	0.923	CPF23	0.925	CPF73	0.924	CPF98
0.515	0.950	CPF49	0.948	CPF24	0.950	CPF74	0.950	CPF99
0.477	0.974	CPF50	0.974	CPF25	0.975	CPF75	0.976	CPF100
0.436	1.000		1.000		1.000		1.000	

Figure 41. Flap F5 external coordinates and location of pressure orifices

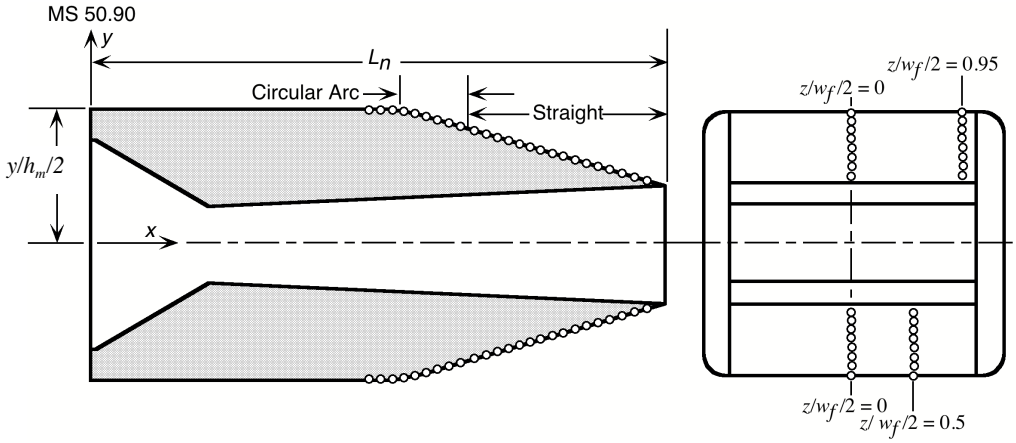

	Top centerline $z/w_f/2 = 0$		Top outboard $z/w_f/2 = 0.95$		Bottom centerline $z/w_f/2 = 0$		Bottom middle $z/w_f/2 = 0.5$	
$y/h_m/2$	x/L_n	orifice	x/L_n	orifice	x/L_n	orifice	x/L_n	orifice
1.000	0.000		0.000		0.000		0.000	
1.000	0.385	CPF26	0.386	CPF1	0.386	CPF51	0.384	CPF76
1.000	0.435	CPF27	0.437	CPF2	0.438	CPF52	0.437	CPF77
1.000	0.463	CPF28	0.462	CPF3	0.462	CPF53	0.461	CPF78
1.000	0.487	CPF29	0.487	CPF4	0.489	CPF54	0.487	CPF79
1.000	0.492	CPF30	0.492	CPF5	0.495	CPF55	0.491	CPF80
0.999	0.501	CPF31	0.499	CPF6	0.502	CPF56	0.500	CPF81
0.996	0.513	CPF32	0.512	CPF7	0.514	CPF57	0.513	CPF82
0.984	0.537	CPF33	0.538	CPF8	0.542	CPF58	0.540	CPF83
0.964	0.563	CPF34	0.564	CPF9	0.566	CPF59	0.567	CPF84
0.934	0.589	CPF35	0.589	CPF10	0.591	CPF60	0.591	CPF85
0.903	0.615	CPF36	0.614	CPF11	0.619	CPF61	0.616	CPF86
0.872	0.641	CPF37	0.641	CPF12	0.644	CPF62	0.644	CPF87
0.839	0.668	CPF38	0.667	CPF13	0.668	CPF63	0.667	CPF88
0.810	0.692	CPF39	0.691	CPF14	0.694	CPF64	0.692	CPF89
0.778	0.718	CPF40	0.717	CPF15	0.719	CPF65	0.720	CPF90
0.747	0.743	CPF41	0.743	CPF16	0.746	CPF66	0.747	CPF91
0.716	0.769	CPF42	0.769	CPF17	0.768	CPF67	0.770	CPF92
0.686	0.794	CPF43	0.794	CPF18	0.798	CPF68	0.797	CPF93
0.654	0.820	CPF44	0.820	CPF19	0.823	CPF69	0.822	CPF94
0.622	0.847	CPF45	0.846	CPF20	0.846	CPF70	0.847	CPF95
0.592	0.872	CPF46	0.871	CPF21	0.873	CPF71	0.874	CPF96
0.561	0.897	CPF47	0.898	CPF22	0.898	CPF72	0.899	CPF97
0.529	0.924	CPF48	0.923	CPF23	0.927	CPF73	0.924	CPF98
0.497	0.950	CPF49	0.949	CPF24	0.948	CPF74	0.949	CPF99
0.467	0.975	CPF50	0.975	CPF25	0.973	CPF75	0.974	CPF100
0.436	1.000		1.000		1.000		1.000	

Figure 42. Flap F6 external coordinates and location of pressure orifices

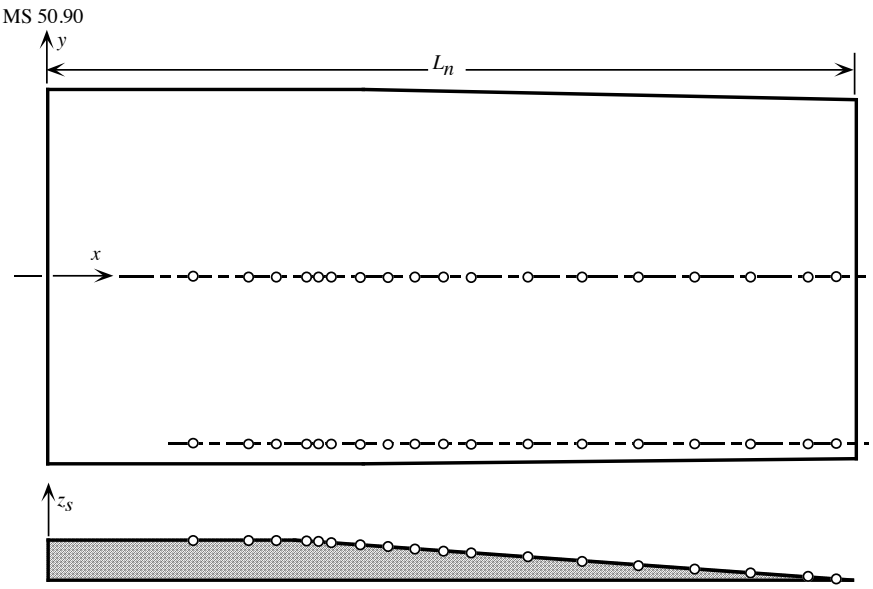

	Centerline row $y/h_m/2 = 0$		Outboard row $y/h_m/2 = -0.87$	
$z/z_{s,max}$	x/L_n	orifice	x/L_n	orifice
1.000	0.000		0.000	
1.000	0.173	CPS1	0.173	CPS21
1.000	0.242	CPS2	0.241	CPS22
1.000	0.276	CPS3	0.276	CPS23
0.958	0.318	CPS5	0.316	CPS25
0.943	0.328	CPS6	0.328	CPS26
0.920	0.344	CPS7	0.345	CPS27
0.872	0.379	CPS8	0.380	CPS28
0.823	0.414	CPS9	0.413	CPS29
0.774	0.448	CPS10	0.448	CPS30
0.728	0.481	CPS11	0.482	CPS31
0.679	0.516	CPS12	0.518	CPS32
0.581	0.586	CPS13	0.585	CPS33
0.484	0.655	CPS14	0.654	CPS34
0.387	0.724	CPS15	0.723	CPS35
0.290	0.793	CPS16	0.792	CPS36
0.195	0.861	CPS17	0.862	CPS37
0.098	0.930	CPS18	0.931	CPS38
0.055	0.961	CPS19	0.964	CPS39
0.015	1.000		1.000	

Figure 43. Sidewall S1 external coordinates and location of pressure orifices

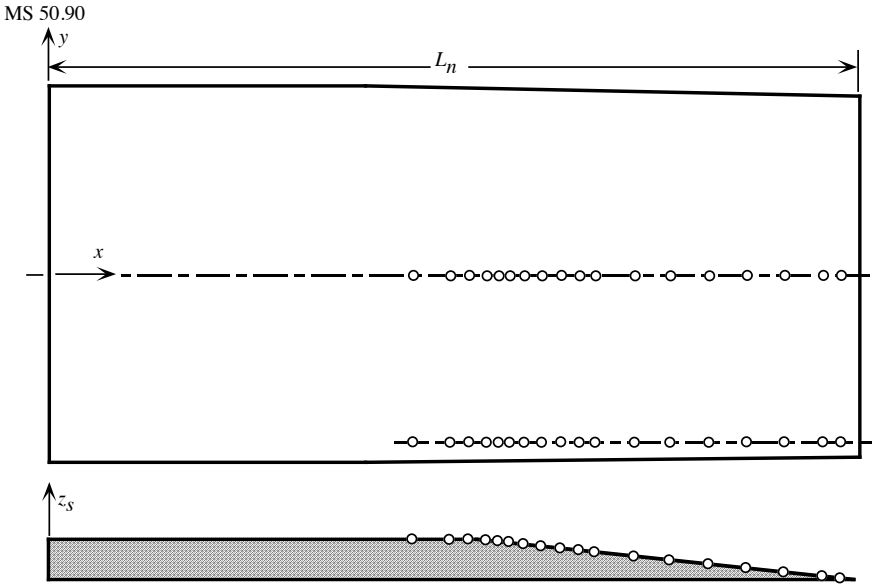

	Centerline row $y/h_m/2 = 0$		Outboard row $y/h_m/2 = -0.87$	
$z/z_{s,max}$	x/L_n	orifice	x/L_n	orifice
1.000	0.000		0.000	
1.000	0.450	CPS1	0.446	CPS21
1.000	0.496	CPS2	0.493	CPS22
1.000	0.517	CPS3	0.515	CPS23
0.965	0.543	CPS5	0.545	CPS24
0.948	0.551	CPS6	0.552	CPS25
0.923	0.563	CPS7	0.564	CPS26
0.875	0.585	CPS8	0.586	CPS27
0.825	0.609	CPS9	0.610	CPS28
0.775	0.633	CPS10	0.631	CPS29
0.729	0.655	CPS11	0.654	CPS30
0.682	0.677	CPS12	0.677	CPS31
0.583	0.724	CPS13	0.723	CPS32
0.489	0.768	CPS14	0.770	CPS33
0.391	0.815	CPS15	0.815	CPS34
0.294	0.861	CPS16	0.861	CPS35
0.201	0.905	CPS17	0.906	CPS36
0.102	0.952	CPS18	0.952	CPS37
0.054	0.974	CPS19	0.978	CPS38
0.015	1.000		1.000	

Figure 44. Sidewall S2 external coordinates and location of pressure orifices.

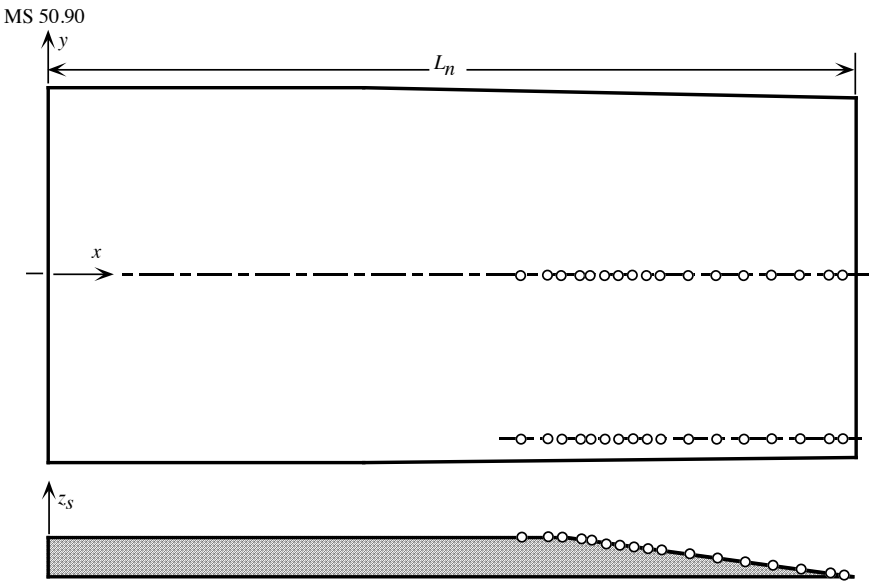

	Centerline row $y/h_m/2 = 0$		Outboard row $y/h_m/2 = -0.87$	
$z/z_{s,max}$	x/L_n	orifice	x/L_n	orifice
1.000	0.000		0.000	
1.000	0.590	CPS1	0.589	CPS21
1.000	0.624	CPS2	0.623	CPS22
1.000	0.640	CPS3	0.637	CPS23
0.957	0.661	CPS5	0.660	CPS25
0.910	0.678	CPS7	0.670	CPS27
0.866	0.693	CPS8	0.689	CPS28
0.827	0.707	CPS9	0.708	CPS29
0.774	0.726	CPS10	0.725	CPS30
0.726	0.743	CPS11	0.743	CPS31
0.675	0.761	CPS12	0.760	CPS32
0.580	0.795	CPS13	0.794	CPS33
0.485	0.828	CPS14	0.829	CPS34
0.386	0.863	CPS15	0.863	CPS35
0.291	0.897	CPS16	0.898	CPS36
0.193	0.932	CPS17	0.931	CPS37
0.093	0.967	CPS18	0.967	CPS38
0.049	0.983	CPS19	0.983	CPS39
0.015	1.000		1.000	

Figure 45. Sidewall S3 external coordinates and location of pressure orifices

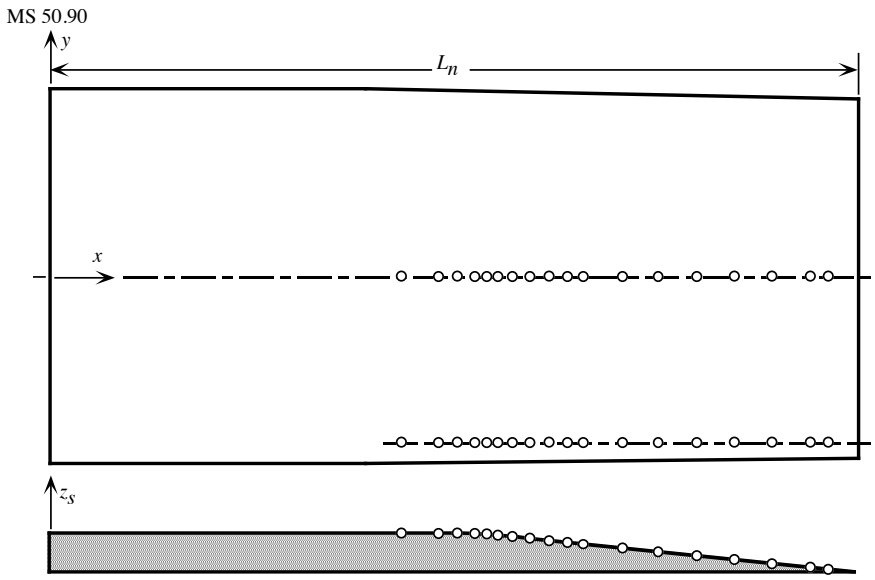

	Centerline row $y/h_m/2 = 0$		Outboard row $y/h_m/2 = -0.87$	
$z/z_{s,max}$	x/L_n	orifice	x/L_n	orifice
1.000	0.000		0.000	
1.000	0.396	CPS1	0.396	CPS21
1.000	0.445	CPS2	0.448	CPS22
1.000	0.470	CPS3	0.473	CPS23
1.000	0.495	CPS5	0.496	CPS25
0.989	0.508	CPS6	0.505	CPS26
0.978	0.521	CPS7	0.519	CPS27
0.943	0.546	CPS8	0.545	CPS28
0.904	0.571	CPS9	0.570	CPS29
0.853	0.596	CPS10	0.598	CPS30
0.799	0.622	CPS11	0.622	CPS31
0.746	0.646	CPS12	0.648	CPS32
0.638	0.698	CPS13	0.697	CPS33
0.532	0.748	CPS14	0.748	CPS34
0.426	0.798	CPS15	0.799	CPS35
0.319	0.849	CPS16	0.849	CPS36
0.212	0.899	CPS17	0.900	CPS37
0.100	0.952	CPS18	0.951	CPS38
0.052	0.975	CPS19	0.974	CPS39
0.015	1.000		1.000	

Figure 46. Sidewall S4 external coordinates and location of pressure orifices

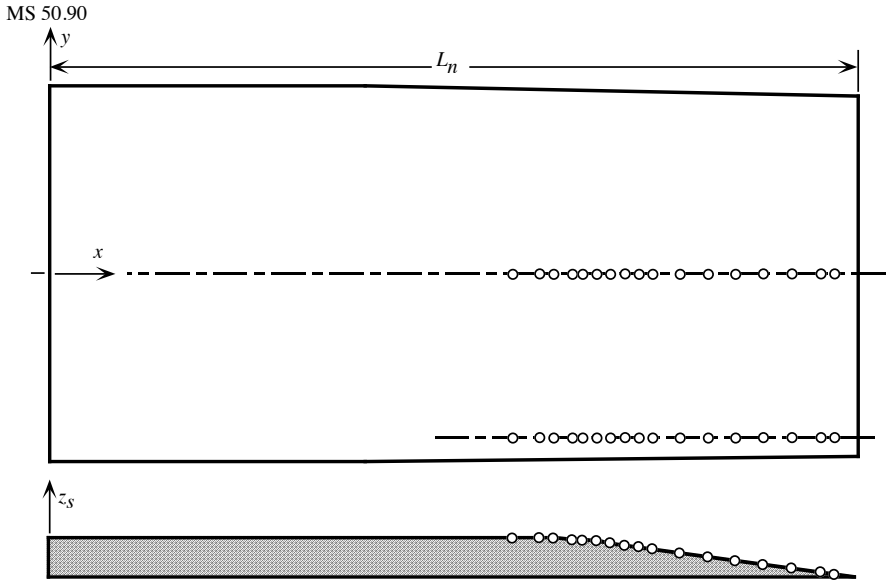

	Centerline row $y/h_m/2 = 0$		Outboard row $y/h_m/2 = -0.87$	
$z/z_{s,max}$	x/L_n	orifice	x/L_n	orifice
1.000	0.000		0.000	
1.000	0.540	CPS1	0.550	CPS21
1.000	0.584	CPS2	0.585	CPS22
1.000	0.604	CPS3	0.604	CPS23
1.000	0.623	CPS5	0.623	CPS25
0.989	0.630	CPS6	0.632	CPS26
0.969	0.641	CPS7	0.641	CPS27
0.940	0.660	CPS8	0.660	CPS28
0.901	0.679	CPS9	0.679	CPS29
0.856	0.697	CPS10	0.698	CPS30
0.800	0.717	CPS11	0.717	CPS31
0.750	0.734	CPS12	0.736	CPS32
0.646	0.771	CPS13	0.774	CPS33
0.535	0.811	CPS14	0.811	CPS34
0.427	0.849	CPS15	0.849	CPS35
0.320	0.887	CPS16	0.887	CPS36
0.211	0.925	CPS17	0.925	CPS37
0.105	0.963	CPS18	0.963	CPS38
0.053	0.981	CPS19	0.982	CPS39
0.015	1.000		1.000	

Figure 47. Sidewall S5 external coordinates and location of pressure orifices

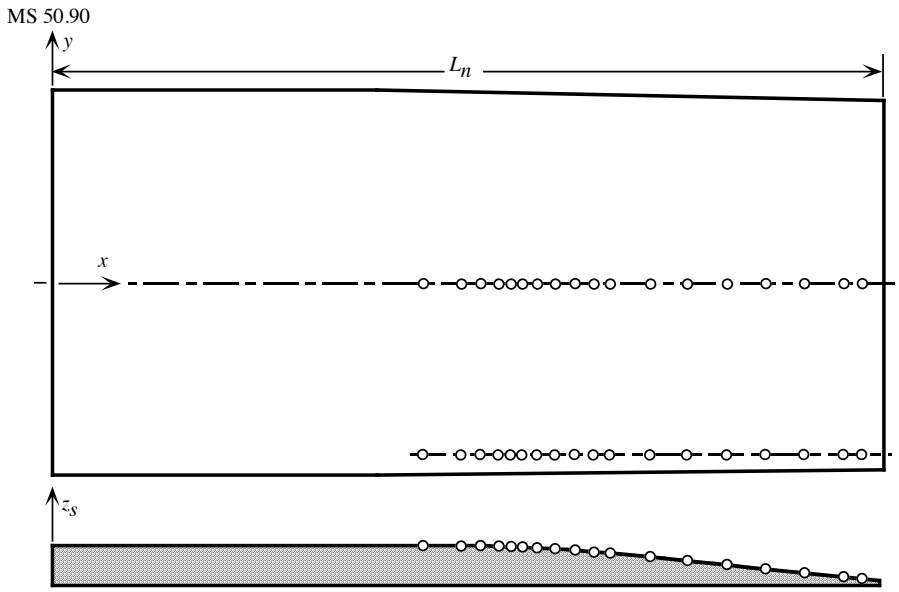

	Centerline row $y/h_m/2 = 0$		Outboard row $y/h_m/2 = -0.87$	
$z/z_{s,max}$	x/L_n	orifice	x/L_n	orifice
1.000	0.000		0.000	
1.000	0.327	CPS1	0.323	CPS21
1.000	0.384	CPS2	0.383	CPS22
1.000	0.410	CPS3	0.408	CPS23
1.000	0.440	CPS5	0.440	CPS25
0.999	0.453	CPS6	0.453	CPS26
0.998	0.465	CPS7	0.465	CPS27
0.990	0.495	CPS8	0.492	CPS28
0.977	0.523	CPS9	0.524	CPS29
0.959	0.552	CPS10	0.551	CPS30
0.936	0.580	CPS11	0.579	CPS31
0.908	0.608	CPS12	0.608	CPS32
0.818	0.664	CPS13	0.662	CPS33
0.709	0.721	CPS14	0.720	CPS34
0.590	0.776	CPS15	0.776	CPS35
0.476	0.833	CPS16	0.833	CPS36
0.359	0.888	CPS17	0.887	CPS37
0.237	0.945	CPS18	0.944	CPS38
0.180	0.971	CPS19	0.973	CPS39
0.113	1.000		1.000	

Figure 48. Sidewall S6 external coordinates and location of pressure orifices

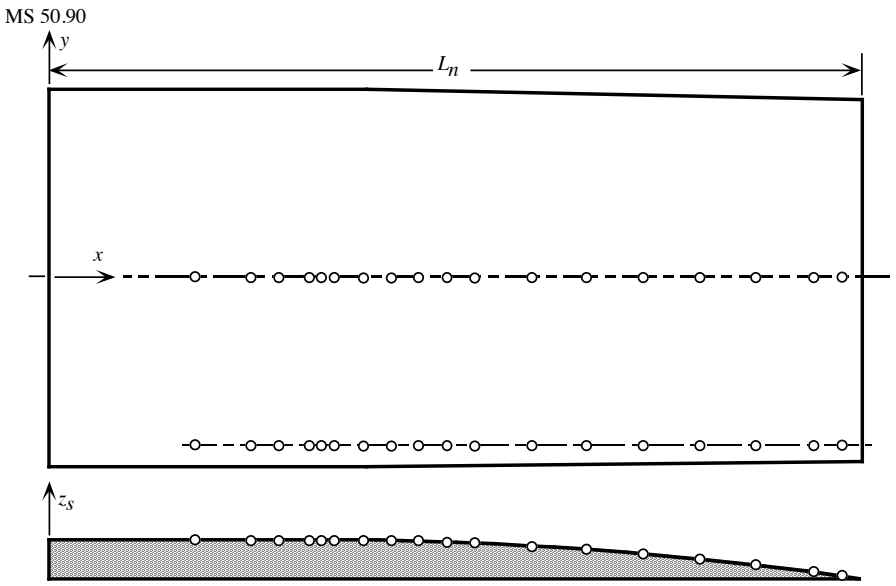

	Centerline row $y/h_m/2 = 0$		Outboard row $y/h_m/2 = -0.87$	
$z/z_{s,max}$	x/L_n	orifice	x/L_n	orifice
1.000	0.000		0.000	
1.000	0.173	CPS1	0.173	CPS21
1.000	0.242	CPS2	0.242	CPS22
1.000	0.276	CPS3	0.276	CPS23
1.000	0.318	CPS5	0.318	CPS25
0.999	0.328	CPS6	0.328	CPS26
0.998	0.345	CPS7	0.345	CPS27
0.990	0.379	CPS8	0.379	CPS28
0.968	0.437	CPS9	0.413	CPS29
0.962	0.447	CPS10	0.449	CPS30
0.940	0.483	CPS11	0.483	CPS31
0.913	0.518	CPS12	0.520	CPS32
0.846	0.586	CPS13	0.585	CPS33
0.759	0.655	CPS14	0.655	CPS34
0.654	0.724	CPS15	0.724	CPS35
0.528	0.793	CPS16	0.793	CPS36
0.382	0.862	CPS17	0.862	CPS37
0.218	0.930	CPS18	0.932	CPS38
0.129	0.965	CPS19	0.966	CPS39
0.015	1.000		1.000	

Figure 49. Sidewall S7 external coordinates and location of pressure orifices.

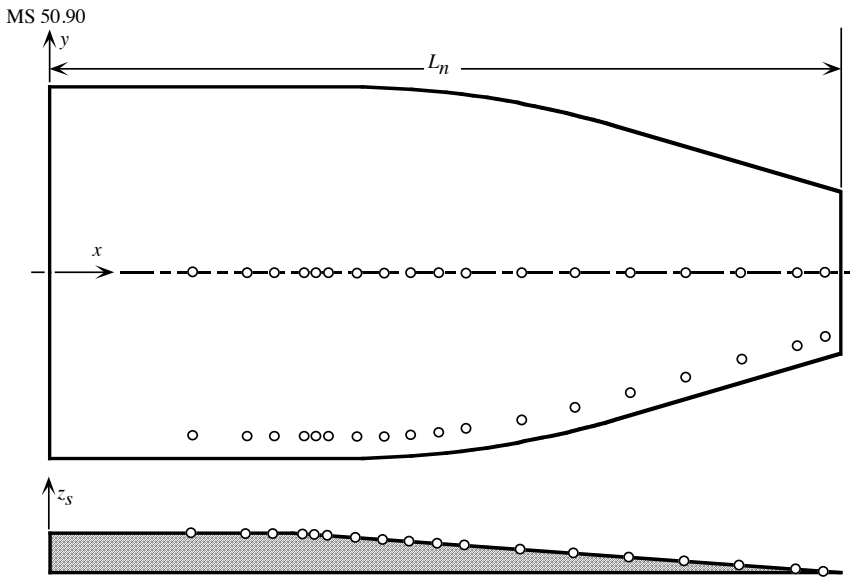

	Centerline row			Outboard row		
$z/z_{s,max}$	x/L_n	$y/h_m/2 = 0$	orifice	x/L_n	$y/h_m/2 = 0$	orifice
1.000	0.000			0.000		
1.000	0.172	0.000	CPS1	0.173	-0.871	CPS21
1.000	0.240	0.000	CPS2	0.242	-0.871	CPS22
1.000	0.276	0.000	CPS3	0.278	-0.871	CPS23
0.957	0.318	0.000	CPS5	0.319	-0.871	CPS25
0.943	0.328	0.000	CPS6	0.327	-0.871	CPS26
0.919	0.345	0.000	CPS7	0.344	-0.871	CPS27
0.870	0.381	0.000	CPS8	0.383	-0.871	CPS28
0.821	0.415	0.000	CPS9	0.417	-0.871	CPS29
0.774	0.448	0.000	CPS10	0.449	-0.865	CPS30
0.724	0.484	0.000	CPS11	0.482	-0.839	CPS31
0.676	0.518	0.000	CPS12	0.516	-0.829	CPS32
0.580	0.587	0.000	CPS13	0.586	-0.787	CPS33
0.484	0.655	0.000	CPS14	0.654	-0.719	CPS34
0.387	0.725	0.000	CPS15	0.725	-0.639	CPS35
0.288	0.795	0.000	CPS16	0.793	-0.561	CPS36
0.195	0.861	0.000	CPS17	0.862	-0.468	CPS37
0.096	0.932	0.000	CPS18	0.935	-0.384	CPS38
0.056	0.960	0.000	CPS19	0.965	-0.339	CPS39
0.015	1.000			1.000		

Figure 50. Sidewall S8 external coordinates and location of pressure orifices.

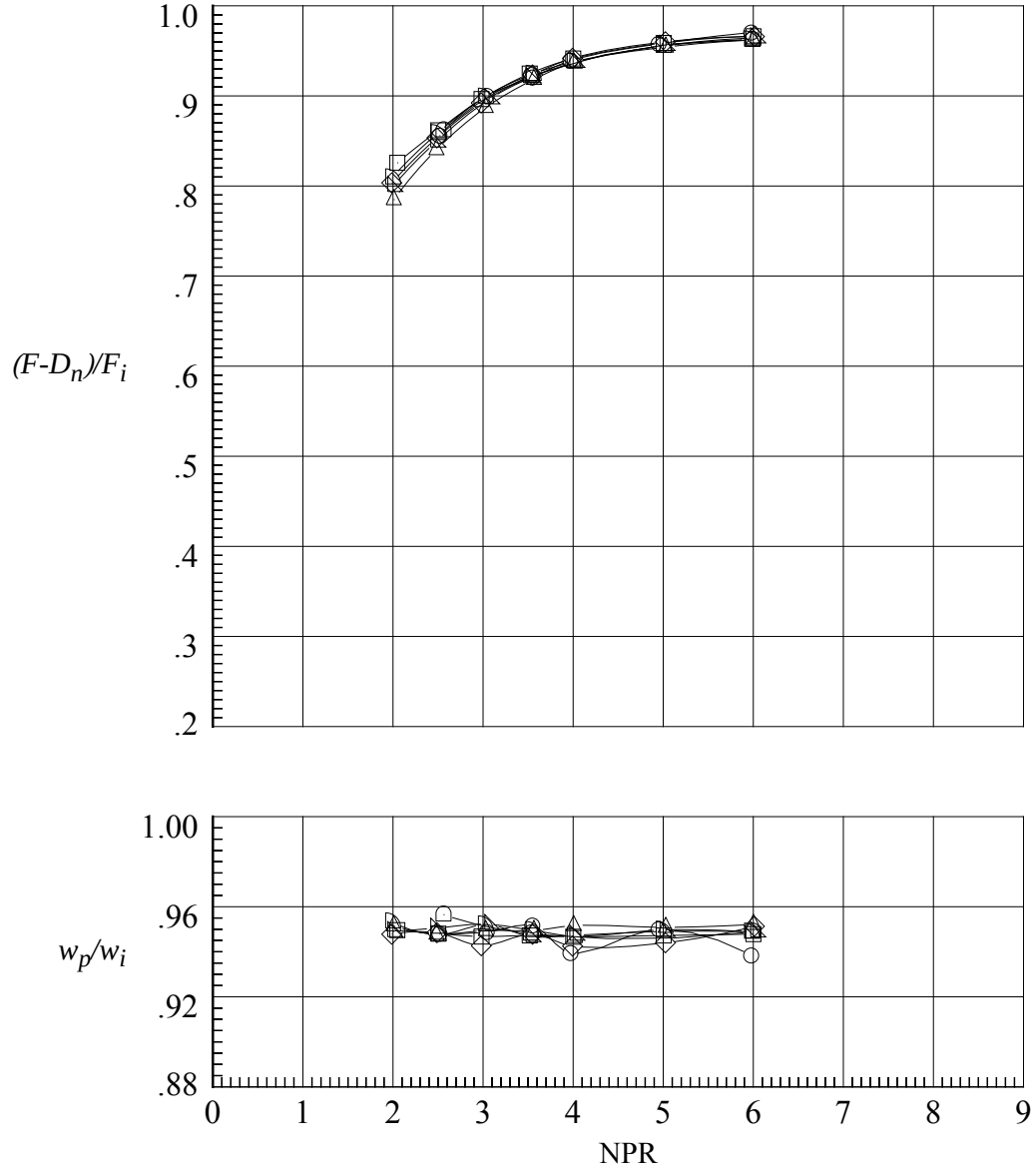

(a) Variation of $(F-D_n)/F_i$ and w_p/w_i.

Figure 51. Aeropropulsive performance data repeatability for nozzle N1. Symbols represent different runs.

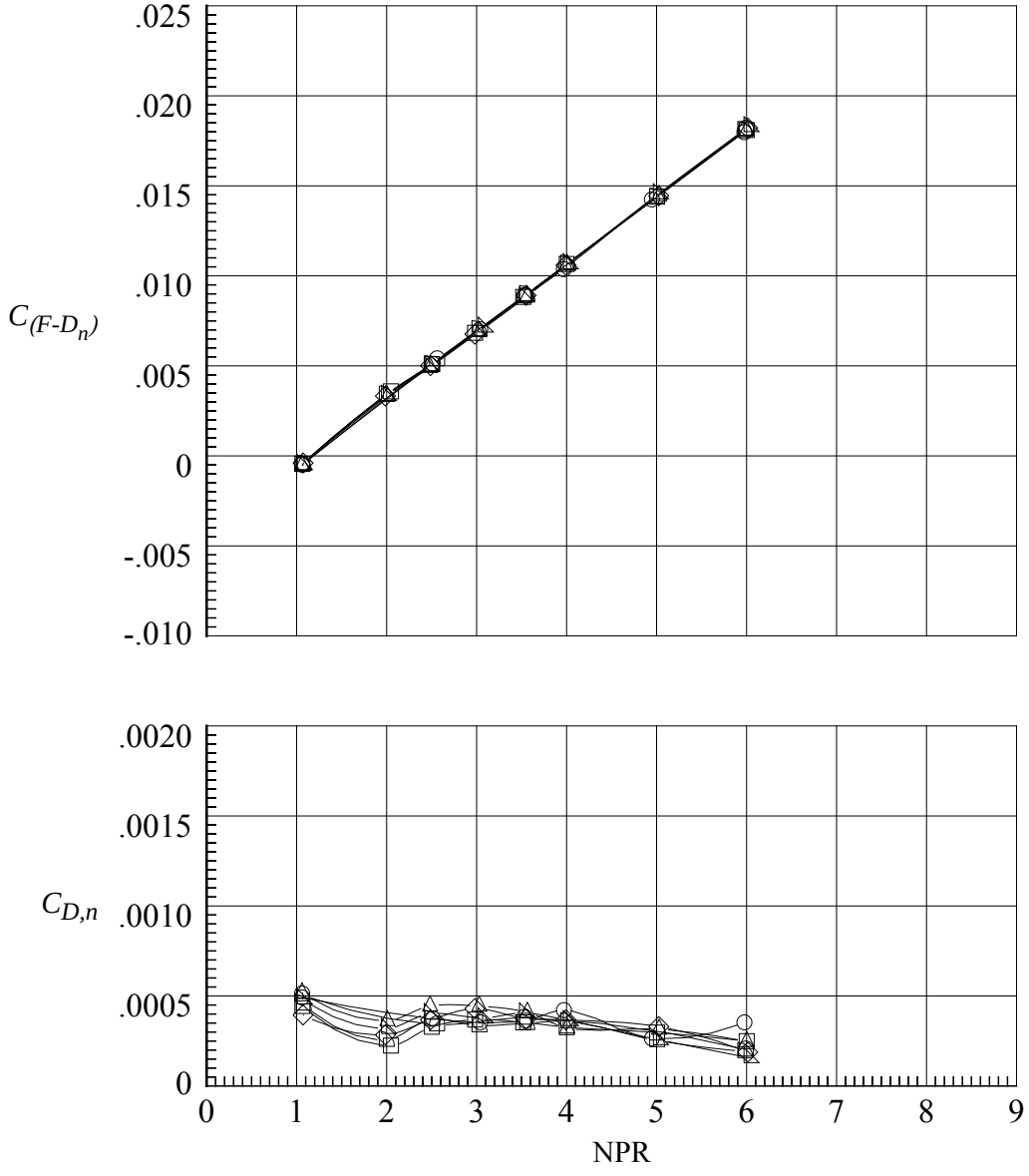

(b) Variation of $C_{(F\text{-}D_n)}$ and $C_{D,n}$.

Figure 51. Continued.

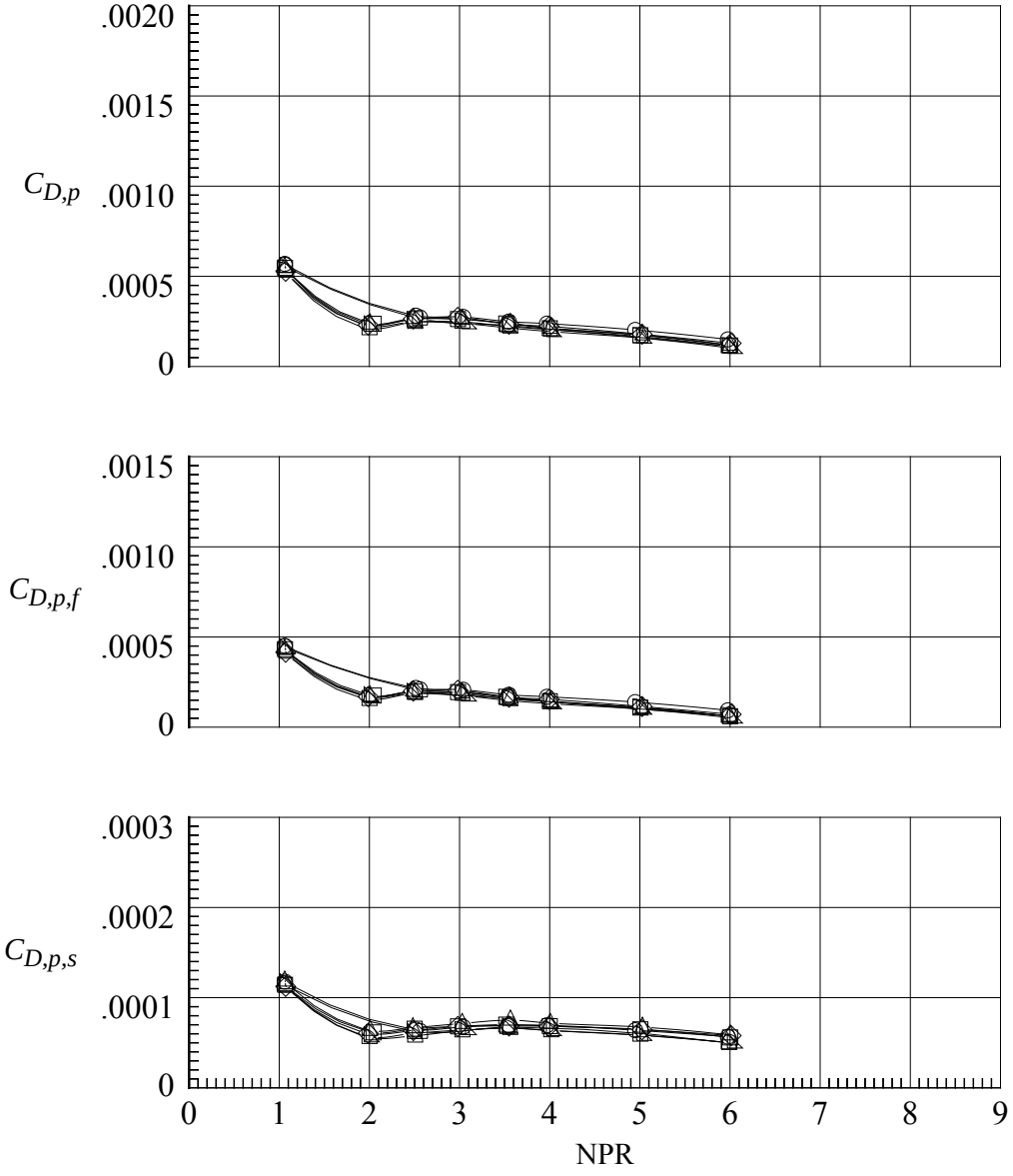

(c) Variation of $C_{D,p}$, $C_{D,p,f}$, and $C_{D,p,s}$.

Figure 51. Continued.

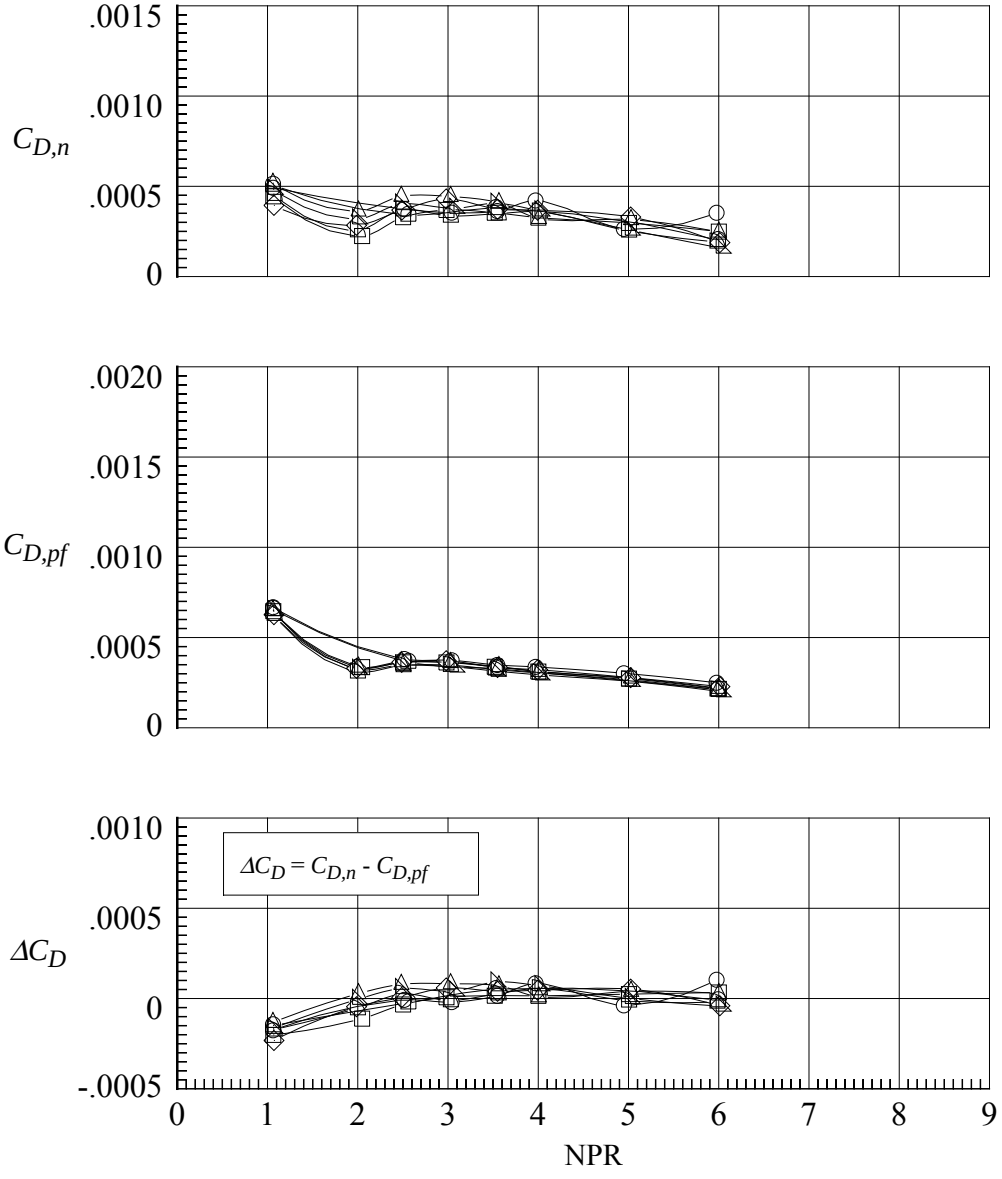

(d) Variation of $C_{D,n}$, $C_{D,pf}$, and ΔC_D.

Figure 51. Concluded.

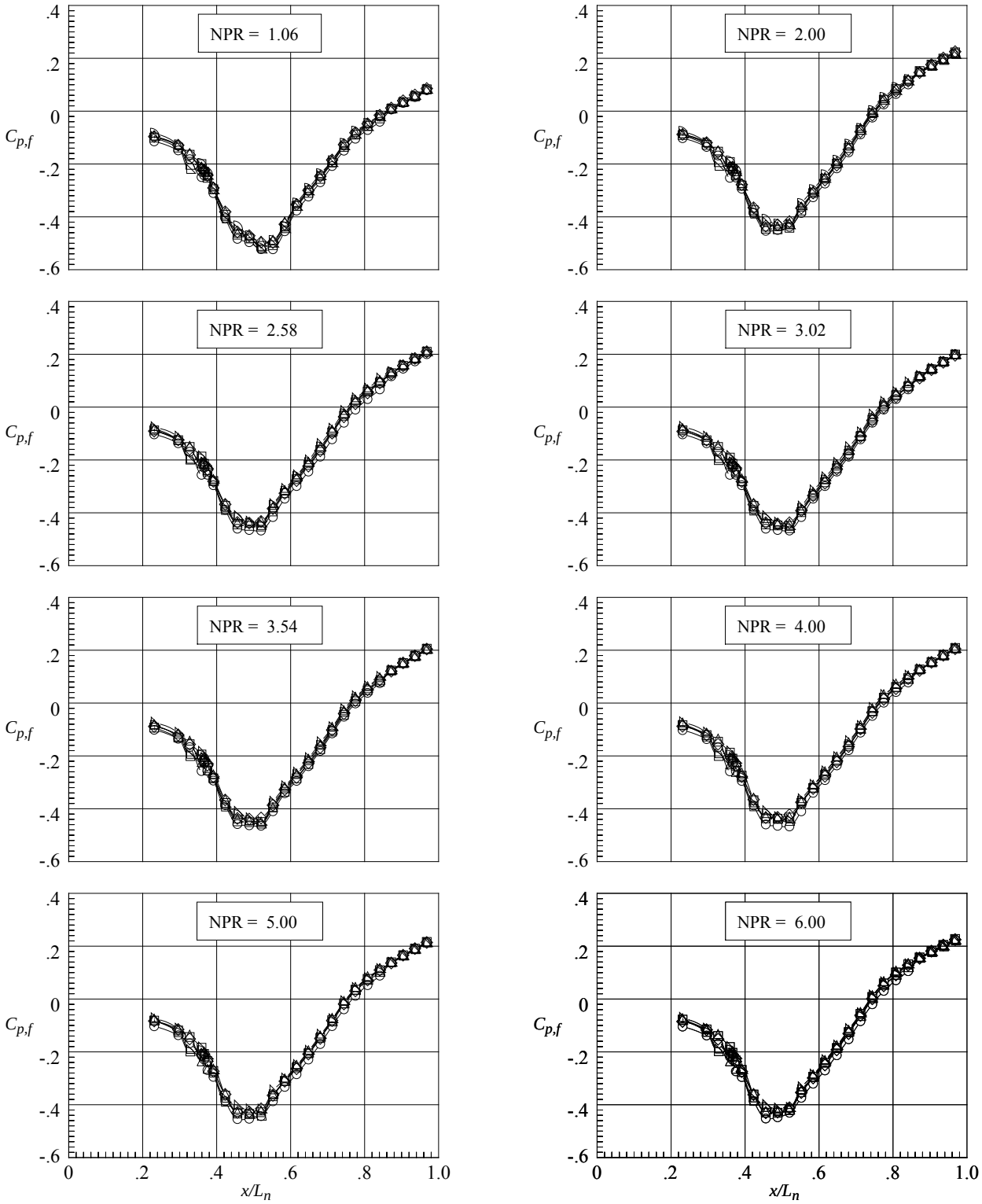

(a) Flap top center row, $z/w_f/2 = 0$.

Figure 52. Nozzle N1 pressure coefficient repeatability from different runs.
Symbols represent different runs.

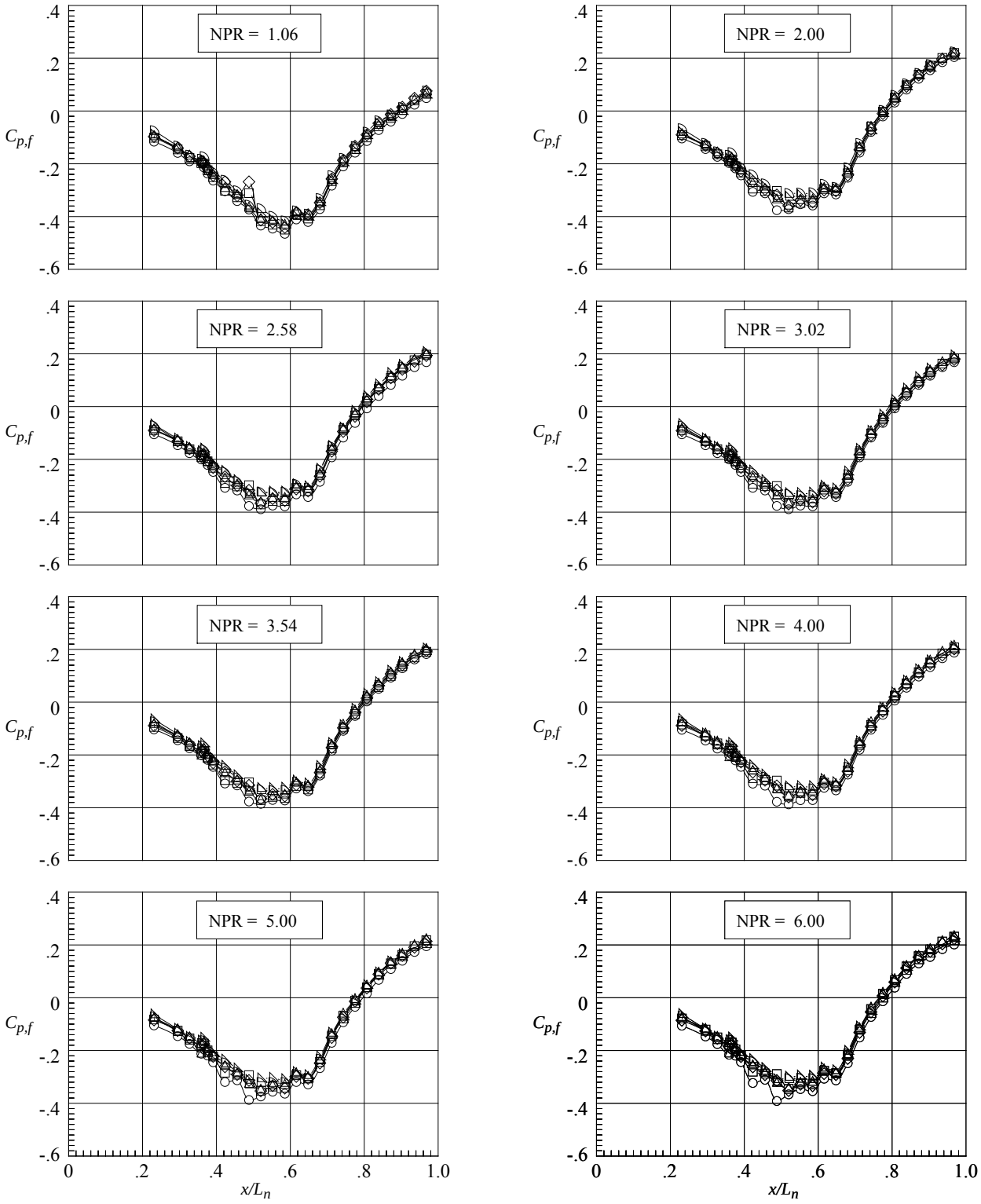

(b) Flap top outboard row, $z/w_f/2 = 0.95$

Figure 52. Continued.

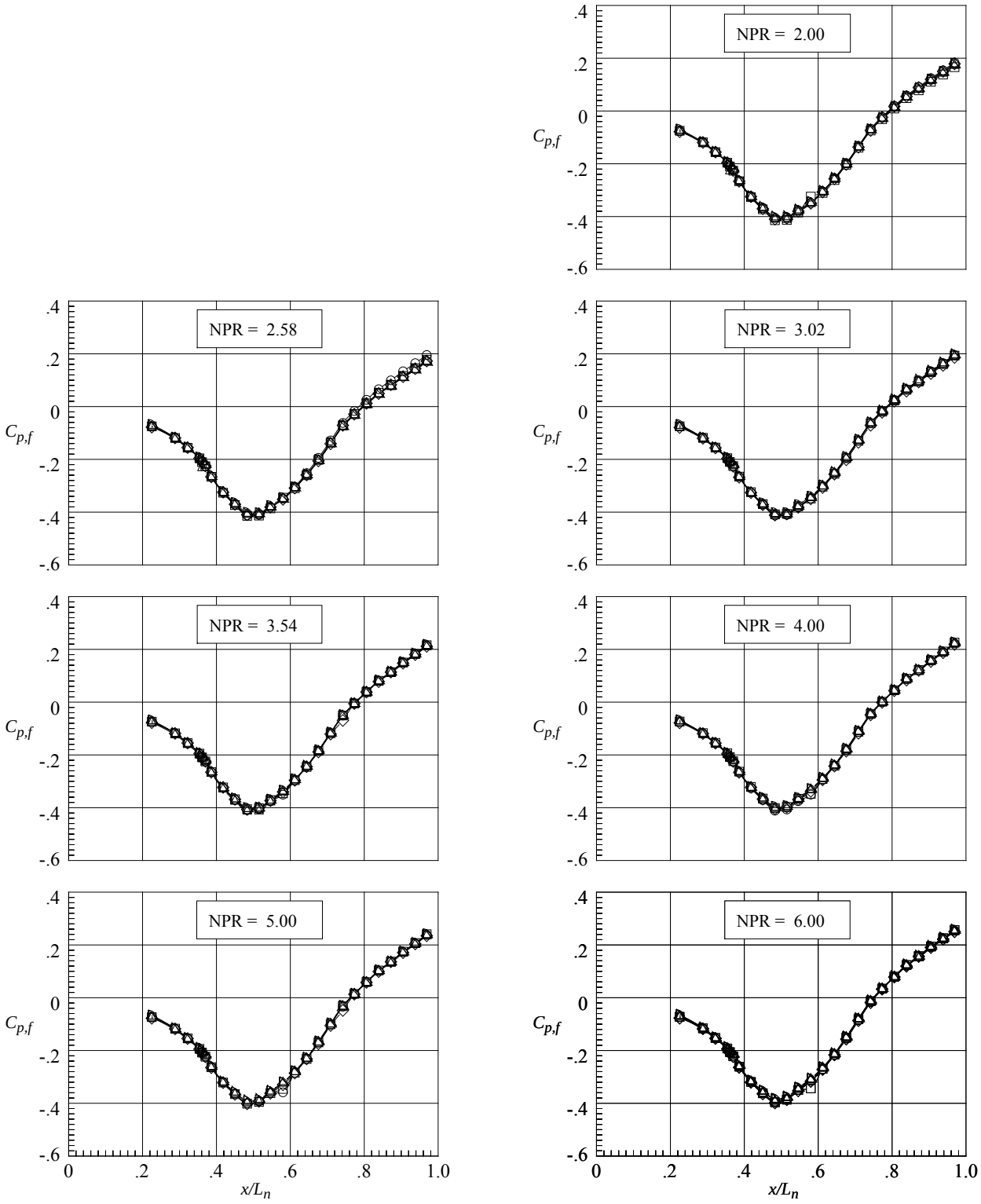

(c) Flap bottom center row, $z/w_f/2 = 0$.

Figure 52. Continued.

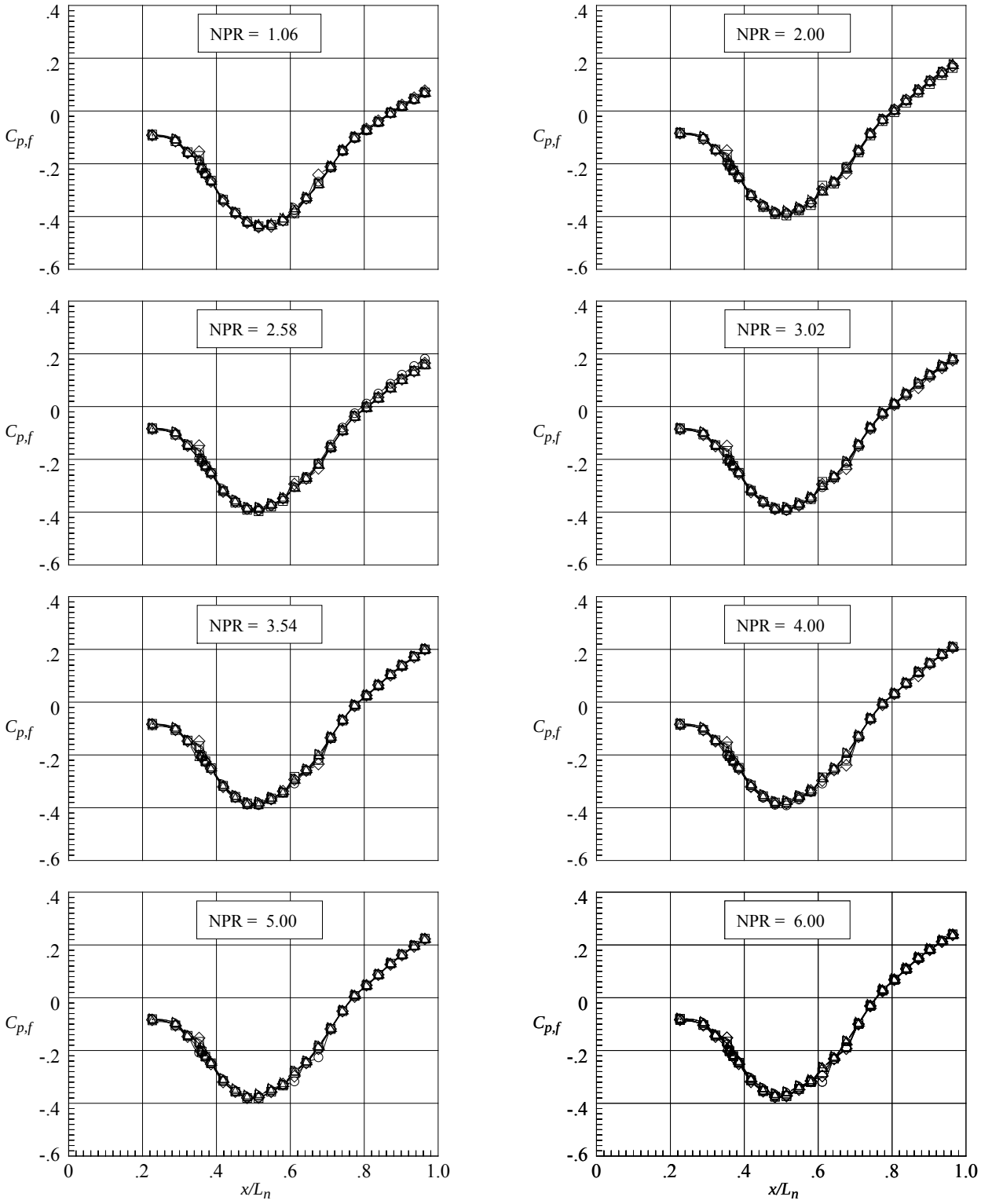

(d) Flap bottom middle row, $z/w_f/2 = 5$.

Figure 52. Continued.

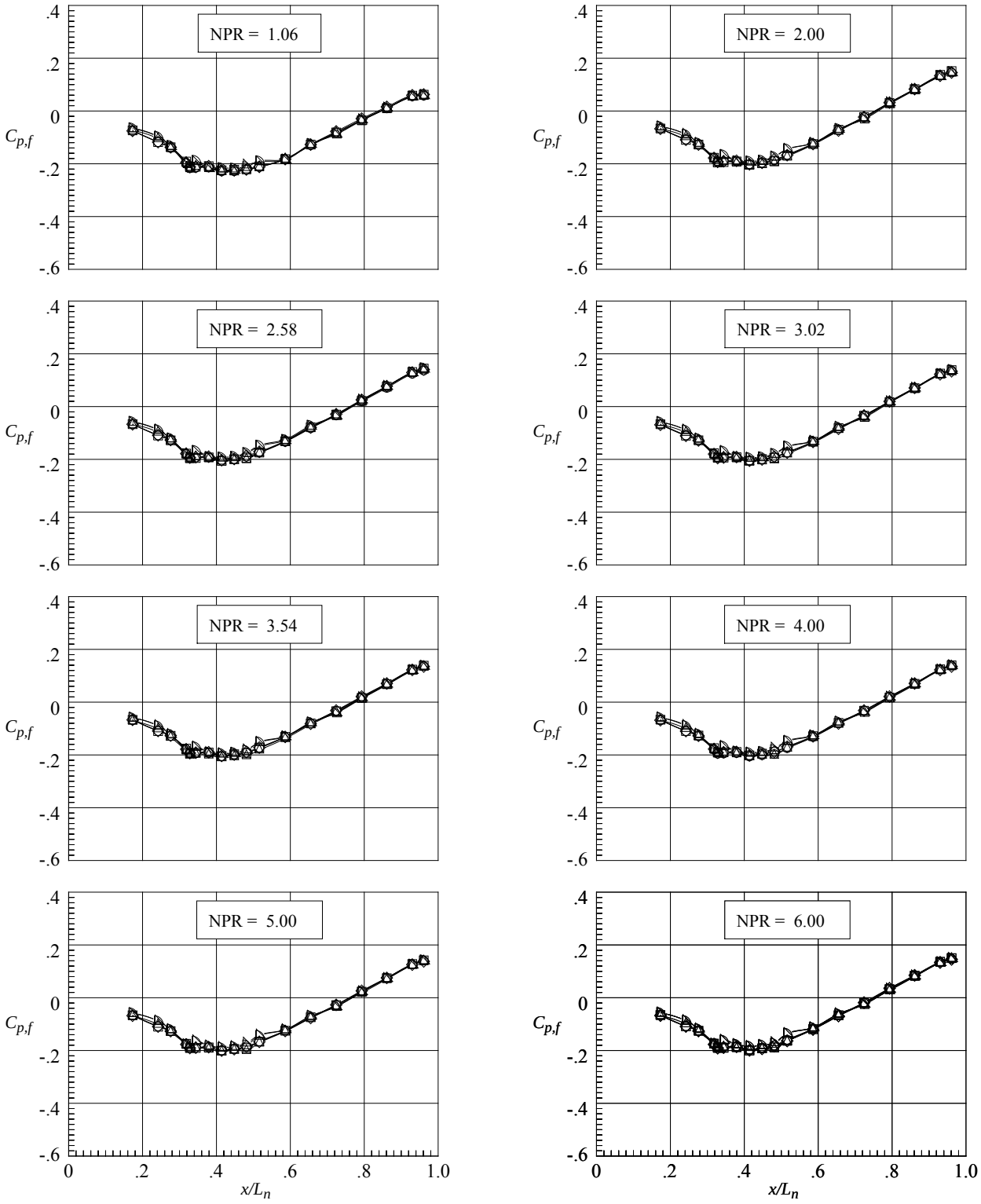

(e) Sidewall center row, $y/h_m/2 = 0$.

Figure 52. Continued.

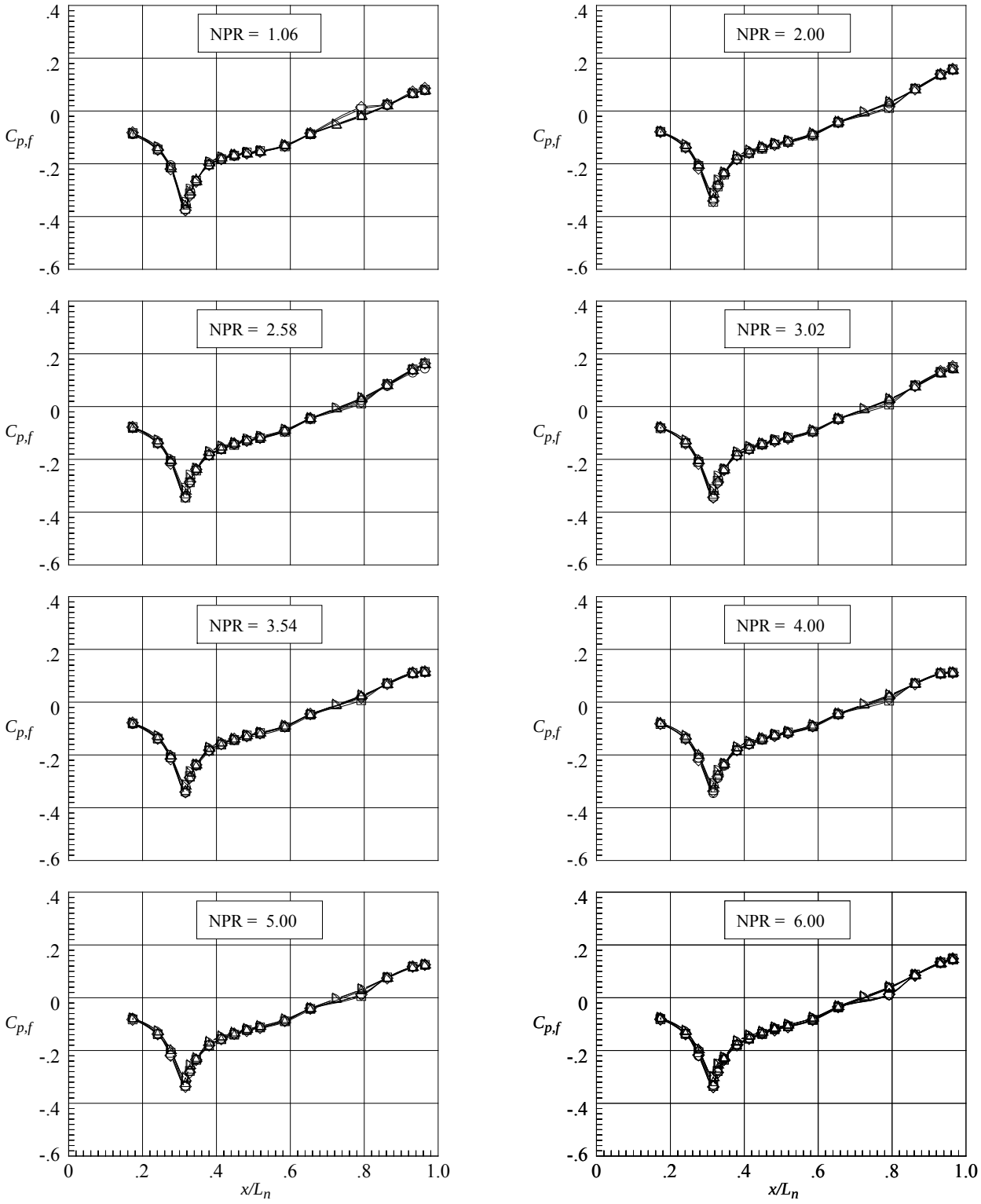

(f) Sidewall outboard row, $y/h_m/2$ = -0.87.

Figure 52. Concluded.

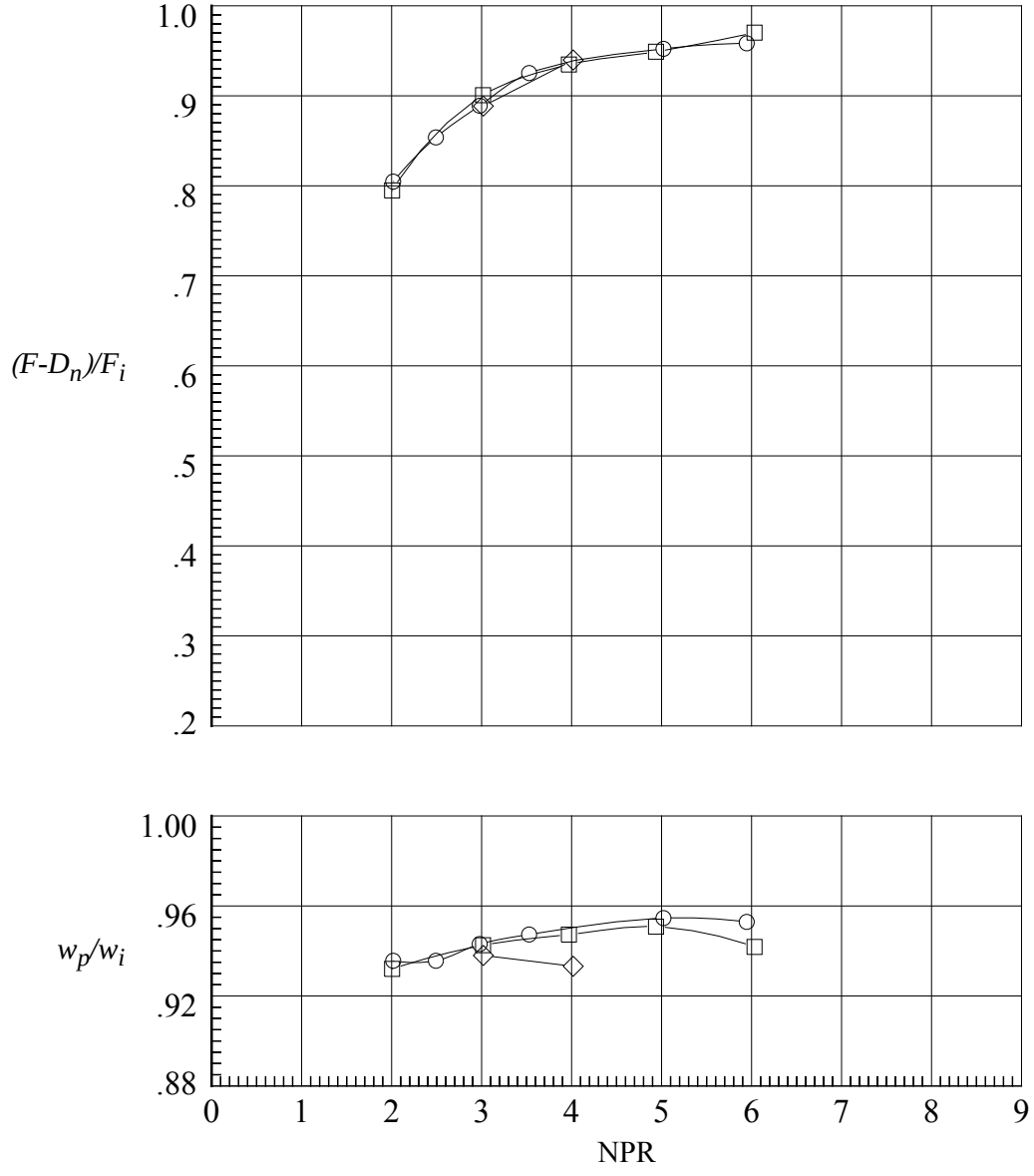

(a) Variation of $(F\text{-}D_n)/F_i$ and w_p/w_i.

Figure 53. Aeropropulsive performance data repeatability for nozzle N6. Symbols represent different runs.

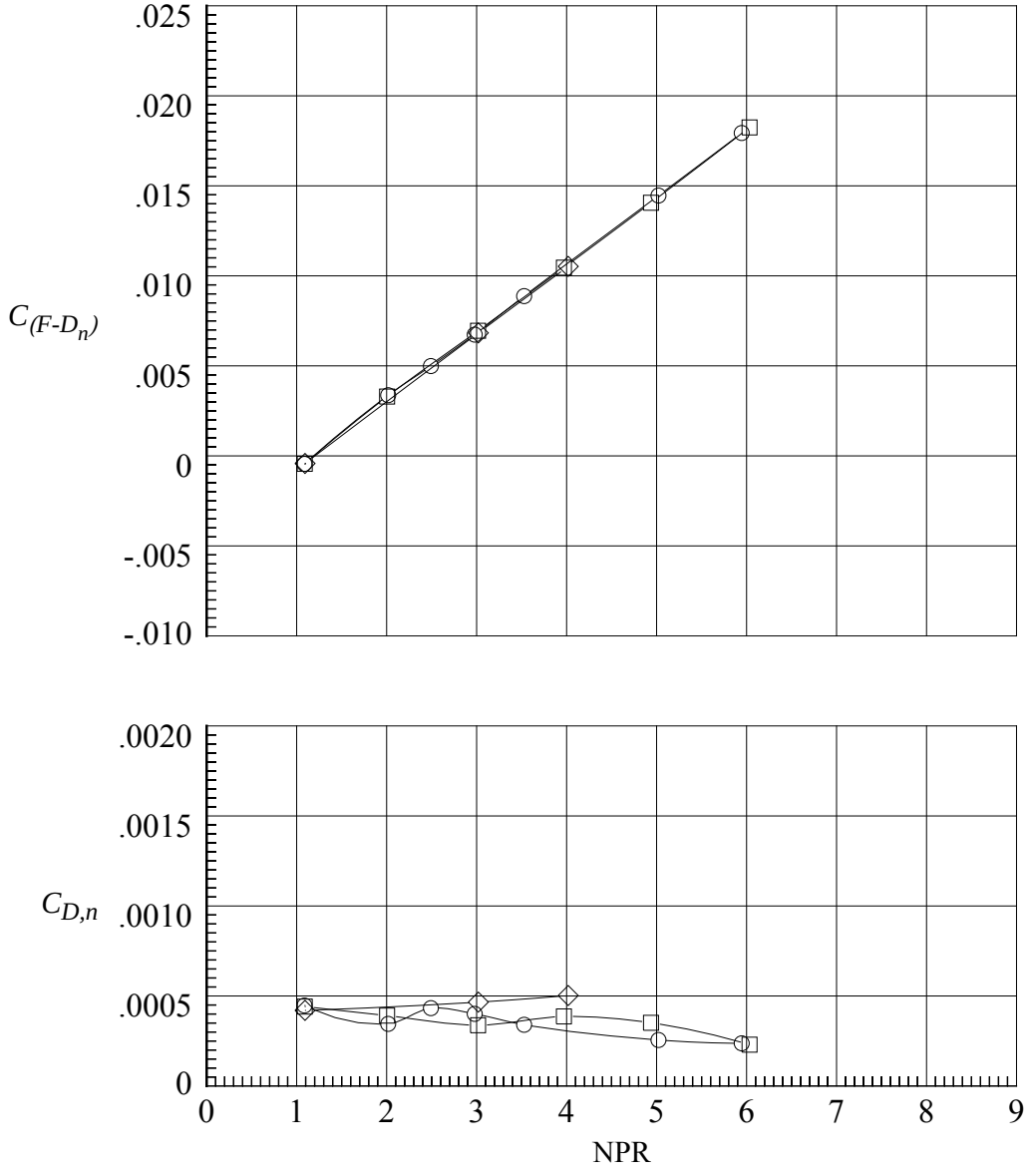

(b) Variation of $C_{(F\text{-}D_n)}$ and $C_{D,n}$.

Figure 53. Continued.

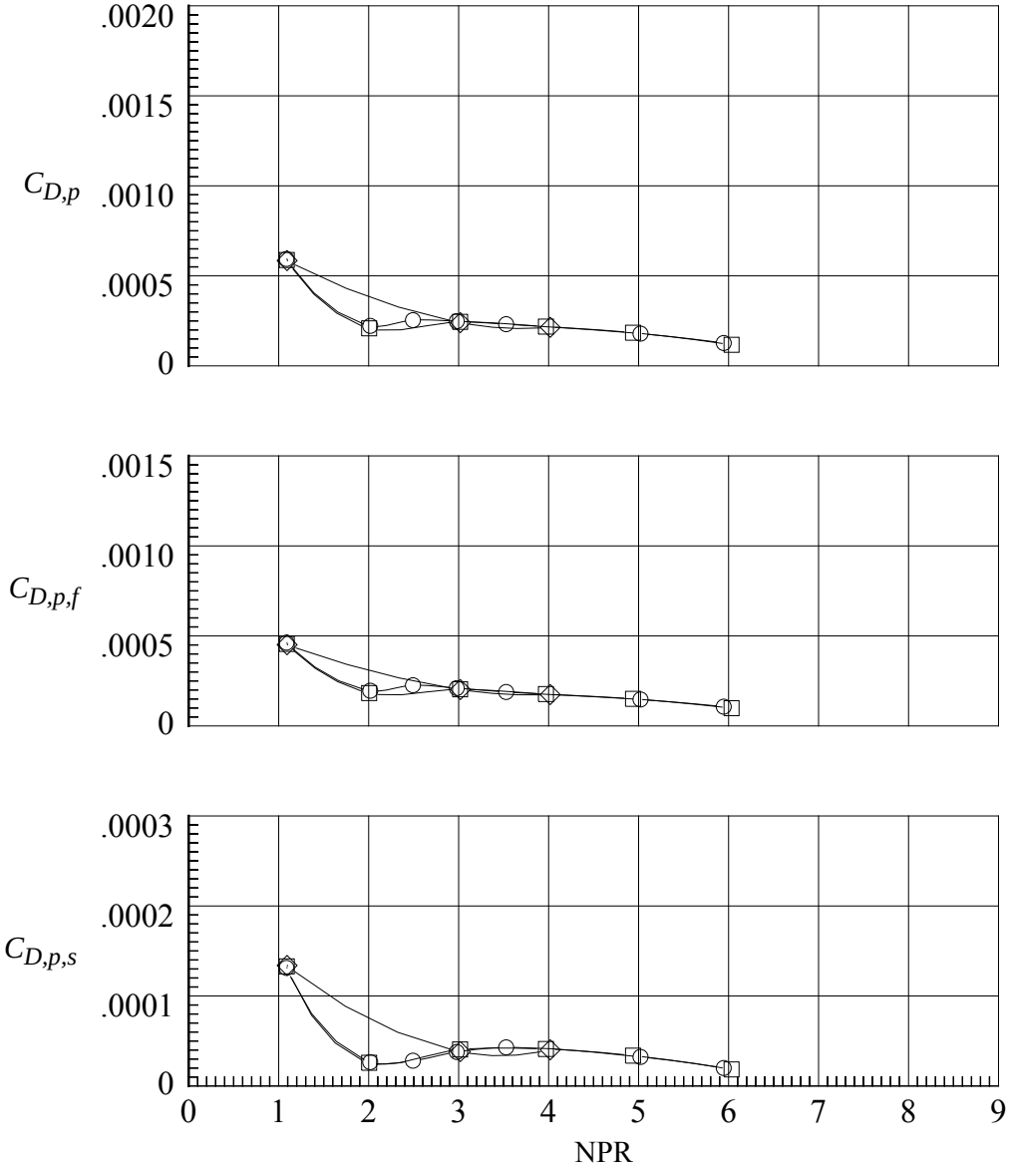

(c) Variation of $C_{D,p}$, $C_{D,p,f}$, and $C_{D,p,s}$.

Figure 53. Continued.

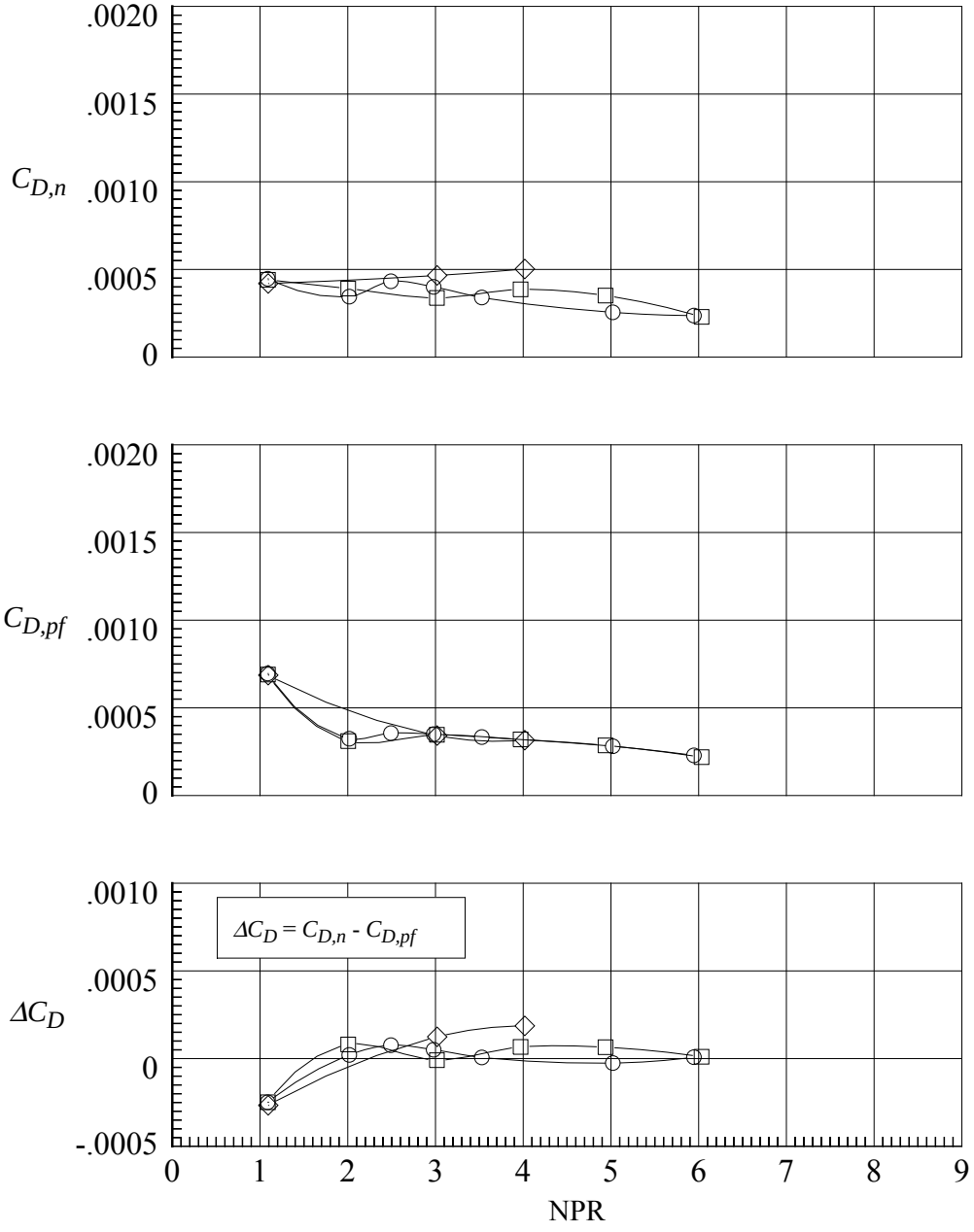

(d) Variation of $C_{D,n}$, $C_{D,pf}$, and ΔC_D.

Figure 53. Concluded.

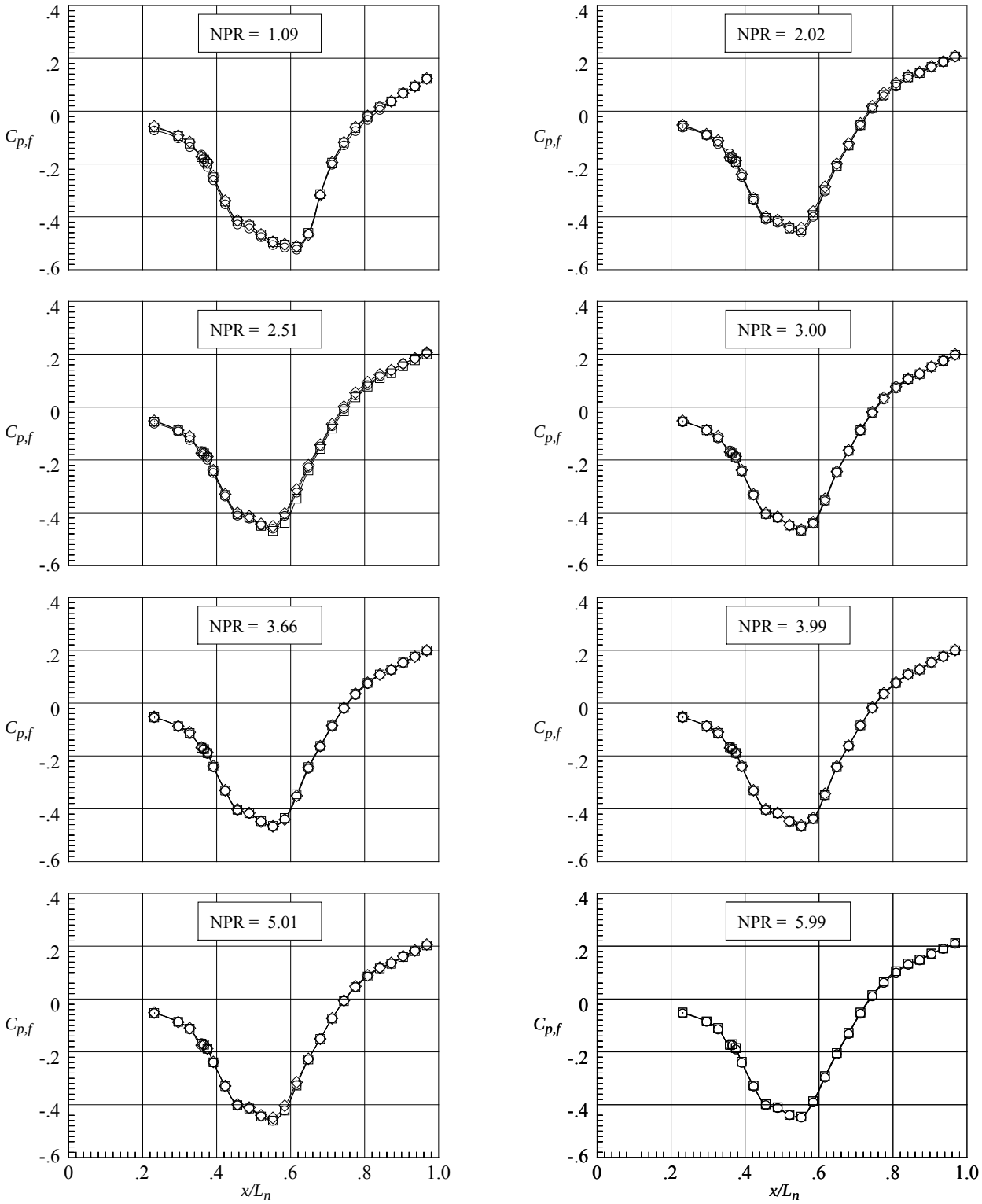

(a) Flap top center row, $z/w_f/2 = 0$.

Figure 54. Nozzle N6 pressure coefficient repeatability from different runs.
Symbols represent different runs.

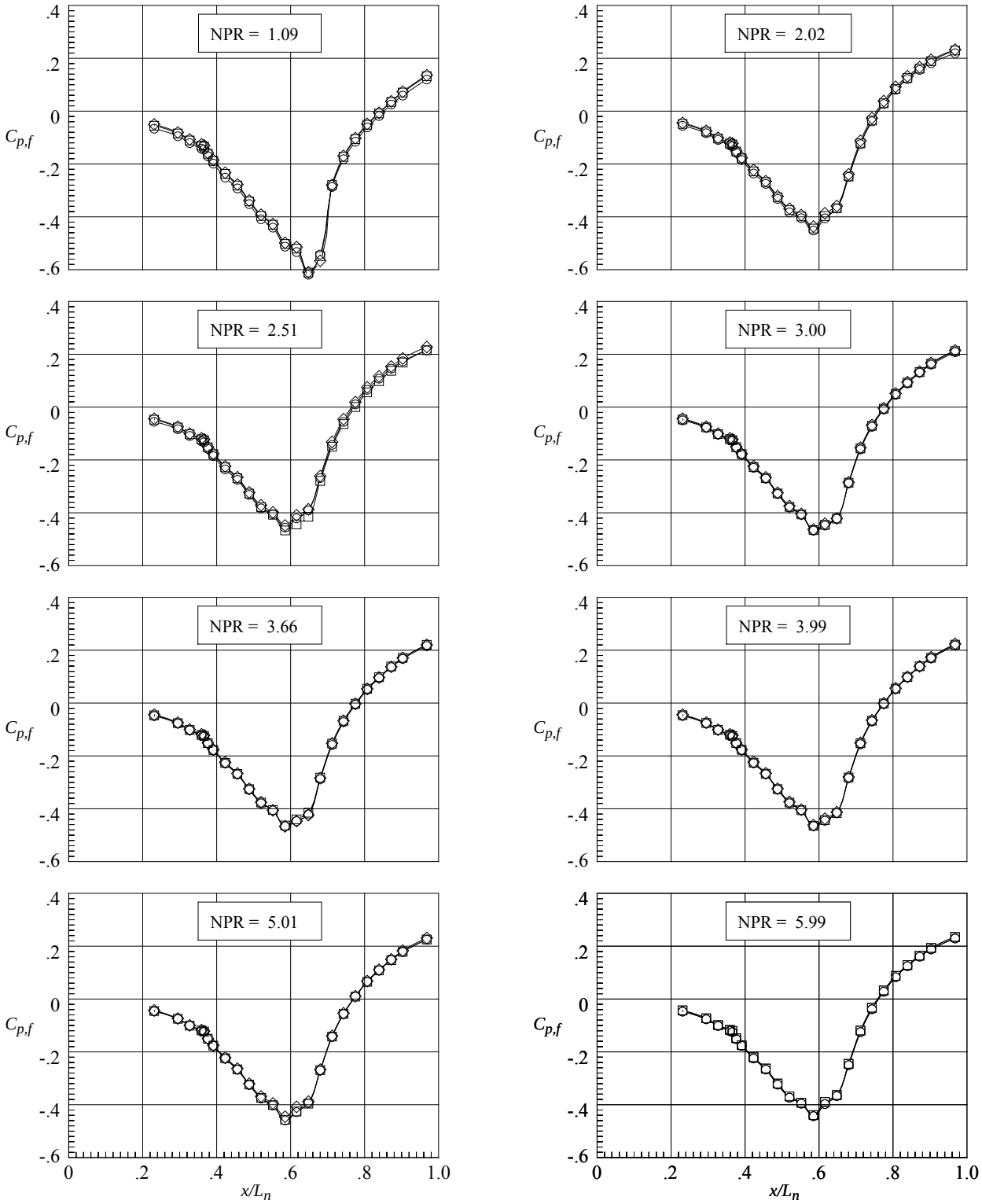

(b) Flap top outboard row, $z/w_f/2 = 0.95$

Figure 54. Continued.

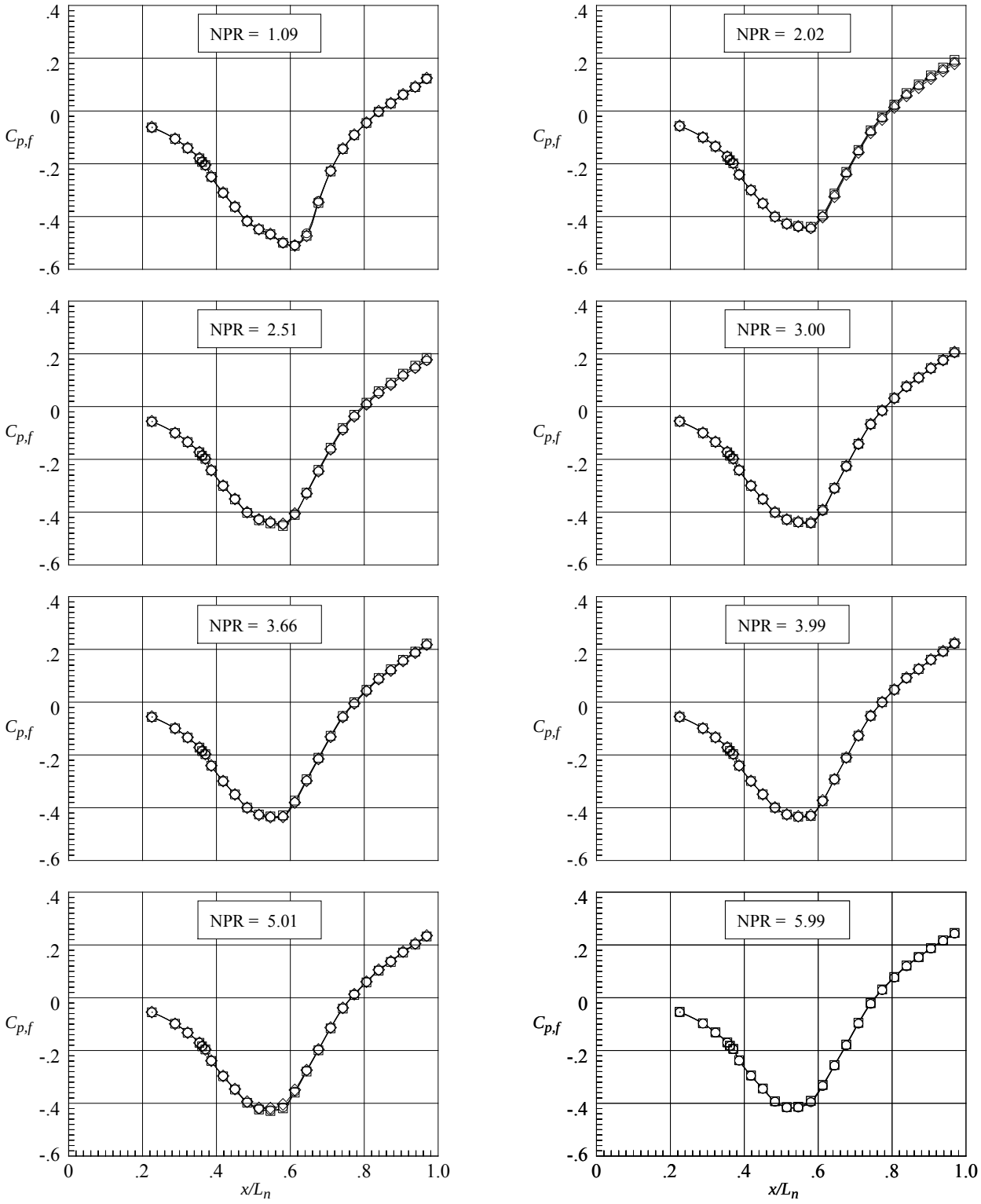

(c) Flap bottom center row, $z/w_f/2 = 0$.

Figure 54. Continued.

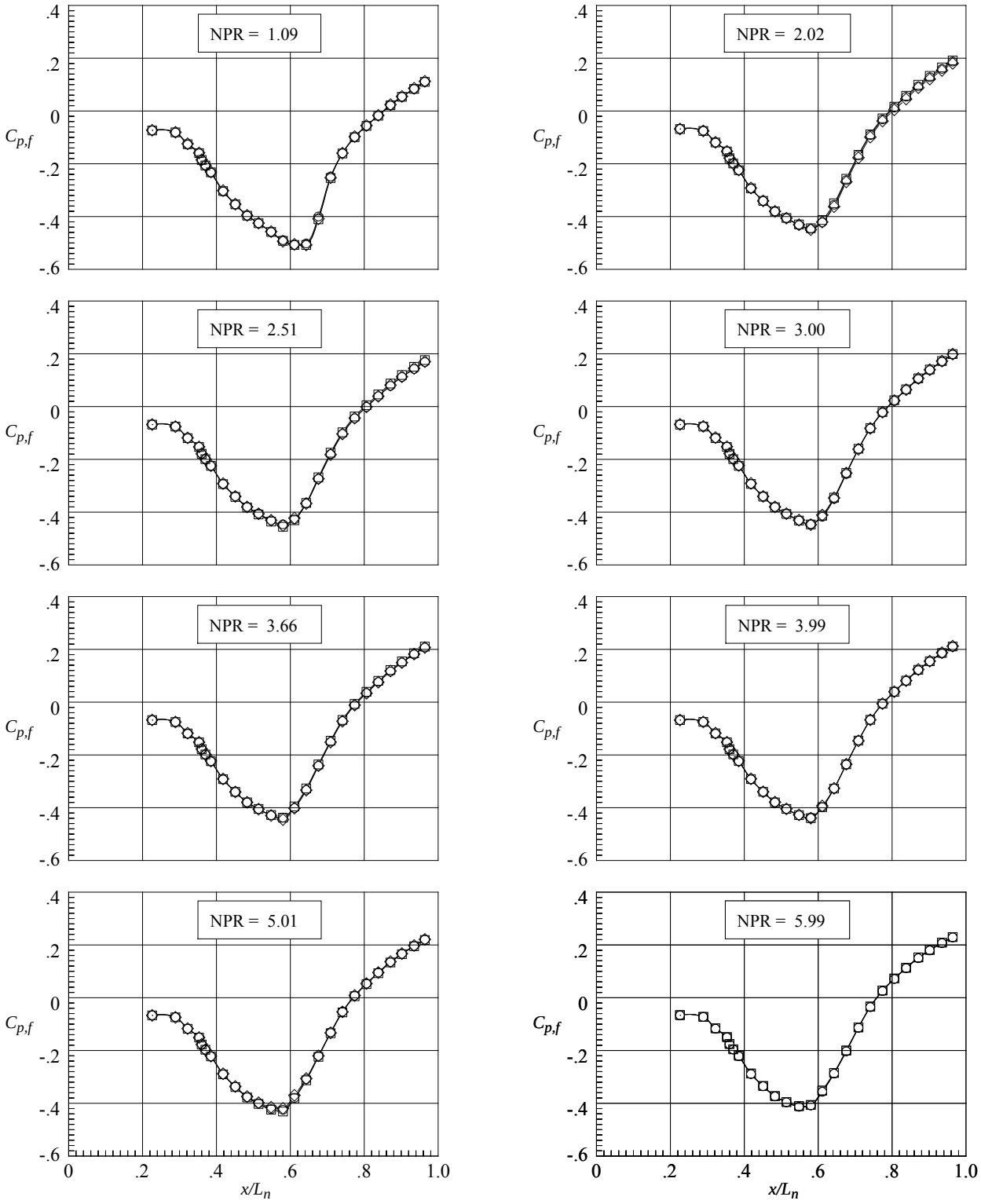

(d) Flap bottom middle row, $z/w_f/2 = 5$.

Figure 54. Continued.

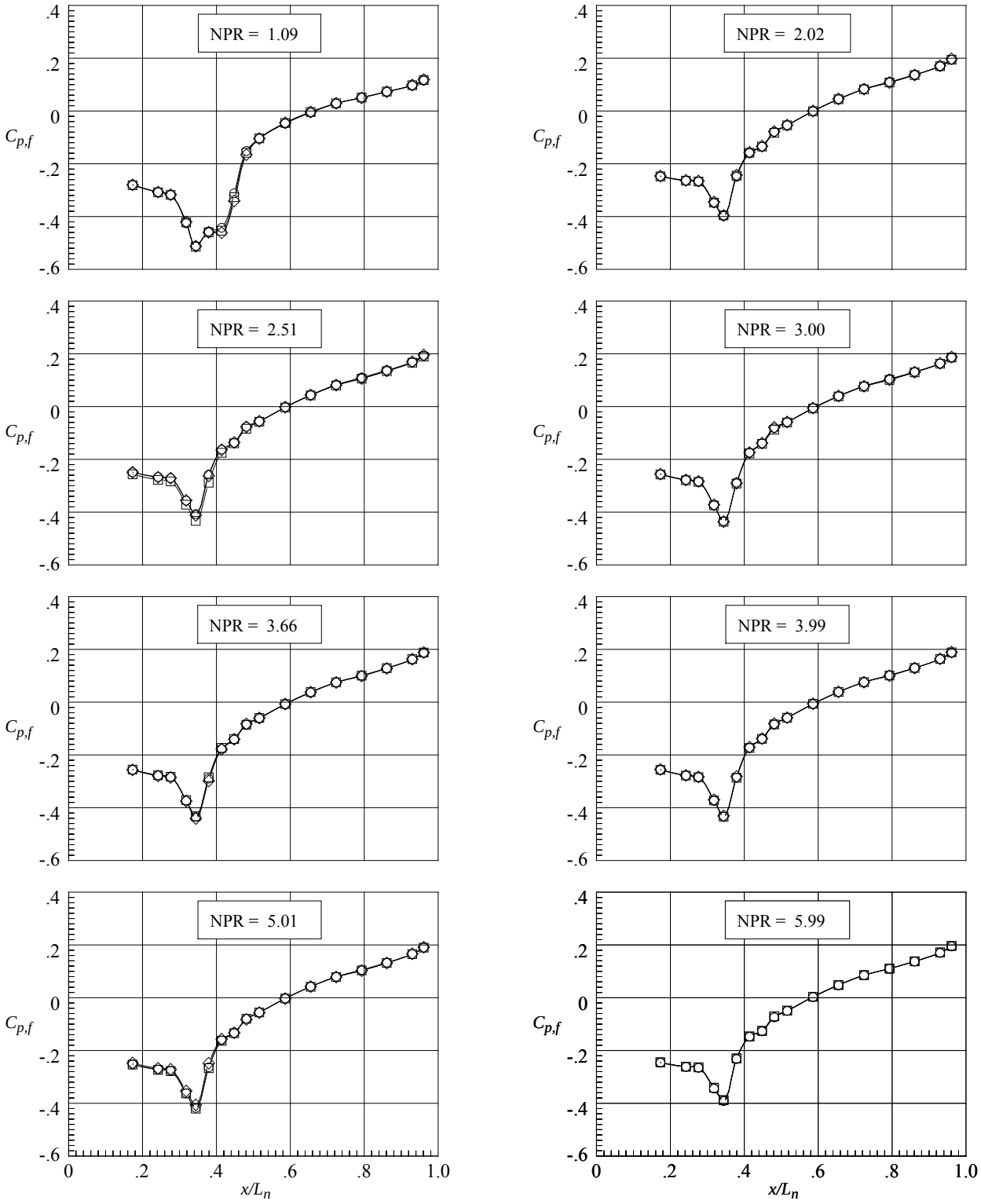

(e) Sidewall center row, $y/h_m/2 = 0$.

Figure 54. Continued.

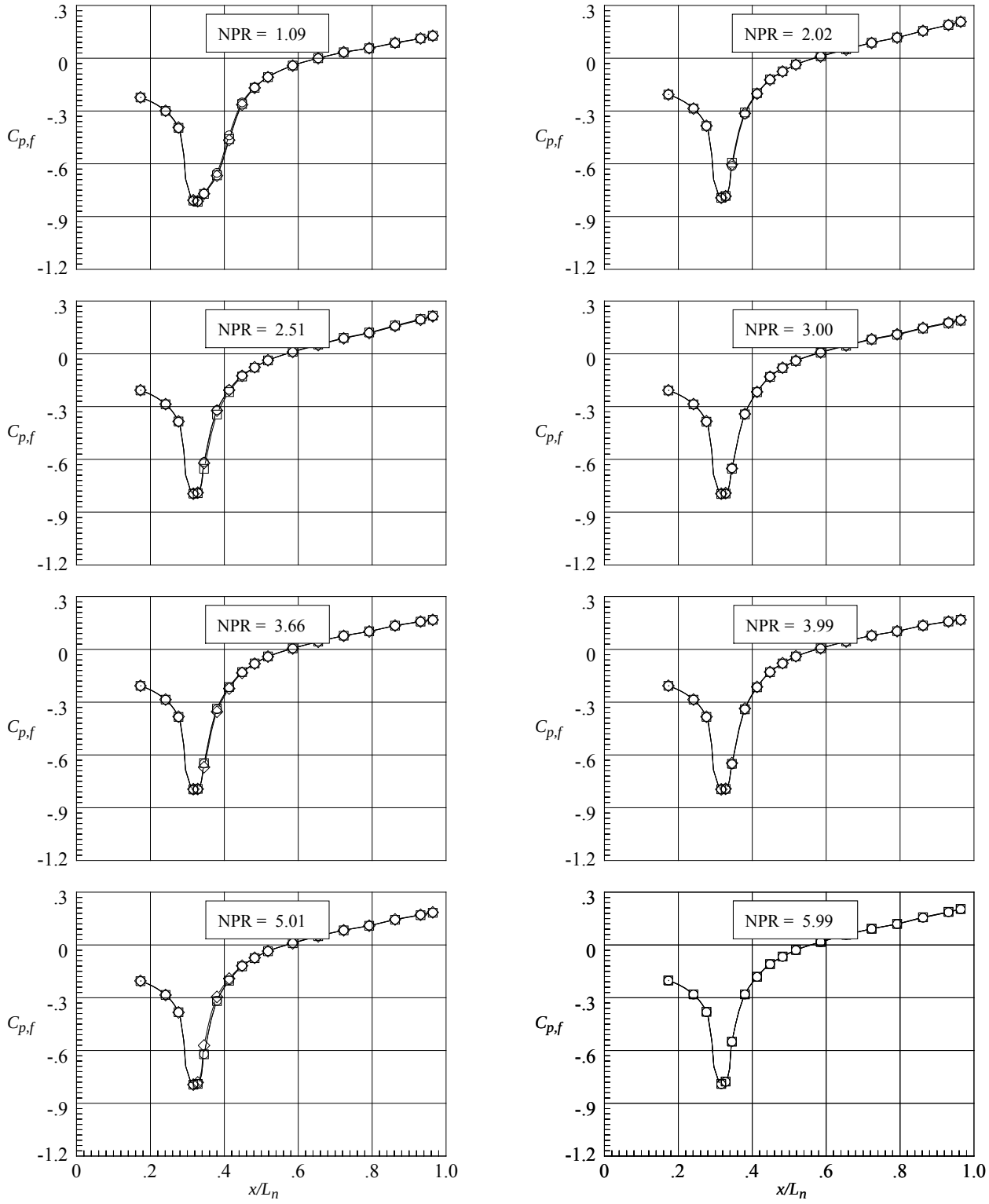

(f) Sidewall outboard row, $y/h_m/2$ = -0.87.

Figure 54. Concluded.

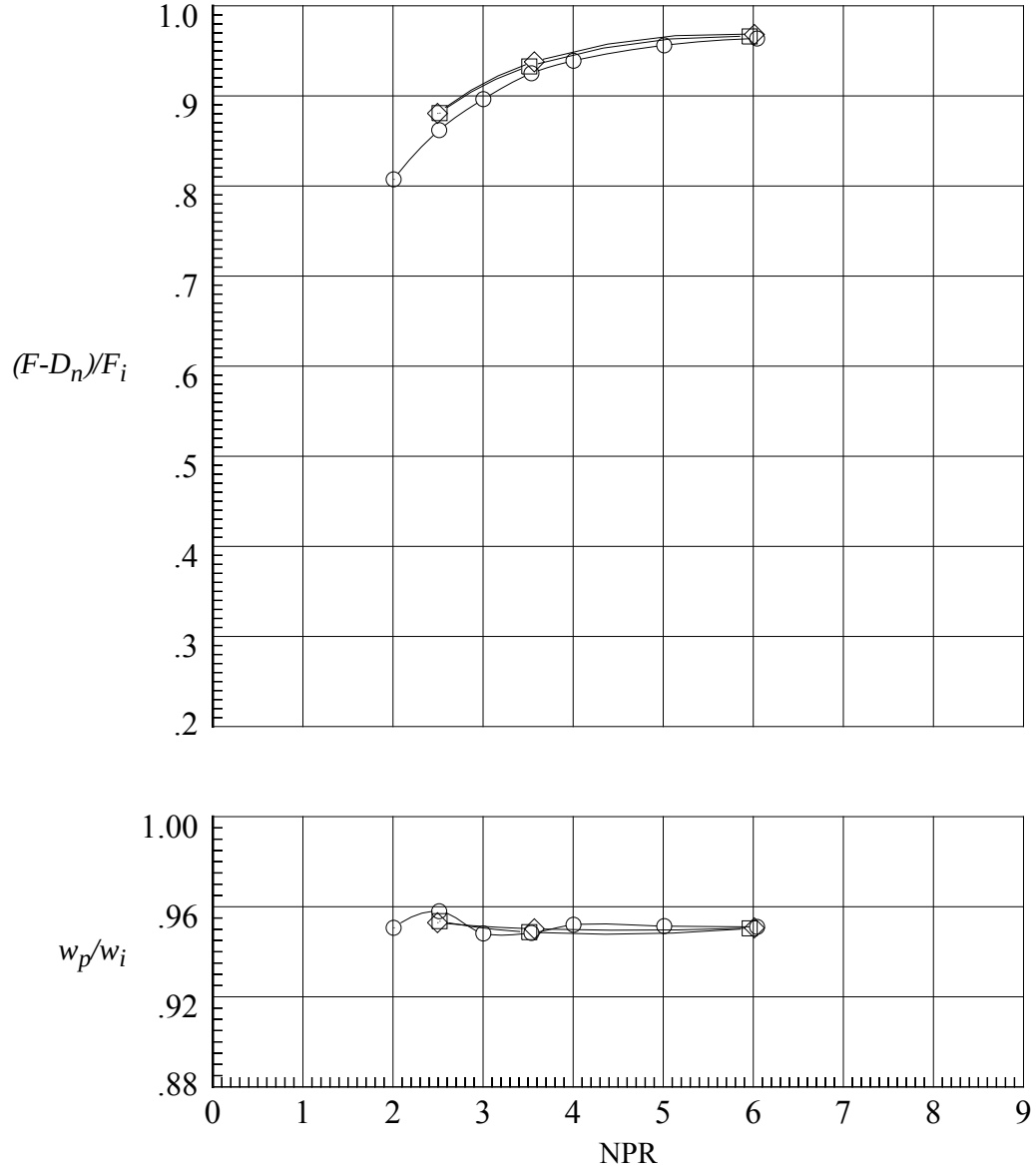

(a) Variation of $(F\text{-}D_n)/F_i$ and w_p/w_i.

Figure 55. Aeropropulsive performance data repeatability for nozzle N11. Symbols represent different run numbers.

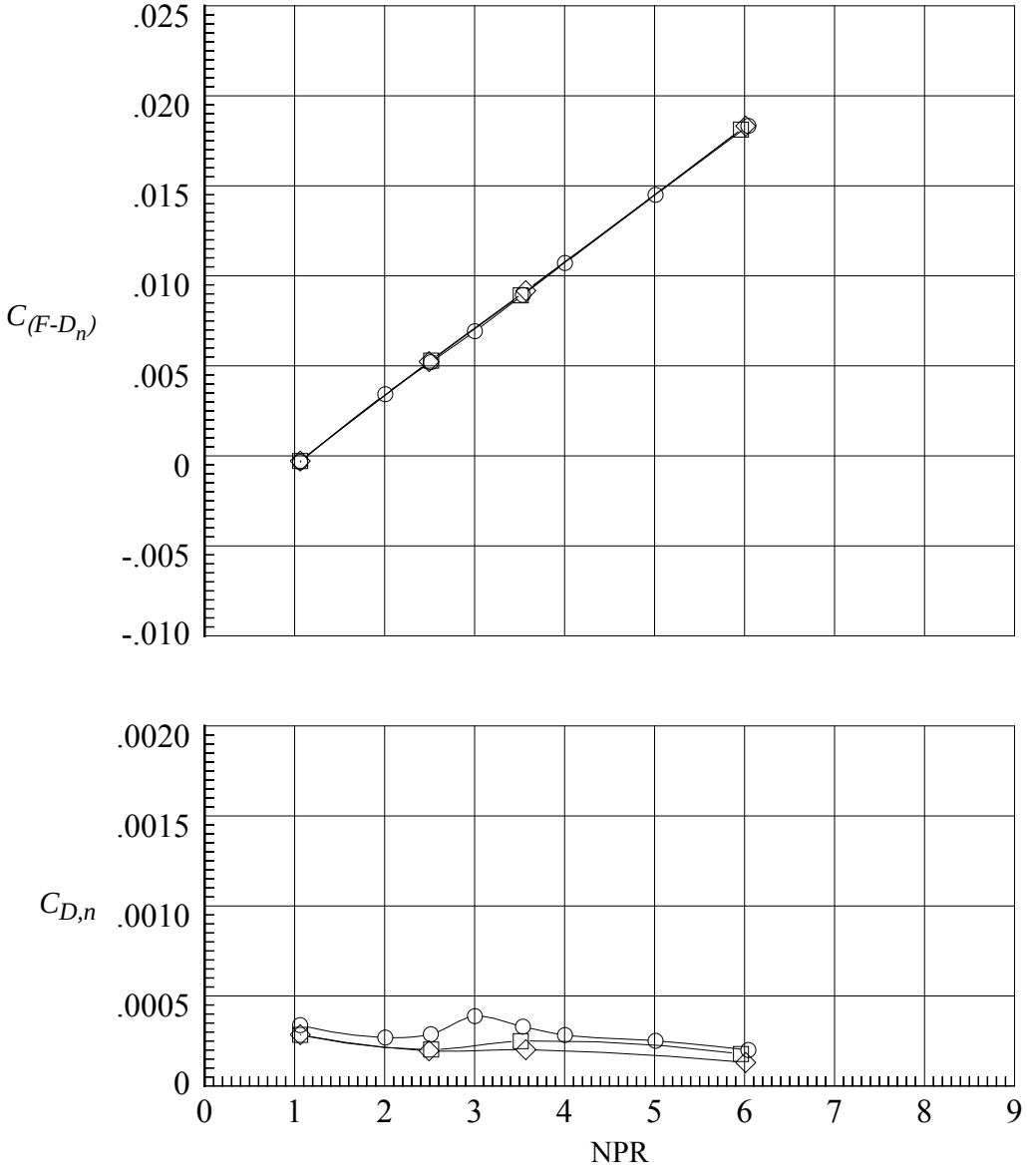

(b) Variation of $C_{(F\text{-}D_n)}$ and $C_{D,n}$.

Figure 55. Continued.

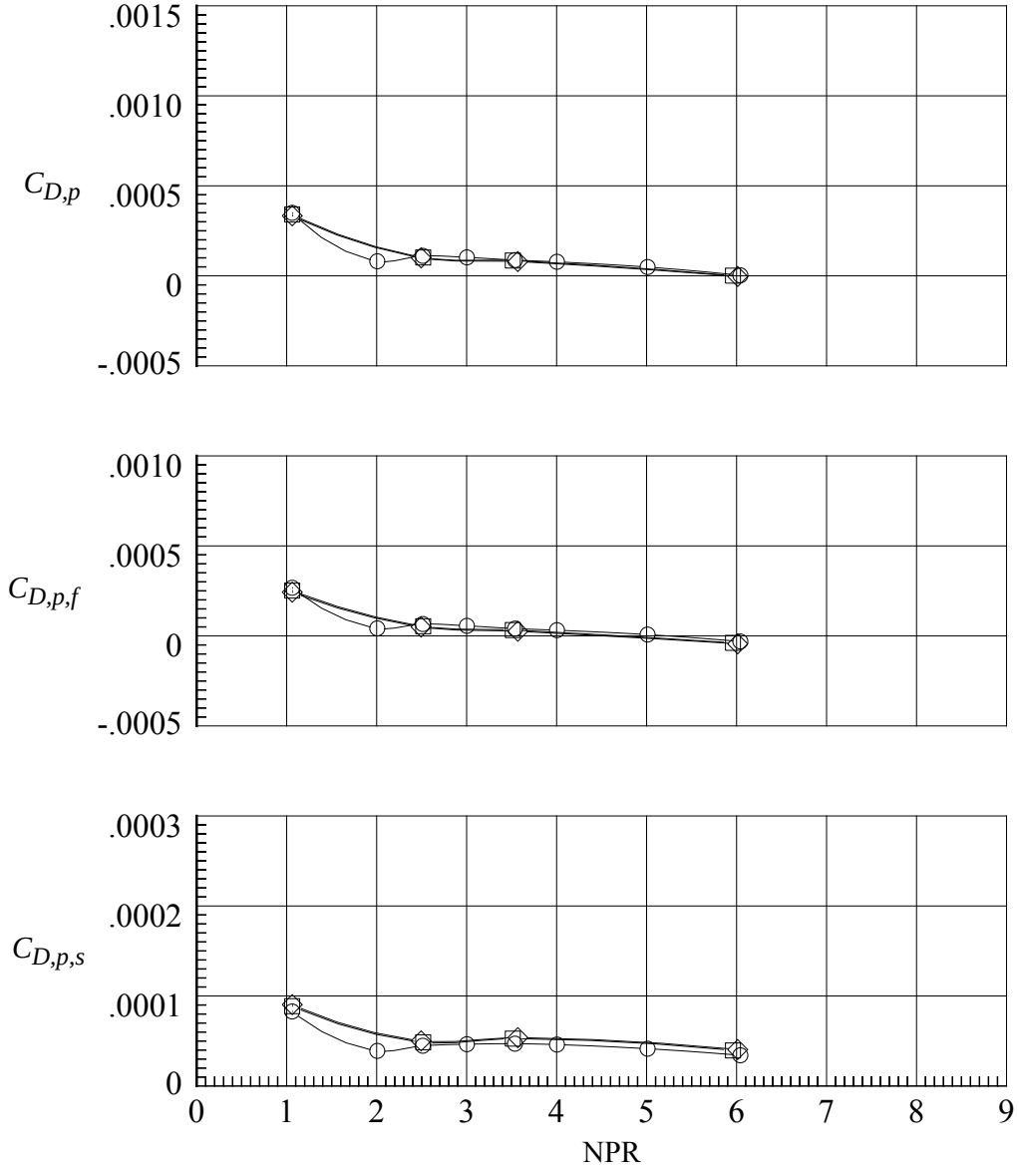

(c) Variation of $C_{D,p}$, $C_{D,p,f}$, and $C_{D,p,s}$.

Figure 55. Continued.

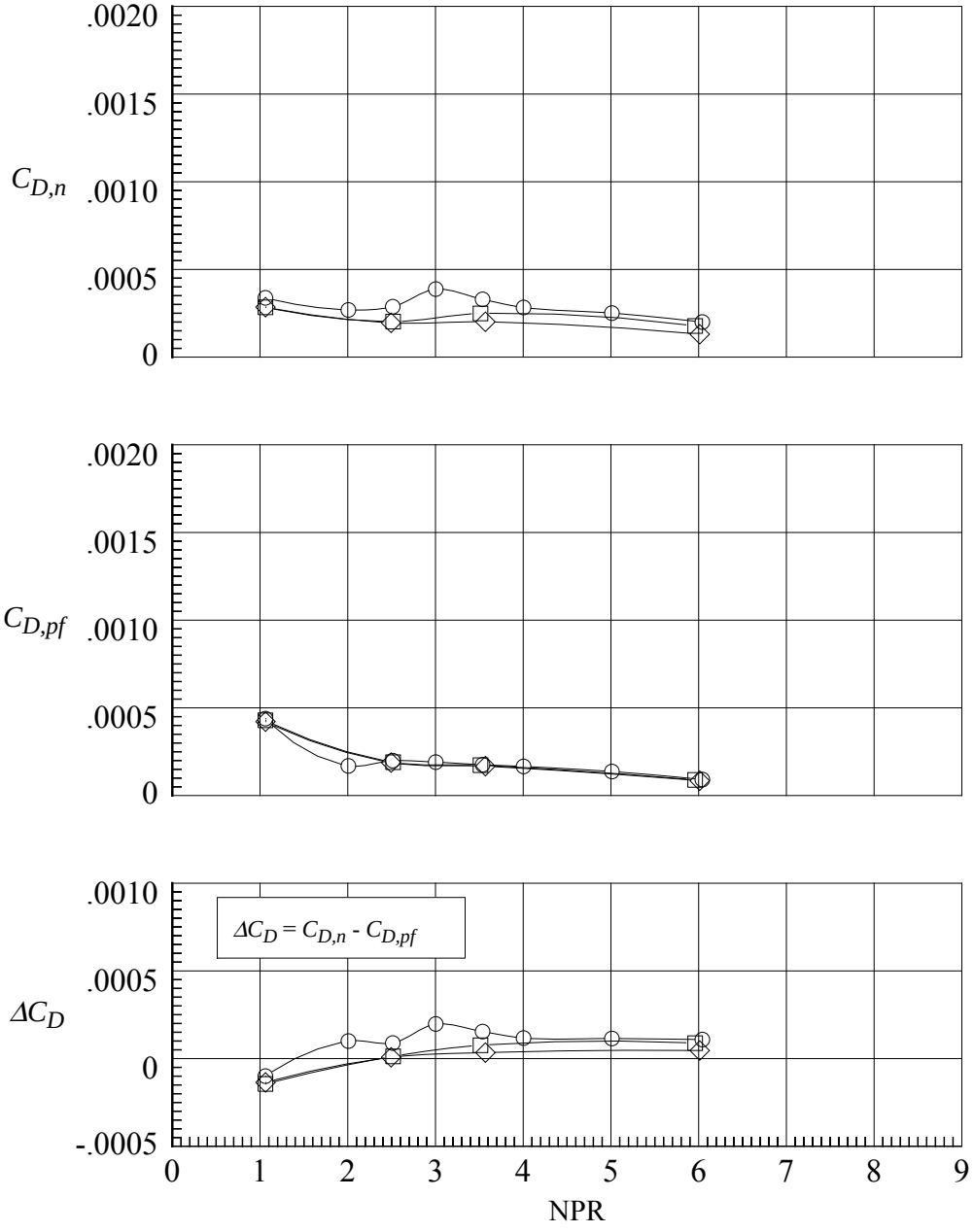

(d) Variation of $C_{D,n}$, $C_{D,pf}$, and ΔC_D.

Figure 55. Concluded.

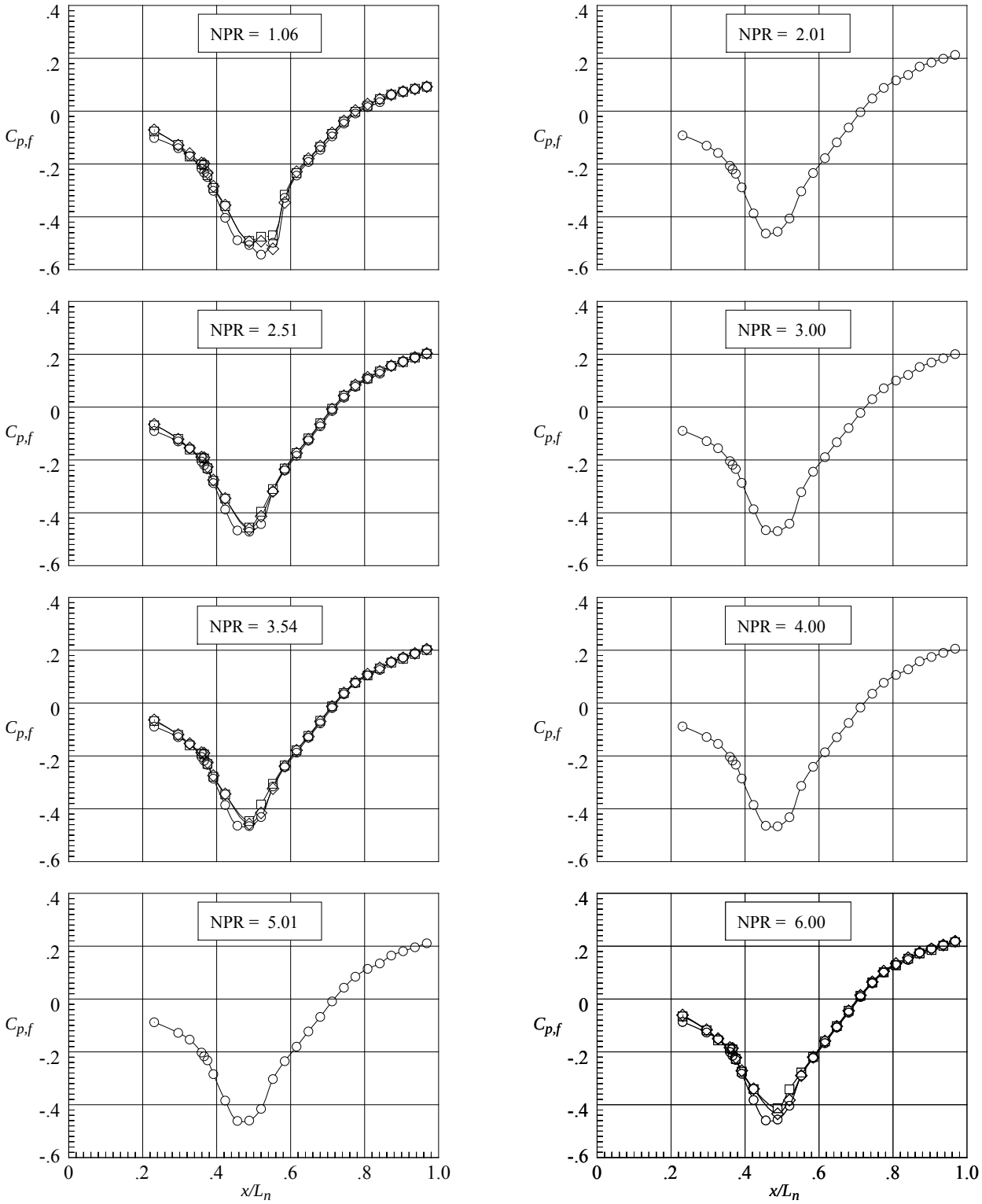

(a) Flap top center row, $z/w_f/2 = 0$.

Figure 56. Nozzle N11 pressure coefficient repeatability from different runs.
Symbols represent different runs.

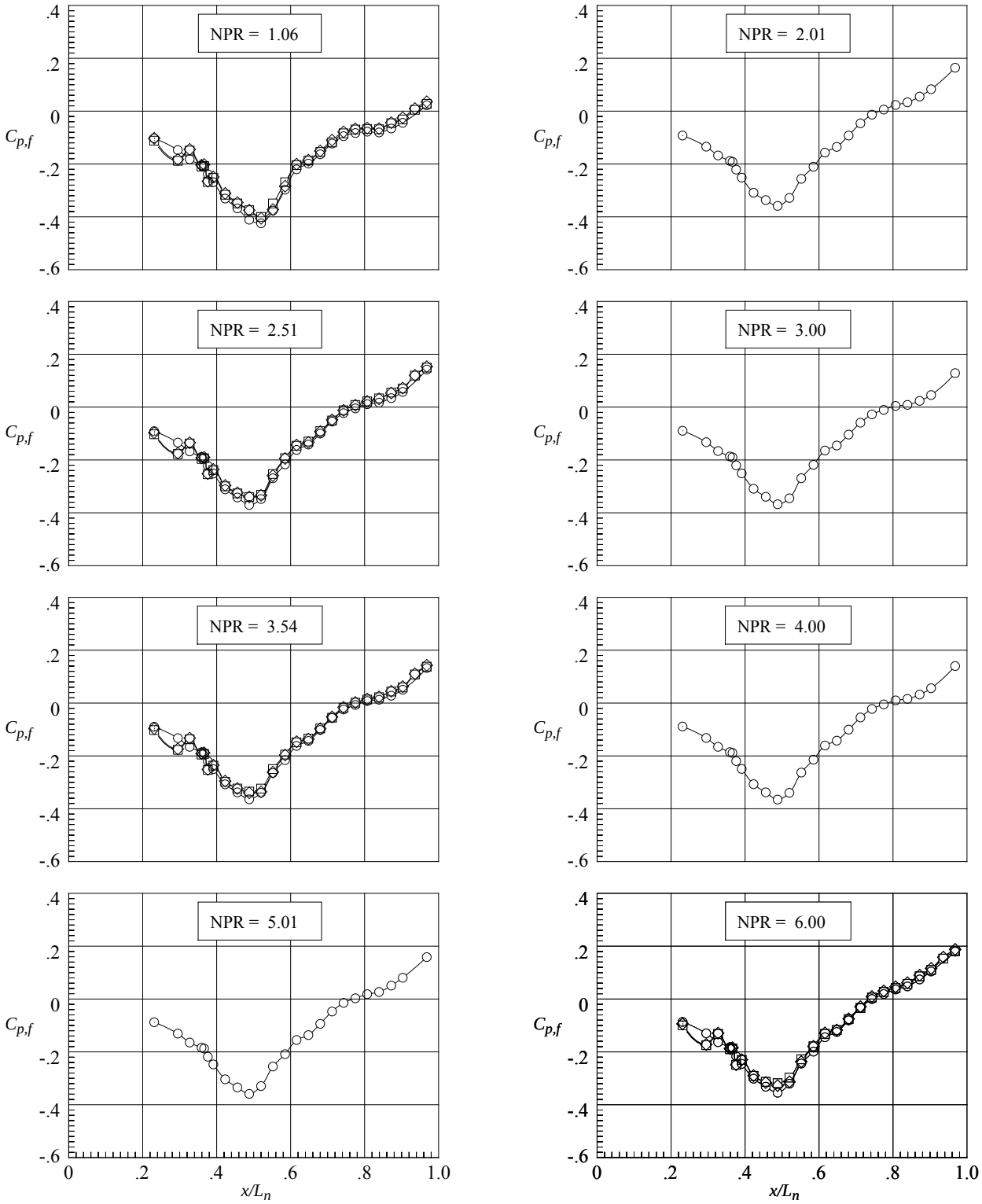

(b) Flap top outboard row, $z/w_f/2 = 0.95$

Figure 56. Continued.

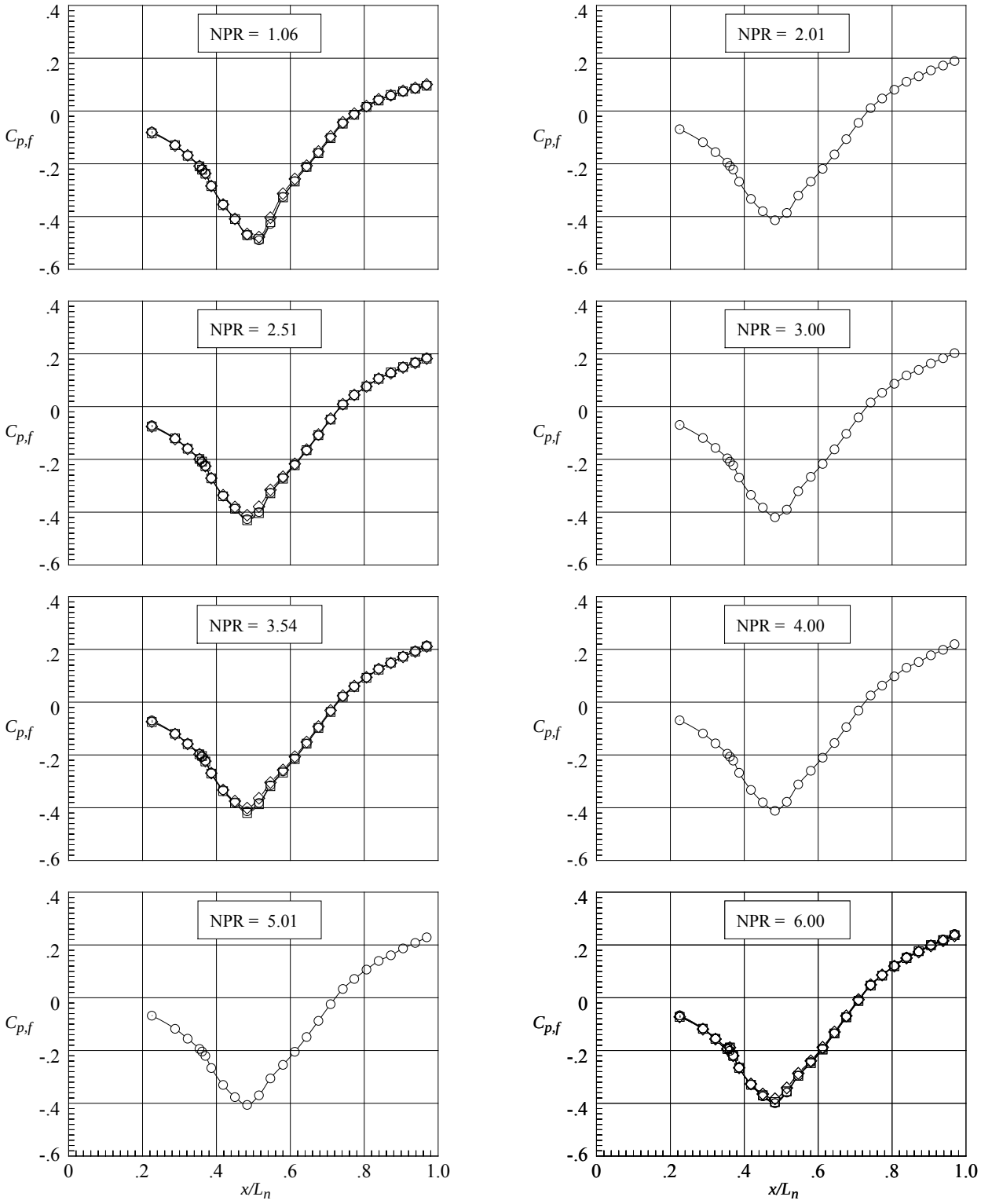

(c) Flap bottom center row, $z/w_f/2 = 0$.

Figure 56. Continued.

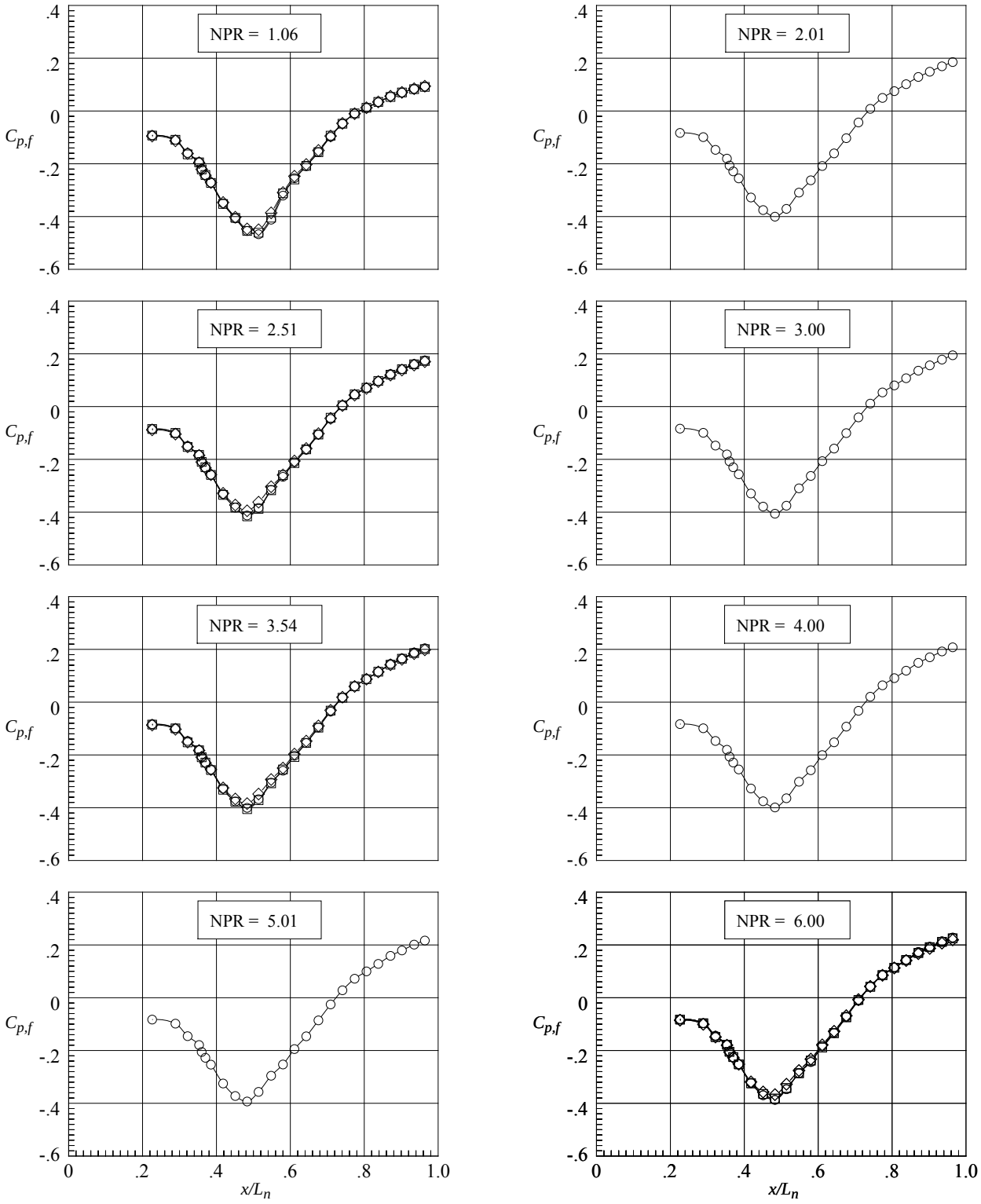

(d) Flap bottom middle row, $z/w_f/2 = 5$.

Figure 56. Continued.

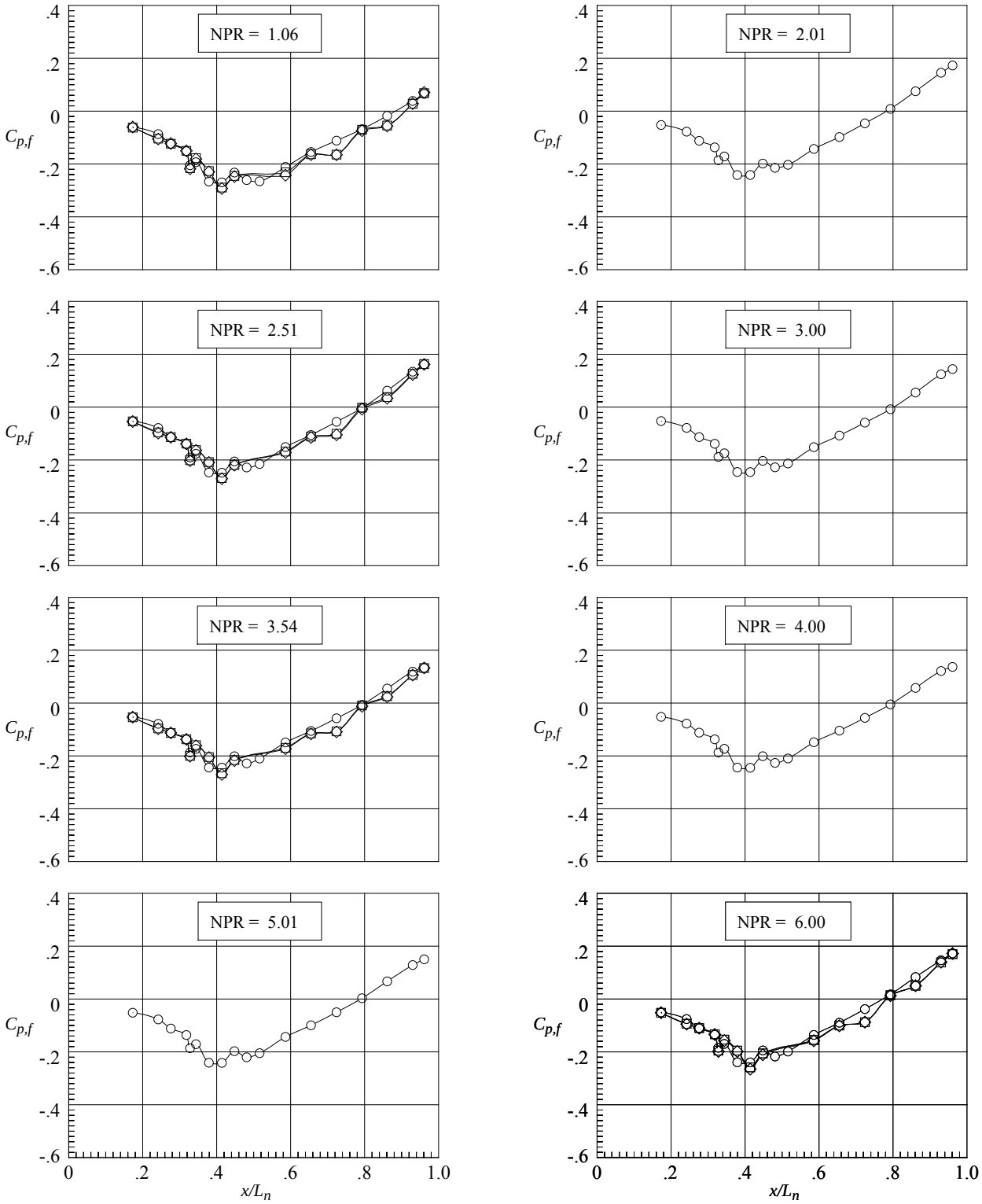

(e) Sidewall center row, $y/h_m/2 = 0$.

Figure 56. Continued.

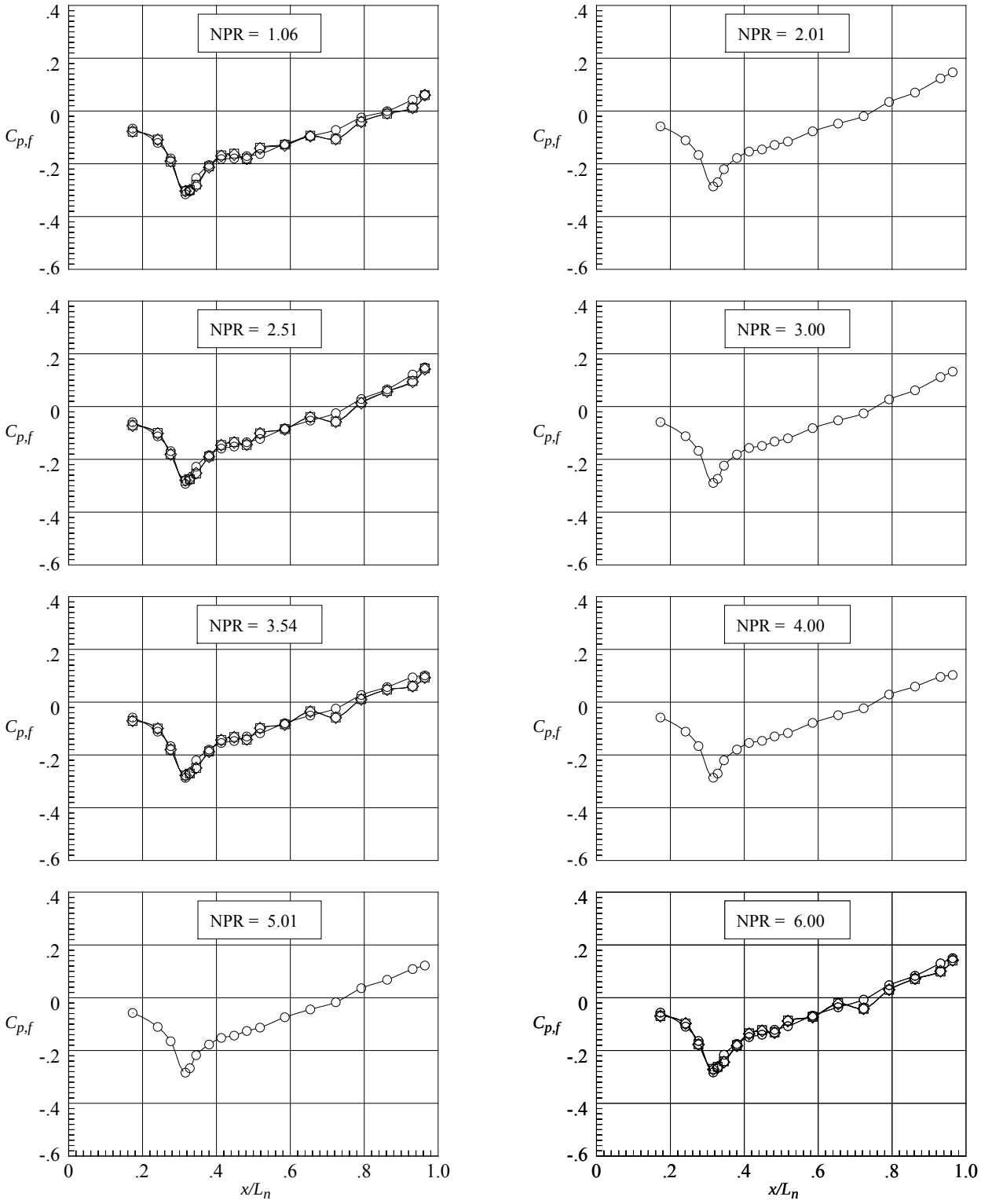

(f) Sidewall outboard row, $y/h_m/2$ = -0.87.

Figure 56. Concluded.

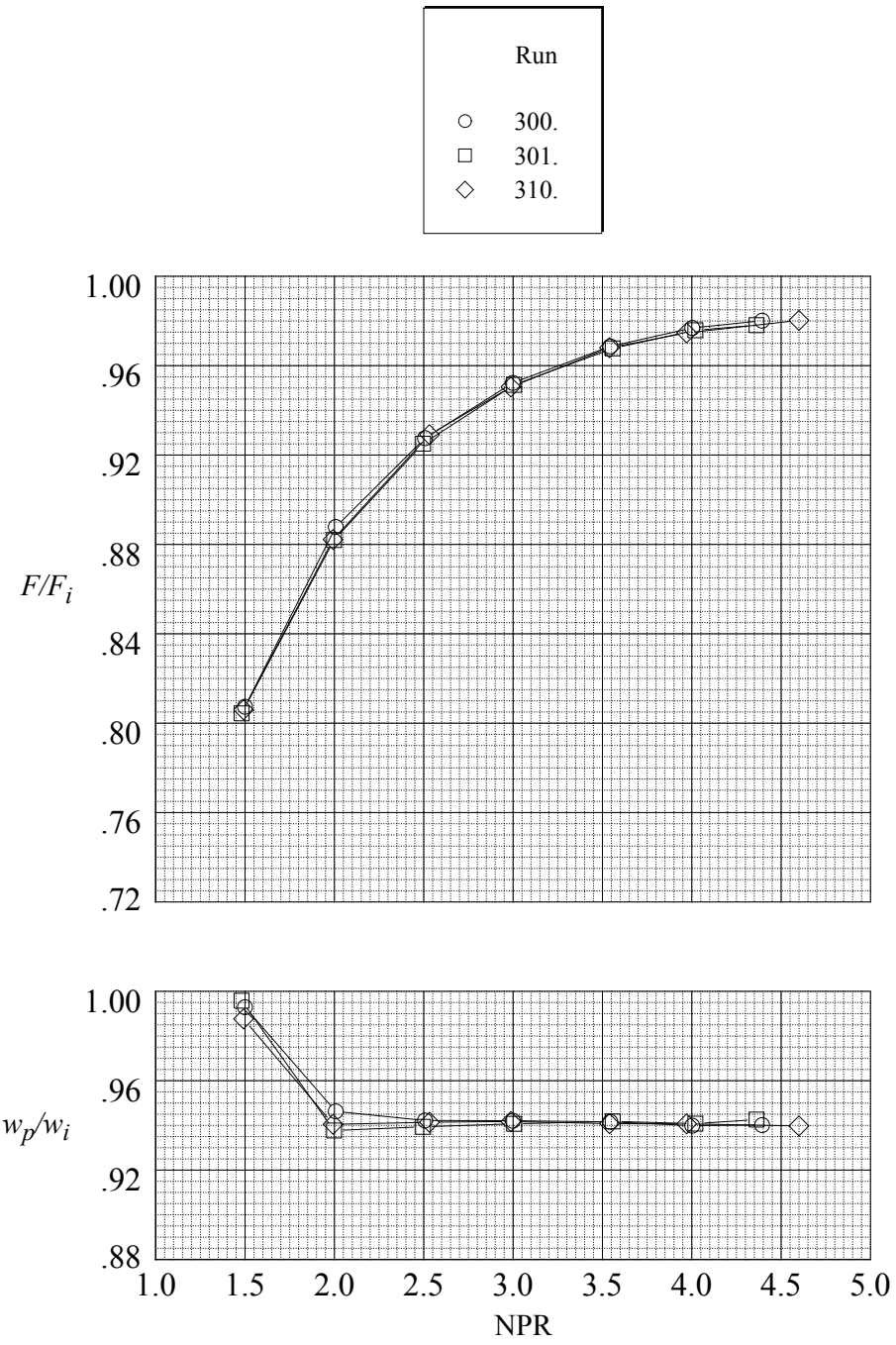

Figure 57. Static performance for Nozzle N1 with flap F1 and sidewall S1.
$r_f/r_{f,max} = 0.4$; $\beta_f = 16.38°$; $L_f/h_m = 1.4$; $\beta_s = 4.0°$; $r_s/r_{s,max} = 0$.

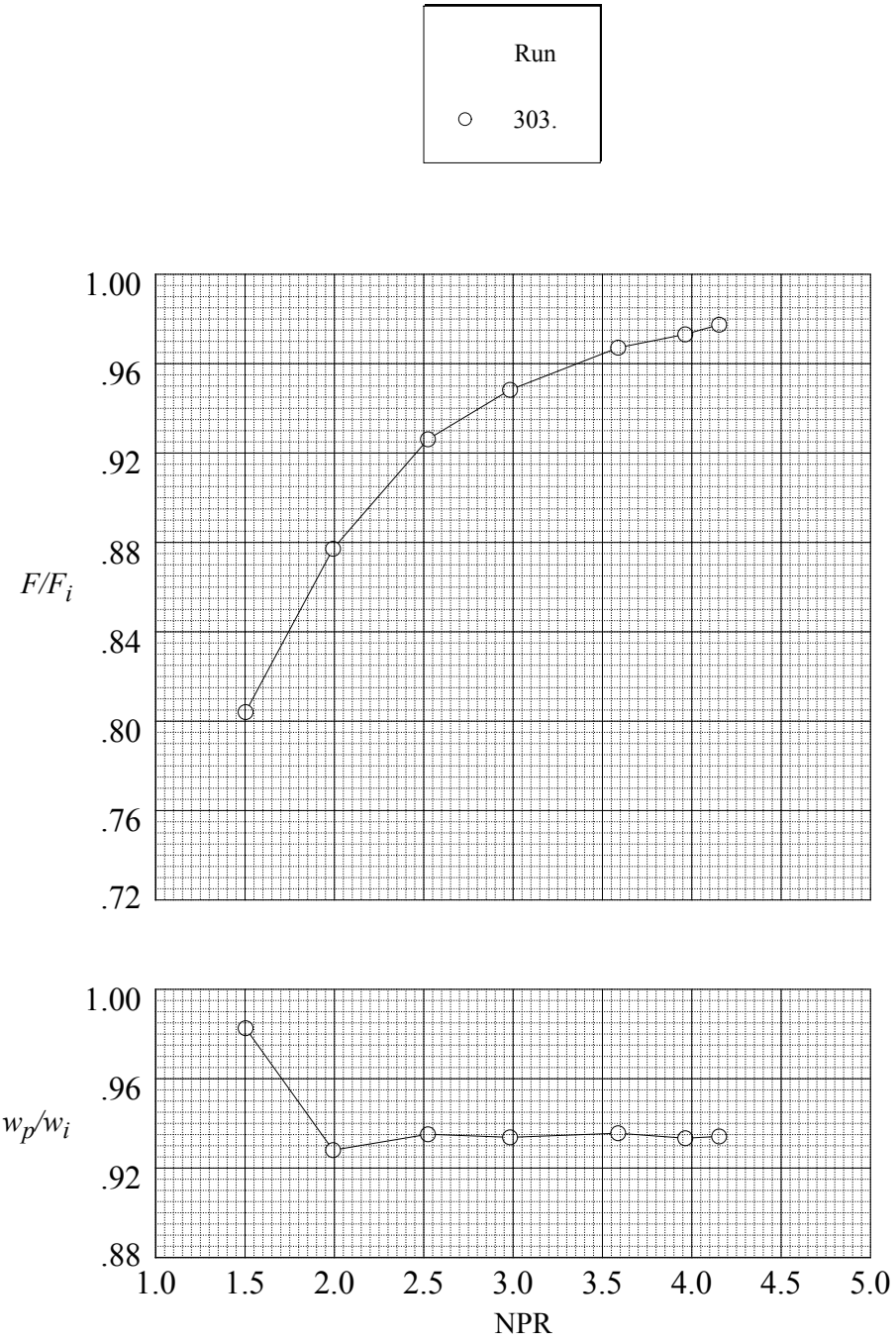

Figure 58. Static performance for Nozzle N2 with flap F2 and sidewall S1. $r_f/r_{f,max} = 0.1$; $\beta_f = 12.88°$; $L_f/h_m = 1.4$; $\beta_s = 4.0°$; $r_s/r_{s,max} = 0$.

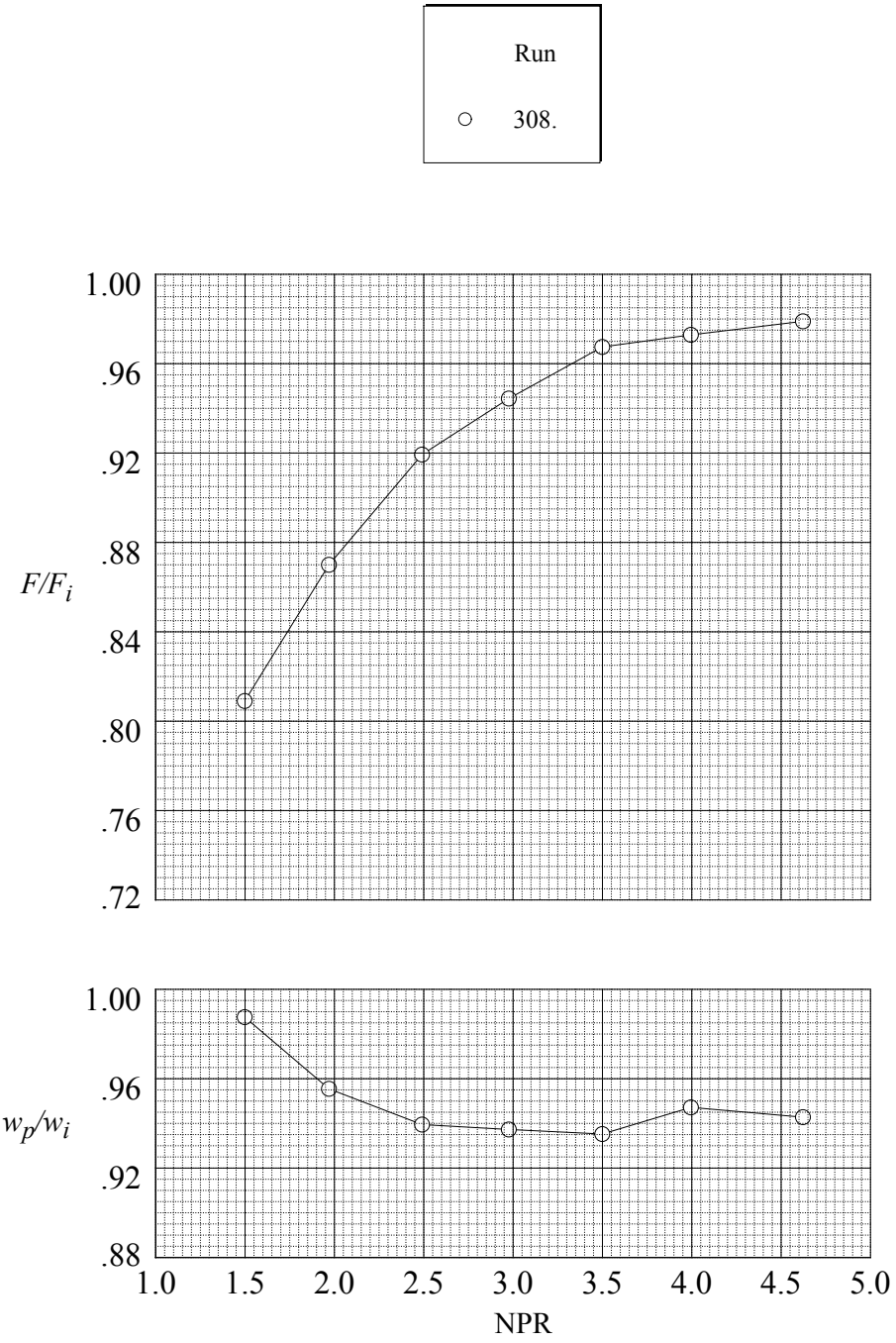

Figure 59. Static performance for Nozzle N3 with flap F3 and sidewall S1.
$r_f/r_{f,max} = 0$; $\beta_f = 11.72°$; $L_f/h_m = 1.4$; $\beta_s = 4.0°$; $r_s/r_{s,max} = 0$.

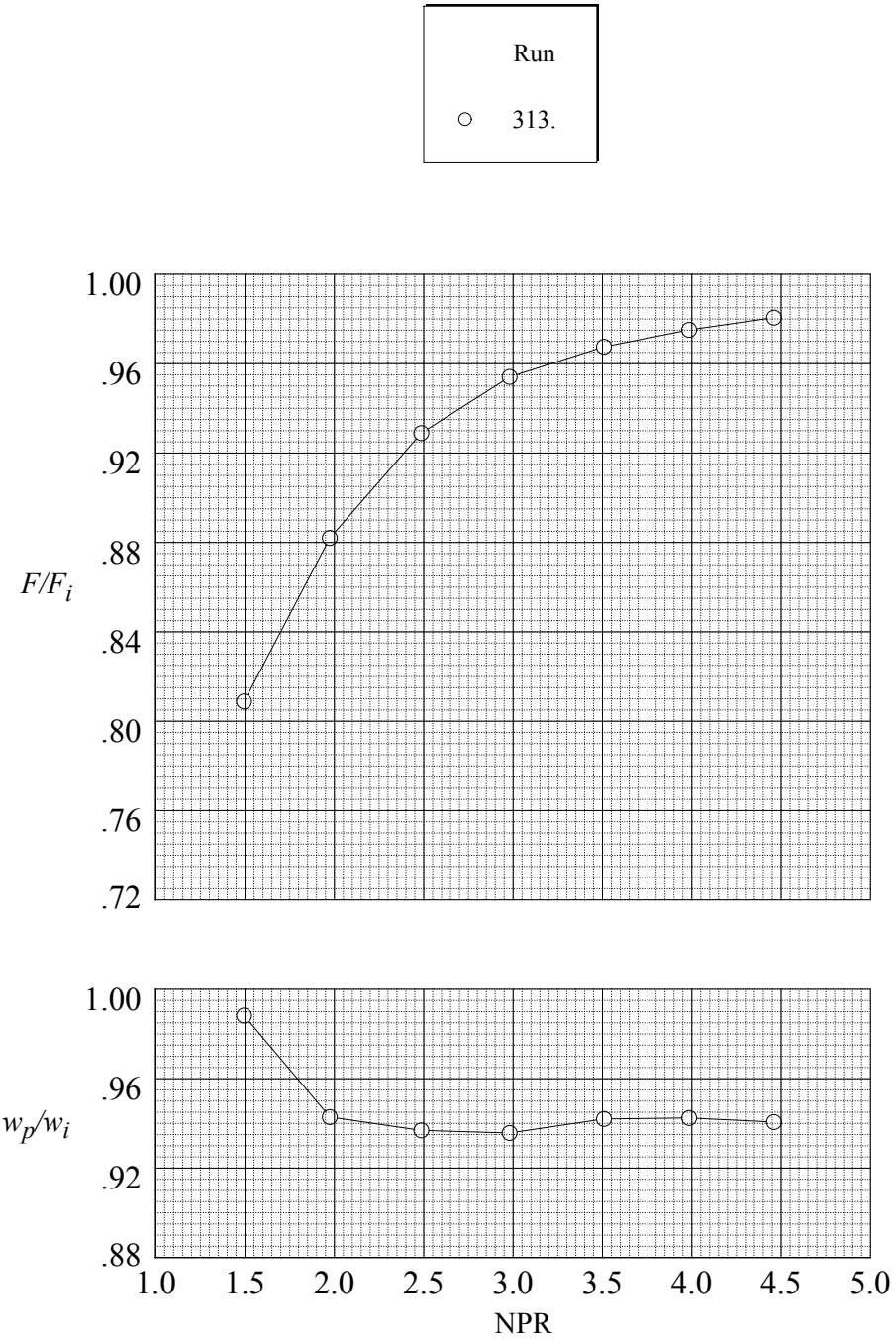

Figure 60. Static performance for Nozzle N4 with flap F4 and sidewall S1.
$r_f/r_{f,max} = 1.0$; $\beta_f = 23.44°$; $L_f/h_m = 1.4$; $\beta_s = 4.0°$; $r_s/r_{s,max} = 0$.

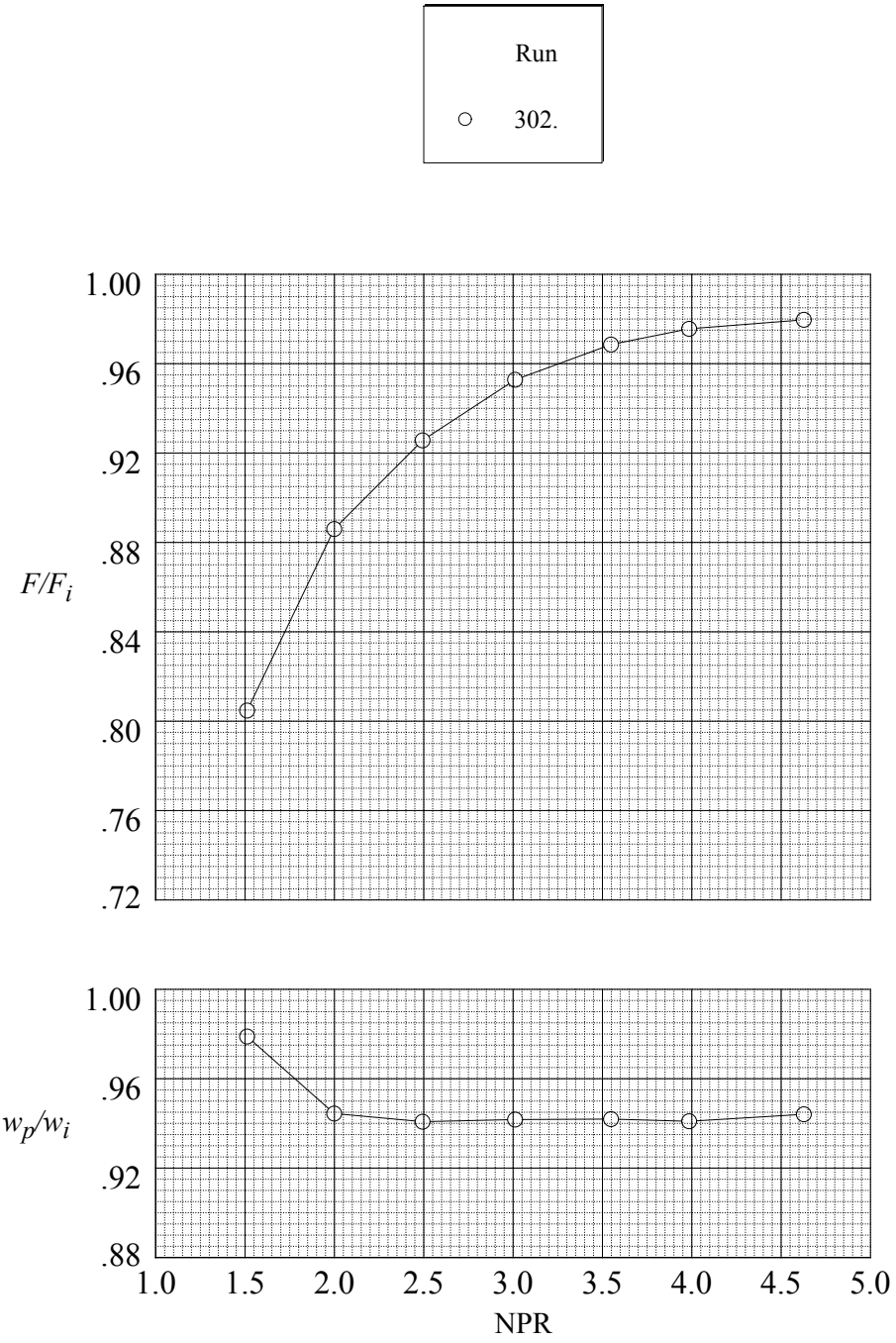

Figure 61. Static performance for Nozzle N5 with flap F1 and sidewall S2.
$r_f/r_{f,max} = 0.4$; $\beta_f = 16.38°$; $L_f/h_m = 1.4$; $\beta_s = 6.0°$; $r_s/r_{s,max} = 0$.

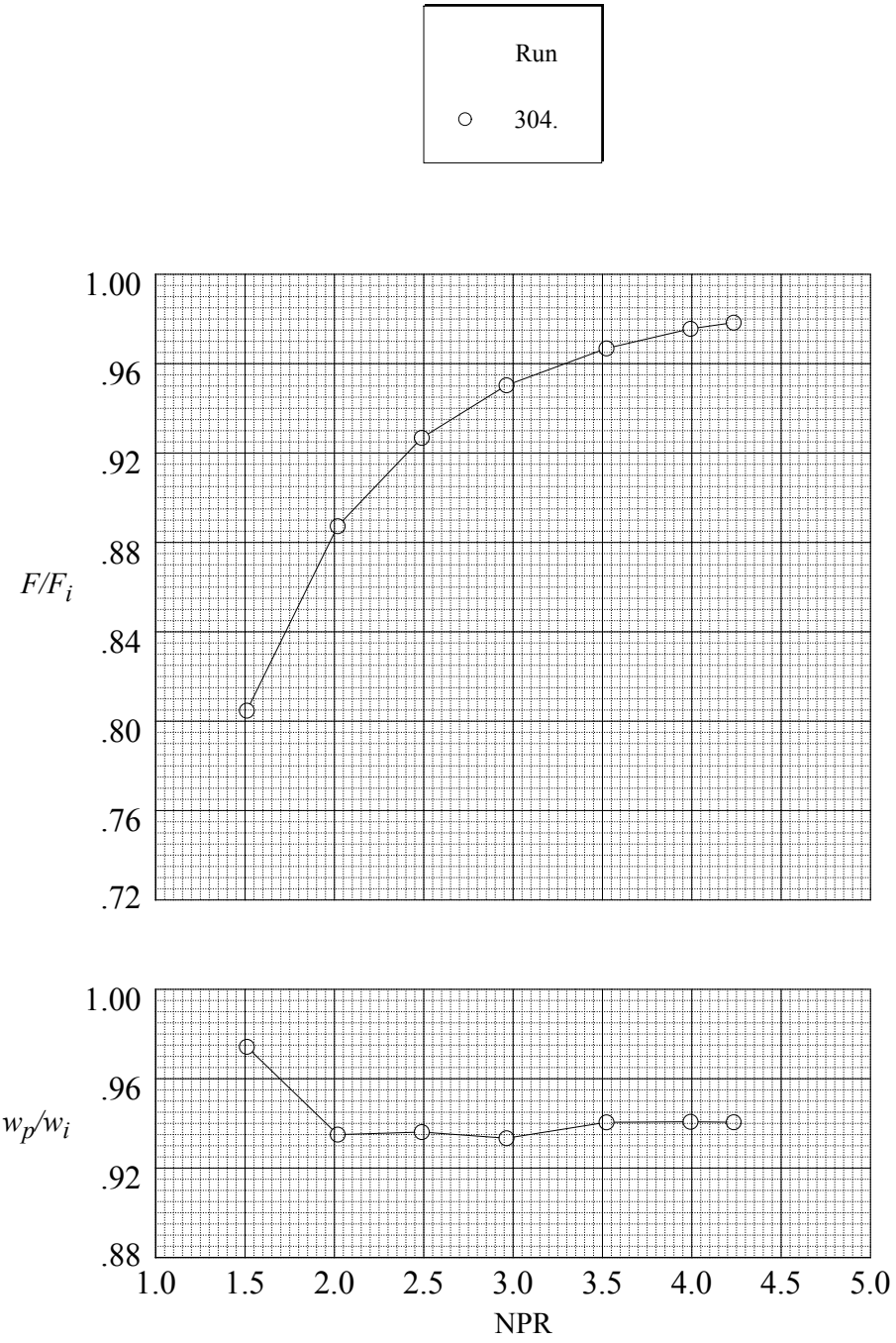

Figure 62. Static performance for Nozzle N6 with flap F1 and sidewall S3.
$r_f/r_{f,max} = 0.4$; $\beta_f = 16.38°$; $L_f/h_m = 1.4$; $\beta_s = 8.0°$; $r_s/r_{s,max} = 0$.

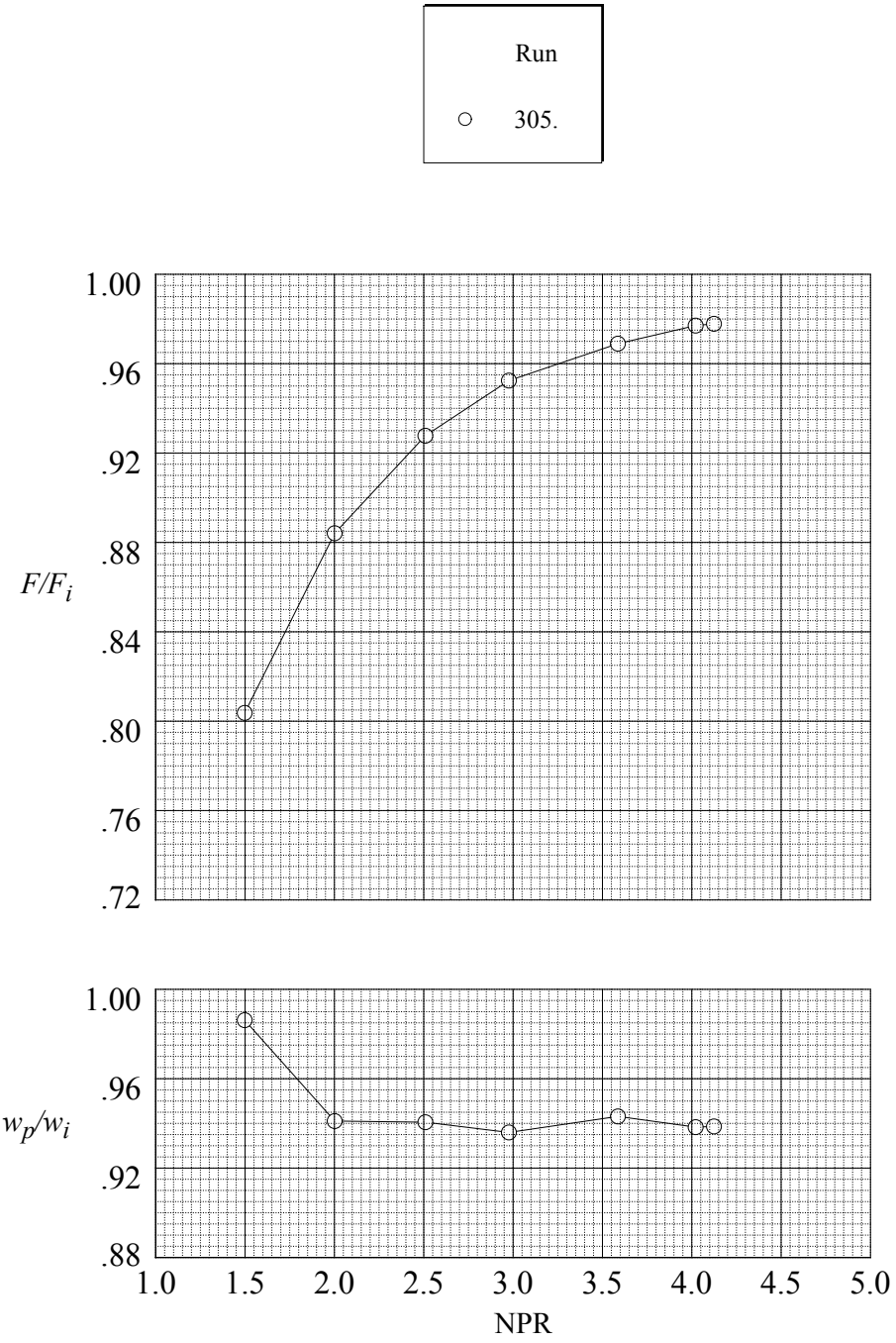

Figure 63. Static performance for Nozzle N7 with flap F1 and sidewall S4.
$r_f/r_{f,max} = 0.4$; $\beta_f = 16.38°$; $L_f/h_m = 1.4$; $\beta_s = 6.0°$; $r_s/r_{s,max} = 0.1$.

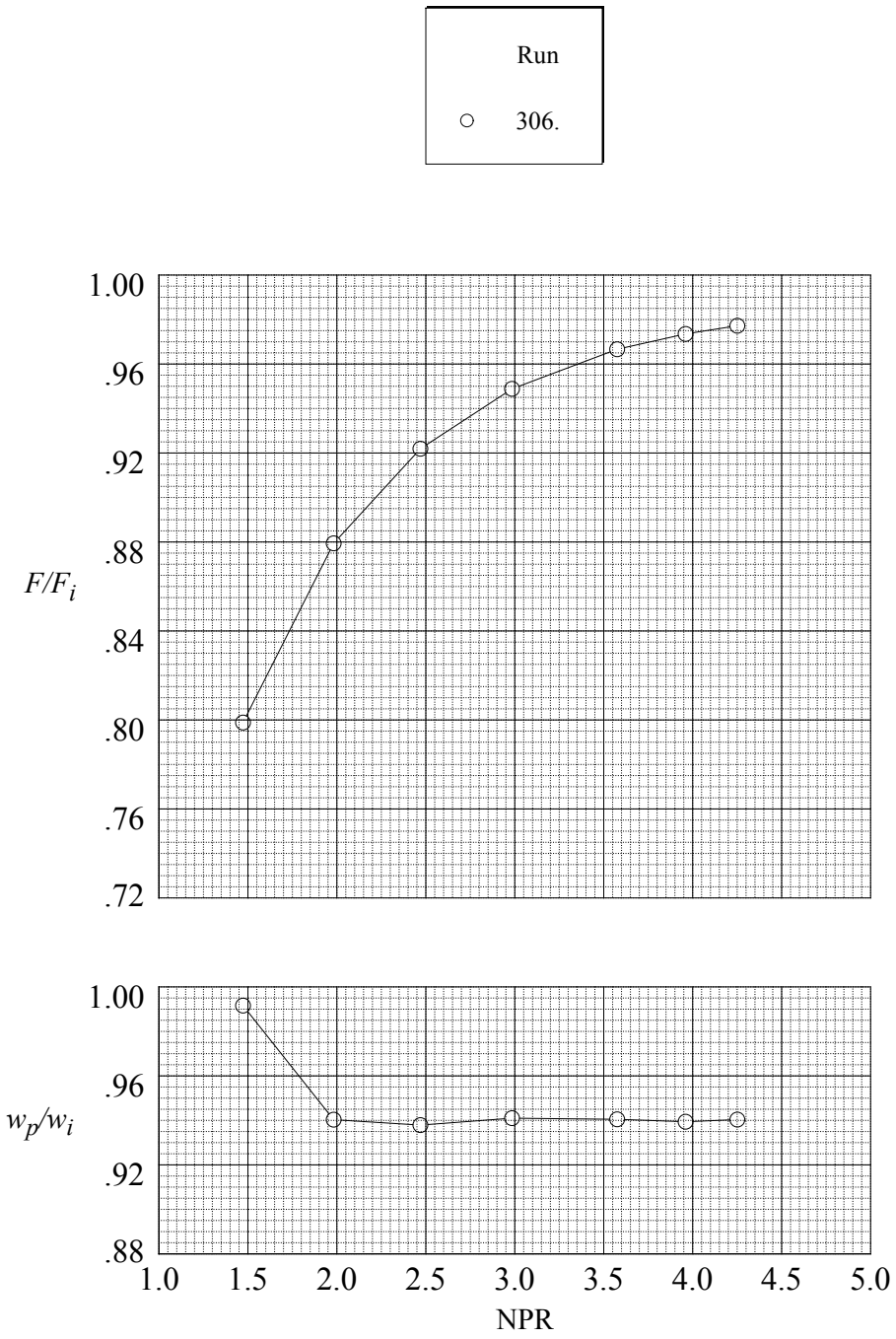

Figure 64. Static performance for Nozzle N8 with flap F1 and sidewall S5.
$r_f/r_{f,max} = 0.4$; $\beta_f = 16.38°$; $L_f/h_m = 1.4$; $\beta_s = 8.0°$; $r_s/r_{s,max} = 0.1$.

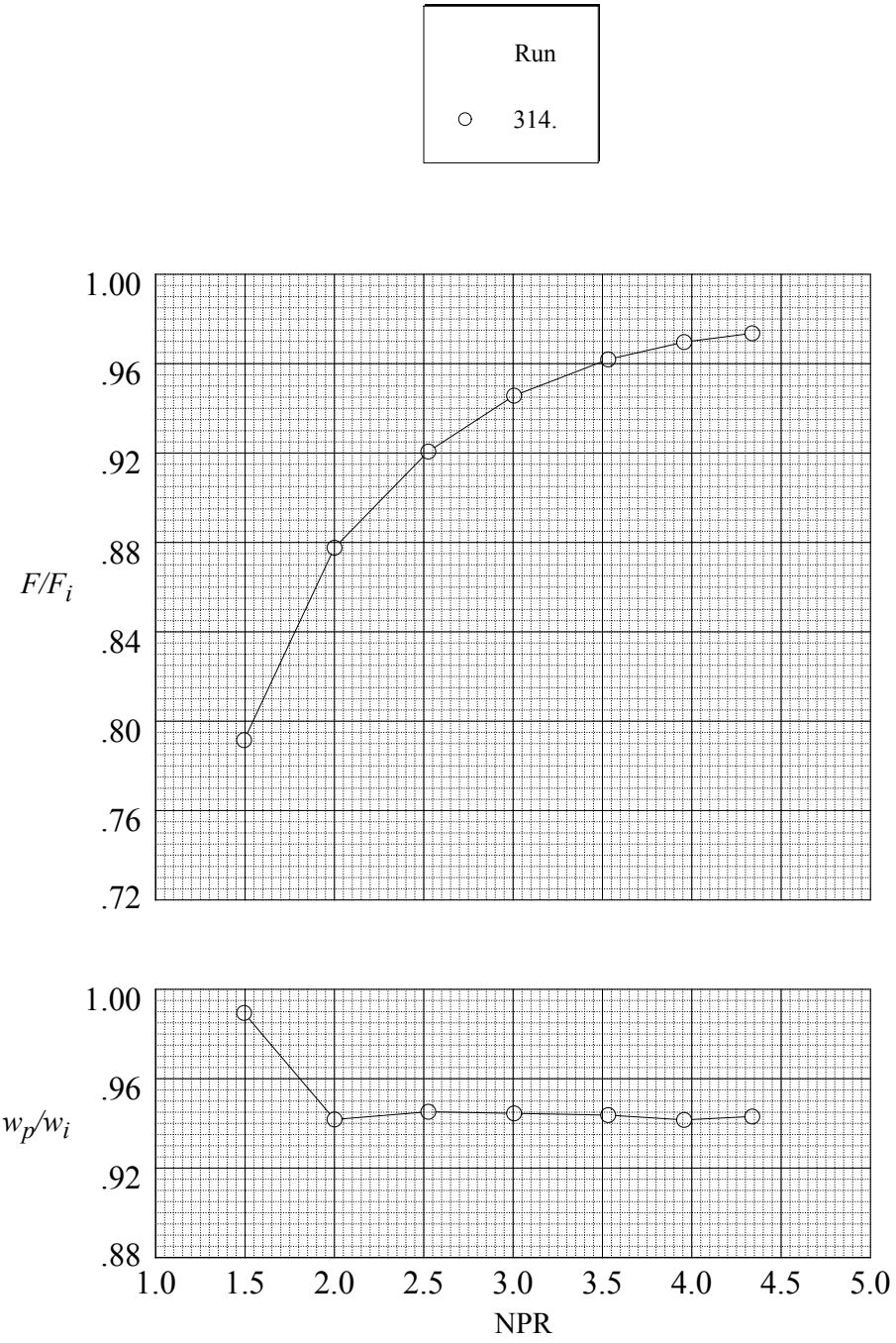

Figure 65. Static performance for Nozzle N9 with flap F1 and sidewall S6.
$r_f/r_{f,max} = 0.4$; $\beta_f = 16.38°$; $L_f/h_m = 1.4$; $\beta_s = 6.0°$; $r_s/r_{s,max} = 0.4$.

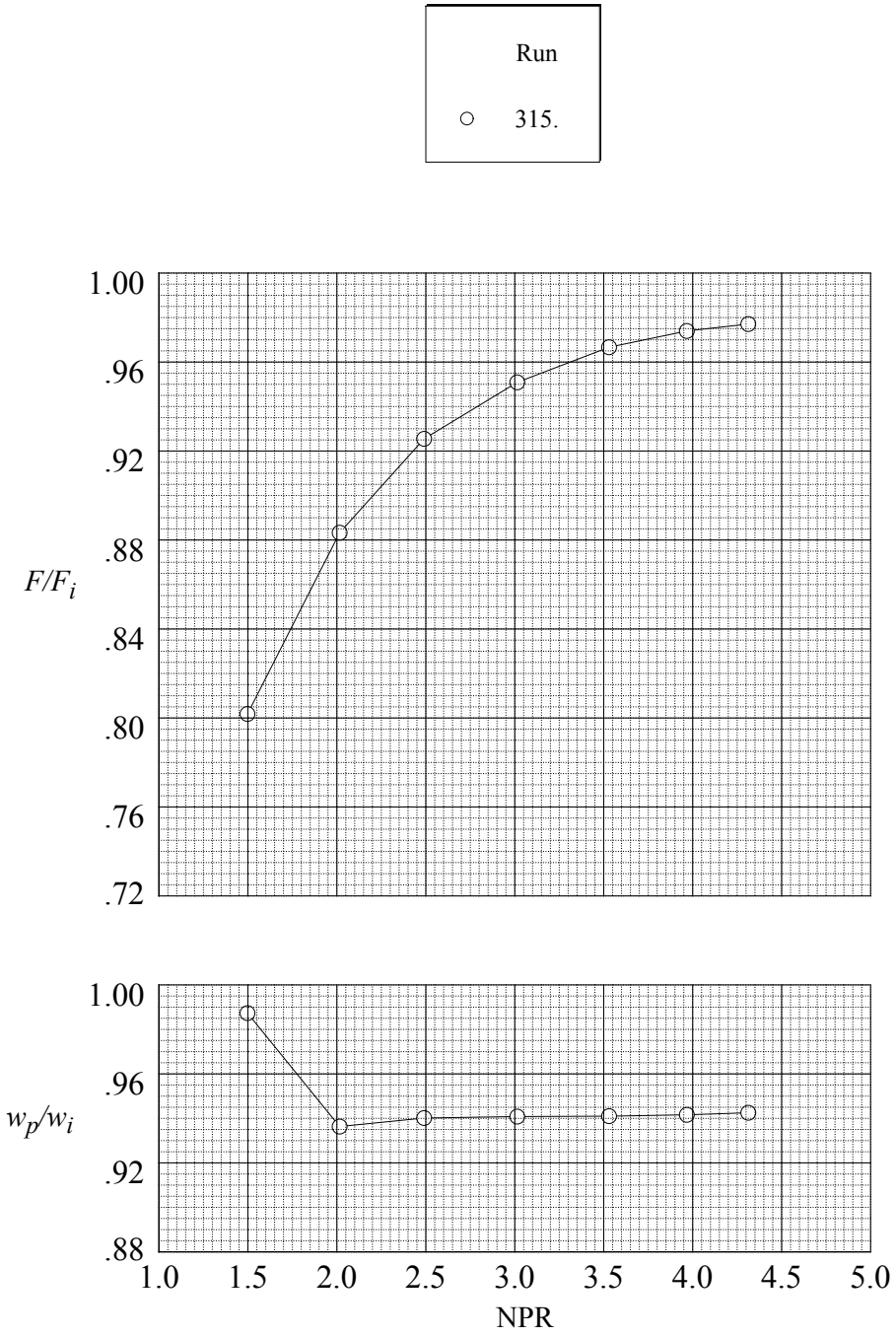

Figure 66. Static performance for Nozzle N10 with flap F1 and sidewall S7.
$r_f/r_{f,max} = 0.4$; $\beta_f = 16.38°$; $L_f/h_m = 1.4$; $\beta_s = 8.0°$; $r_s/r_{s,max} = 1.0$.

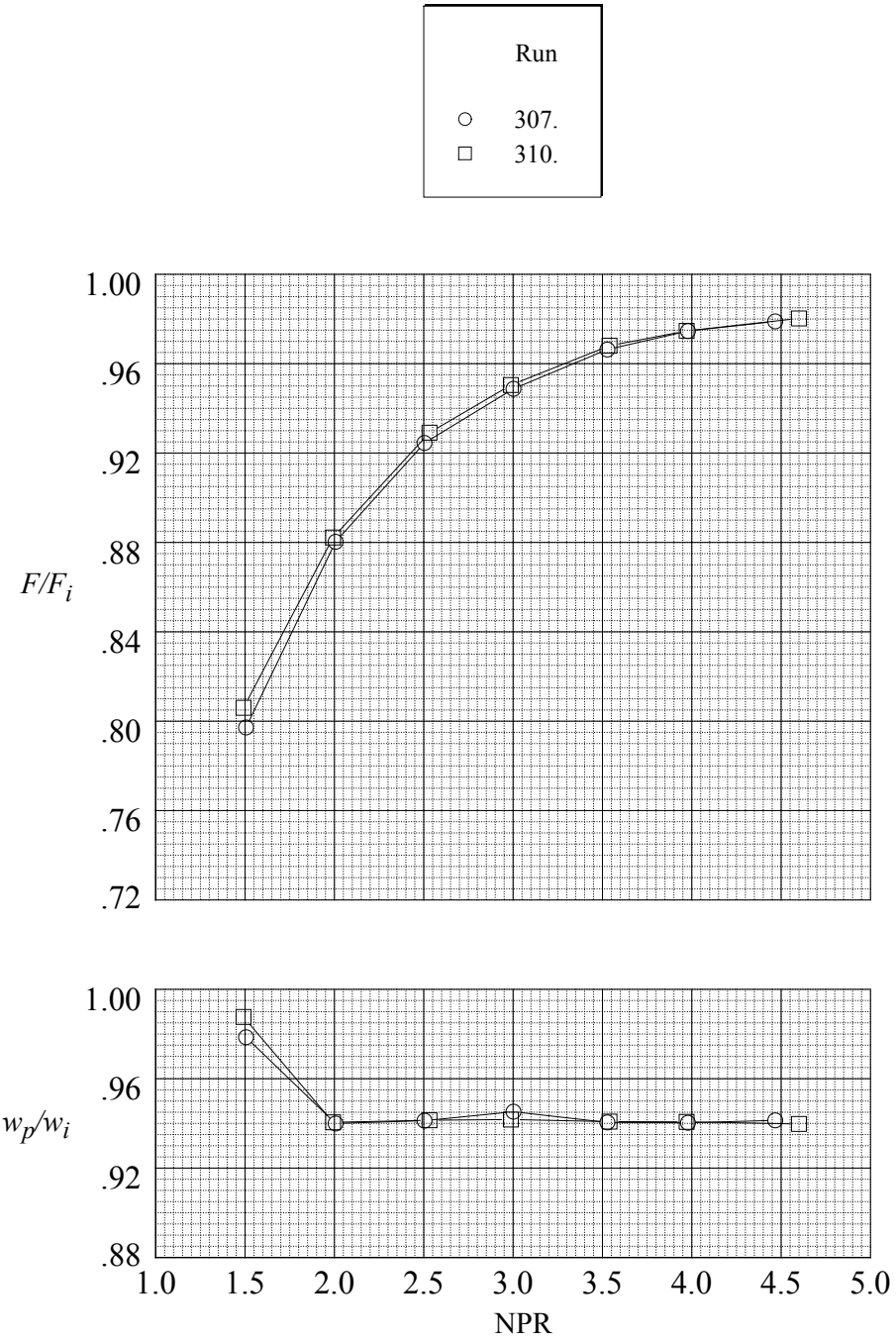

Figure 67. Static performance for Nozzle N11 with flap F1 and sidewall S8.
$r_f/r_{f,max} = 0.4$; $\beta_f = 16.38°$; $L_f/h_m = 1.4$; $\beta_s = 0°$; $r_s/r_{s,max} = 0$.

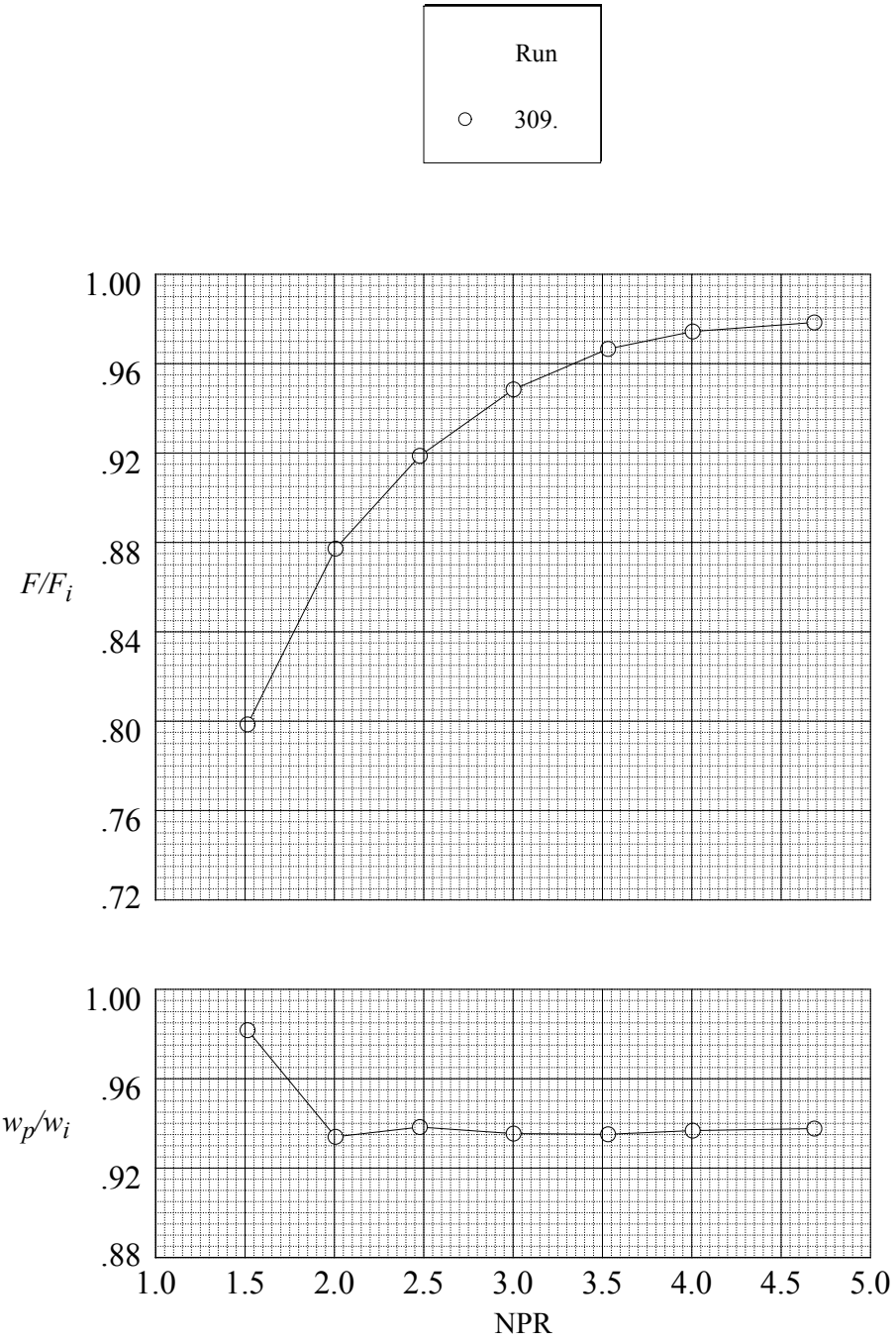

Figure 68. Static performance for Nozzle N12 with flap F2 and sidewall S8.
$r_f/r_{f,max} = 0.1$; $\beta_f = 12.88°$; $L_f/h_m = 1.4$; $\beta_s = 0°$; $r_s/r_{s,max} = 0$.

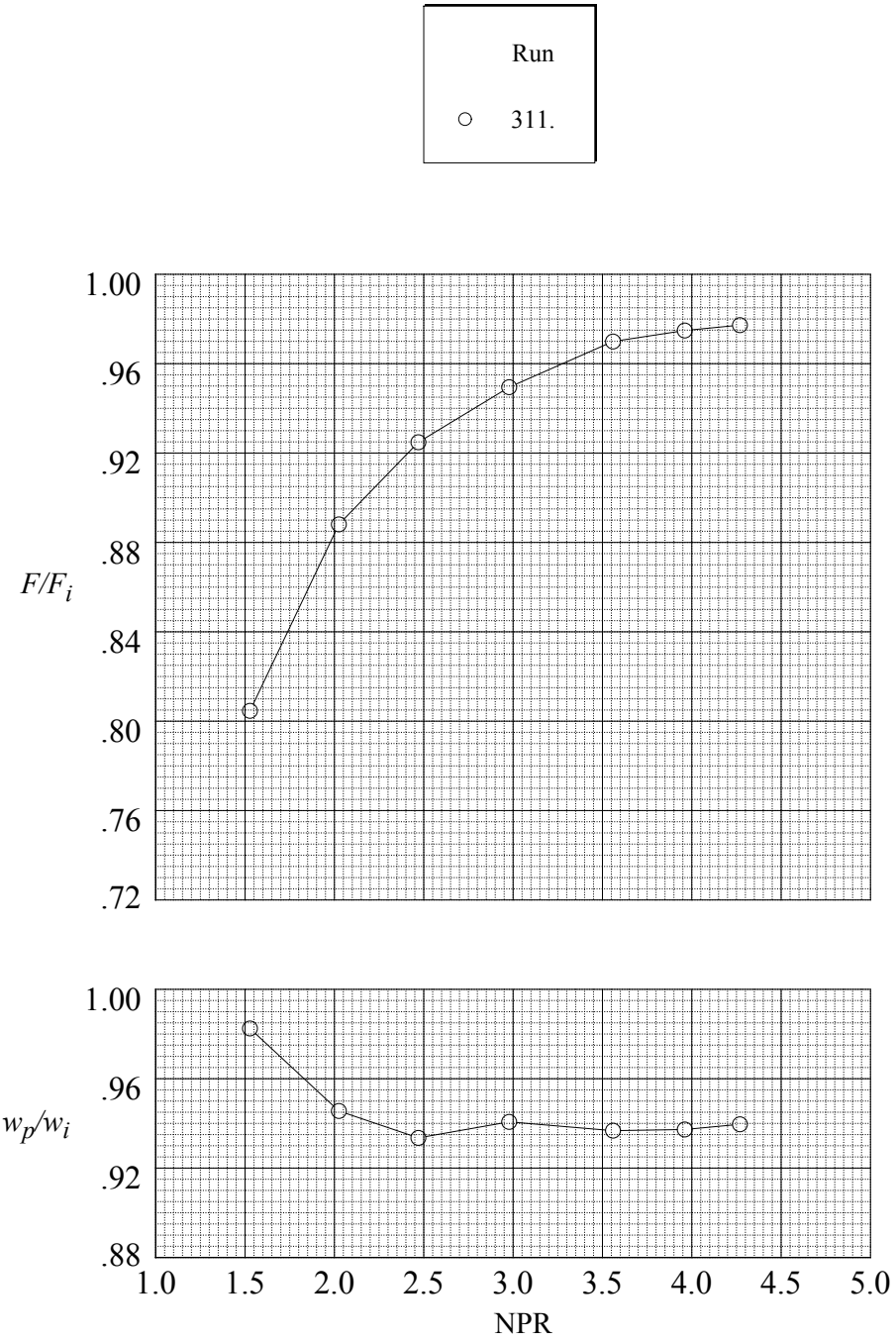

Figure 69. Static performance for Nozzle N13 with flap F5 and sidewall S1.
$r_f/r_{f,max} = 0.4$; $\beta_f = 20.30°$; $L_f/h_m = 1.1$; $\beta_s = 4.0°$; $r_s/r_{s,max} = 0$.

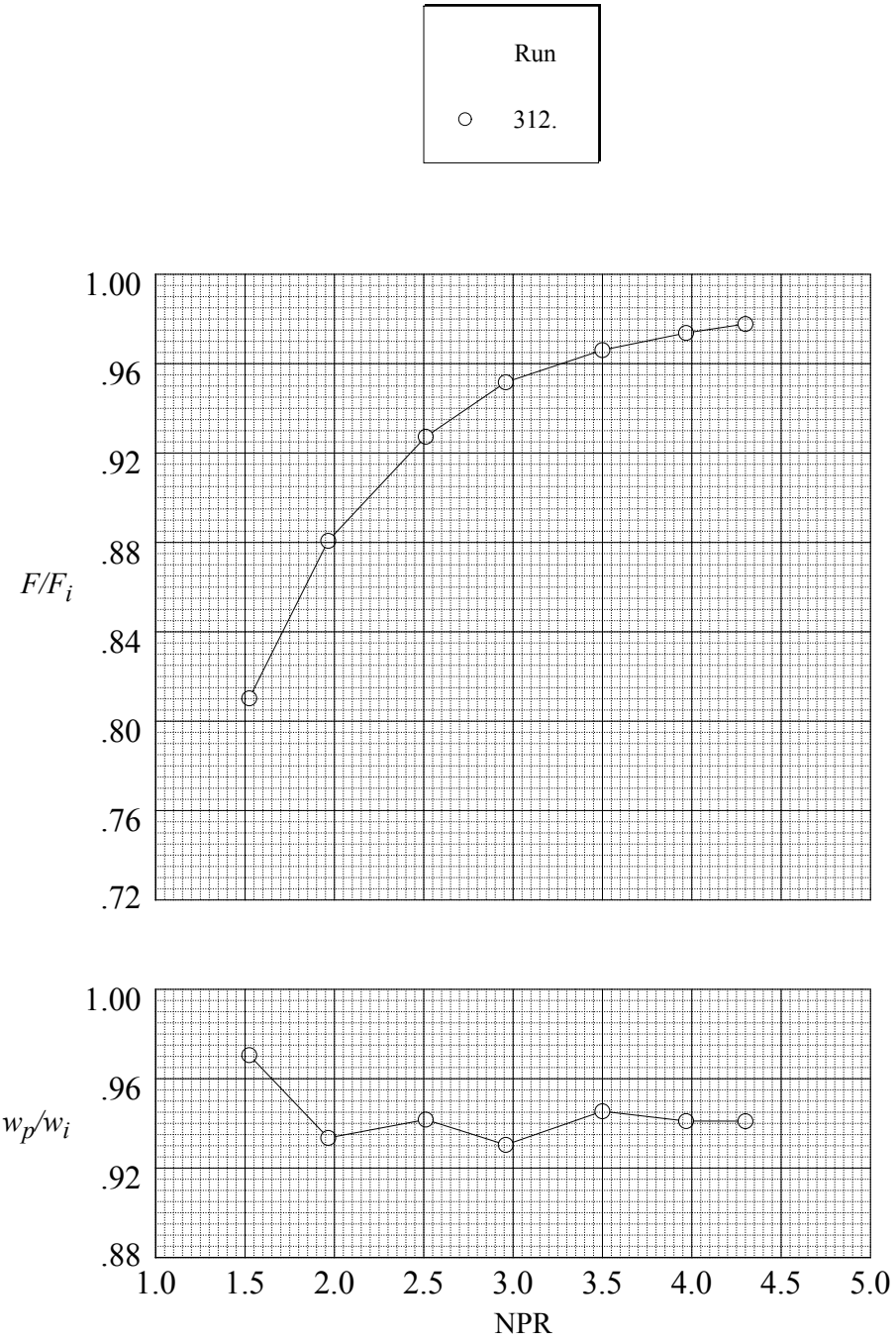

Figure 70. Static performance for Nozzle N14 with flap F6 and sidewall S1.
$r_f/r_{f,max} = 0.1$; $\beta_f = 15.97°$; $L_f/h_m = 1.1$; $\beta_s = 4.0°$; $r_s/r_{s,max} = 0$.

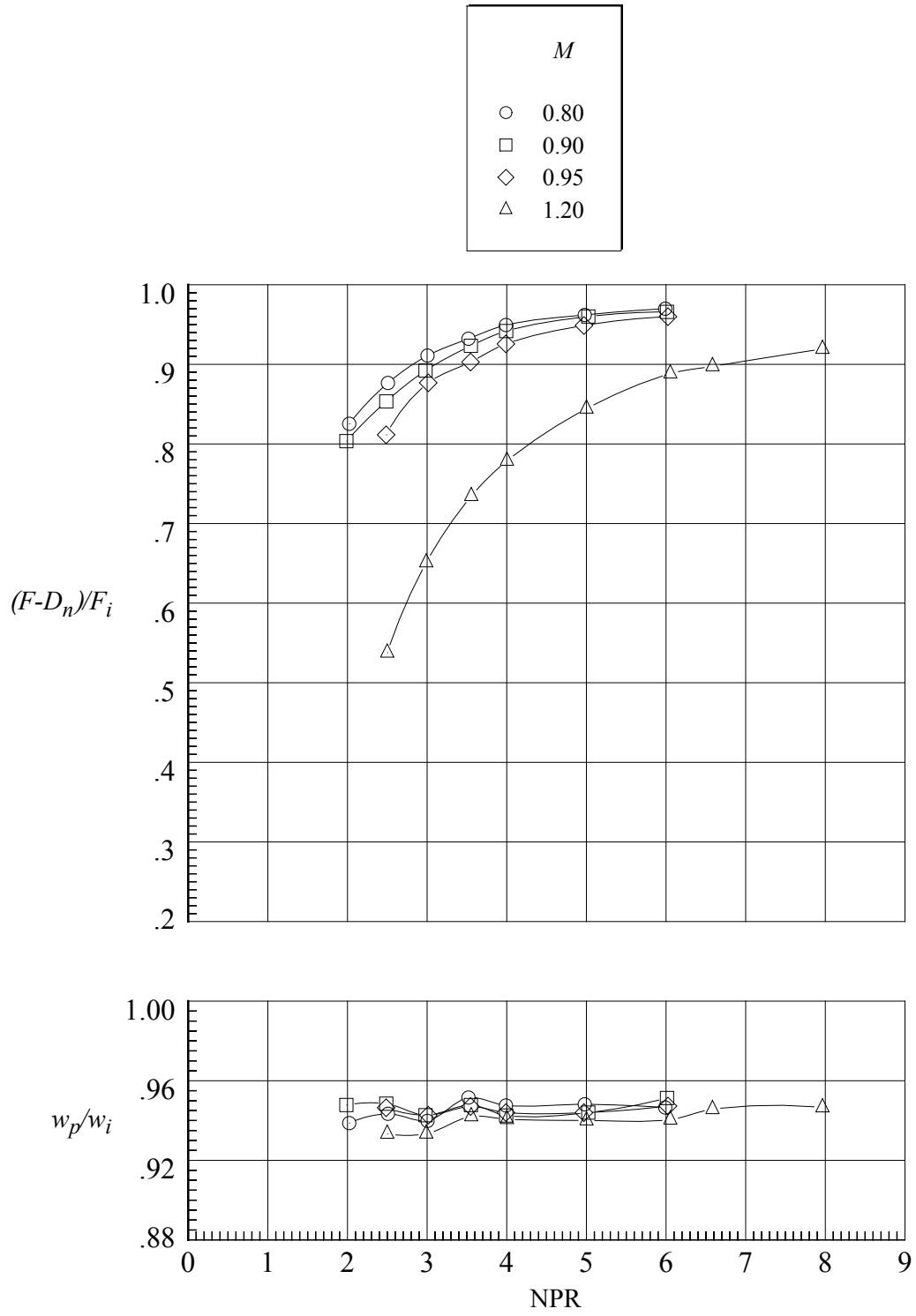

(a) Variation of $(F\text{-}D_n)/F_i$ and w_p/w_i.

Figure 71. Aeropropulsive performance for nozzle N1 with flap F1 and sidewall S1. $r_f/r_{f,max} = 0.4$; $\beta_f = 16.38°$; $L_f/h_m = 1.4$; $\beta_s = 4.0°$; $r_s/r_{s,max} = 0$.

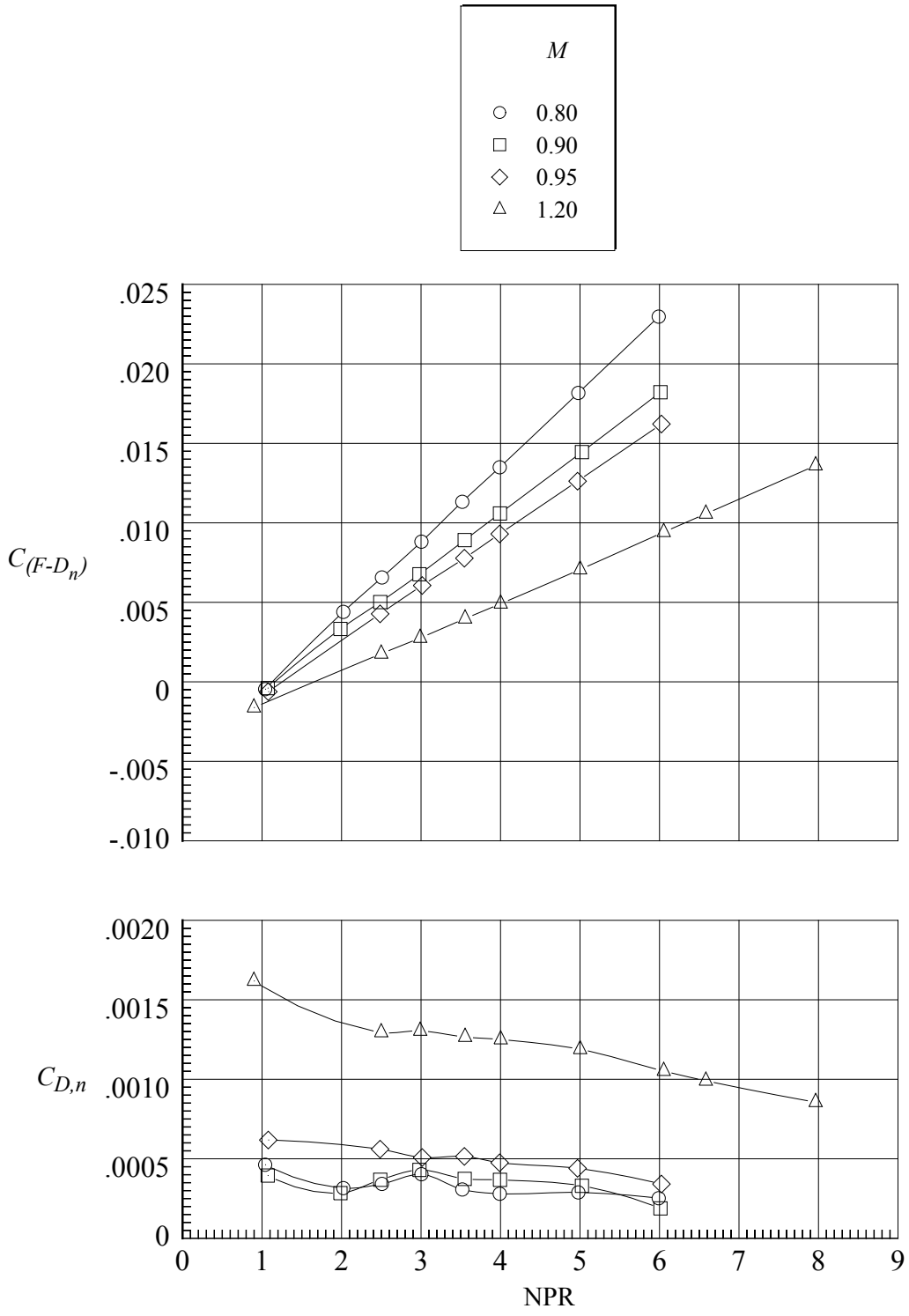

(b) Variation of $C_{(F\text{-}D_n)}$ and $C_{D,n}$.

Figure 71. Continued.

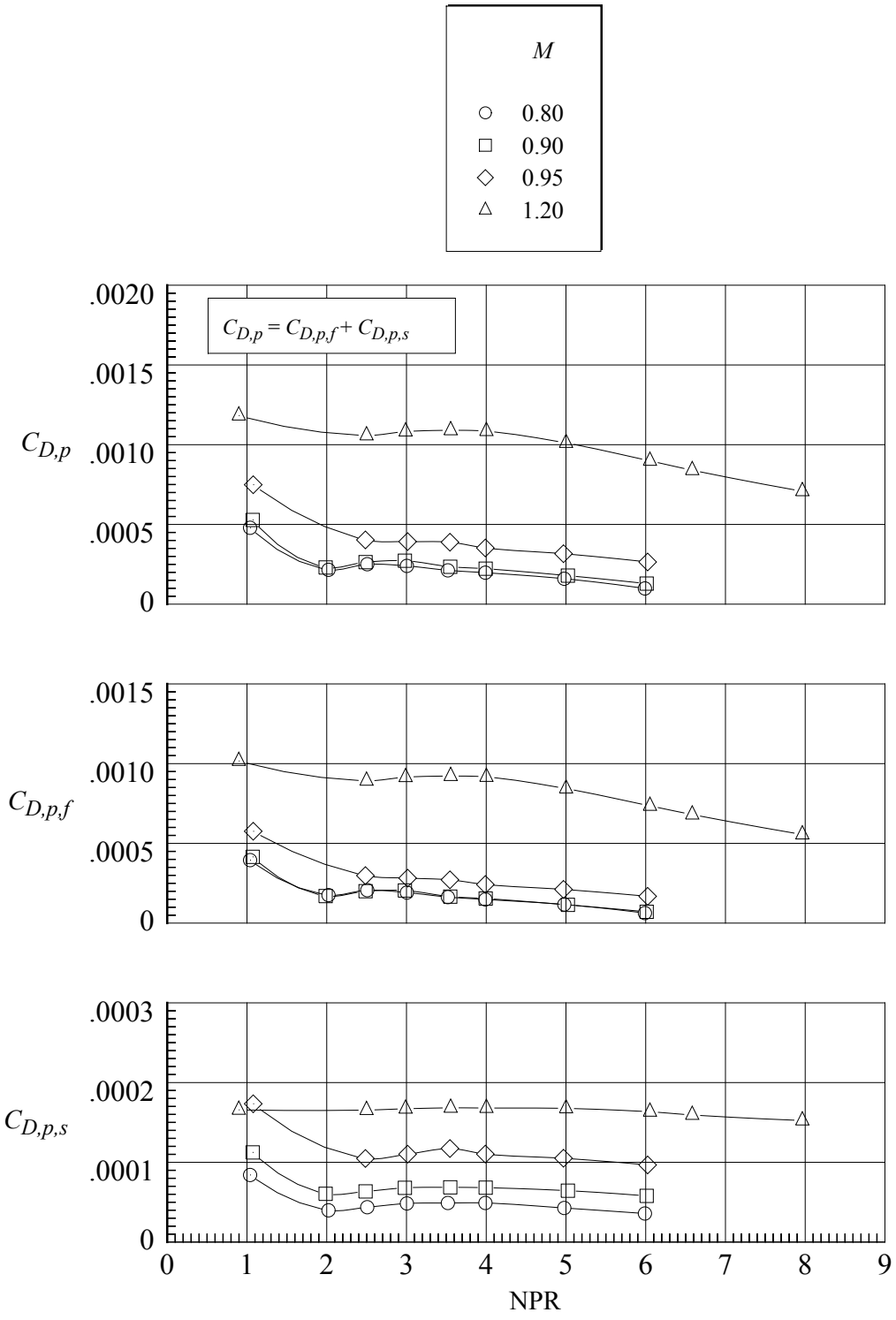

(c) Variation of $C_{D,p}$, $C_{D,p,f}$, and $C_{D,p,s}$.

Figure 71. Continued.

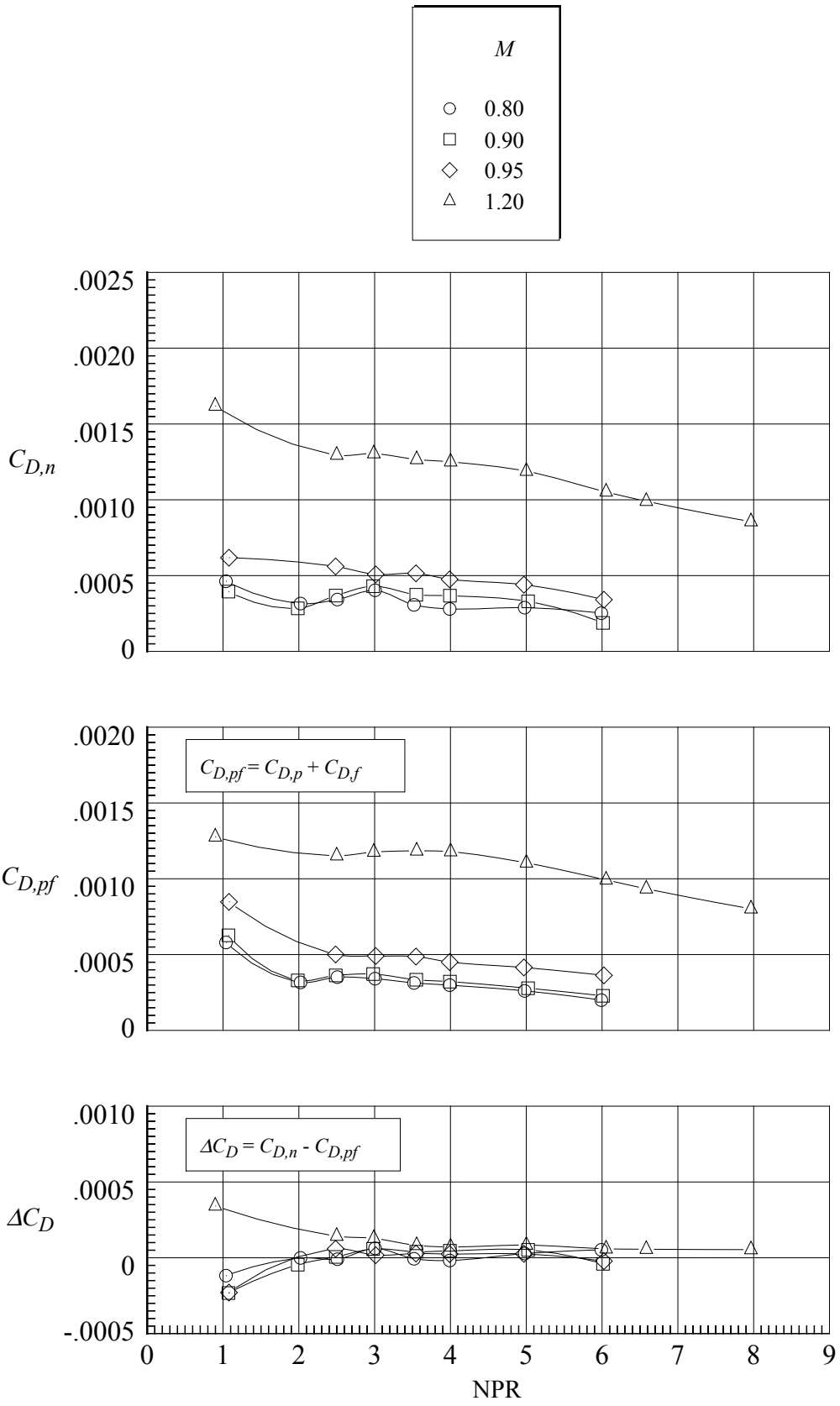

(d) Variation of $C_{D,n}$, $C_{D,pf}$, and ΔC_D.

Figure 71. Concluded.

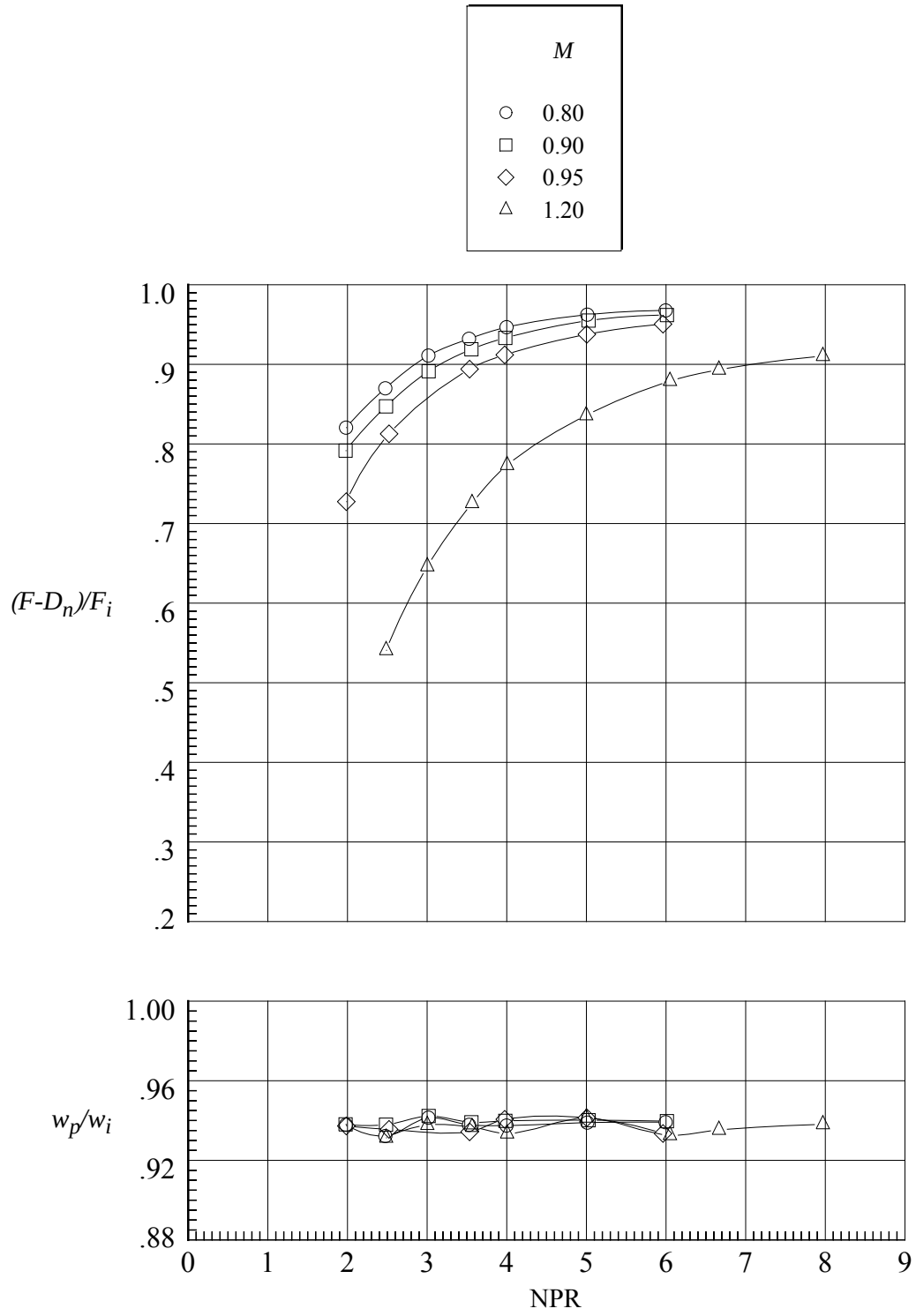

(a) Variation of $(F\text{-}D_n)/F_i$ and w_p/w_i.

Figure 72. Aeropropulsive performance for nozzle N2 with flap F2 and sidewall S1. $r_f/r_{f,max} = 0.1$; $\beta_f = 12.88°$; $L_f/h_m = 1.4$; $\beta_s = 4.0°$; $r_s/r_{s,max} = 0$.

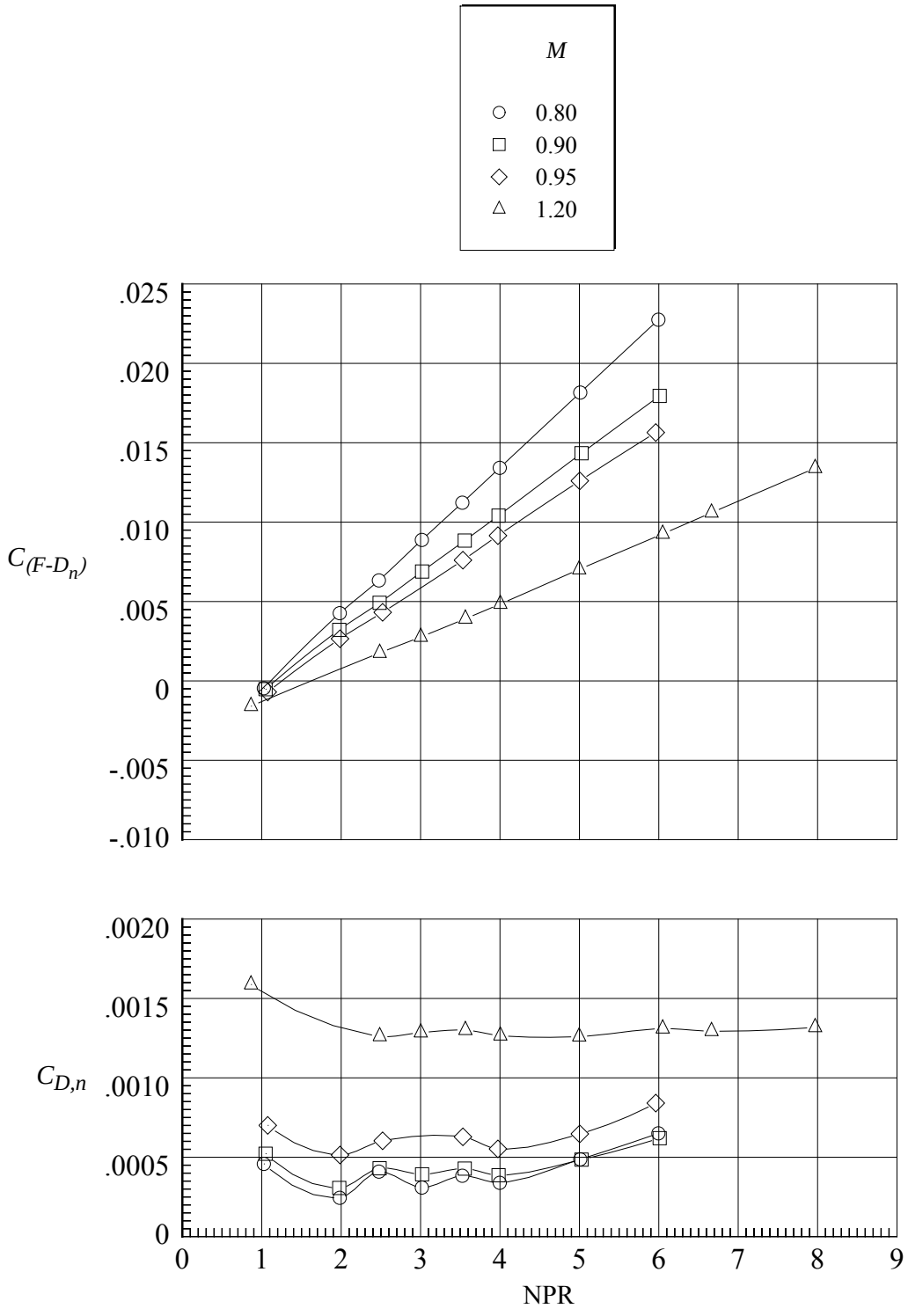

(b) Variation of $C_{(F\text{-}D_n)}$ and $C_{D,n}$.

Figure 72. Continued.

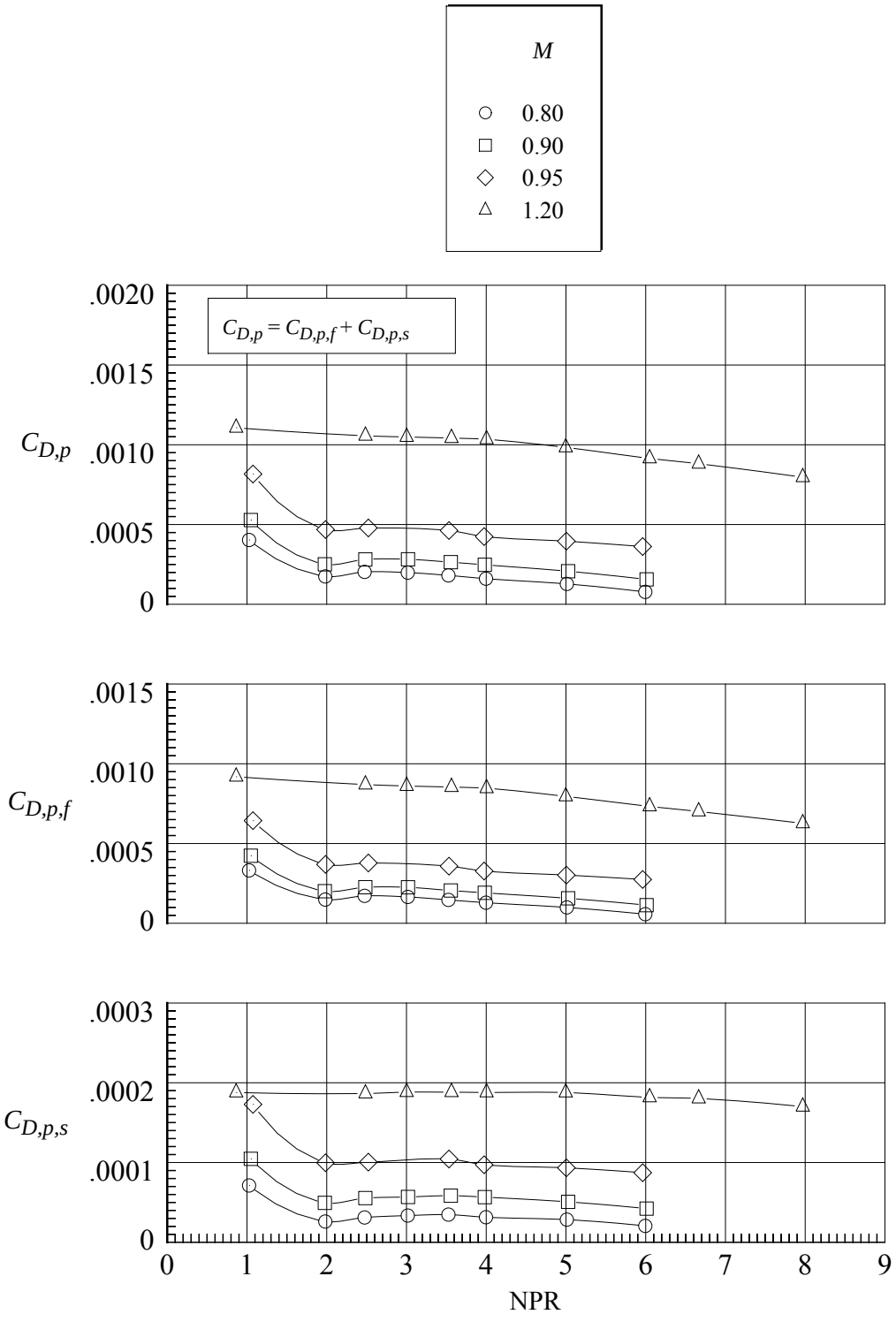

(c) Variation of $C_{D,p}$, $C_{D,p,f}$, and $C_{D,p,s}$.

Figure 72. Continued.

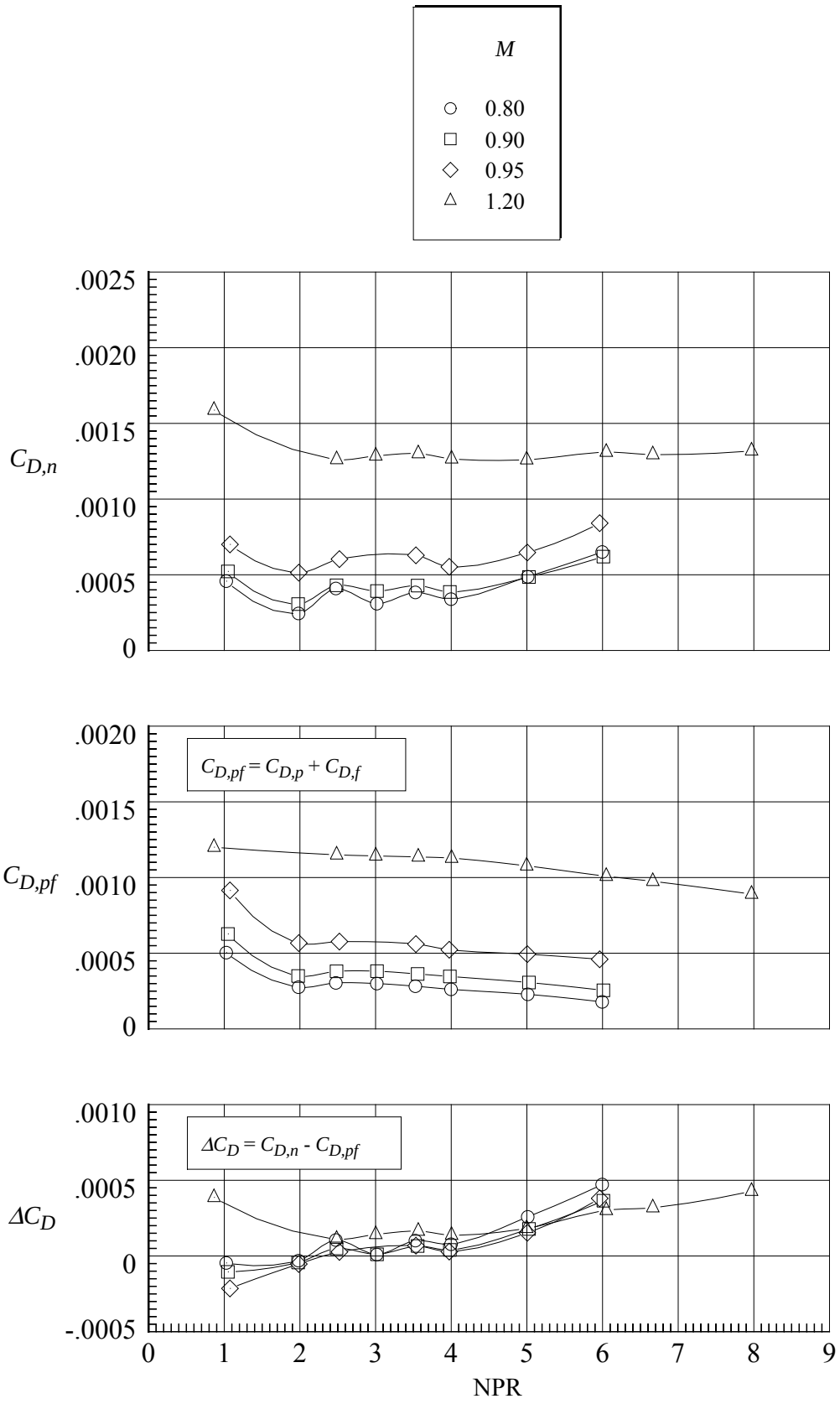

(d) Variation of $C_{D,n}$, $C_{D,pf}$, and ΔC_D.

Figure 72. Concluded.

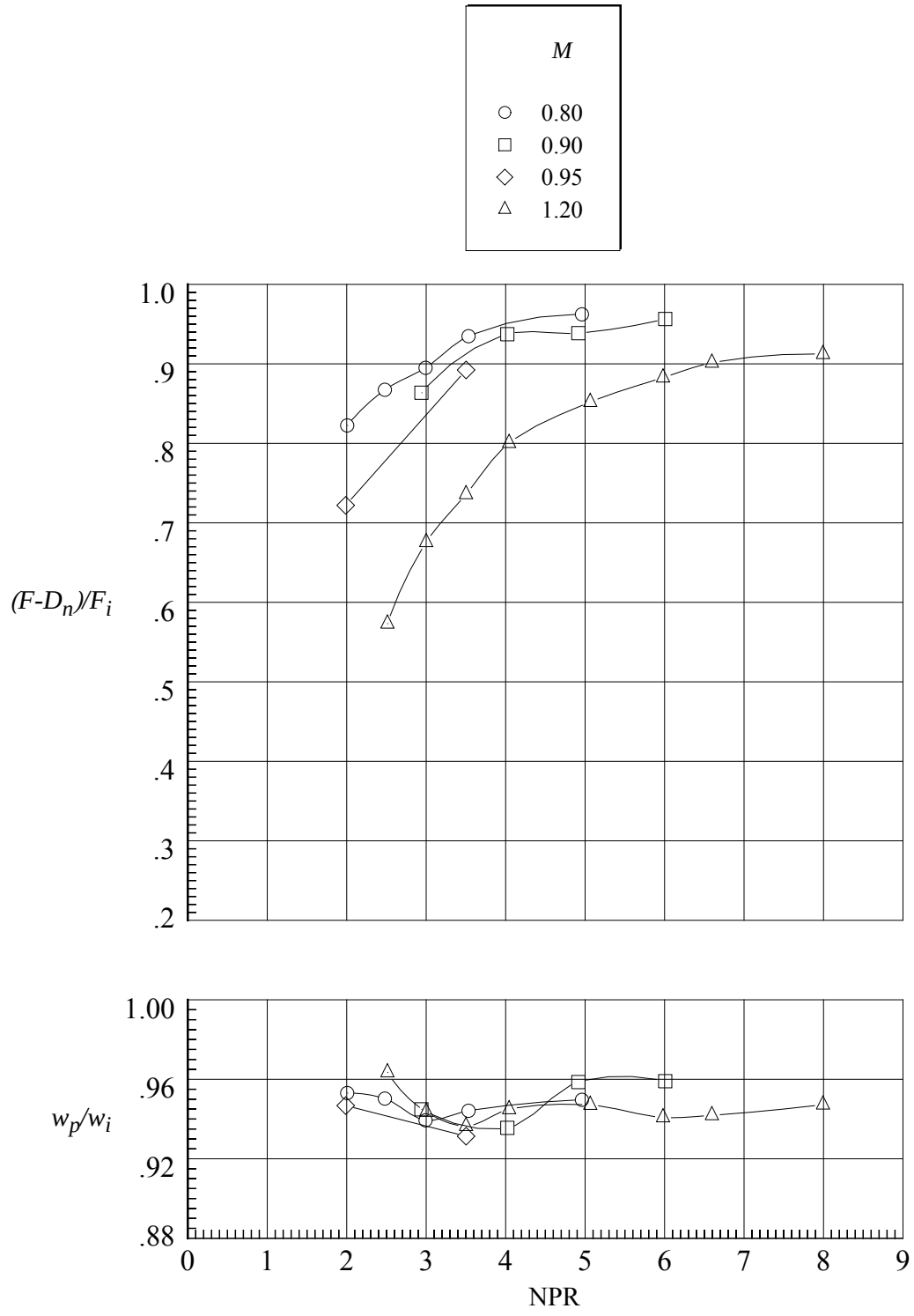

(a) Variation of $(F\text{-}D_n)/F_i$ and w_p/w_i.

Figure 73. Aeropropulsive performance for nozzle N3 with flap F3 and sidewall S1.
$r_f/r_{f,max} = 0$; $\beta_f = 11.72°$; $L_f/h_m = 1.4$; $\beta_s = 4.0°$; $r_s/r_{s,max} = 0$.

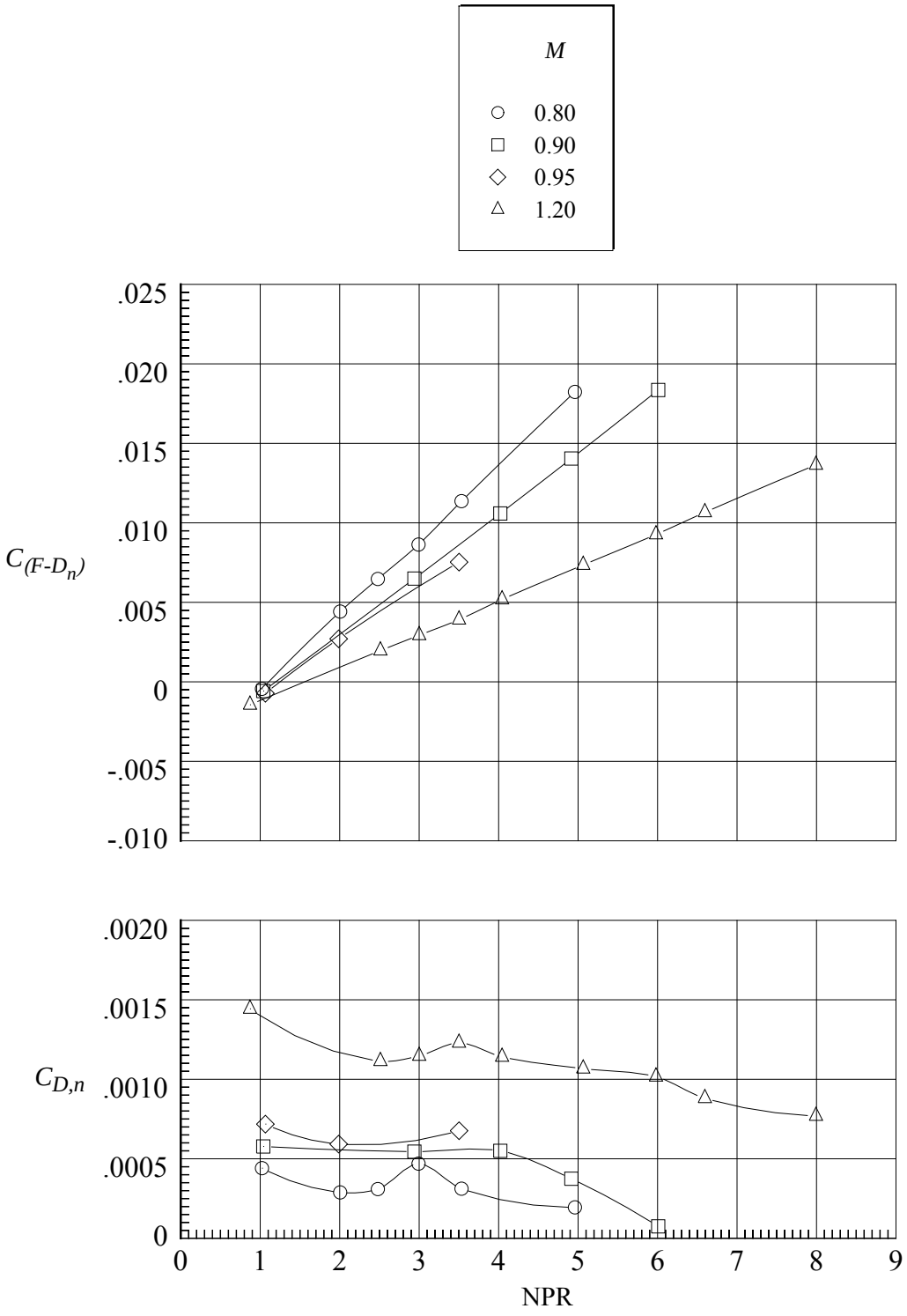

(b) Variation of $C_{(F\text{-}D_n)}$ and $C_{D,n}$.

Figure 73. Continued.

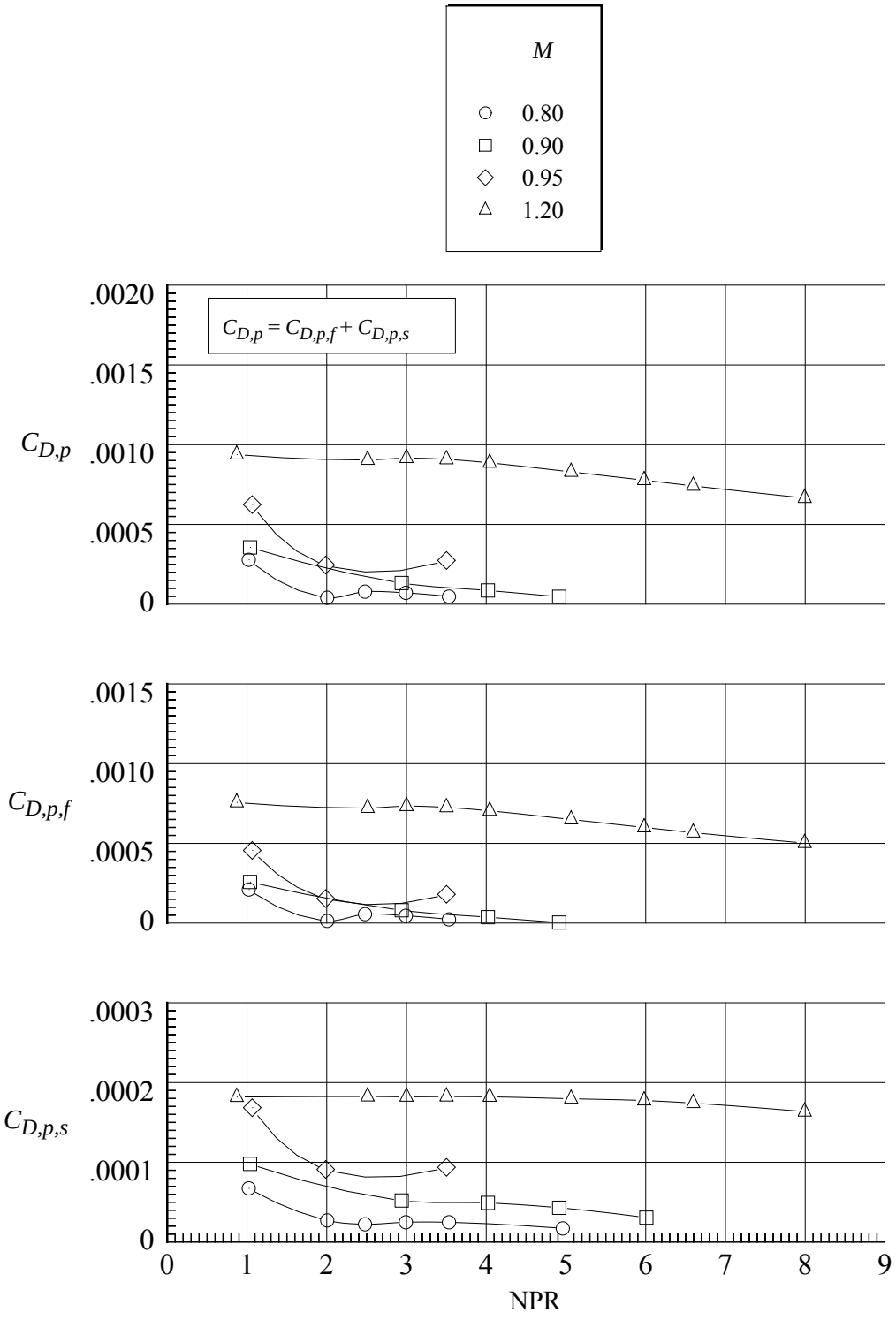

(c) Variation of $C_{D,p}$, $C_{D,p,f}$, and $C_{D,p,s}$.

Figure 73. Continued.

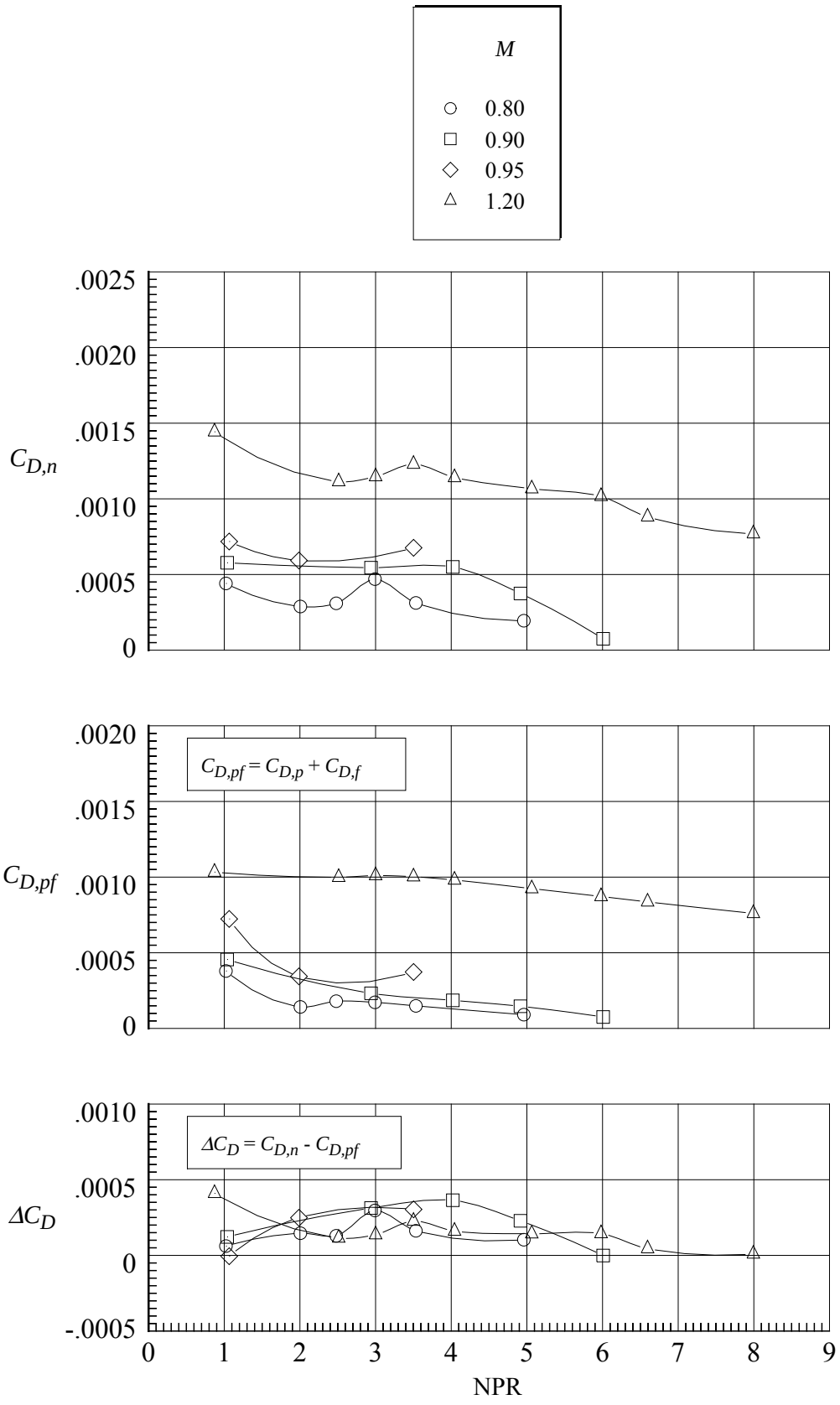

(d) Variation of $C_{D,n}$, $C_{D,pf}$, and ΔC_D.

Figure 73. Concluded.

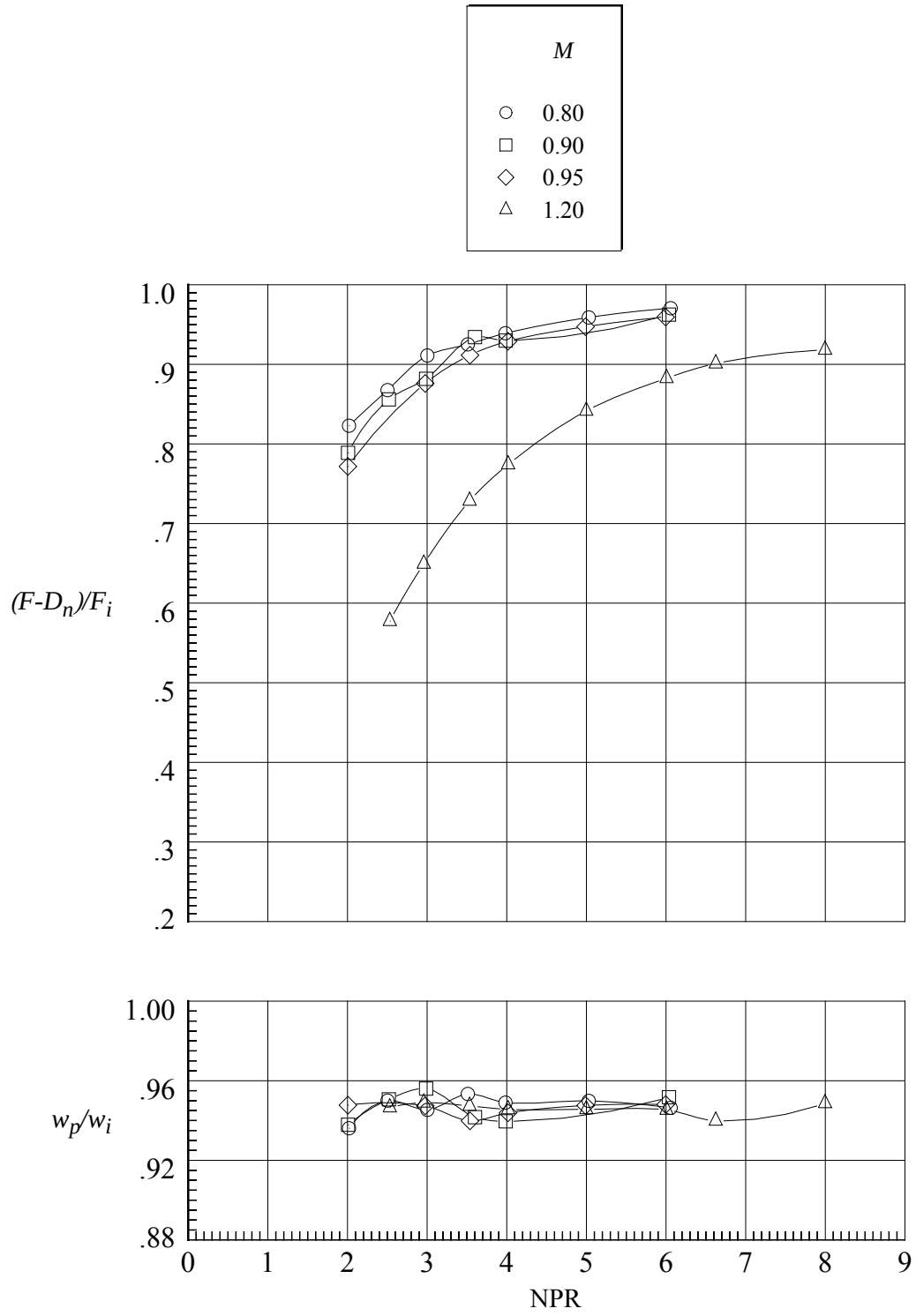

(a) Variation of $(F\text{-}D_n)/F_i$ and w_p/w_i.

Figure 74. Aeropropulsive performance for nozzle N4 with flap F4 and sidewall S1. $r_f/r_{f,max} = 1.0$; $\beta_f = 23.44°$; $L_f/h_m = 1.4$; $\beta_s = 4.0°$; $r_s/r_{s,max} = 0$.

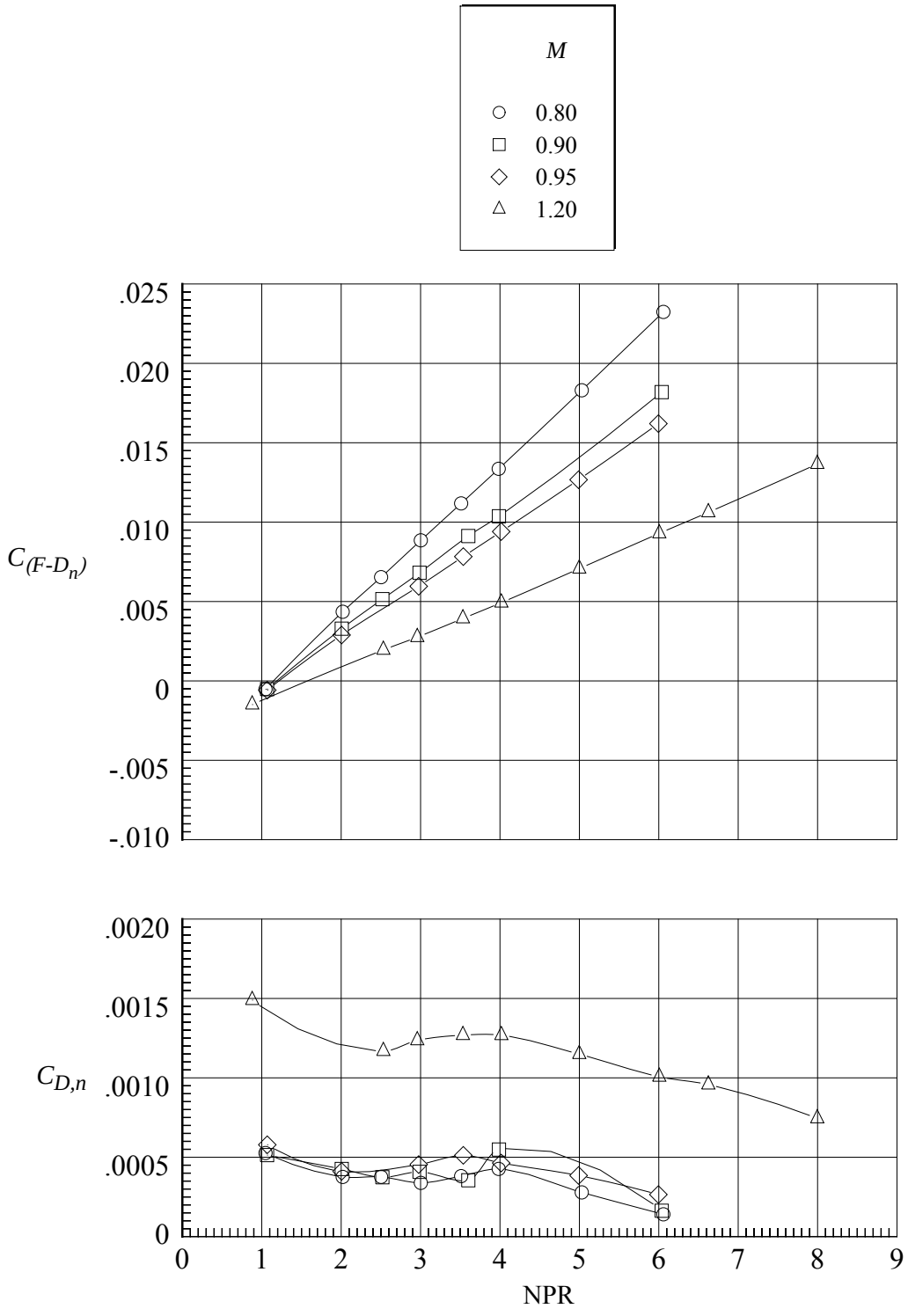

(b) Variation of $C_{(F\text{-}D_n)}$ and $C_{D,n}$.

Figure 74. Continued.

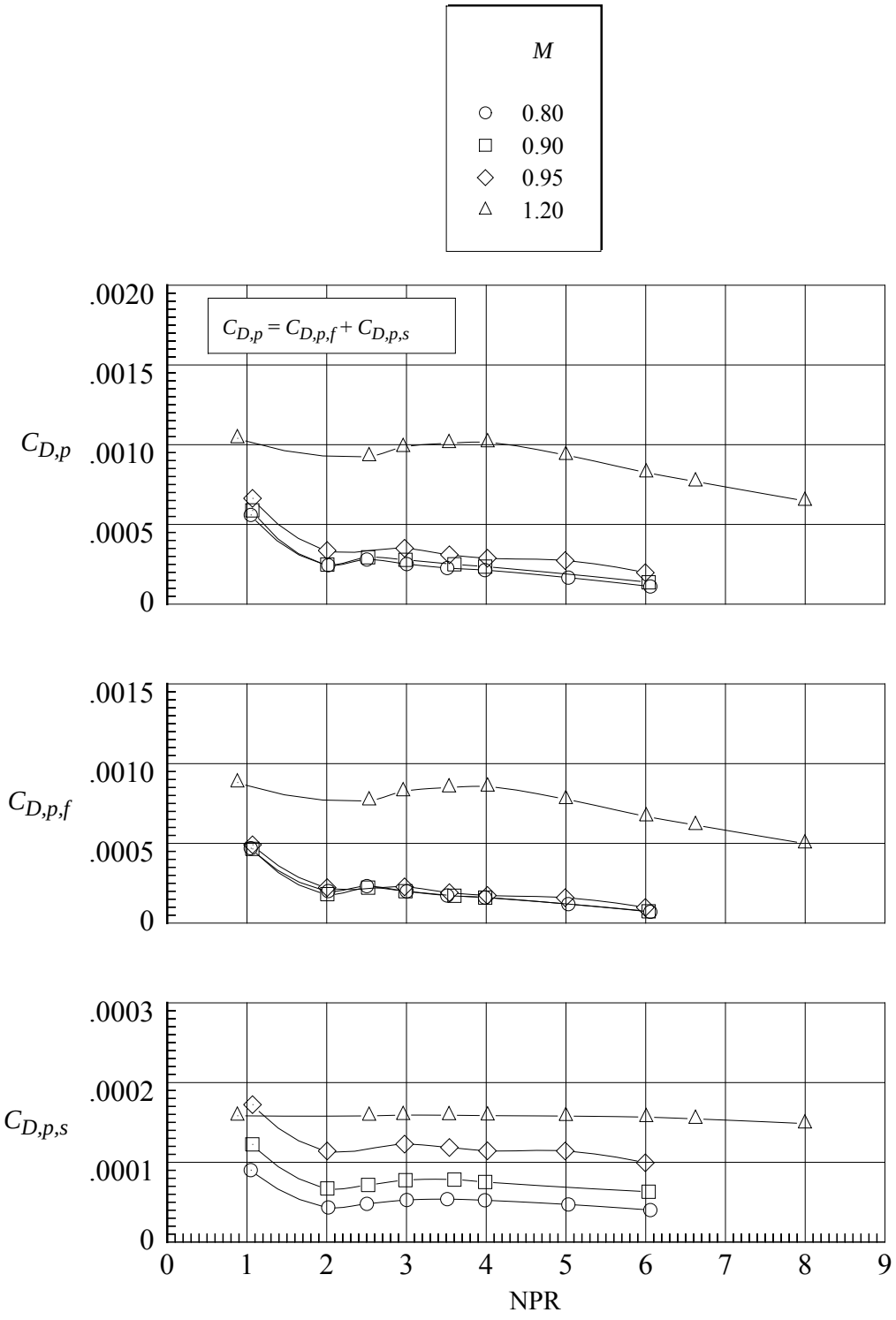

(c) Variation of $C_{D,p}$, $C_{D,p,f}$, and $C_{D,p,s}$.

Figure 74. Continued.

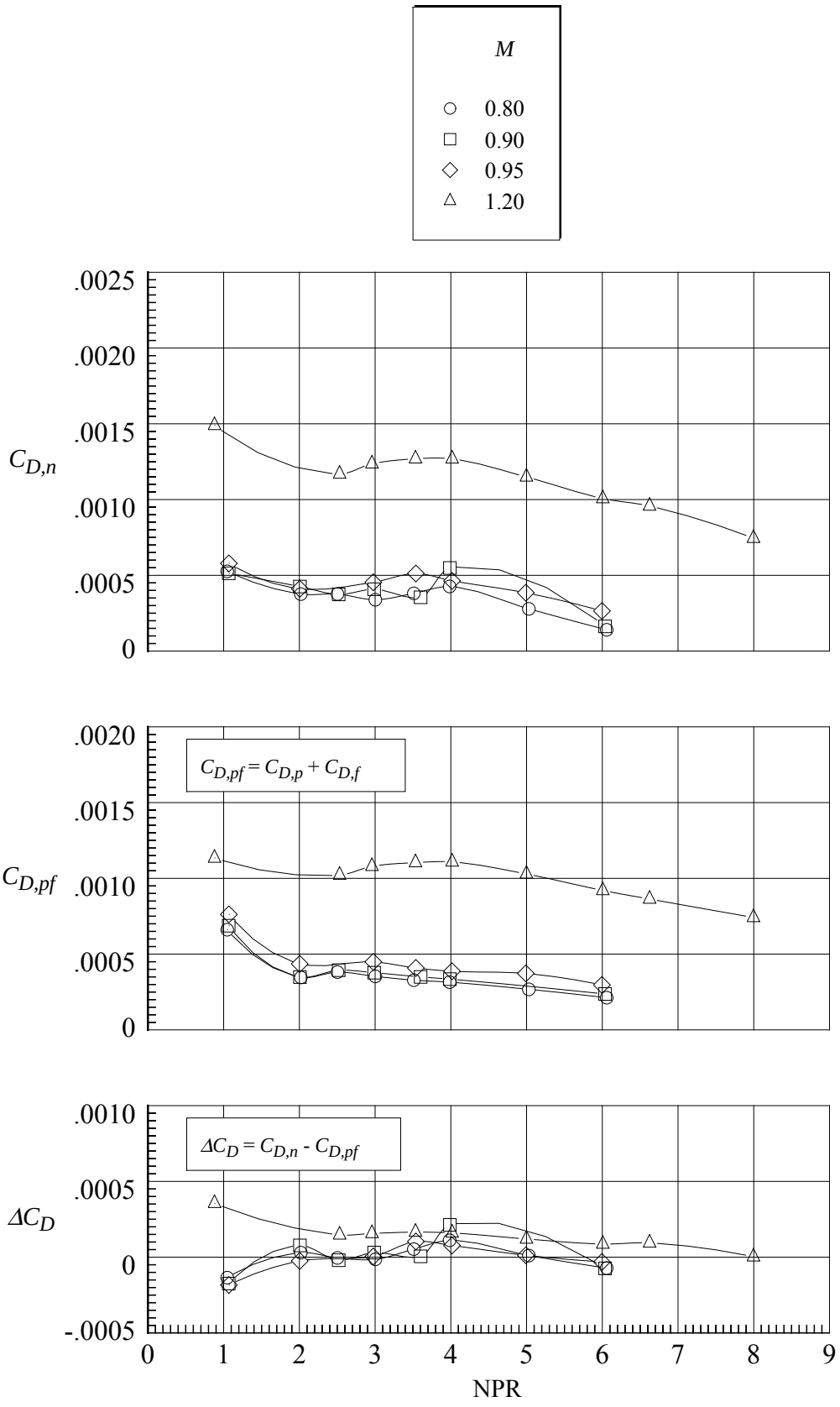

(d) Variation of $C_{D,n}$, $C_{D,pf}$, and ΔC_D.

Figure 74. Concluded.

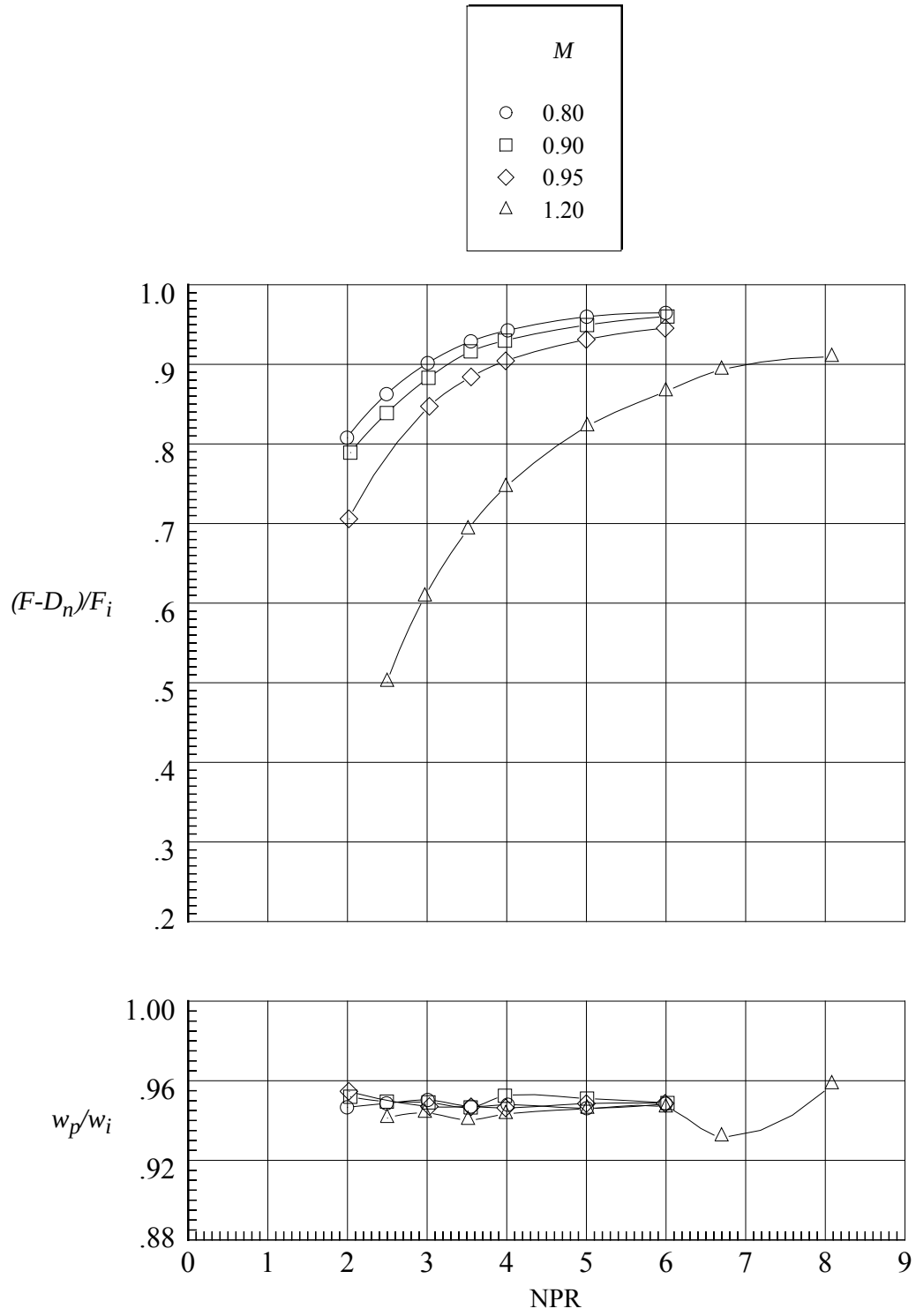

(a) Variation of $(F\text{-}D_n)/F_i$ and w_p/w_i.

Figure 75. Aeropropulsive performance for nozzle N5 with flap F1 and sidewall S2.
$r_f/r_{f,max} = 0.4$; $\beta_f = 16.38°$; $L_f/h_m = 1.4$; $\beta_s = 6.0°$; $r_s/r_{s,max} = 0$.

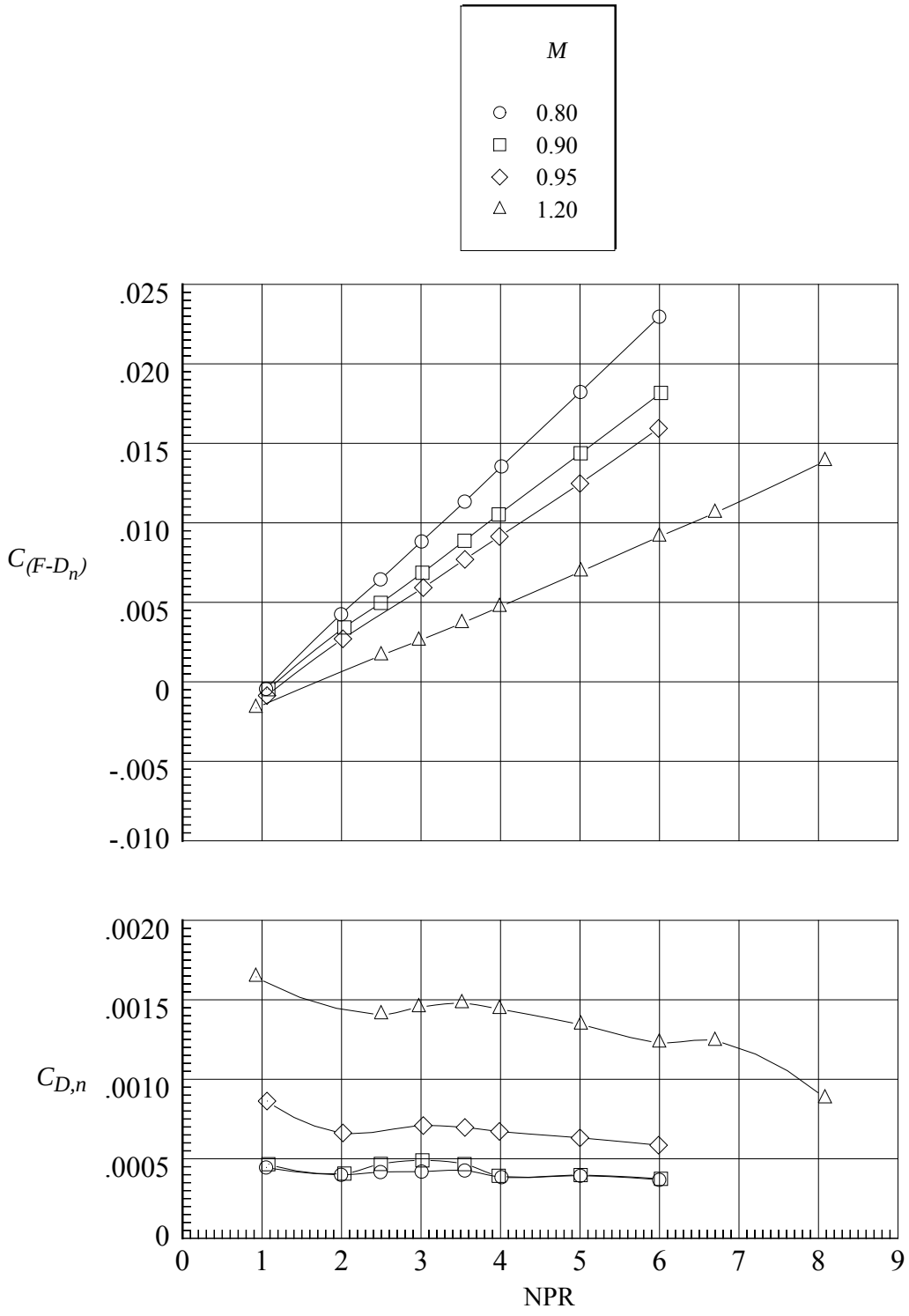

(b) Variation of $C_{(F\text{-}D_n)}$ and $C_{D,n}$.

Figure 75. Continued.

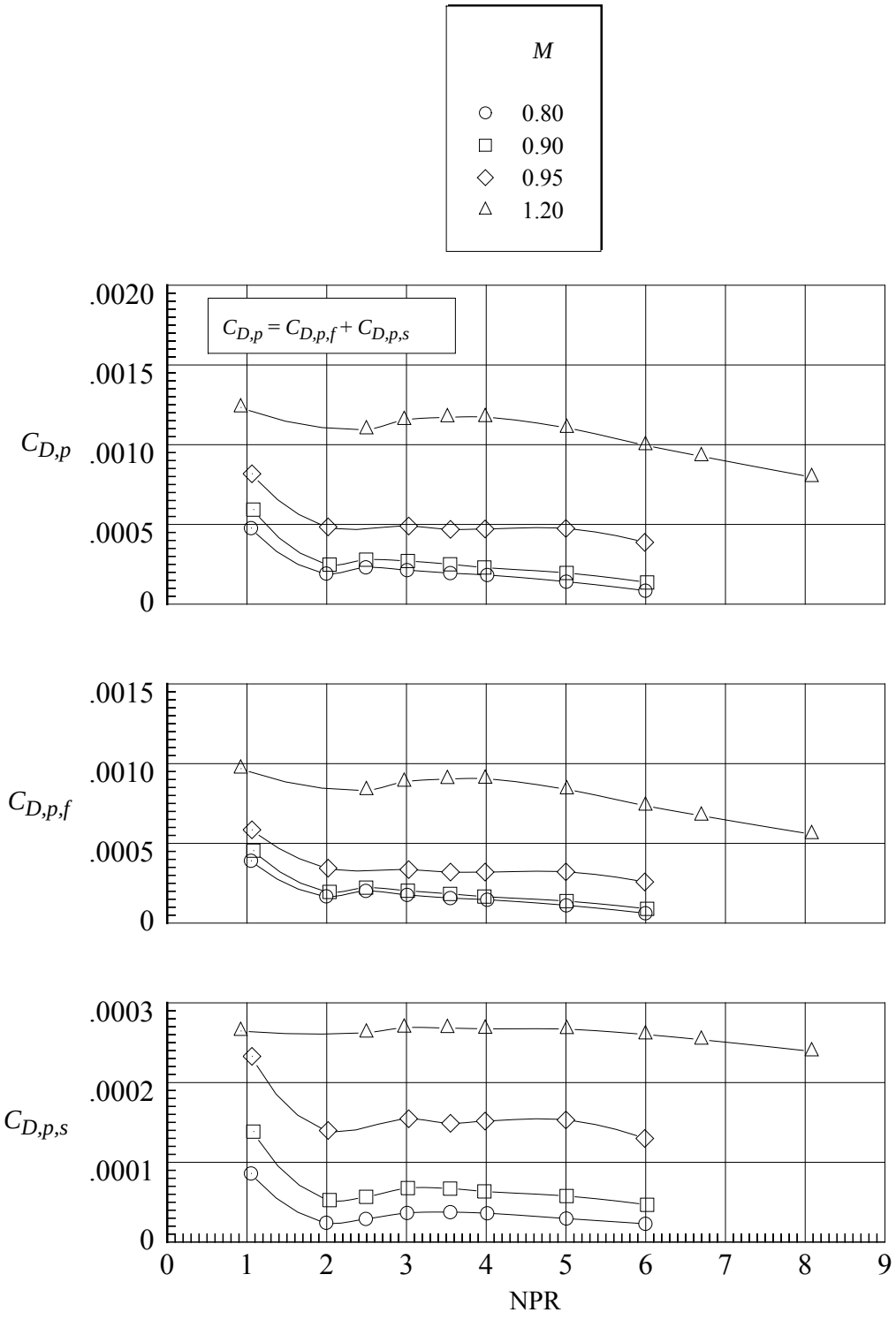

(c) Variation of $C_{D,p}$, $C_{D,p,f}$, and $C_{D,p,s}$.

Figure 75. Continued.

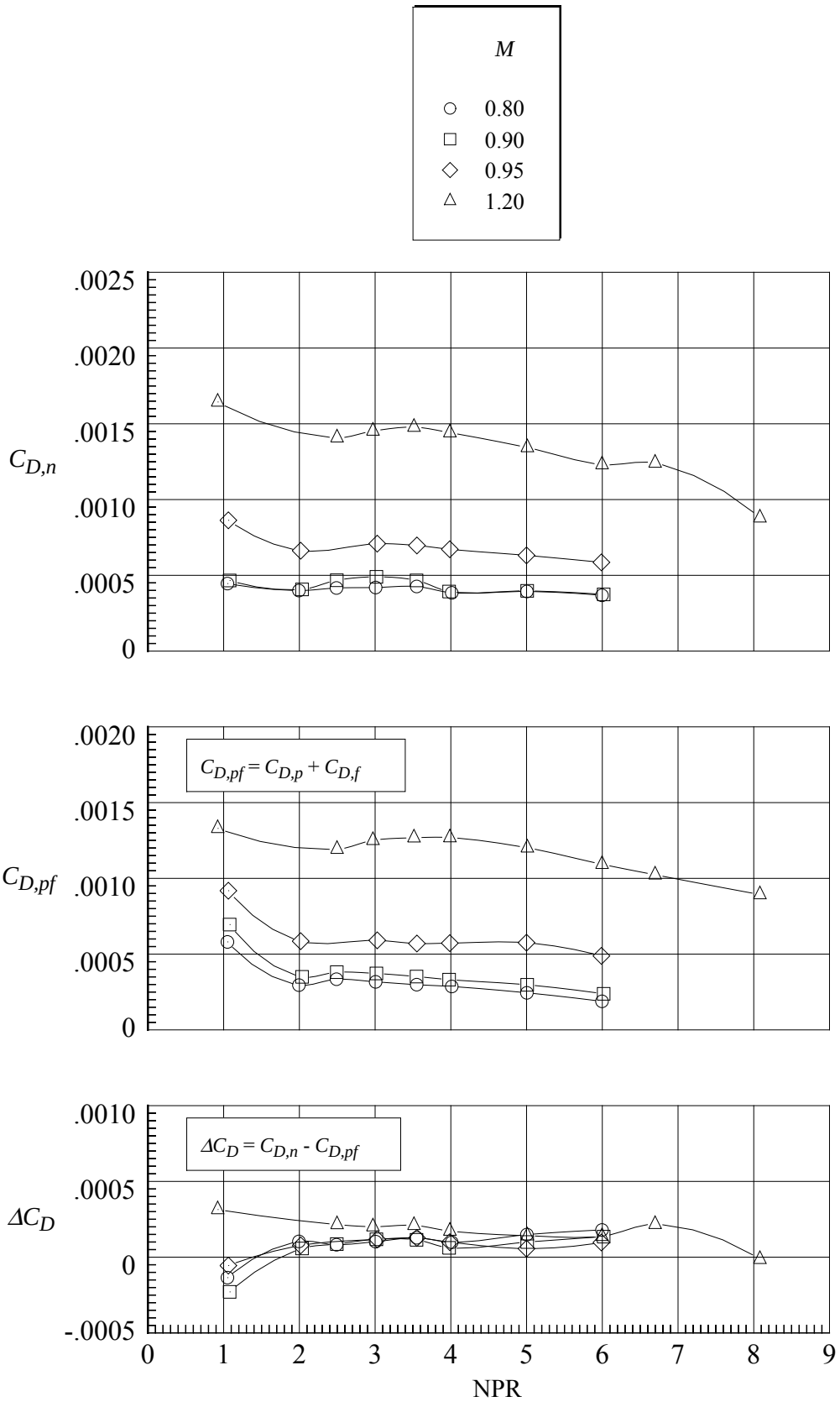

(d) Variation of $C_{D,n}$, $C_{D,pf}$, and ΔC_D.

Figure 75. Concluded.

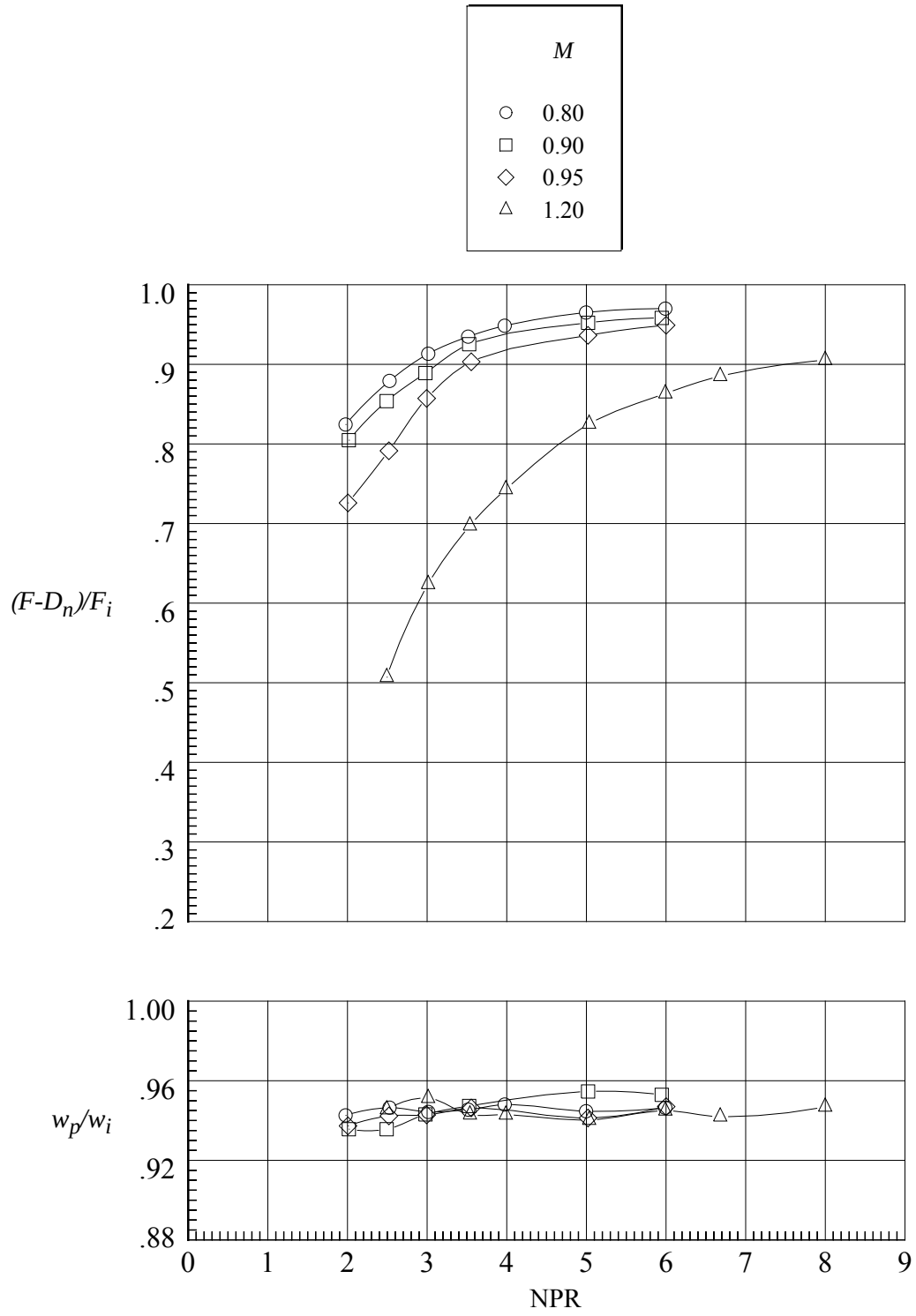

(a) Variation of $(F\text{-}D_n)/F_i$ and w_p/w_i.

Figure 76. Aeropropulsive performance for nozzle N6 with flap F1 and sidewall S3. $r_f/r_{f,max} = 0.4$; $\beta_f = 16.38°$; $L_f/h_m = 1.4$; $\beta_s = 8.0°$; $r_s/r_{s,max} = 0$.

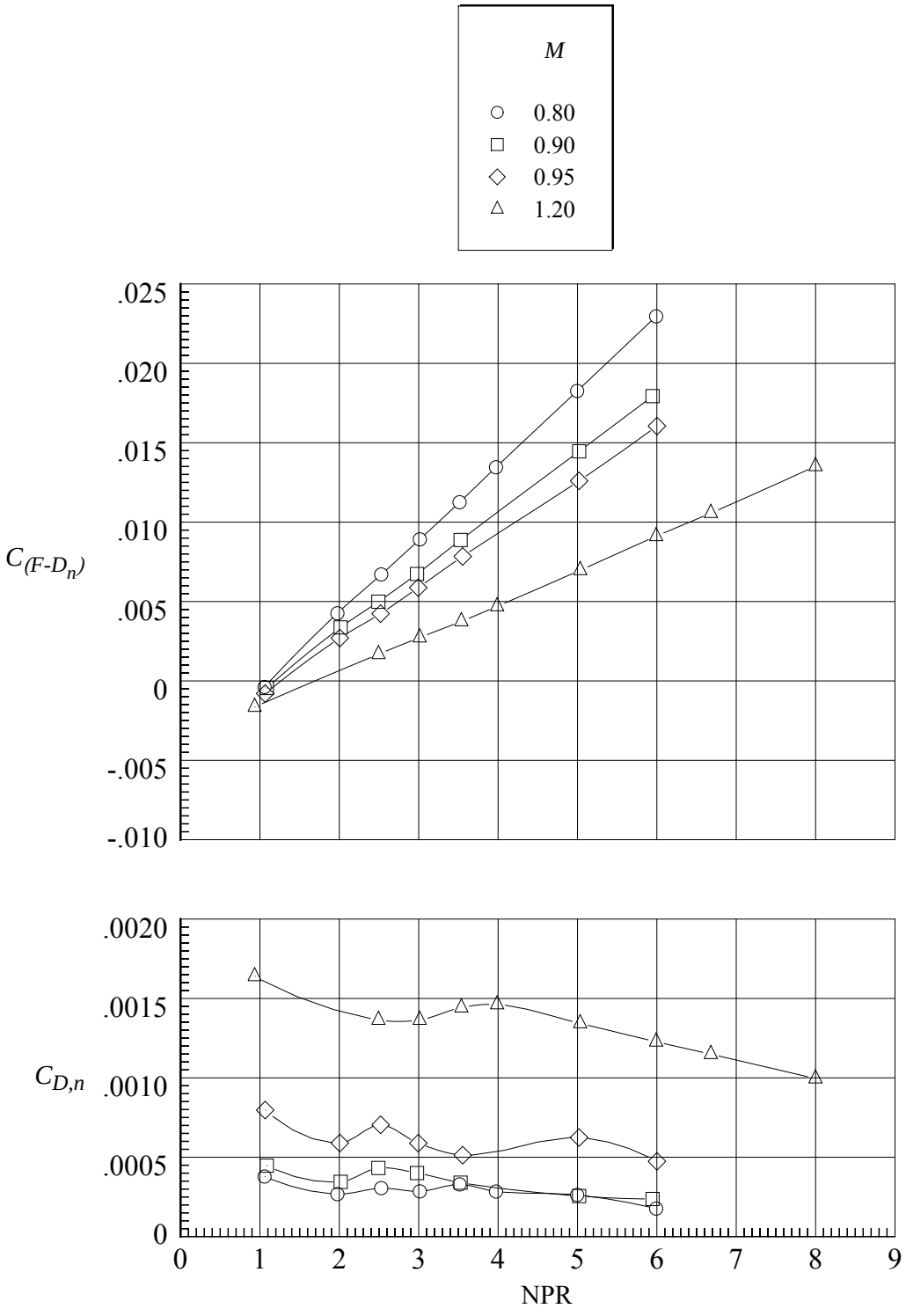

(b) Variation of $C_{(F\text{-}D_n)}$ and $C_{D,n}$.

Figure 76. Continued.

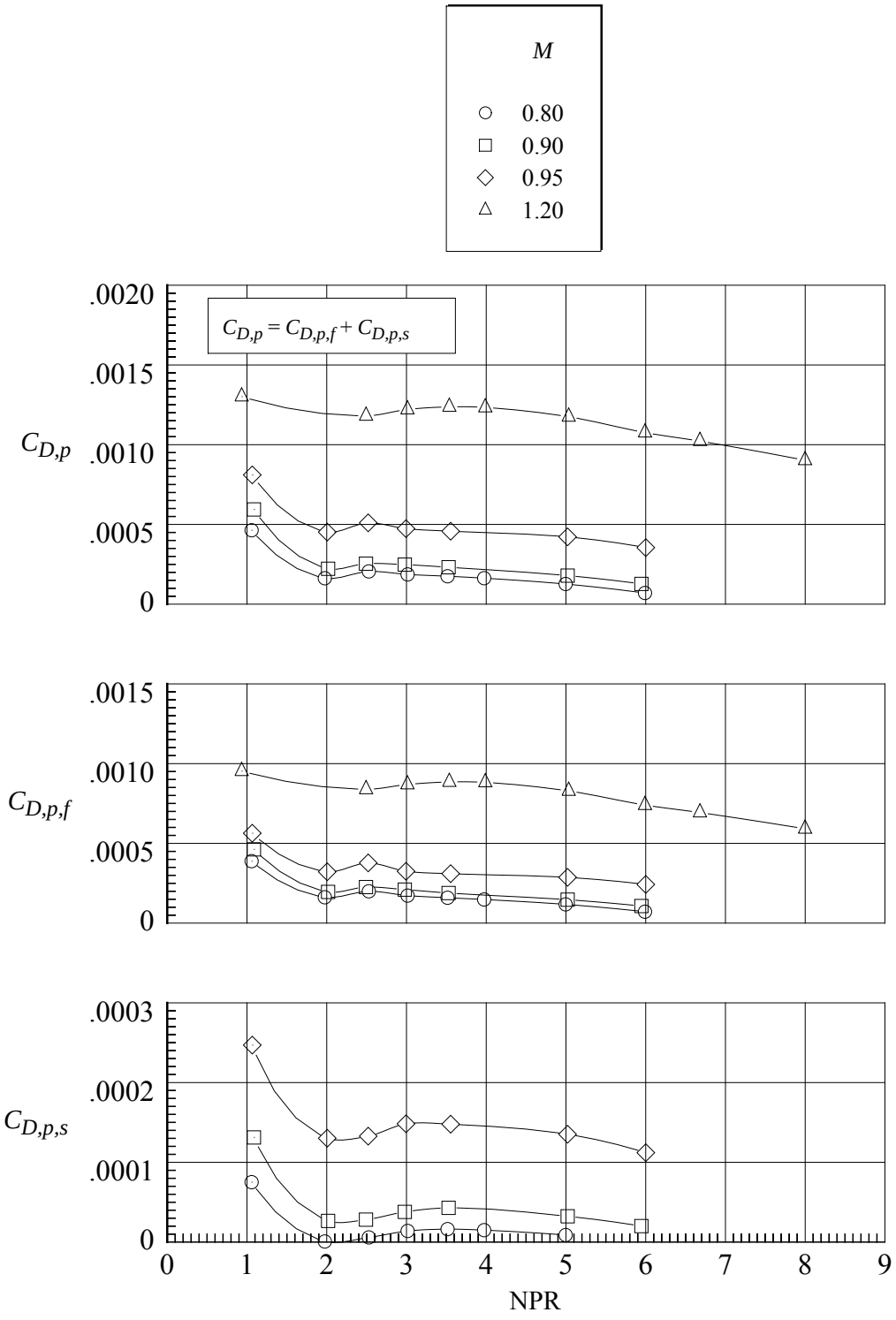

(c) Variation of $C_{D,p}$, $C_{D,p,f}$, and $C_{D,p,s}$.

Figure 76. Continued.

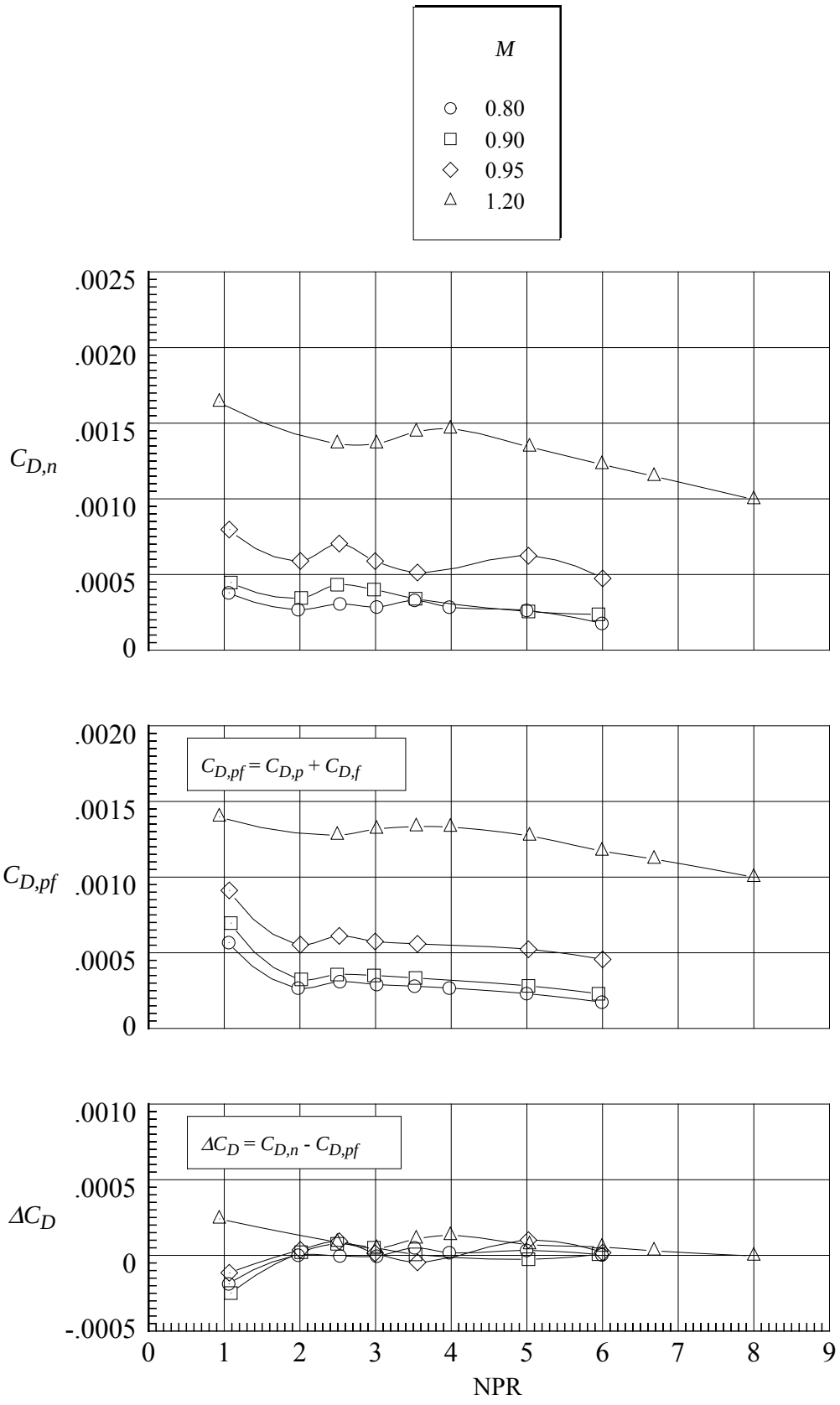

(d) Variation of $C_{D,n}$, $C_{D,pf}$, and ΔC_D.

Figure 76. Concluded.

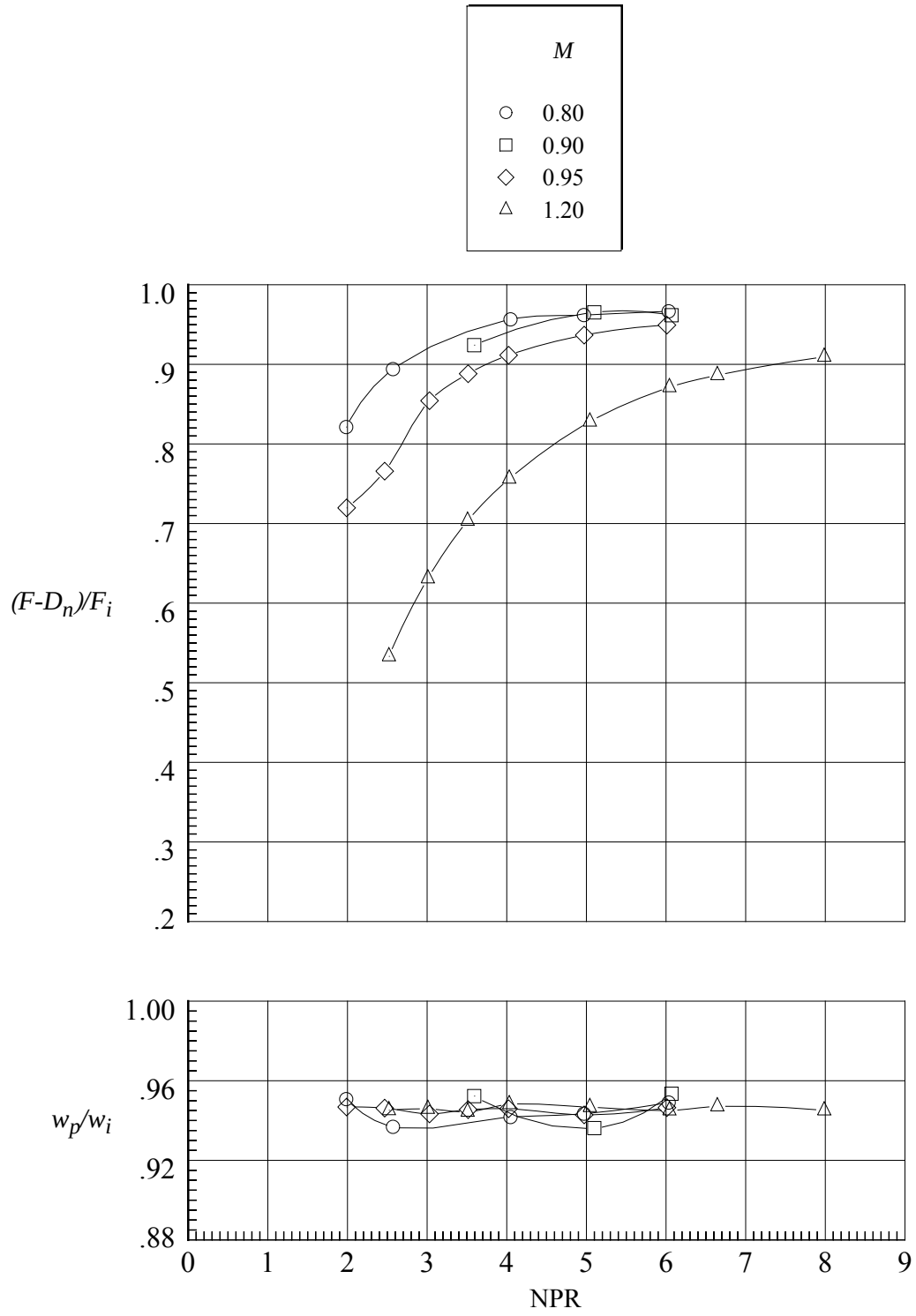

(a) Variation of $(F\text{-}D_n)/F_i$ and w_p/w_i.

Figure 77. Aeropropulsive performance for nozzle N7 with flap F1 and sidewall S4. $r_f/r_{f,max} = 0.4$; $\beta_f = 16.38°$; $L_f/h_m = 1.4$; $\beta_s = 6.0°$; $r_s/r_{s,max} = 0.1$.

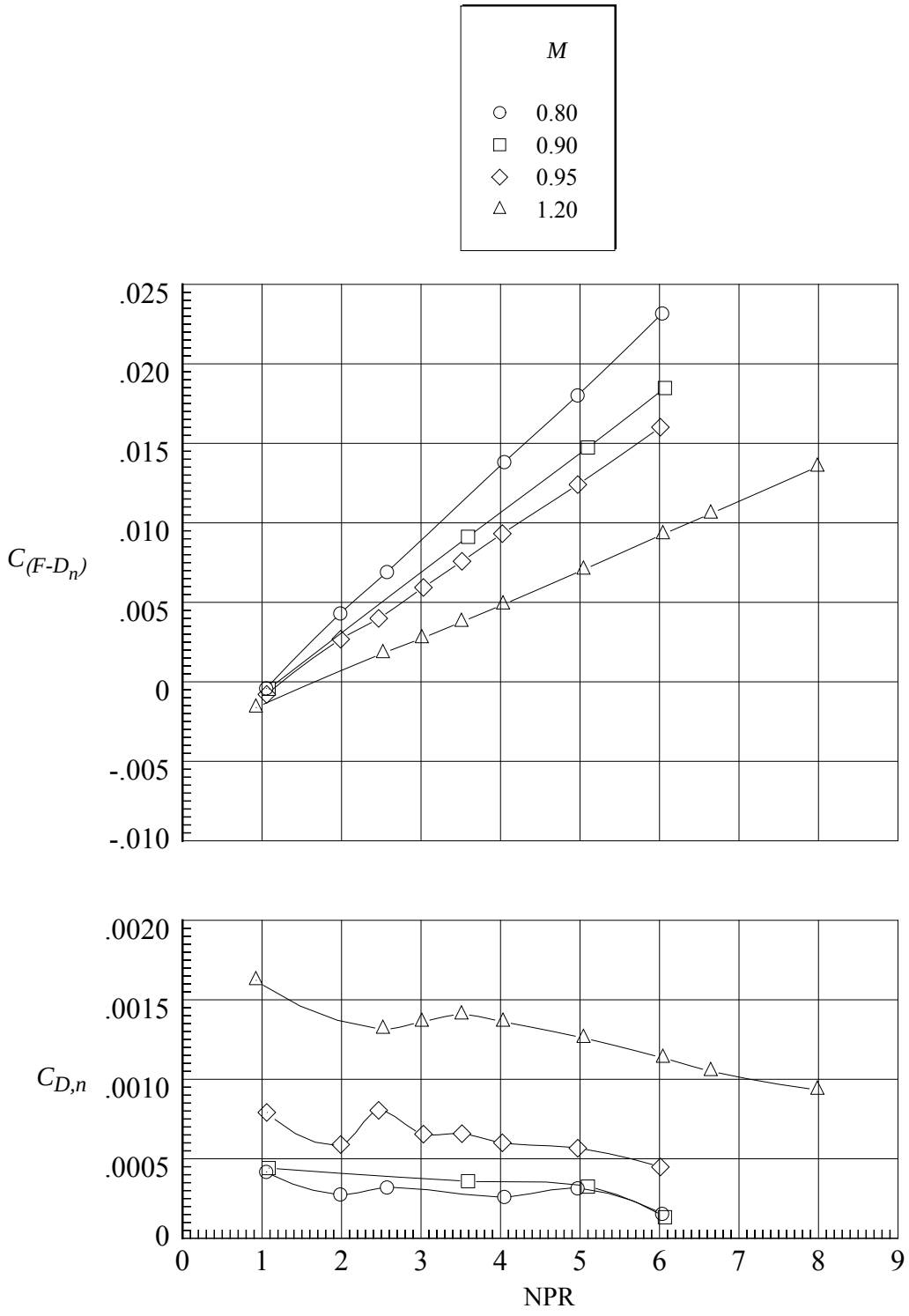

(b) Variation of $C_{(F\text{-}D_n)}$ and $C_{D,n}$.

Figure 77. Continued.

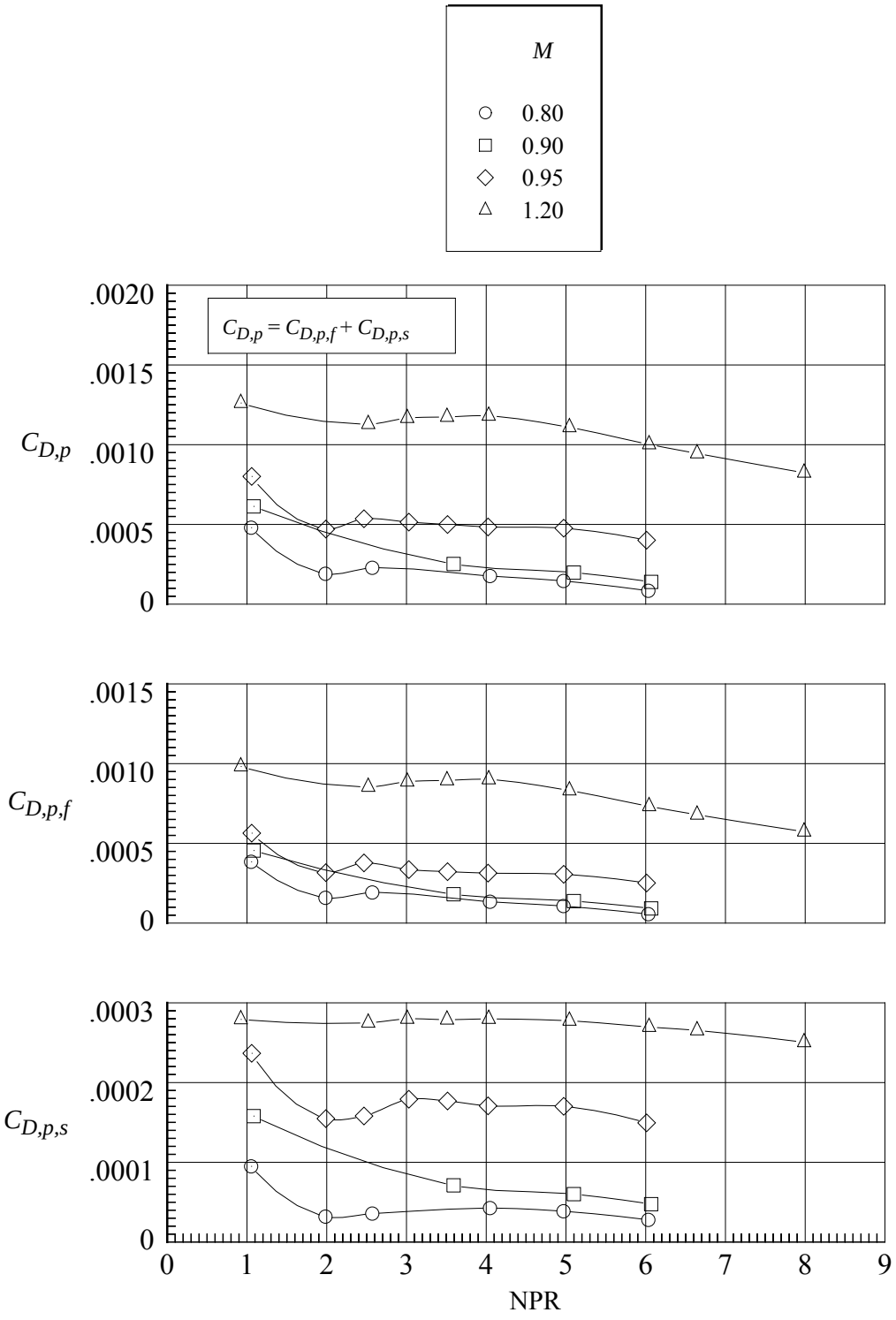

(c) Variation of $C_{D,p}$, $C_{D,p,f}$, and $C_{D,p,s}$.

Figure 77. Continued.

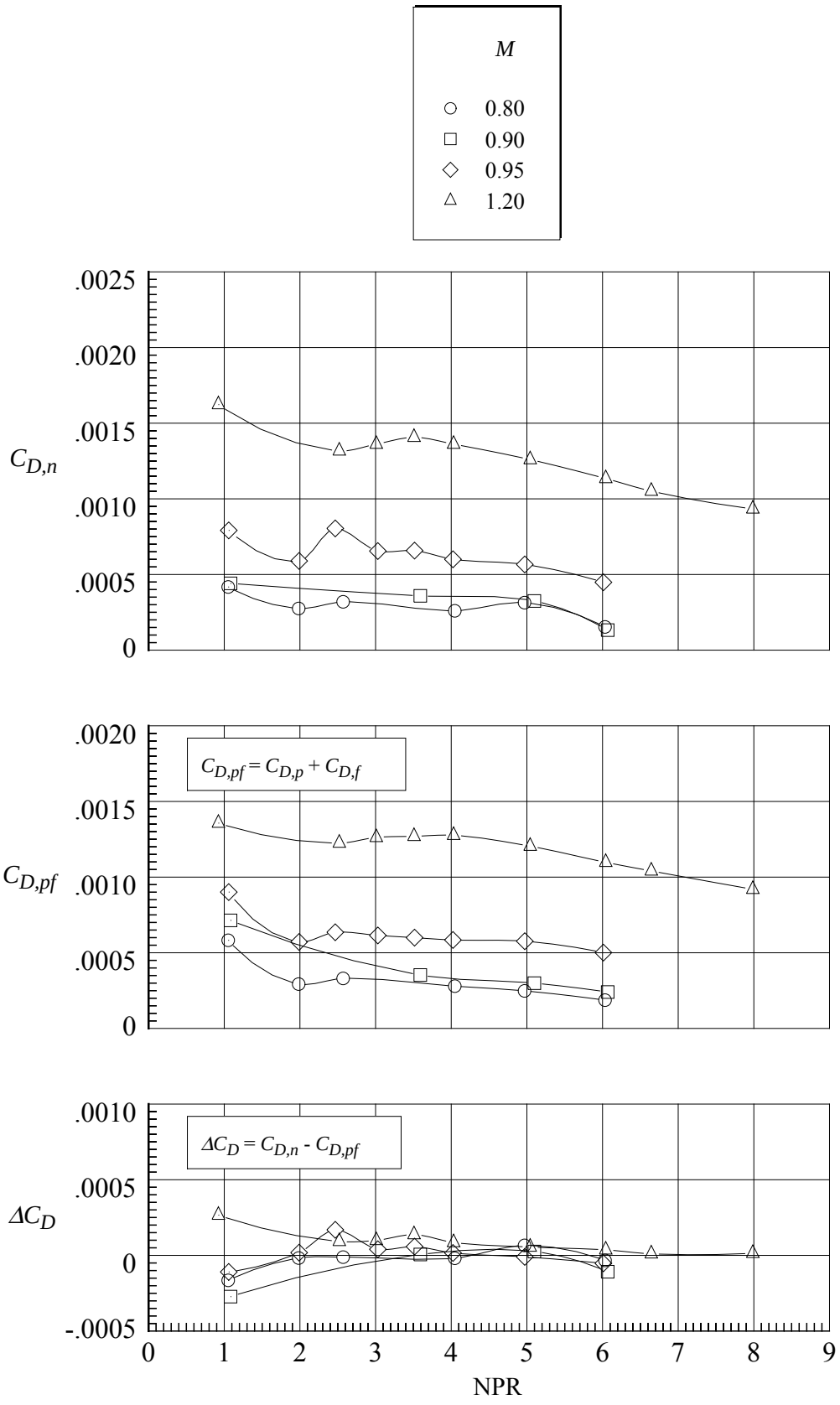

(d) Variation of $C_{D,n}$, $C_{D,pf}$, and ΔC_D.

Figure 77. Concluded.

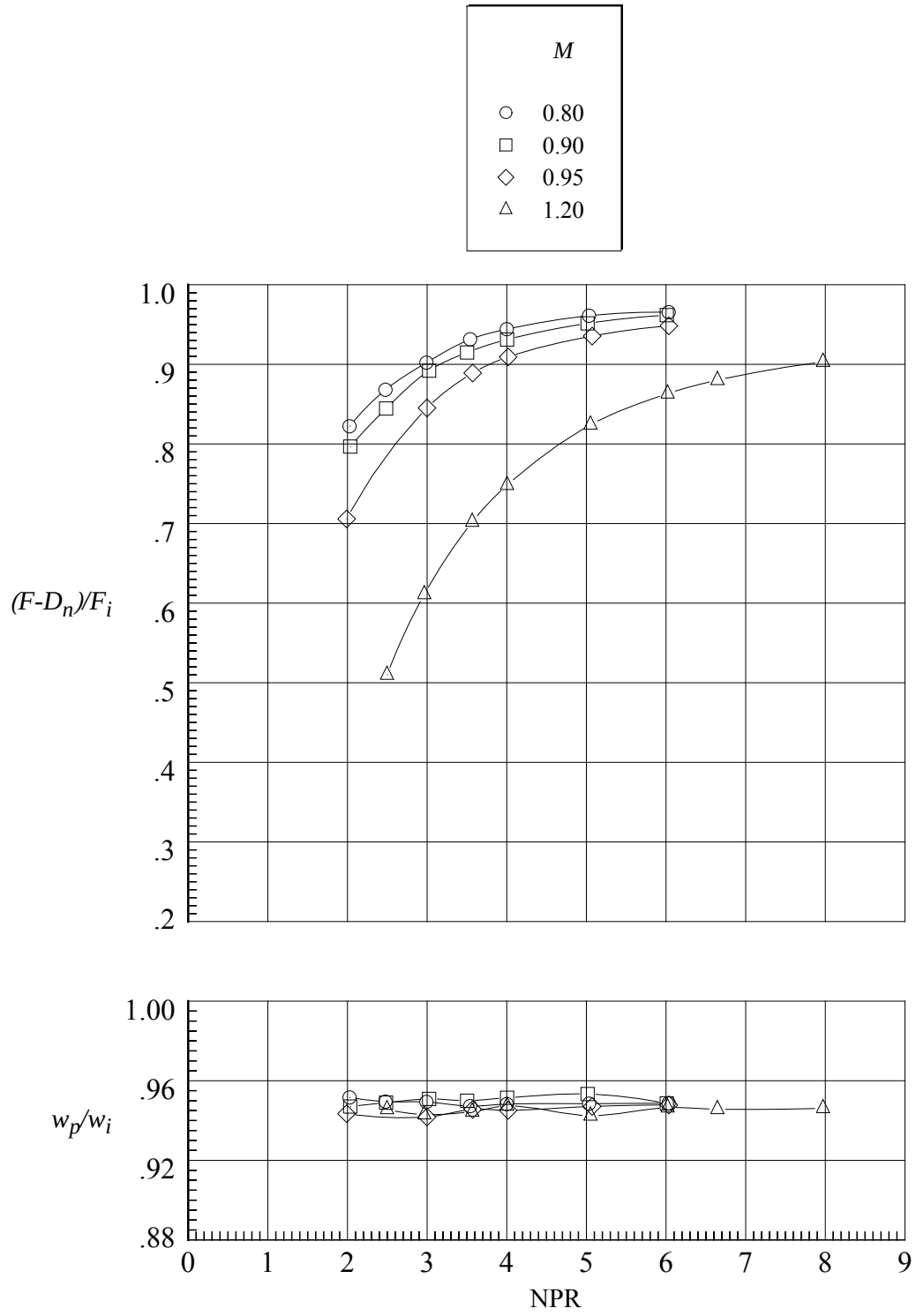

(a) Variation of $(F\text{-}D_n)/F_i$ and w_p/w_i.

Figure 78. Aeropropulsive performance for nozzle N8 with flap F1 and sidewall S5. $r_f/r_{f,max} = 0.4$; $\beta_f = 16.38°$; $L_f/h_m = 1.4$; $\beta_s = 8.0°$; $r_s/r_{s,max} = 0.1$.

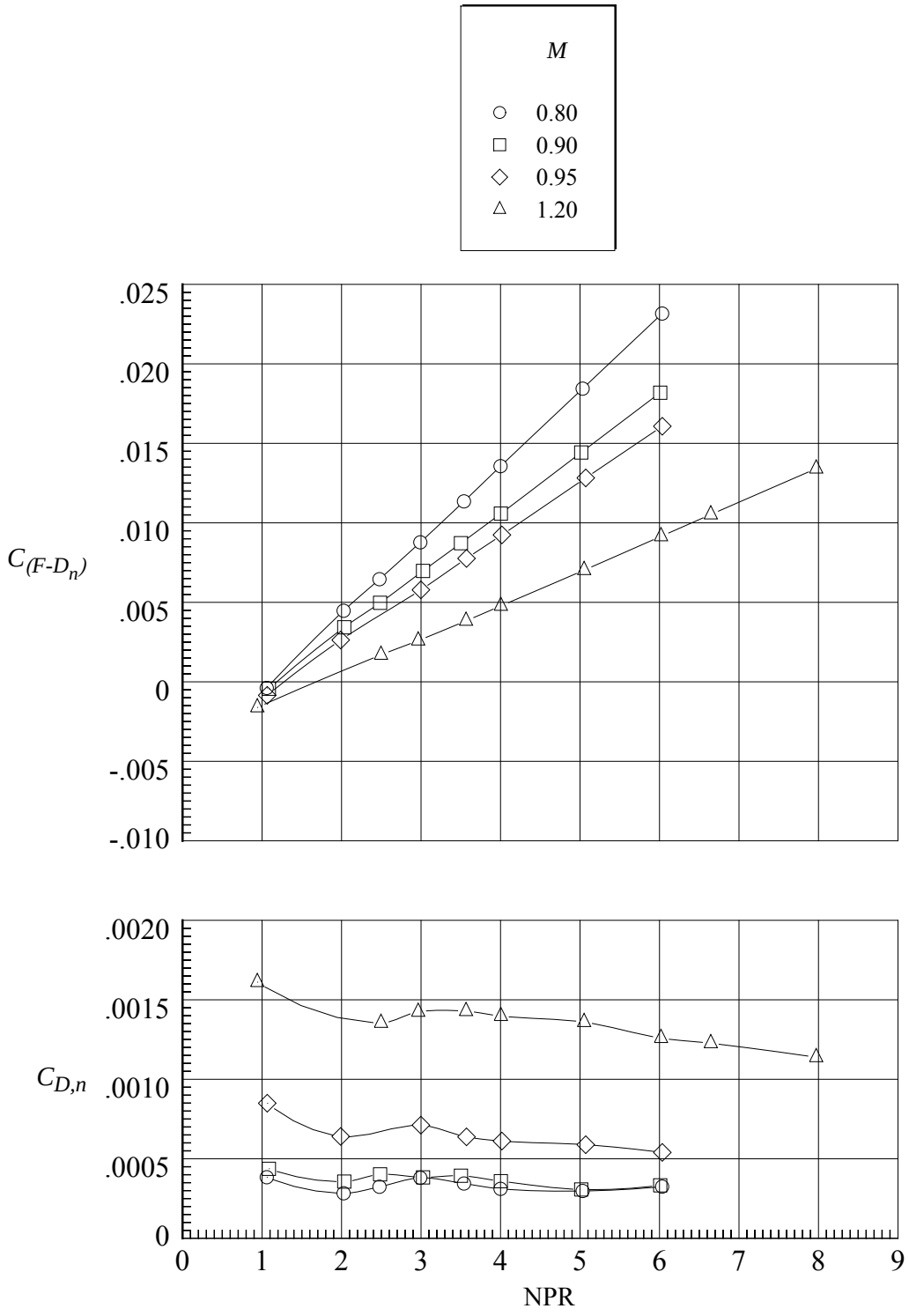

(b) Variation of $C_{(F\text{-}D_n)}$ and $C_{D,n}$.

Figure 78. Continued.

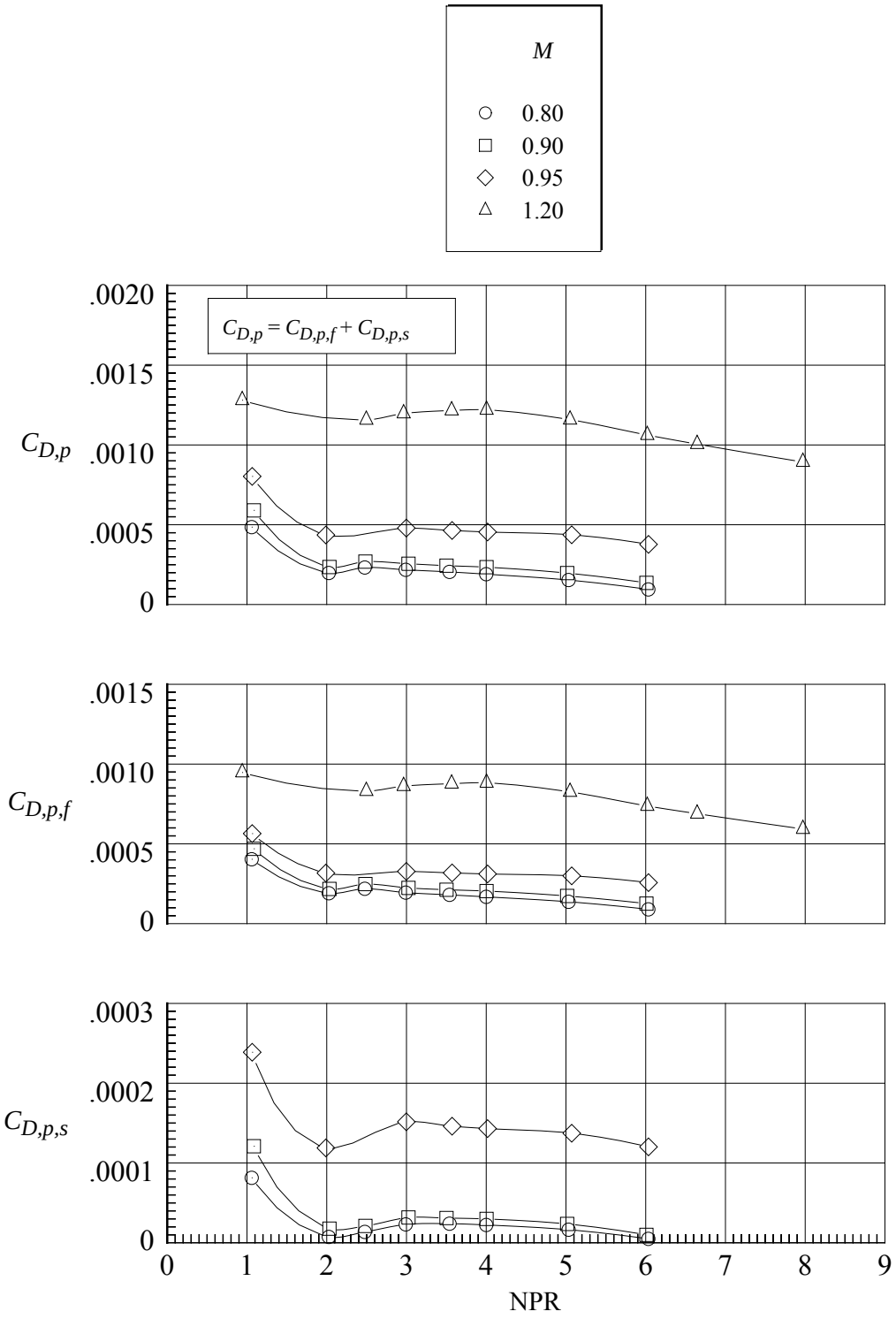

(c) Variation of $C_{D,p}$, $C_{D,p,f}$, and $C_{D,p,s}$.

Figure 78. Continued.

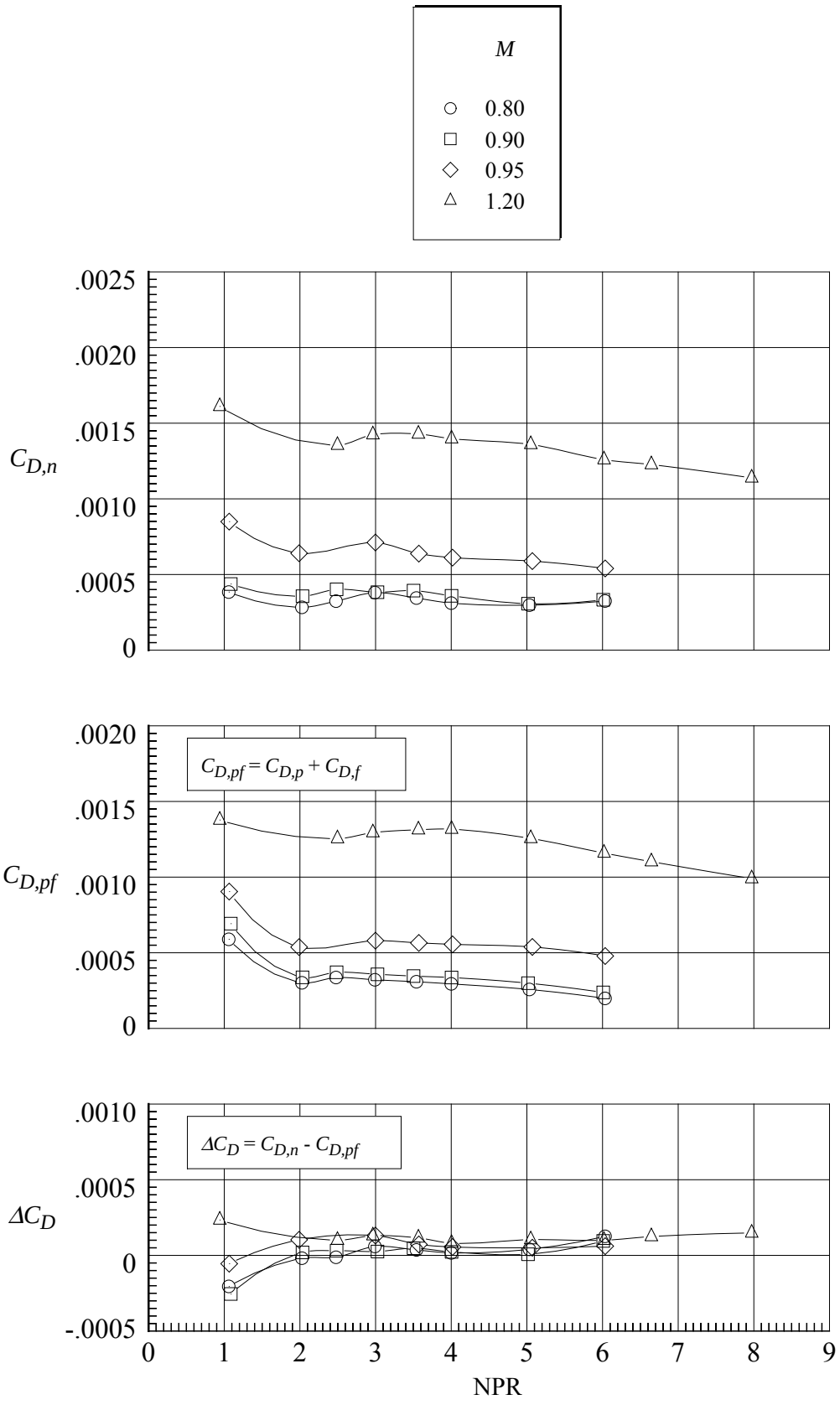

(d) Variation of $C_{D,n}$, $C_{D,pf}$, and ΔC_D.

Figure 78. Concluded.

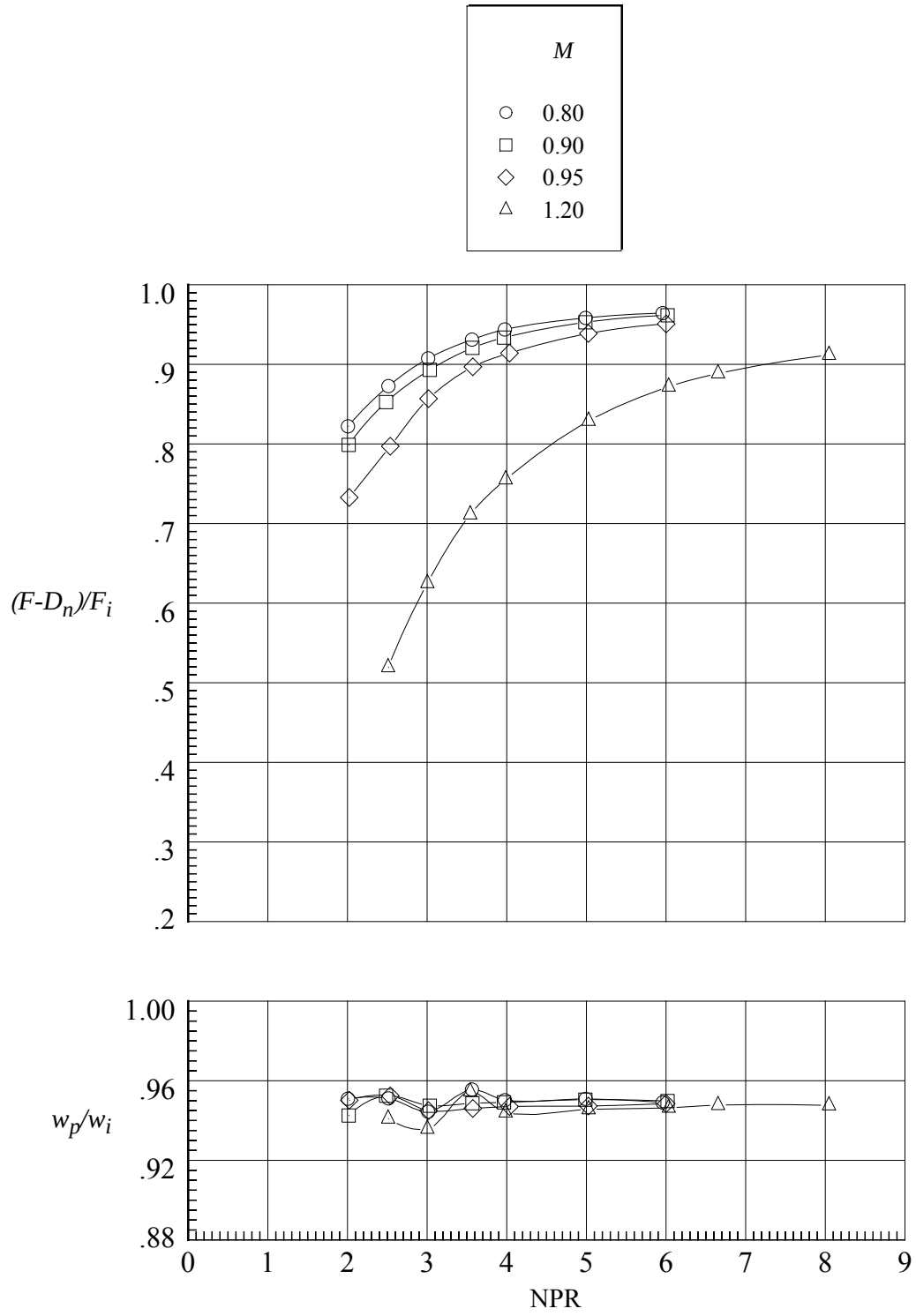

(a) Variation of $(F\text{-}D_n)/F_i$ and w_p/w_i.

Figure 79. Aeropropulsive performance for nozzle N9 with flap F1 and sidewall S6.
$r_f/r_{f,max} = 0.4$; $\beta_f = 16.38°$; $L_f/h_m = 1.4$; $\beta_s = 6.0°$; $r_s/r_{s,max} = 0.4$.

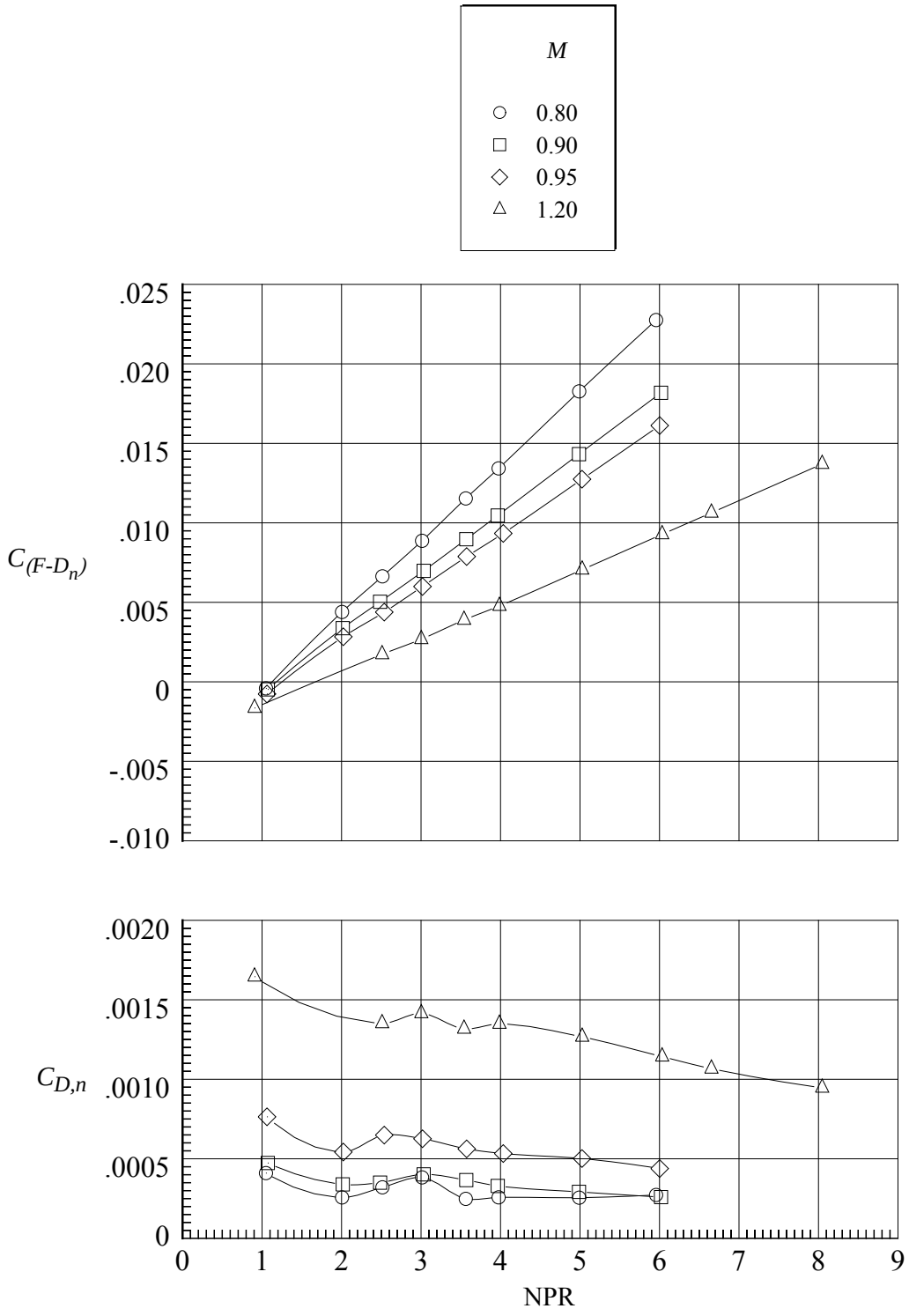

(b) Variation of $C_{(F\text{-}D_n)}$ and $C_{D,n}$.

Figure 79. Continued.

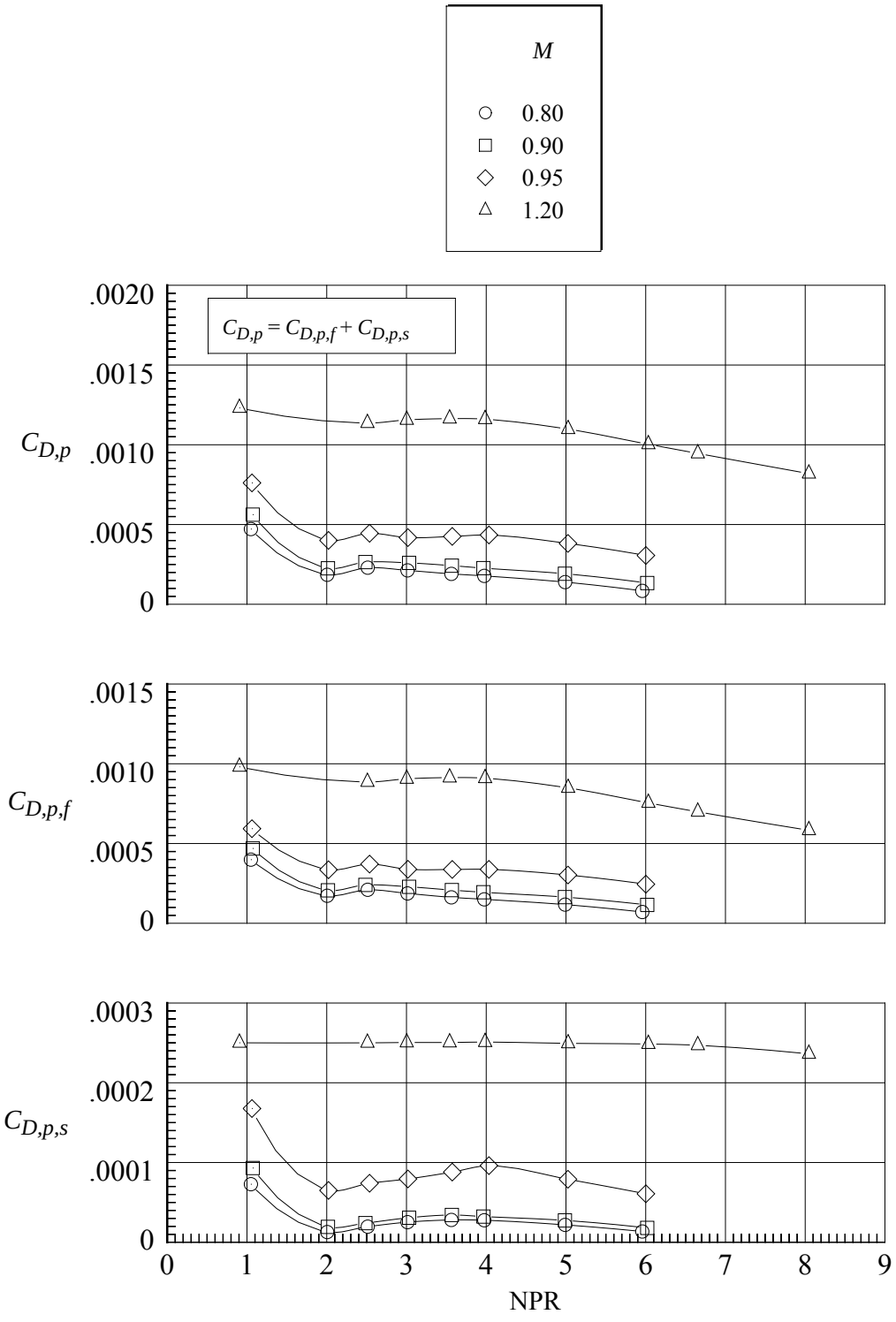

(c) Variation of $C_{D,p}$, $C_{D,p,f}$, and $C_{D,p,s}$.

Figure 79. Continued.

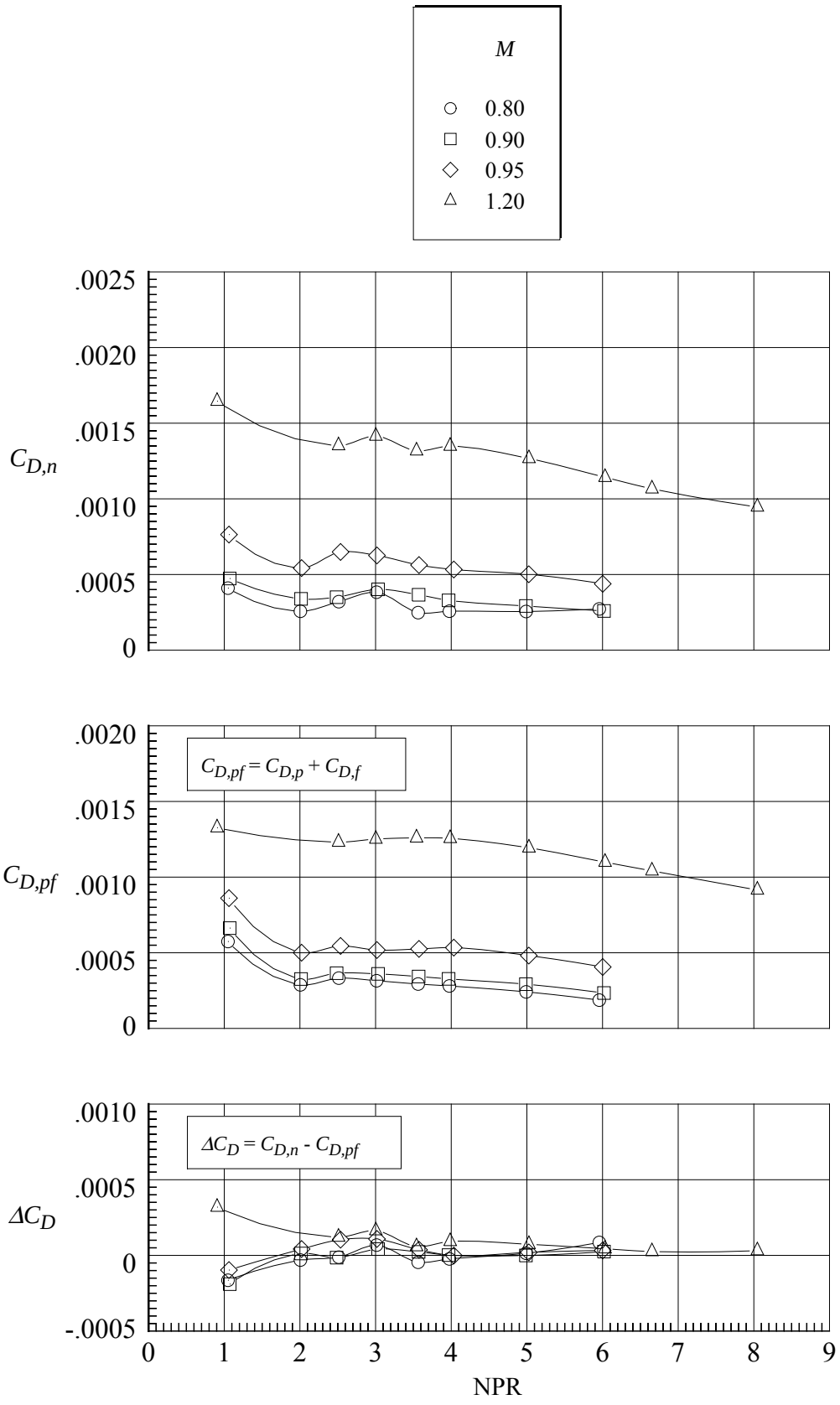

(d) Variation of $C_{D,n}$, $C_{D,pf}$, and ΔC_D.

Figure 79. Concluded.

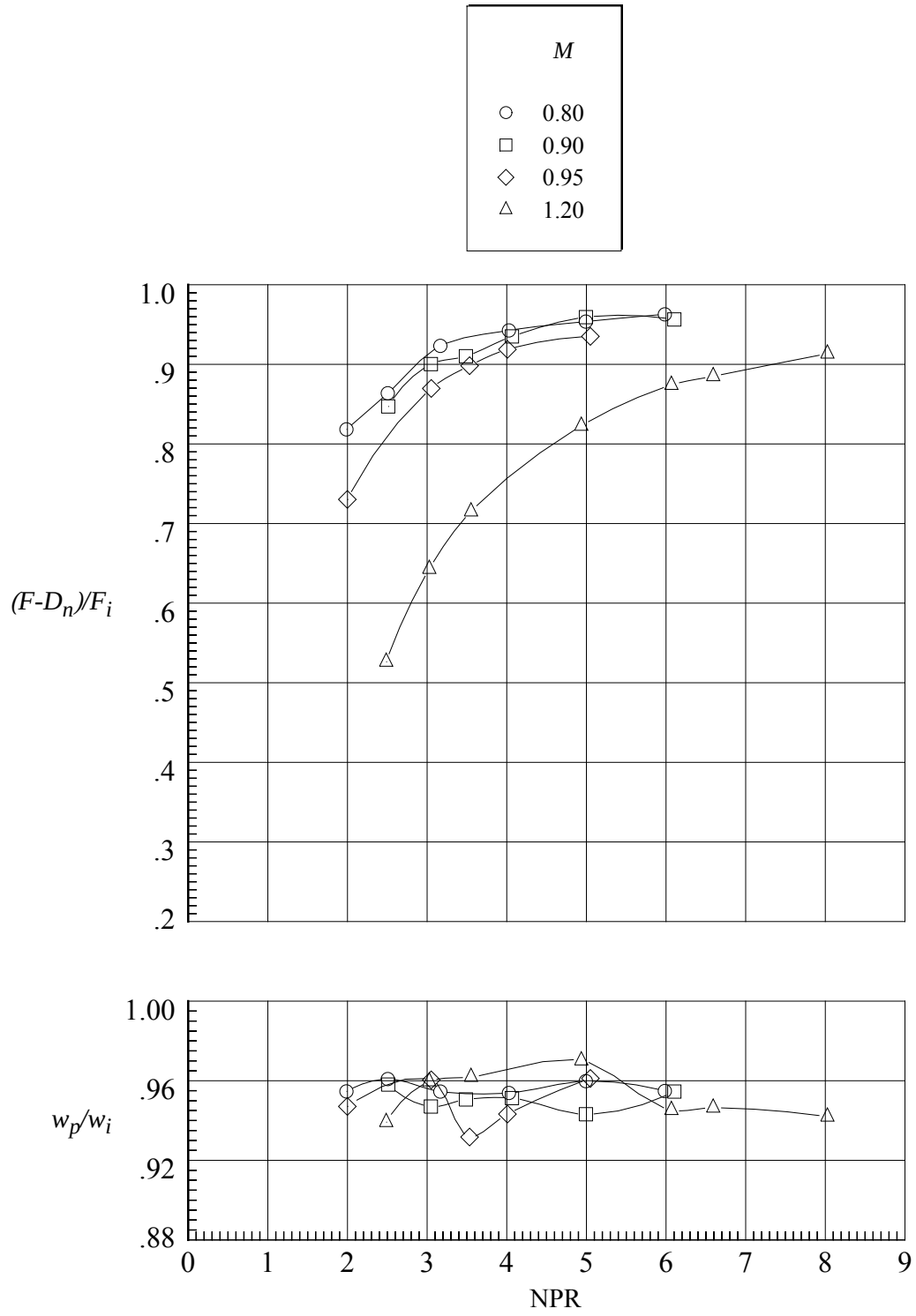

(a) Variation of $(F\text{-}D_n)/F_i$ and w_p/w_i.

Figure 80. Aeropropulsive performance for nozzle N10 with flap F1 and sidewall S7. $r_f/r_{f,max} = 0.4$; $\beta_f = 16.38°$; $L_f/h_m = 1.4$; $\beta_s = 8.0°$; $r_s/r_{s,max} = 1.0$.

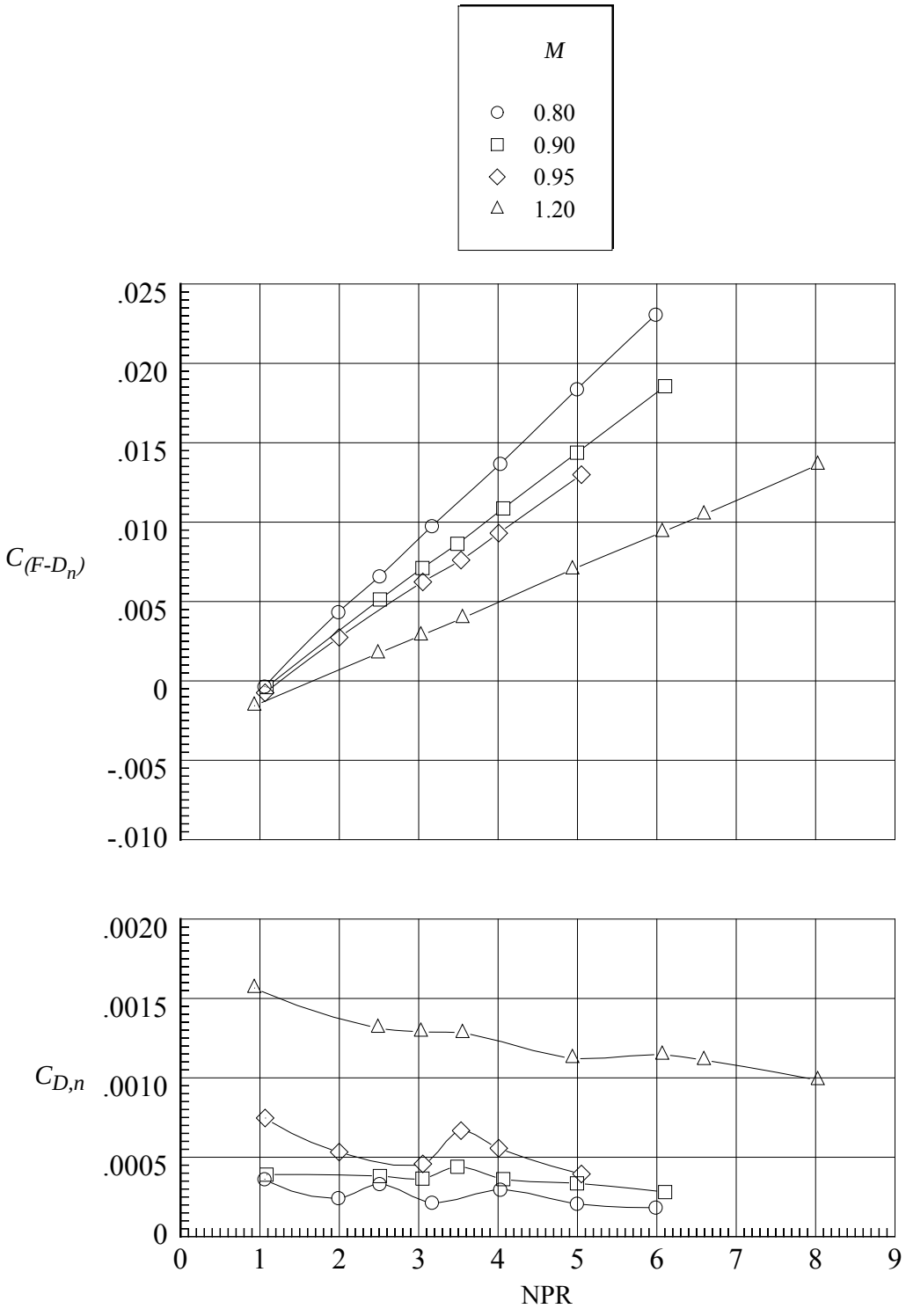

(b) Variation of $C_{(F\text{-}D_n)}$ and $C_{D,n}$.

Figure 80. Continued.

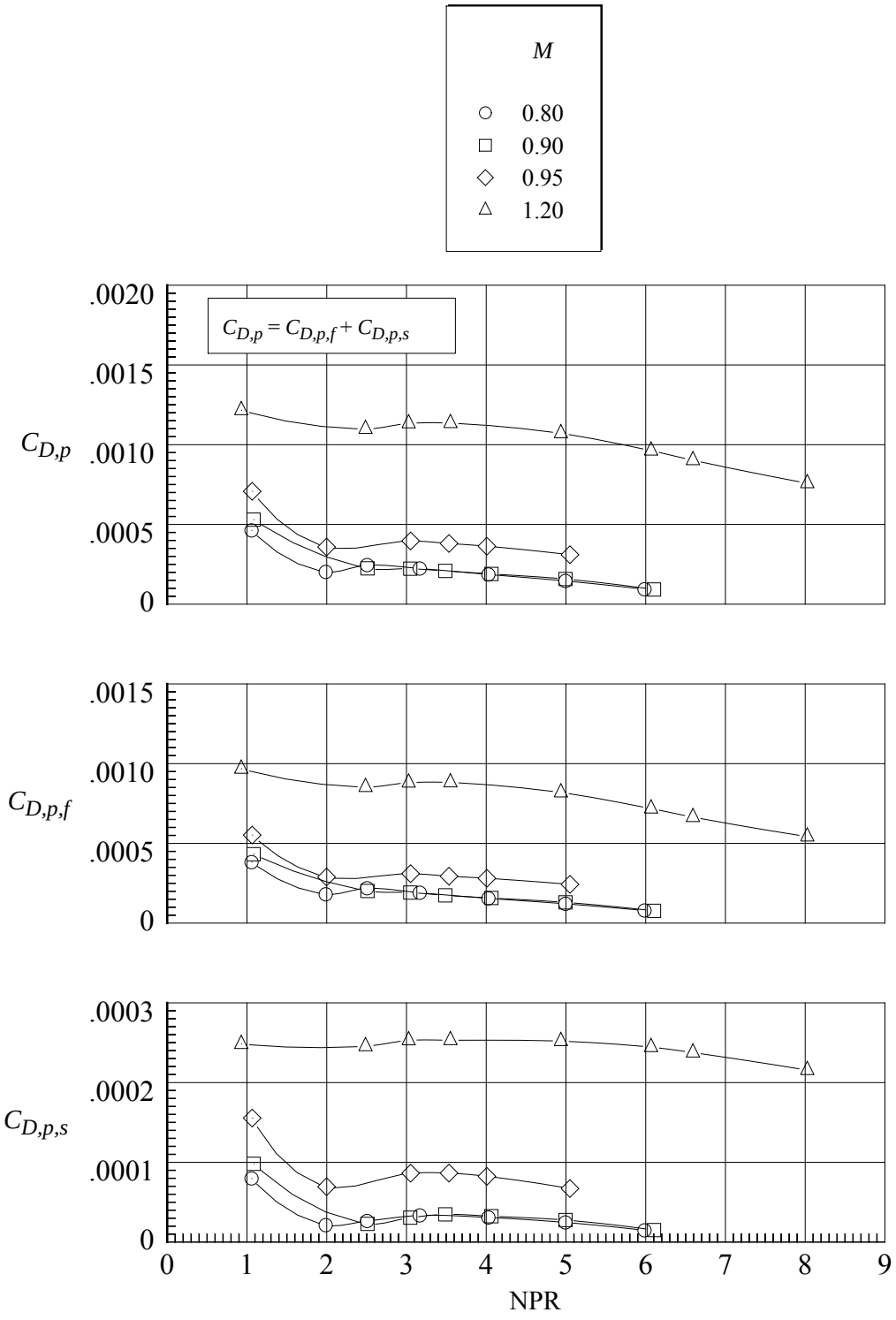

(c) Variation of $C_{D,p}$, $C_{D,p,f}$, and $C_{D,p,s}$.

Figure 80. Continued.

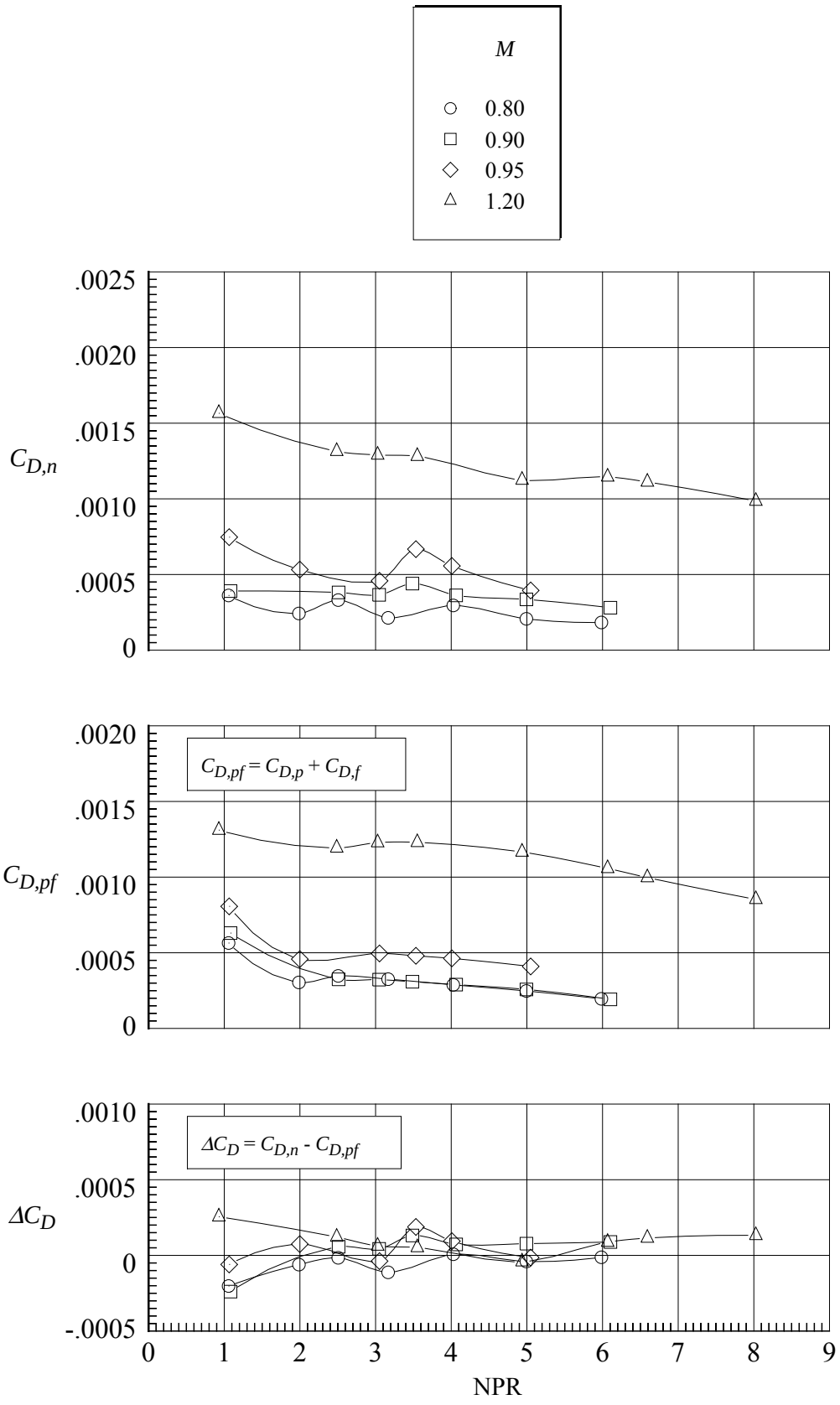

(d) Variation of $C_{D,n}$, $C_{D,pf}$, and ΔC_D.

Figure 80. Concluded.

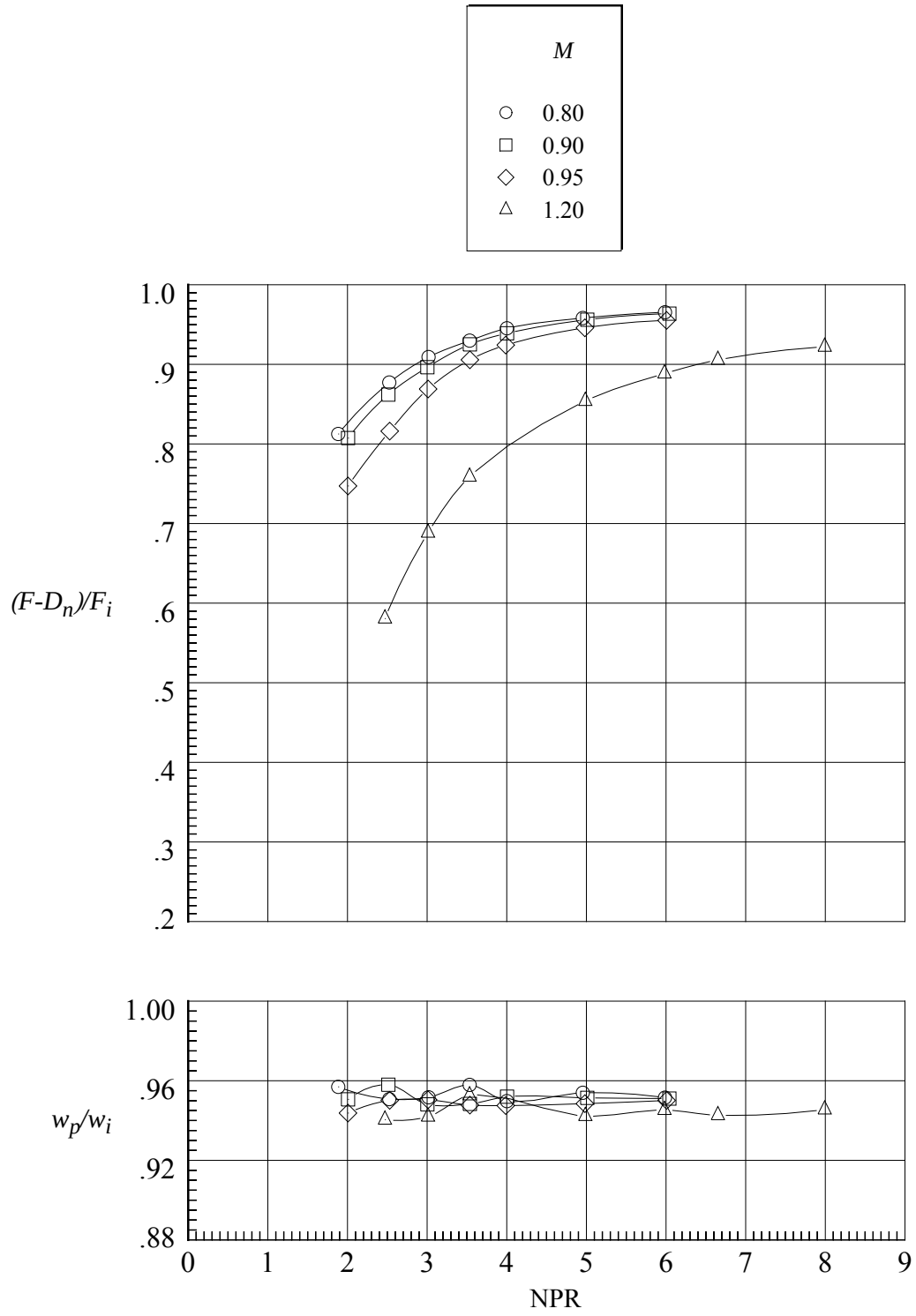

(a) Variation of $(F\text{-}D_n)/F_i$ and w_p/w_i.

Figure 81. Aeropropulsive performance for nozzle N11 with flap F1 and sidewall S8.
$r_f/r_{f,max} = 0.4$; $\beta_f = 16.38°$; $L_f/h_m = 1.4$; $\beta_s = 4°$; $r_s/r_{s,max} = 0$.

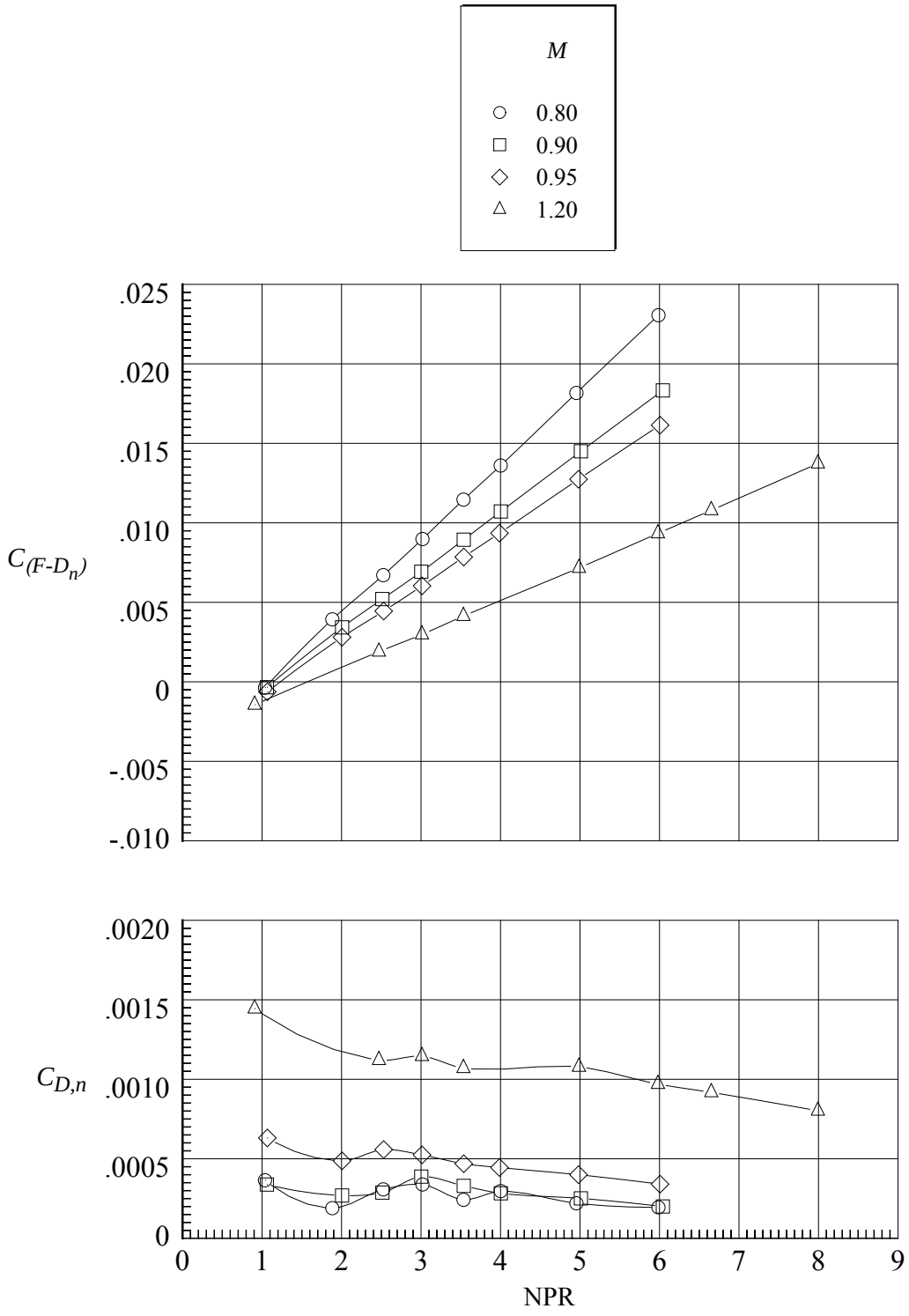

(b) Variation of $C_{(F\text{-}D_n)}$ and $C_{D,n}$.

Figure 81. Continued.

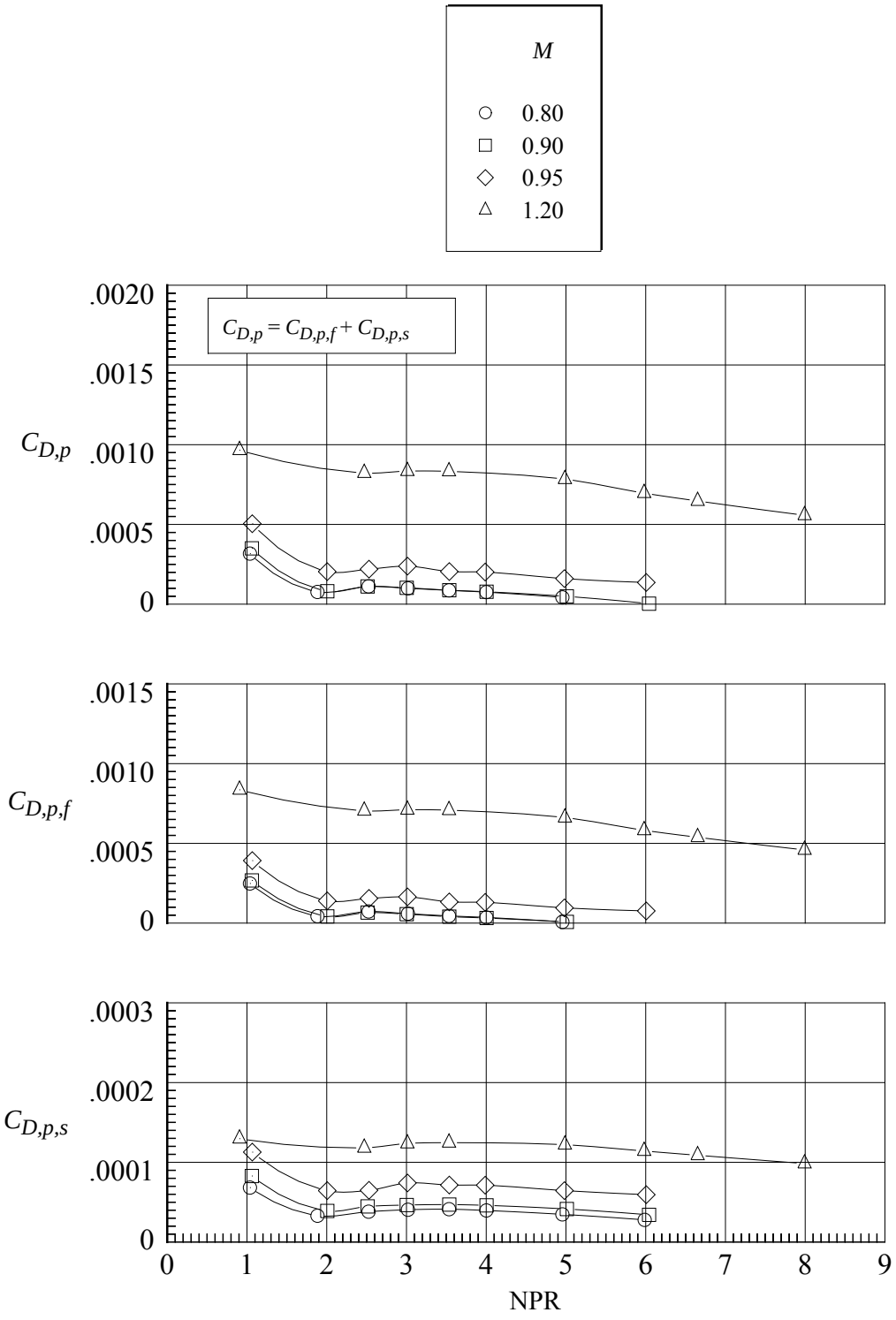

(c) Variation of $C_{D,p}$, $C_{D,p,f}$, and $C_{D,p,s}$.

Figure 81. Continued.

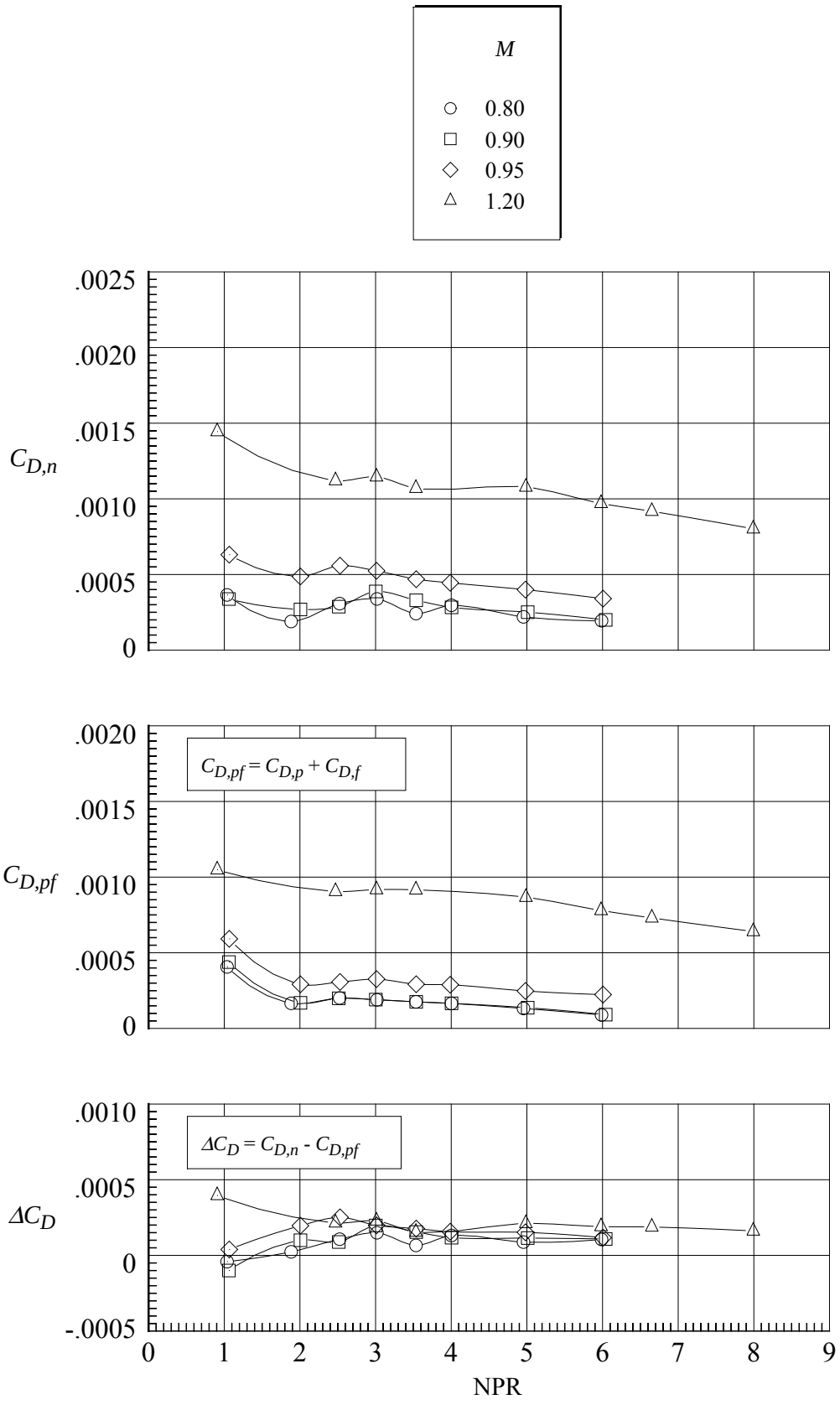

(d) Variation of $C_{D,n}$, $C_{D,pf}$, and ΔC_D.

Figure 81. Concluded.

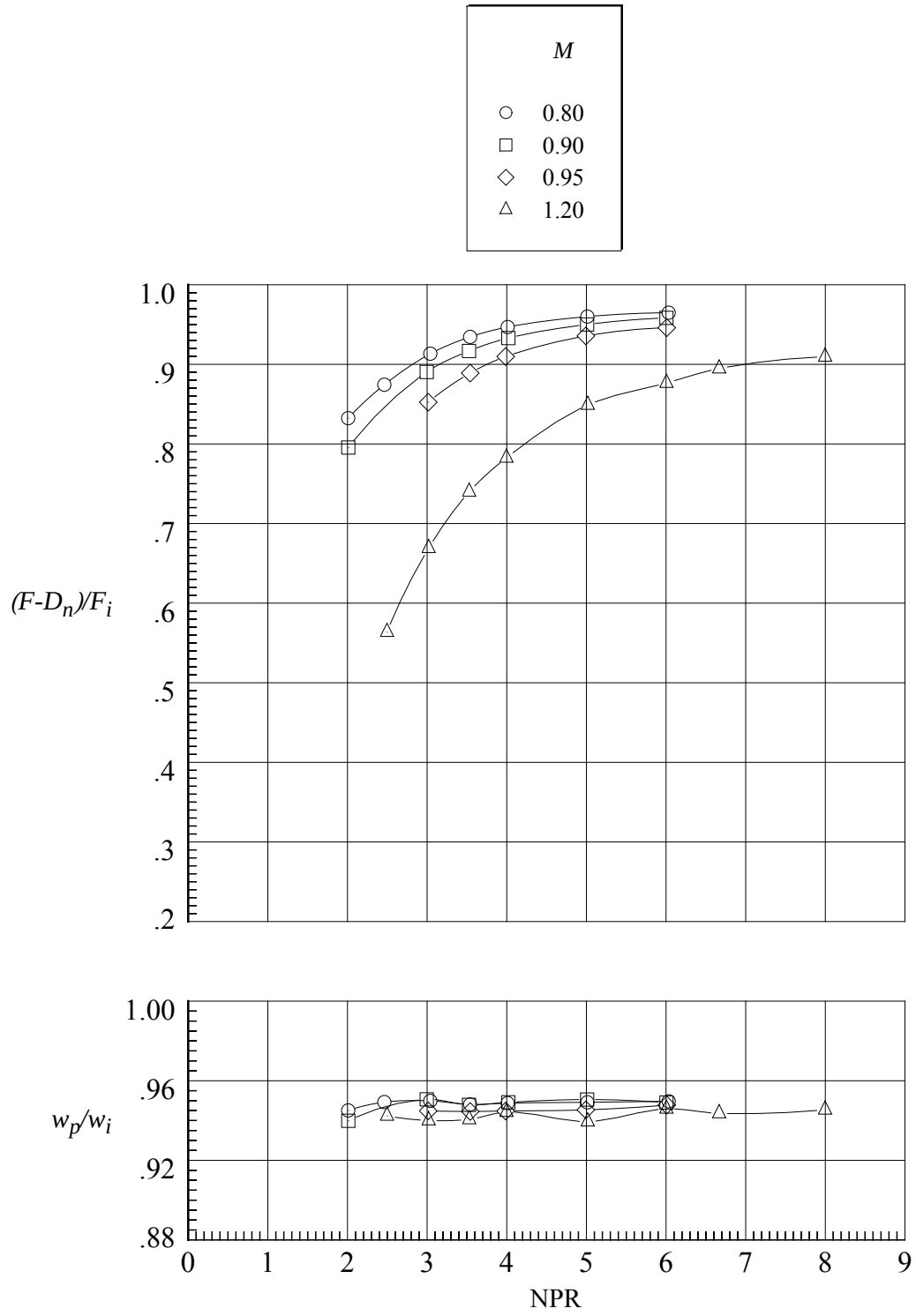

(a) Variation of $(F\text{-}D_n)/F_i$ and w_p/w_i.

Figure 82. Aeropropulsive performance for nozzle N12 with flap F2 and sidewall S8.
$r_f/r_{f,max} = 0.1$; $\beta_f = 12.88°$; $L_f/h_m = 1.4$; $\beta_s = 4°$; $r_s/r_{s,max} = 0$.

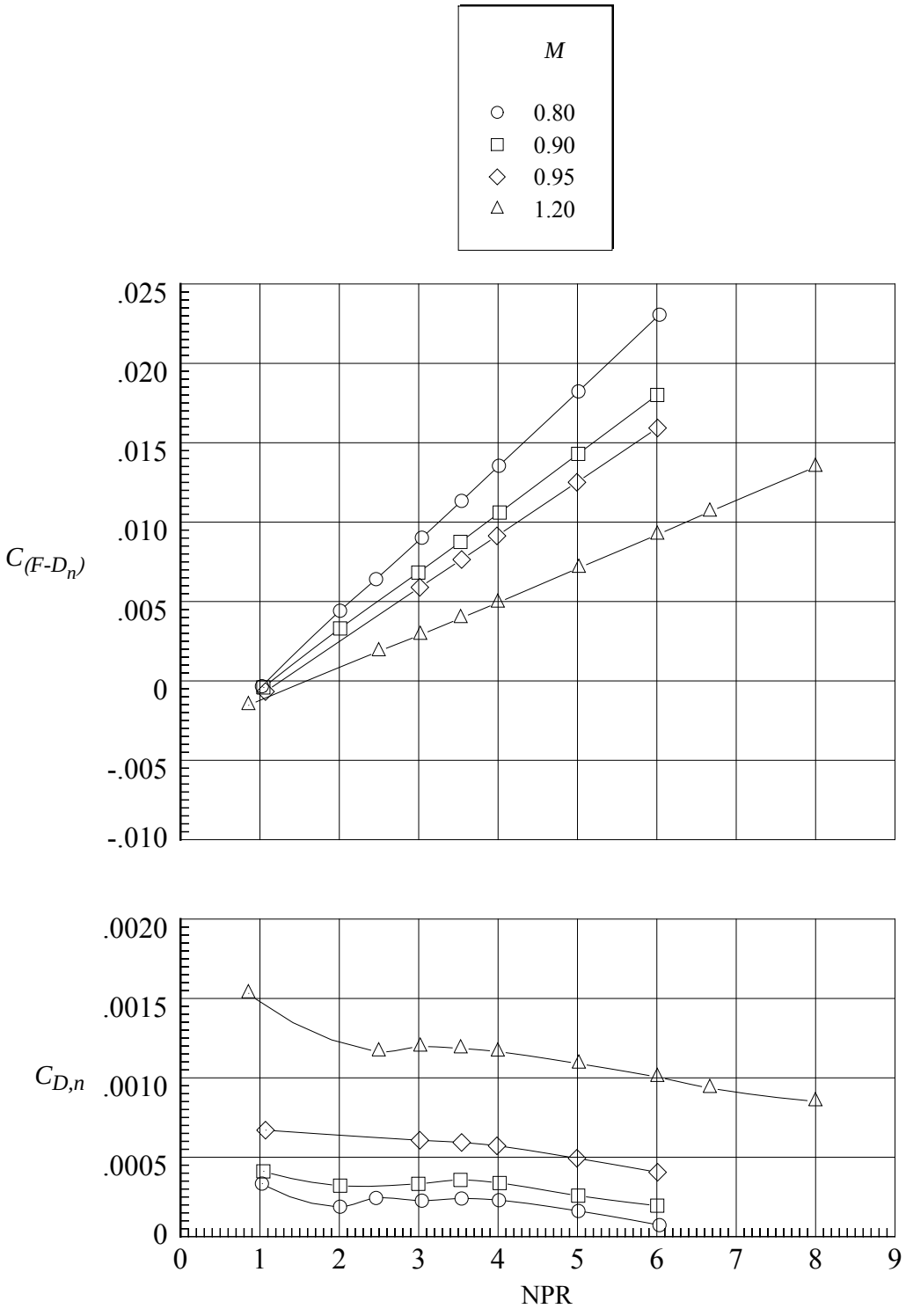

(b) Variation of $C_{(F\text{-}D_n)}$ and $C_{D,n}$.

Figure 82. Continued.

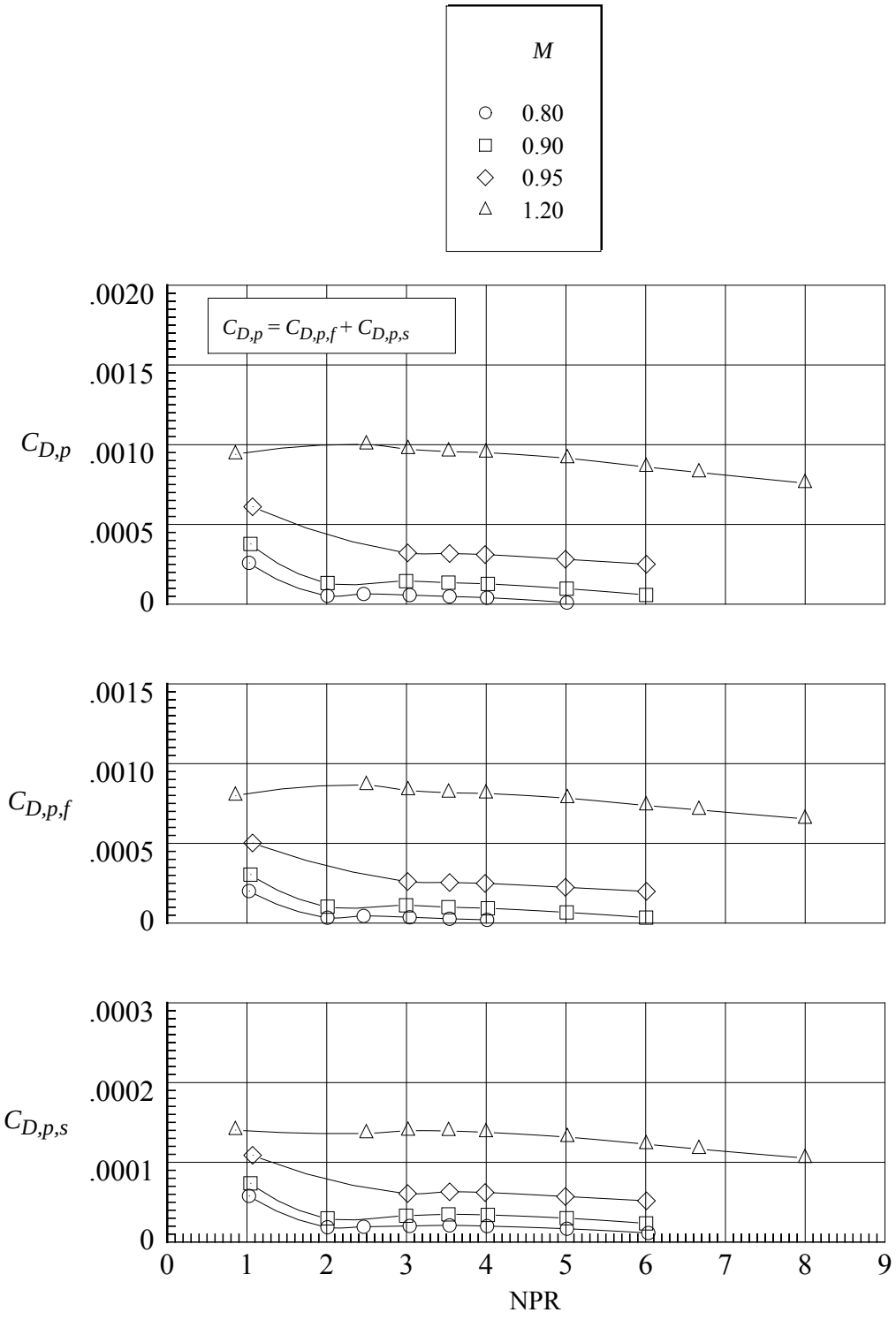

(c) Variation of $C_{D,p}$, $C_{D,p,f}$, and $C_{D,p,s}$.

Figure 82. Continued.

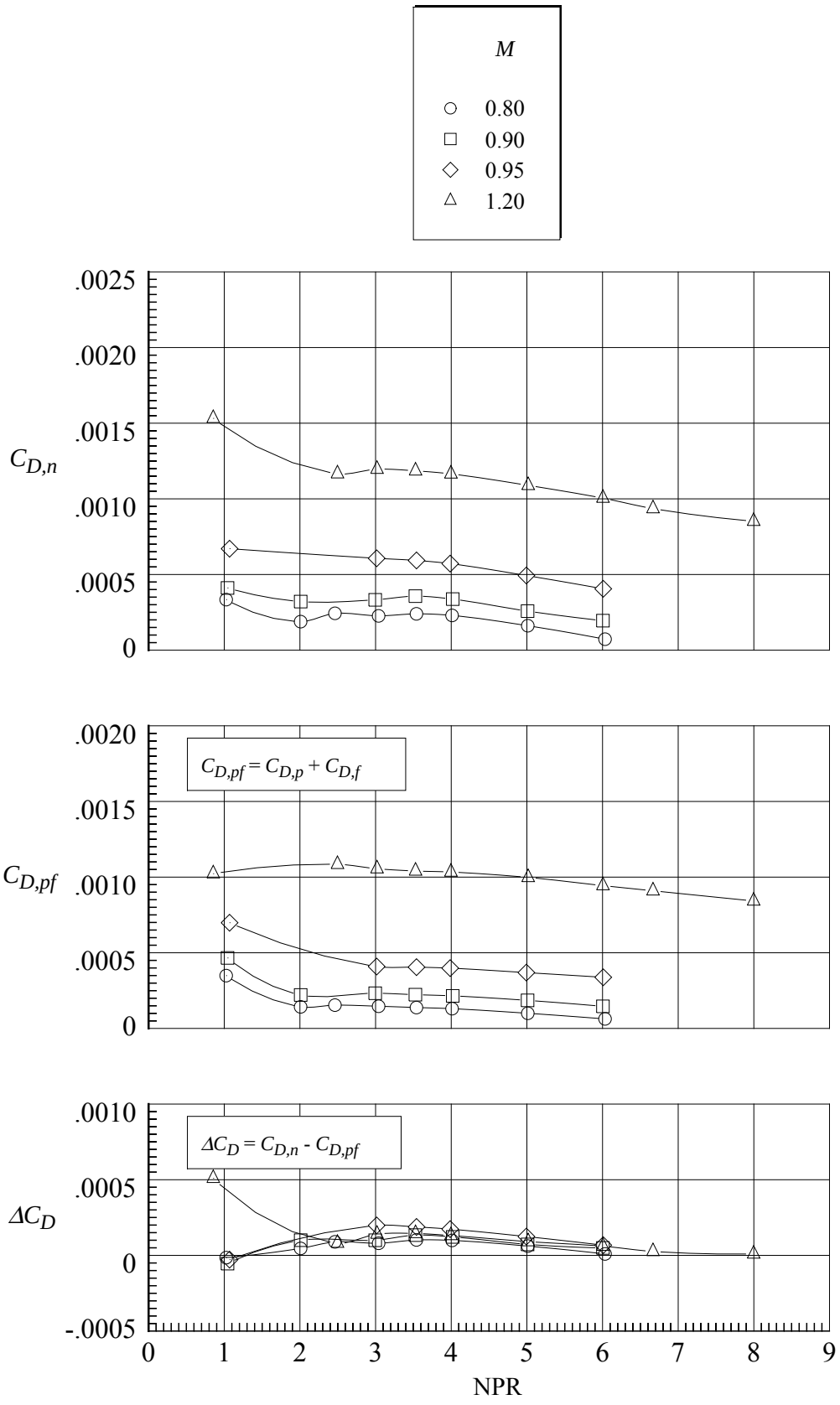

(d) Variation of $C_{D,n}$, $C_{D,pf}$, and ΔC_D.

Figure 82. Concluded.

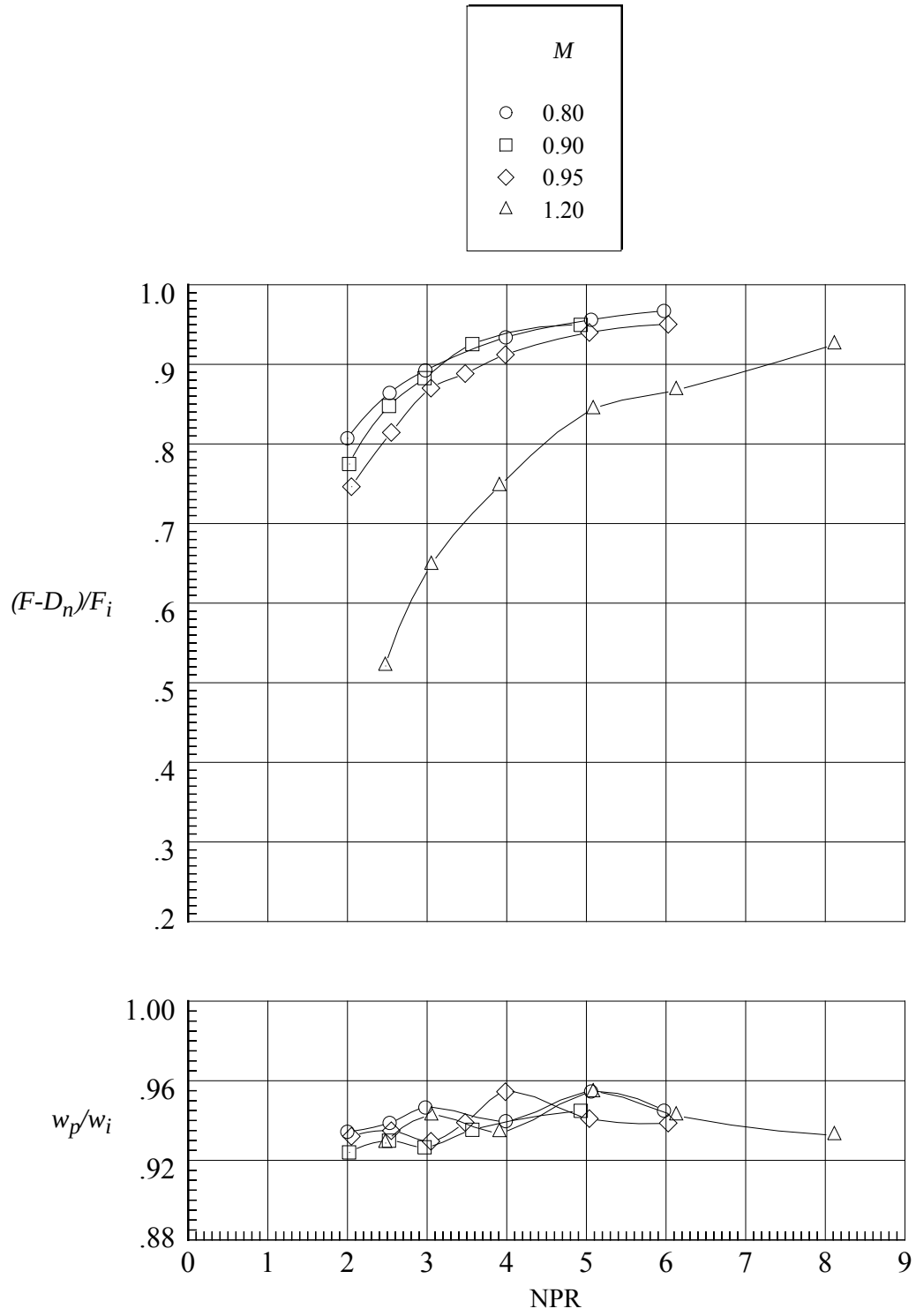

(a) Variation of $(F\text{-}D_n)/F_i$ and w_p/w_i.

Figure 83. Aeropropulsive performance for nozzle N13 with flap F5 and sidewall S1.
$r_f/r_{f,max} = 0.4$; $\beta_f = 20.30°$; $L_f/h_m = 1.1$; $\beta_s = 4.0°$; $r_s/r_{s,max} = 0$.

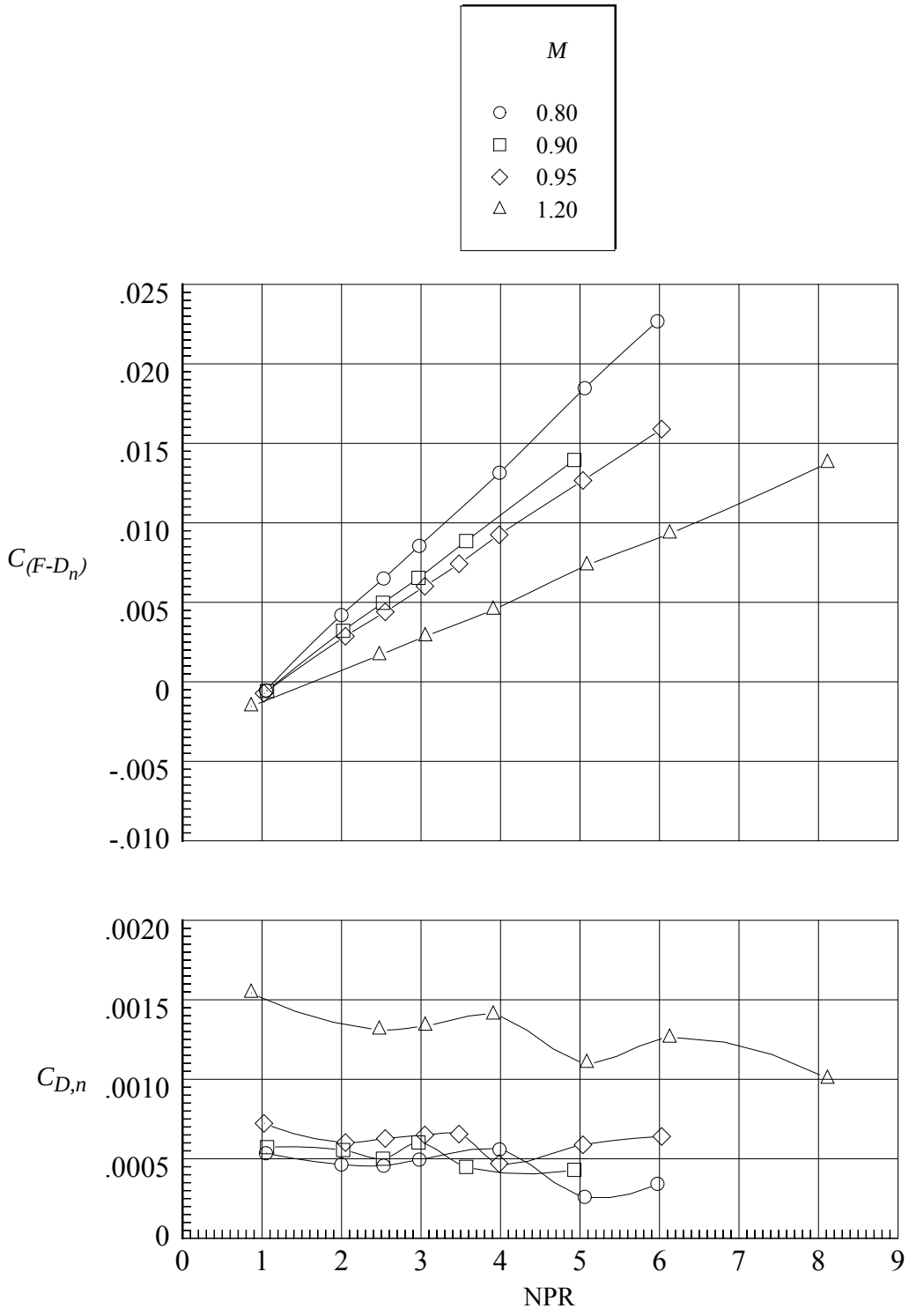

(b) Variation of $C_{(F\text{-}D_n)}$ and $C_{D,n}$.

Figure 83. Continued.

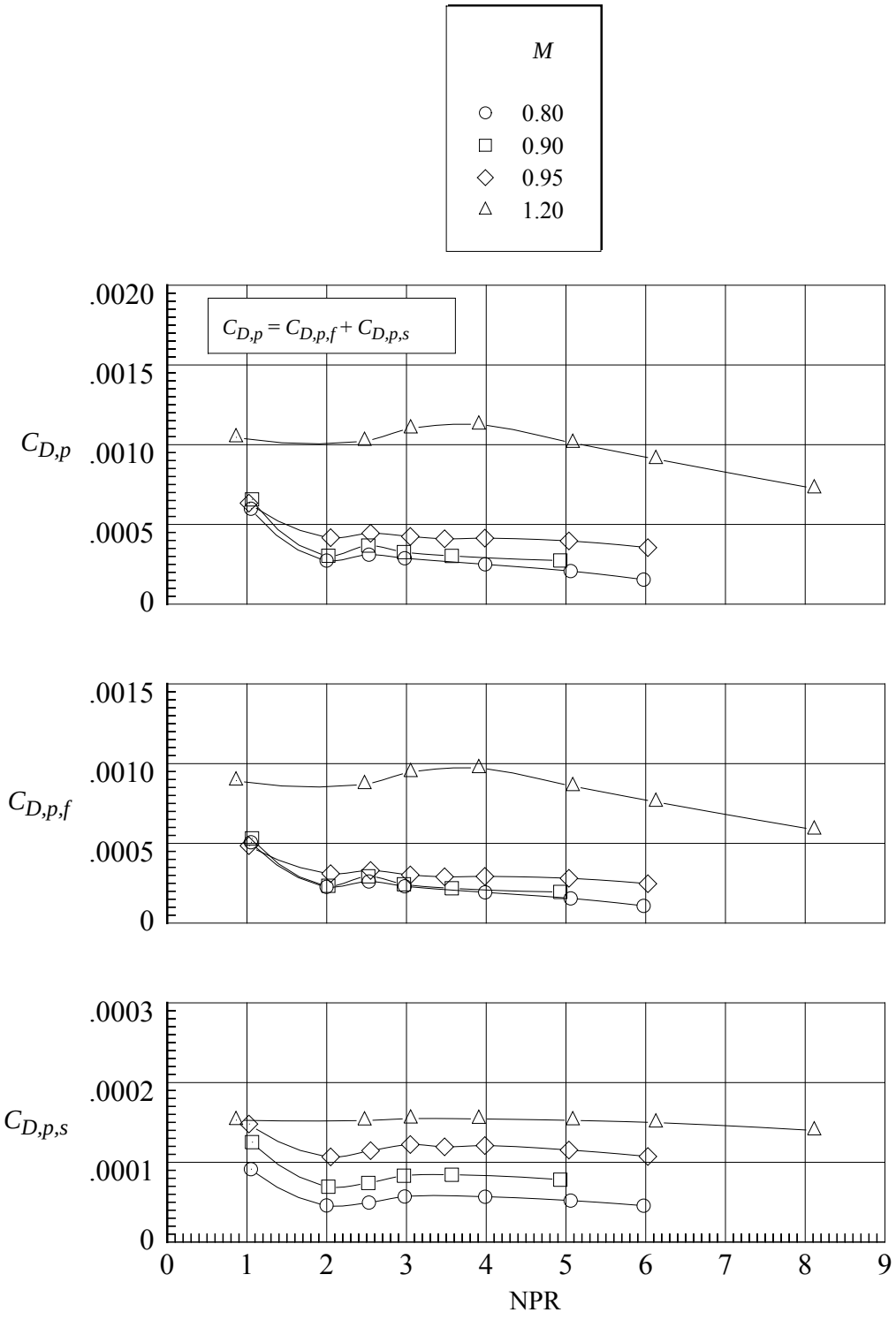

(c) Variation of $C_{D,p}$, $C_{D,p,f}$, and $C_{D,p,s}$.

Figure 83. Continued.

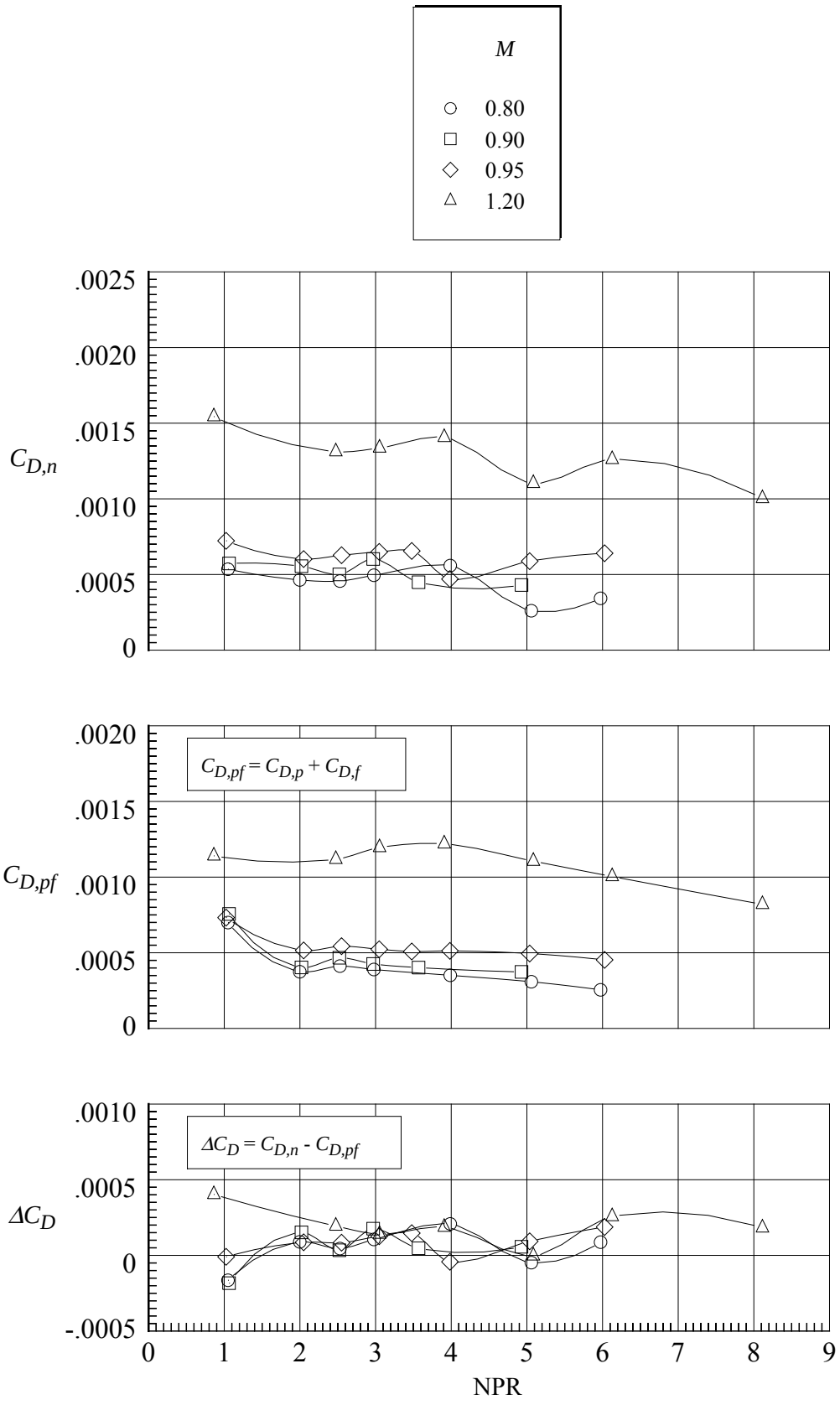

(d) Variation of $C_{D,n}$, $C_{D,pf}$, and ΔC_D.

Figure 83. Concluded.

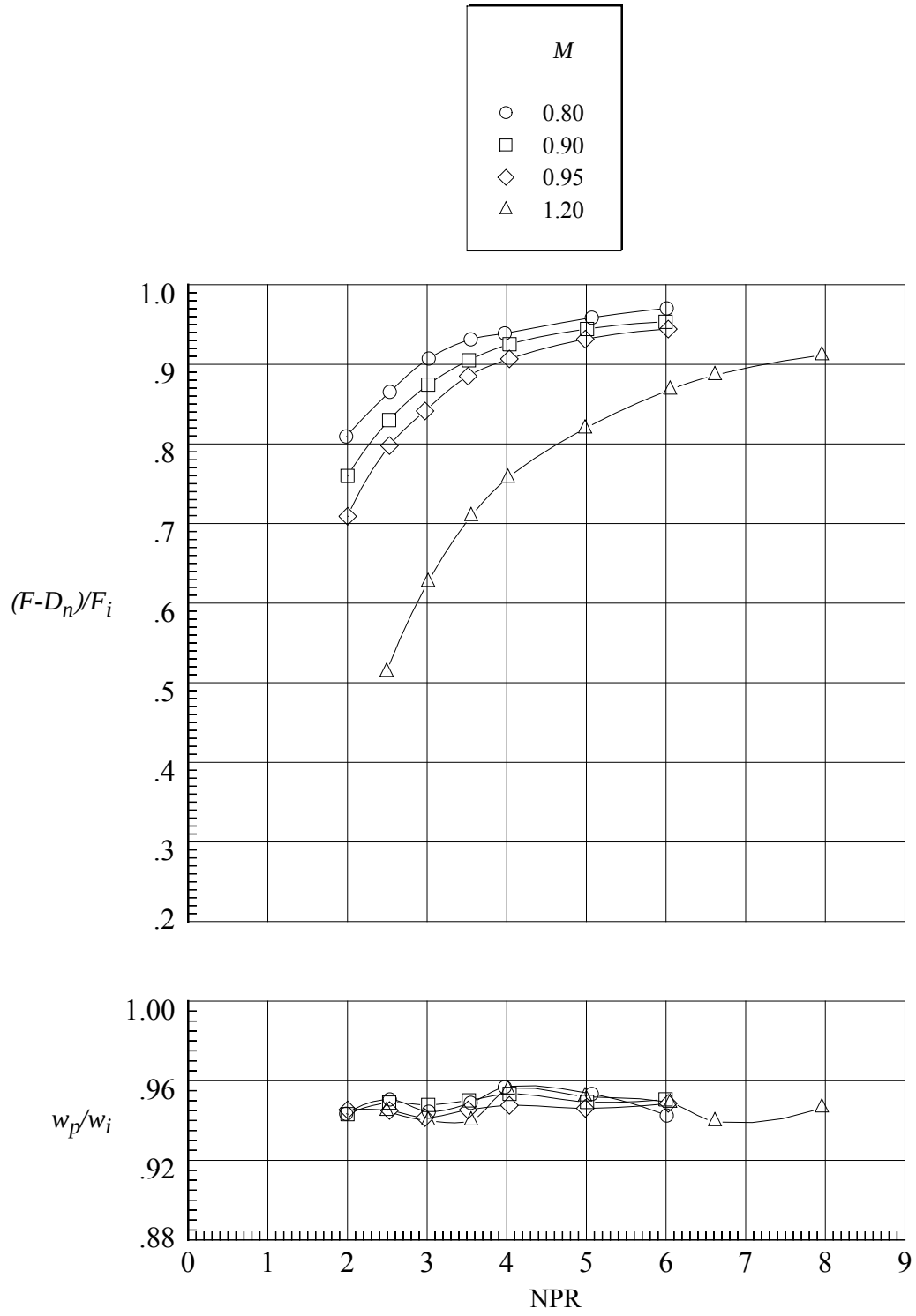

(a) Variation of $(F\text{-}D_n)/F_i$ and w_p/w_i.

Figure 84. Aeropropulsive performance for nozzle N14 with flap F6 and sidewall S1.
$r_f/r_{f,max} = 0.1$; $\beta_f = 15.97°$; $L_f/h_m = 1.1$; $\beta_s = 4.0°$; $r_s/r_{s,max} = 0$.

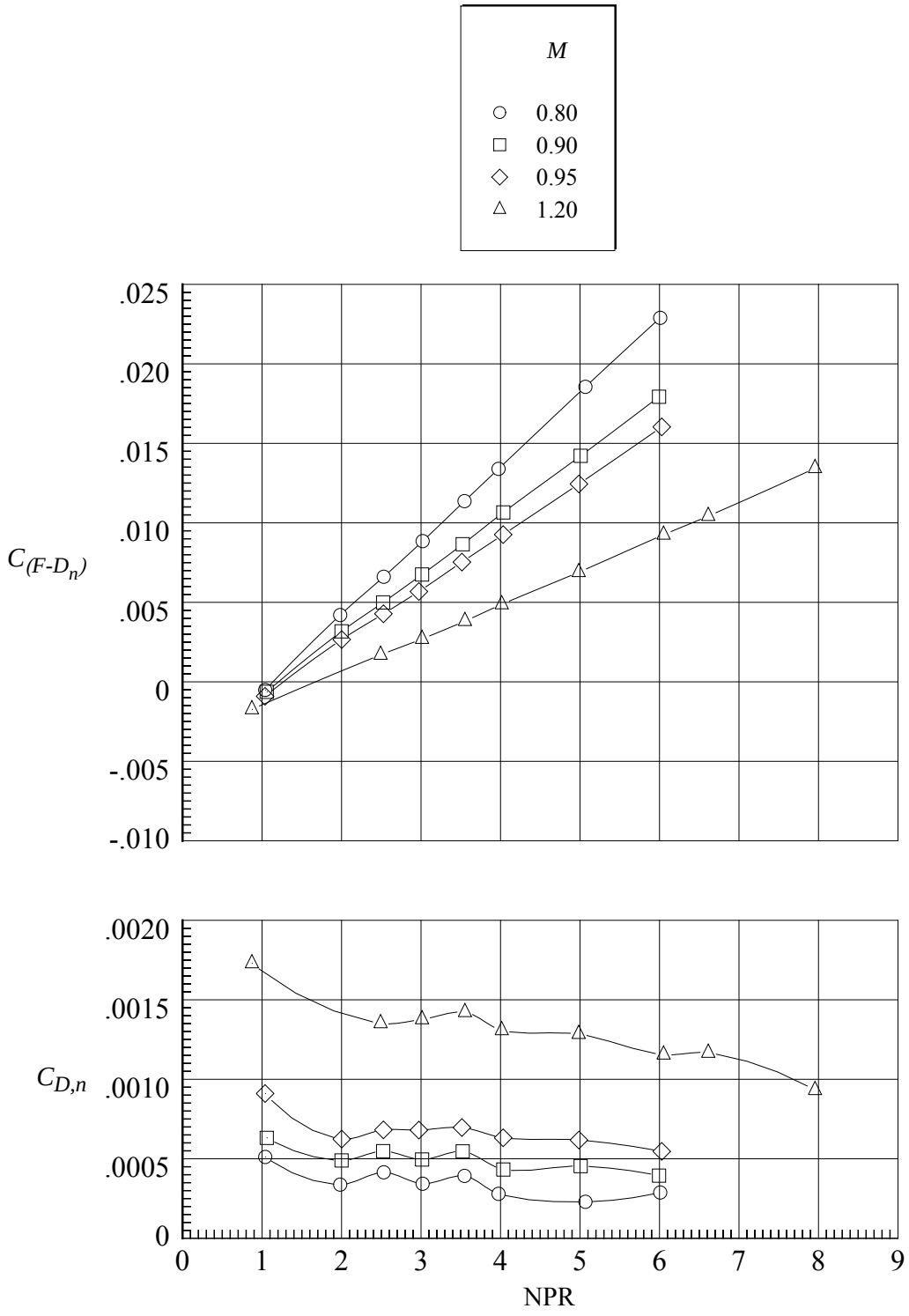

(b) Variation of $C_{(F\text{-}D_n)}$ and $C_{D,n}$.

Figure 84. Continued.

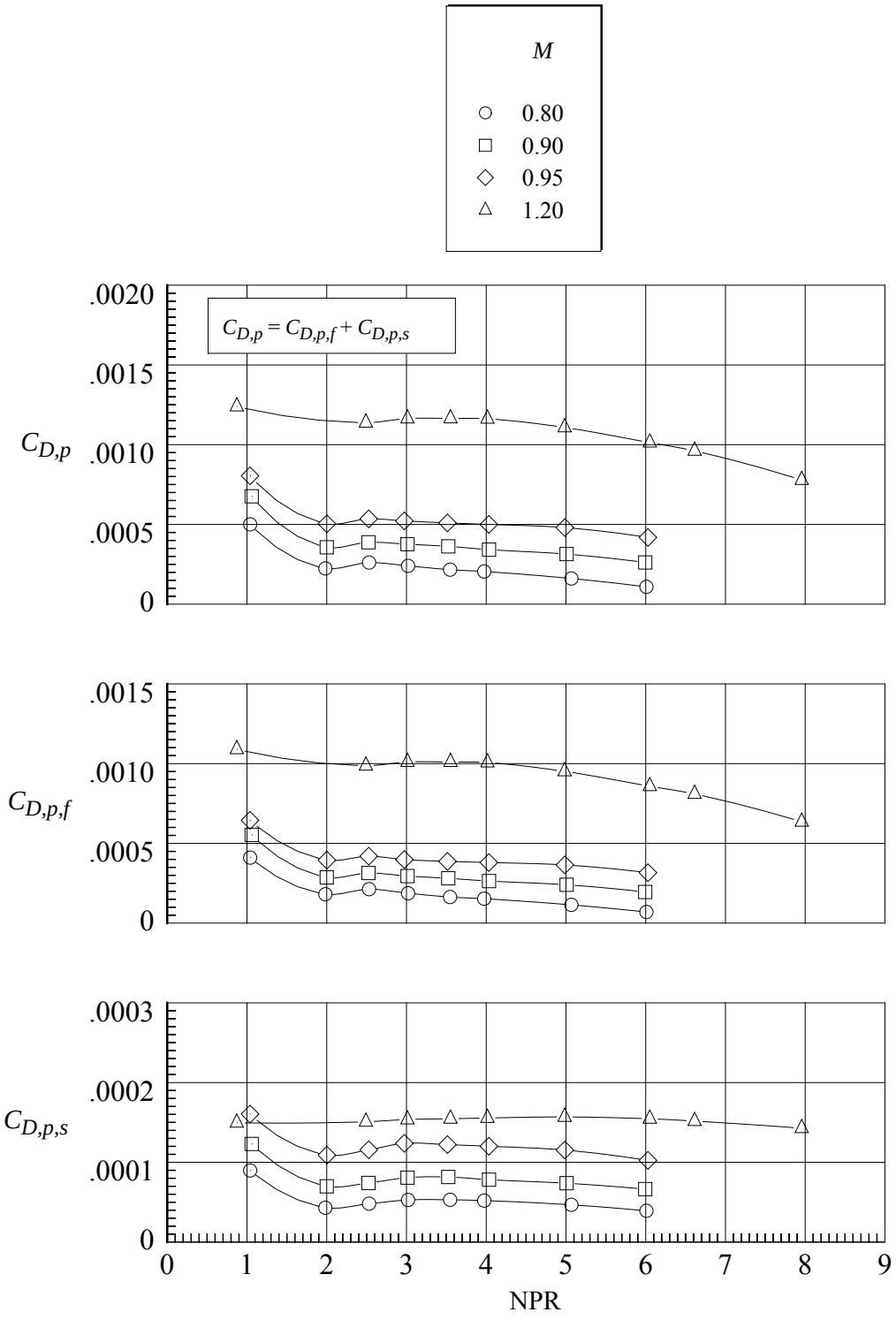

(c) Variation of $C_{D,p}$, $C_{D,p,f}$, and $C_{D,p,s}$.

Figure 84. Continued.

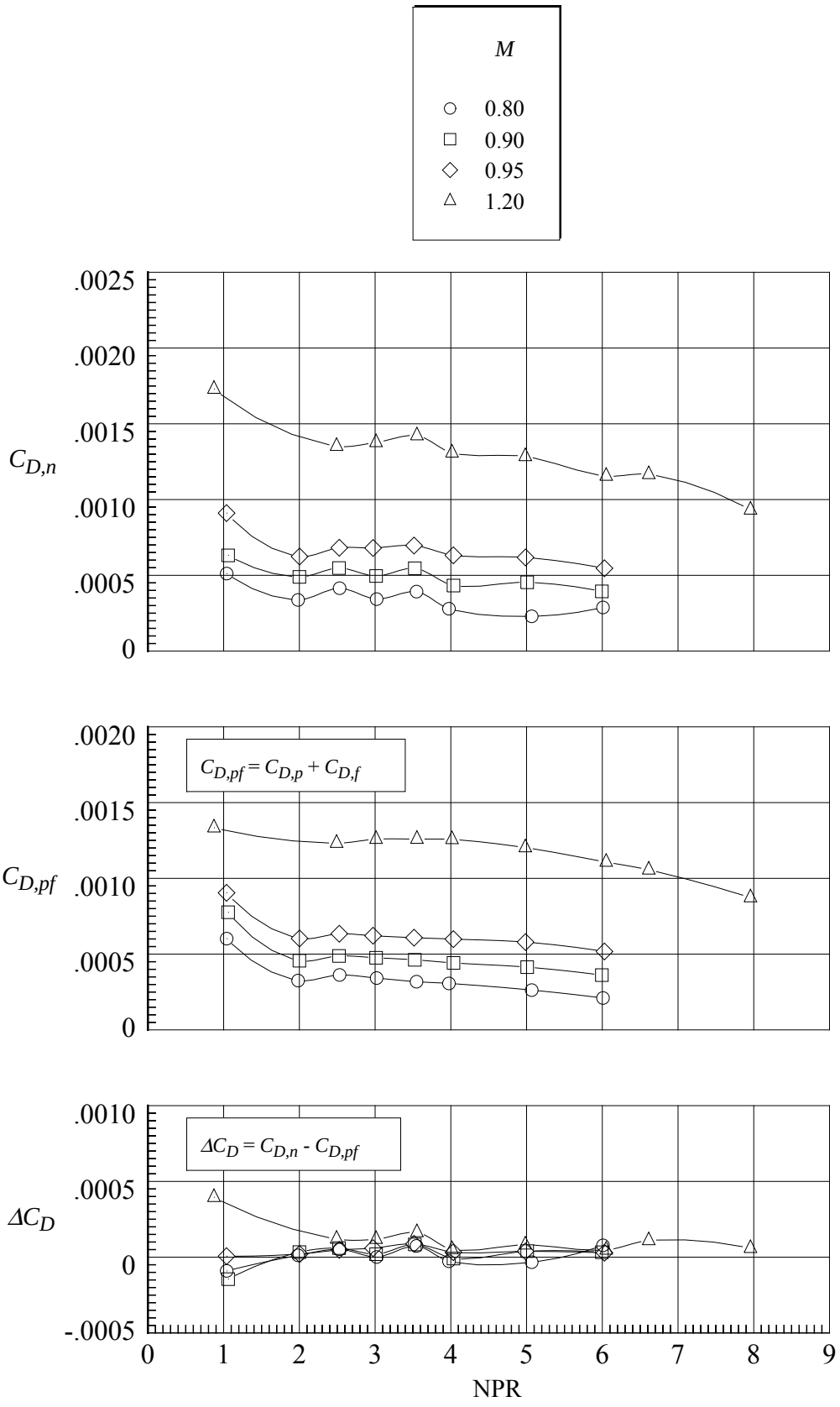

(d) Variation of $C_{D,n}$, $C_{D,pf}$, and ΔC_D.

Figure 84. Concluded.

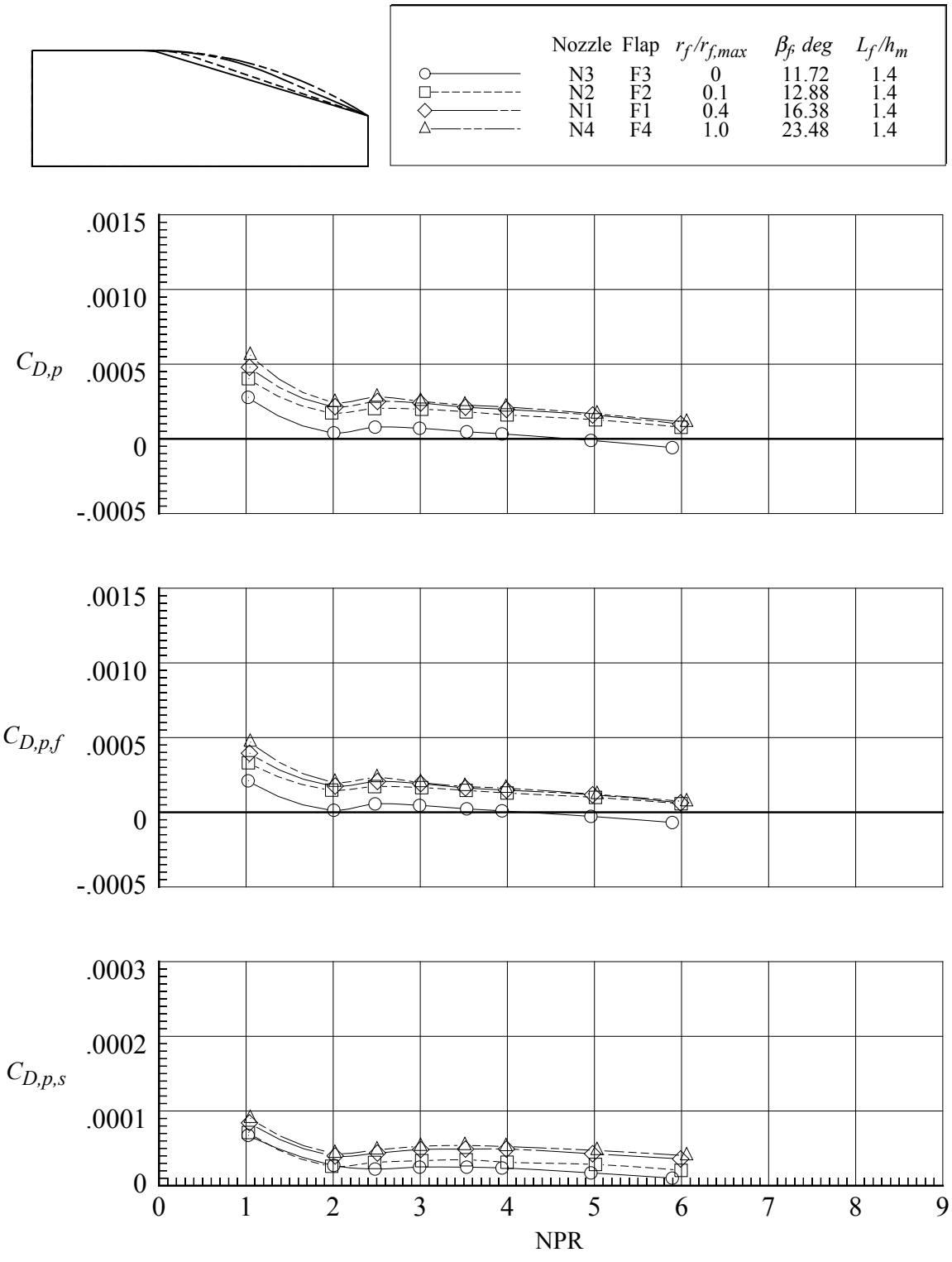

(a) $M = 0.80$.

Figure 85. Effect of flap radius of curvature on pressure drag coefficients for nozzles with sidewall S1. $\beta_s = 4.0°$; $r_s / r_{s,max} = 0$.

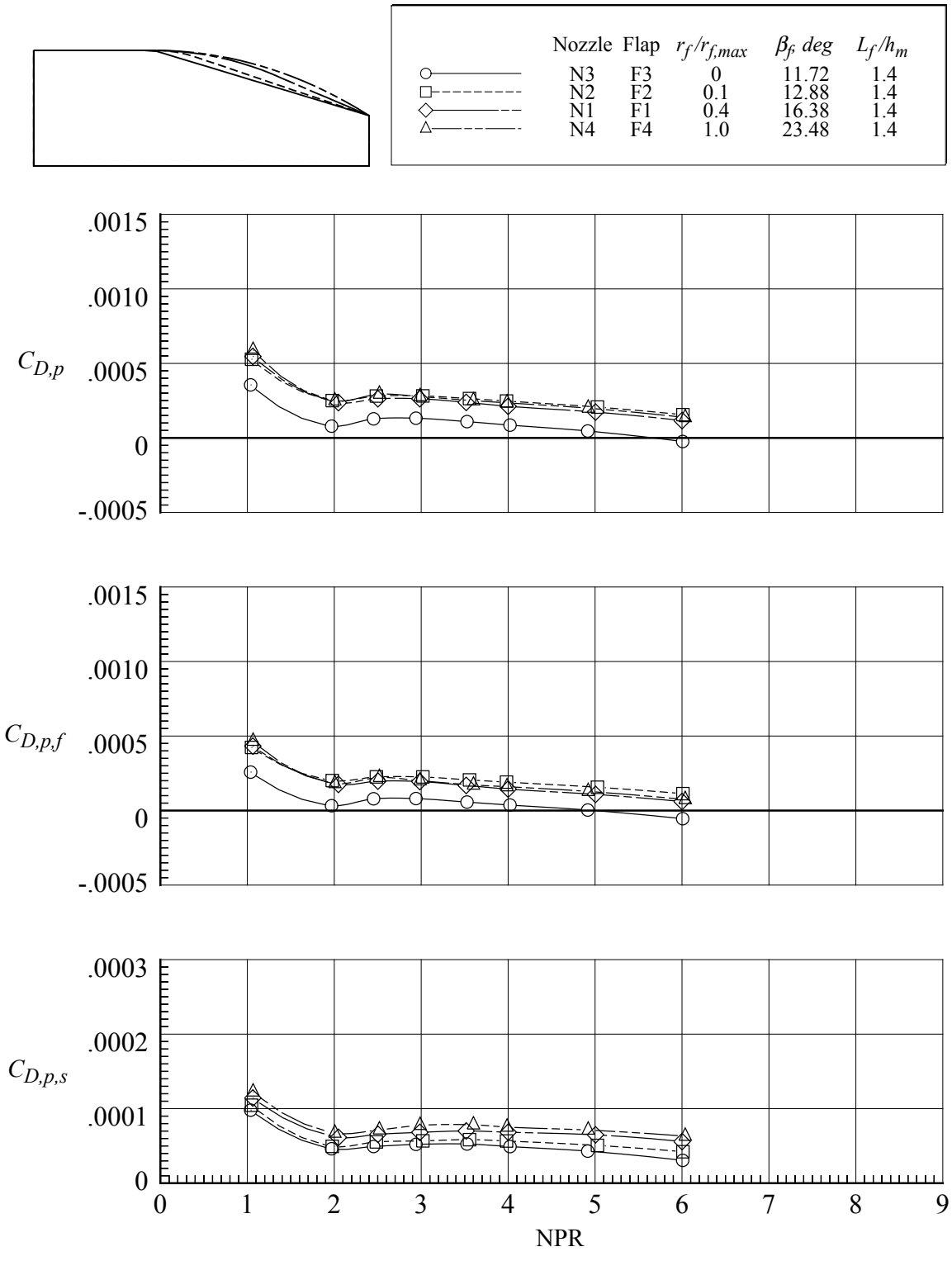

(b) $M = 0.90$.

Figure 85. Continued.

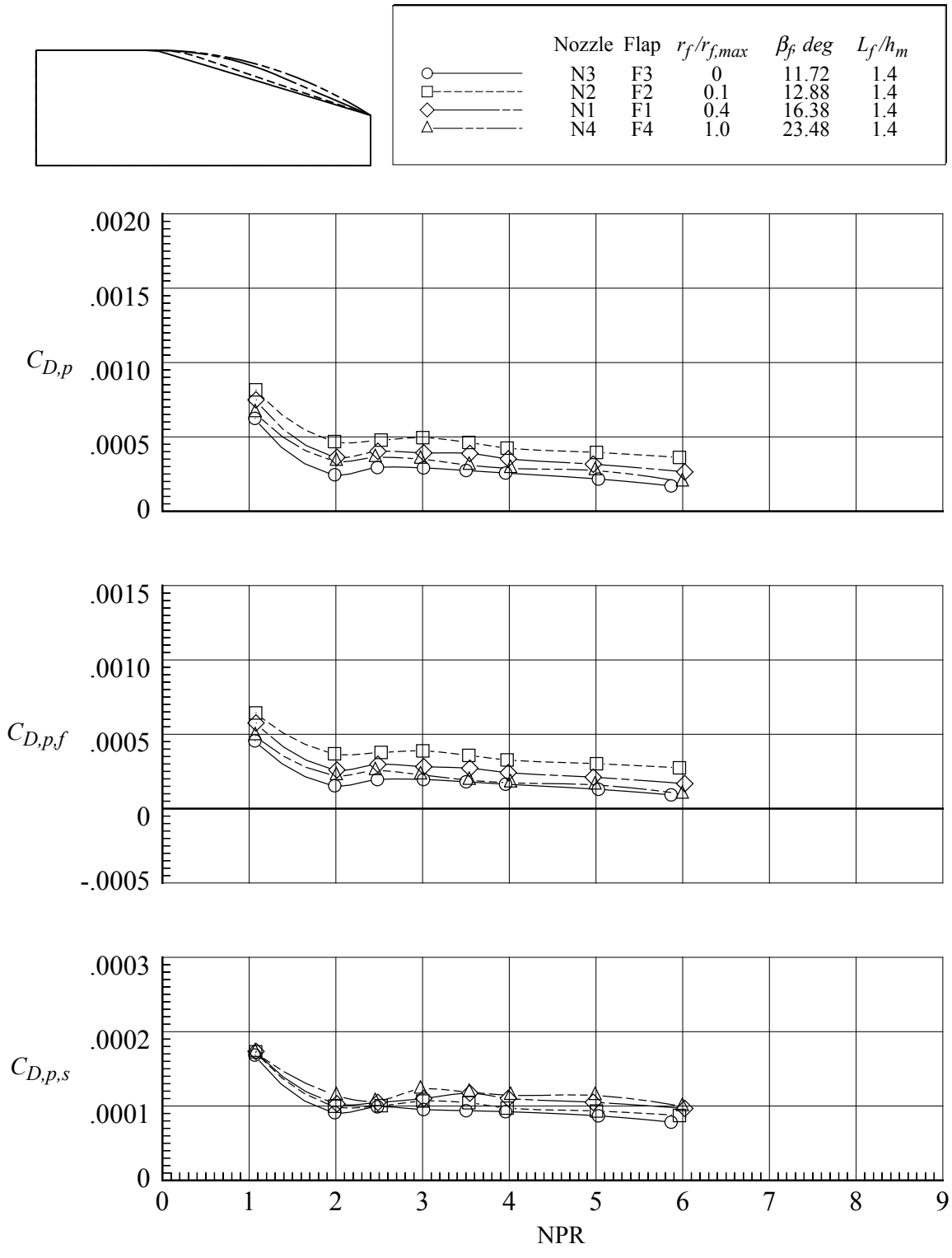

(c) $M = 0.95$.

Figure 85. Continued.

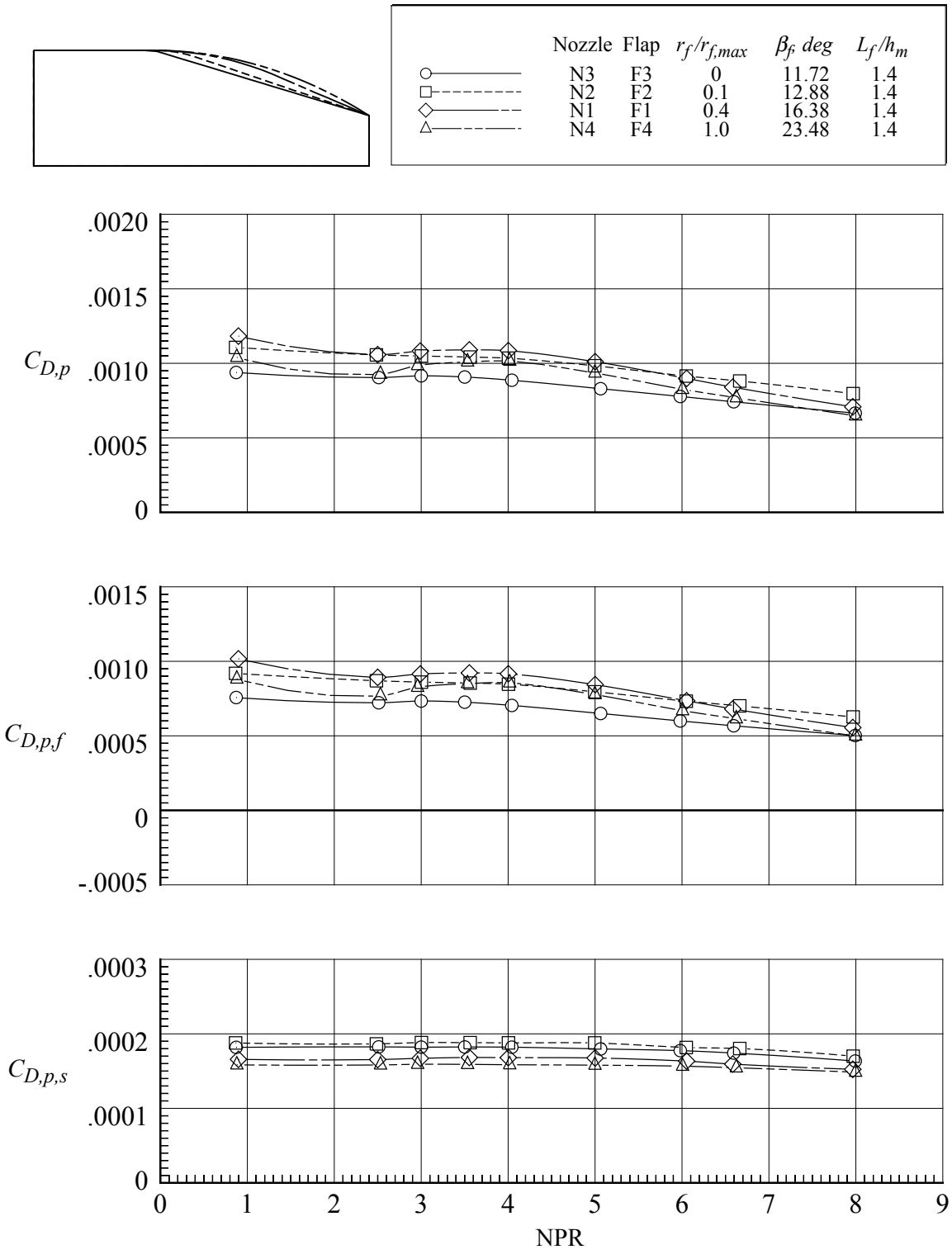

(d) $M = 1.20$.

Figure 85. Concluded.

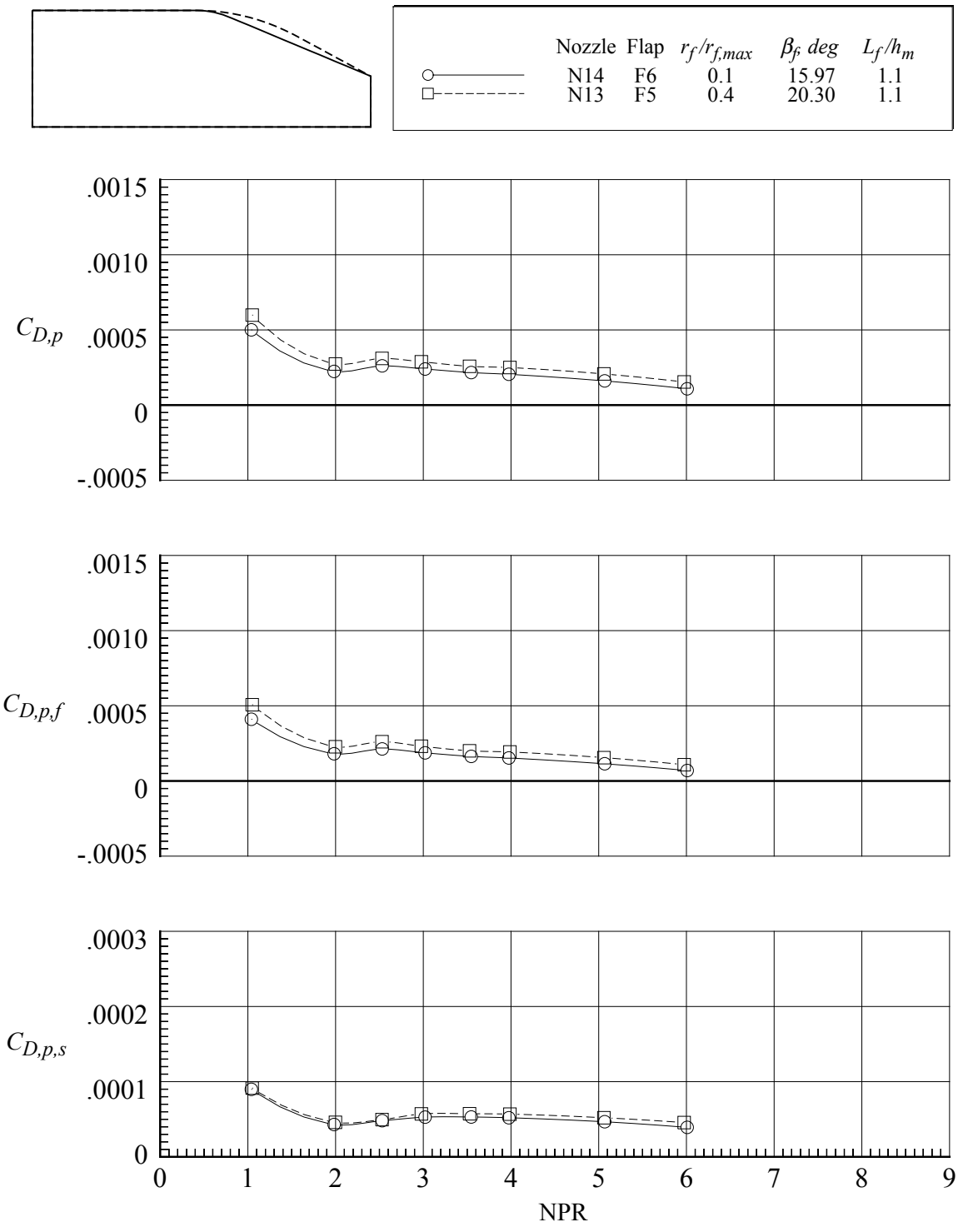

(a) $M = 0.80$.

Figure 86. Effect of flap radius of curvature on pressure drag coefficients for nozzles with sidewall S1. $\beta_s = 4.0°$; $r_s / r_{s,max} = 0$.

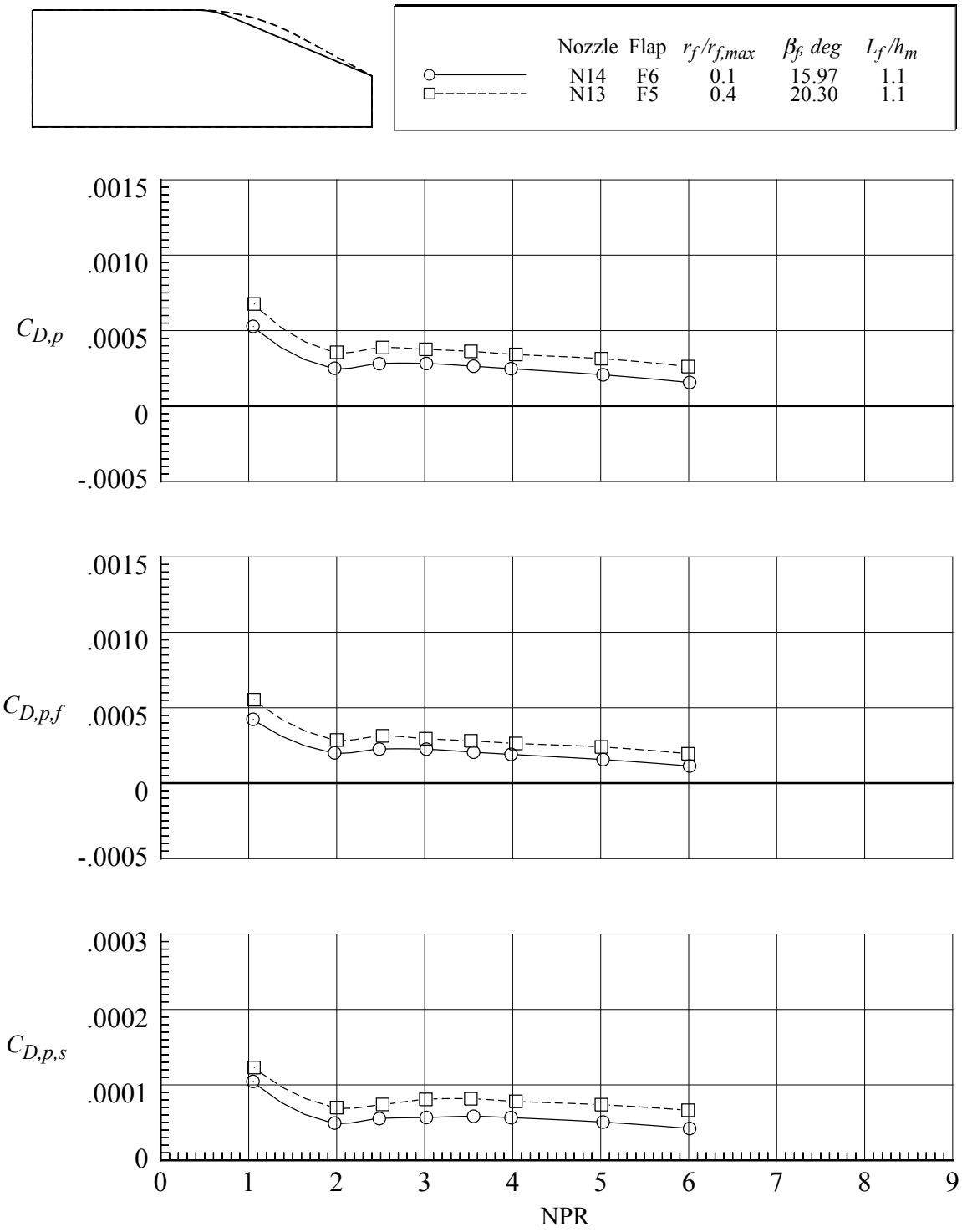

(b) $M = 0.90$.

Figure 86. Continued.

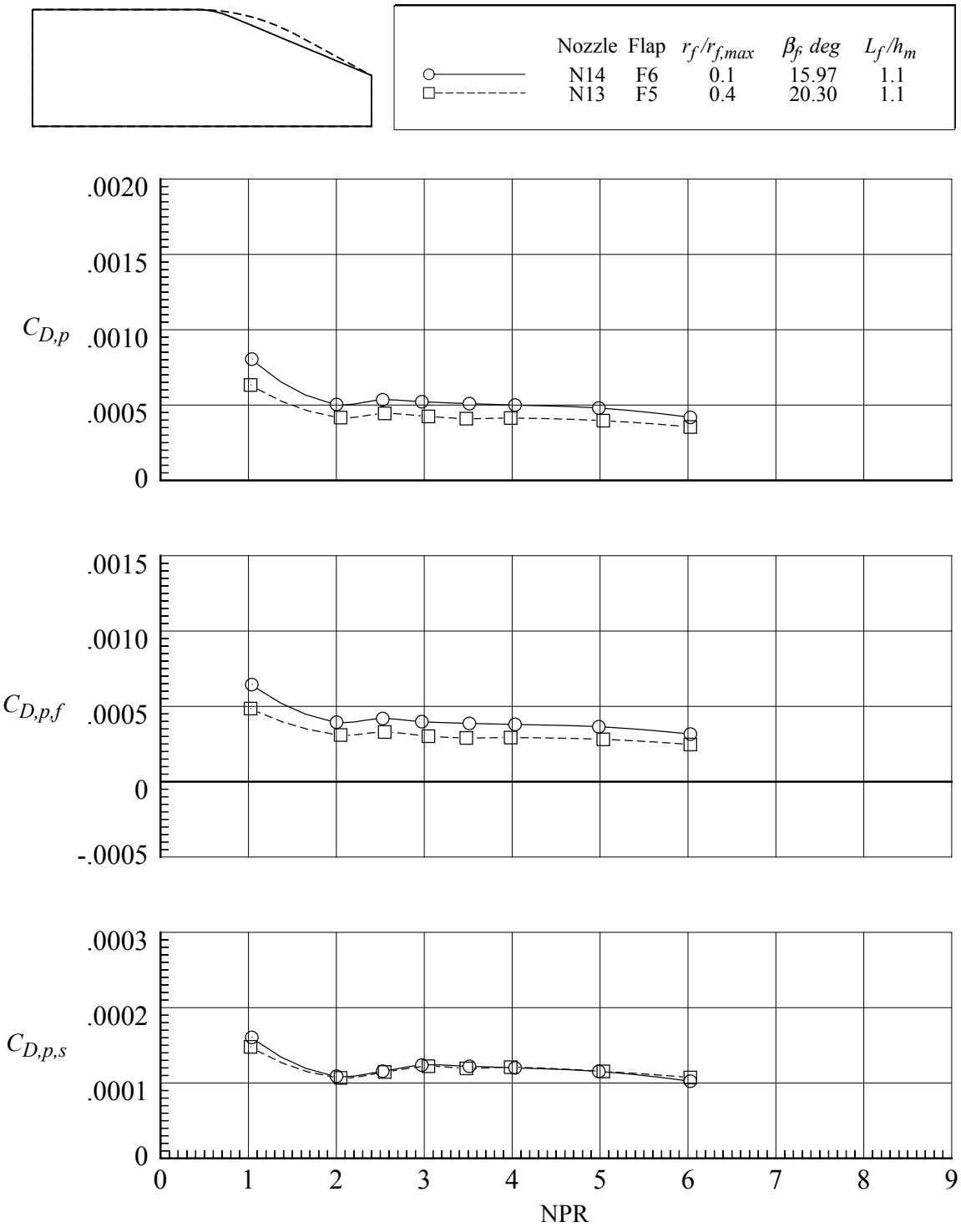

(c) $M = 0.95$.

Figure 86. Continued.

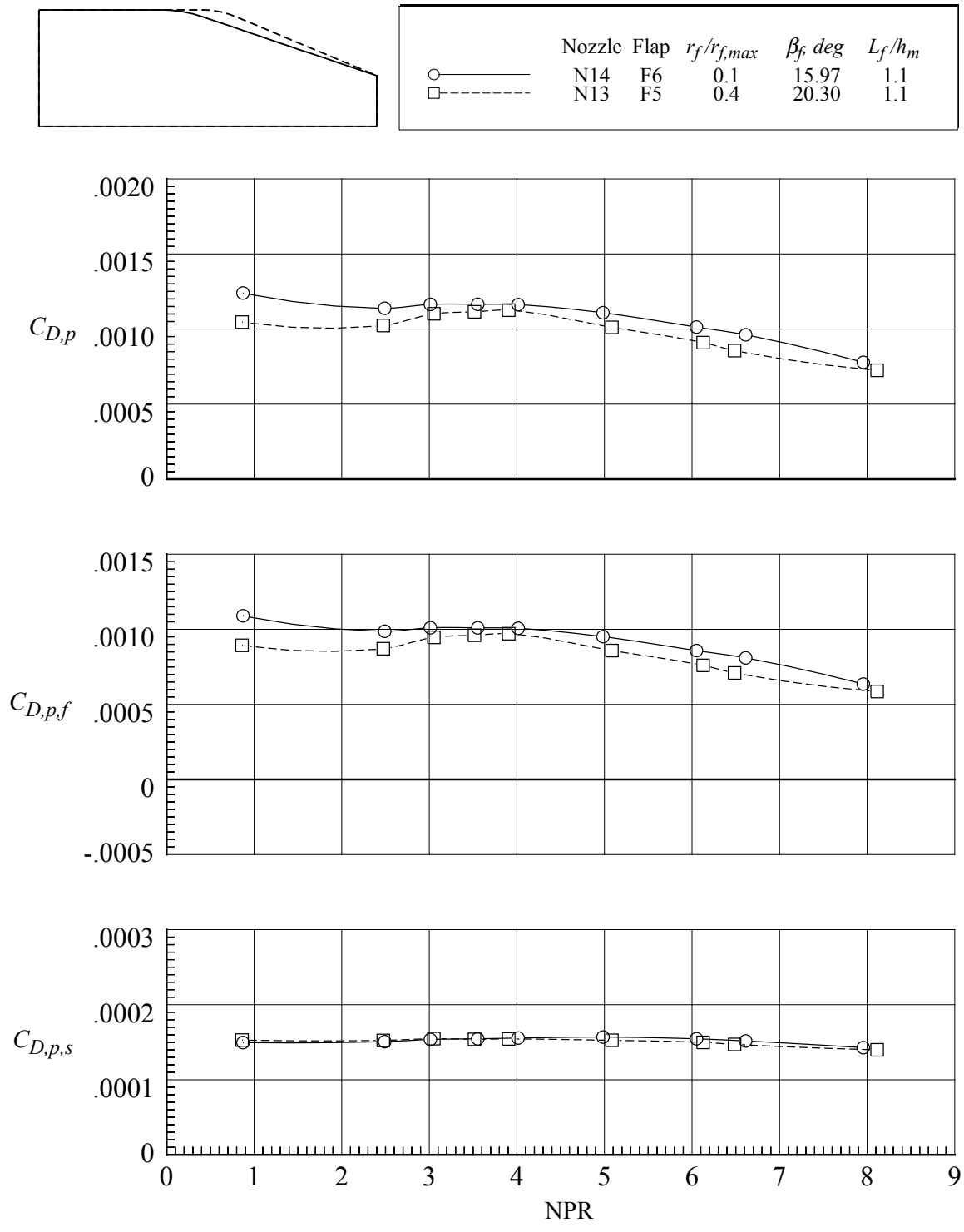

(d) $M = 1.20$.

Figure 86. Concluded.

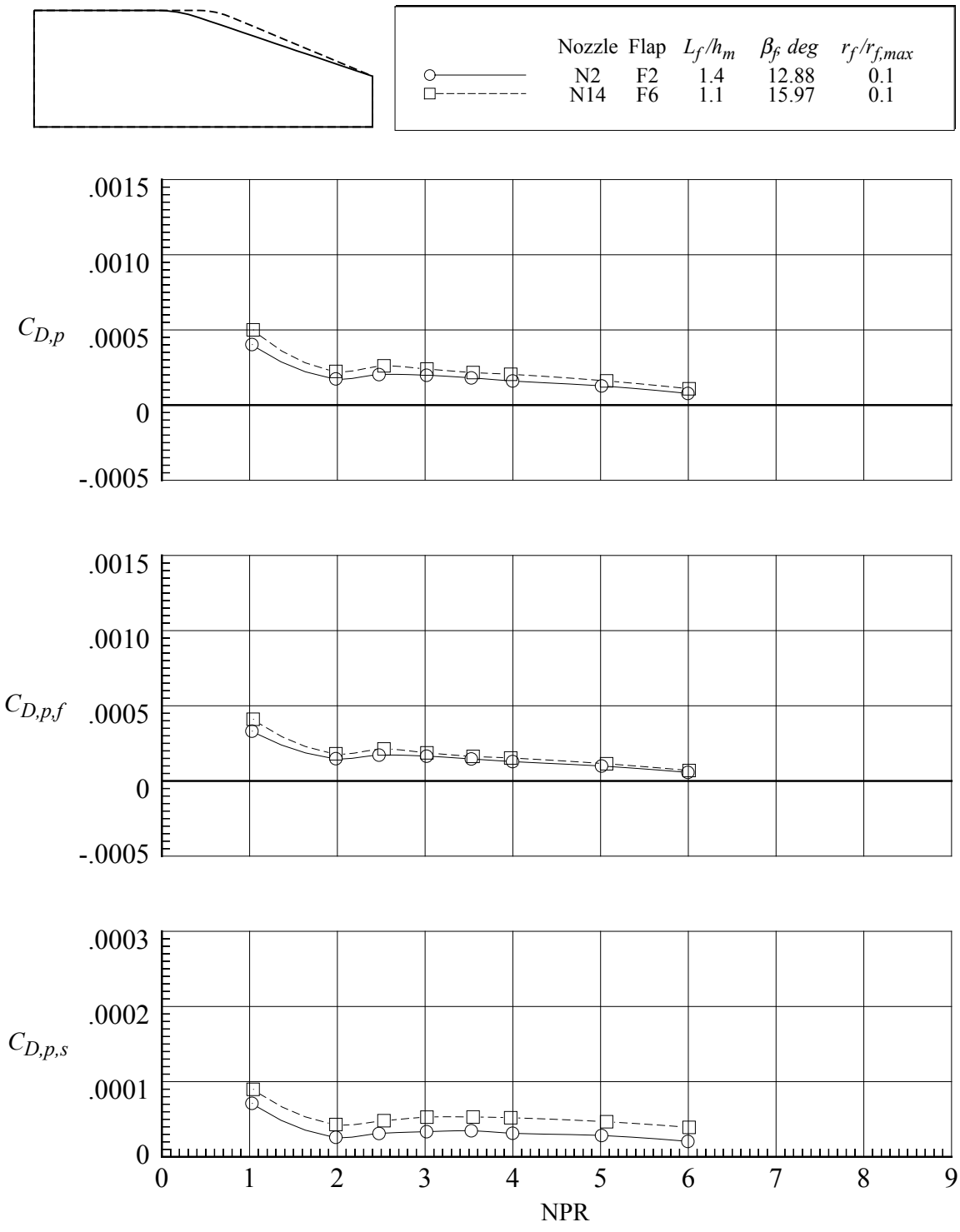

(a) $M = 0.80$.

Figure 87. Effect of flap length on pressure drag coefficients for nozzles with sidewall S1. $\beta_s = 4.0°$; $r_s / r_{s,max} = 0$.

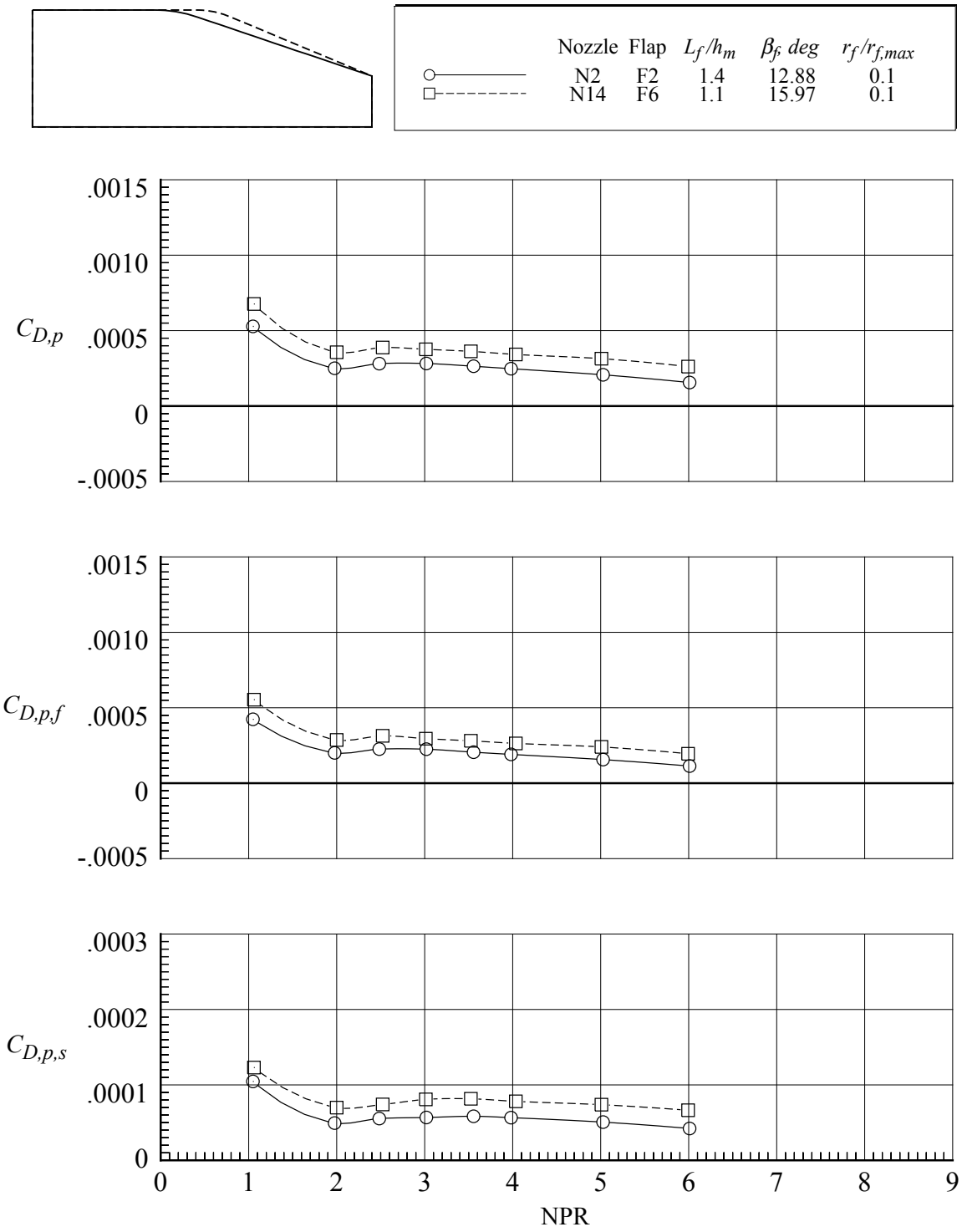

(b) $M = 0.90$.

Figure 87. Continued.

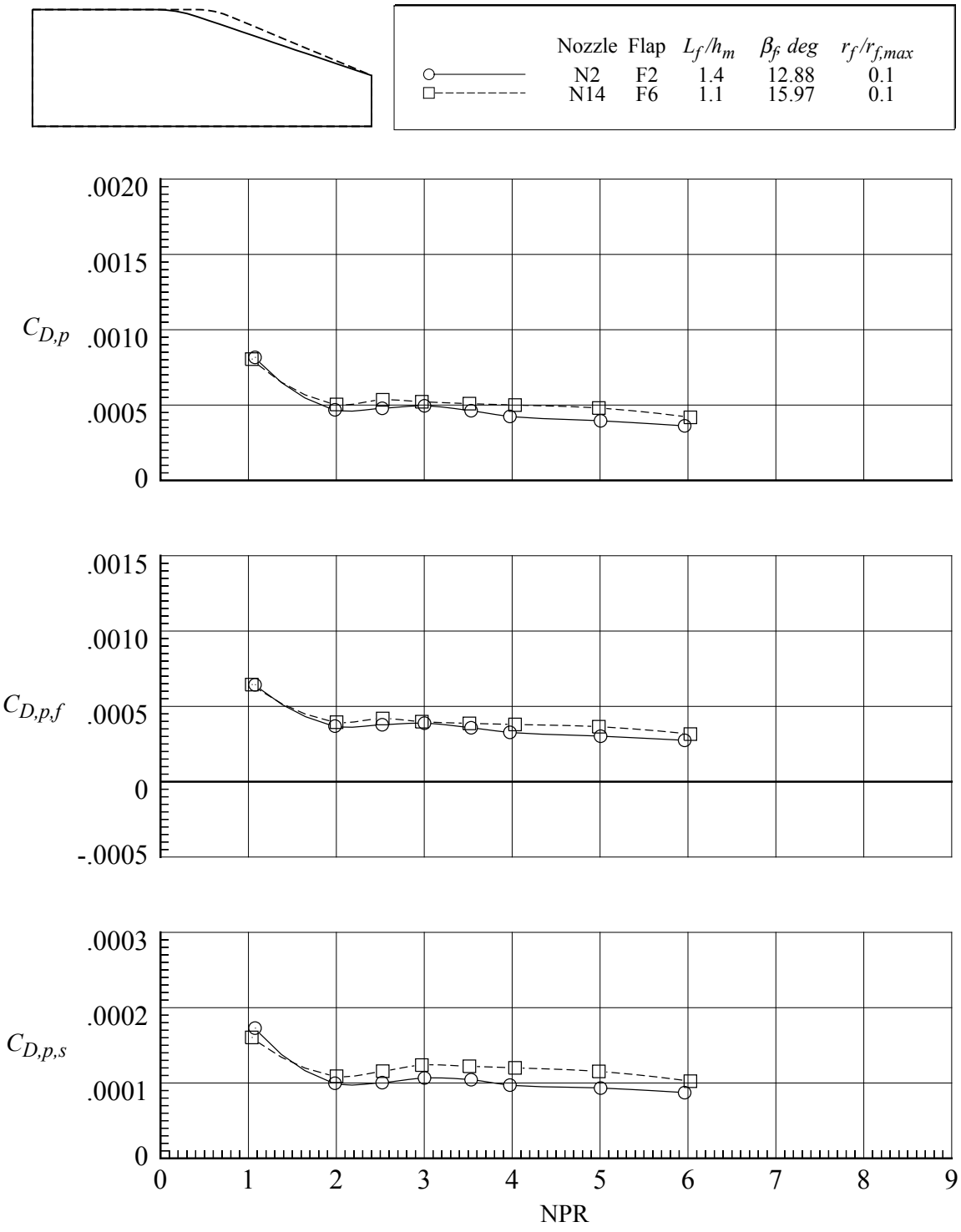

(c) $M = 0.95$.

Figure 87. Continued.

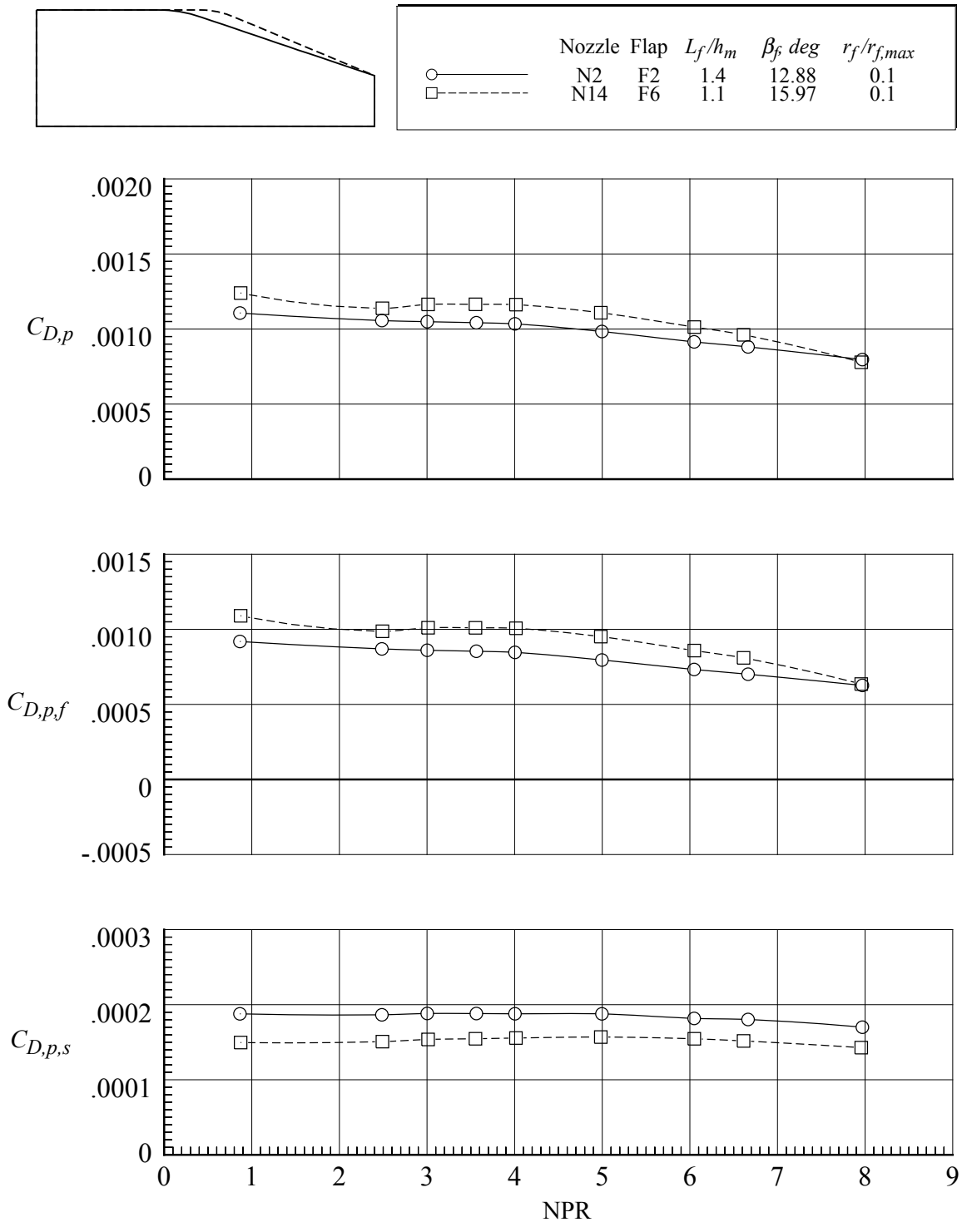

(d) $M = 1.20$.

Figure 87. Concluded.

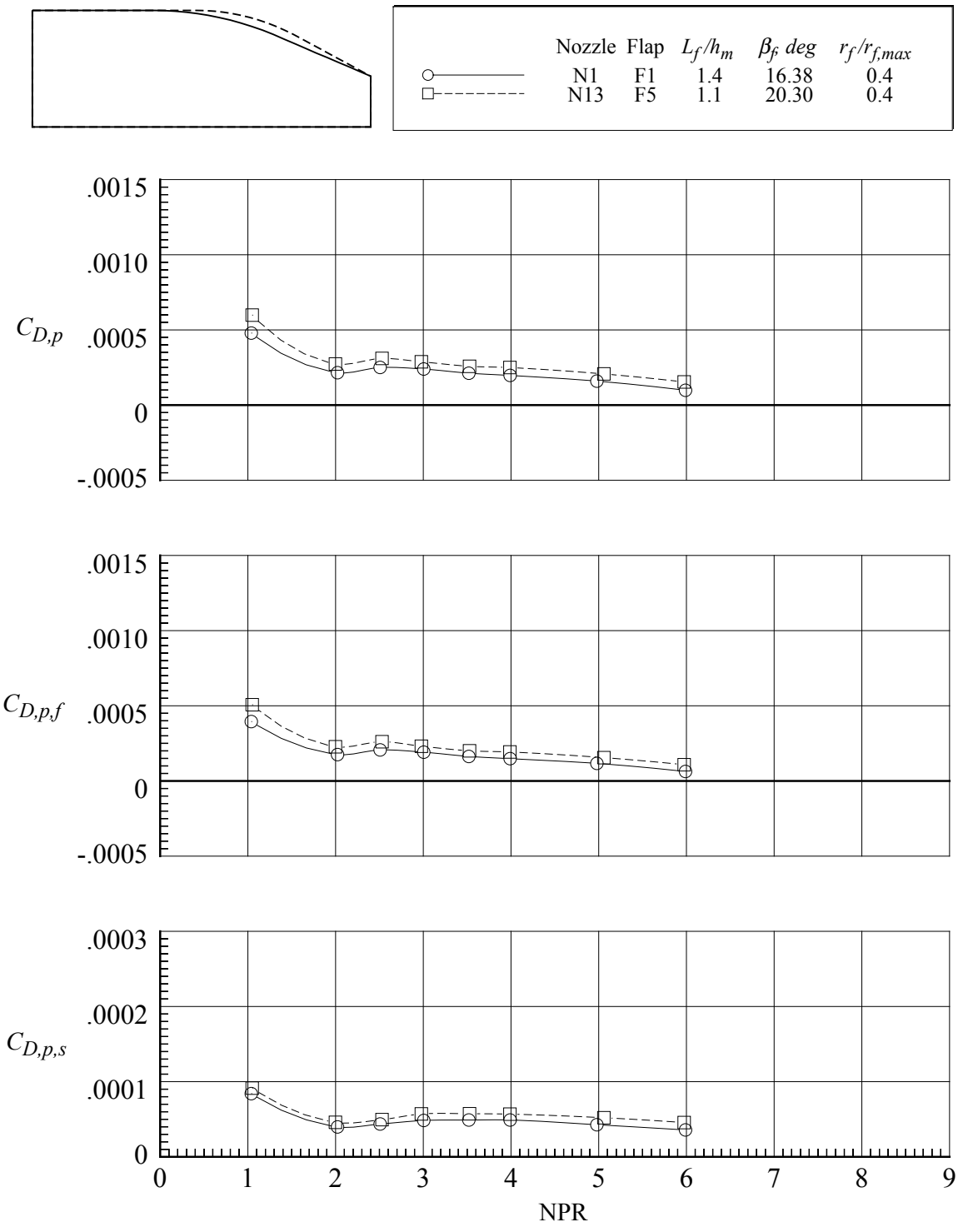

(a) $M = 0.80$.

Figure 88. Effect of flap length on pressure drag coefficients for nozzles with sidewall S1. $\beta_s = 4.0°$; $r_s / r_{s,max} = 0$.

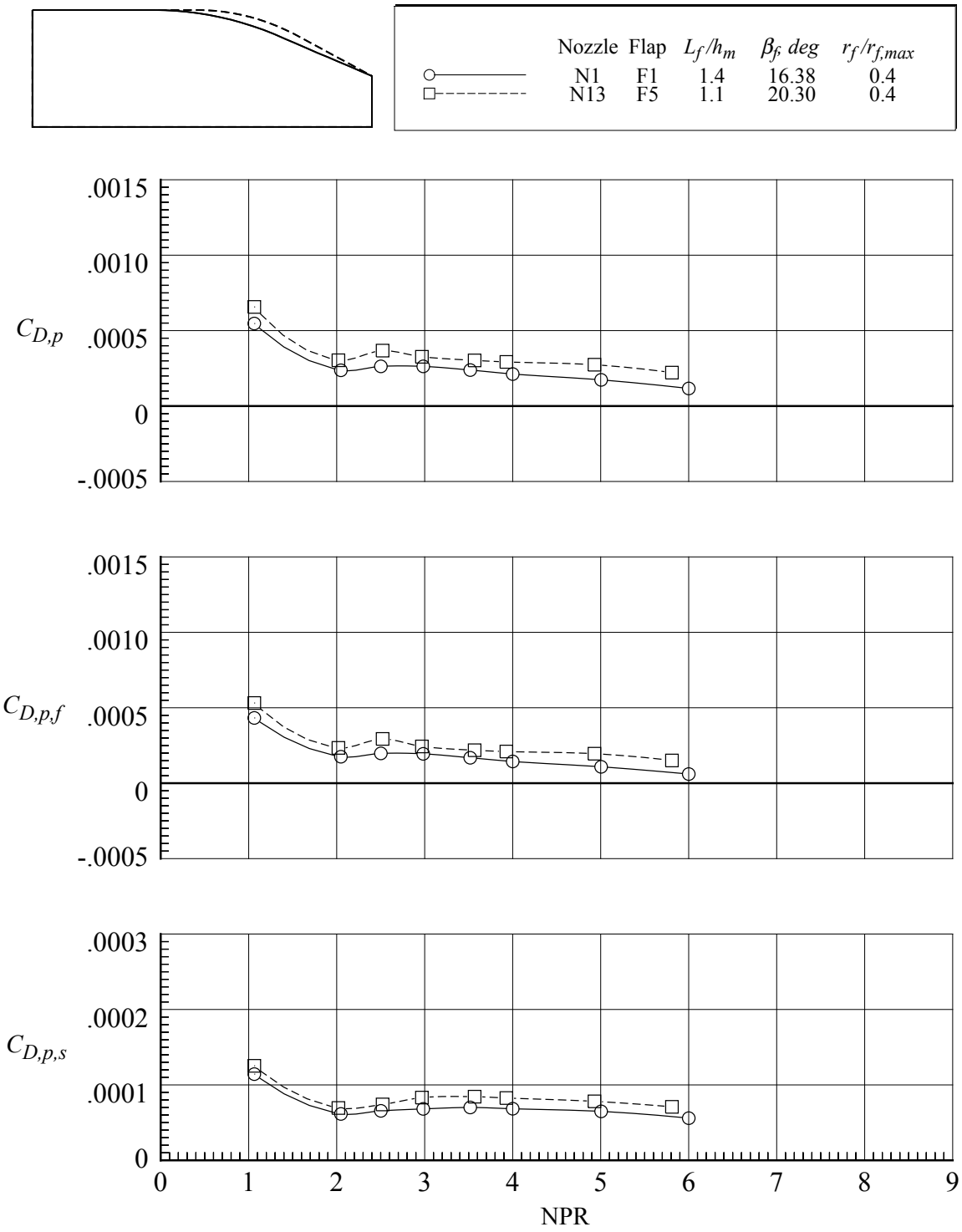

(b) $M = 0.90$.

Figure 88. Continued.

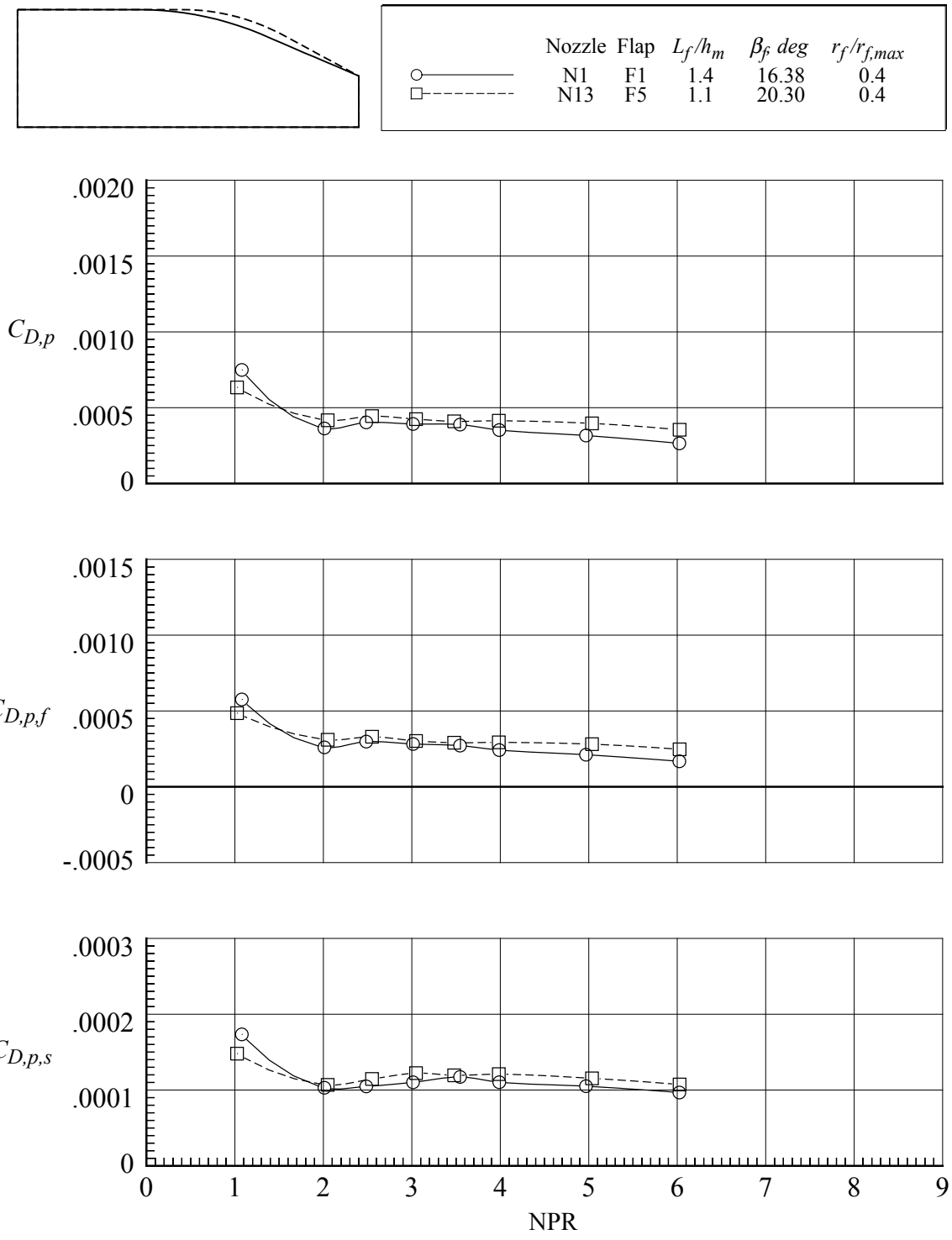

(c) $M = 0.95$.

Figure 88. Continued.

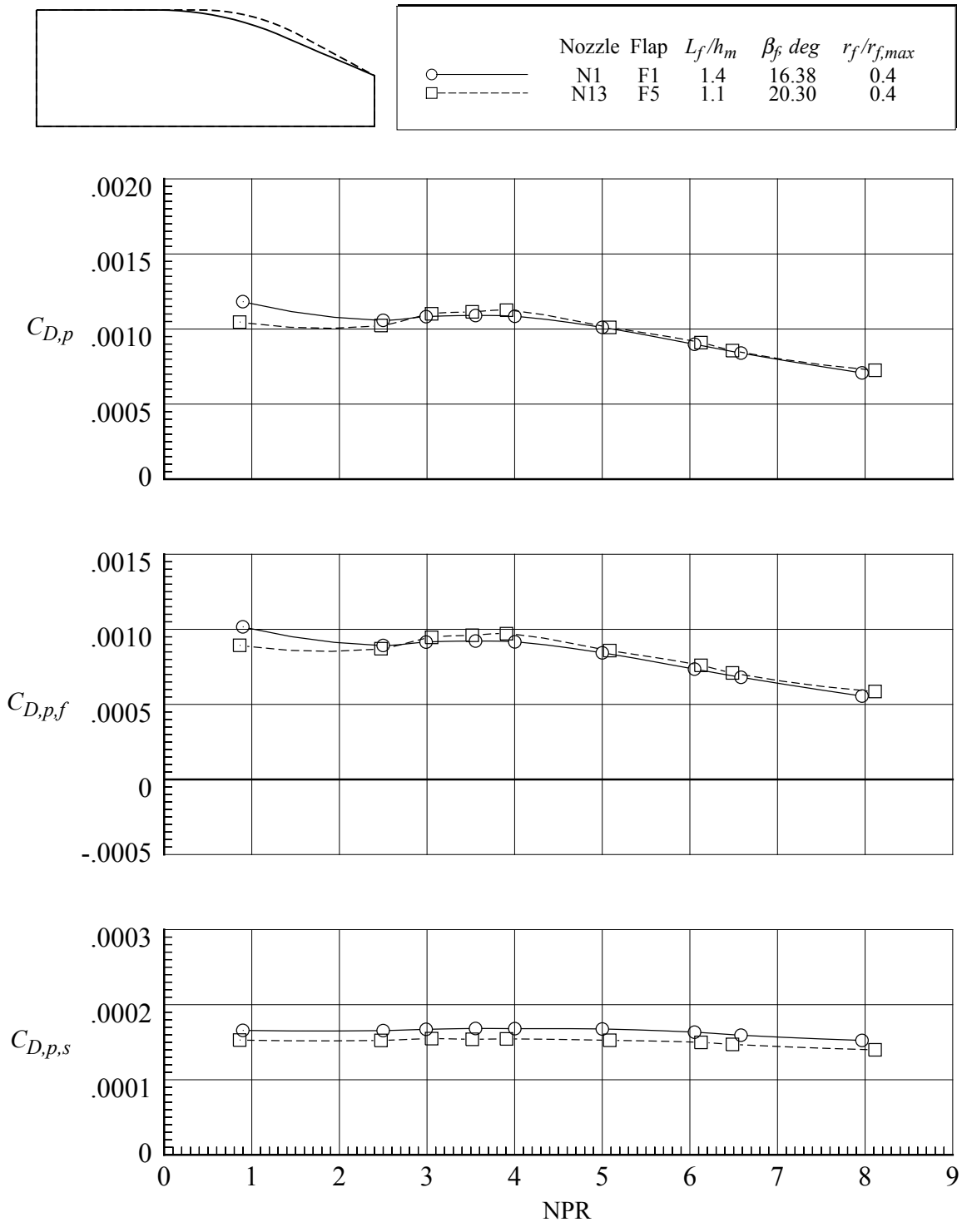

(d) $M = 1.20$.

Figure 88. Concluded.

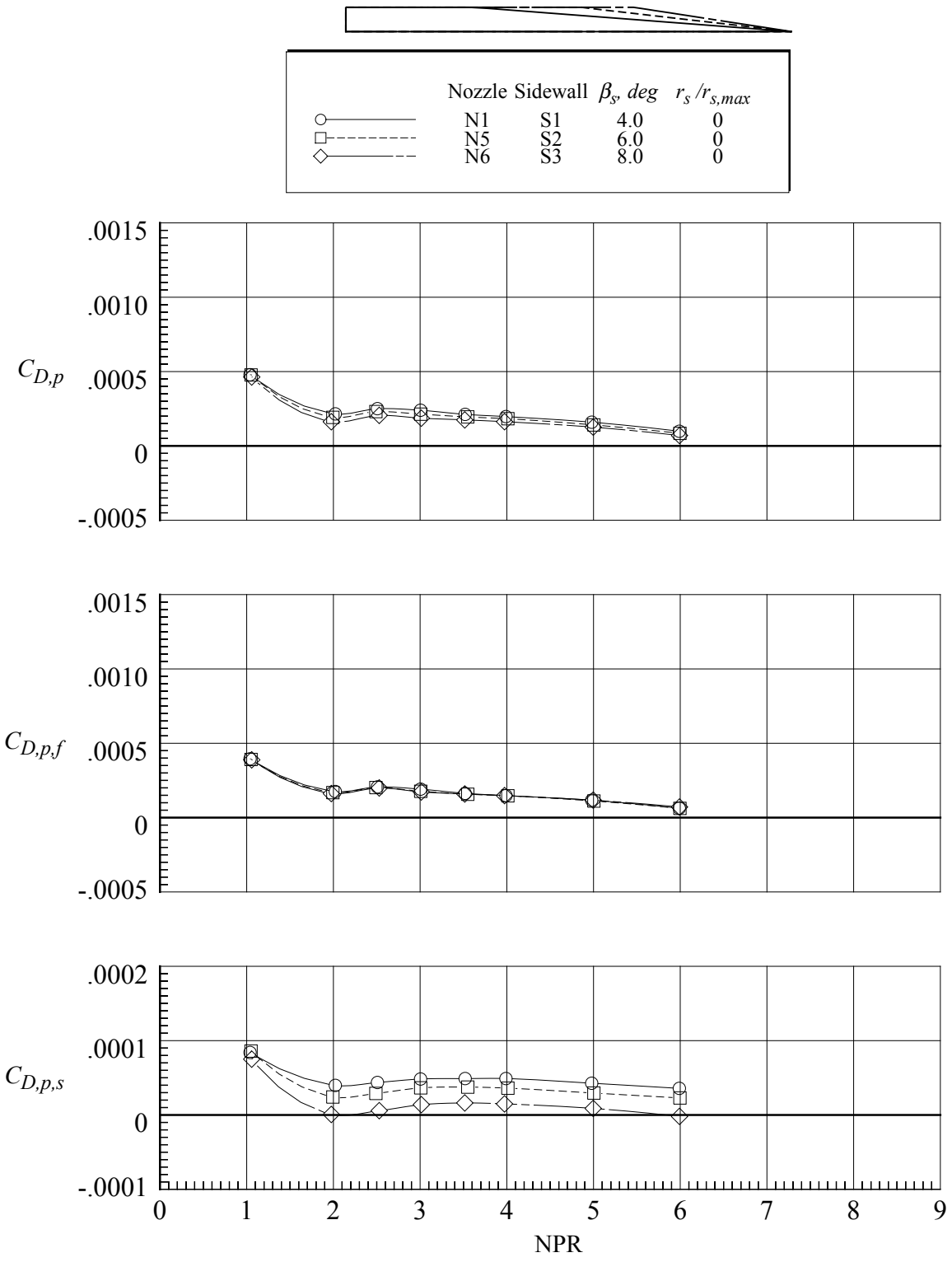

(a) $M = 0.80$.

Figure 89. Effect of sidewall boattail angle on pressure drag coefficients for nozzles with flap F1. $r_f/r_{f,max} = 0.4$; $\beta_f = 16.38°$; $L_f/h_m = 1.4$.

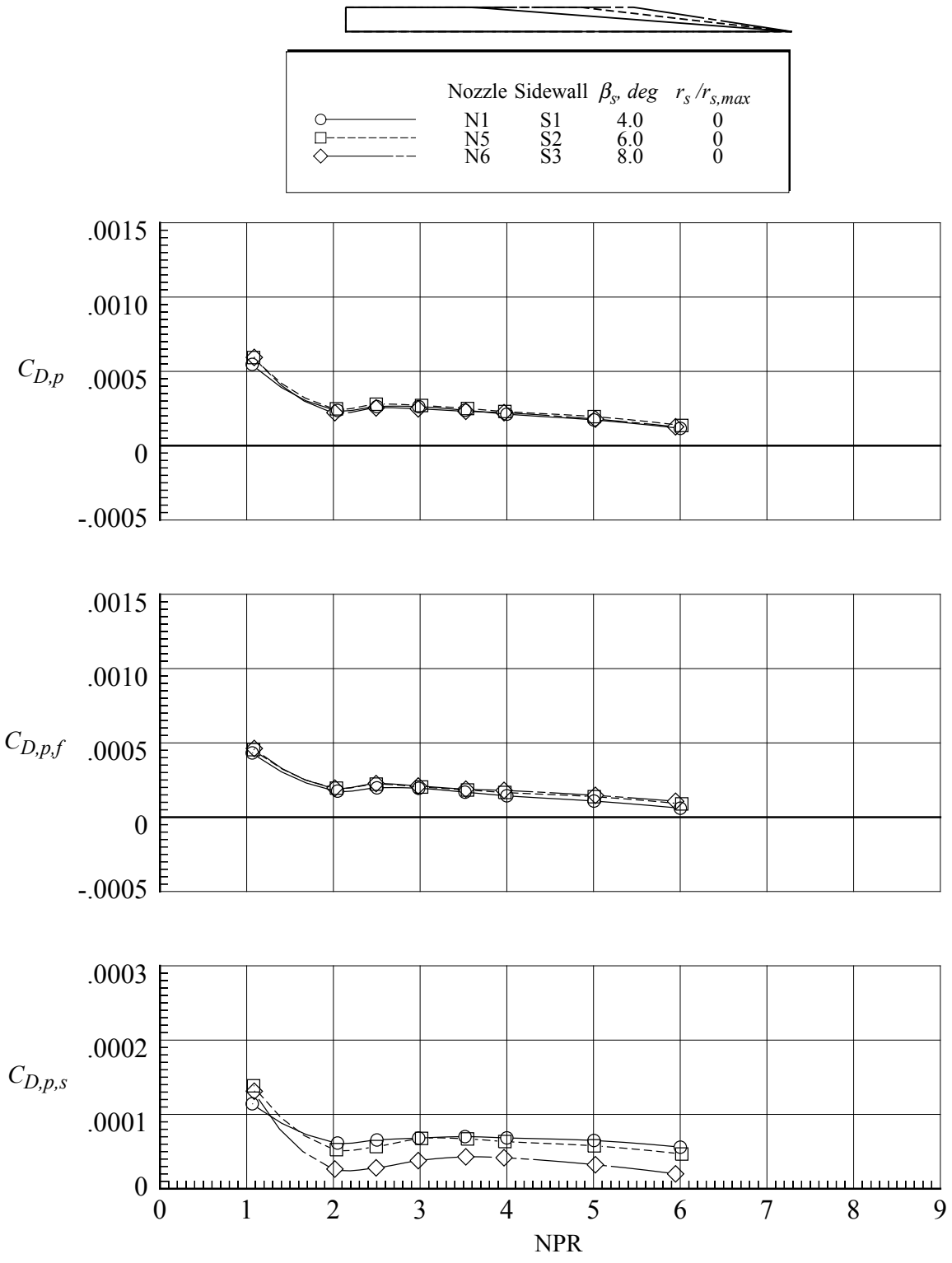

(b) $M = 0.90$.

Figure 89. Continued.

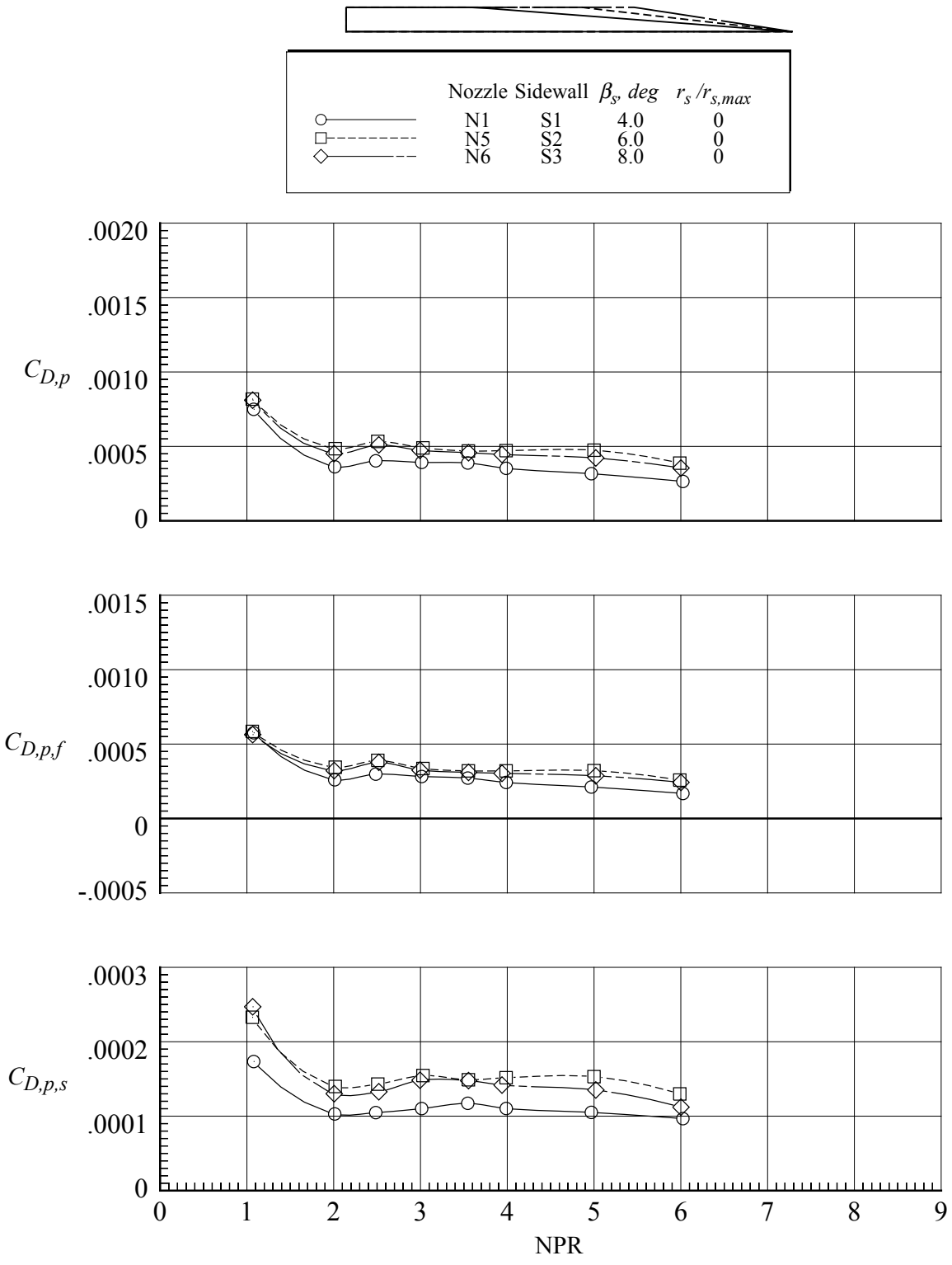

(c) $M = 0.95$.

Figure 89. Continued.

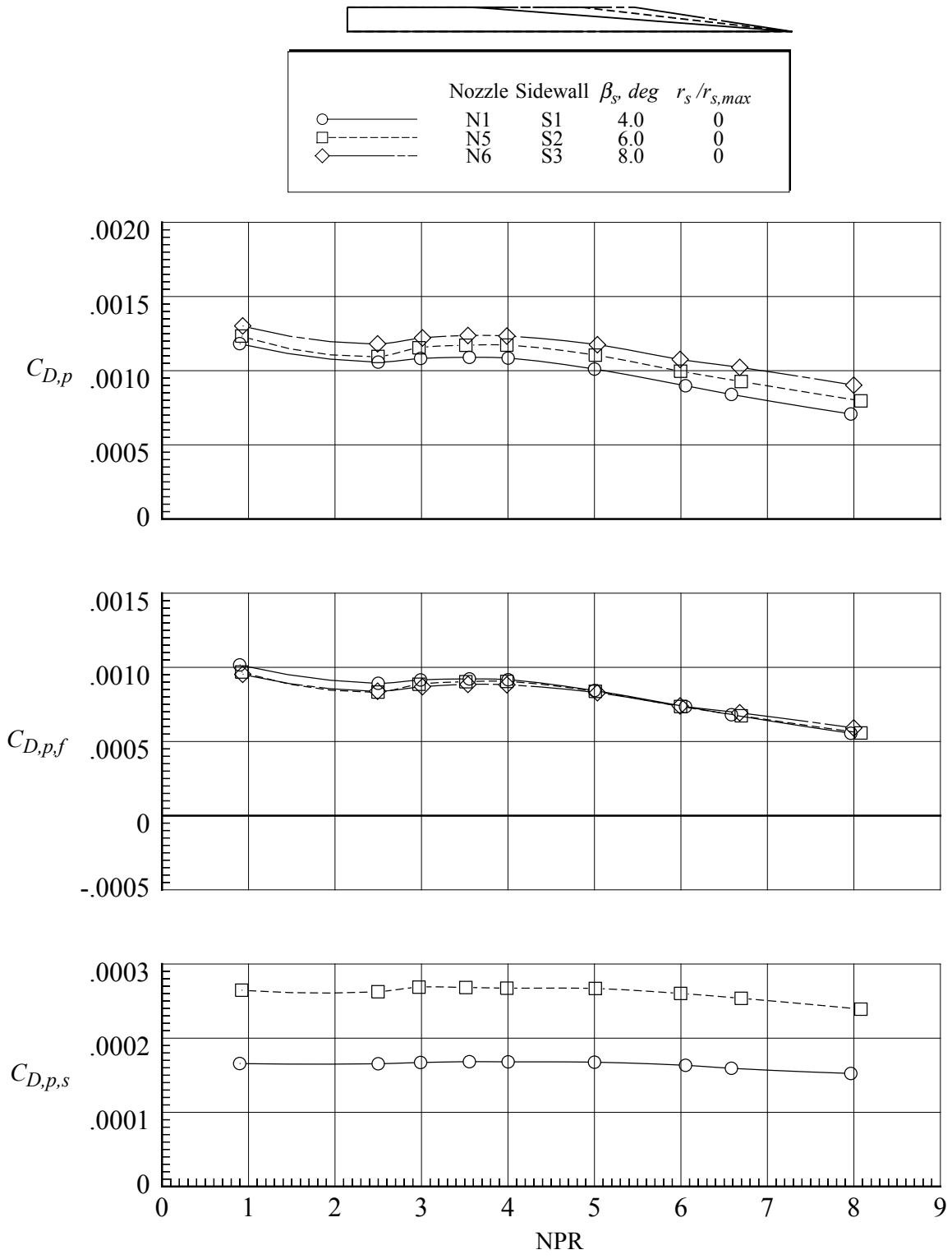

(d) $M = 1.20$.

Figure 89. Concluded.

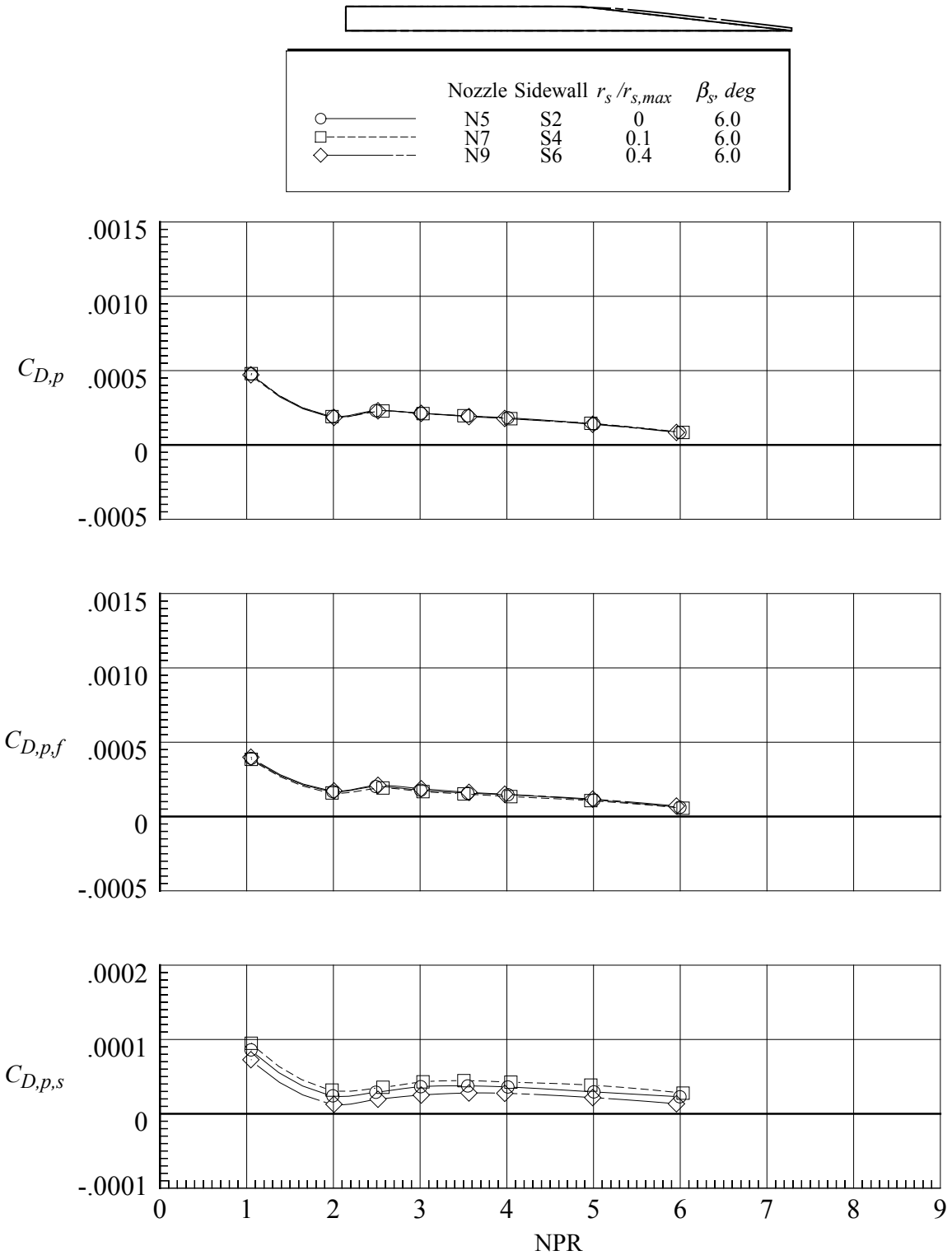

(a) $M = 0.80$.

Figure 90. Effect of sidewall radius of curvature on pressure drag coefficients for nozzles with flap F1. $r_f/r_{f,max} = 0.4$; $\beta_f = 16.38°$; $L_f/h_m = 1.4$.

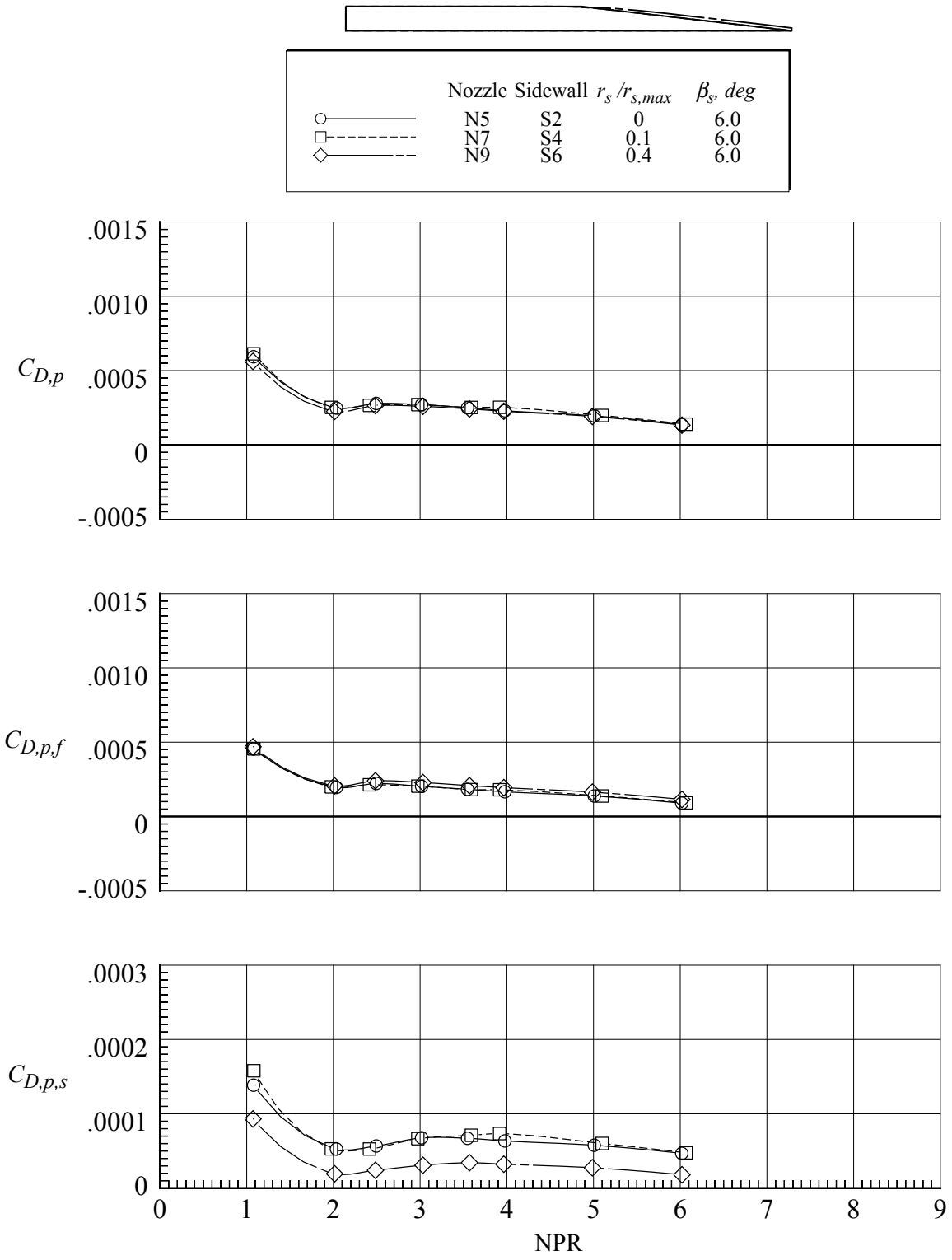

(b) $M = 0.90$.

Figure 90. Continued.

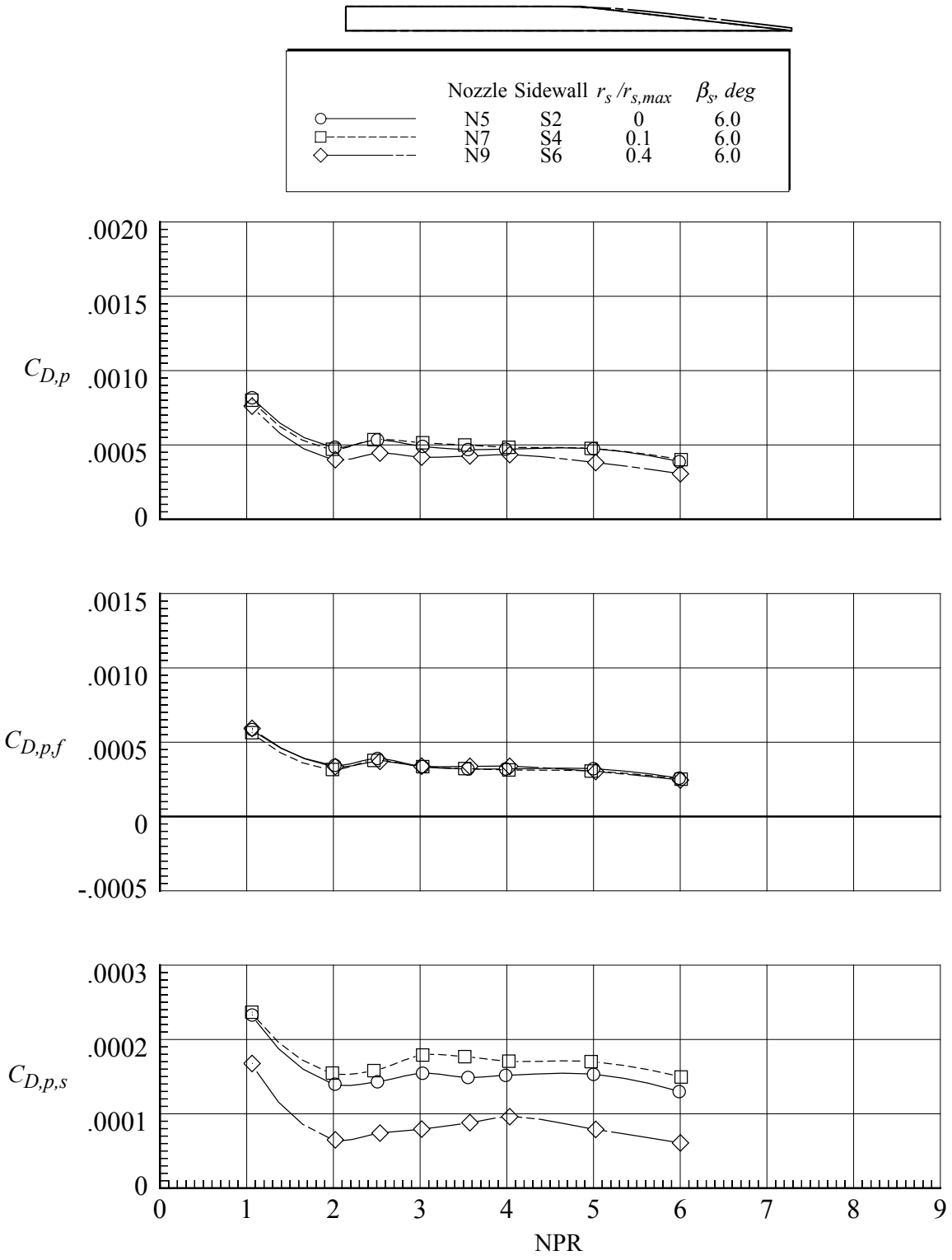

(c) $M = 0.95$.

Figure 90. Continued.

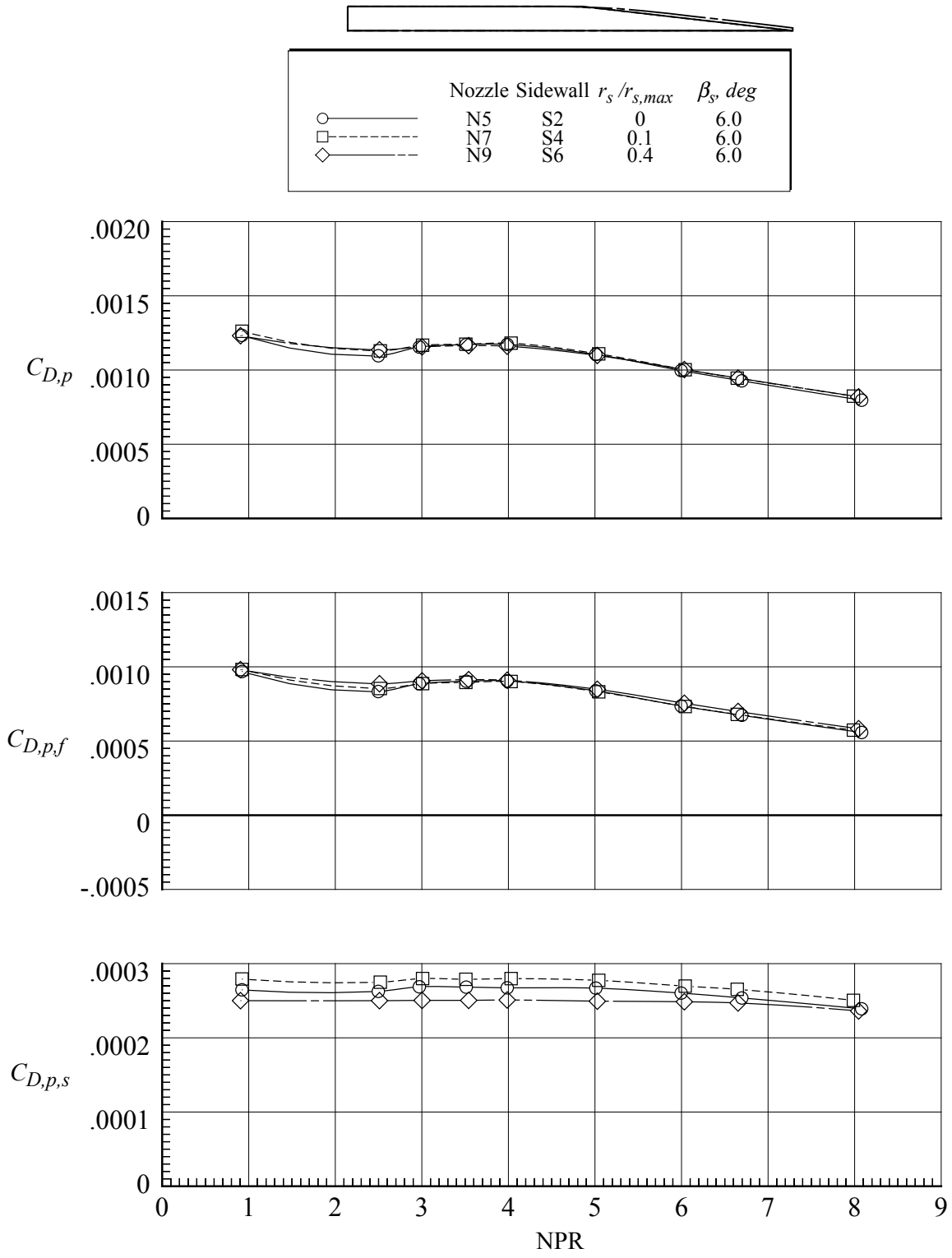

(d) $M = 1.20$.

Figure 90. Concluded.

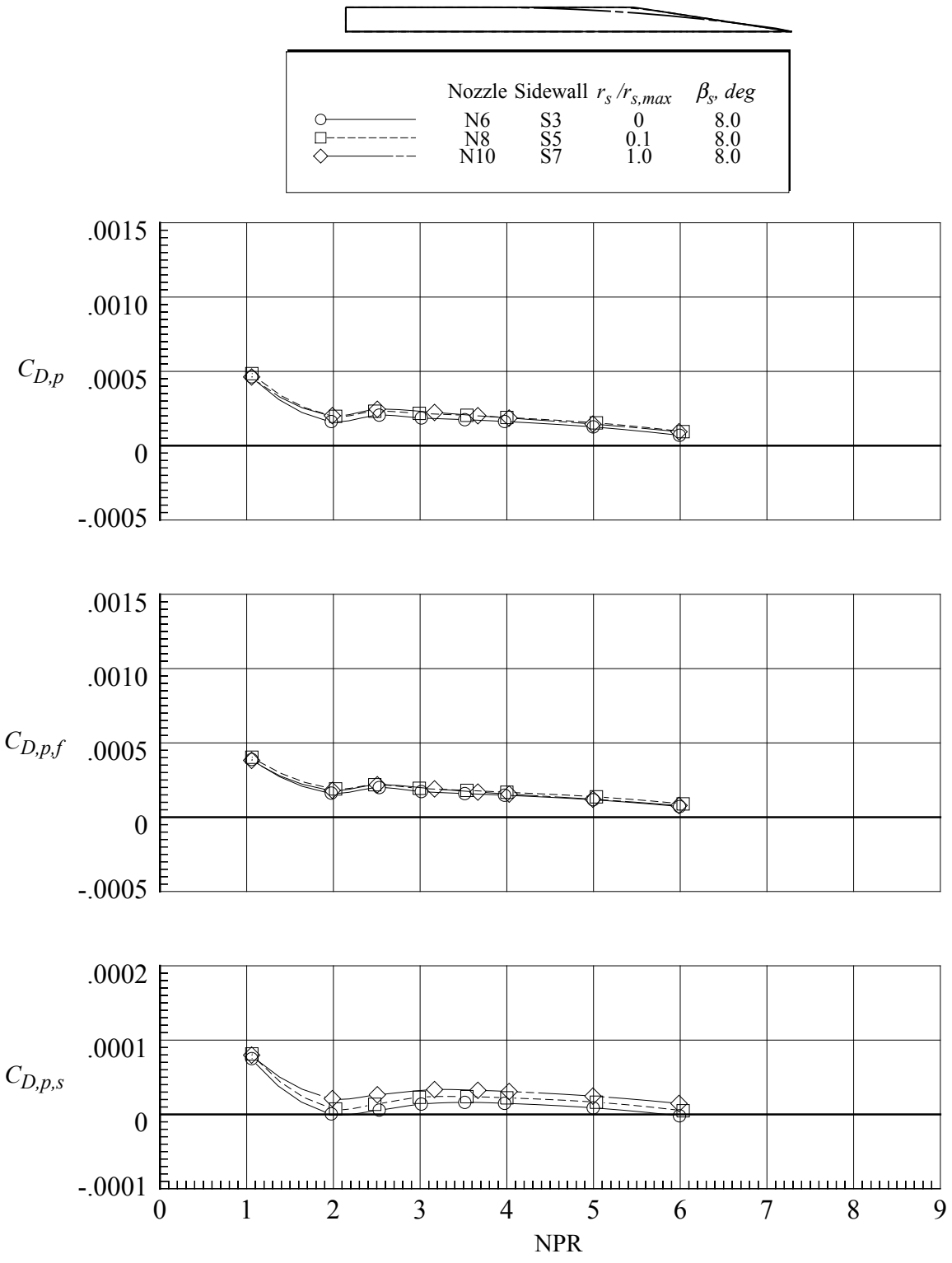

(a) $M = 0.80$.

Figure 91. Effect of sidewall radius of curvature on pressure drag coefficients for nozzles with flap F1. $r_f/r_{f,max} = 0.4$; $\beta_f = 16.38°$; $L_f/h_m = 1.4$.

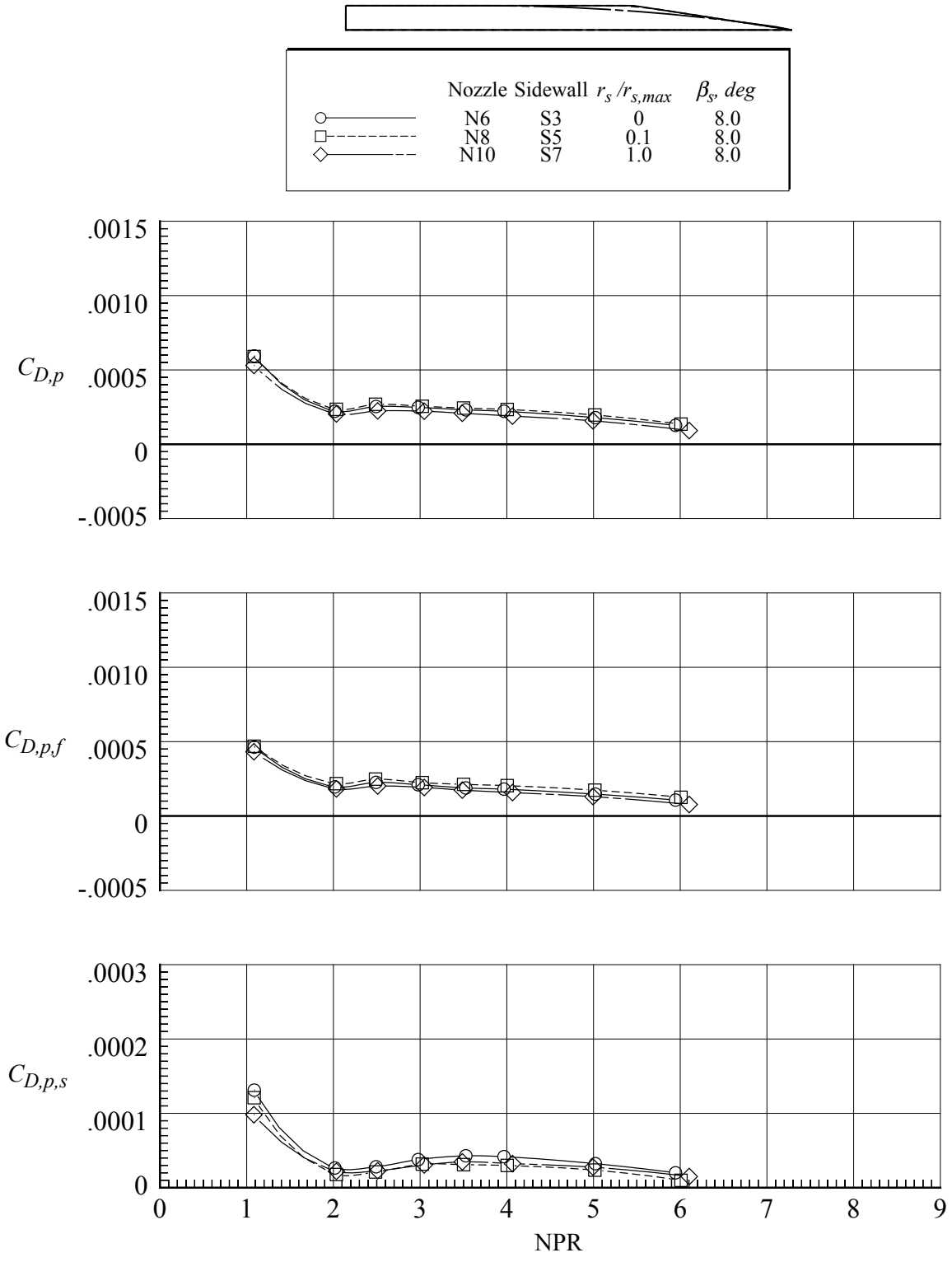

(b) $M = 0.90$.

Figure 91. Continued.

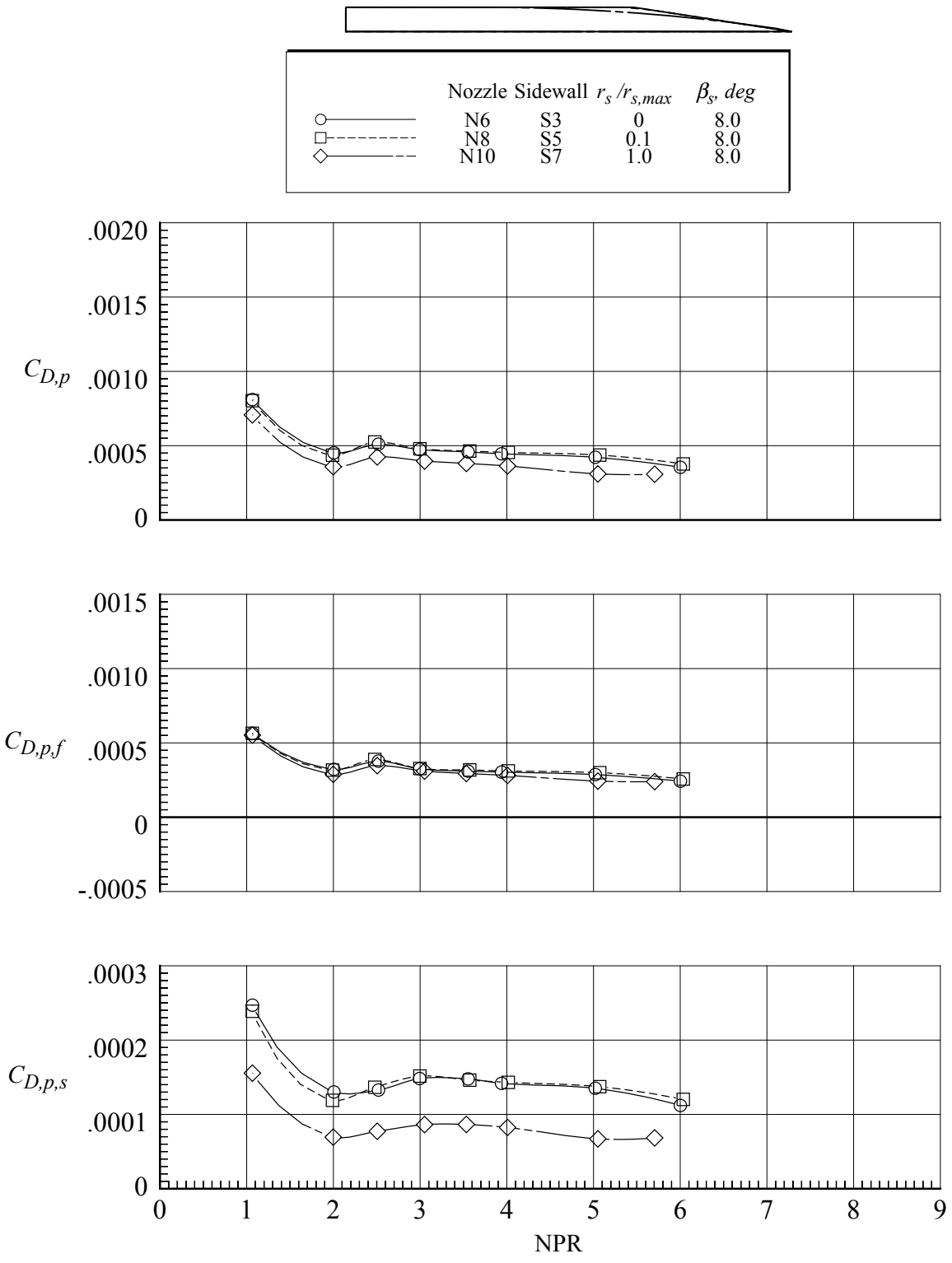

(c) $M = 0.95$.

Figure 91. Continued.

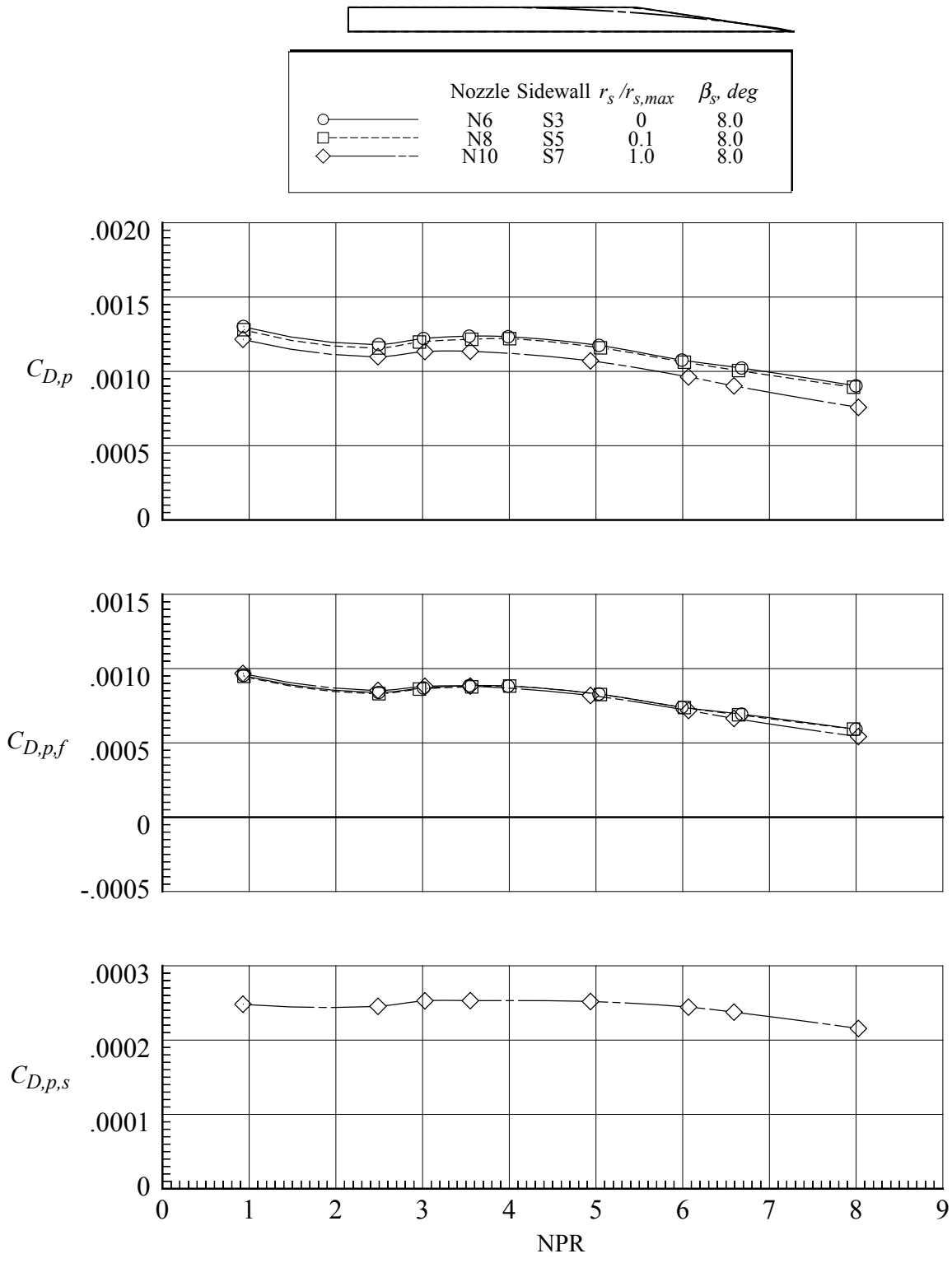

(d) $M = 1.20$.

Figure 91. Concluded.

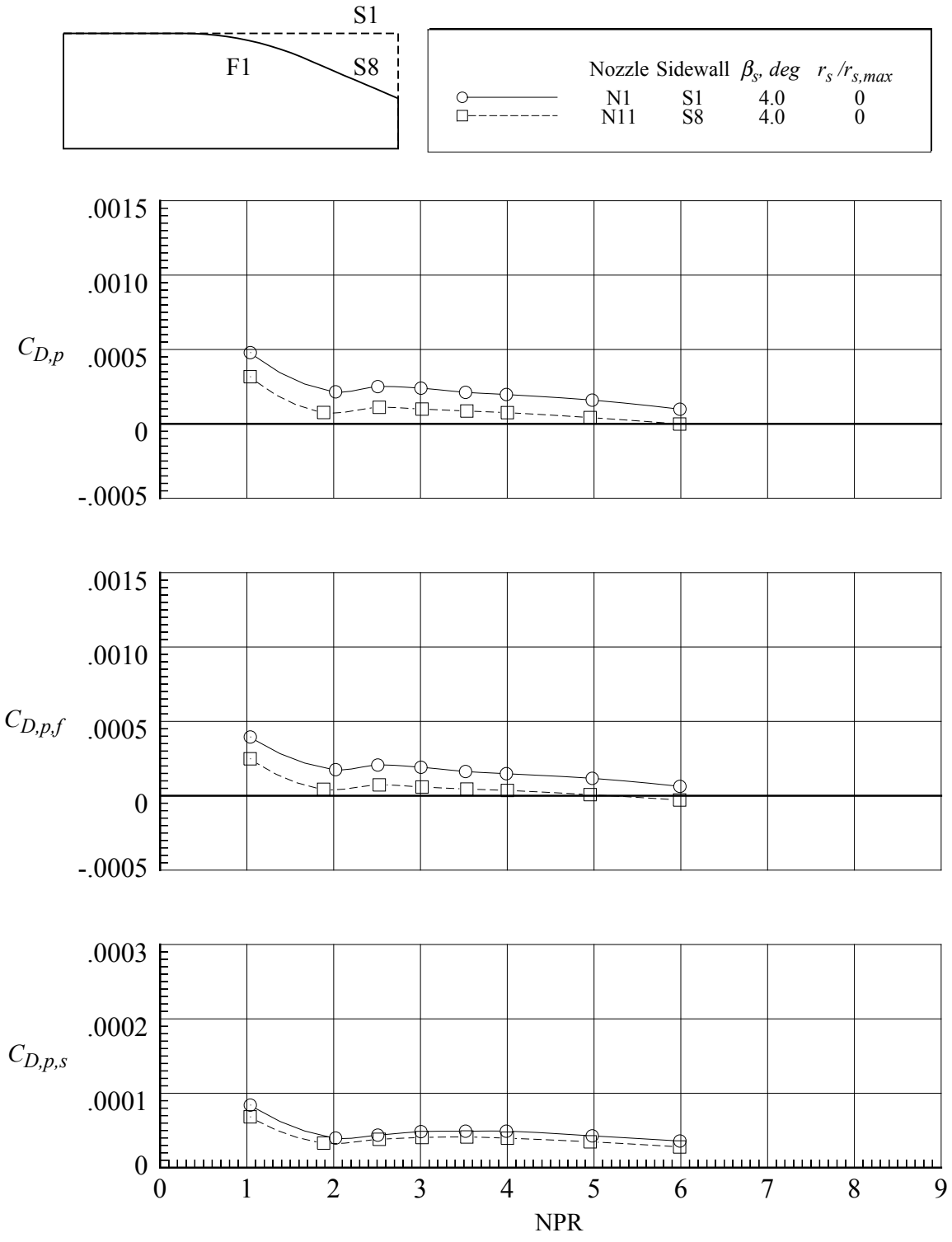

(a) $M = 0.80$.

Figure 92. Effect of reduced sidewall height on pressure drag coefficients for nozzles with flap F1. $r_f/r_{f,max} = 0.4$; $\beta_f = 16.38°$; $L_f/h_m = 1.4$.

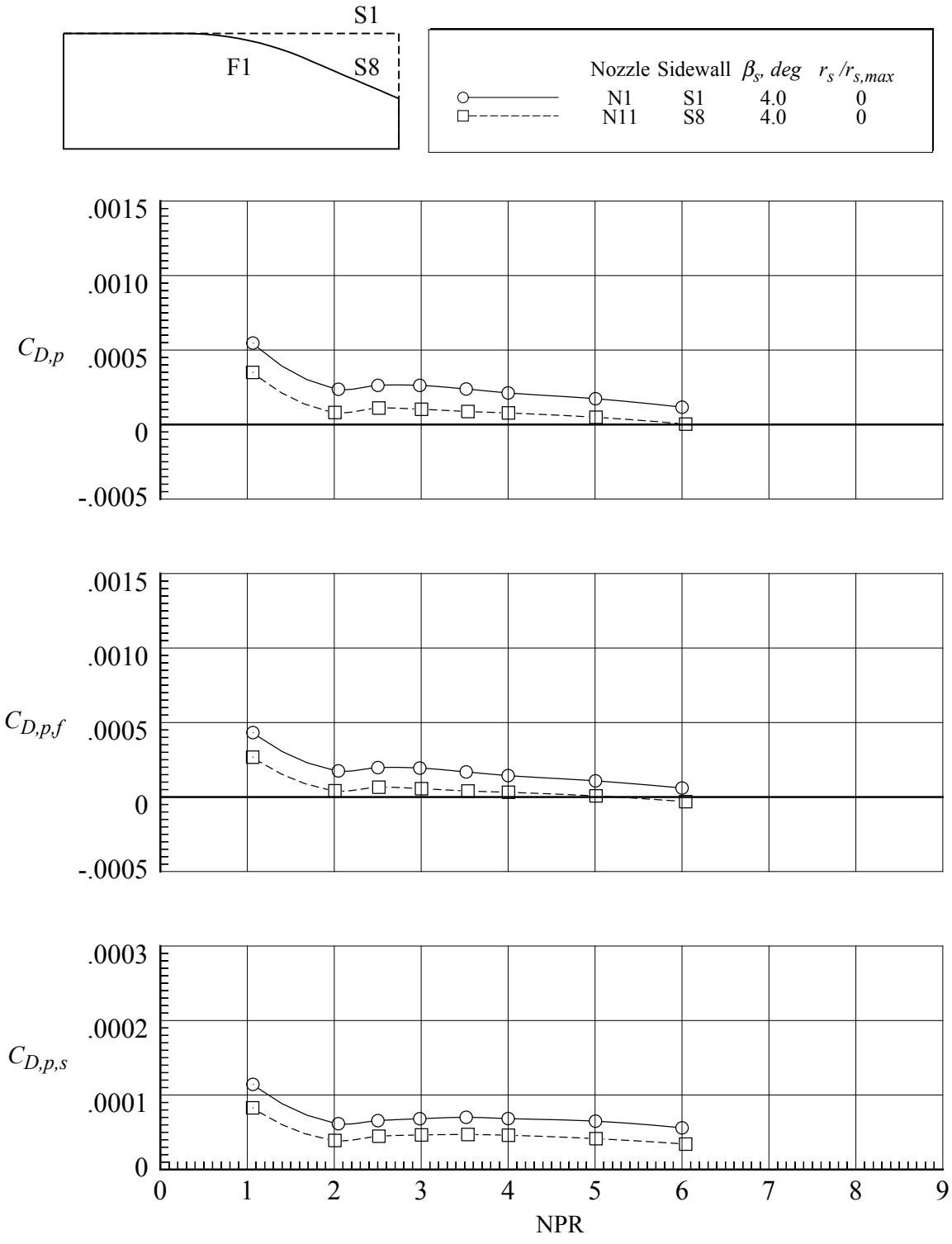

(b) $M = 0.90$.

Figure 92. Continued.

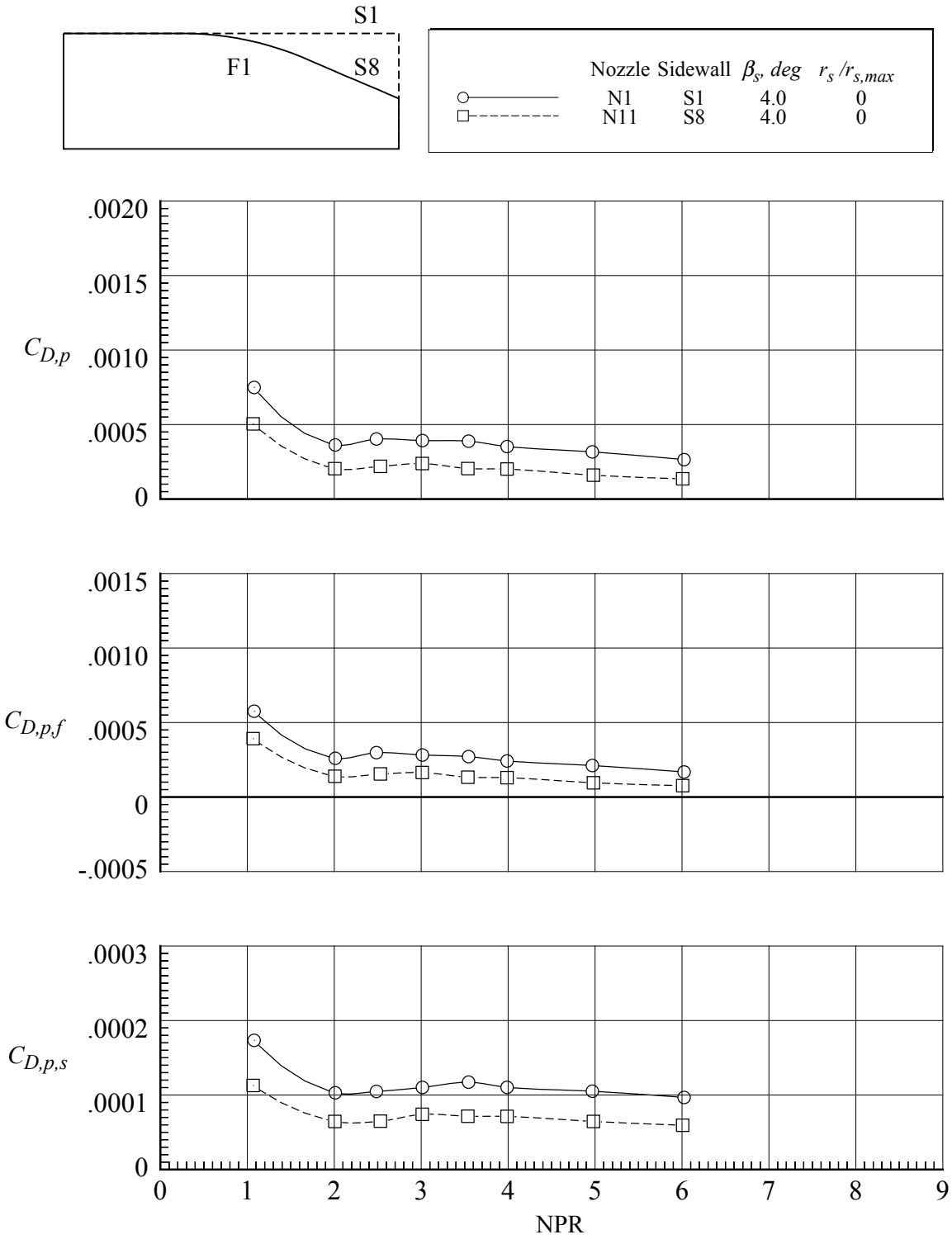

(c) $M = 0.95$.

Figure 92. Continued.

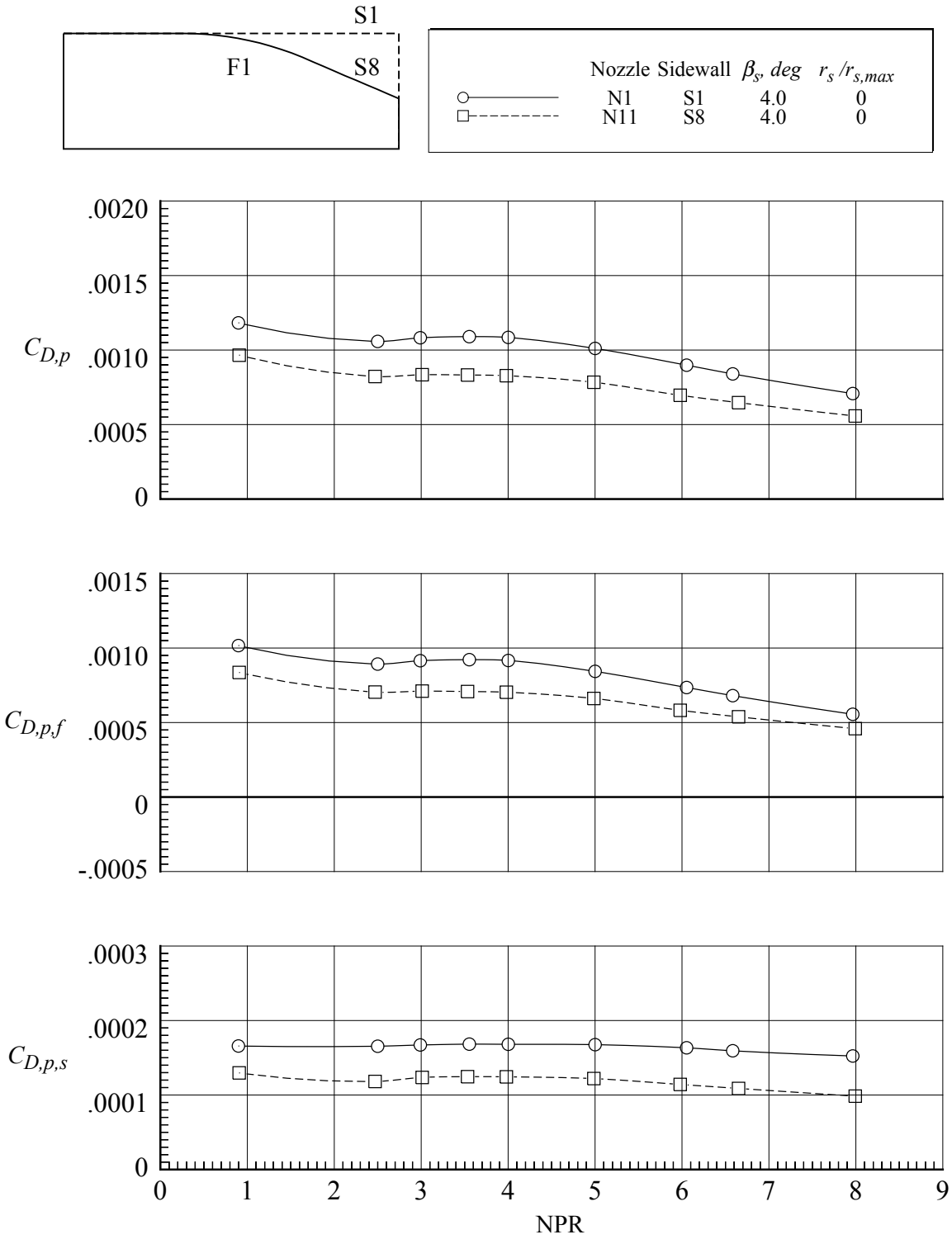

(d) $M = 1.20$.

Figure 92. Concluded.

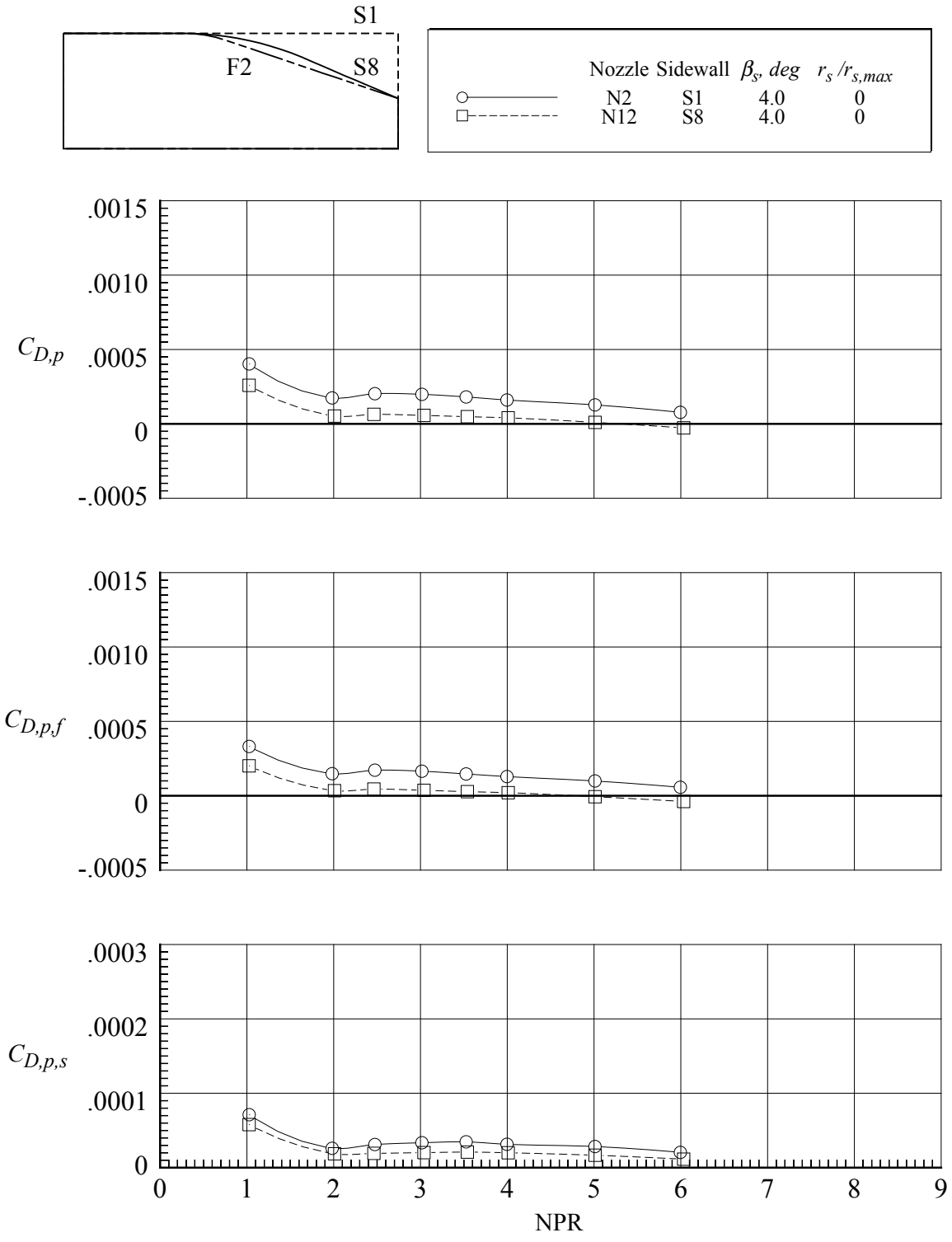

(a) $M = 0.80$.

Figure 93. Effect of reduced sidewall height on pressure drag coefficients for nozzles with flap F2. $r_f/r_{f,max} = 0.1$; $\beta_f = 12.88°$; $L_f/h_m = 1.4$.

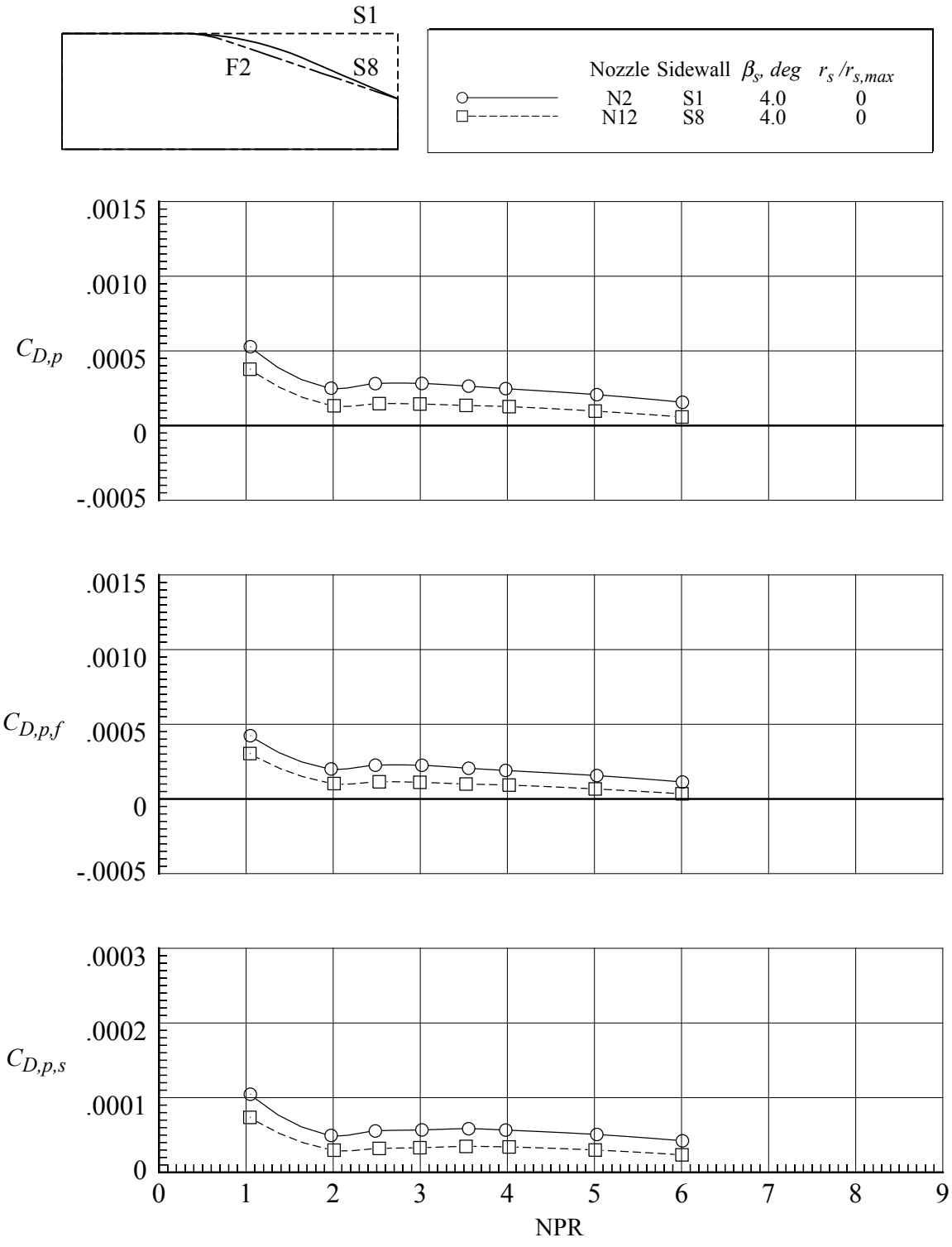

(b) $M = 0.90$.

Figure 93. Continued.

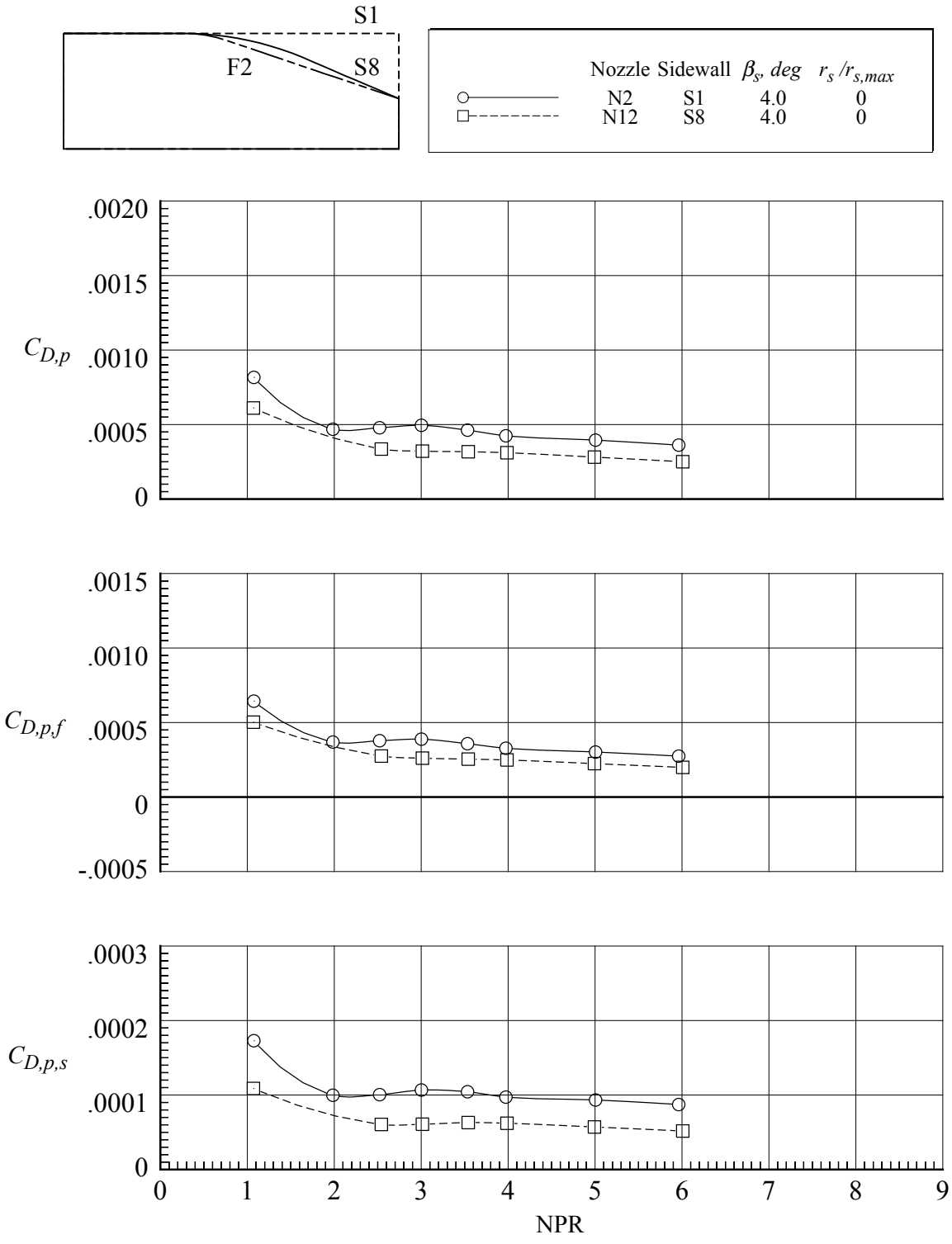

(c) $M = 0.95$.

Figure 93. Continued.

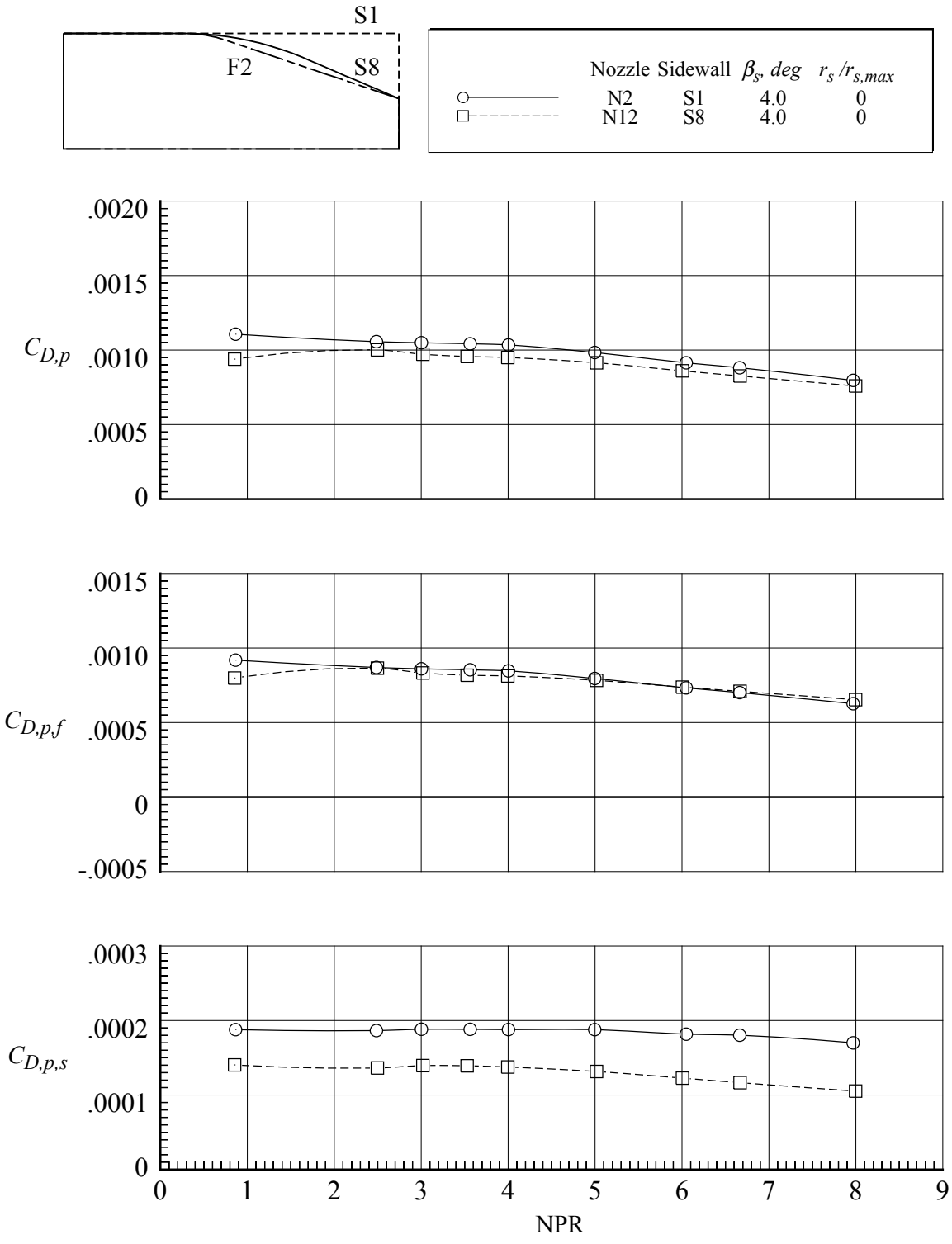

(d) $M = 1.20$.

Figure 93. Concluded.

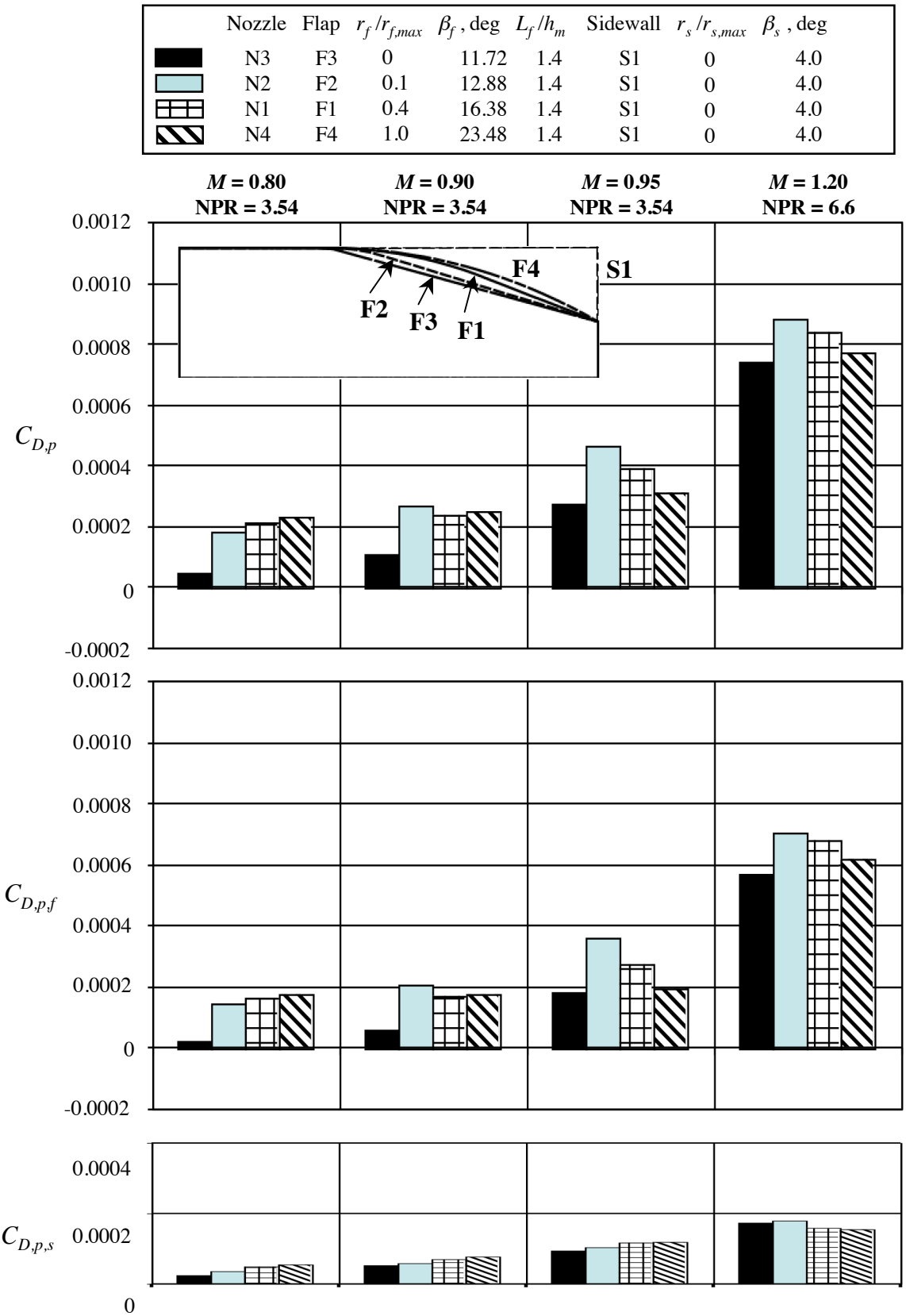

Figure 94. Effect of flap radius of curvature on pressure drag coefficients for nozzles with sidewall S1 at scheduled NPR.

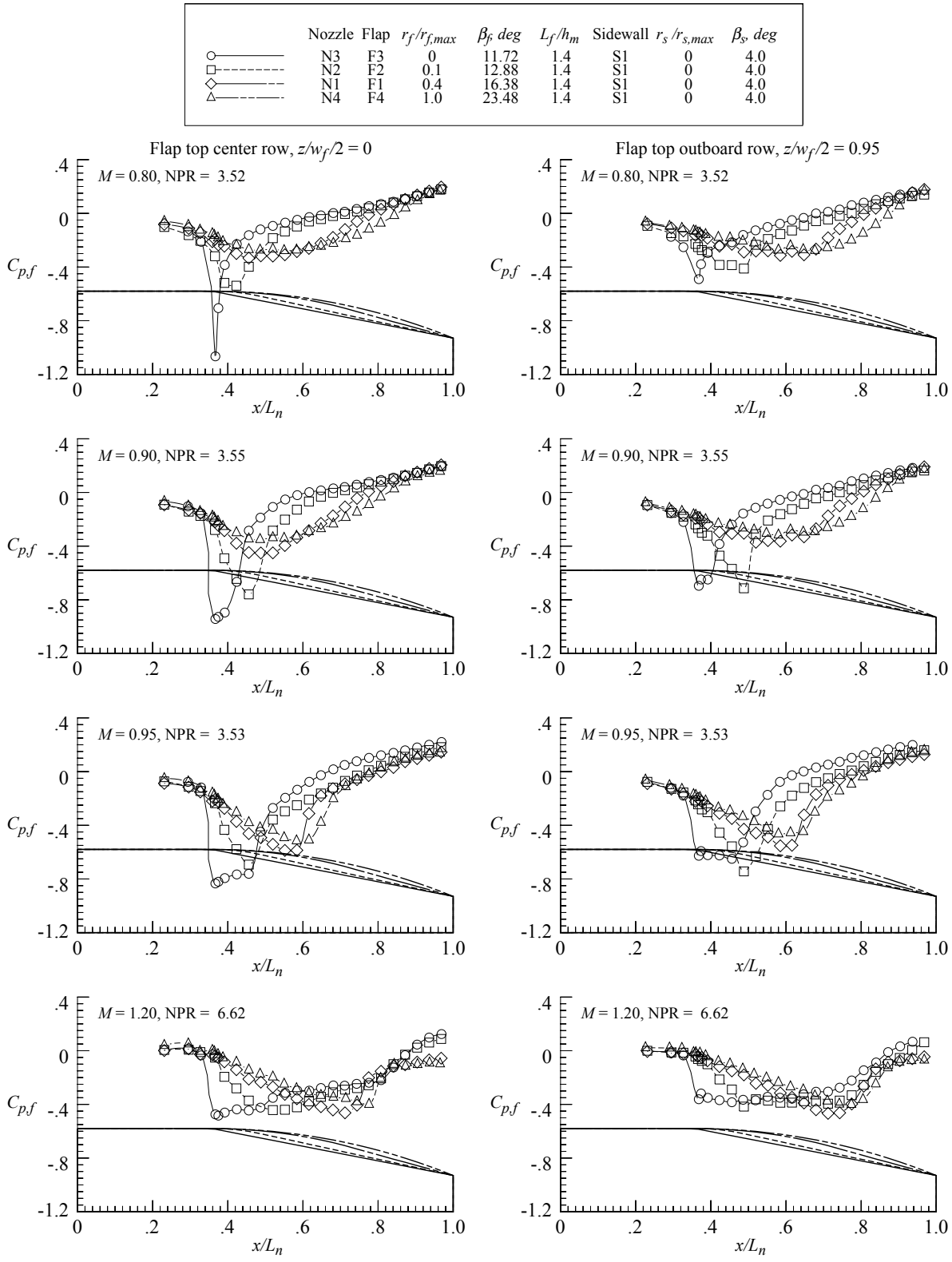

Figure 95. Effect of flap radius of curvature on upper flap pressure distributions for nozzles with sidewall S1 at scheduled NPR.

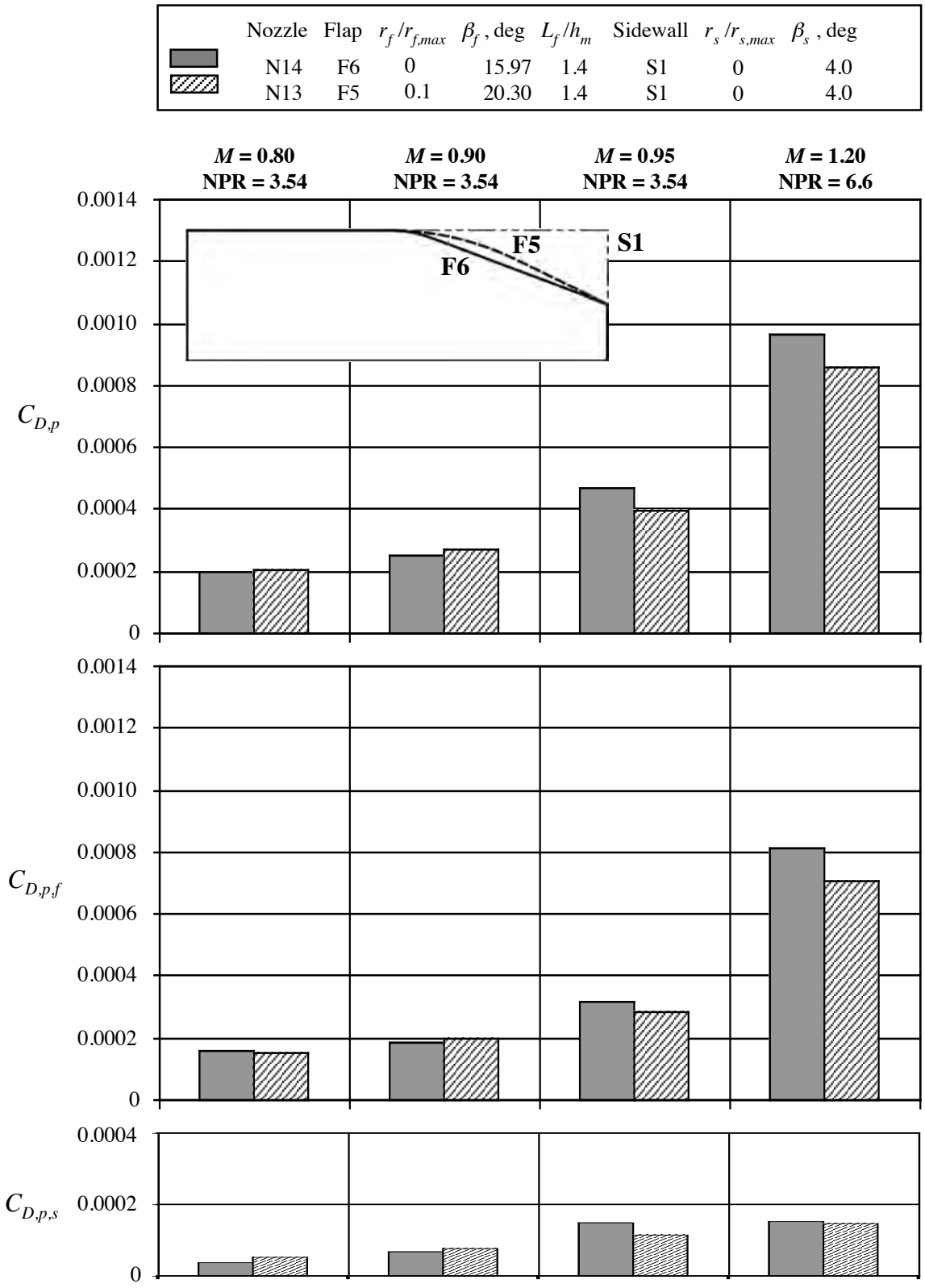

Figure 96. Effect of flap radius of curvature on pressure drag coefficients for nozzles with sidewall S1 at scheduled NPR.

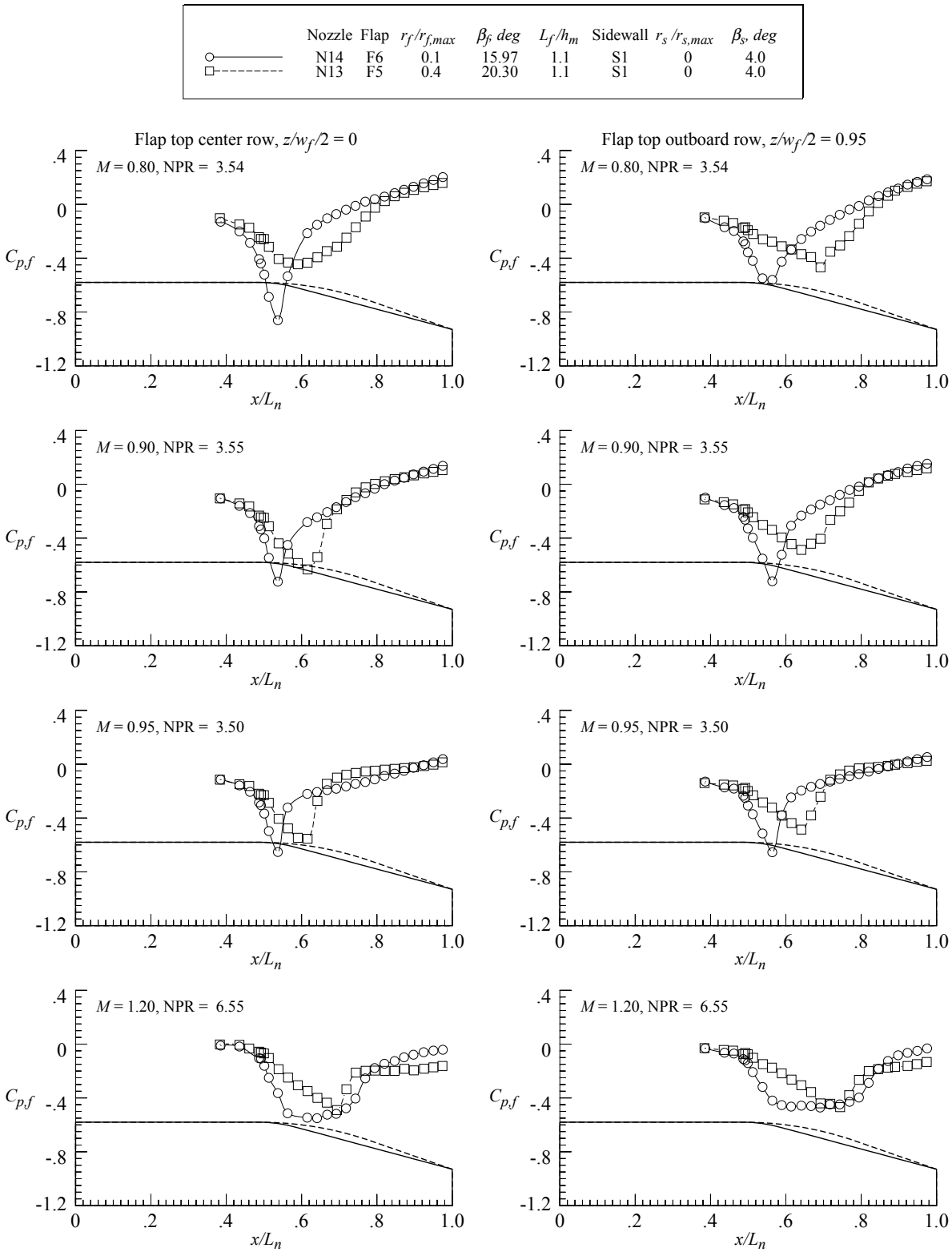

Figure 97. Effect of flap radius of curvature on upper flap pressure distributions for nozzles with sidewall S1 at scheduled NPR.

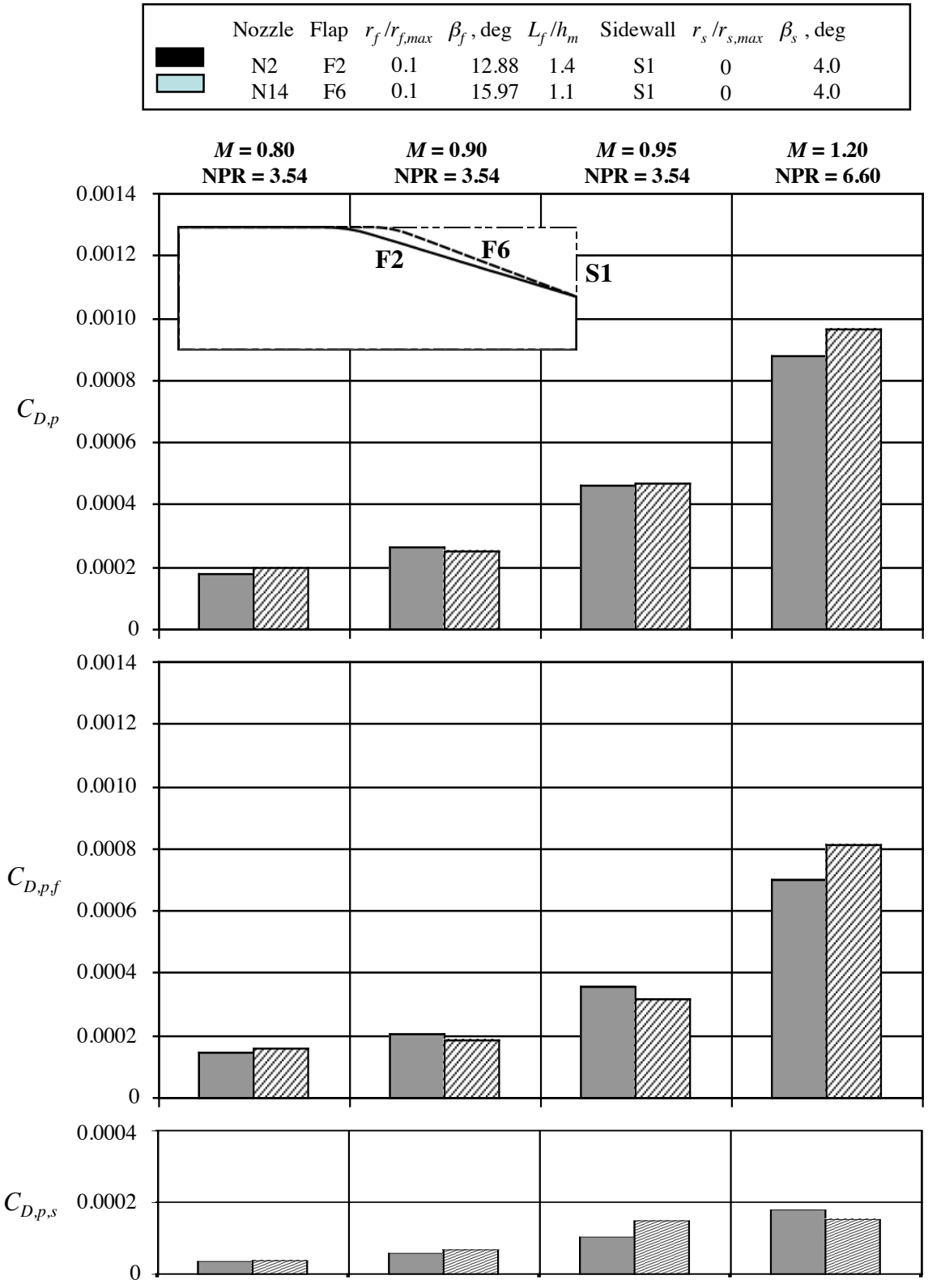

Figure 98. Effect of flap length on pressure drag coefficients for nozzles with sidewall S1 at scheduled pressure.

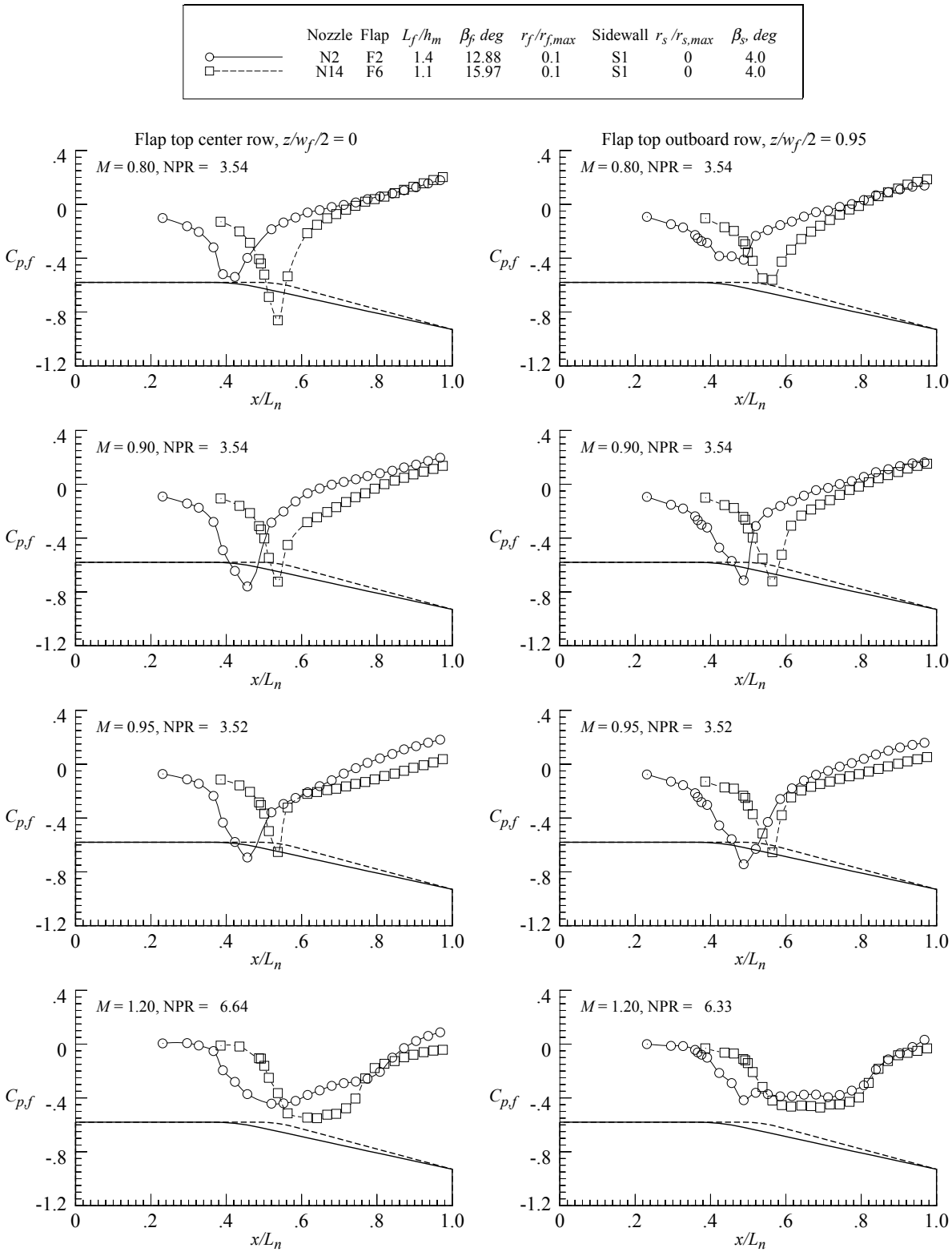

Figure 99. Effect of flap length on upper flap pressure distributions for nozzles with sidewall S1 at scheduled NPR.

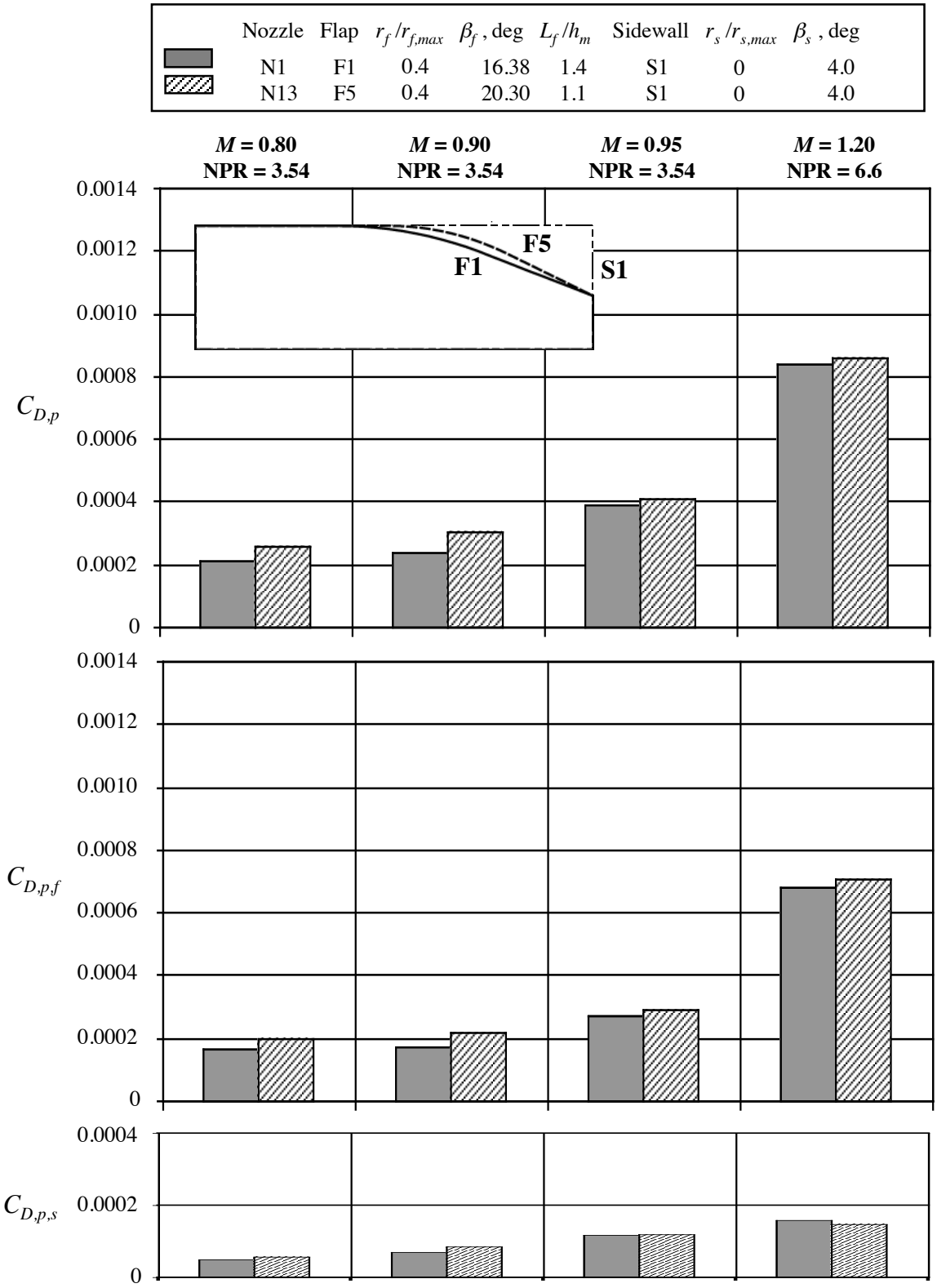

Figure 100. Effect of flap length on pressure drag coefficients for nozzles with sidewall S1 at scheduled pressure.

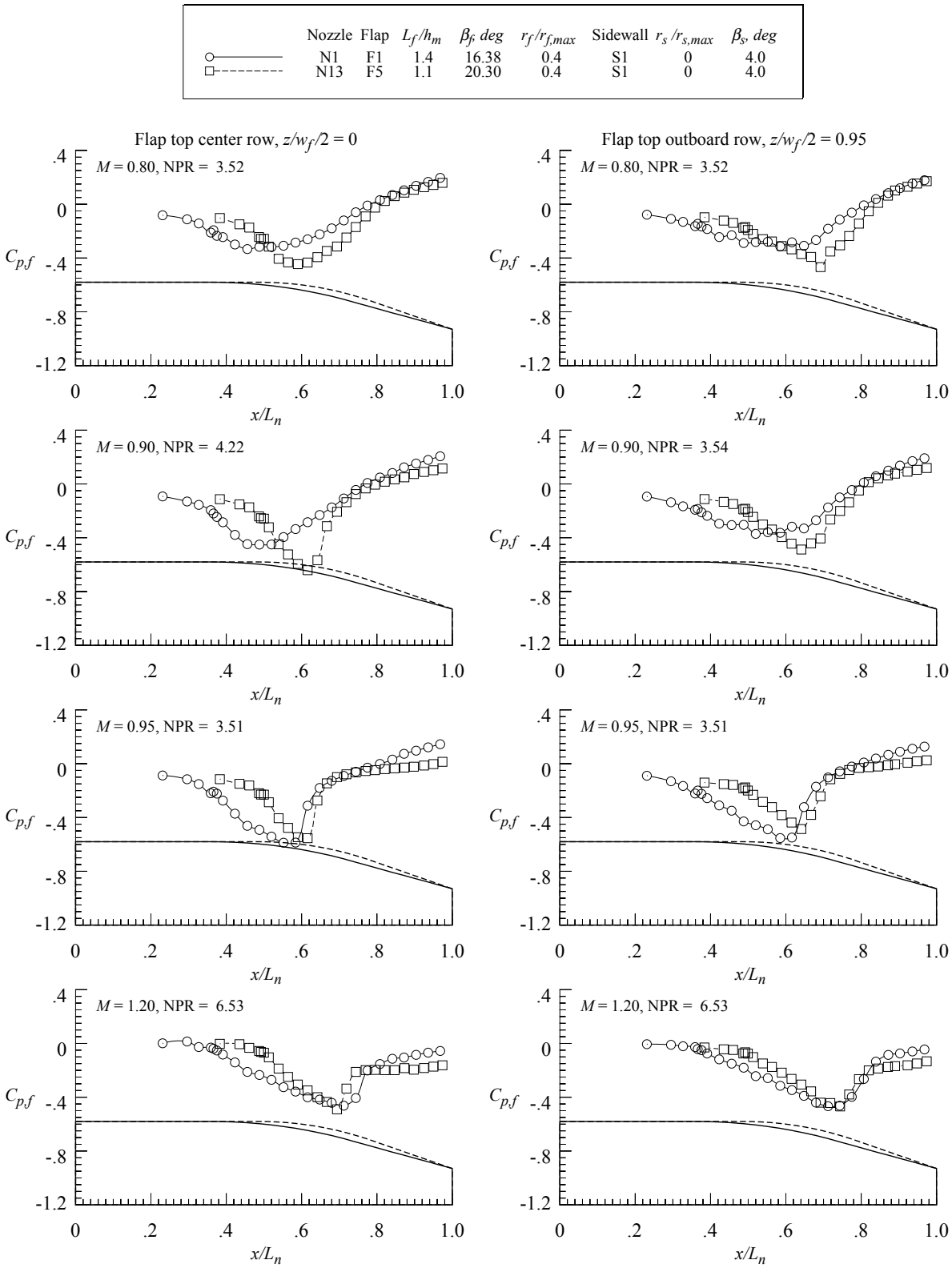

Figure 101. Effect of flap length on upper flap pressure distributions for nozzles with sidewall S1 at scheduled NPR.

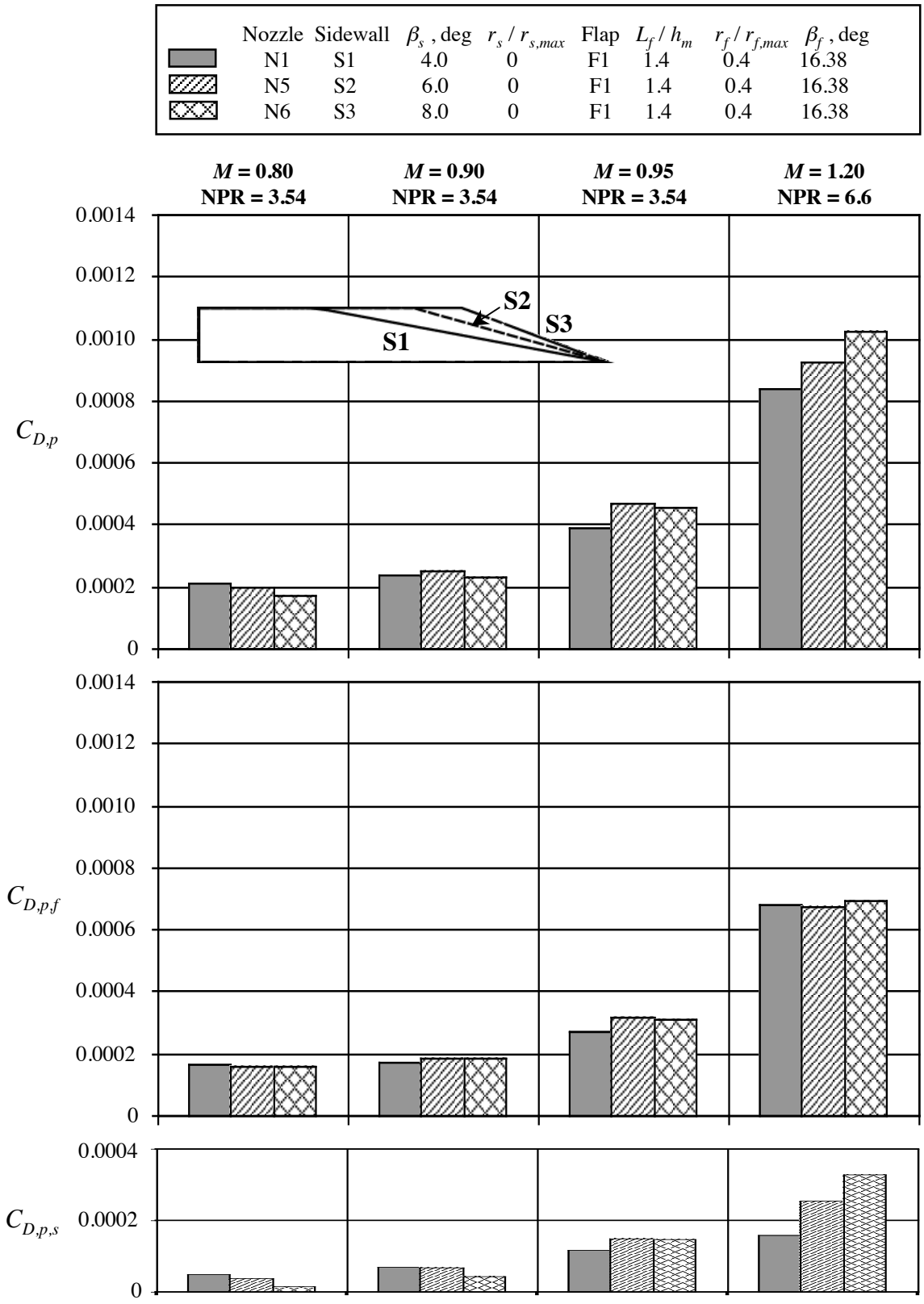

Figure 102. Effect of sidewall boattail angle on pressure drag coefficients for nozzles with flap F1 at scheduled pressure ratio.

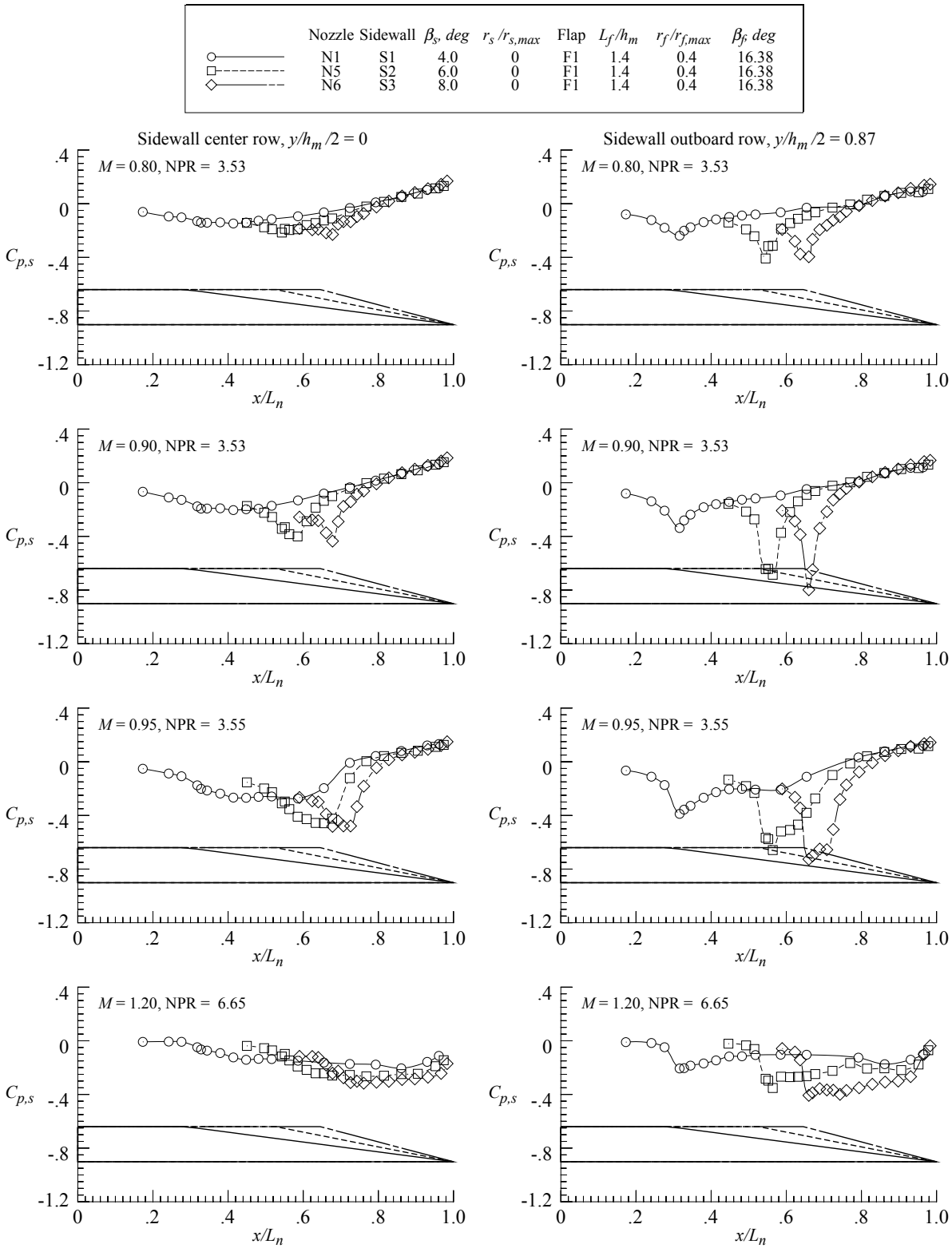

Figure 103. Effect of sidewall boattail angle on sidewall pressure distributions for nozzles with flap F1 at scheduled NPR.

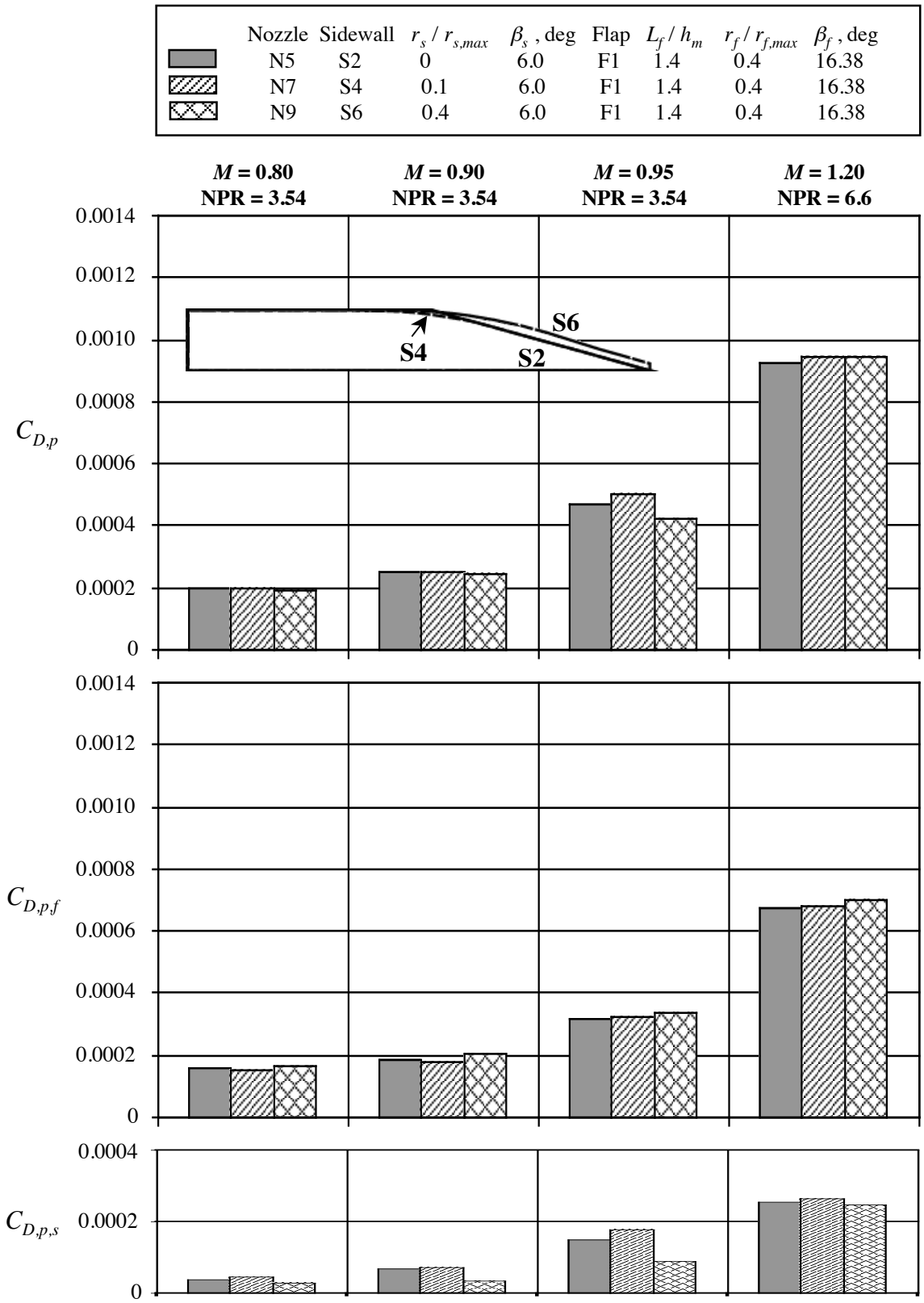

Figure 104. Effect of sidewall radius of curvature and base on pressure drag coefficients for nozzles with flap F1 at scheduled pressure ratio.

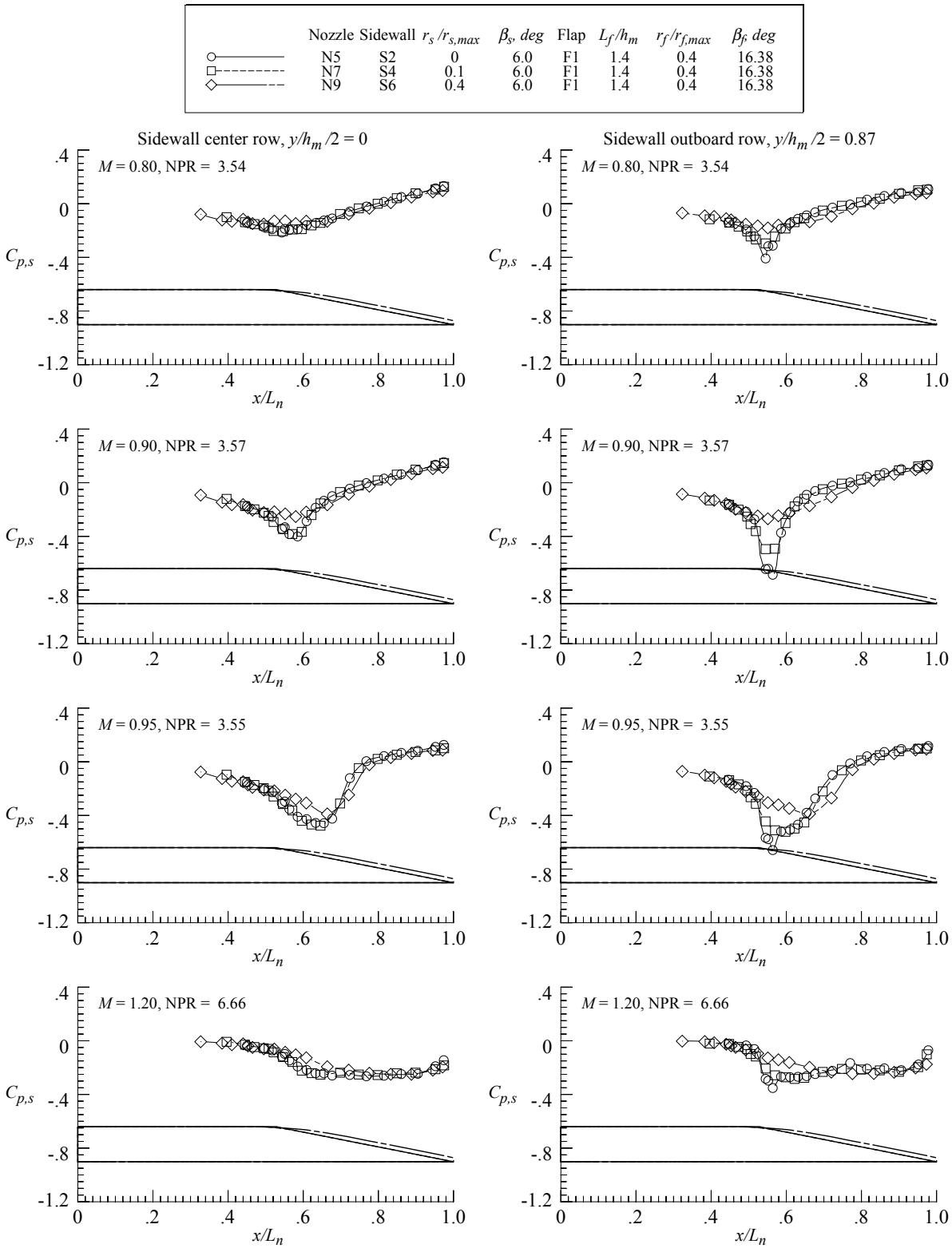

Figure 105. Effect of sidewall radius of curvature and base on sidewall pressure distributions for nozzles with. flap F1 at scheduled NPR.

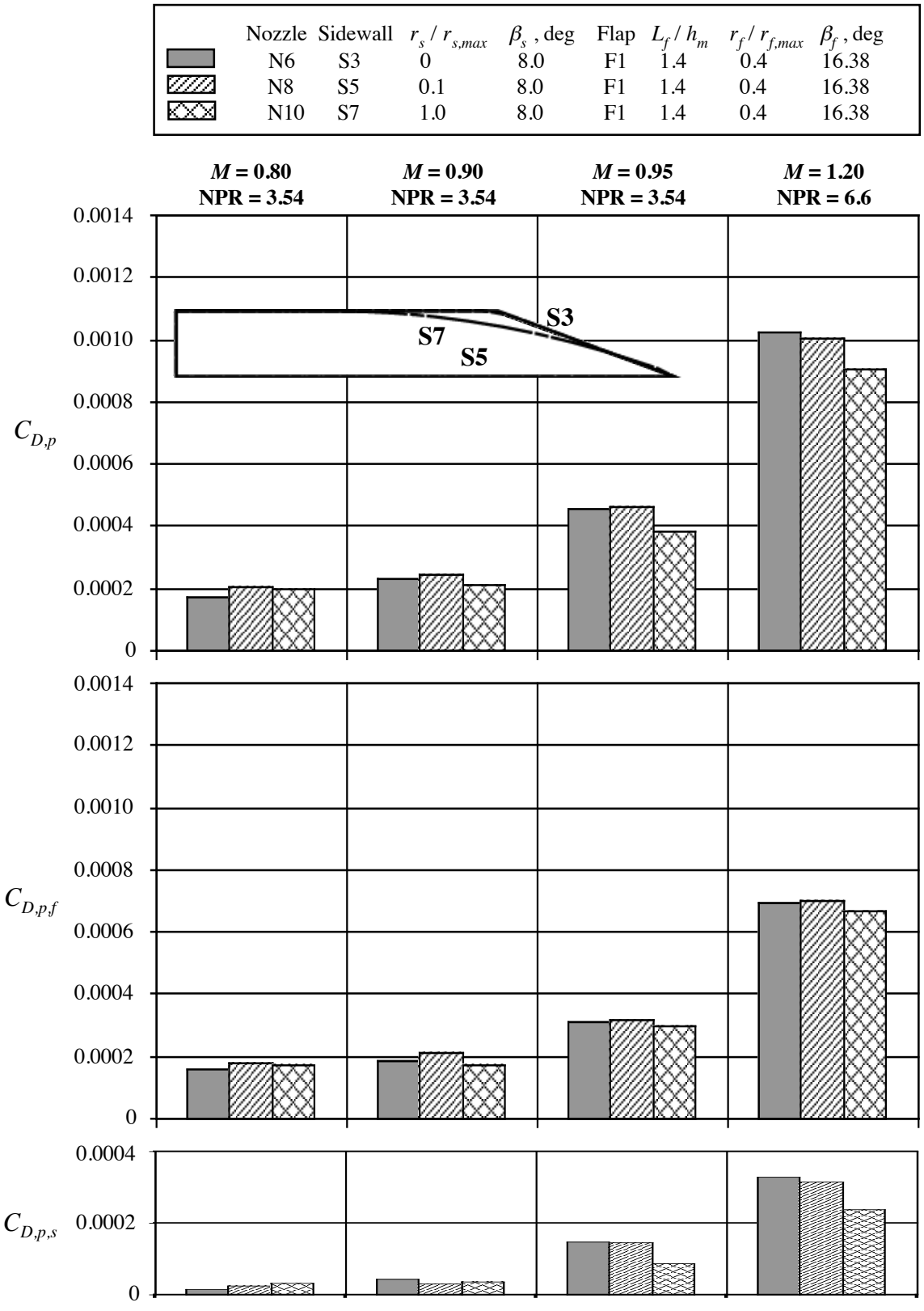

Figure 106. Effect of sidewall radius of curvature on pressure drag coefficients for nozzles with flap F1 at scheduled pressure ratio.

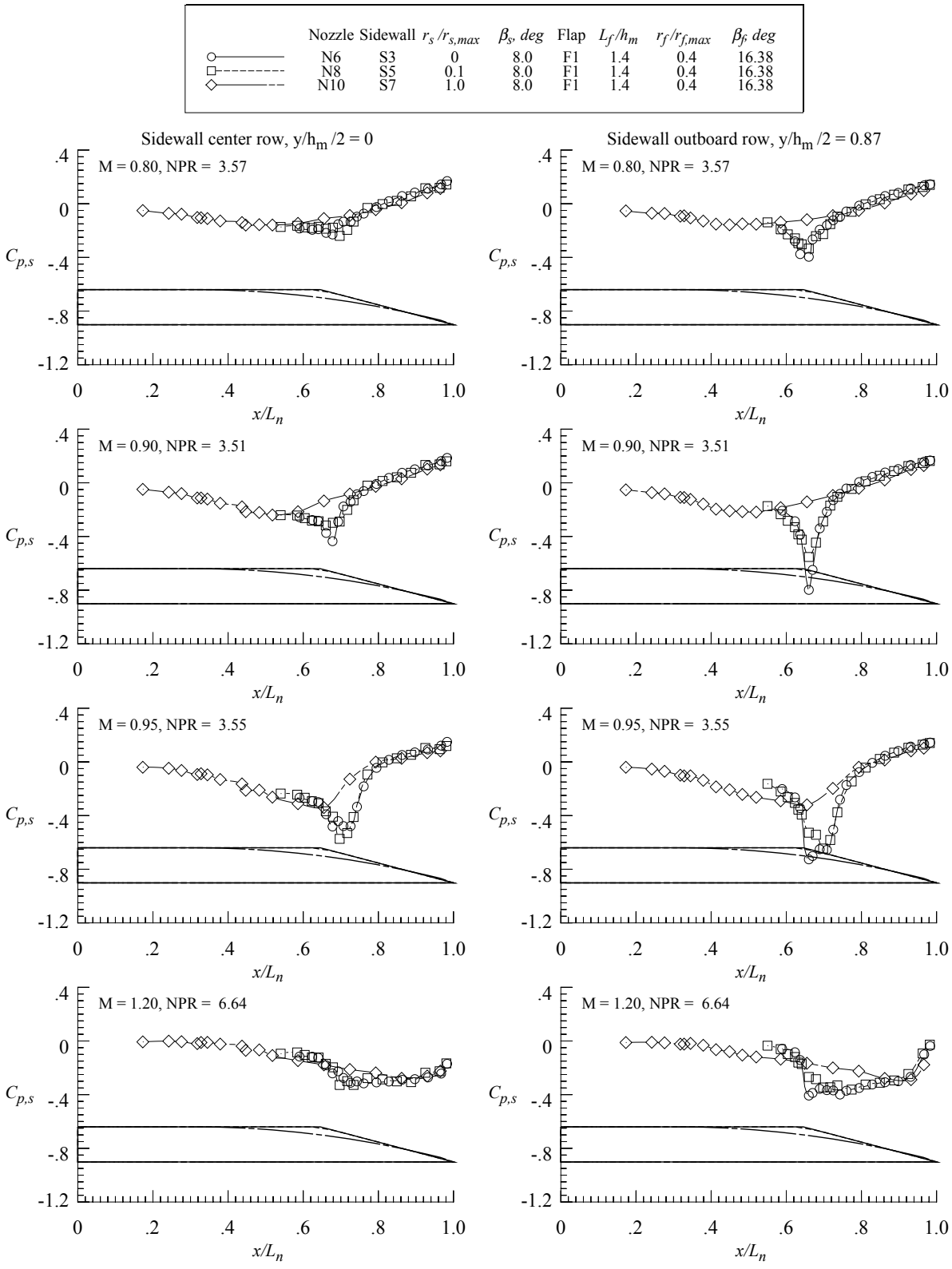

Figure 107. Effect of sidewall radius of curvature on sidewall pressure distributions for nozzles with flap F1 at scheduled NPR.

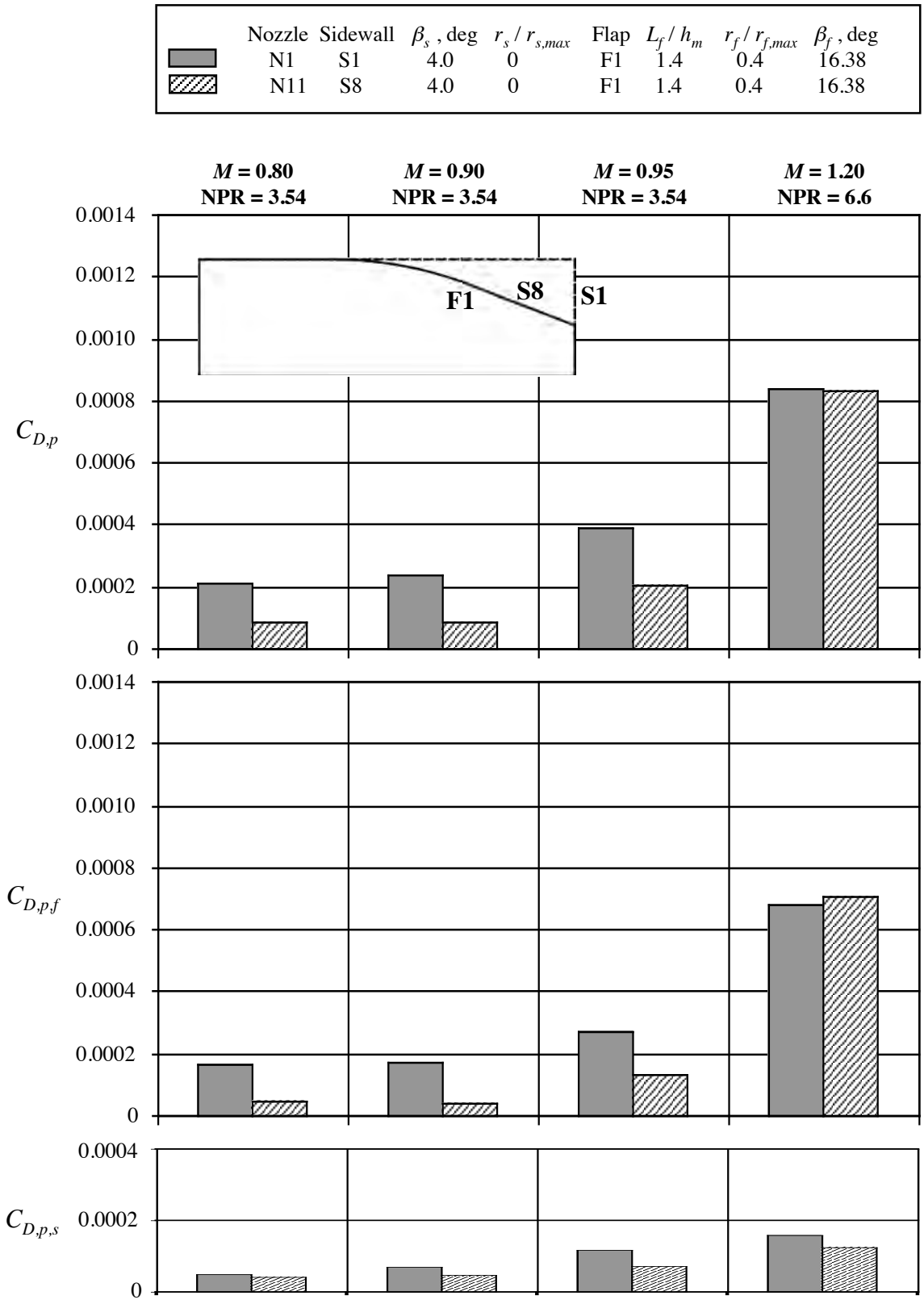

Figure 108. Effect of reduced sidewall height on pressure drag coefficients for nozzles with flap F1 at scheduled pressure ratio.

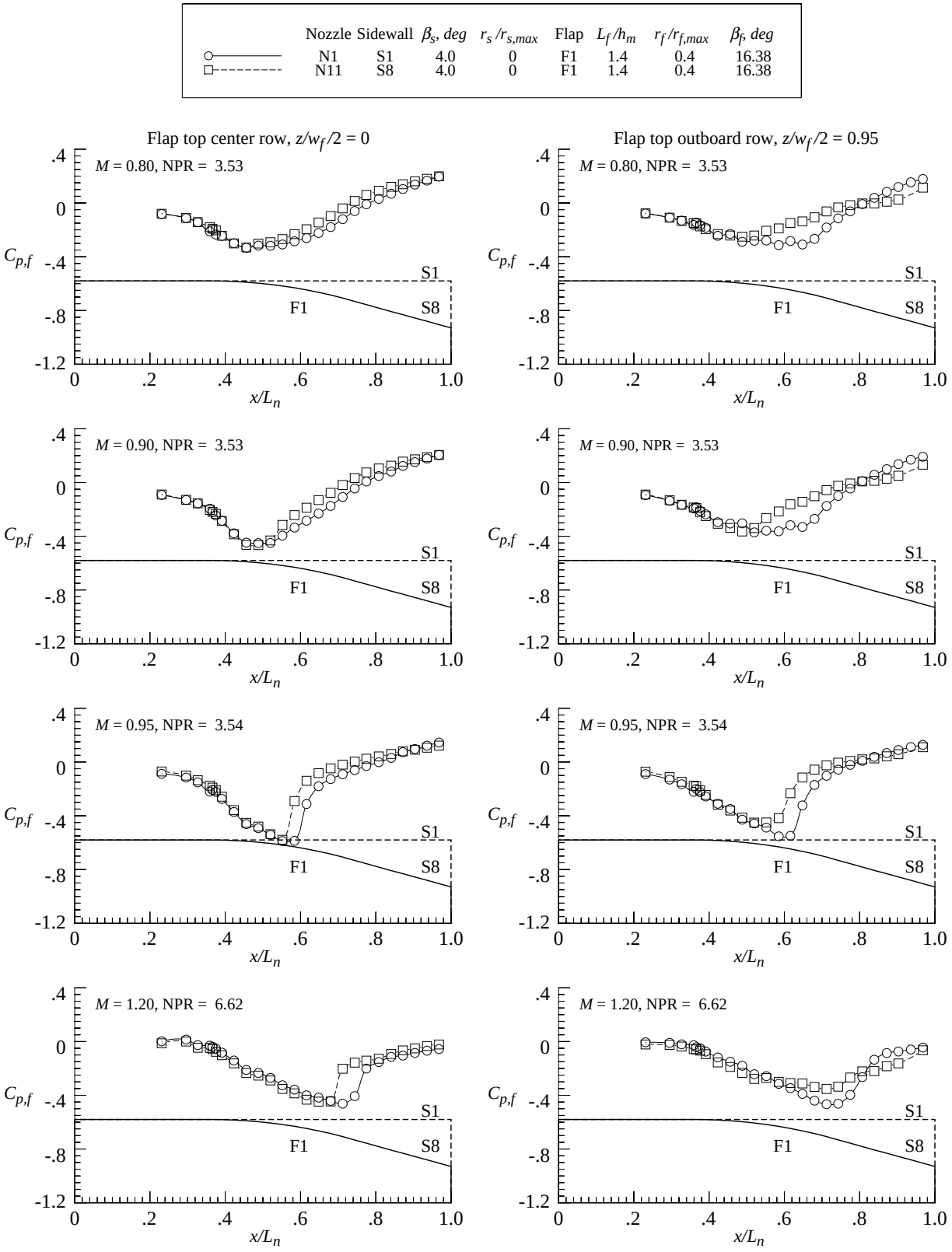

Figure 109. Effect of reduced sidewall height on nozzle pressure distributions for nozzles with flap F1 at scheduled NPR.

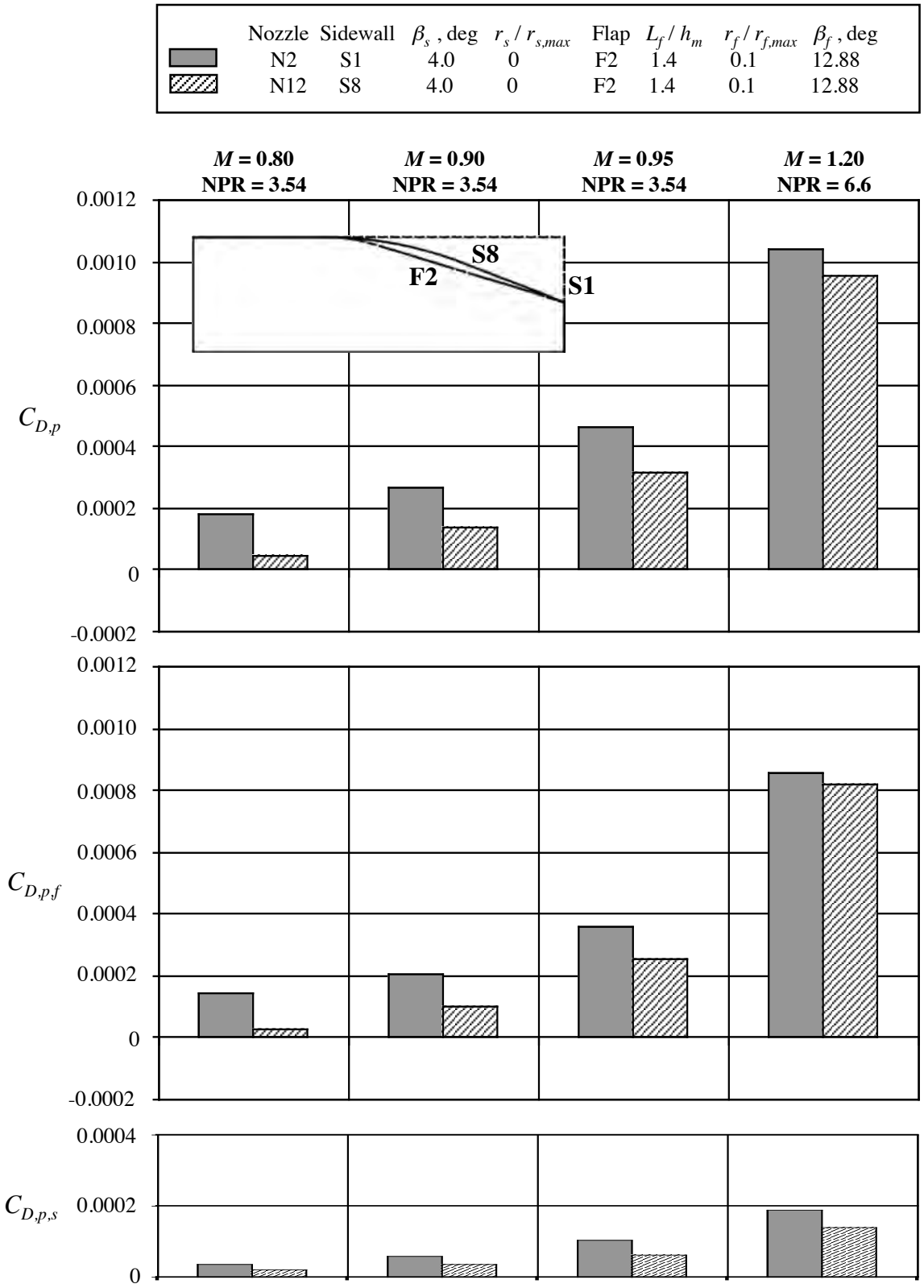

Figure 110. Effect of reduced sidewall height on pressure drag coefficients for nozzles with flap F2 at scheduled pressure ratio.

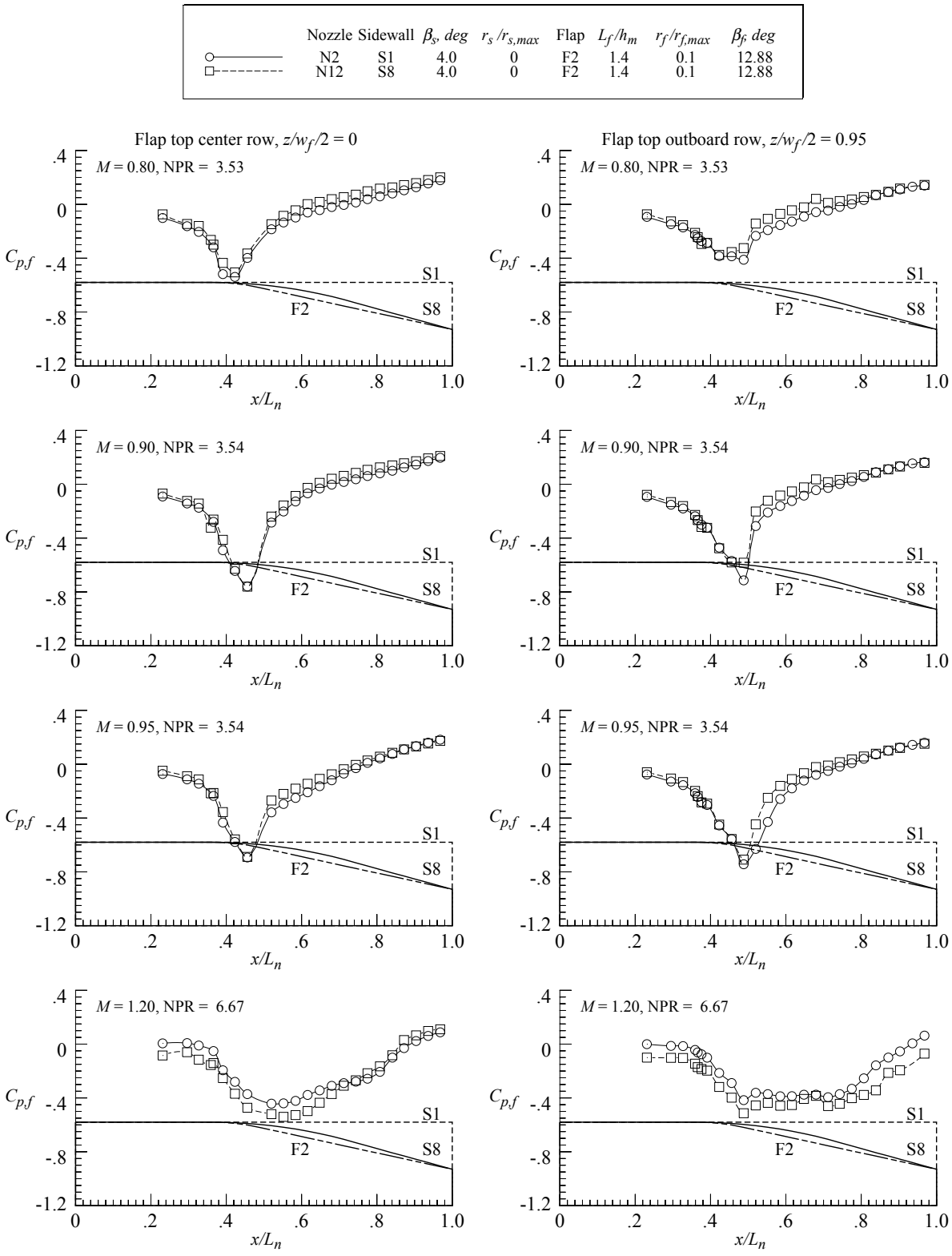

Figure 111. Effect of reduced sidewall height on nozzle pressure distributions for nozzles with flap F2 at scheduled NPR.

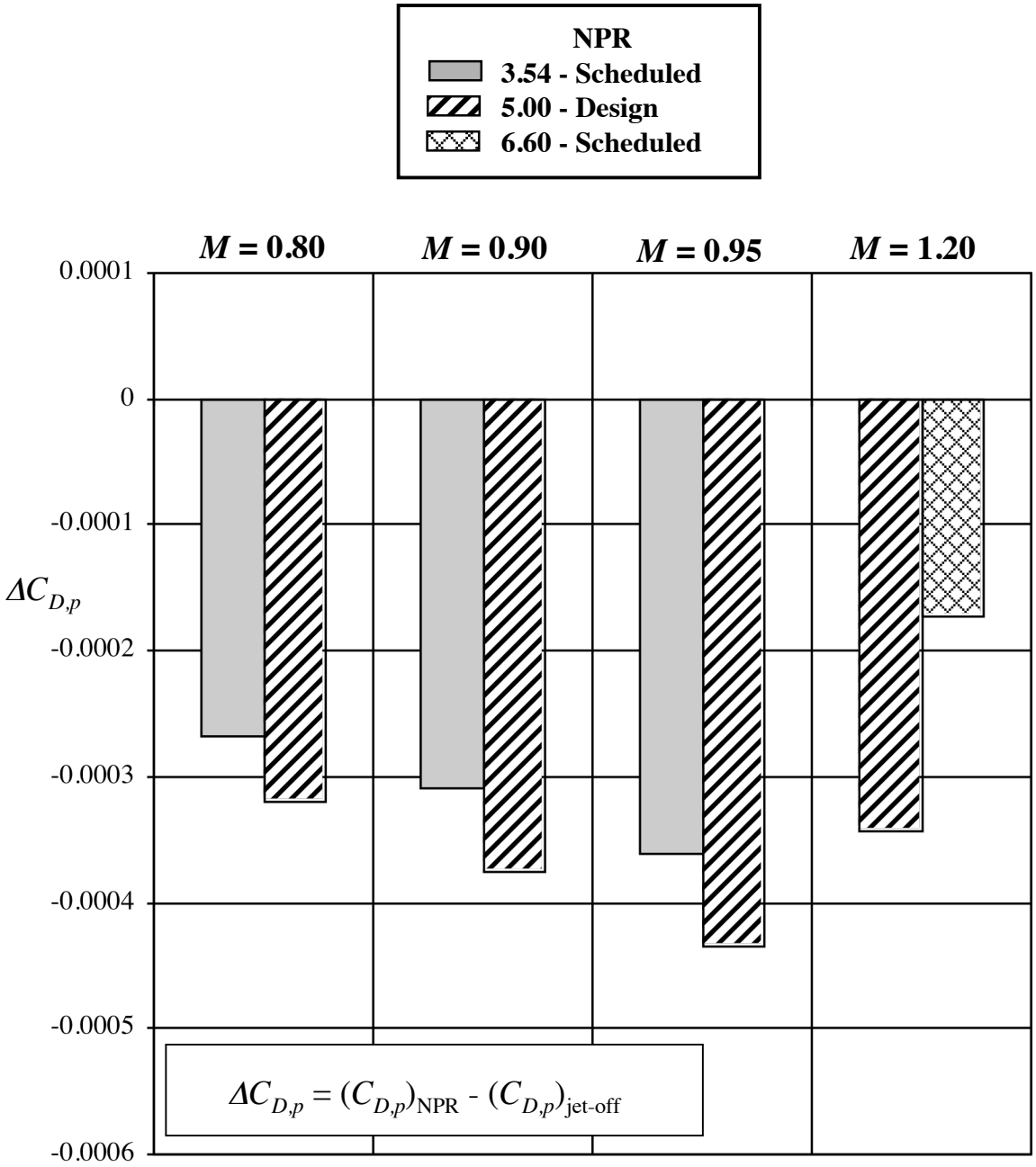

Figure 112. Incremental nozzle pressure drag for nozzle N1 with flap F1 and sidewall S1. $r_f / r_{f,max} = 0.4$; $\beta_f = 16.38°$; $L_f / h_m = 1.4$: $\beta_s = 4.0°$; $r_s / r_{s,max} = 0$.

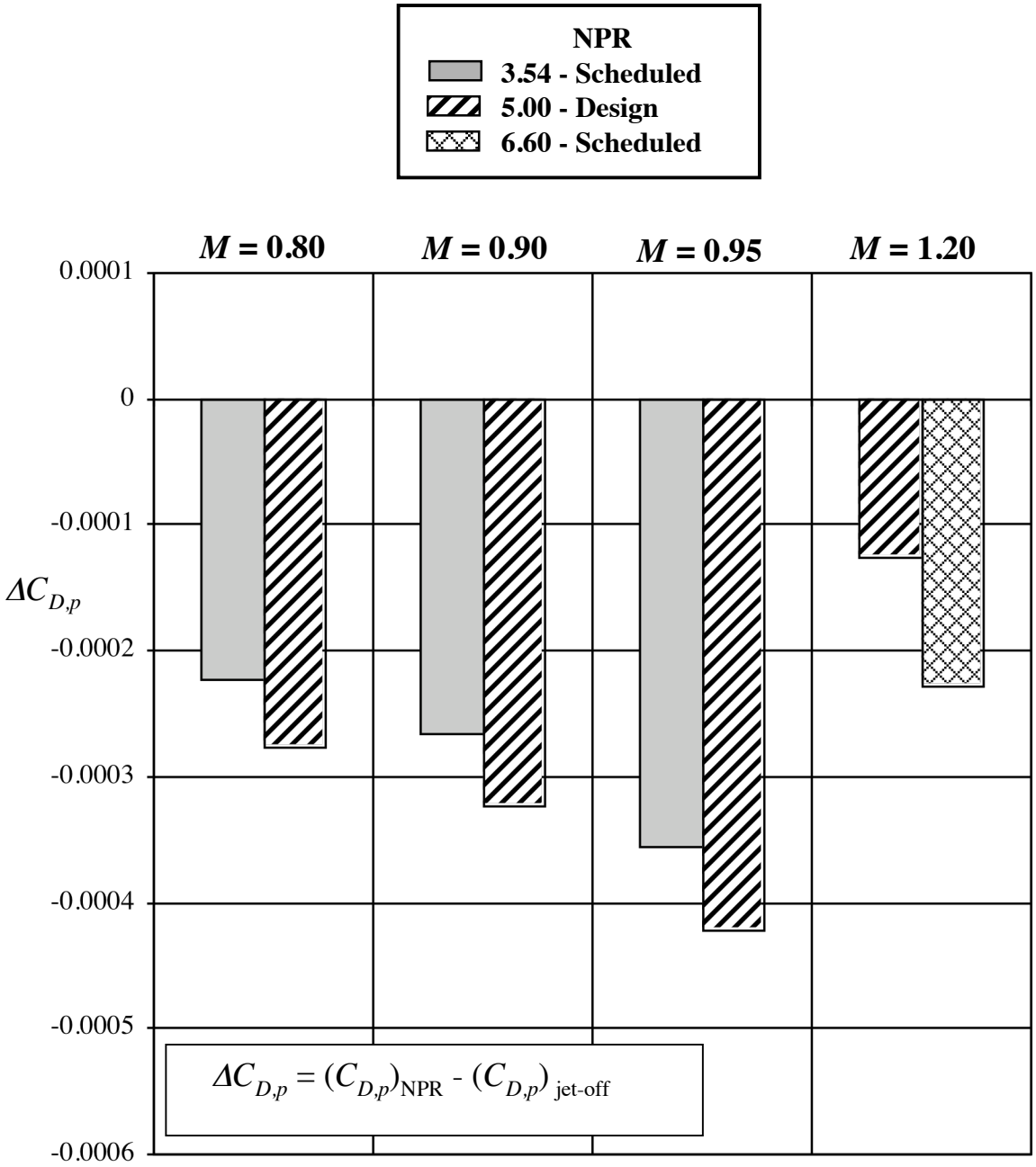

Figure 113. Incremental nozzle pressure drag for nozzle N2 with flap F2 and sidewall S1. $r_f / r_{f,max} = 0.1$; $\beta_f = 12.88°$; $L_f / h_m = 1.4$: $\beta_s = 4.0°$; $r_s / r_{s,max} = 0$.

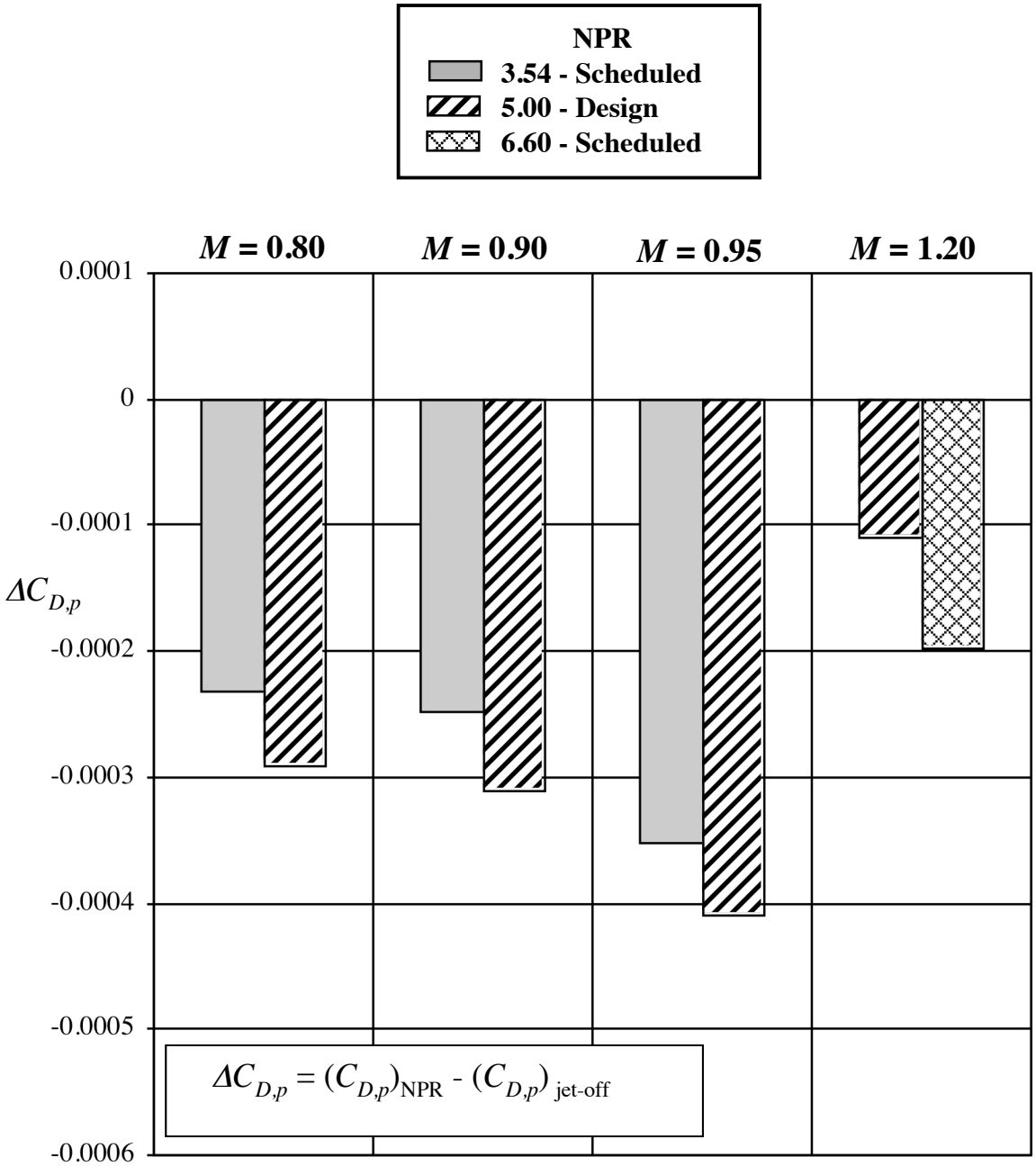

Figure 114. Incremental nozzle pressure drag for nozzle N3 with flap F3 and sidewall S1. $r_f / r_{f,max} = 0$; $\beta_f = 11.72°$; $L_f / h_m = 1.4$: $\beta_s = 4.0°$; $r_s / r_{s,max} = 0$.

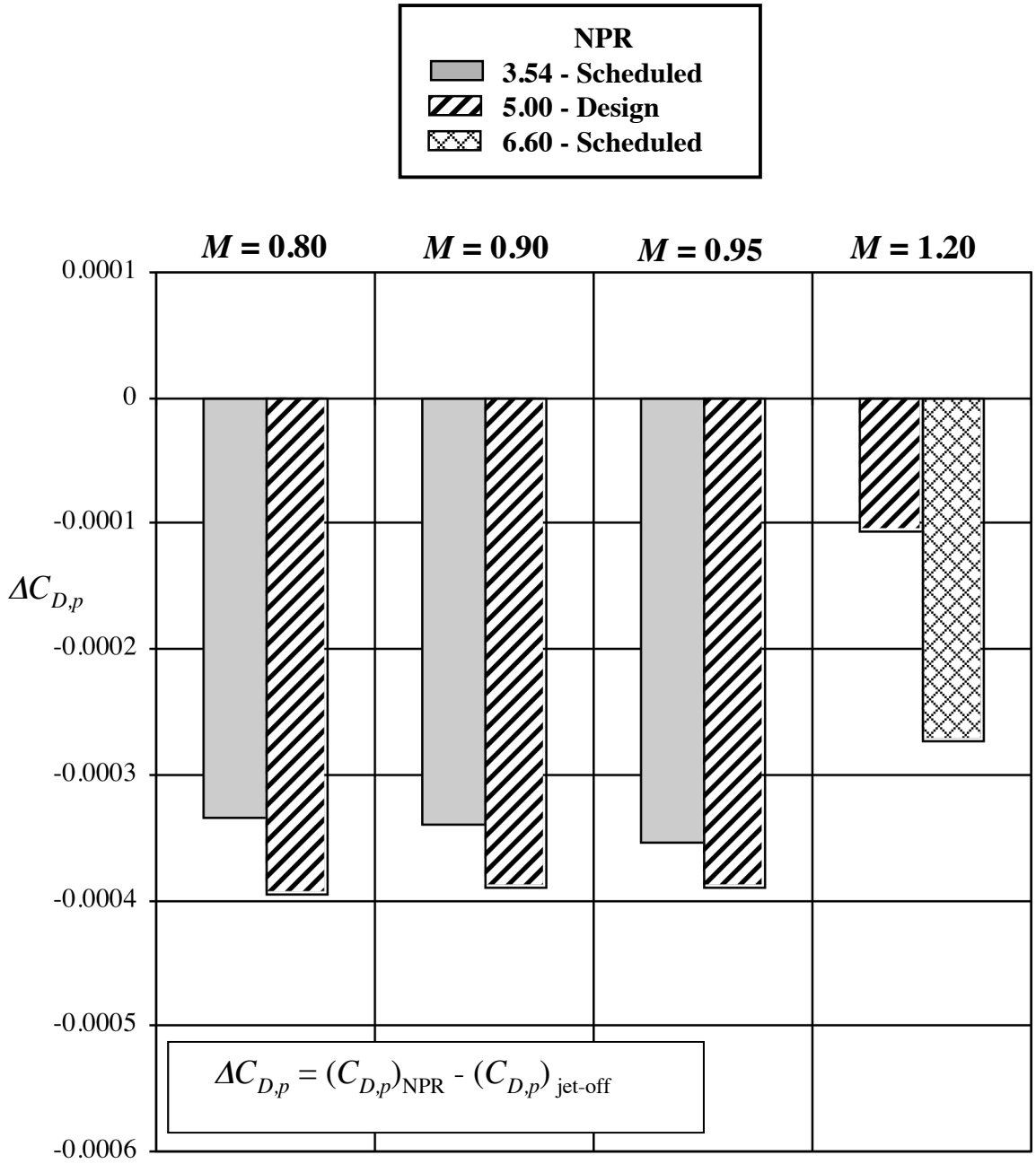

Figure 115. Incremental nozzle pressure drag for nozzle N4 with flap F4 and sidewall S1. $r_f / r_{f,max} = 1.0$; $\beta_f = 23.44°$; $L_f / h_m = 1.4$: $\beta_s = 4.0°$; $r_s / r_{s,max} = 0$.

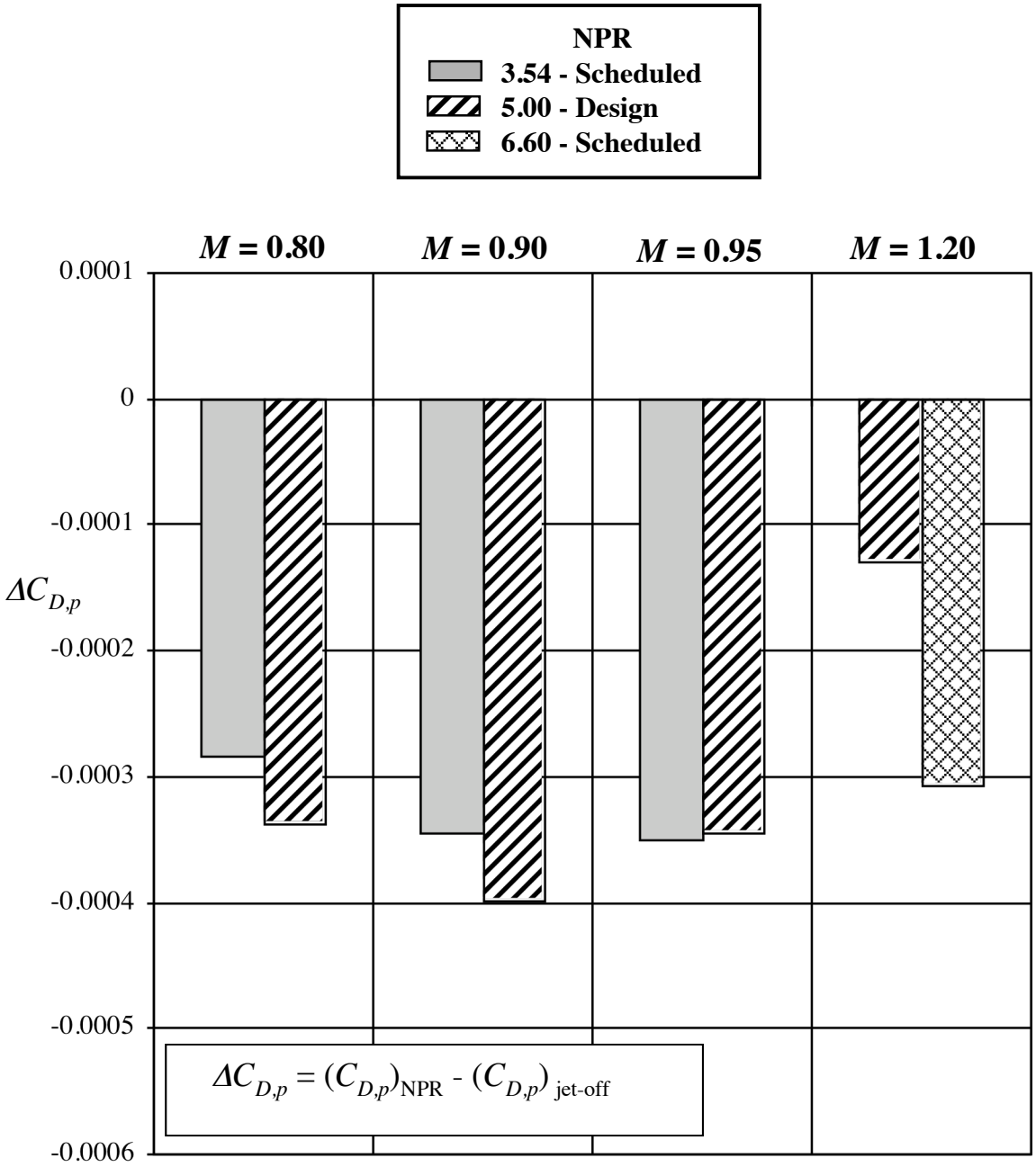

Figure 116. Incremental nozzle pressure drag for nozzle N5 with flap F1 and sidewall S2. $r_f / r_{f,max} = 0.4$; $\beta_f = 16.38°$; $L_f / h_m = 1.4$: $\beta_s = 6.0°$; $r_s / r_{s,max} = 0$.

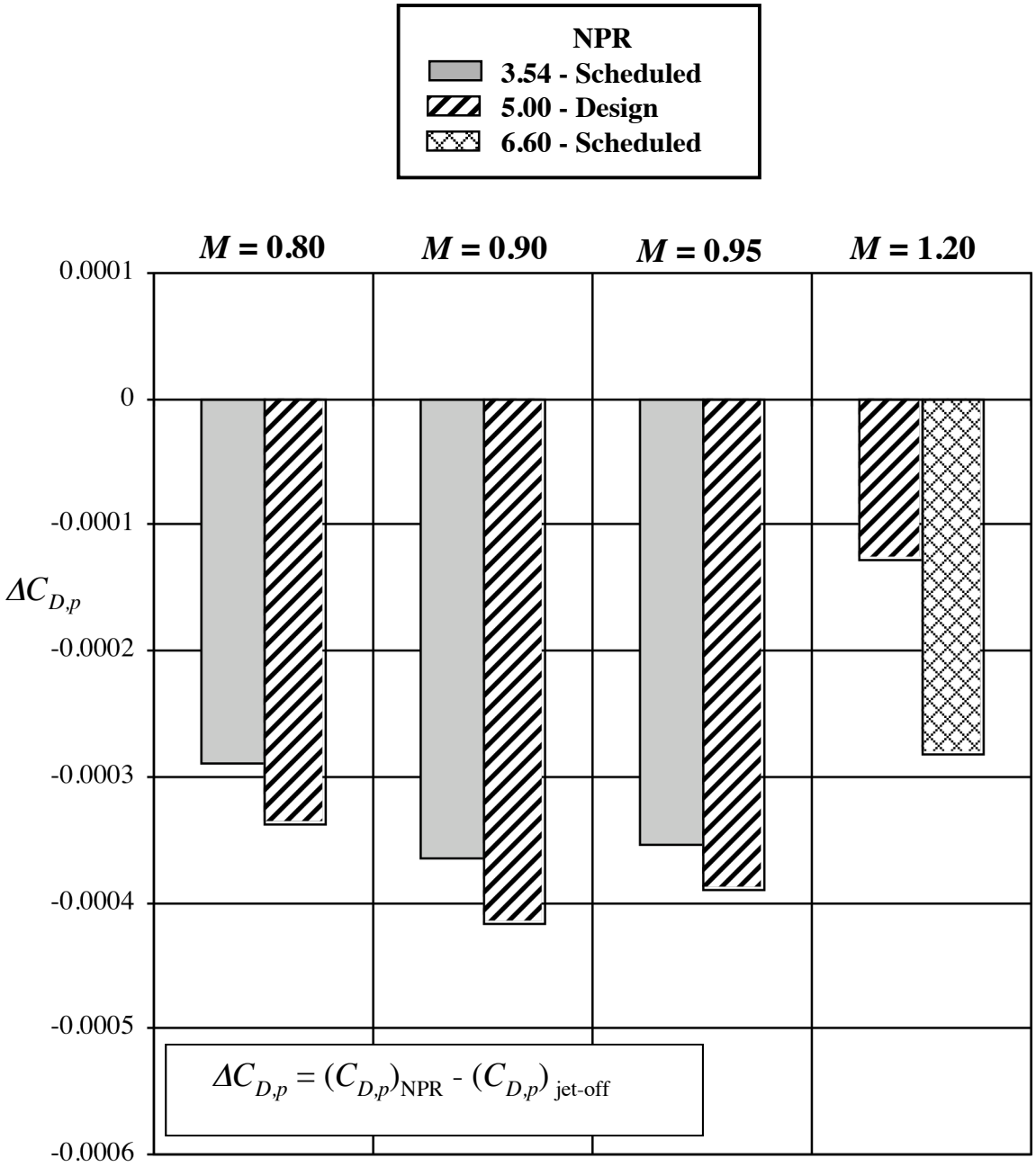

Figure 117. Incremental nozzle pressure drag for nozzle N6 with flap F1 and sidewall S3. $r_f / r_{f,max} = 0.4$; $\beta_f = 16.38°$; $L_f / h_m = 1.4$: $\beta_s = 8.0°$; $r_s / r_{s,max} = 0$.

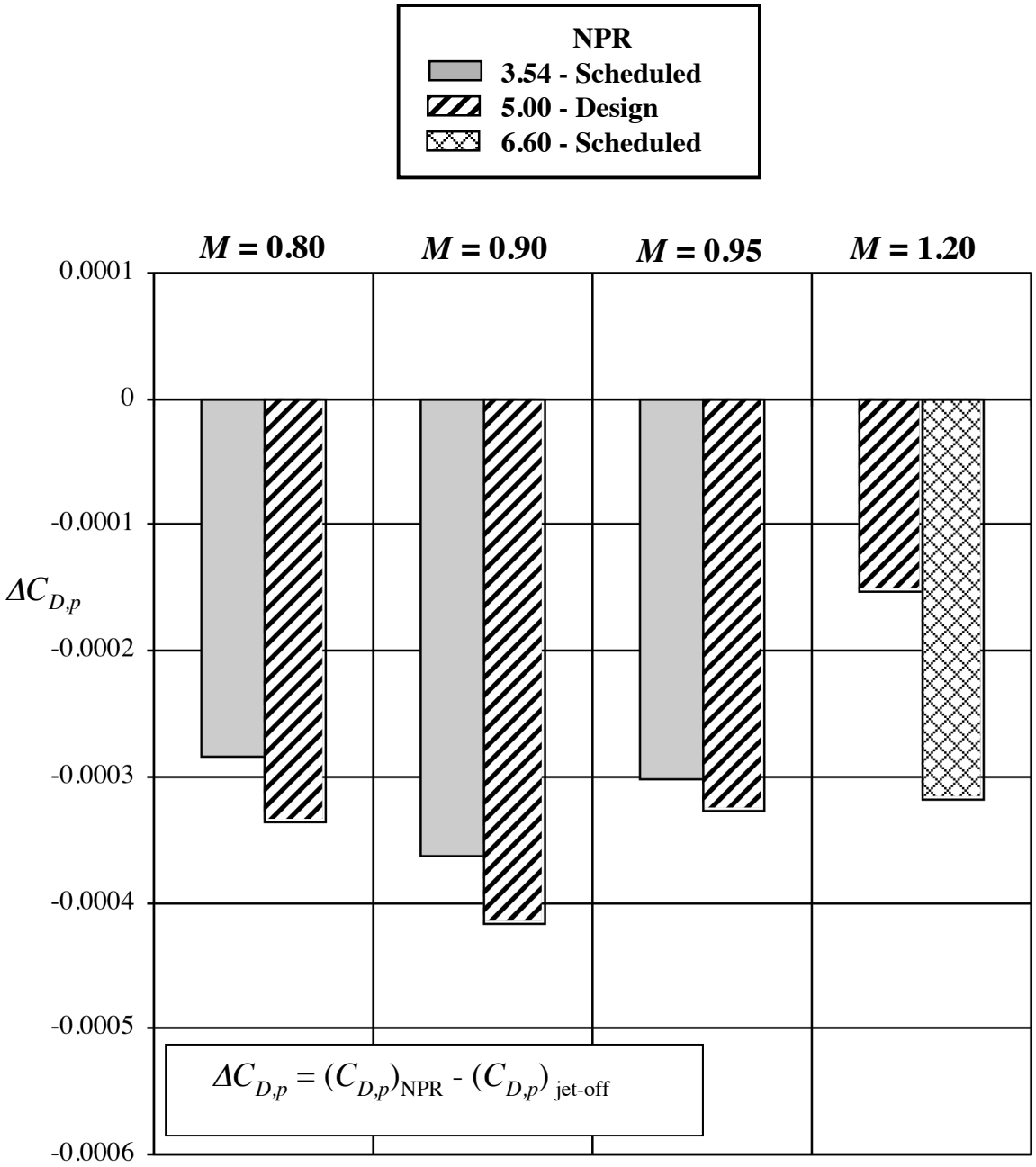

Figure 118. Incremental nozzle pressure drag for nozzle N7 with flap F1 and sidewall S4. $r_f / r_{f,max} = 0.4$; $\beta_f = 16.38°$; $L_f / h_m = 1.4$: $\beta_s = 6.0°$; $r_s / r_{s,max} = 0.1$.

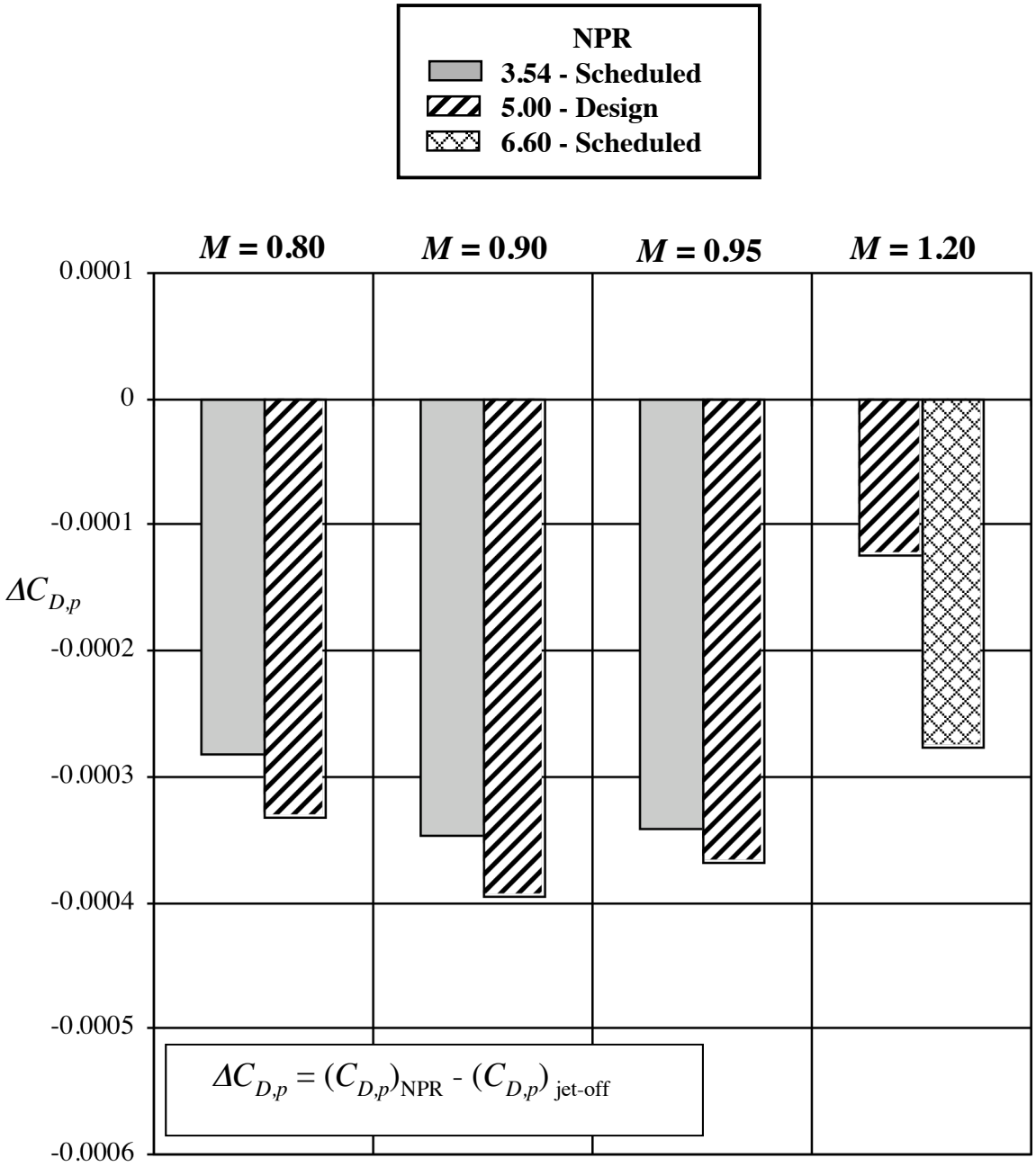

Figure 119. Incremental nozzle pressure drag for nozzle N8 with flap F1 and sidewall S5. $r_f / r_{f,max} = 0.4$; $\beta_f = 16.38°$; $L_f / h_m = 1.4$: $\beta_s = 8.0°$; $r_s / r_{s,max} = 0.1$.

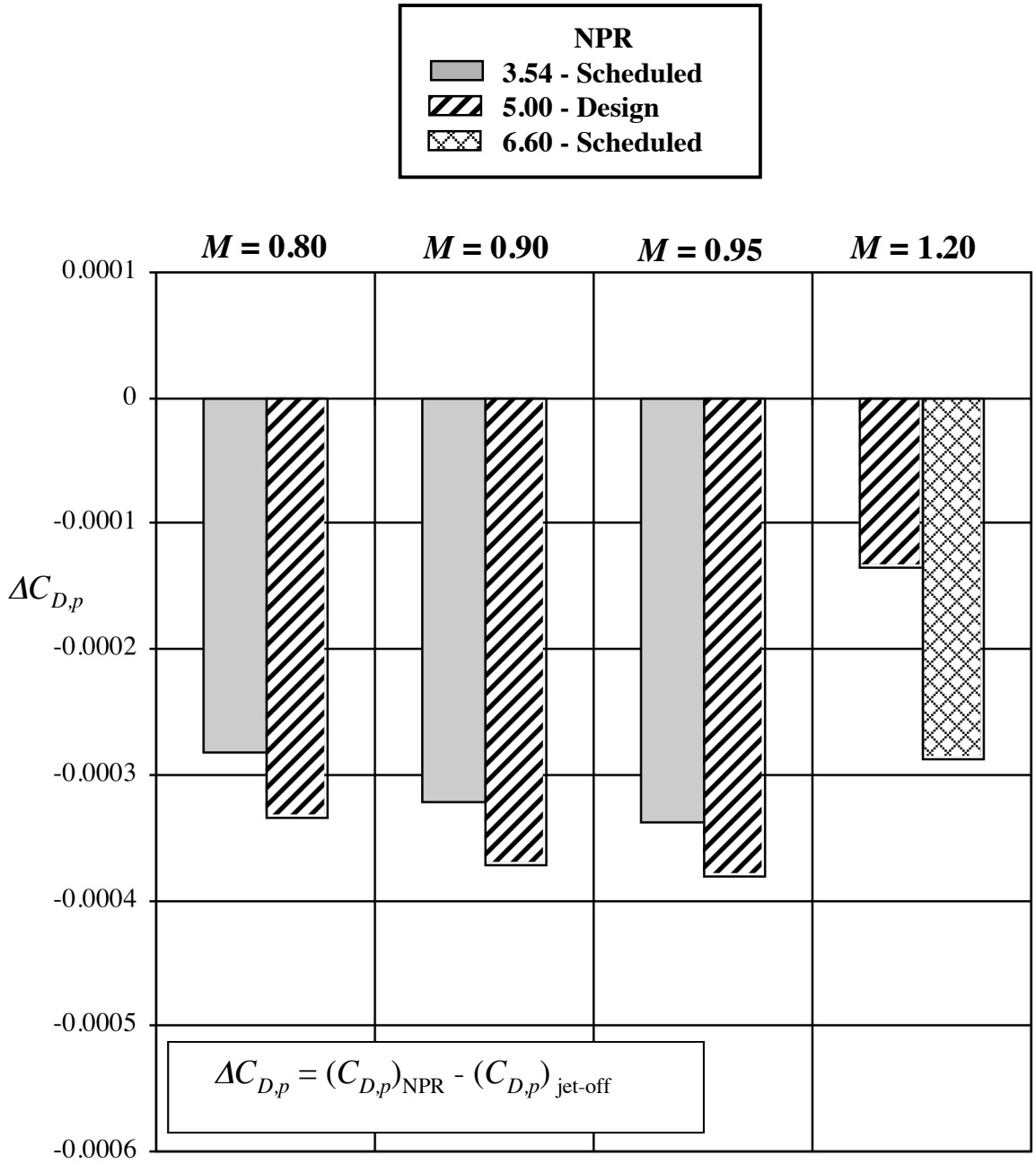

Figure 120. Incremental nozzle pressure drag for nozzle N9 with flap F1 and sidewall S6. $r_f / r_{f,max} = 0.4$; $\beta_f = 16.38°$; $L_f / h_m = 1.4$: $\beta_s = 6.0°$; $r_s / r_{s,max} = 0.4$.

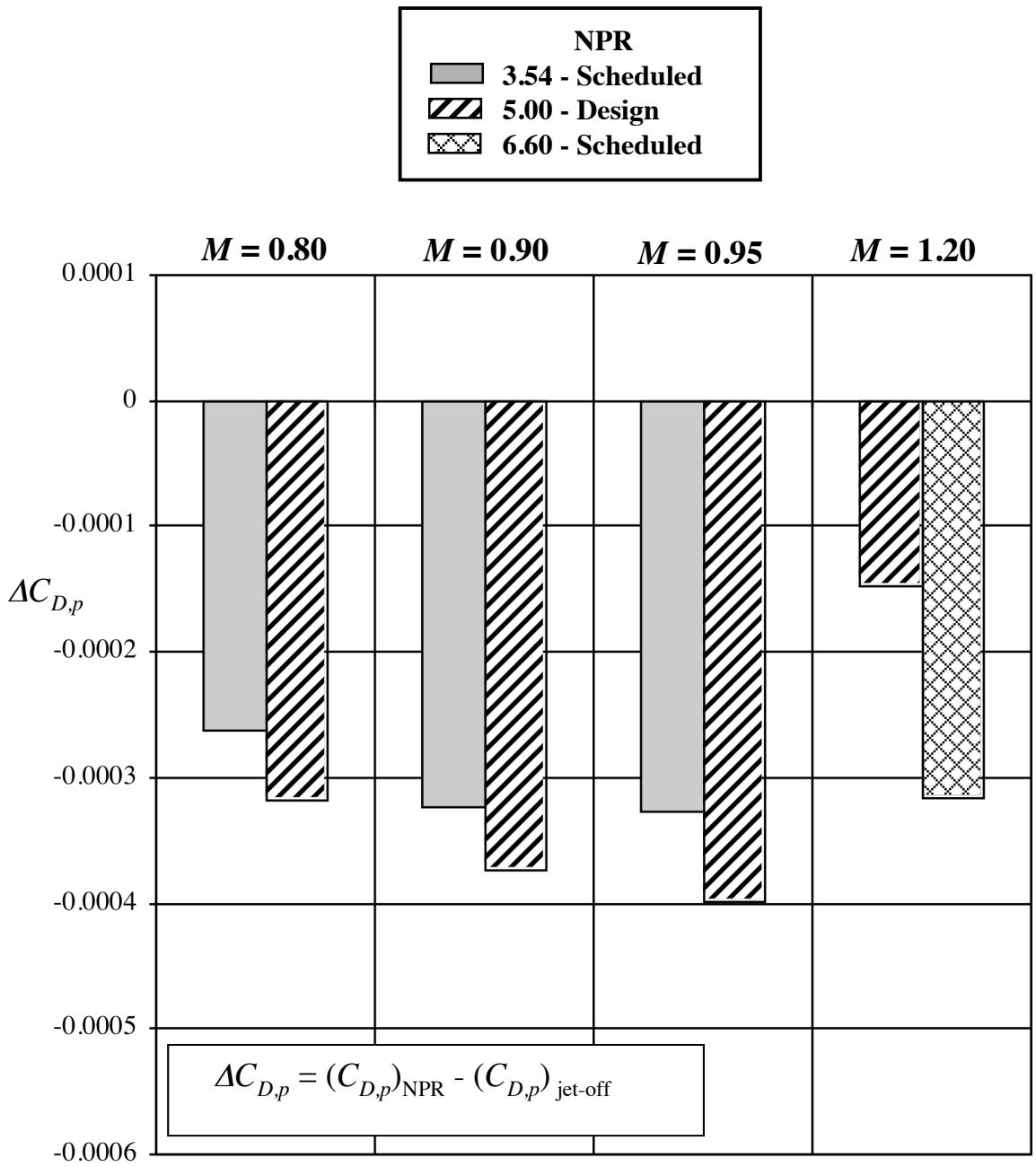

Figure 121. Incremental nozzle pressure drag for nozzle N10 with flap F1 and sidewall S7. $r_f / r_{f,max} = 0.4$; $\beta_f = 16.38°$; $L_f / h_m = 1.4$: $\beta_s = 8.0°$; $r_s / r_{s,max} = 1.0$.

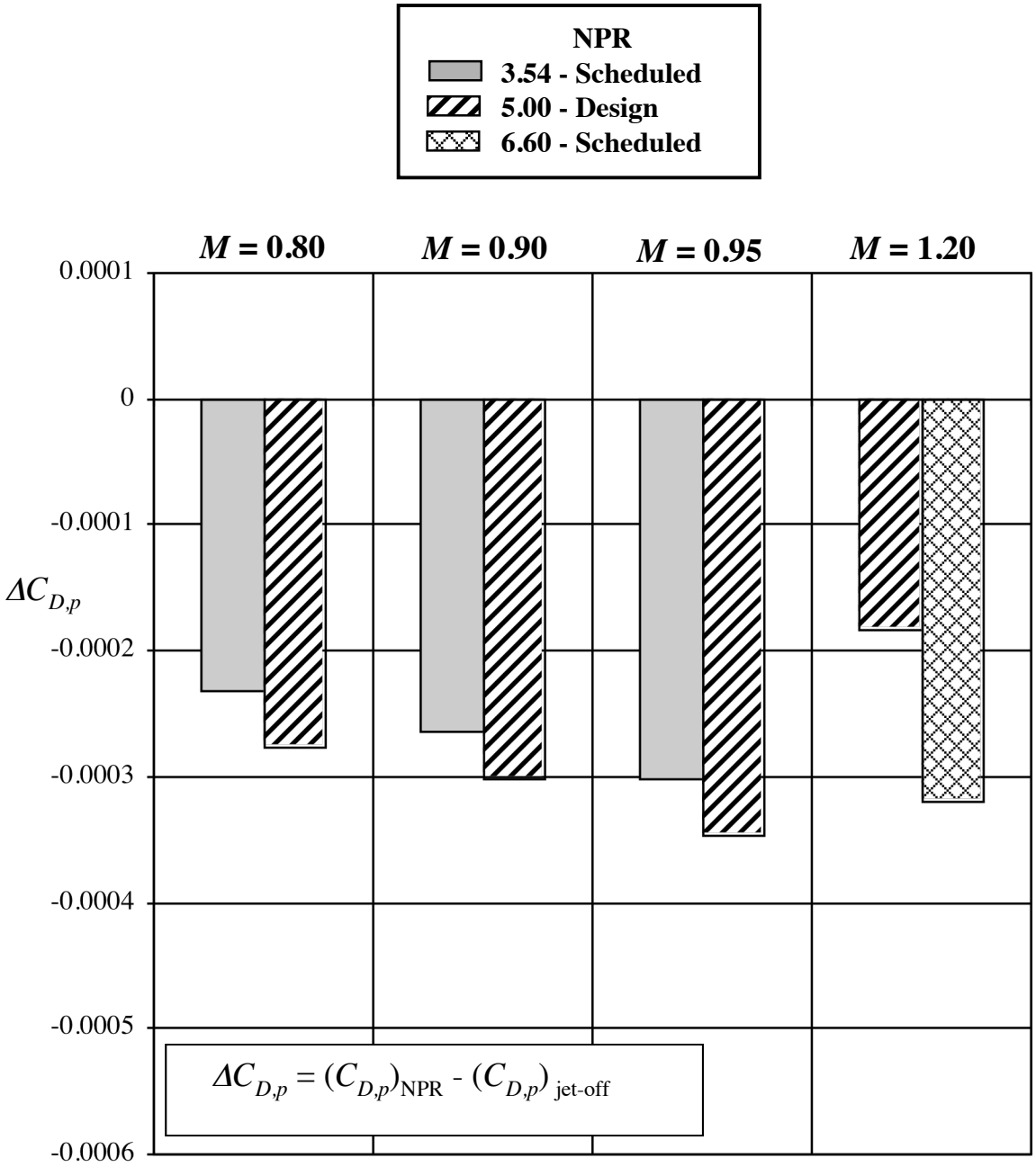

Figure 122. Incremental nozzle pressure drag for nozzle N11 with flap F1 and sidewall S8. $r_f / r_{f,max} = 0.4$; $\beta_f = 16.38°$; $L_f / h_m = 1.4$: $\beta_s = 4°$; $r_s / r_{s,max} = 1.0$.

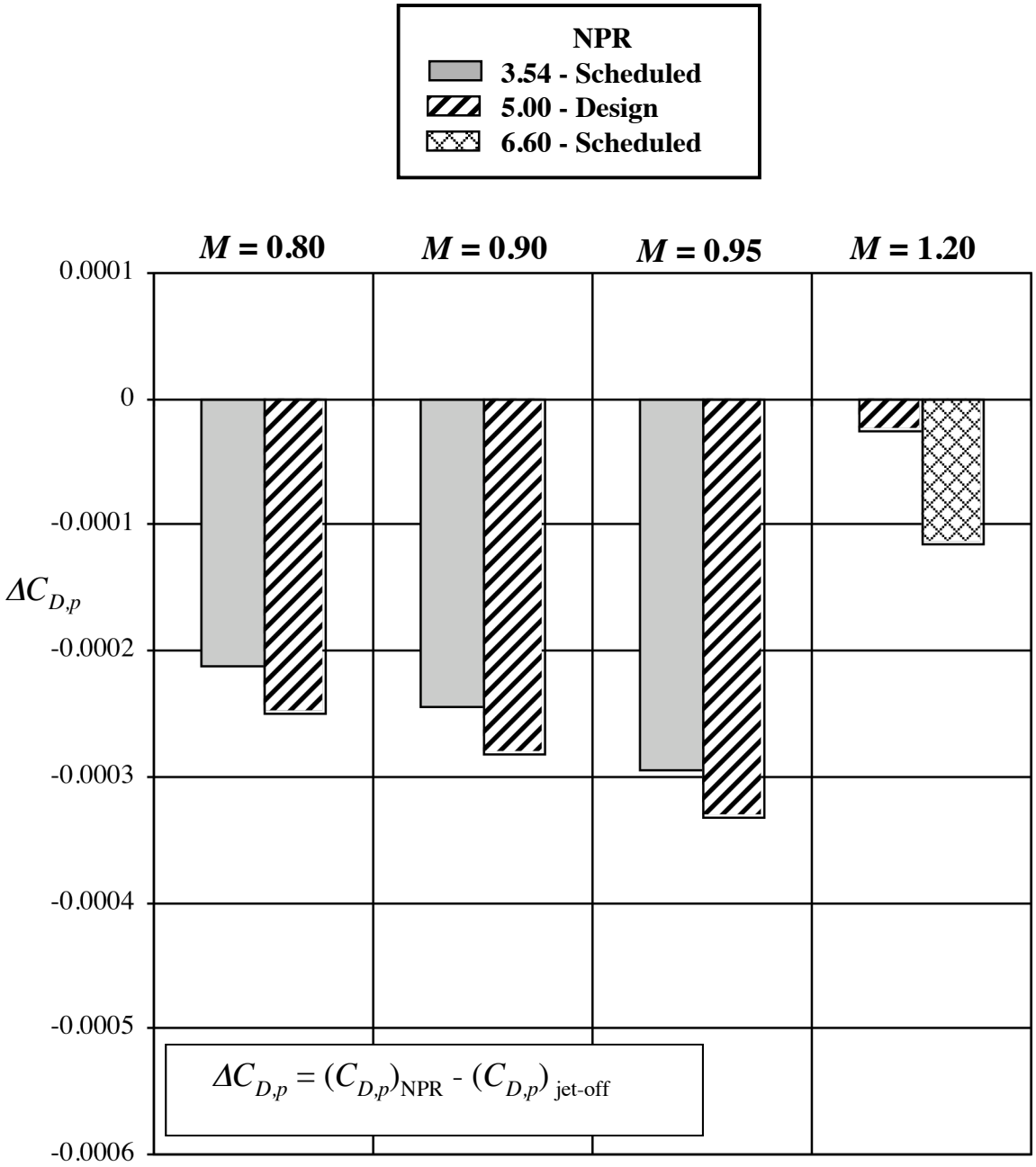

Figure 123. Incremental nozzle pressure drag for nozzle N12 with flap F2 and sidewall S8. $r_f / r_{f,max} = 0.1$; $\beta_f = 12.88°$; $L_f / h_m = 1.4$: $\beta_s = 4°$; $r_s / r_{s,max} = 1.0$.

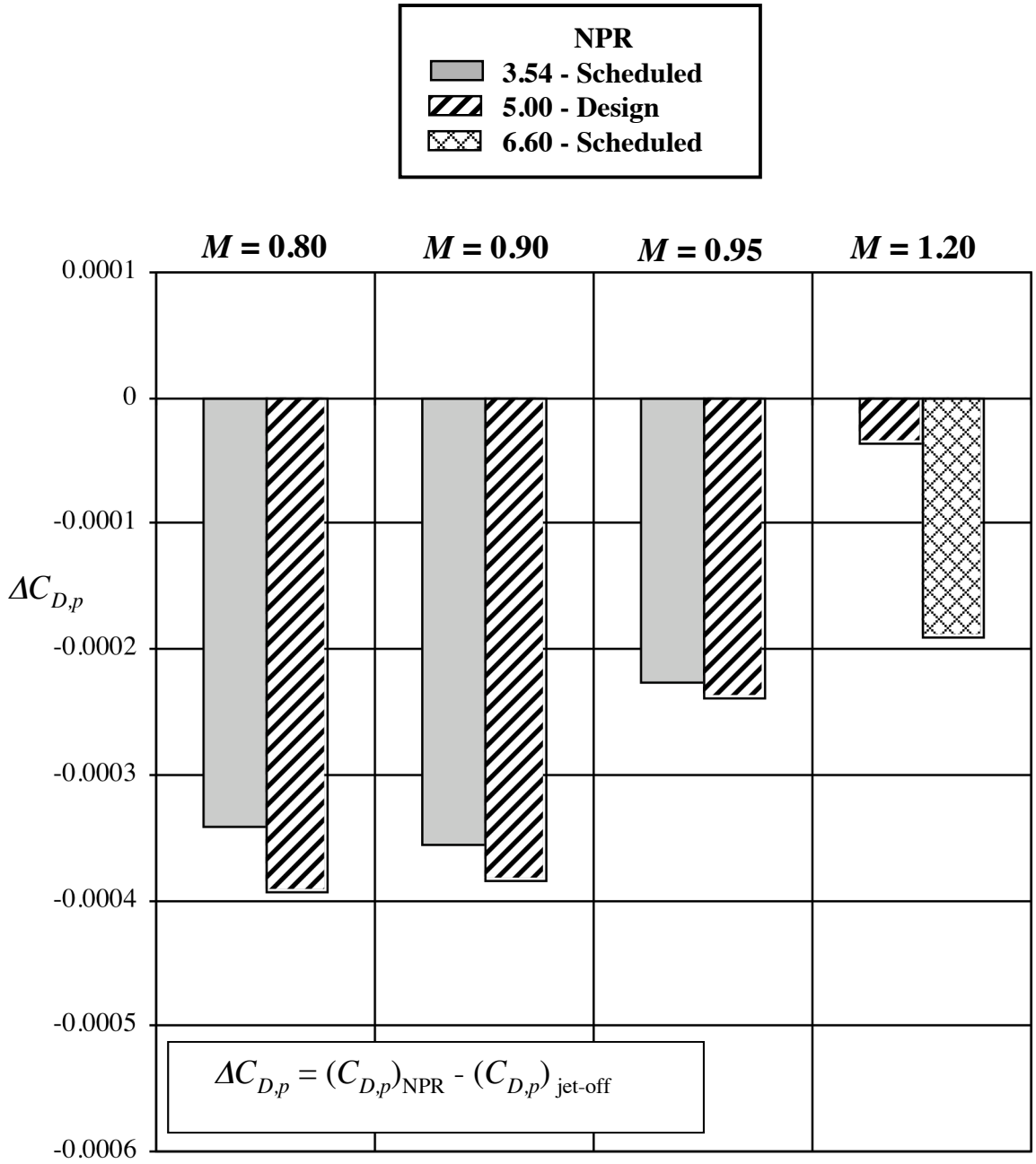

Figure 124. Incremental nozzle pressure drag for nozzle N13 with flap F5 and sidewall S1. $r_f / r_{f,max} = 0.4$; $\beta_f = 20.30°$; $L_f / h_m = 1.1$: $\beta_s = 4°$; $r_s / r_{s,max} = 1.0$.

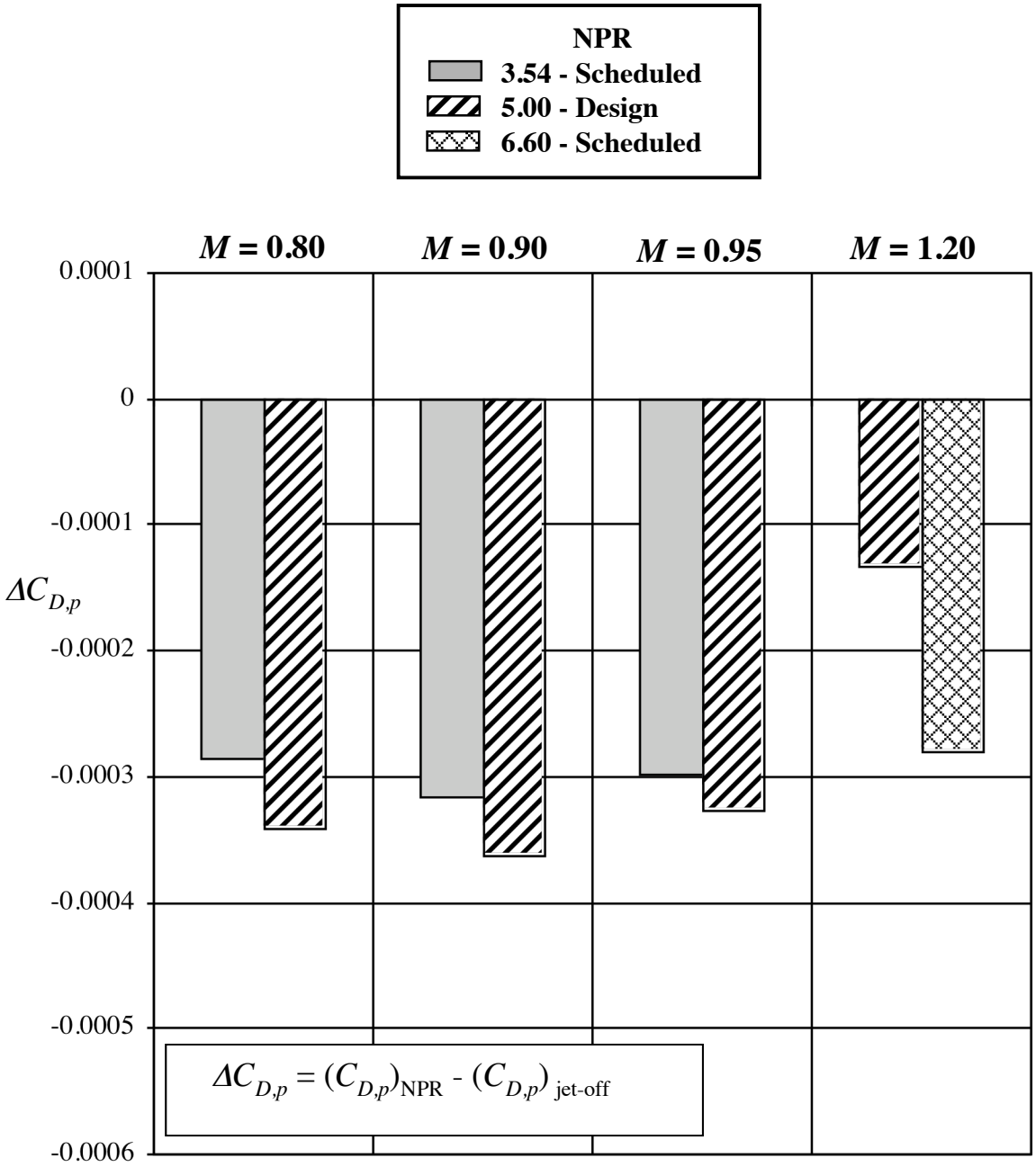

Figure 125. Incremental nozzle pressure drag for nozzle N14 with flap F6 and sidewall S1. $r_f / r_{f,max} = 0.1$; $\beta_f = 15.97°$; $L_f / h_m = 1.1$: $\beta_s = 4°$; $r_s / r_{s,max} = 1.0$.

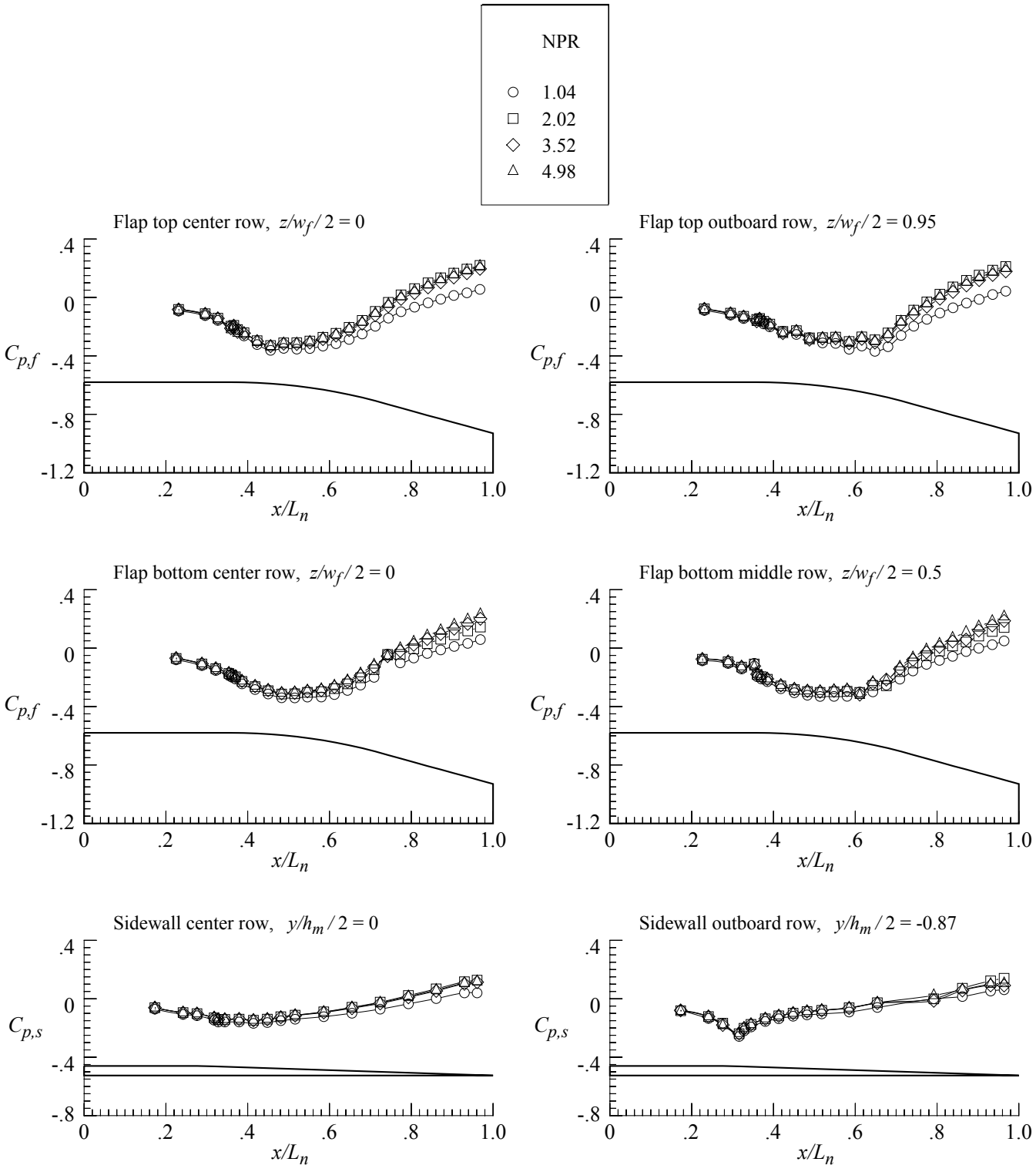

(a) $M = 0.80$.

Figure 126. External pressure distributions for nozzle N1 with flap F1 and sidewall S1. $r_f/r_{f,max} = 0.4$; $\beta_f = 16.38°$; $L_f/h_m = 1.4$; $\beta_s = 4.0°$; $r_s/r_{s,max} = 0$.

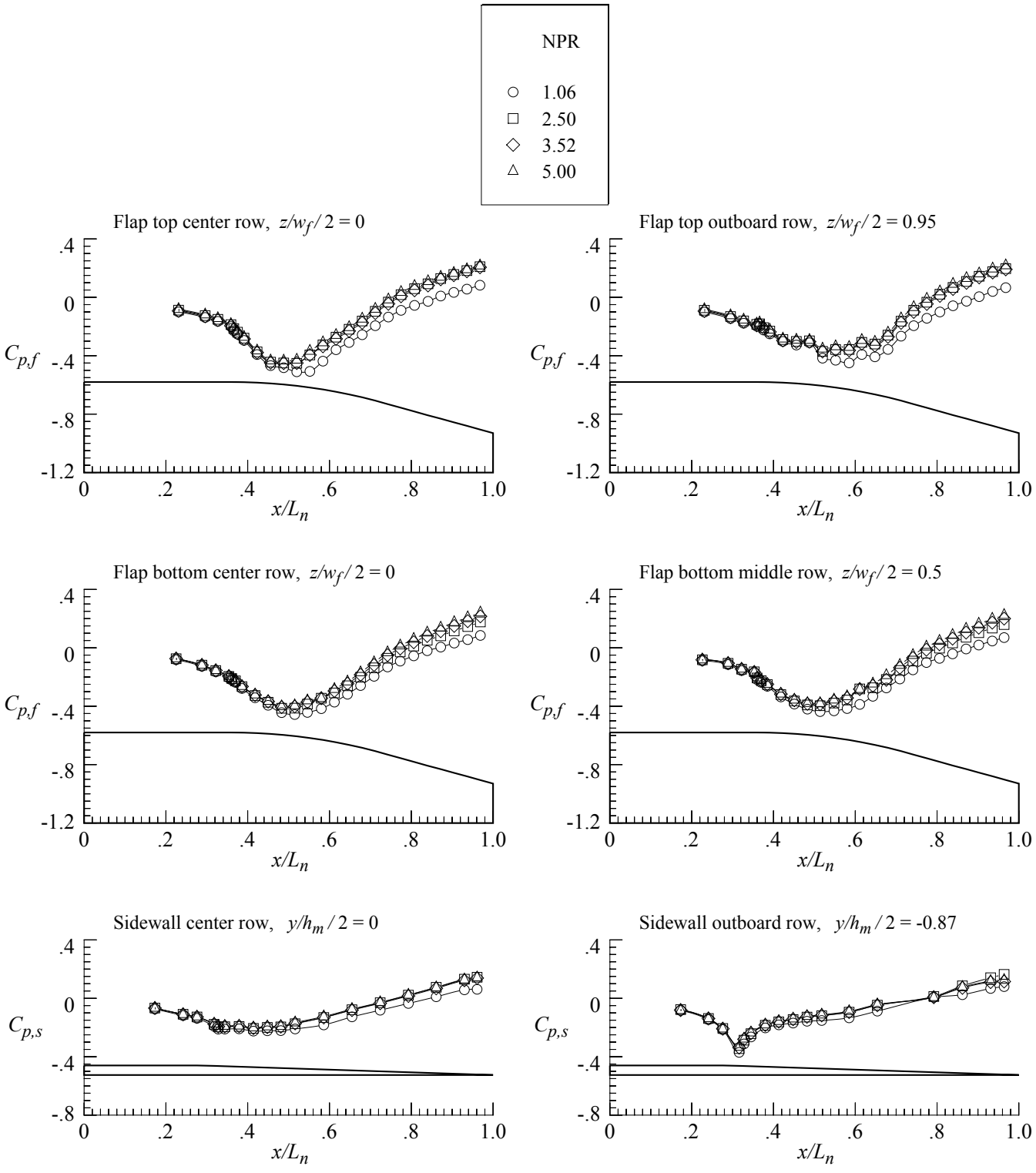

(b) $M = 0.90$.

Figure 126. Continued.

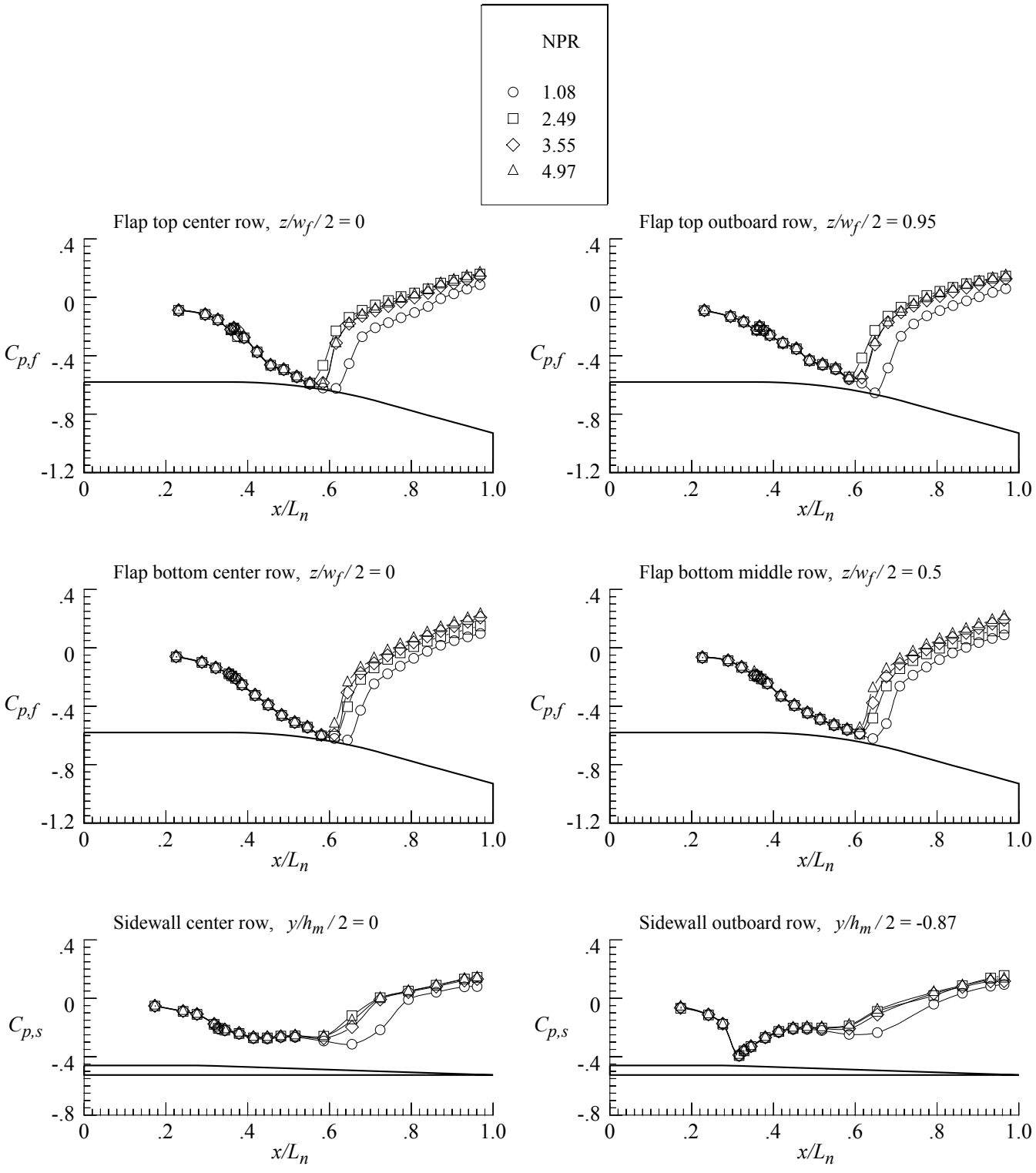

(c) $M = 0.95$.

Figure 126. Continued.

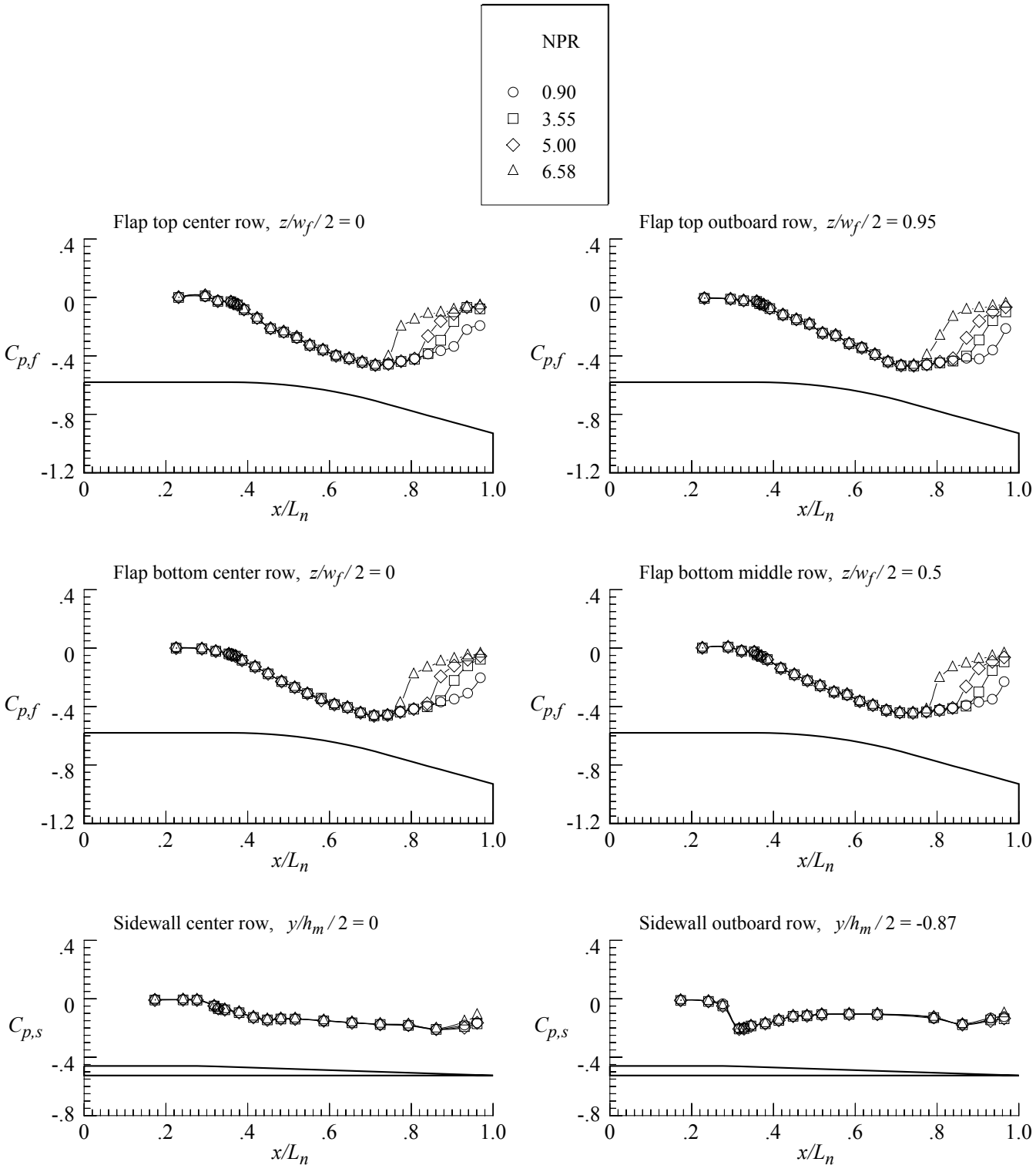

(d) $M = 1.20$.

Figure 126. Concluded.

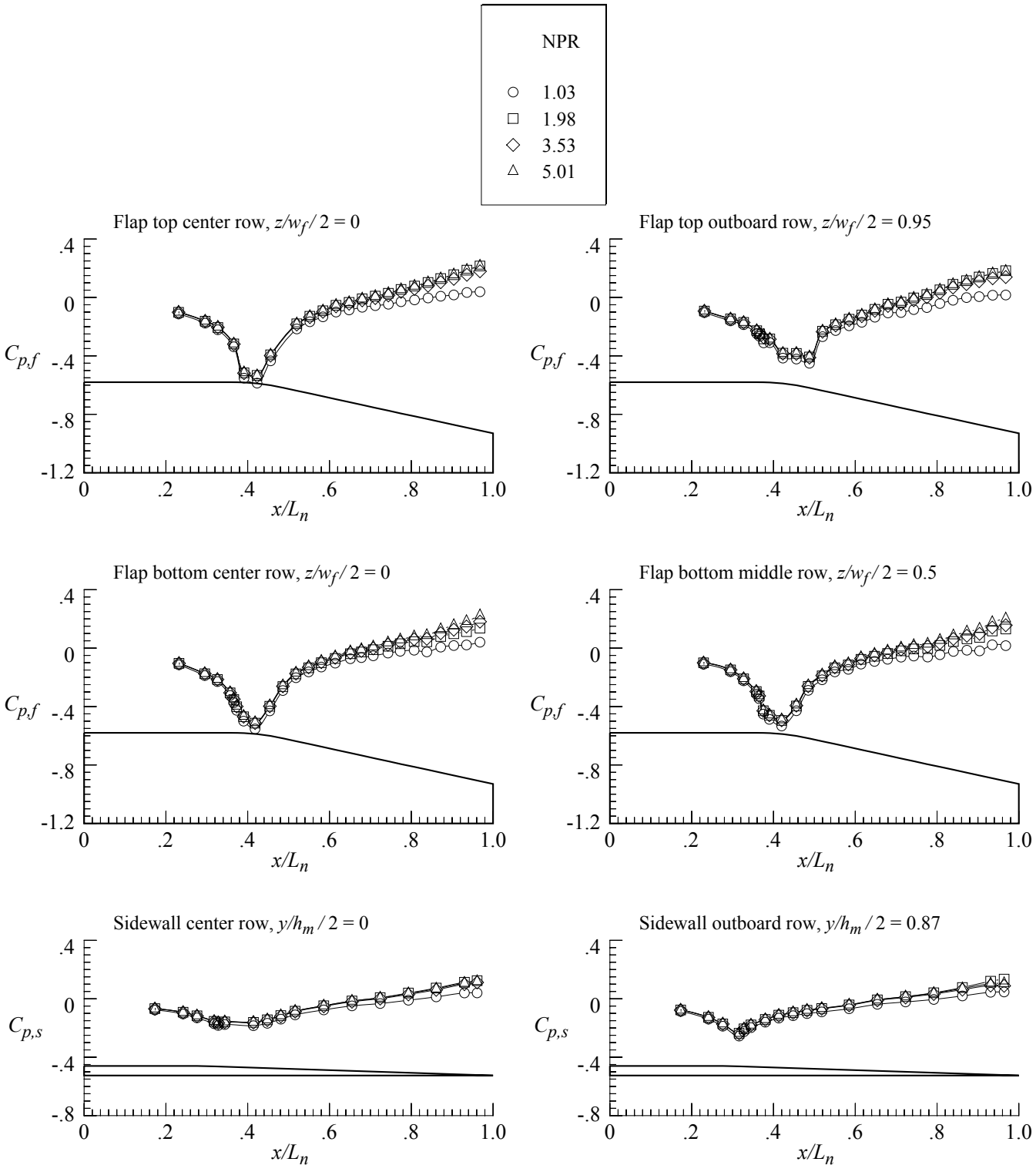

(a) $M = 0.80$.

Figure 127. External pressure distributions for nozzle N2 with flap F2 and sidewall S1.
$r_f/r_{f,max} = 0.1$; $\beta_f = 12.88°$; $L_f/h_m = 1.4$; $\beta_s = 4.0°$; $r_s/r_{s,max} = 0$.

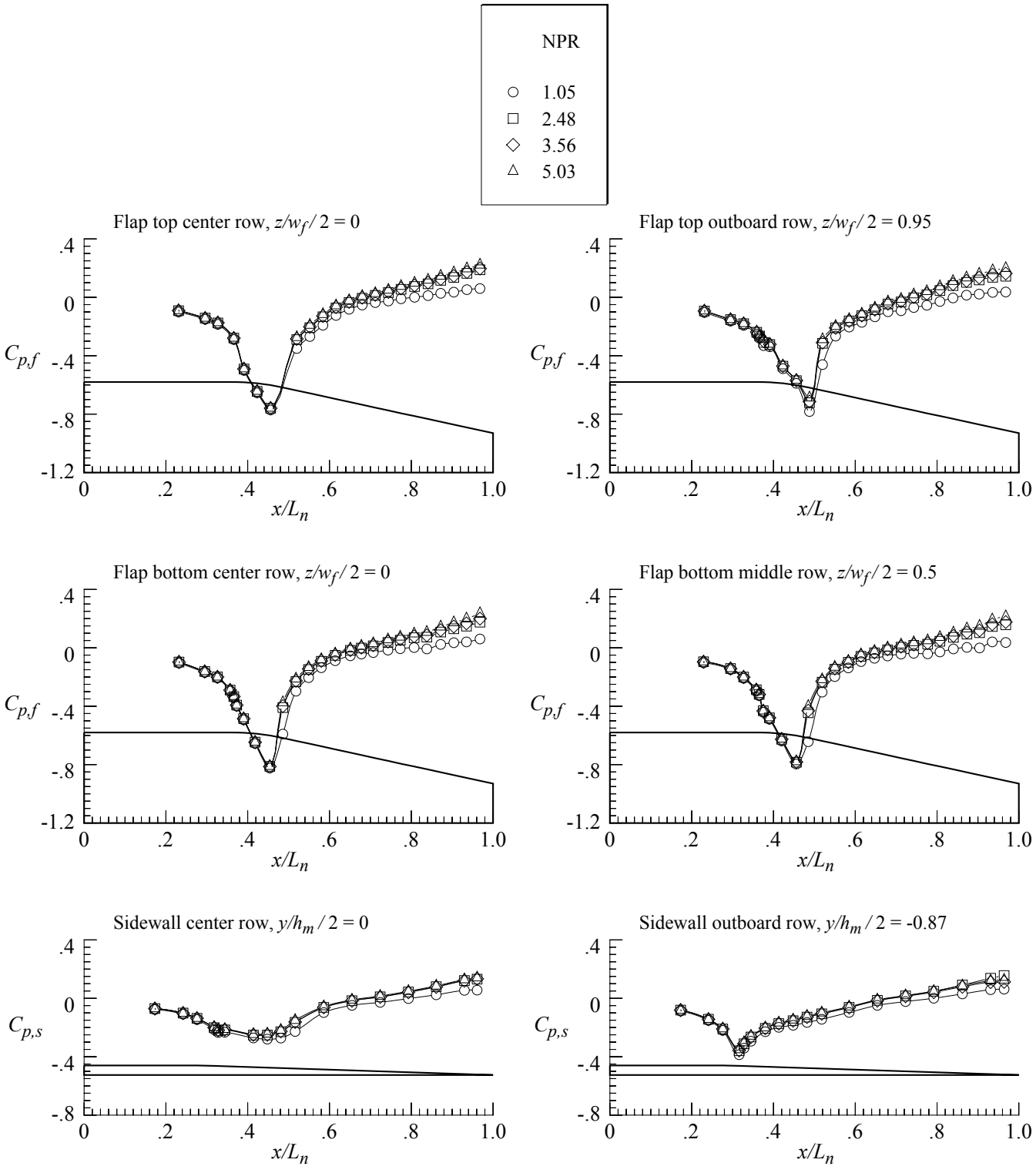

(b) $M = 0.90$.

Figure 127. Continued.

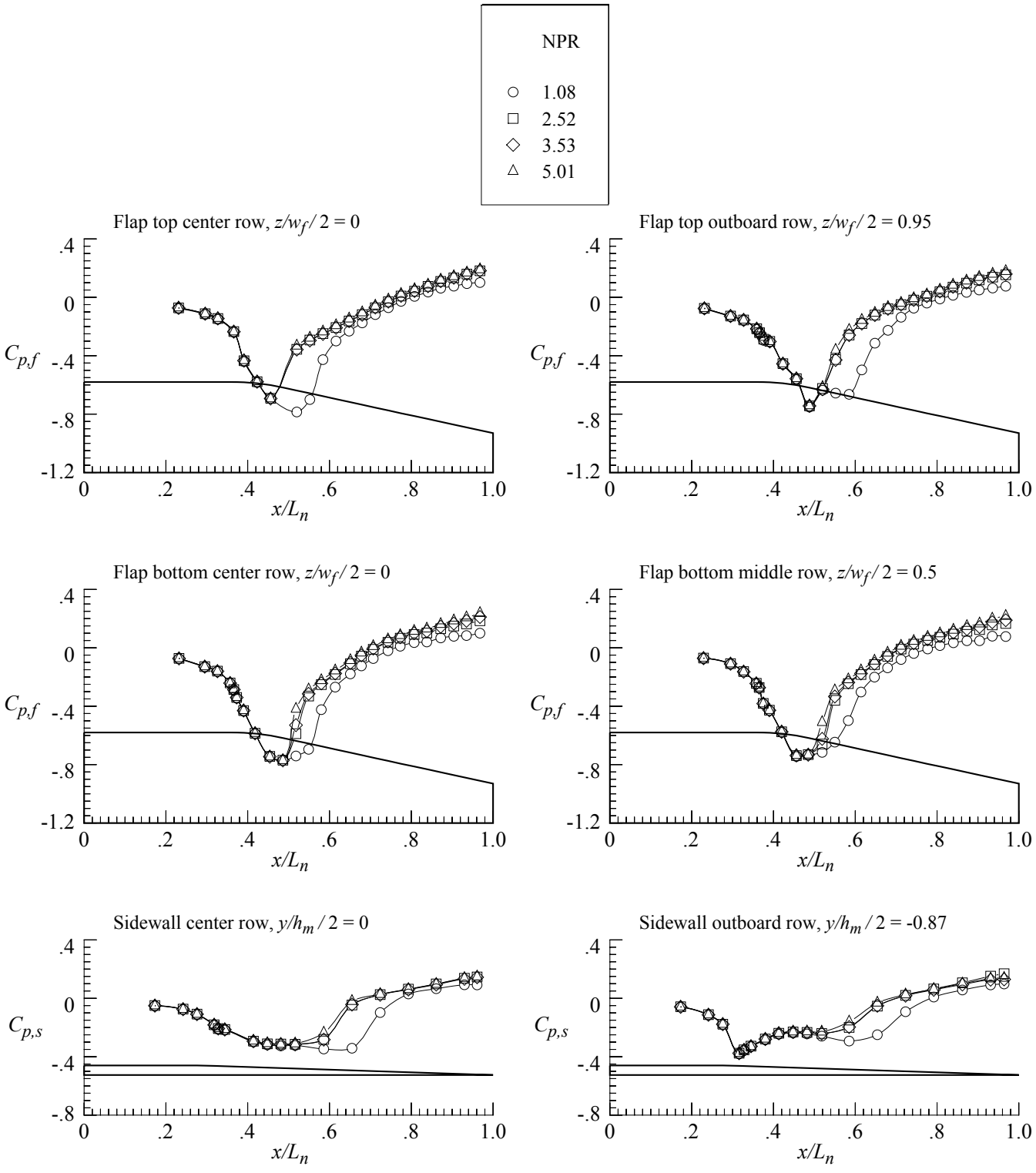

(c) $M = 0.95$.

Figure 127. Continued.

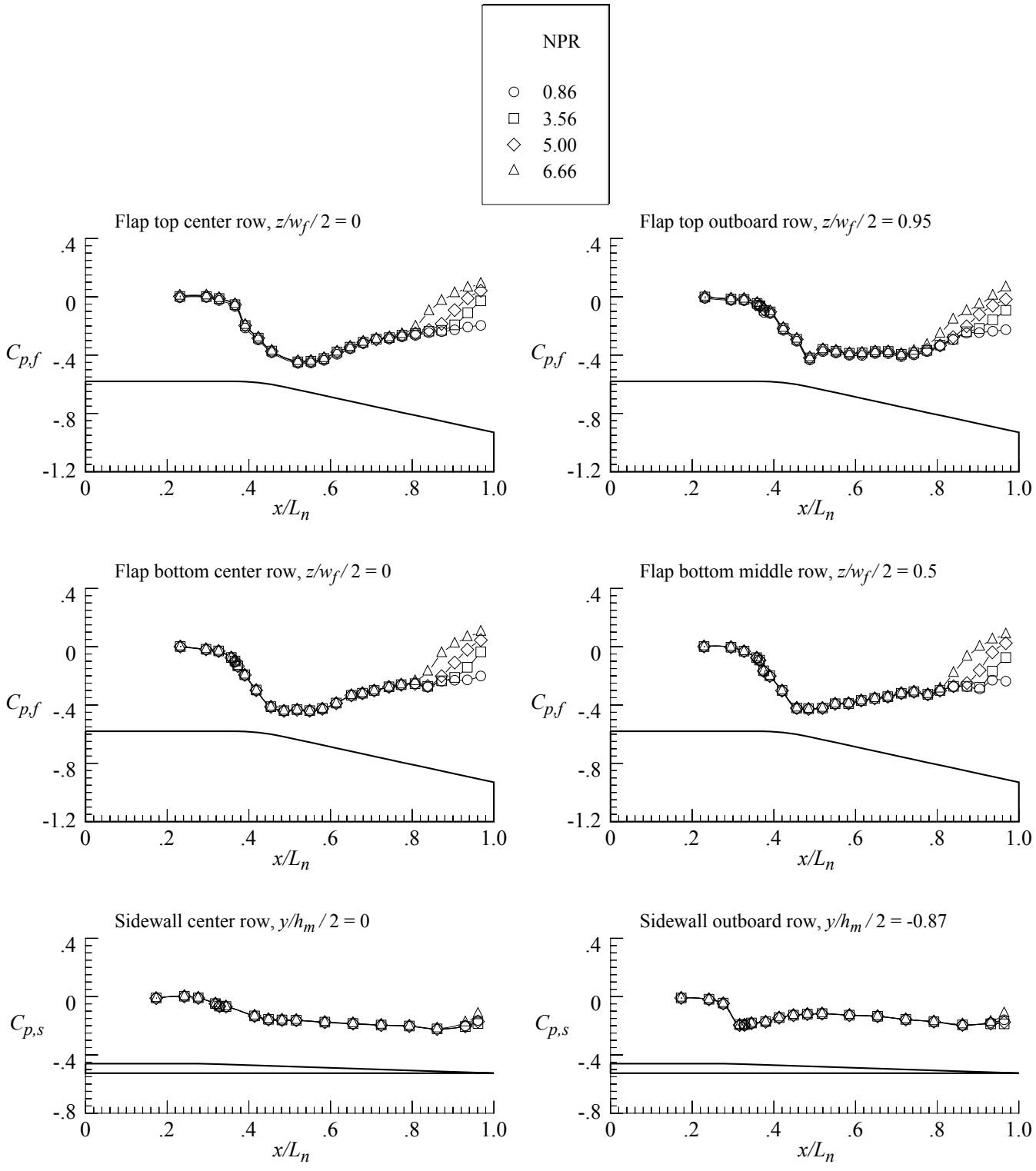

(d) $M = 1.20$.

Figure 127. Concluded.

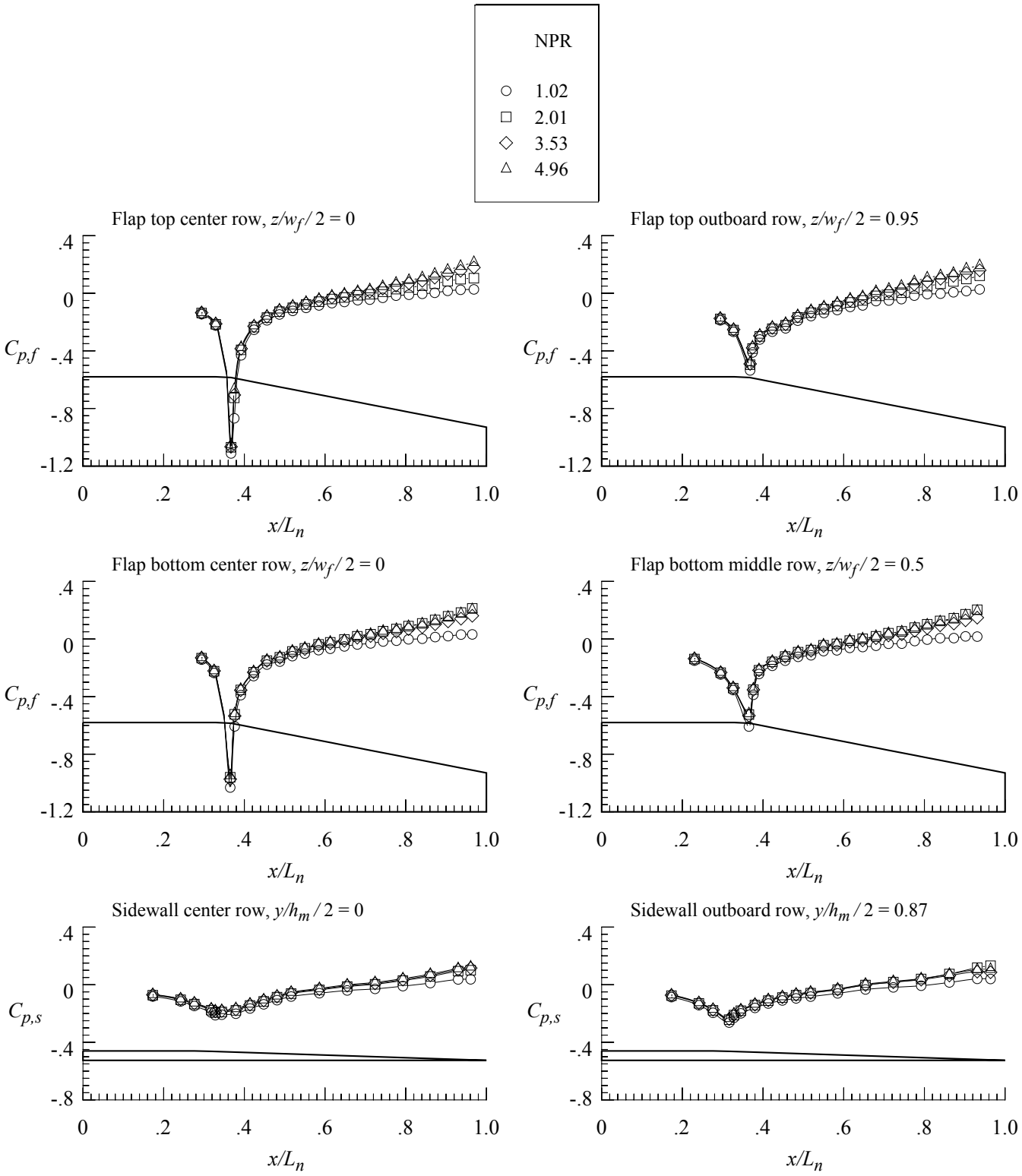

(a) $M = 0.80$.

Figure 128. External pressure distributions for nozzle N3 with flap F3 and sidewall S1.
$r_f/r_{f,max} = 0$; $\beta_f = 11.72°$; $L_f/h_m = 1.4$; $\beta_s = 4.0°$; $r_s/r_{s,max} = 0$.

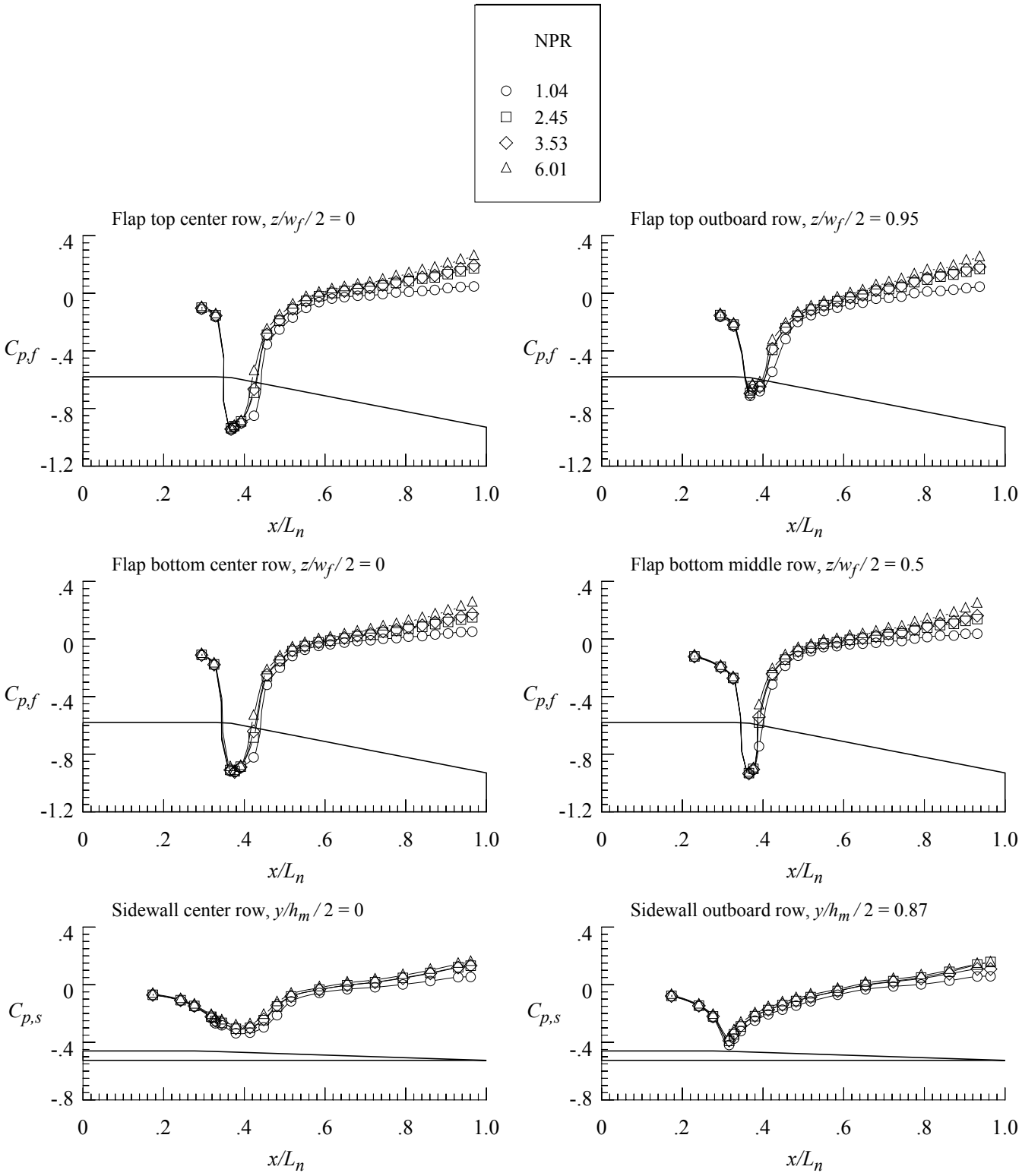

(b) $M = 0.90$.

Figure 128. Continued.

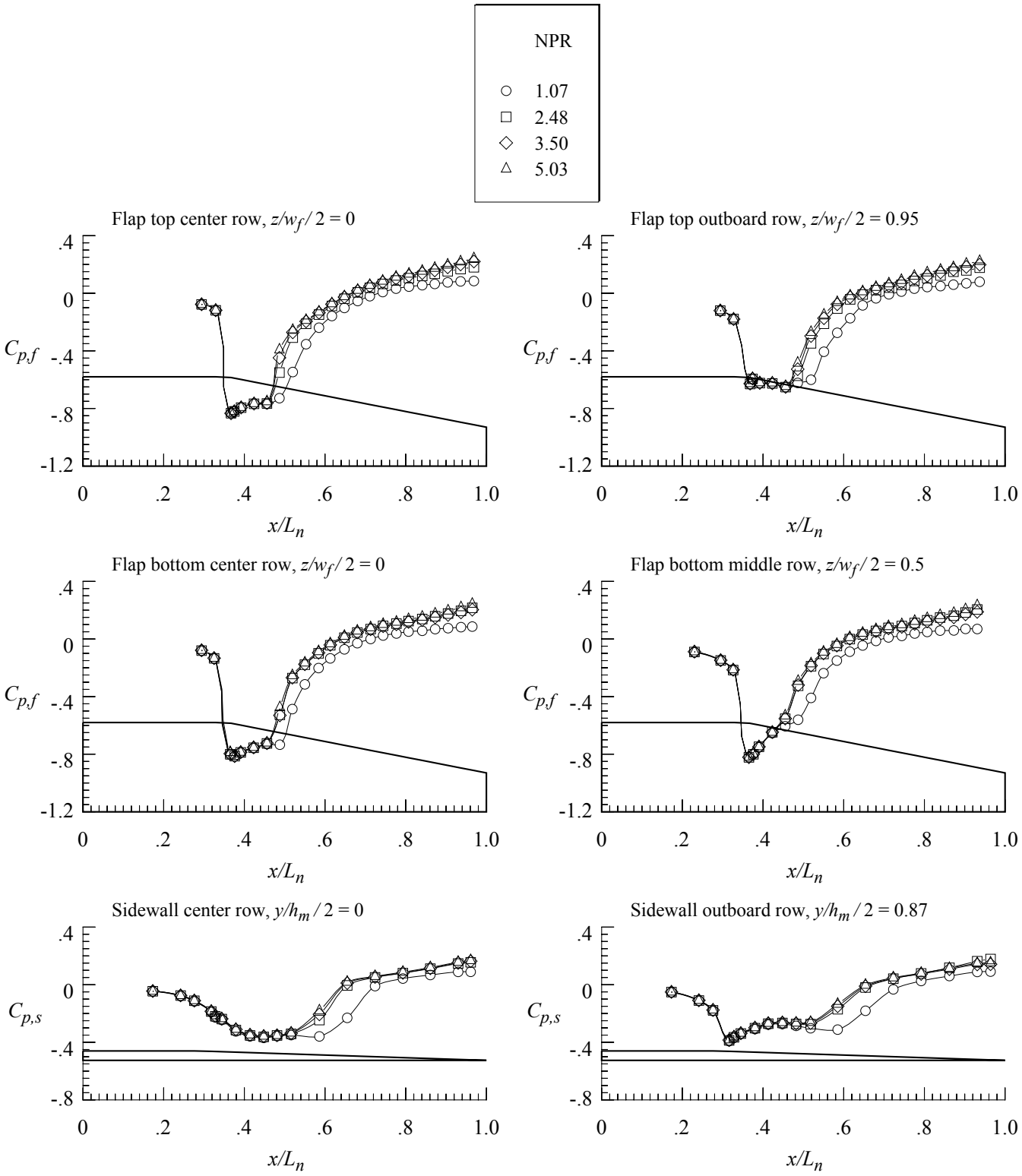

(c) $M = 0.95$.

Figure 128. Continued.

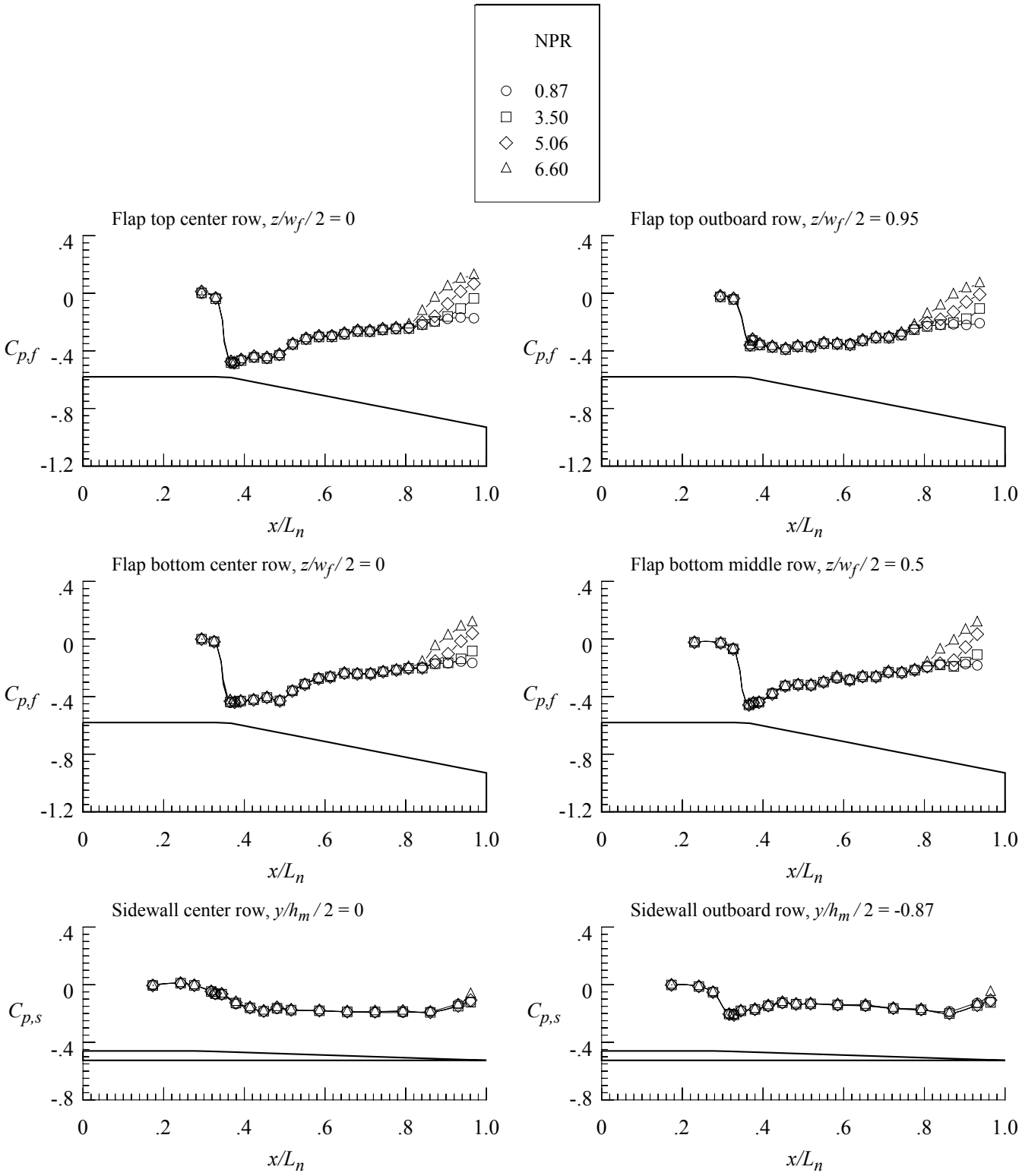

(d) $M = 1.20$.

Figure 128. Concluded.

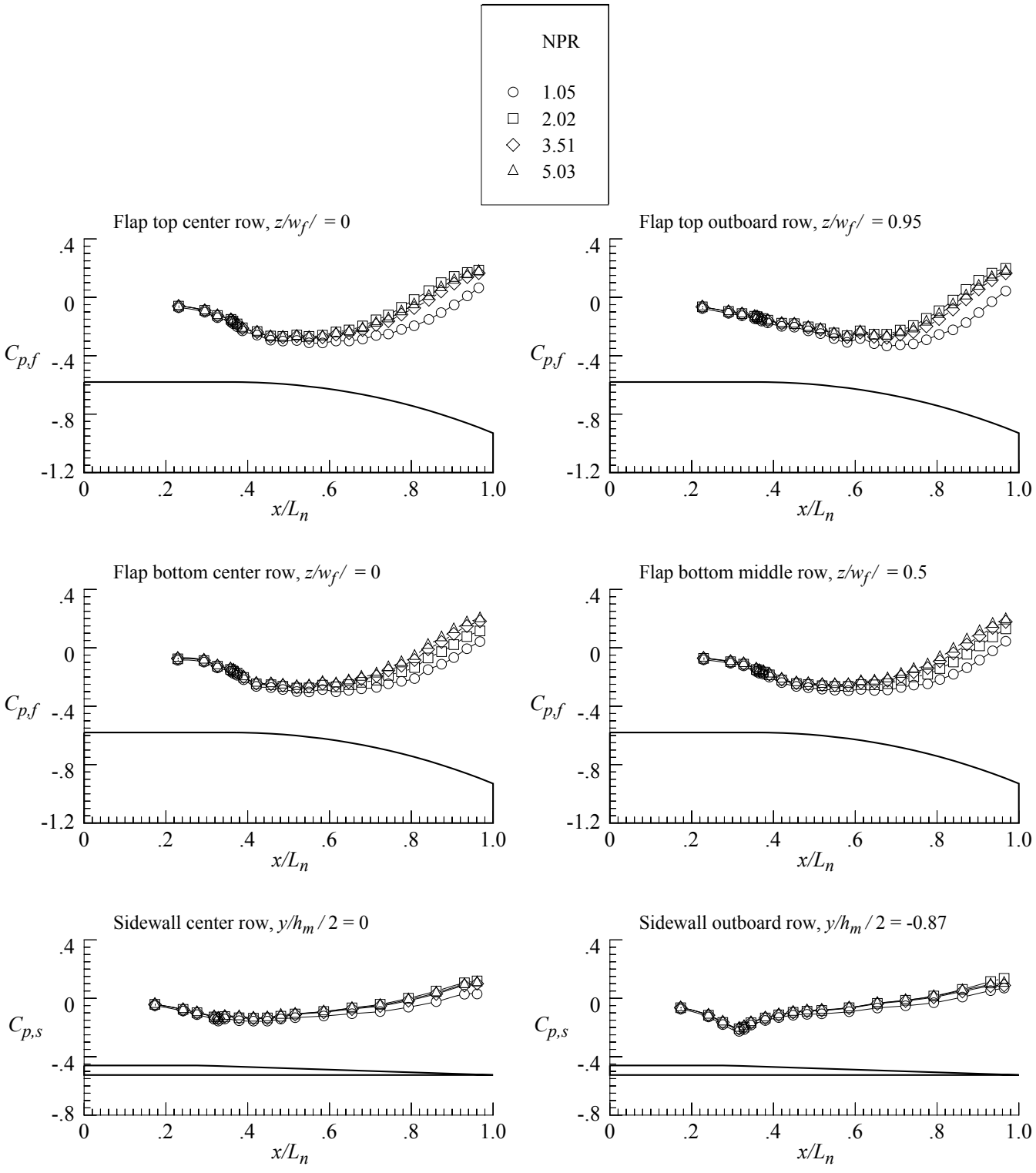

(a) $M = 0.80$.

Figure 129. External pressure distributions for nozzle N4 with flap F4 and sidewall S1.
$r_f/r_{f,max} = 1.0$; $\beta_f = 23.44°$; $L_f/h_m = 1.4$; $\beta_s = 4.0°$; $r_s/r_{s,max} = 0$.

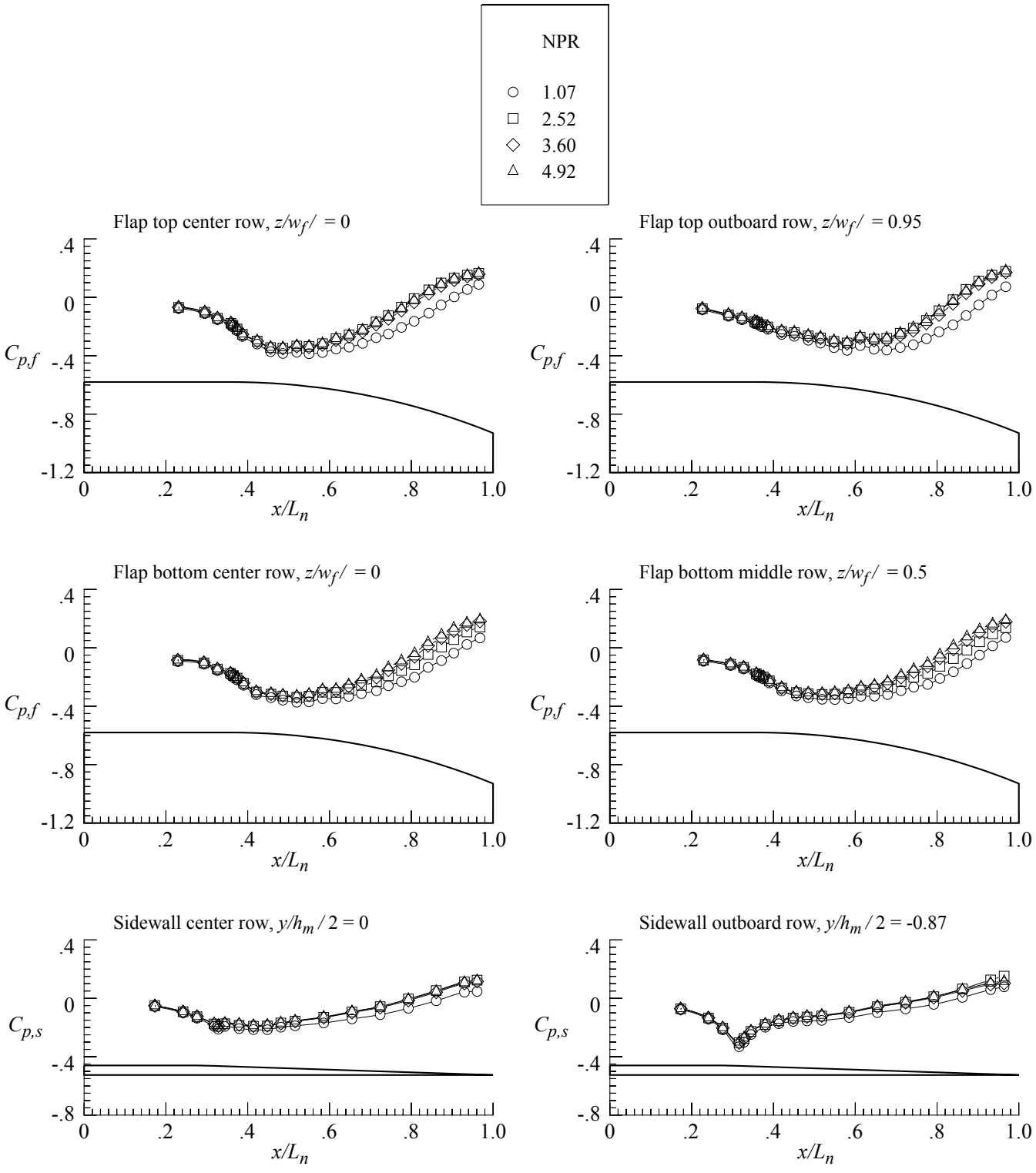

(b) $M = 0.90$.

Figure 129. Continued.

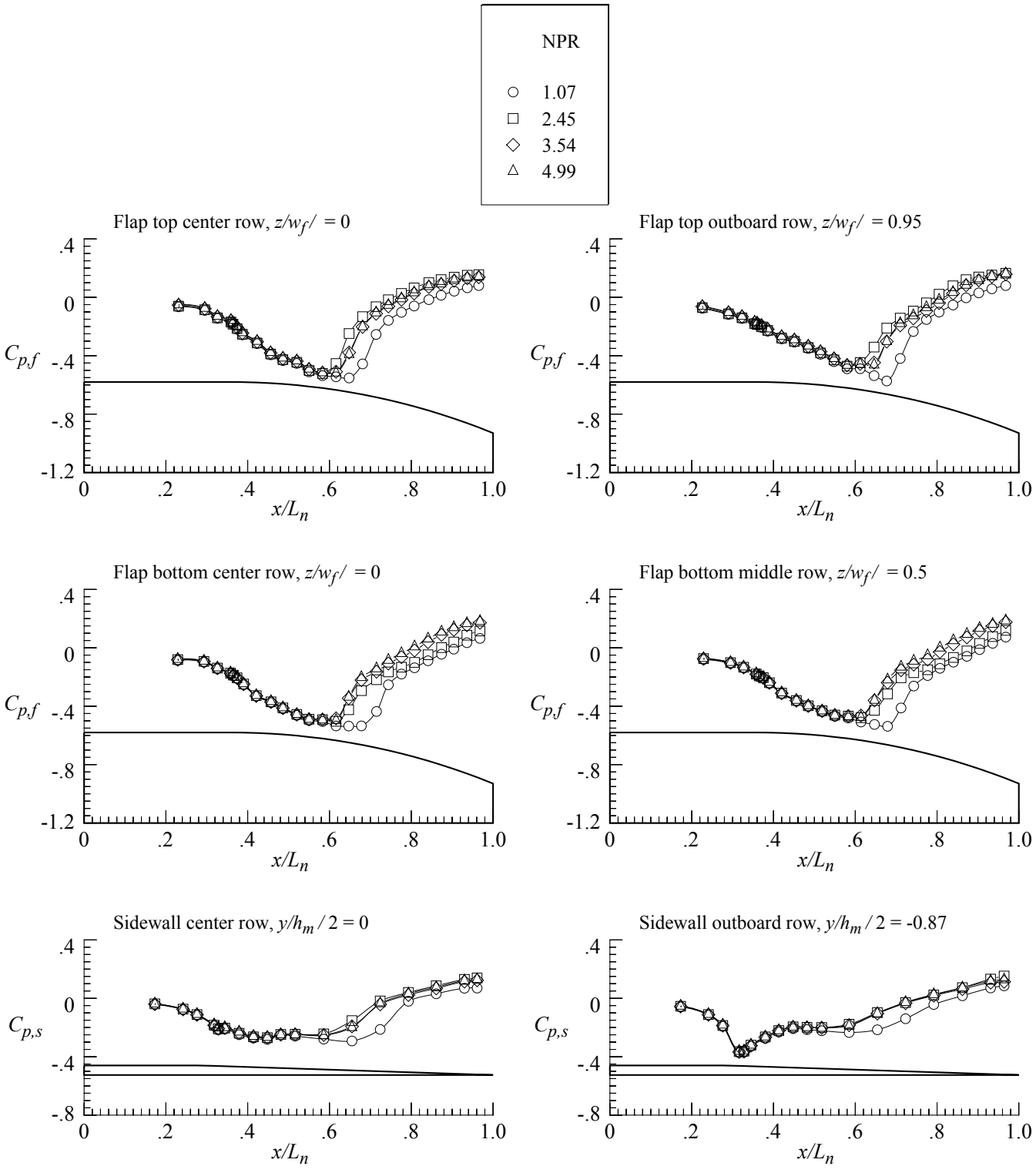

(c) $M = 0.95$.

Figure 129. Continued.

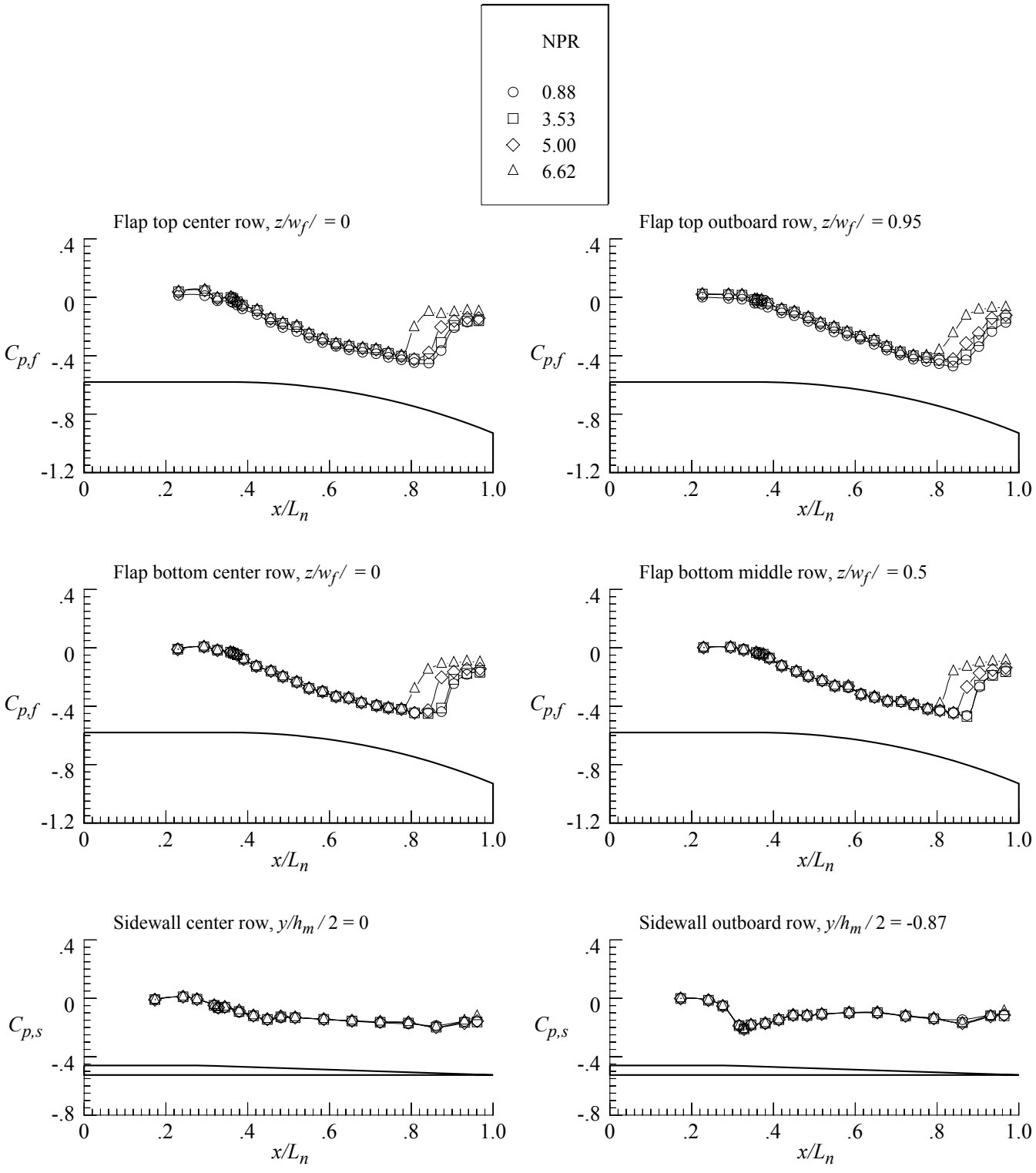

(d) $M = 1.20$.

Figure 129. Concluded.

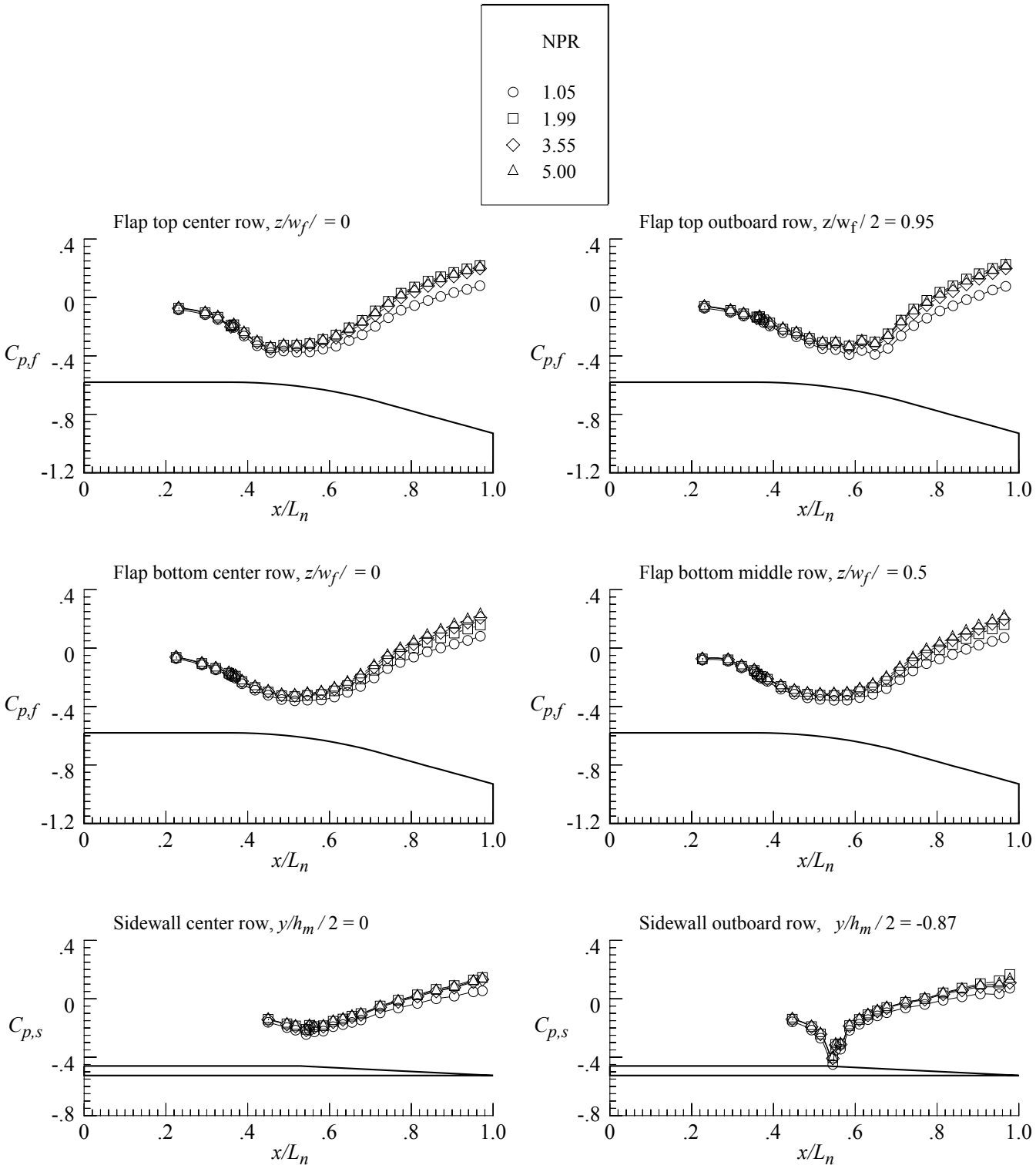

(a) $M = 0.80$.

Figure 130. External pressure distributions for nozzle N5 with flap F1 and sidewall S2. $r_f/r_{f,max} = 0.4$; $\beta_f = 16.38°$; $L_f/h_m = 1.4$; $\beta_s = 6.0°$; $r_s/r_{s,max} = 0$.

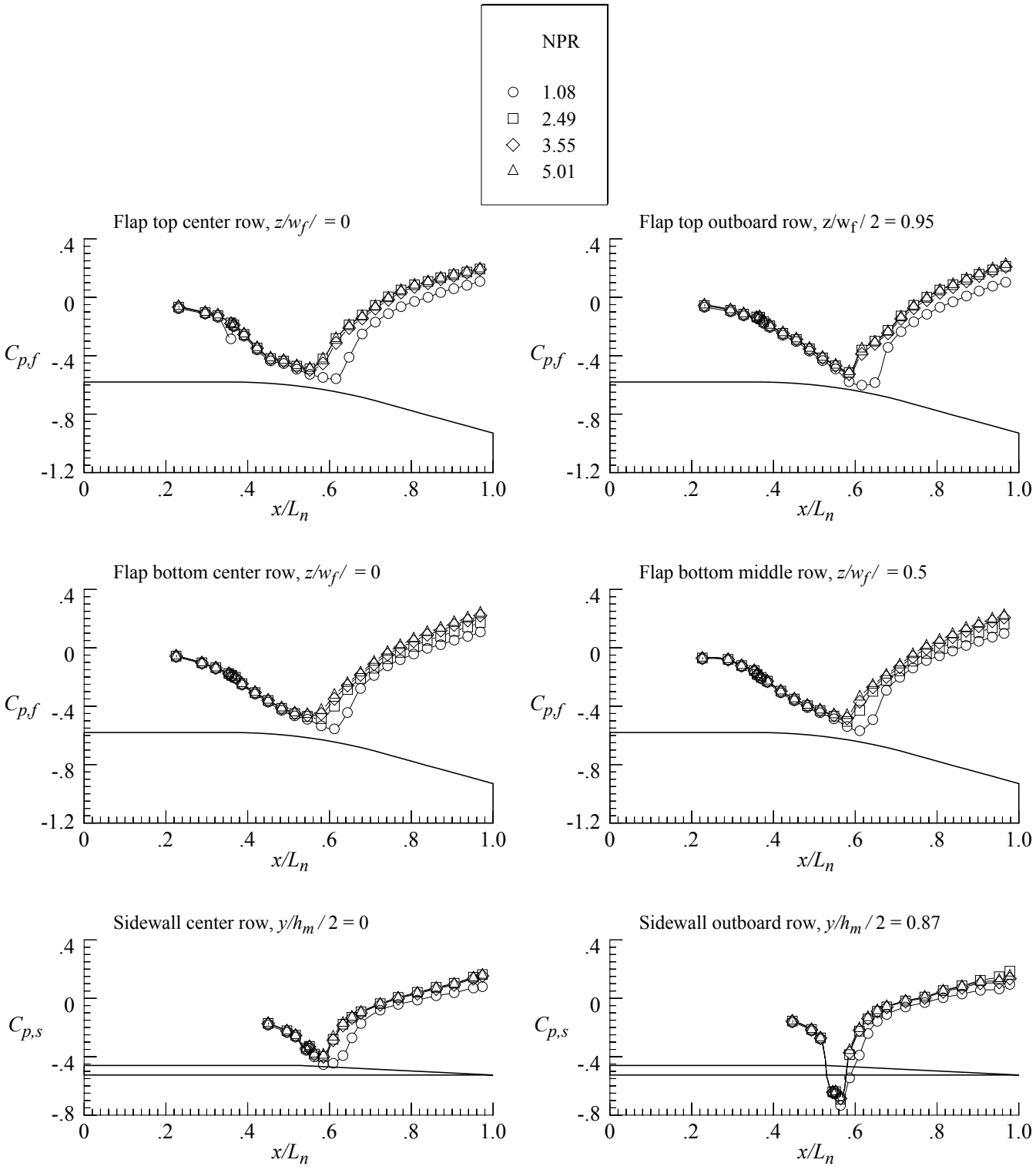

(b) $M = 0.90$.

Figure 130. Continued.

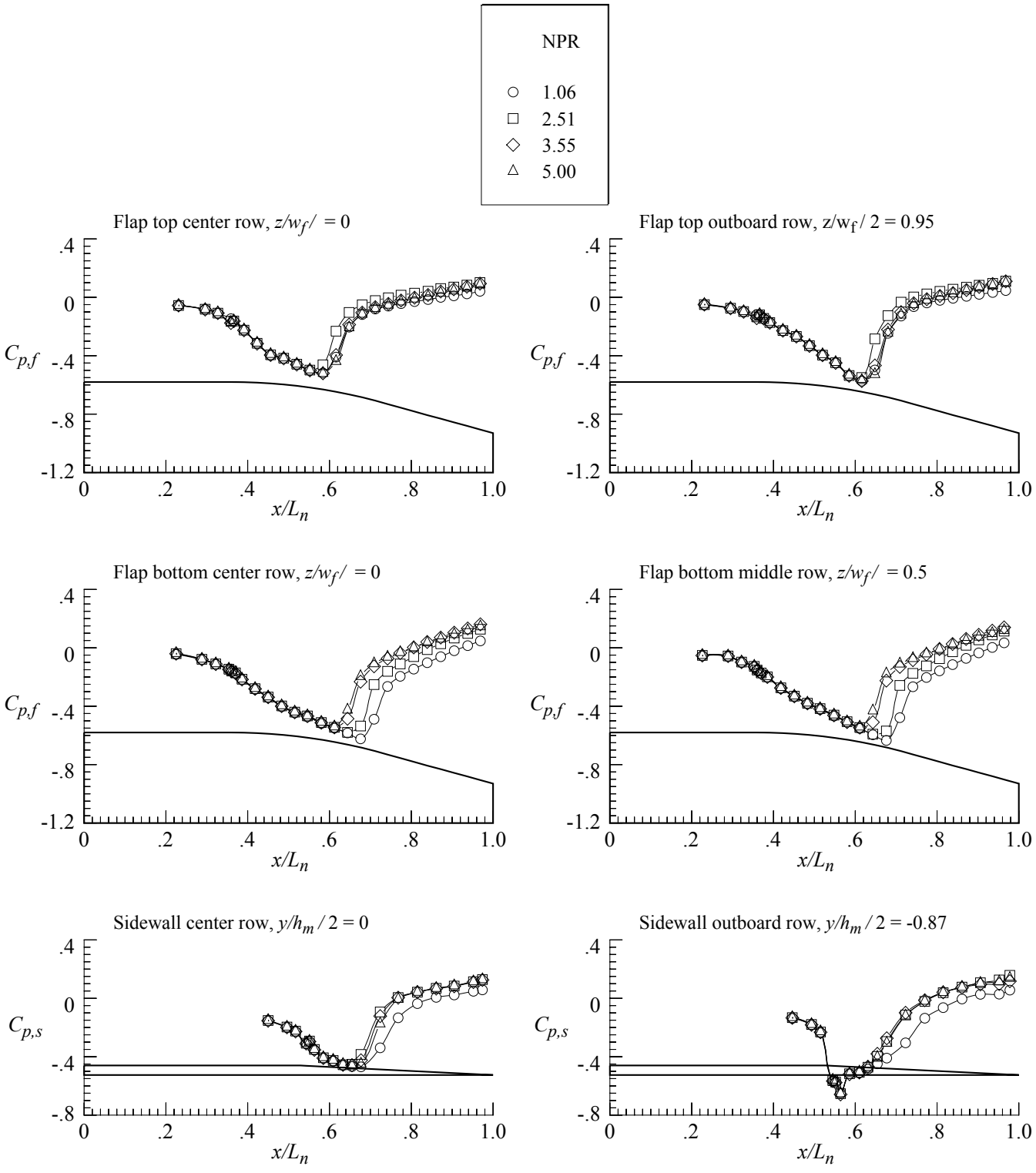

(c) $M = 0.95$.

Figure 130. Continued.

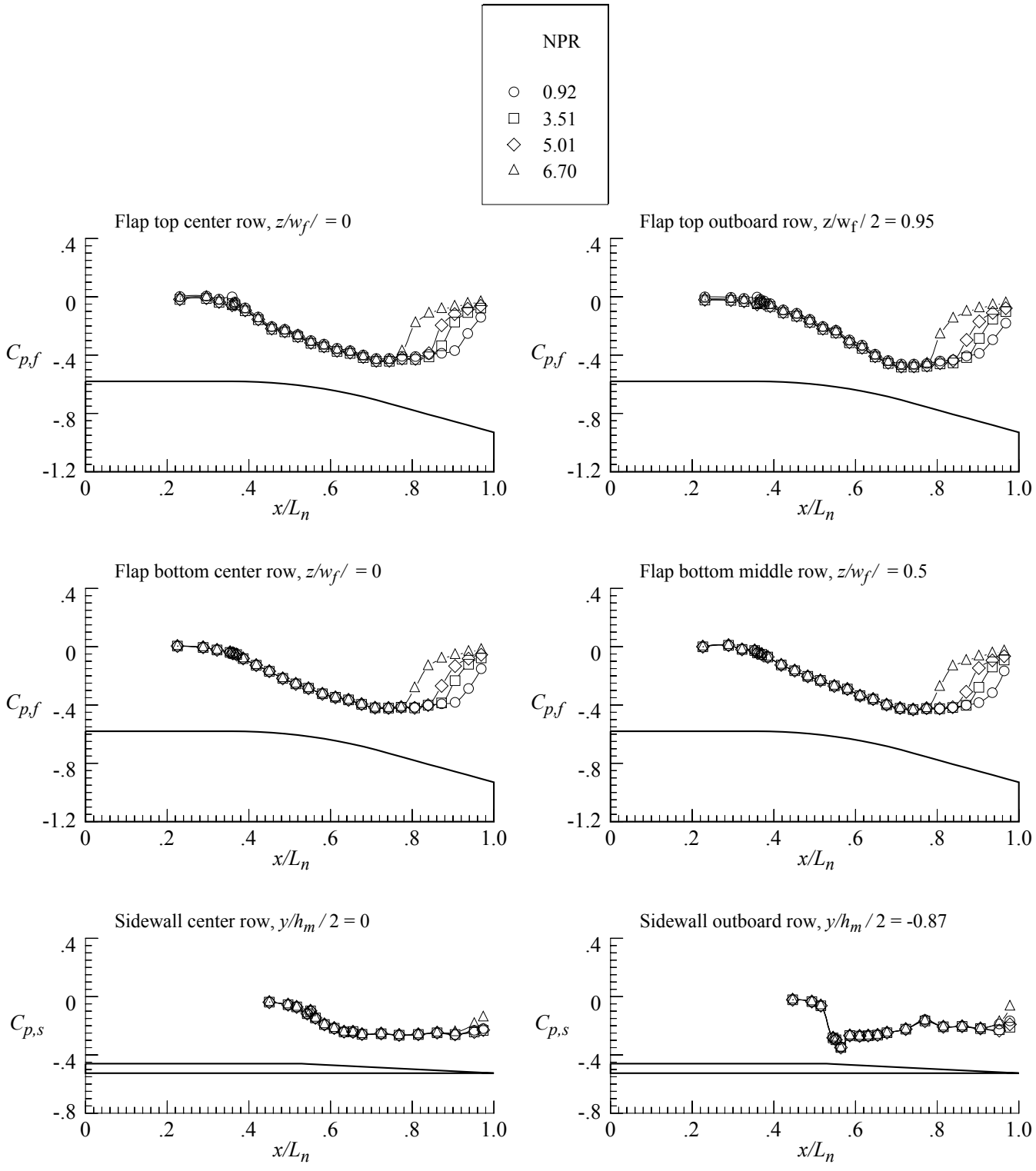

(d) $M = 1.20$.

Figure 130. Concluded.

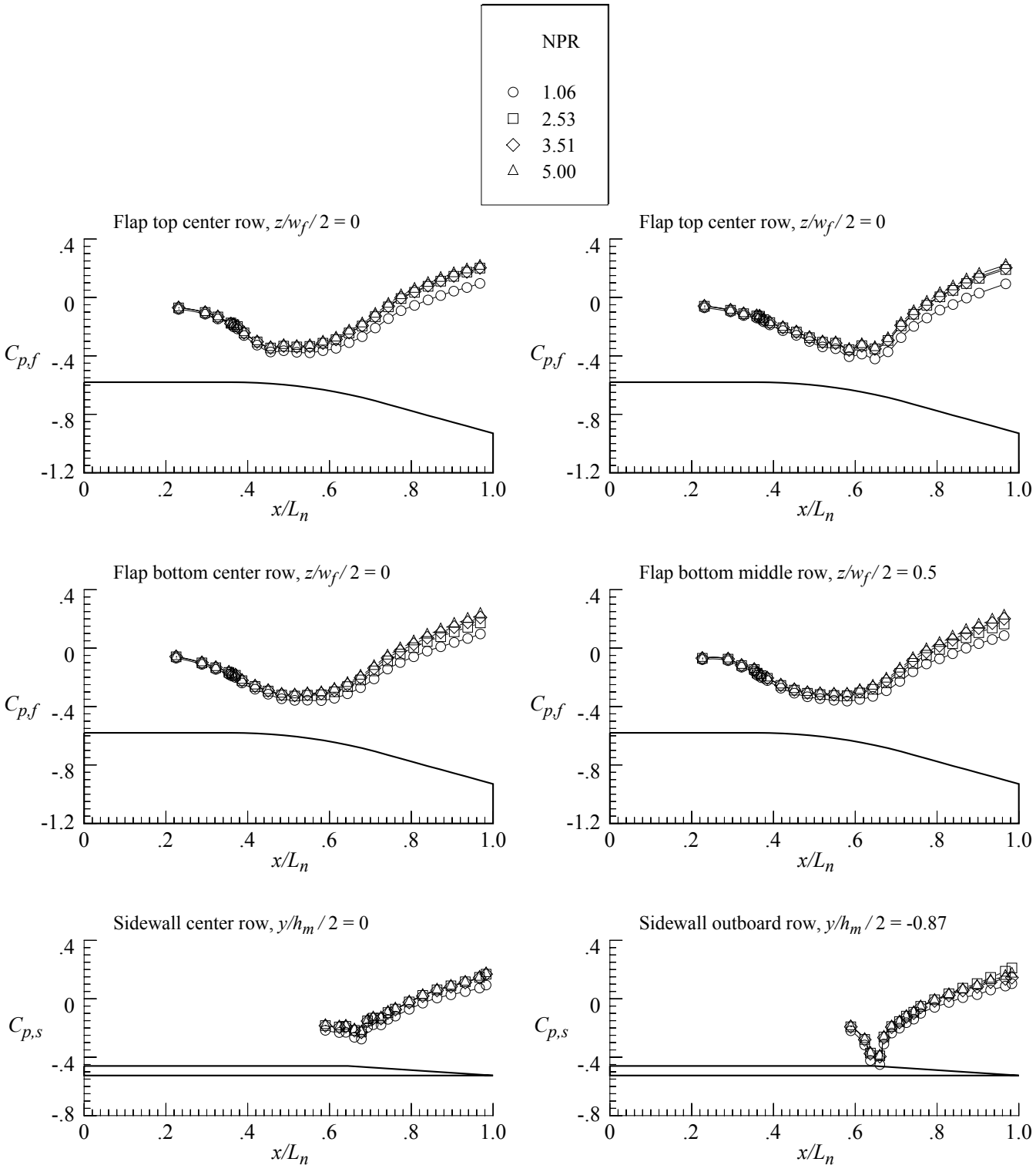

(a) $M = 0.80$.

Figure 131. External pressure distributions for nozzle N6 with flap F1 and sidewall S3. $r_f/r_{f,max} = 0.4$; $\beta_f = 16.38°$; $L_f/h_m = 1.4$; $\beta_s = 8.0°$; $r_s/r_{s,max} = 0$.

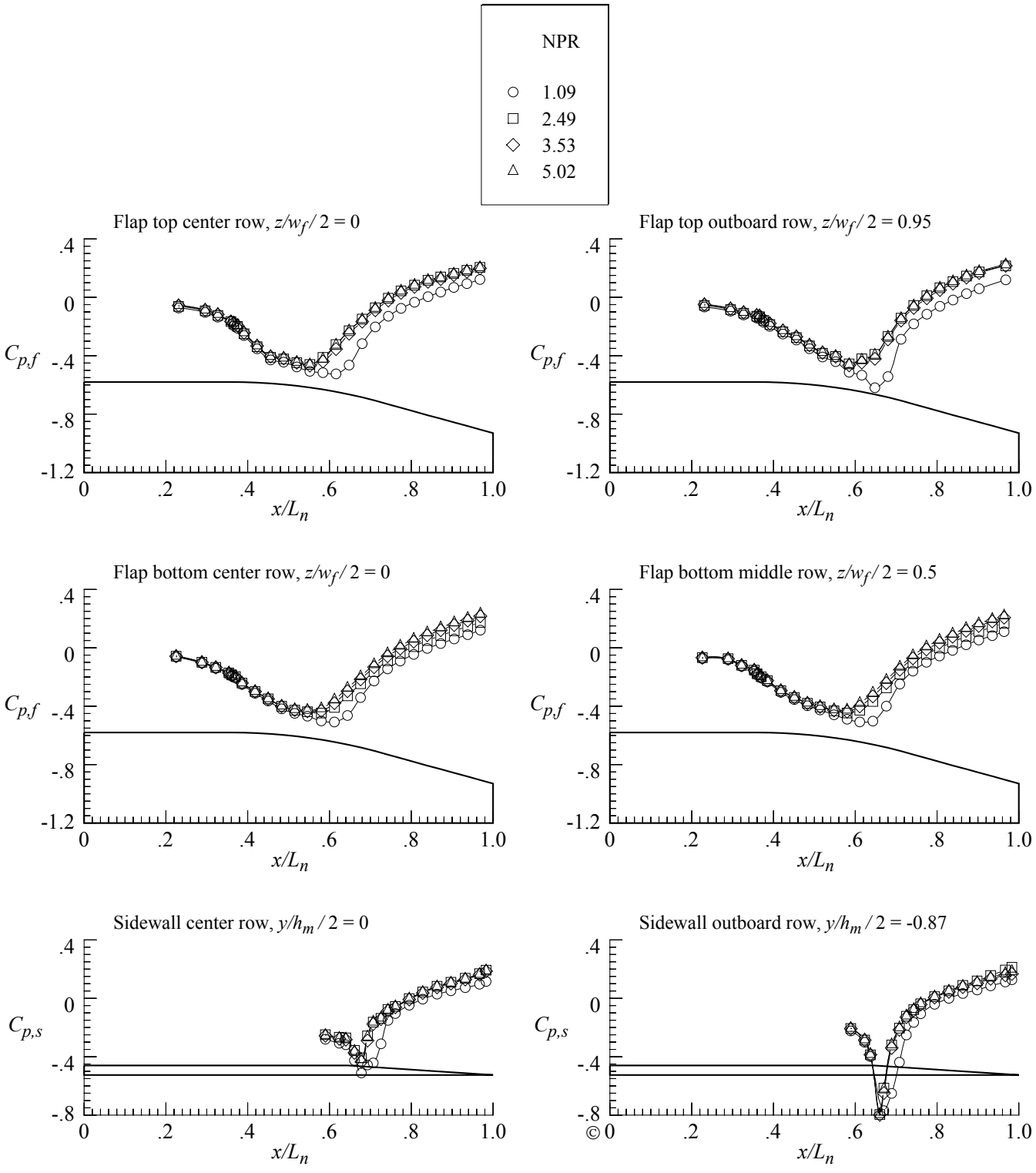

(b) $M = 0.90$.

Figure 131. Continued.

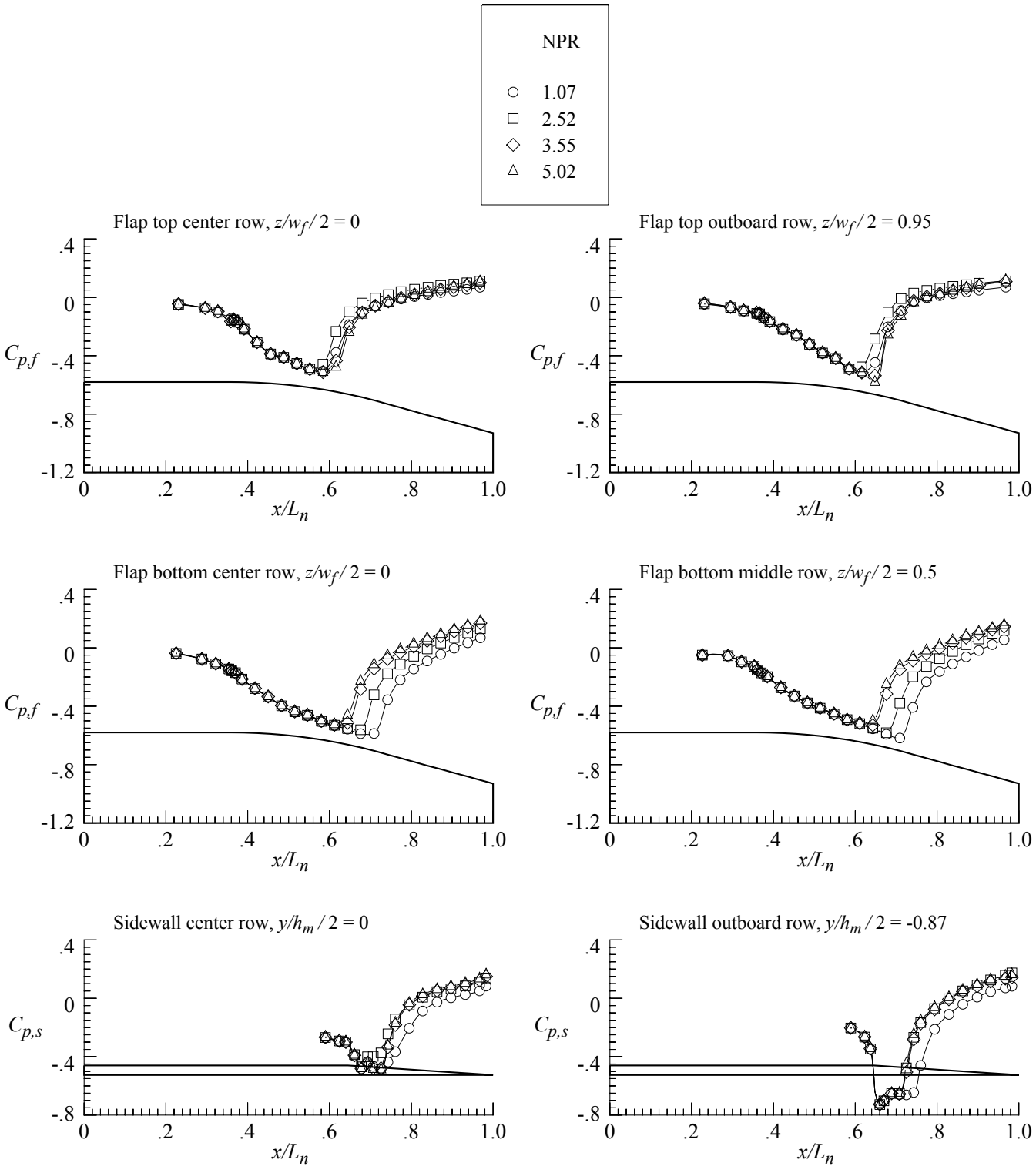

(c) $M = 0.95$.

Figure 131. Continued.

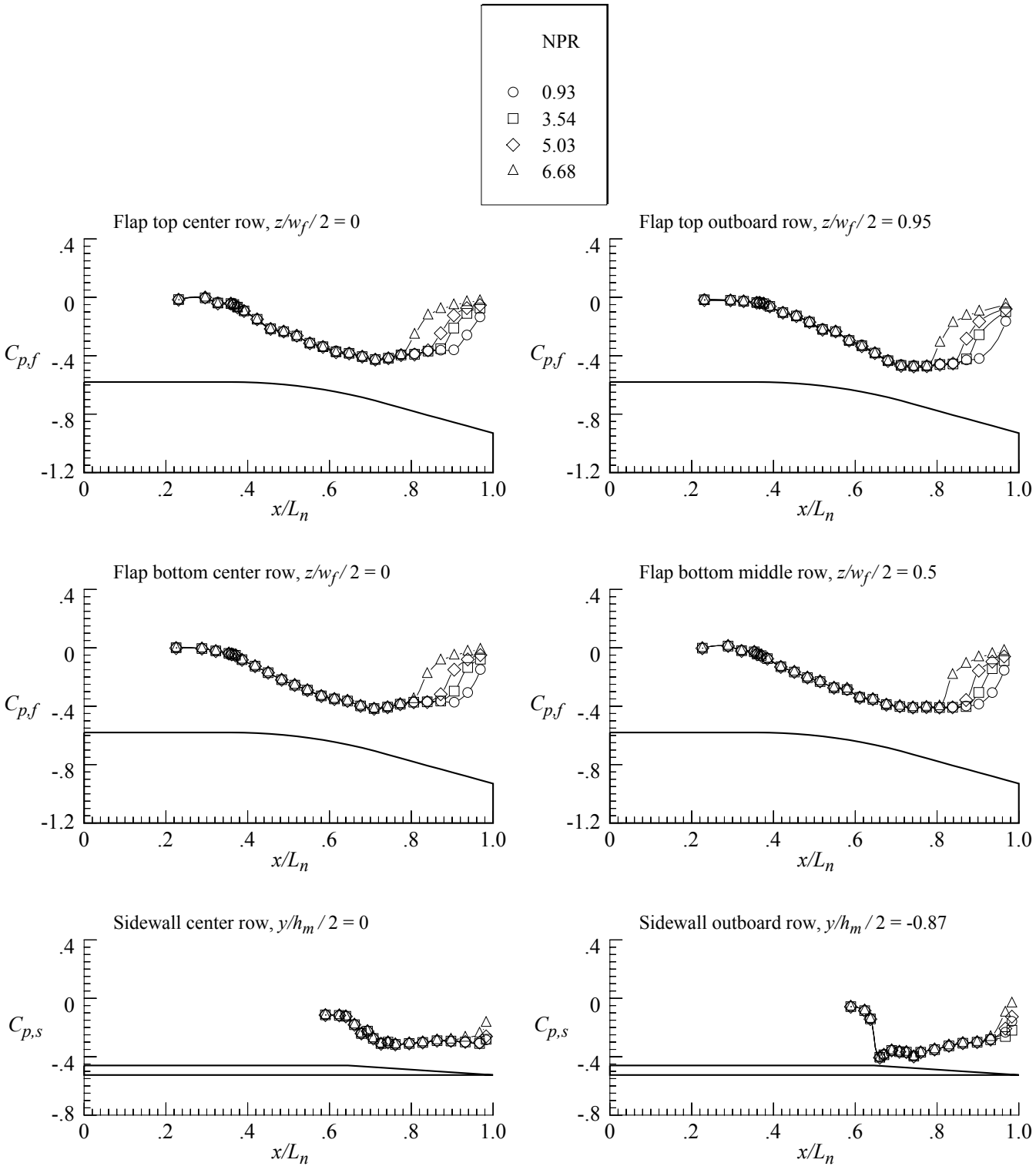

(d) $M = 1.20$.

Figure 131. Concluded.

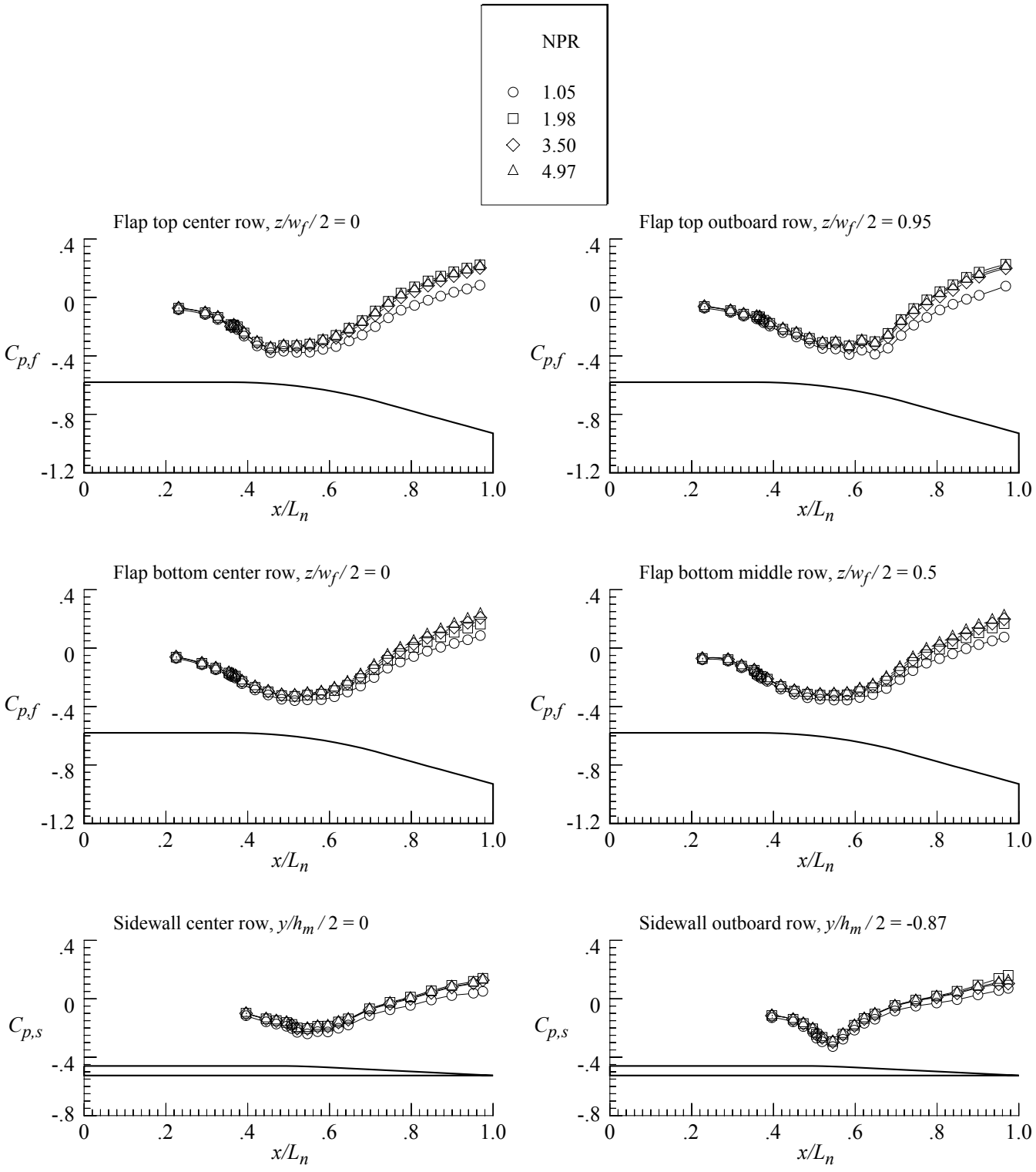

(a) $M = 0.80$.

Figure 132. External pressure distributions for nozzle N7 with flap F1 and sidewall S4. $r_f/r_{f,max} = 0.4$; $\beta_f = 16.38°$; $L_f/h_m = 1.4$; $\beta_s = 6.0°$; $r_s/r_{s,max} = 0.1$.

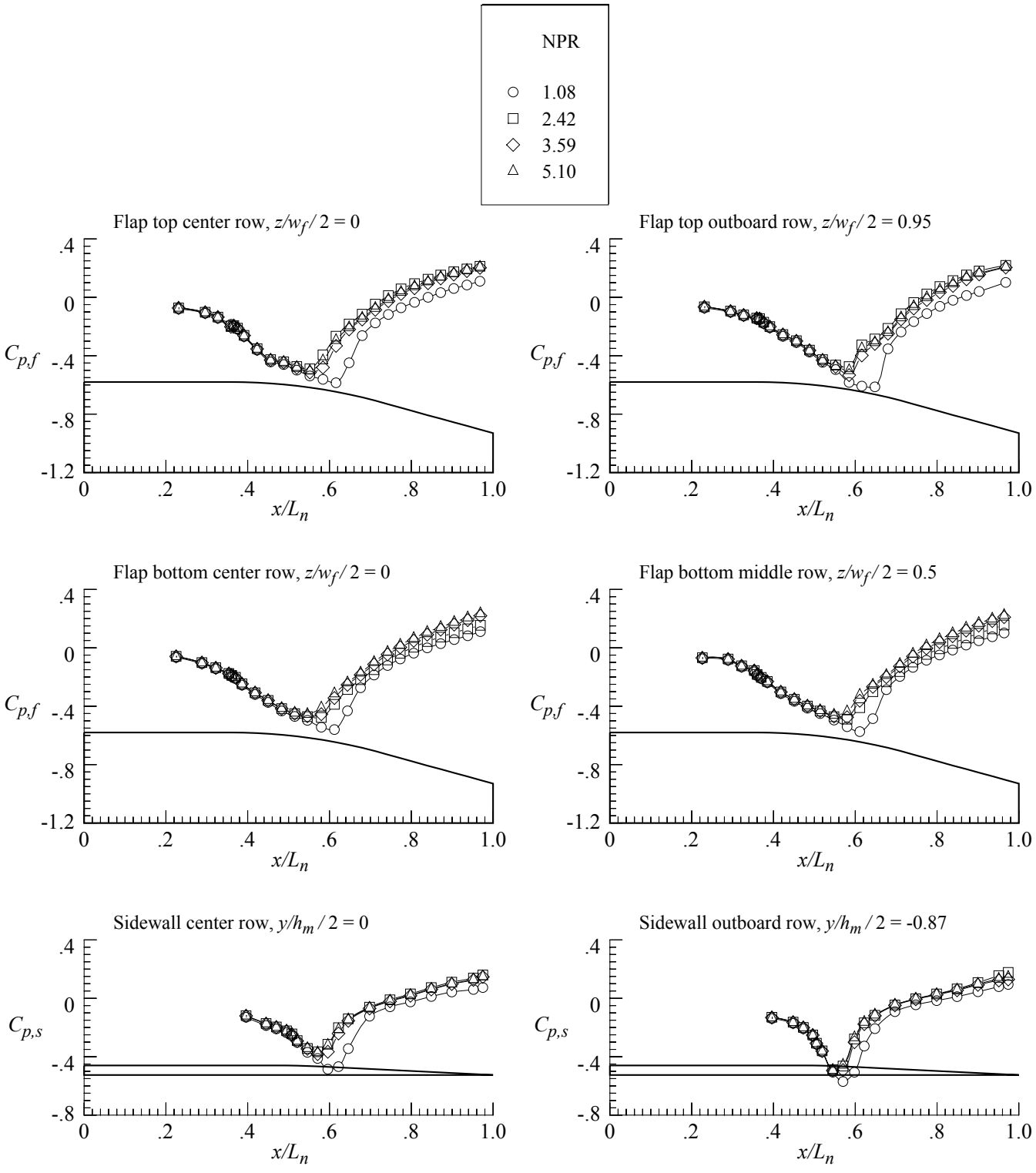

(b) $M = 0.90$.

Figure 132. Continued.

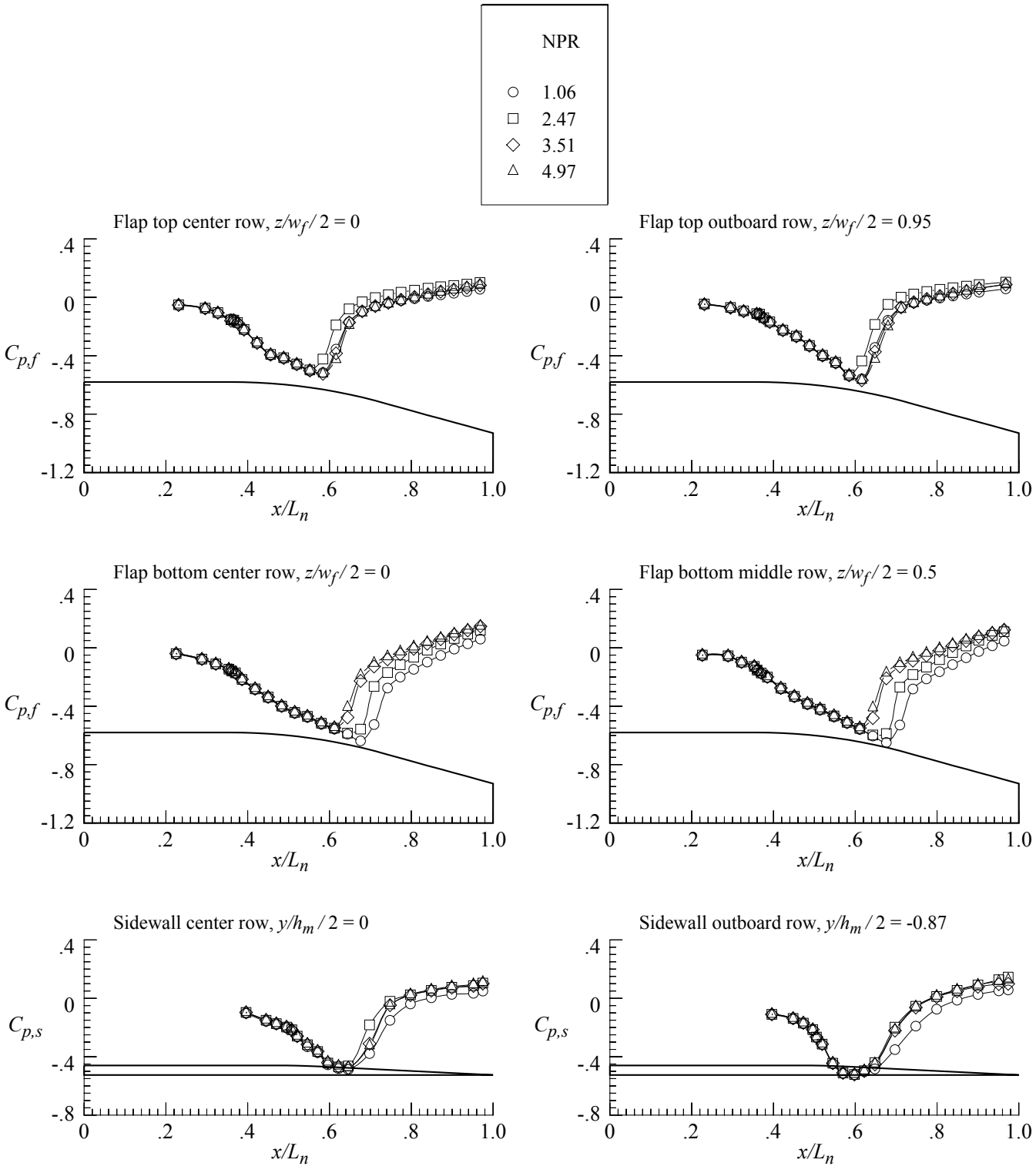

(c) $M = 0.95$.

Figure 132. Continued.

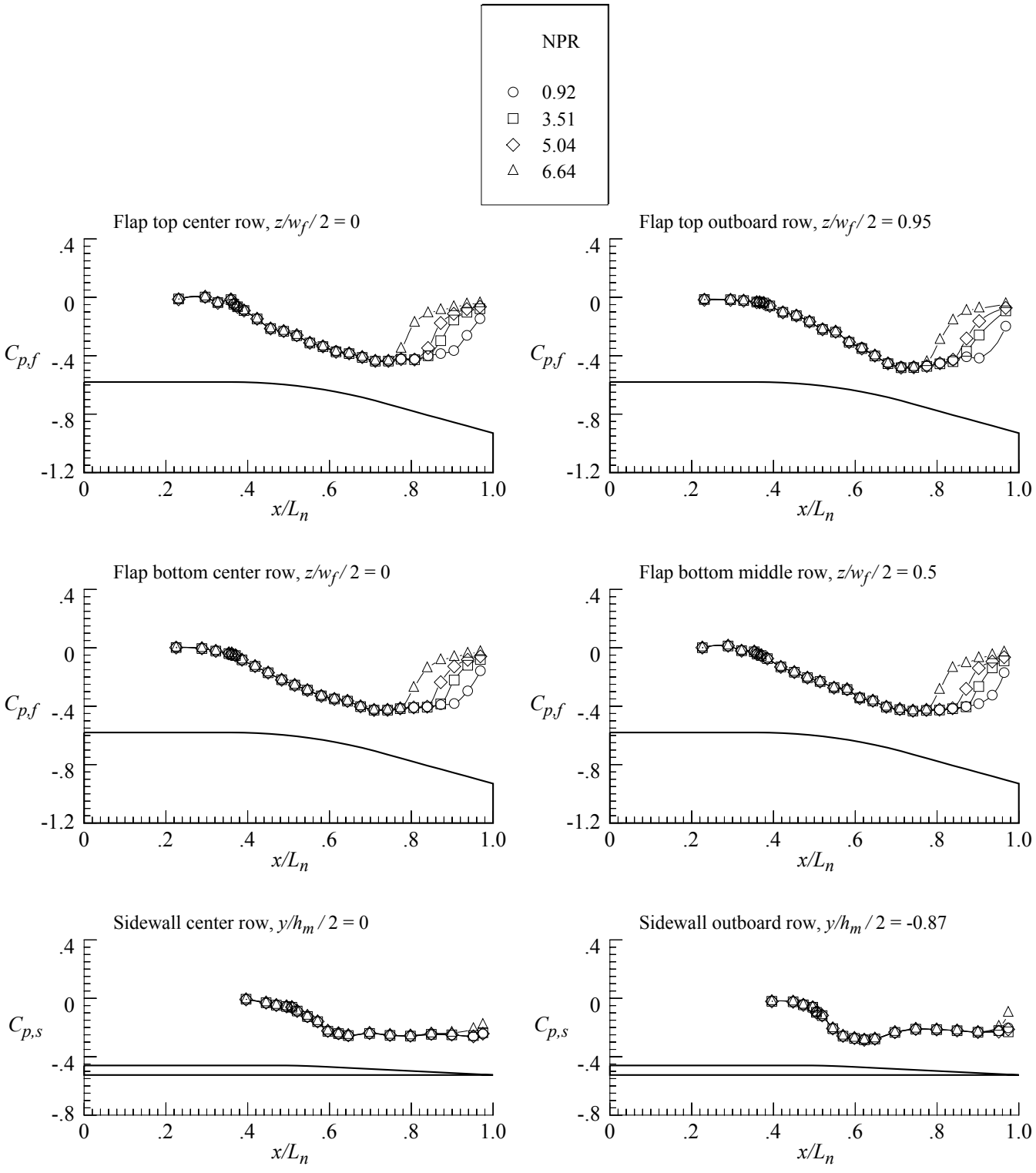

(d) $M = 1.20$.

Figure 132. Concluded.

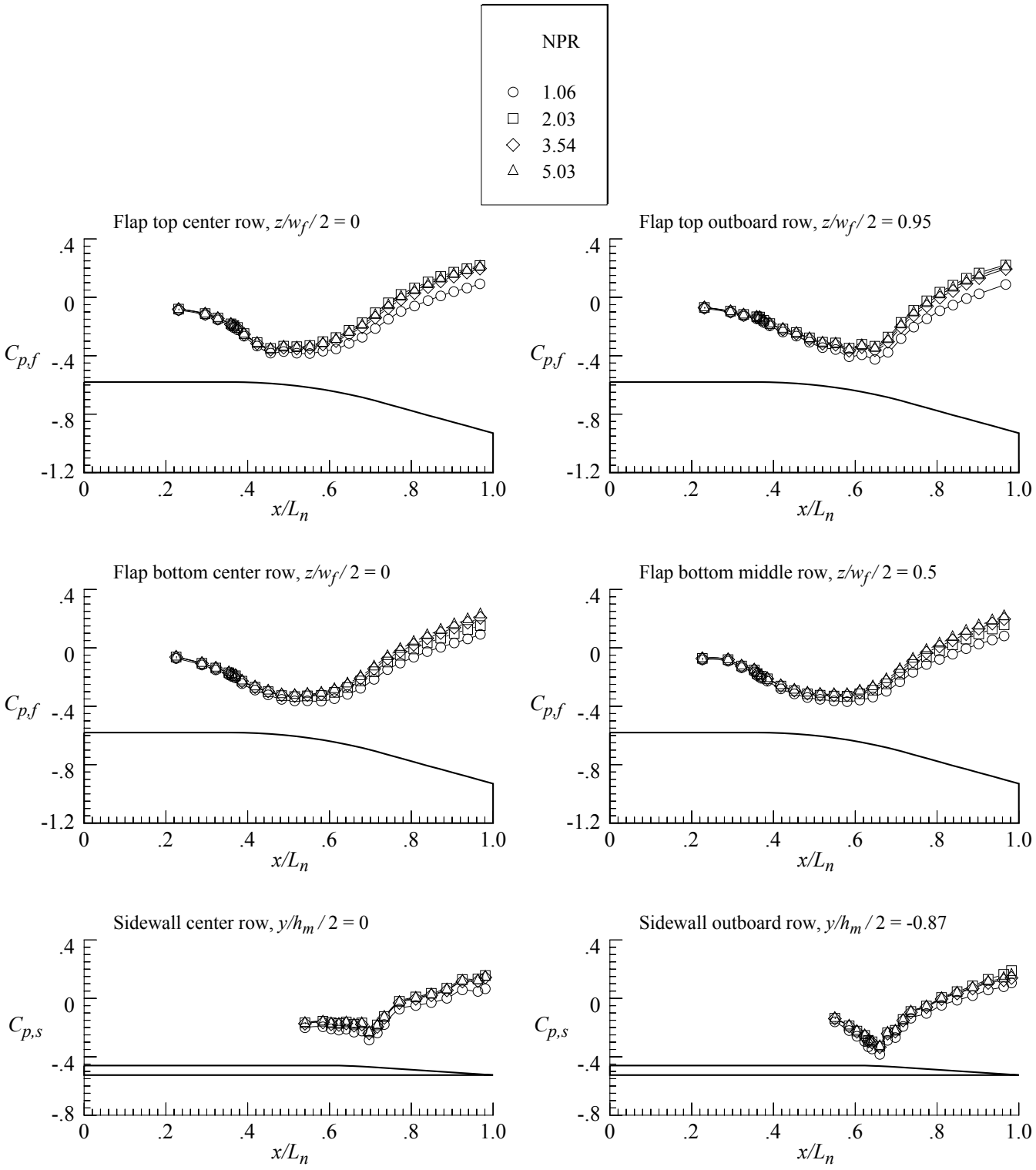

(a) $M = 0.80$.

Figure 133. External pressure distributions for nozzle N8 with flap F1 and sidewall S5. $r_f/r_{f,max} = 0.4$; $\beta_f = 16.38°$; $L_f/h_m = 1.4$; $\beta_s = 8.0°$; $r_s/r_{s,max} = 0.1$.

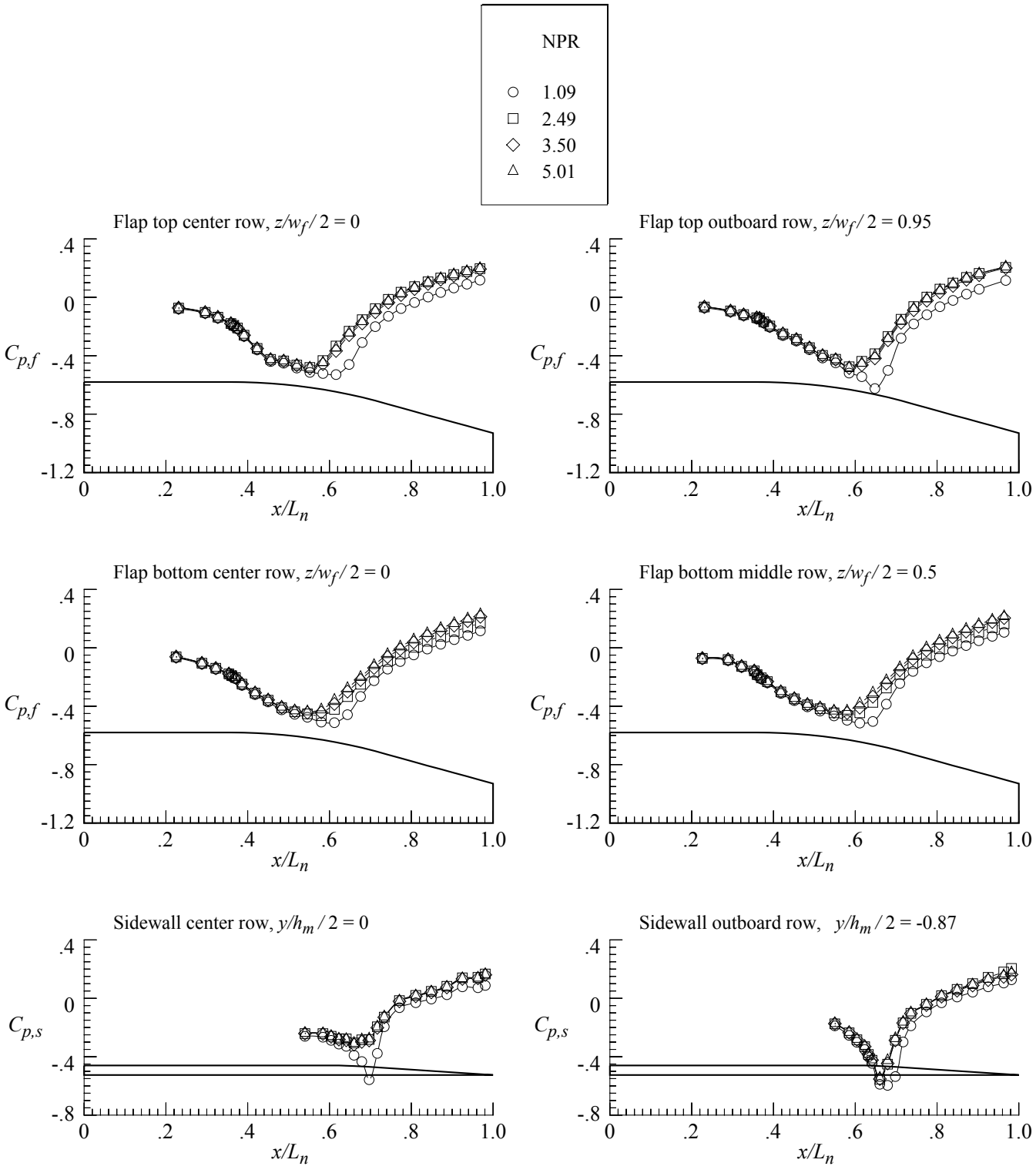

(b) $M = 0.90$.

Figure 133. Continued.

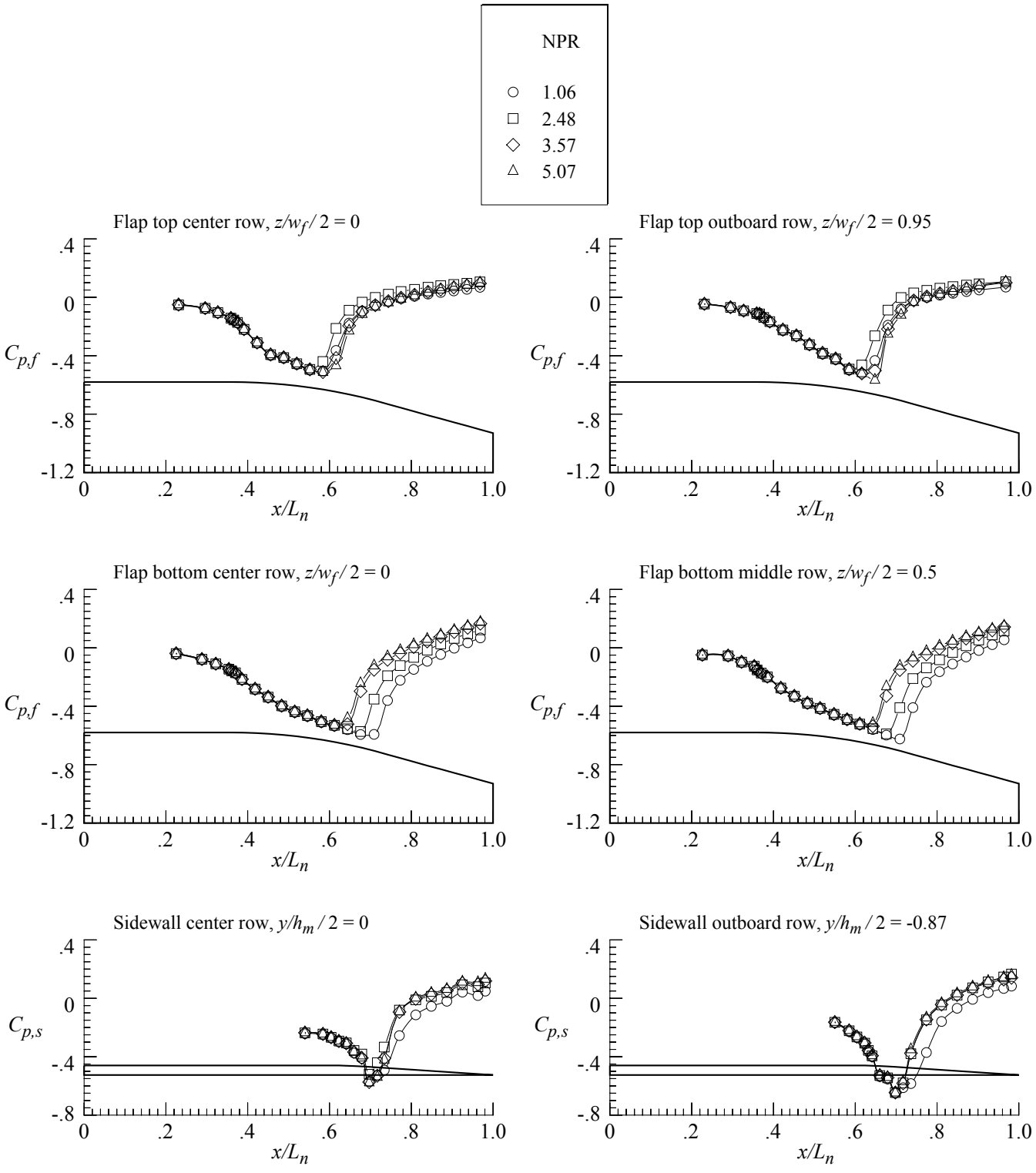

(c) $M = 0.95$.

Figure 133. Continued.

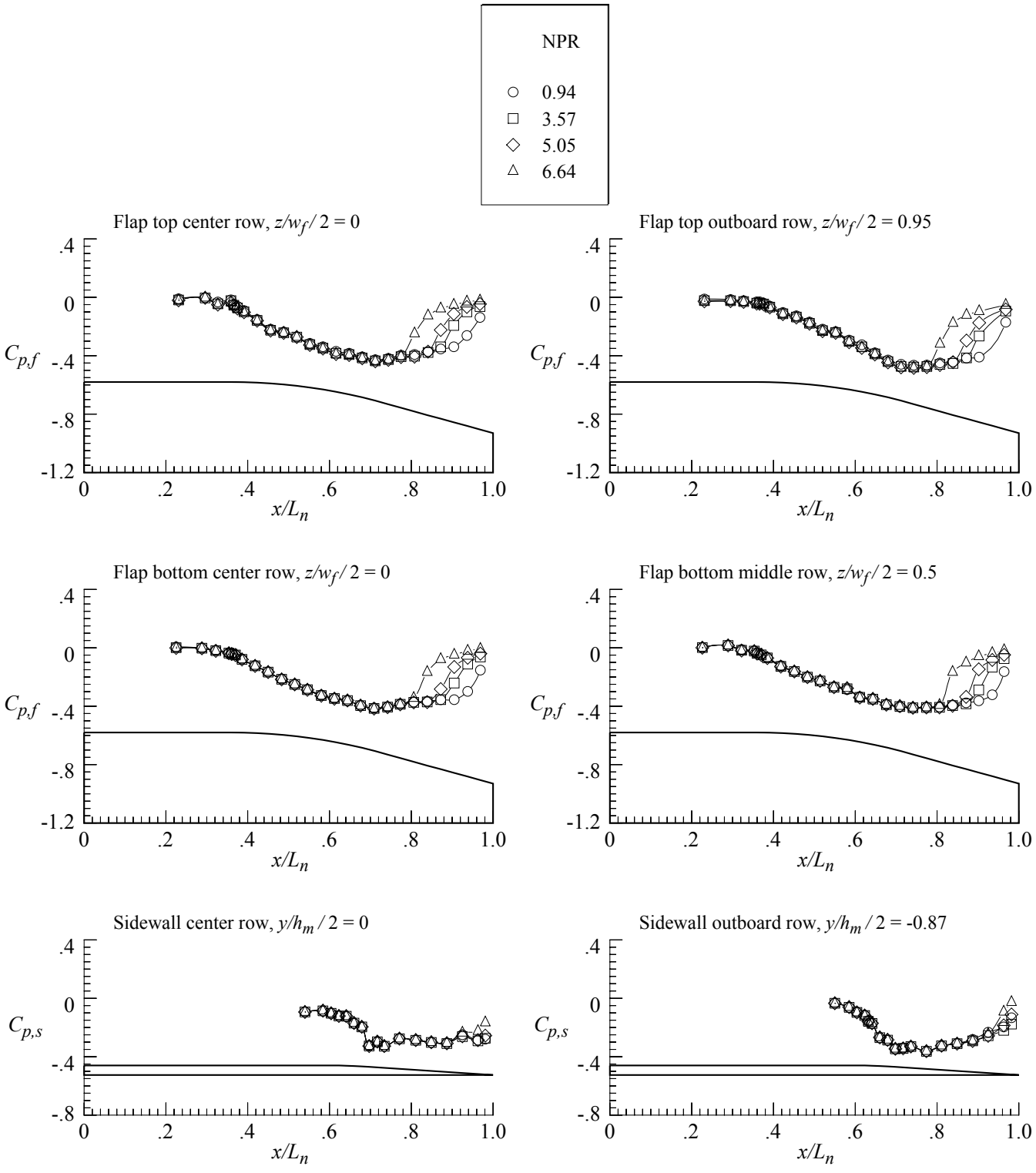

(d) $M = 1.20$.

Figure 133. Concluded.

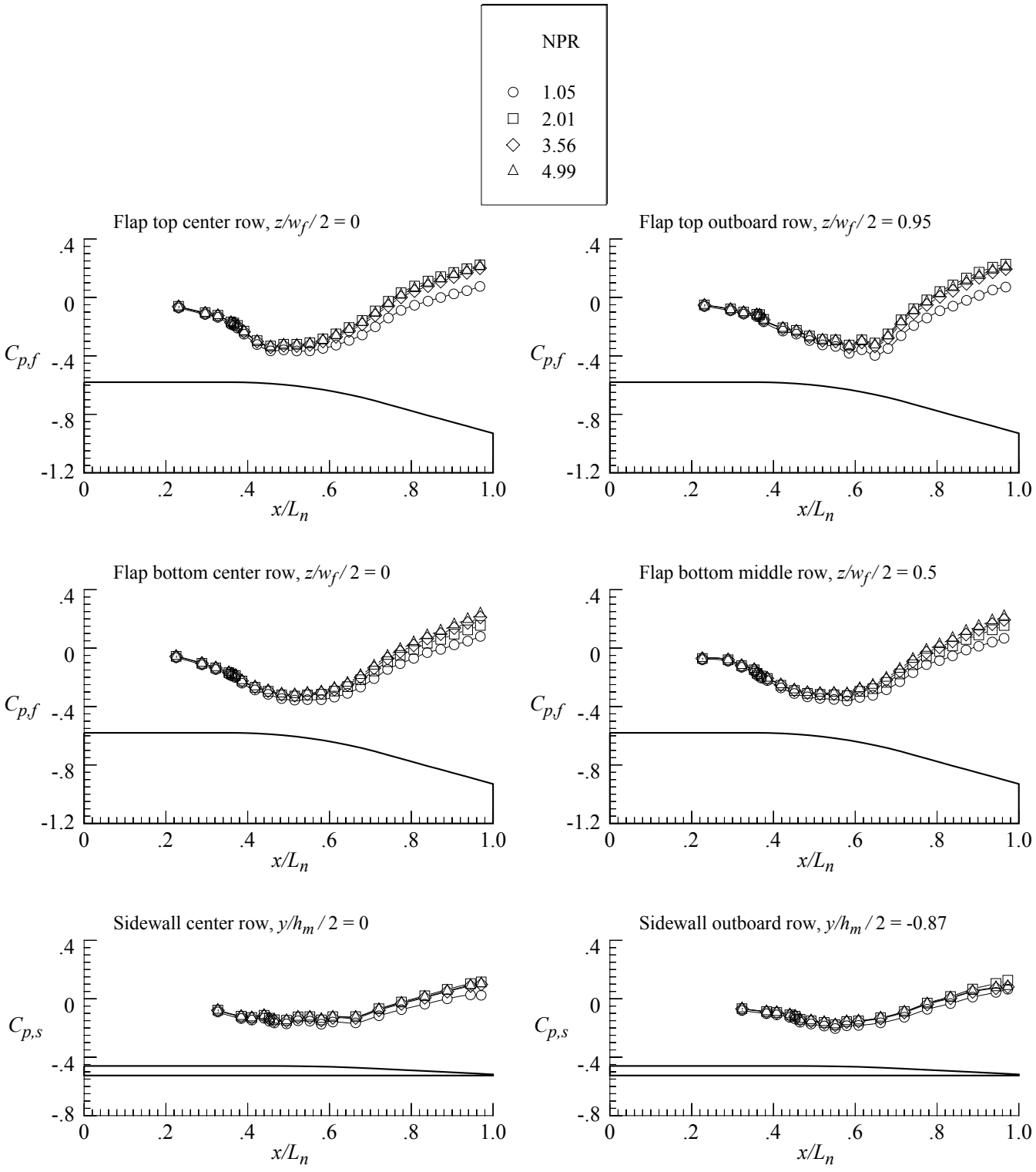

(a) $M = 0.80$.

Figure 134. External pressure distributions for nozzle N9 with flap F1 and sidewall S6.
$r_f/r_{f,max} = 0.4$; $\beta_f = 16.38°$; $L_f/h_m = 1.4$; $\beta_s = 6.0°$; $r_s/r_{s,max} = 0.4$.

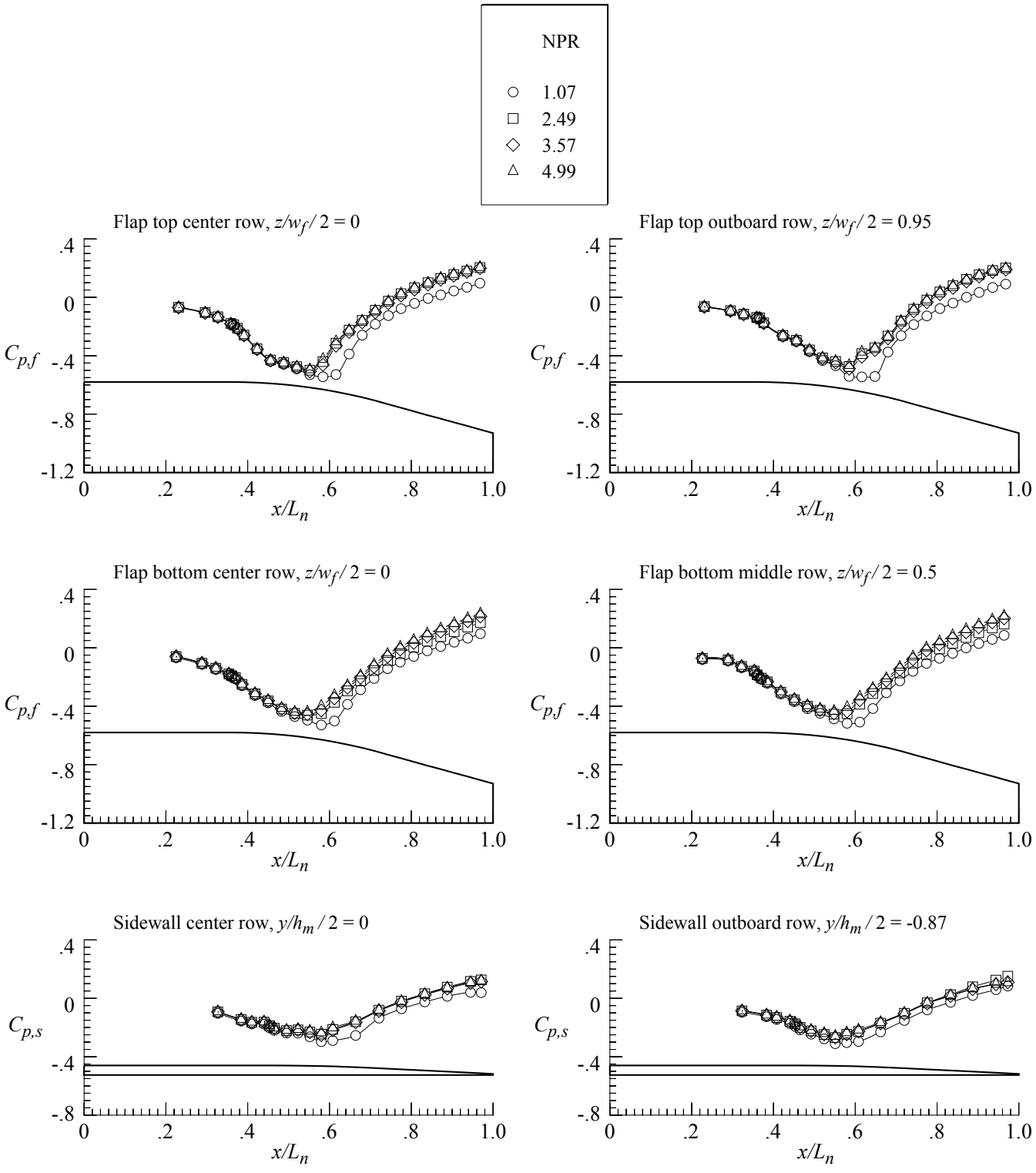

(b) $M = 0.90$.

Figure 134. Continued.

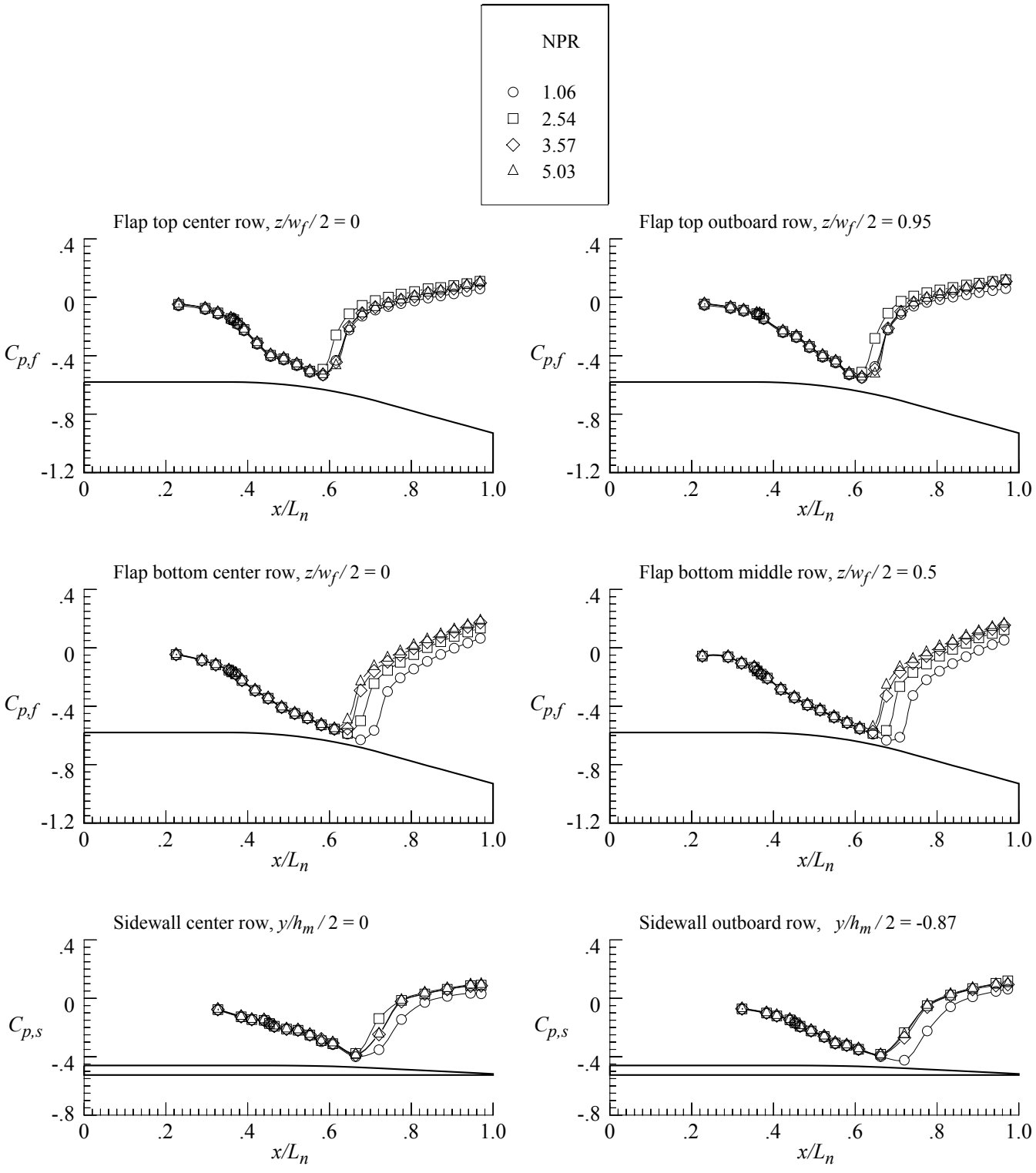

(c) $M = 0.95$.

Figure 134. Continued.

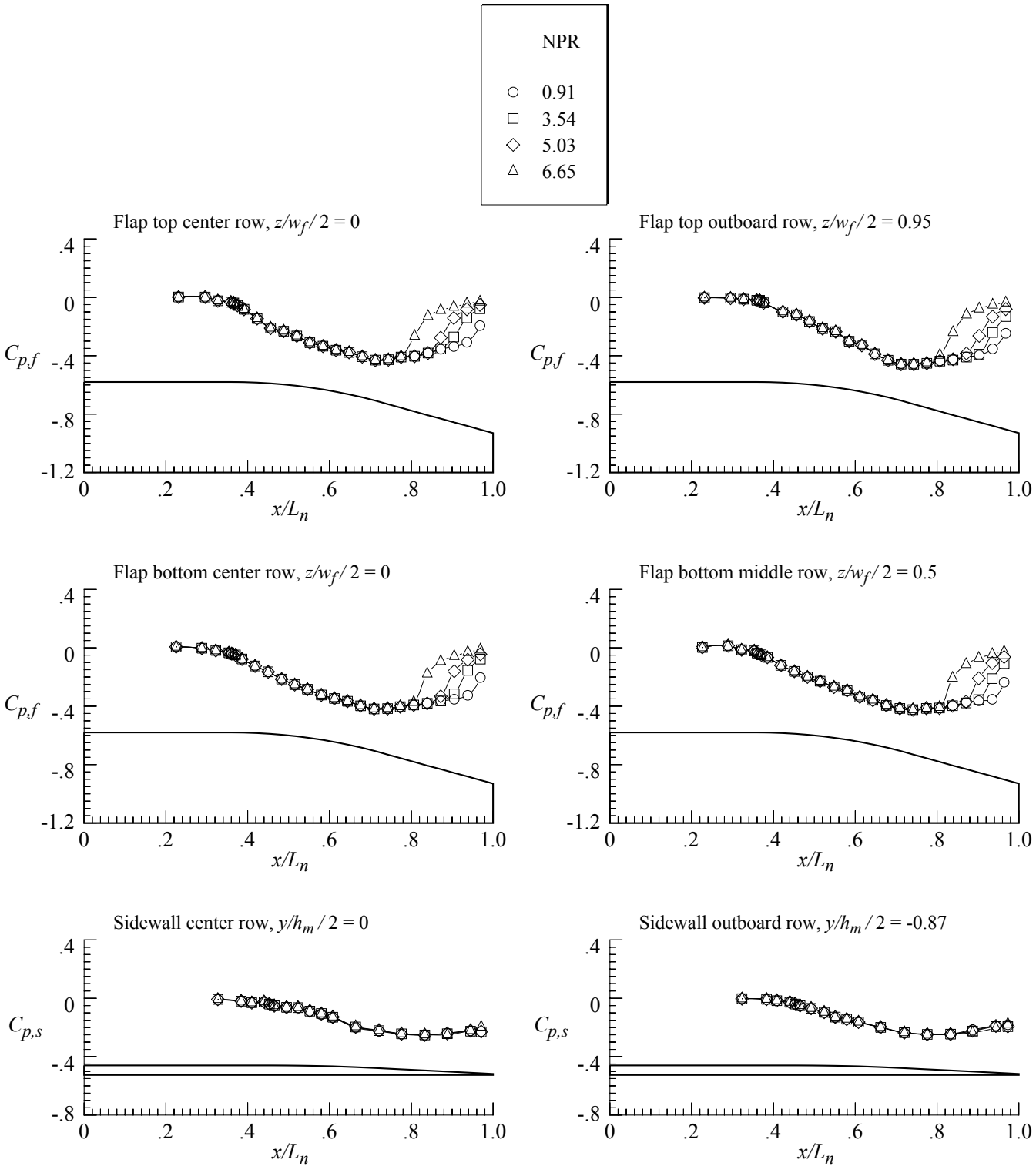

(d) $M = 1.20$.

Figure 134. Concluded.

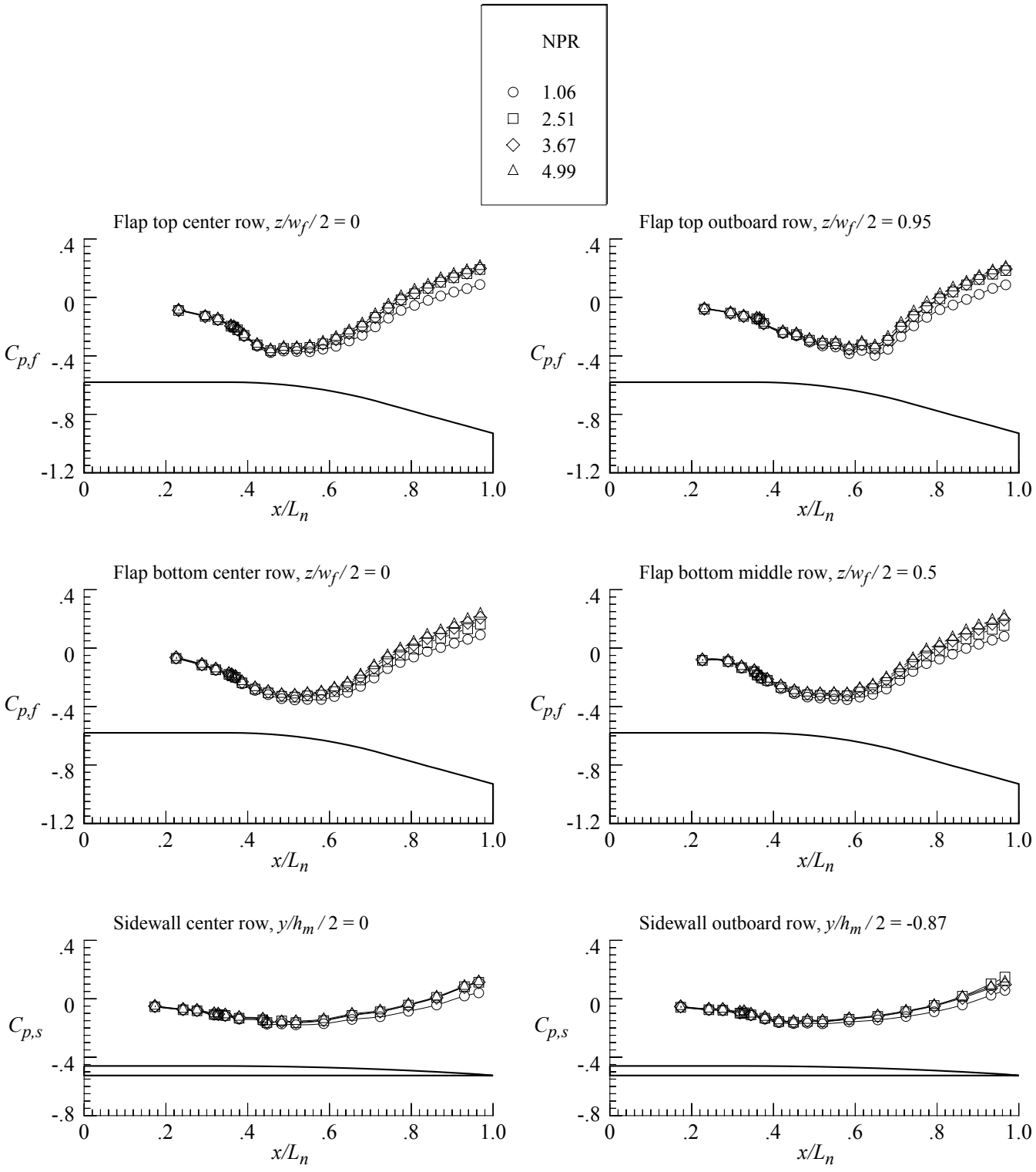

(a) $M = 0.80$.

Figure 135. External pressure distributions for nozzle N10 with flap F1 and sidewall S7. $r_f/r_{f,max} = 0.4$; $\beta_f = 16.38°$; $L_f/h_m = 1.4$; $\beta_s = 8.0°$; $r_s/r_{s,max} = 1.0$.

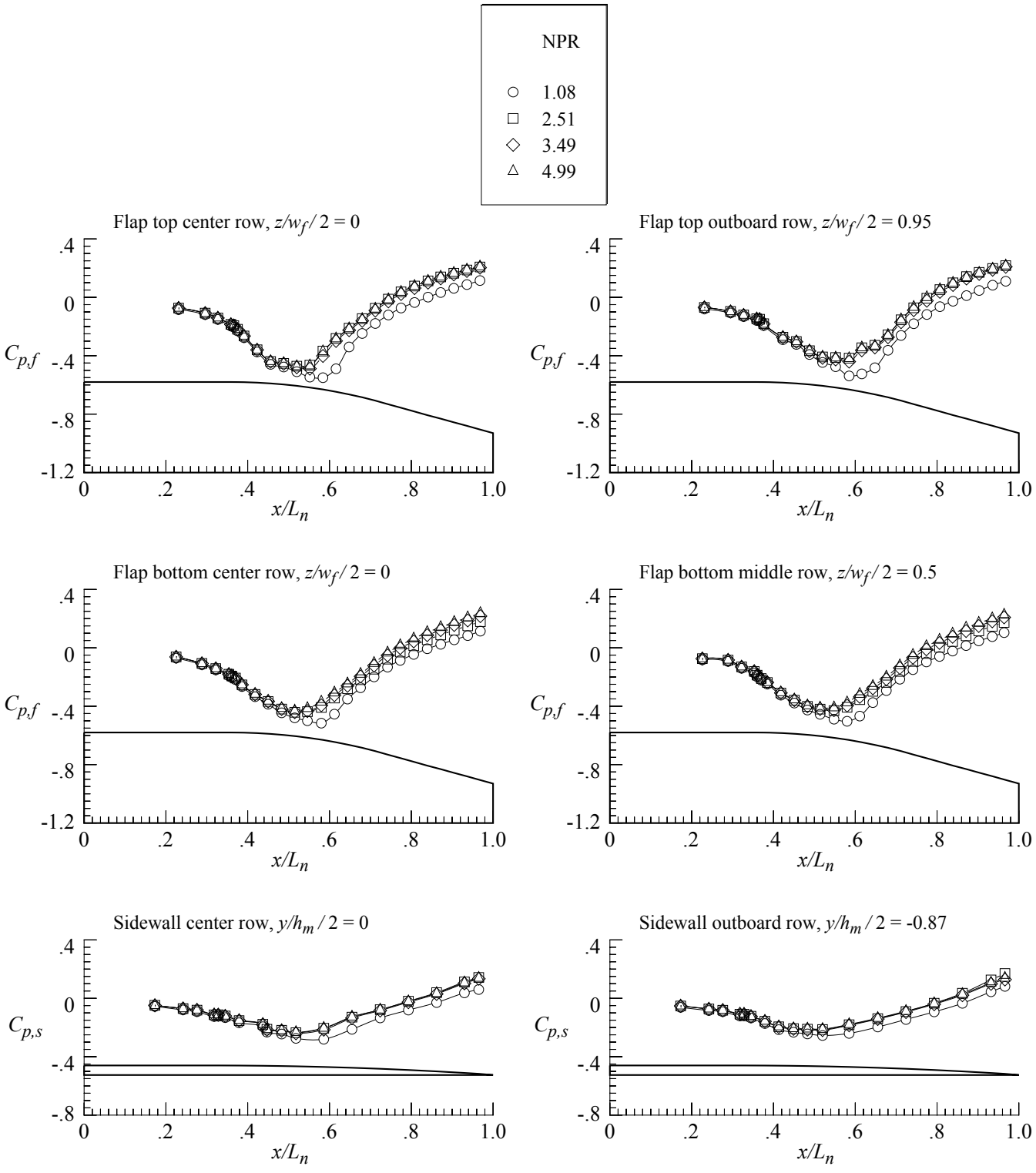

(b) $M = 0.90$.

Figure 135. Continued.

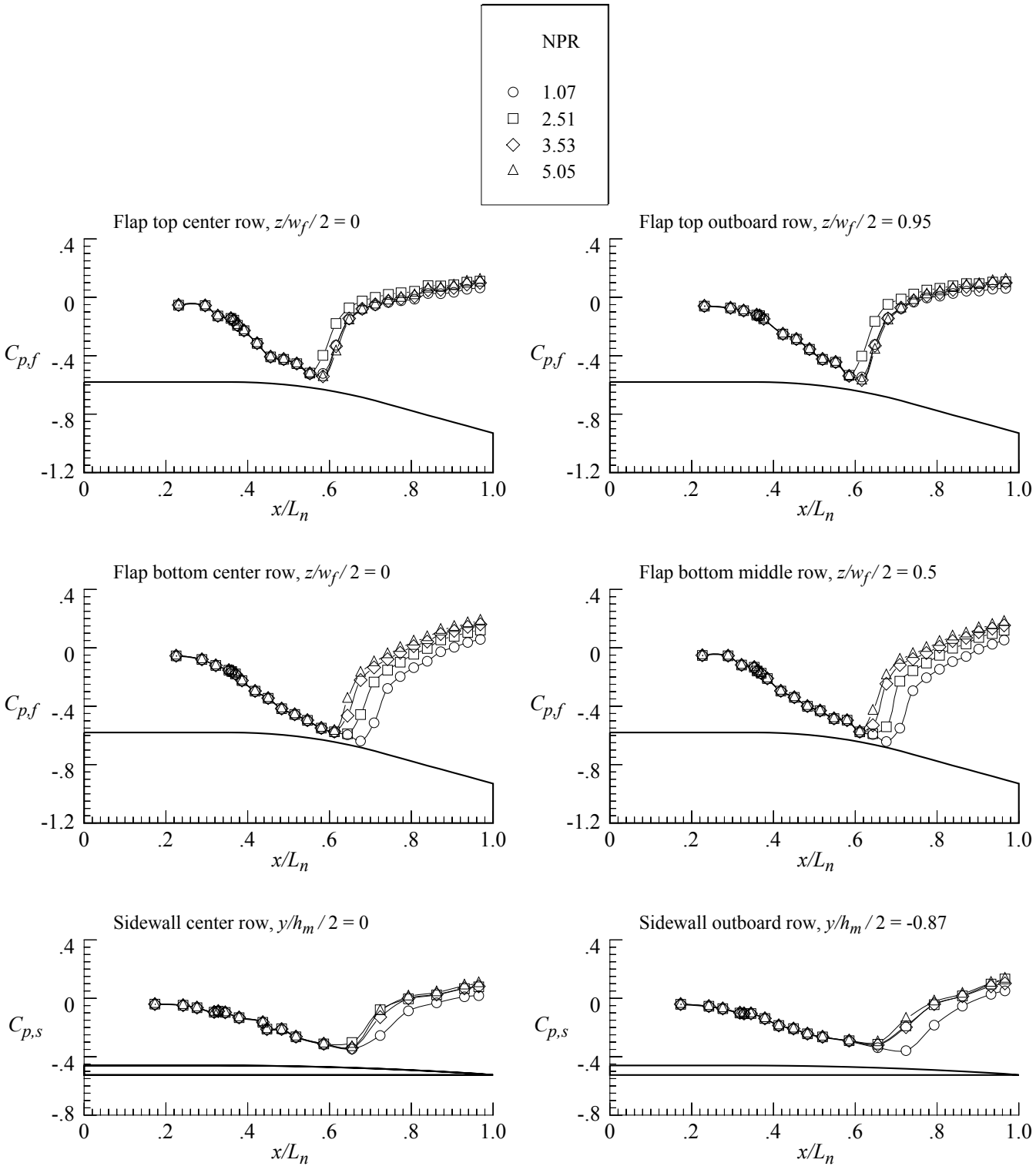

(c) $M = 0.95$.

Figure 135. Continued.

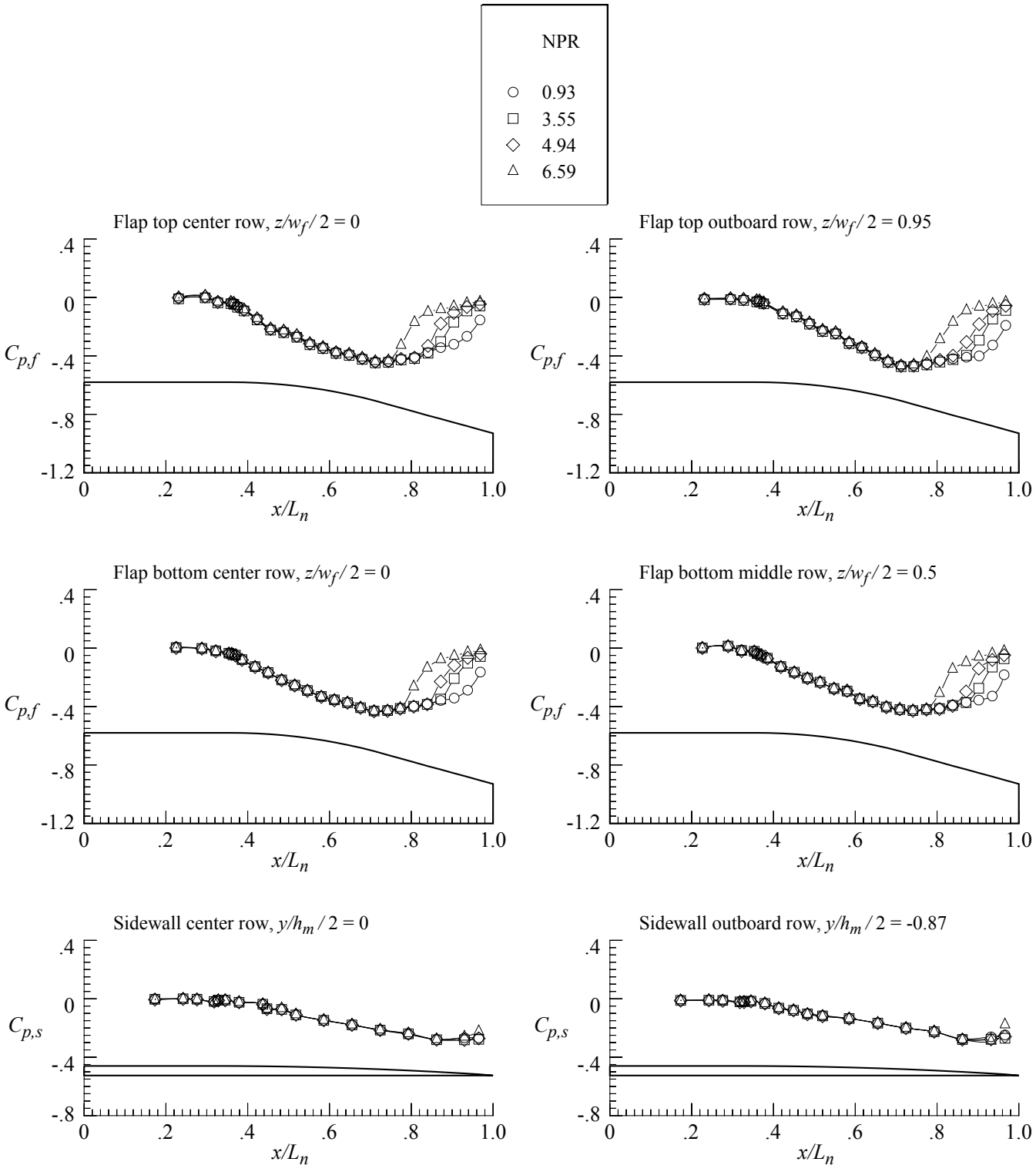

(d) $M = 1.20$.

Figure 135. Concluded.

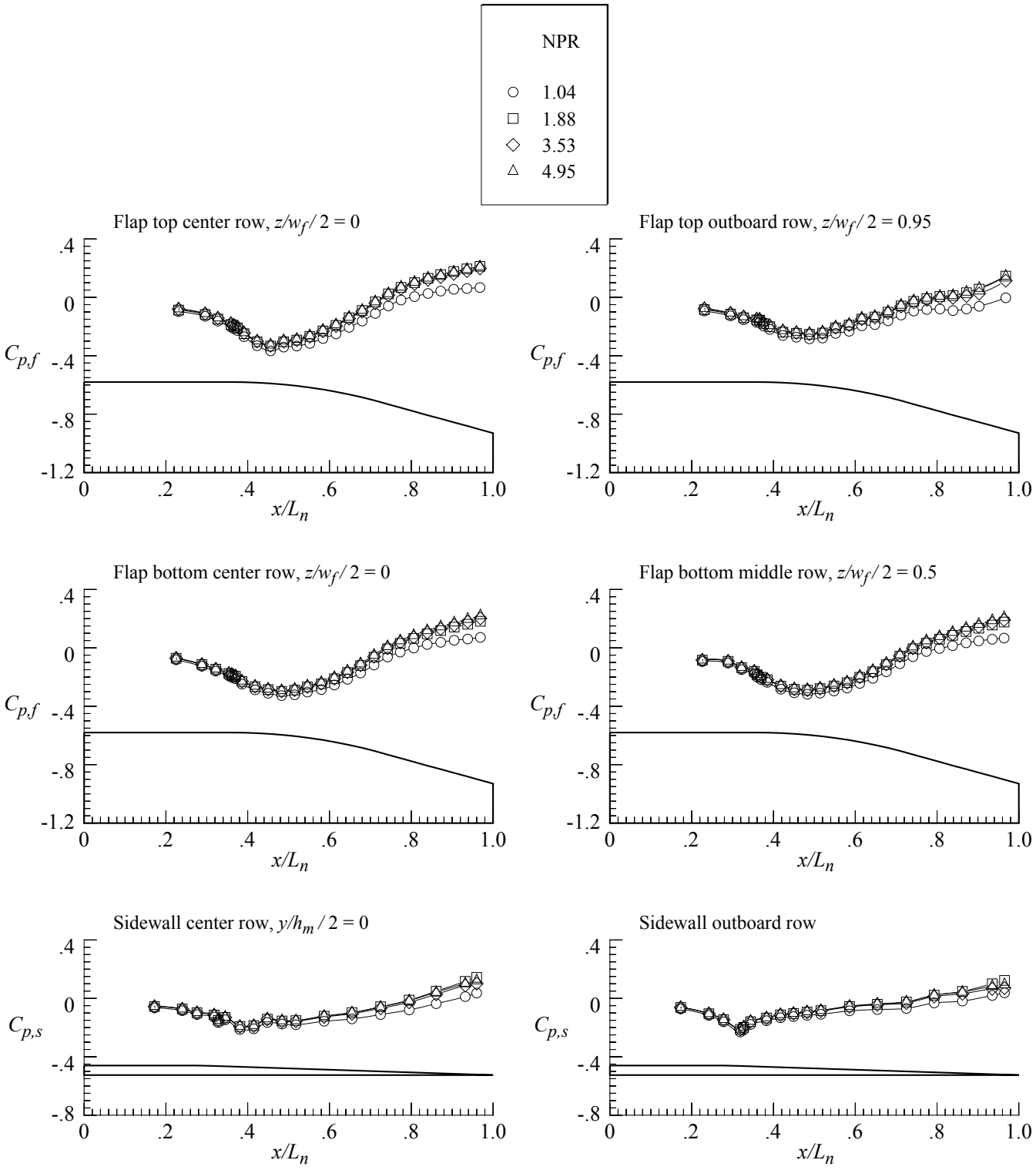

(a) $M = 0.80$.

Figure 136. External pressure distributions for nozzle N11 with flap F1 and sidewall S8. $r_f/r_{f,max} = 0.4$; $\beta_f = 16.38°$; $L_f/h_m = 1.4$; $\beta_s = 4.0°$; $r_s/r_{s,max} = 0$.

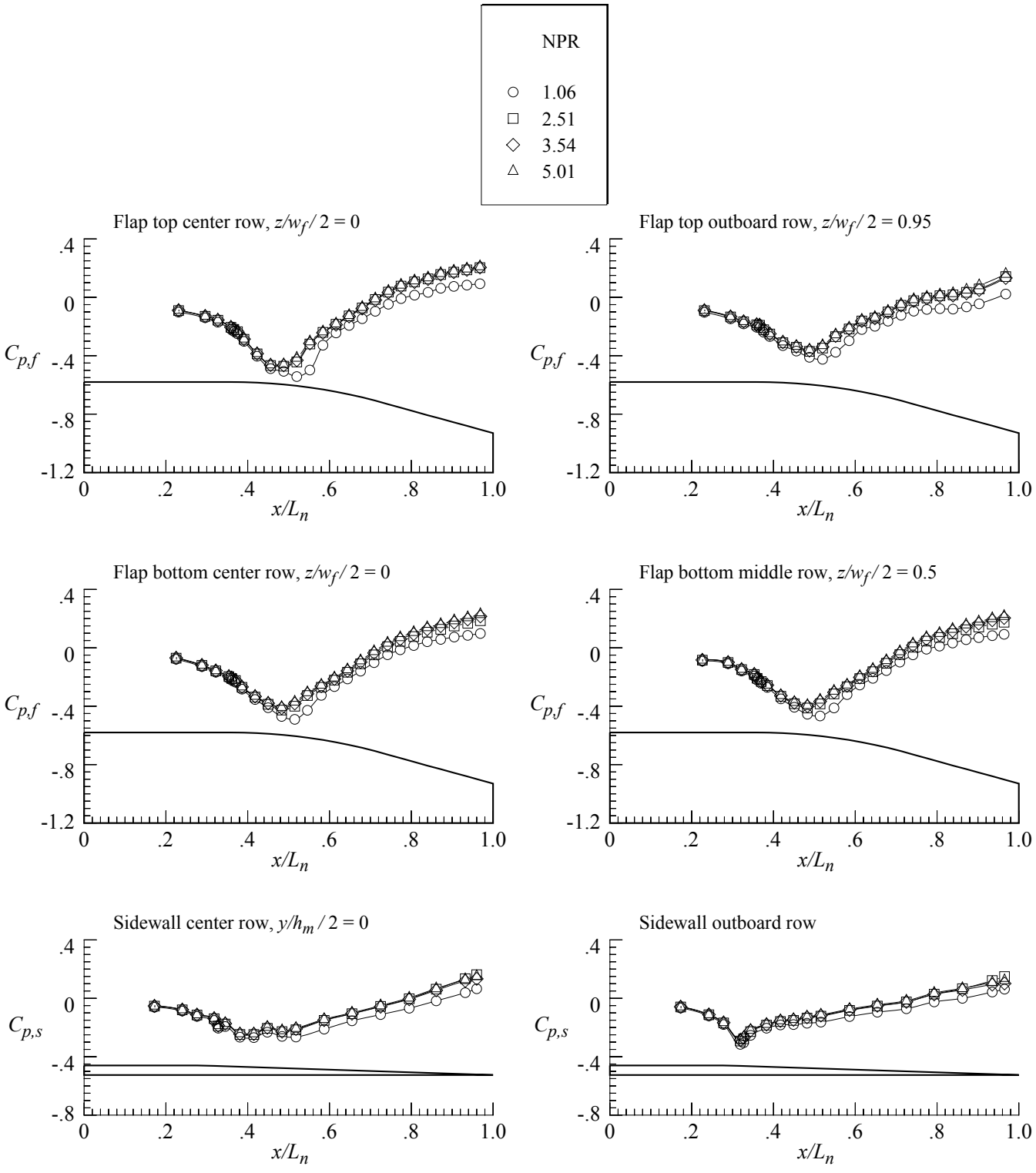

(b) $M = 0.90$.

Figure 136. Continued.

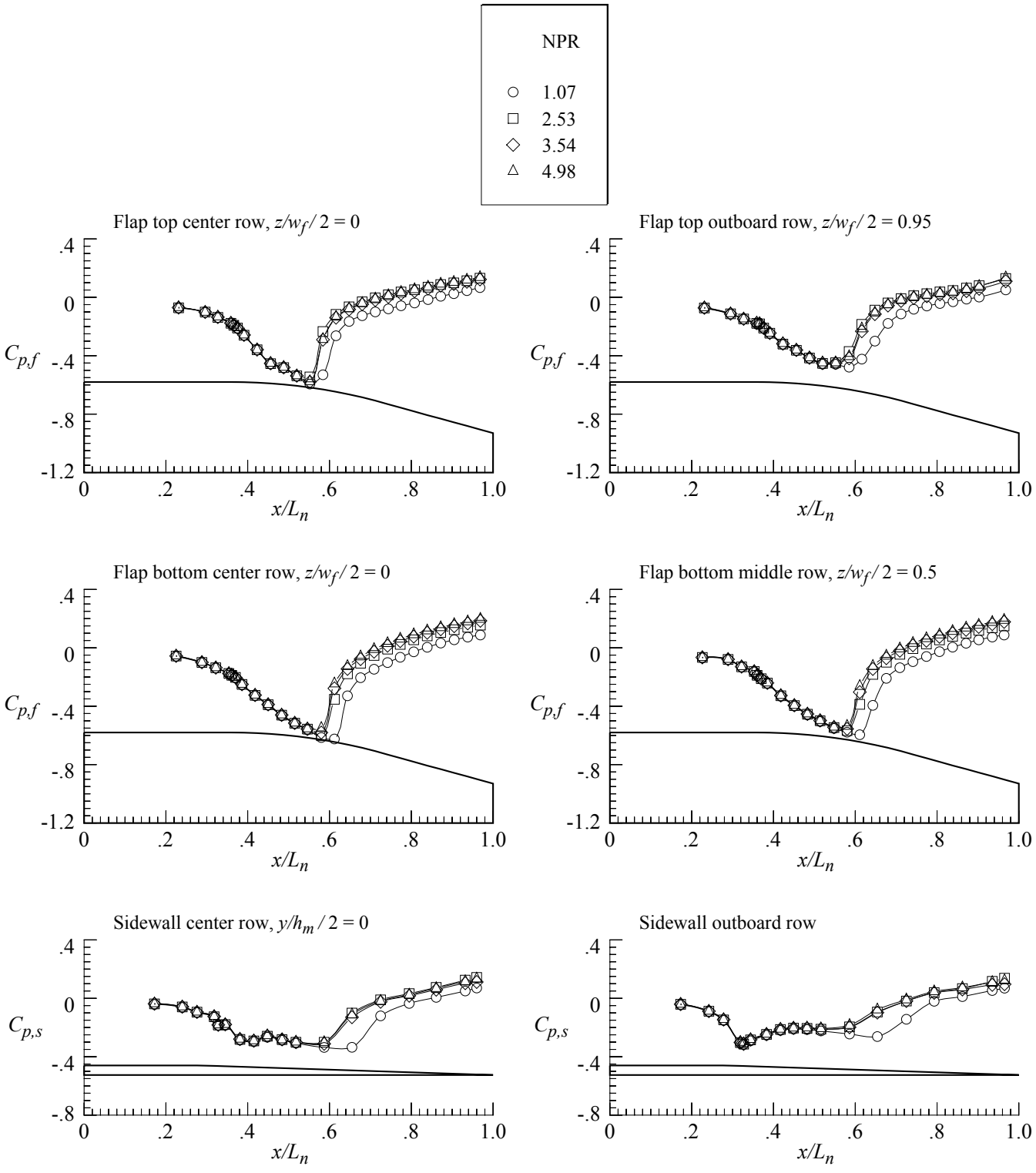

(c) $M = 0.95$.

Figure 136. Continued.

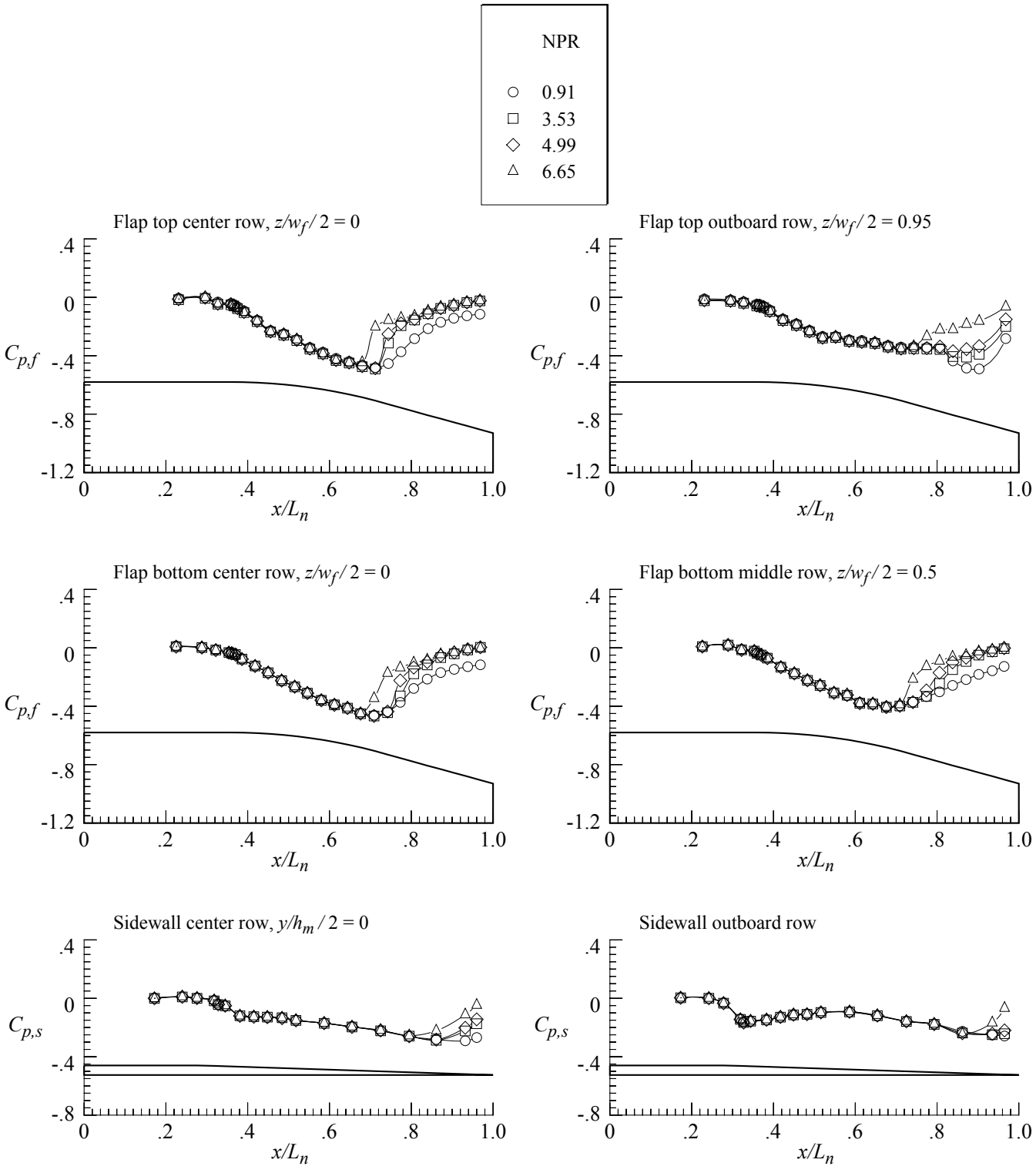

(d) $M = 1.20$.

Figure 136. Concluded.

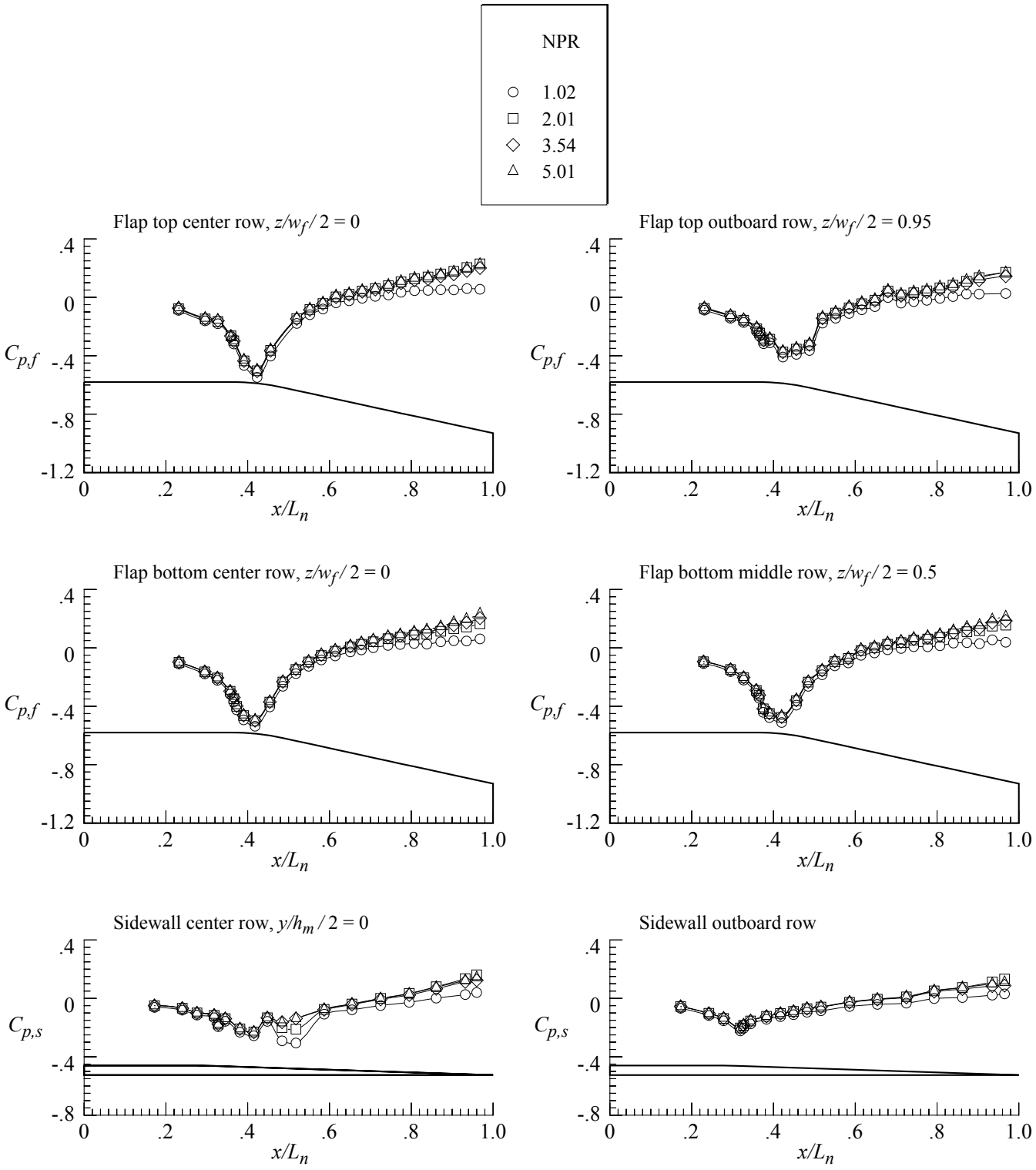

(a) $M = 0.80$.

Figure 137. External pressure distributions for nozzle N12 with flap F2 and sidewall S8.
$r_f/r_{f,max} = 0.1$; $\beta_f = 12.88°$; $L_f/h_m = 1.4$; $\beta_s = 4.0°$; $r_s/r_{s,max} = 0$.

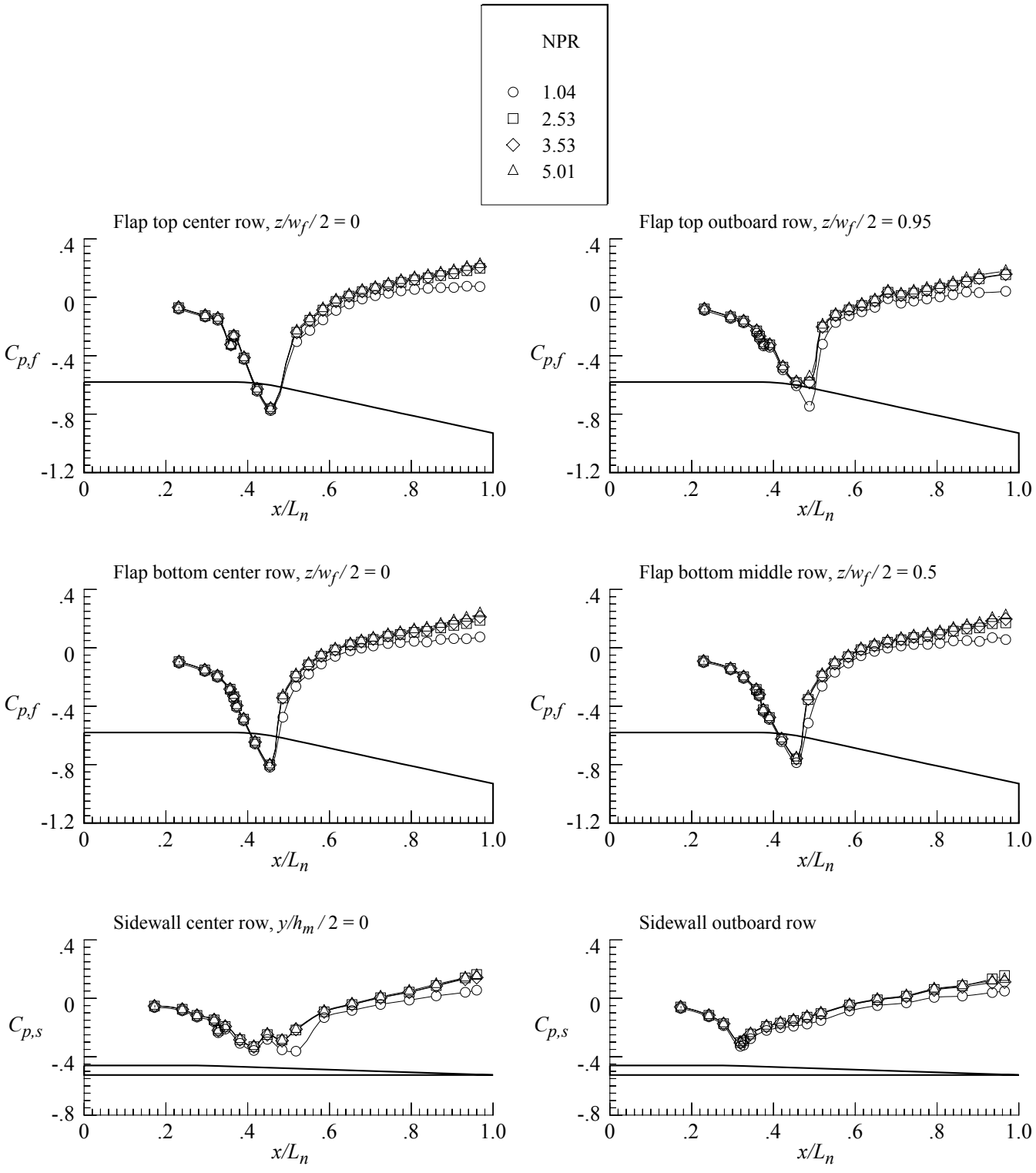

(b) $M = 0.90$.

Figure 137. Continued.

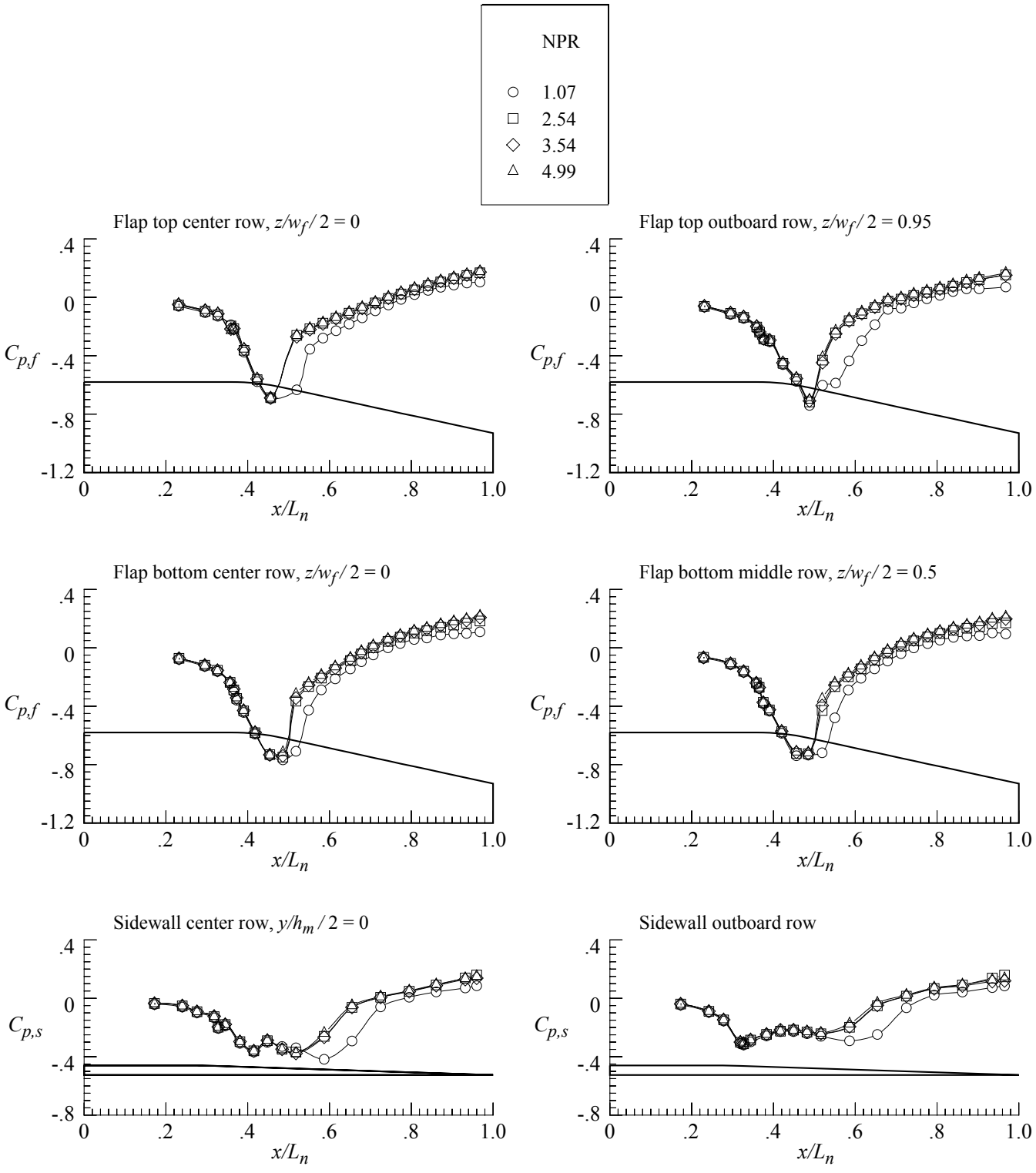

(c) $M = 0.95$.

Figure 137. Continued.

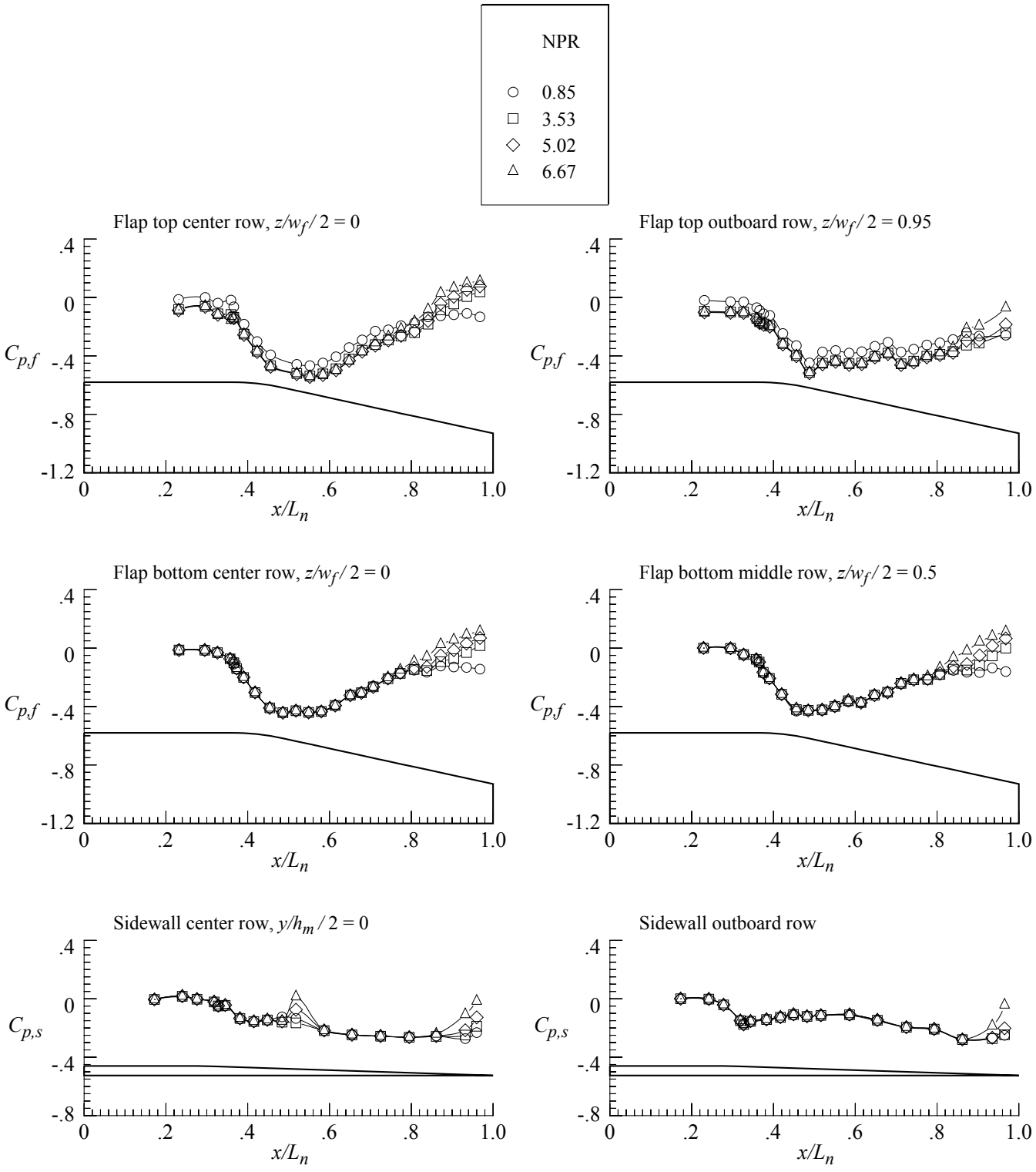

(d) $M = 1.20$.

Figure 137. Concluded.

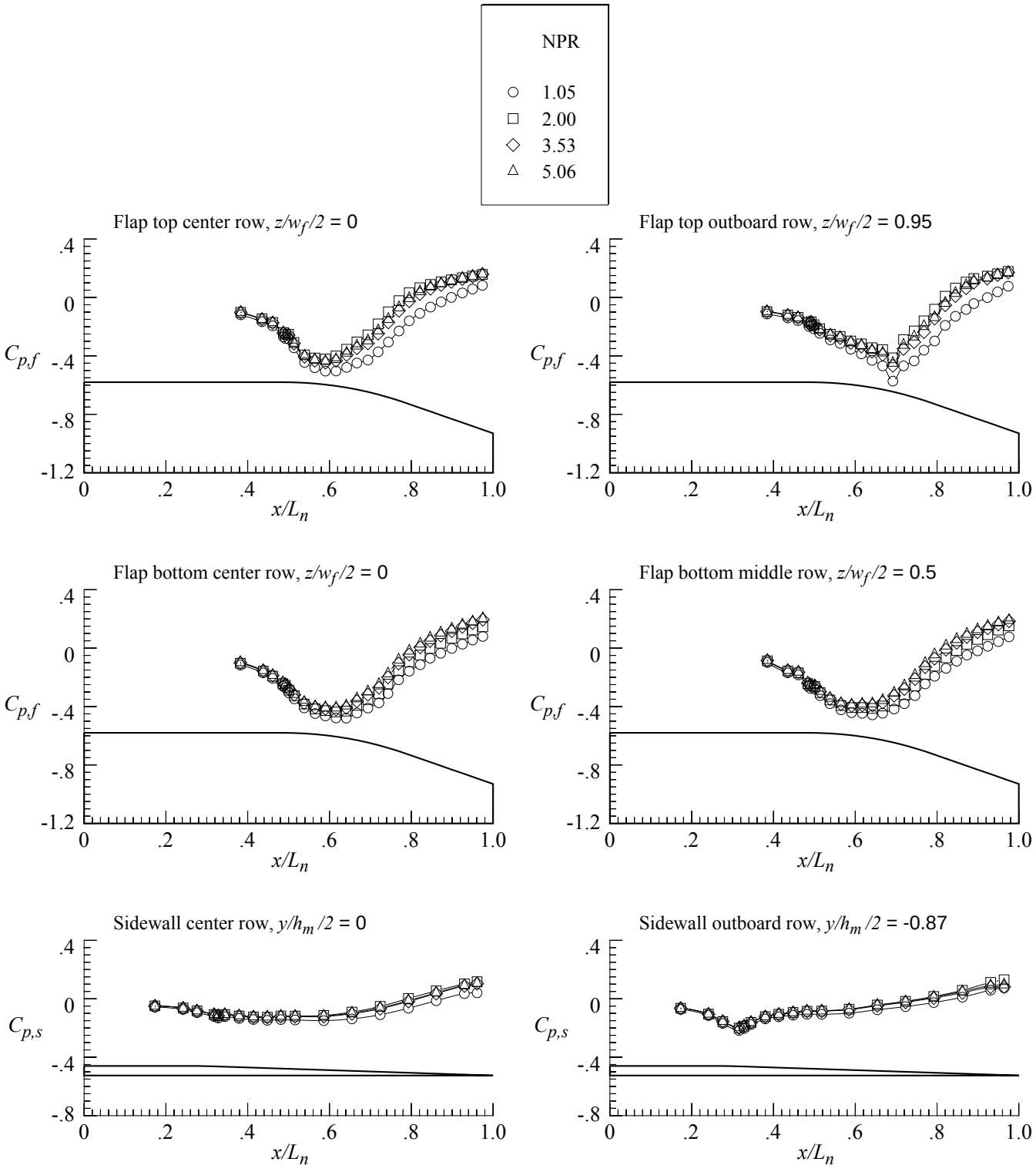

(a) $M = 0.80$.

Figure 138. External pressure distributions for nozzle N13 with flap F5 and sidewall S1.
$r_f/r_{f,max} = 0.4$; $\beta_f = 20.30°$; $L_f/h_m = 1.1$; $\beta_s = 4.0°$; $r_s/r_{s,max} = 0$.

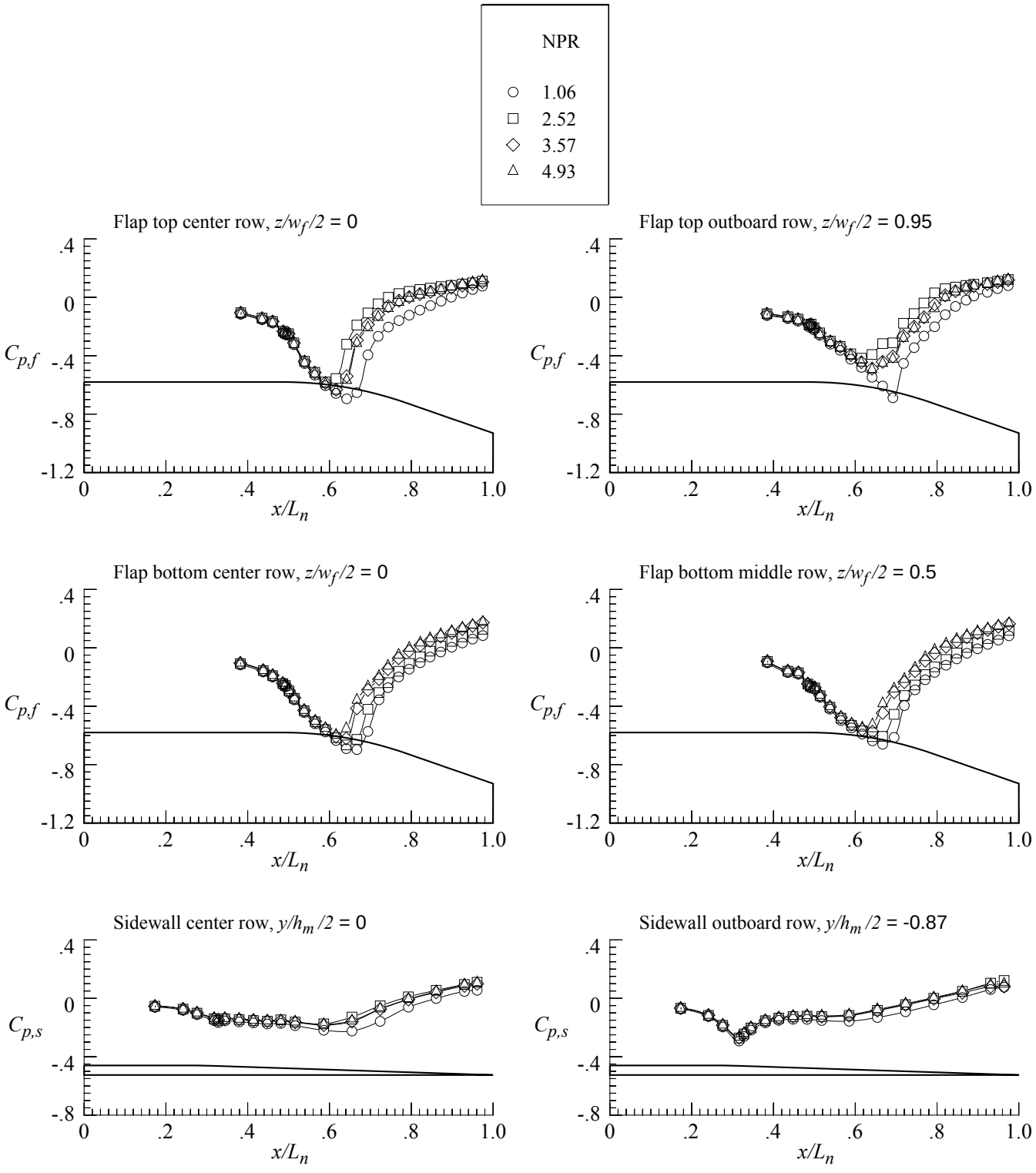

(b) $M = 0.90$.

Figure 138. Continued.

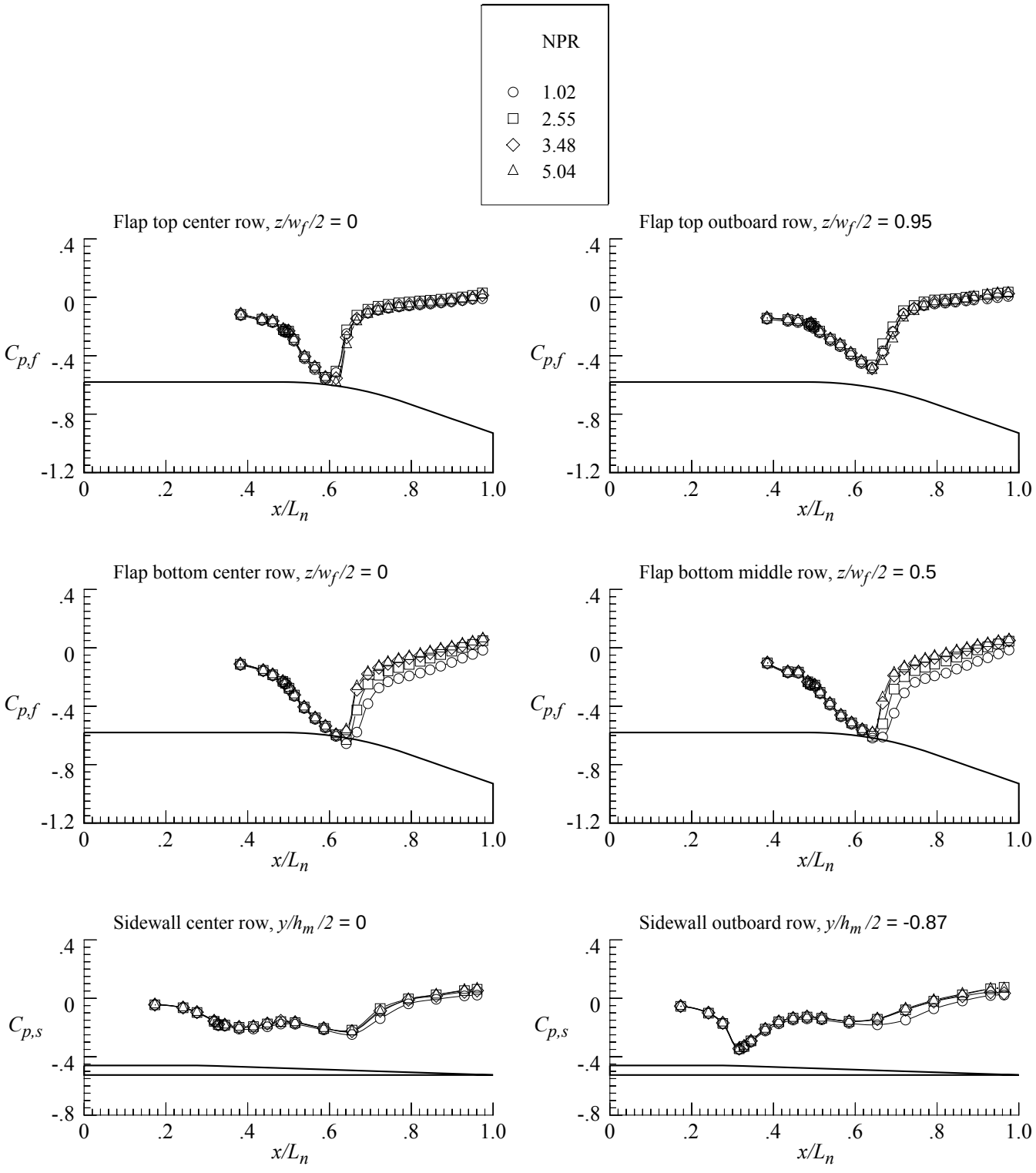

(c) $M = 0.95$.

Figure 138. Continued.

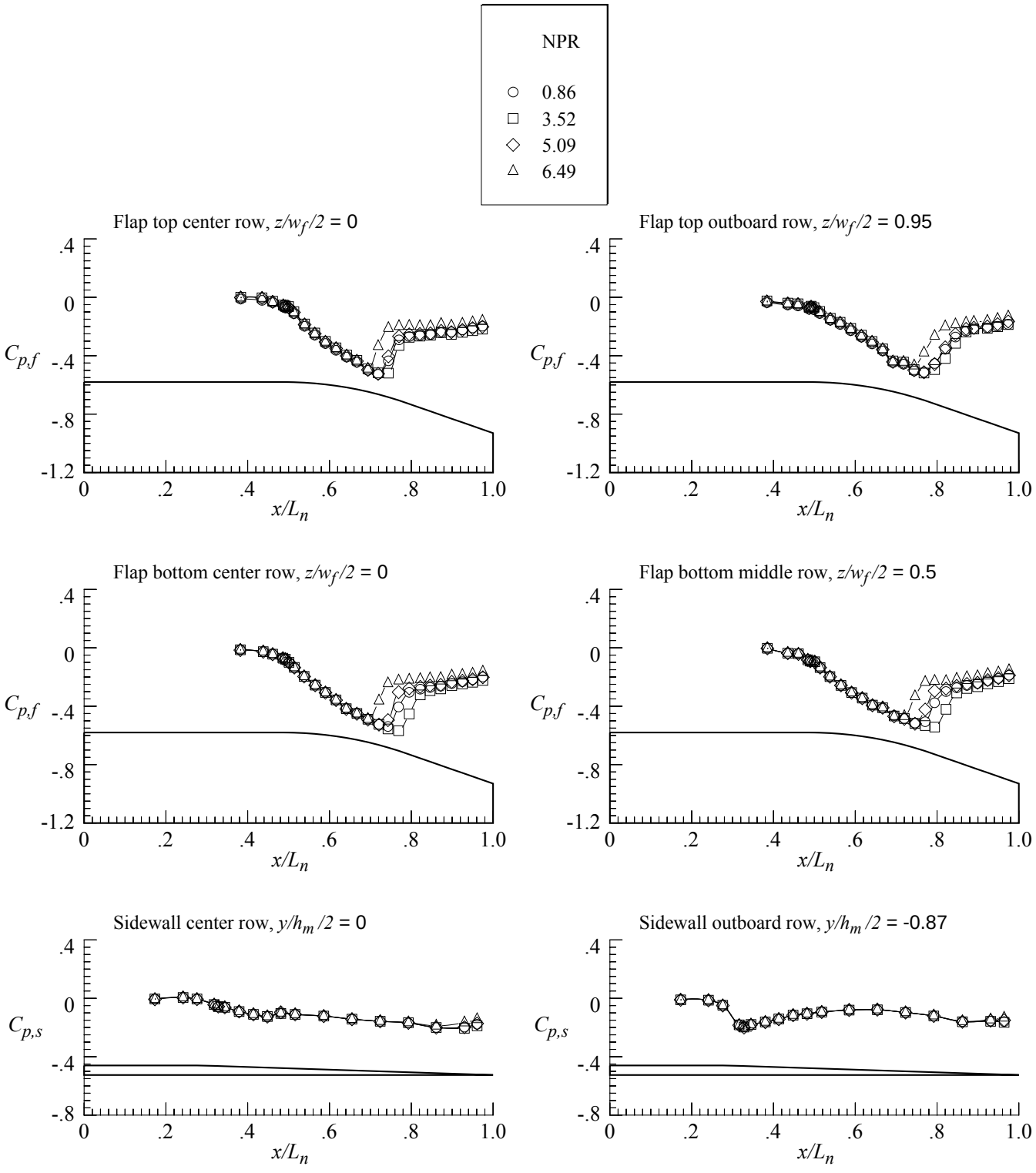

(d) $M = 1.20$.

Figure 138. Concluded.

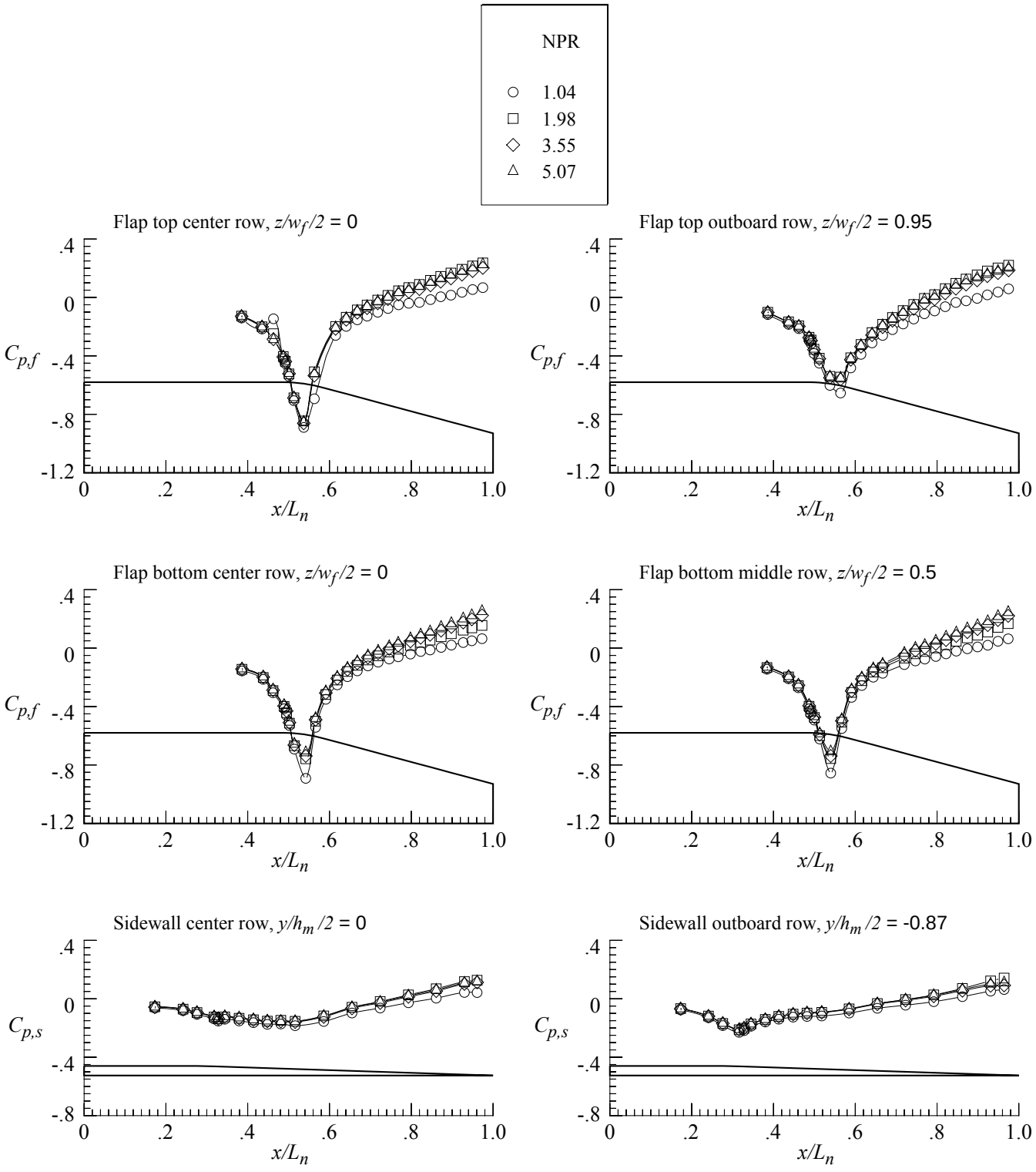

(a) $M = 0.80$.

Figure 139. External pressure distributions for nozzle N14 with flap F6 and sidewall S1.
$r_f/r_{f,max} = 0.1$; $\beta_f = 15.97°$; $L_f/h_m = 1.1$; $\beta_s = 4.0°$; $r_s/r_{s,max} = 0$.

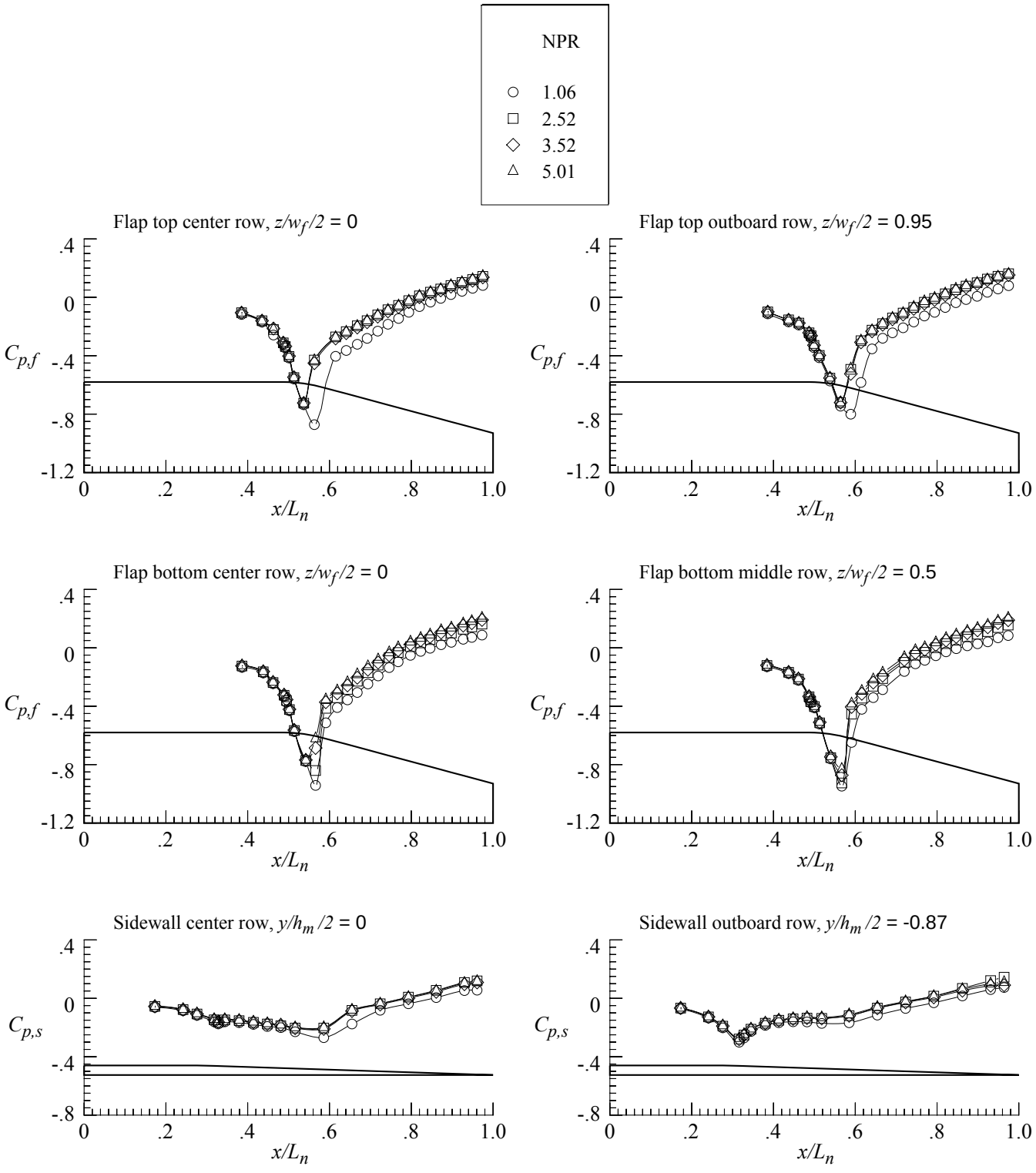

(b) $M = 0.90$.

Figure 139. Continued.

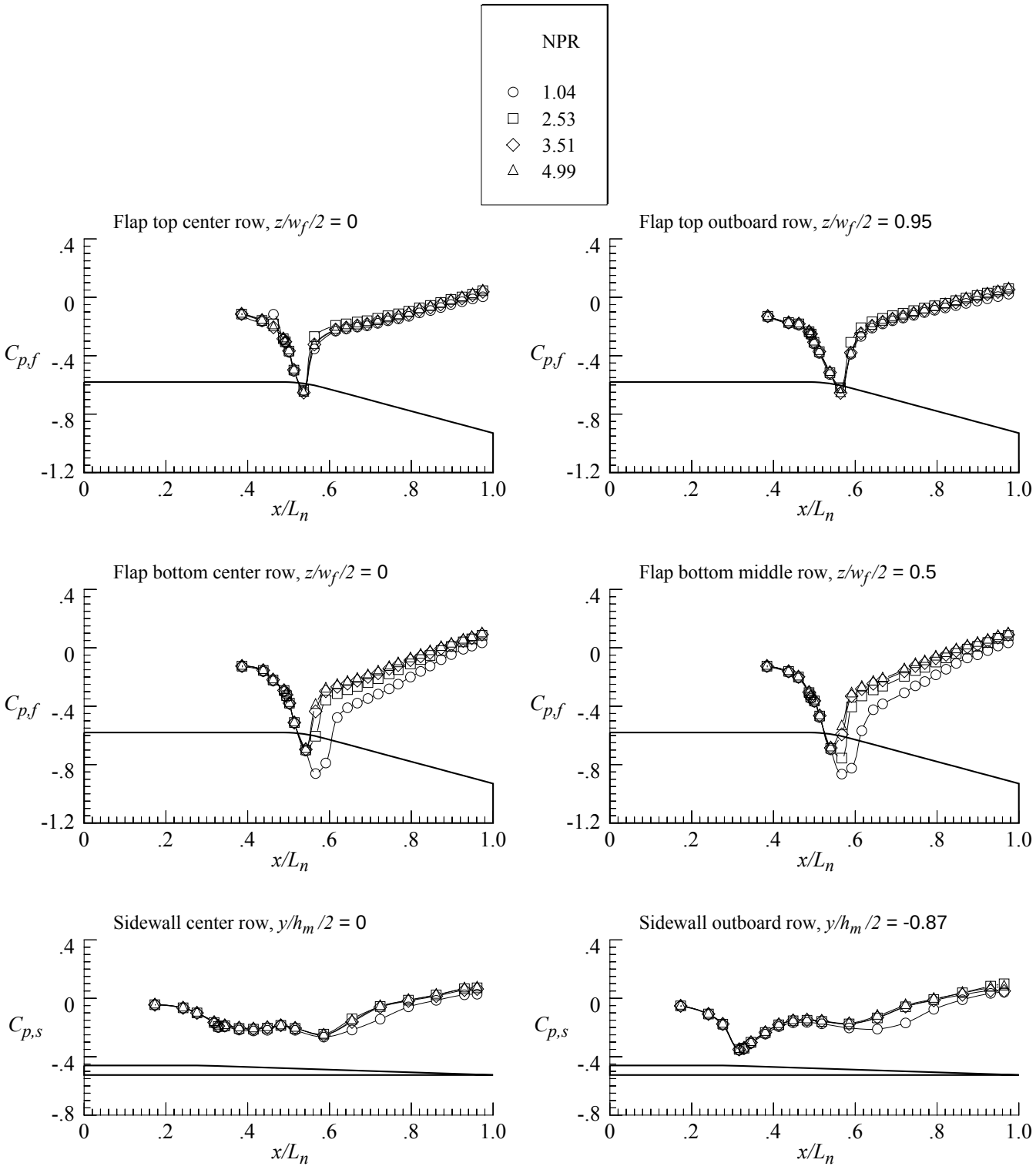

(c) $M = 0.95$.

Figure 139. Continued.

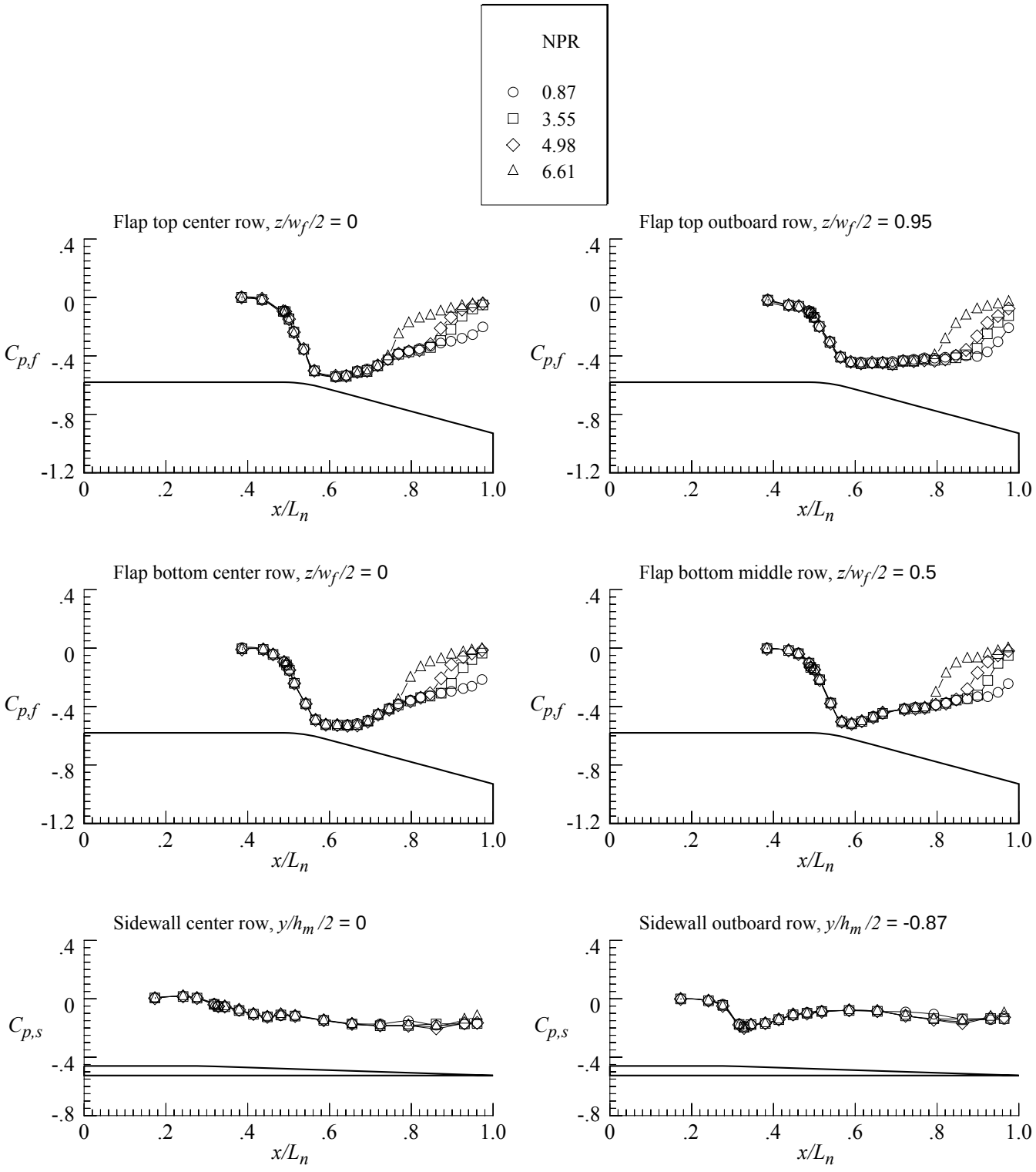

(d) $M = 1.20$.

Figure 139. Concluded.

REPORT DOCUMENTATION PAGE

Form Approved
OMB No. 0704-0188

1. REPORT DATE *(DD-MM-YYYY)*	2. REPORT TYPE	3. DATES COVERED *(From - To)*
01-08-2015	Technical Memorandum	

4. TITLE AND SUBTITLE

Transonic Investigation of Two-Dimensional Nozzles Designed for Supersonic Cruise

5a. CONTRACT NUMBER

5b. GRANT NUMBER

5c. PROGRAM ELEMENT NUMBER

6. AUTHOR(S)

Capone, Francis J.; Deere, Karen A.

5d. PROJECT NUMBER

5e. TASK NUMBER

5f. WORK UNIT NUMBER

432938.11.01.07.43.01.01

7. PERFORMING ORGANIZATION NAME(S) AND ADDRESS(ES)

NASA Langley Research Center
Hampton, VA 23681-2199

8. PERFORMING ORGANIZATION REPORT NUMBER

L-20167

9. SPONSORING/MONITORING AGENCY NAME(S) AND ADDRESS(ES)

National Aeronautics and Space Administration
Washington, DC 20546-0001

10. SPONSOR/MONITOR'S ACRONYM(S)

NASA

11. SPONSOR/MONITOR'S REPORT NUMBER(S)

NASA-TM-2015-218790

12. DISTRIBUTION/AVAILABILITY STATEMENT

Unclassified - Unlimited
Subject Category 02
Availability: NASA STI Program (757) 864-9658

13. SUPPLEMENTARY NOTES

14. ABSTRACT

An experimental and computational investigation has been conducted to determine the offdesign uninstalled drag characteristics of a two-dimensional convergent-divergent nozzle designed for a supersonic cruise civil transport. The overall objectives were to: (1) determine the effects of nozzle external flap curvature and sidewall boattail variations on boattail drag; (2) develop an experimental data base for 2D nozzles with long divergent flaps and low boattail angles and (3) provide data for correlating computational fluid dynamic predictions of nozzle boattail drag. The experimental investigation was conducted in the Langley 16-Foot Transonic Tunnel at Mach numbers from 0.80 to 1.20 at nozzle pressure ratios up to 9. Three-dimensional simulations of nozzle performance were obtained with the computational fluid dynamics code PAB3D using turbulence closure and nonlinear Reynolds stress modeling. The results of this investigation indicate that excellent correlation between experimental and predicted results was obtained for the nozzle with a moderate amount of boattail curvature. The nozzle with an external flap having a sharp shoulder (no curvature) had the lowest nozzle pressure drag. At a Mach number of 1.2, sidewall pressure drag doubled as sidewall boattail angle was increased from 4° to 8°. Reducing the height of the sidewall caused large decreases in both the sidewall and flap pressure drags.

15. SUBJECT TERMS

Boattails; Curvature; Flapping; Pressure drag

16. SECURITY CLASSIFICATION OF:			17. LIMITATION OF ABSTRACT	18. NUMBER OF PAGES	19a. NAME OF RESPONSIBLE PERSON
a. REPORT	b. ABSTRACT	c. THIS PAGE			STI Help Desk (email: help@sti.nasa.gov)
					19b. TELEPHONE NUMBER *(Include area code)*
U	U	U	UU	319	(757) 864-9658